Multi-Fidelity Global Low-Thrust Trajectory Optimisation

Marilena Di Carlo

Submitted in fulfilment of the requirements for the
degree of Doctor of Philosophy

Advanced Space Concept Laboratory
Department of Mechanical and Aerospace Engineering
University of Strathclyde, Glasgow

September 2018

Abstract

This research work presents methods and techniques for multi-fidelity global optimisation of low-thrust trajectories. In the early stages of the definition of a space mission, tools that can provide a fast and preliminary estimation of the cost of low-thrust transfers are required; a more accurate optimisation process of the trajectories is left for subsequent phases. Therefore, models of different levels of fidelity are needed, based on the current phase of the design and on the desired accuracy. An efficient global optimisation algorithm has then to be used in conjunction with these models, in order to identify the global optimal solution to a given problem. The development of multi-fidelity methods, of an efficient global optimisation algorithm and their application for the solution of low-thrust global optimisation problems, are addressed in this thesis.

The lower fidelity models consist of analytical laws for the cost of low-thrust transfers. Higher fidelity innovative laws for transfers between Earth's orbits have been derived. Moreover, a set of analytical equations for the motion of the spacecraft subject to low-thrust acceleration and orbital perturbations is presented.

These models are used in conjunction with a novel adaptive multi-population global optimisation algorithm, validated using several test functions and real world problems. To allow for the use of the global solver with higher fidelity, and therefore computationally more expensive models, the use of surrogate model for low-thrust transfer is proposed.

Various applications are presented where these tools and methods are successfully applied, and that represent an original scientific contribution. Missions have been designed to deorbit objects from Low Earth Orbit and deploy a constellation in Medium Earth Orbit. The optimisation of a transfer from Geostationary Transfer Orbit to Geosynchronous Orbit is also presented. Interplanetary applications include missions to visit the asteroids of the inner solar system and of the main belt.

Acknowledgements

I would like to thank my supervisor, Prof. Massimiliano Vasile, for his invaluable guidance and support during the execution of my dissertation research. He has offered precious advice and inspiration for my research and for my professional development.

I am very grateful to Dr. Stephen Kemble, at Airbus Defence and Space, for his technical assistance.

During my research I have received support by different organisations. My special thanks go to Zonta International, for the award of the Amelia Earhart Fellowship. The fellowship has enriched my PhD and given me invaluable experiences. Thank you to the Zontians I have met in the last years and to the members of the Zonta e-club of Italy. I would also like to acknowledge the financial support I received from the University of Strathclyde, the Royal Aeronautical Society, the IEEE Computational Intelligence Society, Woman in Aerospace Europe, the Institution of Engineering and Technology and the NASA National Institute of Aerospace, to attend different conferences during my studies.

I would like to thank the colleagues at the Department of Mechanical and Aerospace Engineering, for sharing these years and for the great experiences we had together. A special thank goes to the members of Team HECATE of the ESA Moon Challenge and Team Strath++ of GTOC9.

I would like to acknowledge the students and friends, from different universities around the world, with whom I have shared the invaluable experiences of the Caltech Space Challenge and the NASA RASC-AL competition. A special thank goes to Davide, for his tireless enthusiasm about space.

To the friends who have supported me throughout this process, I give my appreciation: to my friends from Pisa, Jessica and Claudia, and to my friends in Glasgow, Daniela and Valentina; to Simone, a dedicated friend over many years, and to Luca, who has supported me for part of my years in Glasgow and throughout the experiences that have led me here.

Finally, my greatest thank goes to my parents and to my sister. Thank you for your immense support and encouragement.

Contents

List of Figures

List of Tables

Nomenclature

Acronyms

ADR	Active Debris Removal
CEC	Congress on Evolutionary Computation
CSI	Criticality of Spacecraft Index
DACE	Design and Analysis of Computer Experiments
DE	Differential Evolution
DITAN	Direct Interplanetary Trajectory ANalysis
DT-CTECA	Direct Transcription using Coast and Thrust Element of Constant Acceleration
DT-TEPA	Direct Transcription using Thrust Element at Periapsis and Apoapsis
DT-TEVA	Direct Transcription using Thrust Element of Variable Acceleration
ECI	Earth Centered Inertial system
FET	Finite Elements in Time
FOV	Field Of View
GALLOP	Gravity Assist Low-thrust Local Optimization Program
GEO	Geostationary Equatorial Orbit
GMAT	General Mission Analysis Tool
GPS	Global Positioning System
GTO	Geostationary Transfer Orbit
HEO	High Elliptic Orbit
IDEA	Inflationary Differential Evolution Algorithm
IEO	Inner Earth Object
IPM	Interior Point Method

LEO	Low Earth Orbit
MALTO	Mission Analysis Low-Thrust Optimizer
MBH	Monotonic Basin Hopping
MEO	Medium Earth Orbit
MOID	Minimum Orbital Intersection Distance
MPAIDEA	Multi Population Adaptive Inflationary Differential Evolution Algorithm
NEA	Near Earth Asteroid
NORAD	North American Aerospace Defence Command
RCS	Radar Cross Section
RTN	Radial Transverse Normal reference frame
SQP	Sequential Quadratic Programming
SSO	Sun Synchronous Orbit
TLE	Two-Line Elements
TSP	Travelling Salesman Problem
VRP	Vehicle Routing Problem

Physics Constants

$\mu_\odot$	Gravitational parameter of the Sun	132712439935 km^3/s^2
$\mu_\oplus$	Gravitational parameter of the Earth	398600 km^3/s^2
$f_\oplus$	Earth flattening factor	0.00335
G	Gravitational constant	$6.67\ 10^{-20}$ km^3/kg/s^2
g_0	Gravitational attraction at sea level	9.81 m/s^2
J_2	Second order zonal harmonic of the Earth's gravitational potential	$1082.63\ 10^{-6}$
J_3	Third order zonal harmonic of the Earth's gravitational potential	$-2.5327\ 10^{-6}$
J_4	Fourth order zonal harmonic of the Earth's gravitational potential	$-1.6196\ 10^{-6}$
J_5	Fifth order zonal harmonic of the Earth's gravitational potential	$-2.2730\ 10^{-7}$
$m_\oplus$	Mass of the Earth	$5.972\ 10^{24}$ kg
$R_\oplus$	Radius of the Earth	6378.136 km

Greek Symbols

α	Azimuth angle of the low-thrust acceleration in the RTN reference frame	[rad]
α_{3rd}	Direction cosine of $\mathbf{r}_{3rd}$ with respect to $\hat{\mathbf{f}}$	[rad]
$\bar{\omega}$	Longitude of the periapsis	[rad]
$\bar{\psi}$	Angular amplitude of the thrust arcs for control laws of transfer under the effect of J_2	[rad]
β	Elevation angle of the low-thrust acceleration in the RTN reference frame	[rad]
β_{3rd}	Direction cosine of $\mathbf{r}_{3rd}$ with respect to $\hat{\mathbf{g}}$	[rad]
$\boldsymbol{\beta}_K$	Kriging regression parameters	
$\boldsymbol{\lambda}$	Lagrangian multipliers	
$\boldsymbol{\mu}$	Lagrange multipliers	
$\boldsymbol{\nu}$	Lagrange multipliers	
$\boldsymbol{\psi}$	Boundary conditions of the optimal control problem	
ΔL	Angular span of the thrust leg	[rad]
Δt	Time length of the thrust leg	[s]
ΔV	Variation of velocity required for the transfer	[m/s]
δ	Declination	[rad]
ϵ	Magnitude of the low-thrust acceleration	[m/s^2]
η	Shift of the periapsis thrust arc with respect to the periapsis point	[rad]
γ	Flight path angle	[rad]
γ_{3rd}	Direction cosine of $\mathbf{r}_{3rd}$ with respect to $\hat{\mathbf{w}}$	[rad]
μ	Gravitational parameter	[m^3/s^2]
μ_{3rd}	Gravitational potential of the third body	[m^3/s^2]
Ω	Right ascension of the ascending node	[rad]
ω	Argument of the periapsis	[rad]
ϕ	Phase angle Sun-asteroid-spacecraft	[rad]
Π_I	Elliptic integral of the third kind	
ρ	Atmospheric density	[kg/m^3]

θ	True anomaly	[rad]
ξ	Angle between $\mathbf{r}_{3rd}$ and $\mathbf{r}$	[rad]

Roman Symbols

$\hat{\mathbf{f}}$	First versor of the equinoctial frame	
$\hat{\mathbf{g}}$	Second versor of the equinoctial frame	
$\hat{\mathbf{i}}_R$	Versor of the radial axis of the RTN reference frame	
$\hat{\mathbf{k}}$	Versor of the third axis the ECI reference frame	
$\hat{\mathbf{w}}$	Third versor of the equinoctial frame	
$\mathbf{c}$	Equality constraints	
$\mathbf{f}$	Acceleration of perturbation of the Keplerian motion	[m/s^2]
$\mathbf{f}_{Drag}$	Acceleration due to the atmospheric drag	[m/s^2]
$\mathbf{f}_K$	Kriging regression model	
$\mathbf{g}$	Inequality constraints	
$\mathbf{h}$	Spacecraft's dynamic	
$\mathbf{p}$	Vector of parameters	
$\mathbf{p}_v$	Primer vector	
$\mathbf{r}$	Spacecraft's position vector	[m]
$\mathbf{r}_{3rd}$	Position vector of the third body	[m]
$\mathbf{u}$	Low-thrust control acceleration vector	[m/s^2]
$\mathbf{v}$	Spacecraft's velocity vector	[m/s]
$\mathbf{X}$	State vector of the spacecraft	
$\mathbf{x}^L$	Lower boundary of the search space for the global optimisation	
$\mathbf{x}^U$	Upper boundary of the search space for the global optimisation	
$\mathcal{F}$	Feasible set	
$\mathcal{H}$	Hamiltonian	
$\mathcal{OE}$	Set of orbital elements defining an orbit	
$\mathcal{P}_l$	Legendre polynomial of order l	

$\mathcal{TP}$	Set of training points for surrogate model	
$\mathcal{U}$	Domain of the feasible controls	
A	Area of the spacecraft in the direction of the velocity	[m^2]
a	Semi-major axis	[m]
C_D	Drag coefficient	
E	Eccentric anomaly	[rad]
e	Eccentricity	
E_{Ic}	Complete elliptic integral of the second kind	
E_I	Elliptic integral of the second kind	
F	Engine thrust	[N]
F_{Ic}	Complete elliptic integral of the first kind	
F_I	Elliptic integral of the first kind	
G	Asteroid's slope parameter	
H	Asteroid's absolute magnitude	
h	Angular momentum	[m^2/s]
$h_\oplus$	Geodetic altitude above the Earth surface	[m]
i	Inclination	[rad]
I_{sp}	Specific impulse	[s]
J	Objective function	
k_{LT}	Number of nodes to model the variation of the control parameters	
L	True longitude	[rad]
M	Mean anomaly	[rad]
m	Spacecraft's mass	[kg]
m_p	Propellant's mass	[kg]
n	Mean motion	[s^{-1}]
n_c	Number of variables of the constraints vector	
n_u	Number of variables of the control vector	

n_x	Number of variables of the state vector	
n_{LT}	Number of thrust legs	
n_{tr}	Number of training points for surrogate model	
p	Semilatus rectum	[m]
P_1	Second equinoctial element	
P_2	Third equinoctial element	
p_v	Asteroid's albedo	
Q	Apoapsis	[m]
q	Periapsis	[m]
Q_1	Fourth equinoctial element	
Q_2	Fifth equinoctial element	
r_a	Radius of apoapsis	[m]
r_p	Radius of periapsis	[m]
S_w	Switching function	
T	Orbital period	[s]
t	Time	[s]
ToF	Time of flight	[s]
U	Potential	[m^2/s^2]
u	Argument of latitude	[rad]
U^{3rd}	Potential of the third body perturbation	[m^2/s^2]
V	Asteroid's relative magnitude	
z_K	Kriging stochastic process	

Subscripts and Superscripts

$\bullet^+$	Forward propagation
$\bullet^-$	Backward propagation
$\bullet^{OFF}$	Switching point from a thrust to a coast leg
$\bullet^{ON}$	Switching point from a coast to a thrust leg

$\bullet_0$	Initial conditions
$\bullet_a$	Apoapsis
$\bullet_f$	Final conditions
$\bullet_N$	Normal component
$\bullet_p$	Periapsis
$\bullet_R$	Radial component
$\bullet_s$	Relative to the s-th thurst leg
$\bullet_T$	Transverse component
$\bullet_{ap}$	Thrust leg between apoapsis and periapsis
$\bullet_{arr}$	Arrival
$\bullet_{dep}$	Departure
$\bullet_{pa}$	Thrust leg between periapsis and apoapsis
$\dot{\bullet}$	Time derivation
$\hat{\bullet}$	Versor

Introduction

Low-thrust propulsion is a technology used to provide thrust to a spacecraft by means of electric energy (electro-thermal, electrostatic or electromagnetic), or by means of radiation pressure, as in the case of solar sails. Compared to high-thrust propulsion technologies (such as chemical propulsion systems), low-thrust systems that make use of propellant are characterised by a higher exhaust velocity, or specific impulse, and therefore lower propellant consumption. The first experimental electric propulsion thrusters were launched in the early 60's by US and Russia and geostationary communications satellites have been using electric propulsion since the early 1980[1]. NASA Deep Space 1[2], launched in 1998, was the first NASA deep space mission to use electric propulsion. The use of low-thrust propelled spacecraft has increased in recent years: electric propulsion is now widely used for station keeping and orbit insertion of communication satellites. In March 2015, two Boeing all-electric satellites perfomed, for the first time, an electric-propelled orbit raising to the Geostationary Transfer Orbit (GTO)[3]. Other successful missions have proven the validity of electric propulsion for deep space missions. Examples include JAXA's Hayabusa (2003)[4], ESA's Smart-1 (2003)[5] and NASA's Dawn (2007)[6]. Moreover, future planned missions, such as ESA's BepiColombo to Mercury, will make use of low-thrust propulsion[7].

While the specific impulse is higher for low-thrust rather than high-thrust engines, the thrust level is lower. High-thrust engines can produce thrust levels from few Newton to 10^7 Newton, while the level of thrust of low-thrust engines is generally not higher than a few Newton [35]. This means that the transfers realised by means of low-thrust systems are generally characterised by longer times of flight and more orbital revolutions than the transfers obtained with high-thrust engines. This poses additional challenges when optimising low-thrust trajectories. Moreover, while for high-thrust propulsion the application of the thrust is considered to happen instantaneously and is modelled as single, instantaneous impulses of the engine, the thrust generated by a low-thrust engine can not be approximated with impulses.

Spacecraft trajectories are generally optimised to minimise some quantity of interest, such as the propellant mass or the time of flight. The trajectory defined by the optimisation process

[1] http://sci.esa.int/smart-1/34201-electric-spacecraft-propulsion/?fbodylongid=1534
[2] https://www.jpl.nasa.gov/missions/deep-space-1-ds1/
[3] http://boeing.mediaroom.com/2015-09-10-Boeing-World-s-First-All-Electric-Propulsion-Satellite-Begins-Operations
[4] http://global.jaxa.jp/projects/sat/muses˙c/index.html
[5] http://sci.esa.int/smart-1/
[6] https://dawn.jpl.nasa.gov/
[7] http://sci.esa.int/bepicolombo/

has, moreover, to satisfy same initial and terminal conditions and, possibly, path constraints during the transfer [48]. For high-thrust propulsion the optimisation process consists in defining the times or positions of application of the impulses and their direction. For low-thrust propulsion, a continuous thrust profile has to be determined instead.

The accurate optimisation of low-thrust trajectories can generally be left for the advanced phases of the mission design, while in the early stages of the definition of a space mission, tools that can provide a fast and preliminary estimation of the cost of a low-thrust transfer are used. Different equations are available in the literature to estimate the cost associated to the variation of specific orbital elements using low-thrust propulsion [39, 72, 158, 160]. These analytical equations are generally limited to transfers where only one or two orbital elements undergo a variation, do not take into account the effect of orbital perturbations and provide a low-fidelity estimation of the cost of low-thrust transfers.

In the more advanced phases of the mission design, a higher-fidelity estimation of the cost is needed. At this stage, optimisation algorithms are used in conjunction with a model of the motion of the spacecraft. In general, there is no closed form solution to the motion of a spacecraft subject to low-thrust acceleration. However, if analytical models were to be used in the optimisation process, the time required to obtain an optimal solution would be greatly reduced. Analytical solutions for the motion of the spacecraft subject to low-thrust acceleration have been proposed in the literature only for simple thrust profiles or for trajectories of specific shapes [24, 25, 147, 156, 157, 225]. A tool of more general validity should, however, be able to provide analytical solutions for the motion of the spacecraft under any type of low-thrust control profile, any shape of the trajectory and should include orbital perturbations.

The methods for the solution of the optimal control problem associated to the design of low-thrust trajectories are generally classified as either indirect or direct. Indirect methods solve the differential-algebraic system of equations resulting from the definition of the necessary conditions for optimality, while direct methods transcribe the infinite dimensional optimal control problem in a finite dimensional non-linear programming problem [19]. Both existing indirect and direct methods in the literature generally make use of local optimisation algorithms. However, local algorithms are characterised by local convergence of their iterates, and the local optimum obtained is generally strongly dependent on the choice of the initial guess. Global algorithms have two principal advantages over local ones: they require no initial guess and they are more likely to locate the global minimum, rather than being attracted to a local minimum [48]. Different works in the literature used global algorithms for the solution of impulsive trajectories [69, 208, 214]. The use of global algorithms has been proposed also for the optimisation of low-thrust trajectories [216, 218, 224]. From an operational point of view, the global algorithm should return not only the best solution but also other possible minima, so that different options might be evaluated.

The use of global algorithms for the design of low-thrust trajectories is, however, limited by two factors: the number of function evaluations required by the solver and the computational time of each evaluation. The difficulties related to the optimisation of computationally expensive models have been dealt with in many engineering sectors, such as aerodynamics

and computational fluid dynamics, using surrogate models or reduced order models [82, 237]. Examples of the use of surrogate models or regression techniques for low-thrust transfers are presented in [96, 139], where the focus is on the creation of a surrogate model for the mass of propellant required for the transfers between Near Earth Objects and main belt asteroids. A more general use of surrogate models for low-thrust transfers would consist in the creation of a cartography of the cost of any low-thrust transfer. Moreover, applications for surrogate-based optimisation of optimal low-thrust trajectory can be investigated.

Based on these considerations, the main motivations for this thesis work are:

- the need for multi-fidelity methods that can provide both fast preliminary estimations and higher-fidelity solutions, and in particular:
  - the need to define a computationally efficient model for the motion of the spacecraft subject to a low-thrust acceleration and orbital perturbations;
  - the development of techniques and methods for the use of surrogate models for low-thrust trajectories;
- the need for a global optimisation algorithm to be used in the optimisation of low-thrust trajectories.

Contributions

Following the motivations outlined in the previous section, the key contributions of this thesis are:

- the analysis of the analytical control laws available in the literature for the fast evaluation of low-thrust transfers, in order to define their range of applicability and their accuracy;
- the development of novel laws for low-thrust transfers under orbital perturbations based on the exploitation of the natural orbital dynamic;
- the derivation of analytical or semi-analytical equations for the propagation of the spacecraft motion perturbed by atmospheric drag, Earth's gravitational potential and third body gravitational perturbations;
- the definition of suitable transcription methods for the solution of optimal low-thrust transfers problems;
- the use of surrogate models to create a cartography of the cost of optimal low-thrust transfers;
- the development of a novel adaptive global optimisation algorithm based on the combination of Differential Evolution and Monotonic Basin Hopping;

- the applications of these techniques to design low-thrust space missions to visit the Atira asteroids (inner solar system asteroids), the main asteroid belt, to deorbit spacecraft from Low Earth Orbit (LEO), deploy the satellites of a constellations in Medium Earth Orbit (MEO) and to realise transfers from Geostationary Transfer Orbit (GTO) to Geostationary Equatorial Orbits (GEO).

For some of the mission design studies presented in this thesis, work has been carried out also on the subject of combinatorial optimisation. However, since combinatorial optimisation in not a central theme for this dissertation, only brief descriptions, or references, are given for the proposed methods.

Part of the content of this dissertation and of the work done during the research period was published in different journal articles and conference papers. A list of journal and conference publications and of technical reports is given hereafter:

Journal publications

1. **M. Di Carlo**, M. Vasile and E. Minisci. Multi-Population Adaptive Inflationary Differential Evolution Algorithm with Adaptive Local Restart. Under review. Soft Computing.

2. **M. Di Carlo**, M. Vasile and J. Dunlop. Low-thrust tour of the main belt asteroids. Advances in Space Research. Accepted/in press. doi: 10.1016/j.asr.2017.12.033

3. C. Ortega Absil, L. A. Ricciardi, **M. Di Carlo**, C. Greco, R. Serra, M. Polnik, A. Vroom, A. Riccardi, E. Minisci, and M. Vasile. GTOC 9: Results from University of Strathclyde. Acta Futura, 9 January 2018, Vol. 11, p. 57-70. doi: 10.5281/zenodo.1142858

4. D. Conte, **M. Di Carlo**, K. Ho, D. Spencer and M. Vasile. Earth-Mars Transfer Through Moon Distant Retrograde Orbits. Acta Astronautica, Vol. 143, February 2018, pp. 372-379. doi: 10.1016/j.actaastro.2017.12.007

5. E. Fantino, R. M. Flores, **M. Di Carlo**, A. Di Salvo and E. Cabot. Geosynchronous inclined orbits for high-latitude communications. Acta Astronautica, Vol. 140, November 2017, pp. 570-582. doi: 10.1016/j.actaastro.2017.09.014

6. D. Conte, **M. Di Carlo**, D. Budzyn, H. Burgoyne, D. Fries, M. Grulich, S. Heizmann, H. Jethani, M. Lepotre, T. Roos, E. Serrano Castillo, M. Schermann, R. Vieceli, L. Wilson and C. Wynard. Advanced concept for a crewed mission to the Martian moons. Acta Astronautica, Vol. 139, October 2017, pp. 545-563.
doi: 10.1016/j.actaastro.2017.07.044

7. **M. Di Carlo**, J. M. Romero Martin, and M. Vasile. CAMELOT, Computational-Analytical Multi-fidElity Low-thrust Optimisation Toolbox. CEAS Space Journal, September 2017.
doi: 10.1007/s12567-017-0172-6

8. **M. Di Carlo**, J. M . Romero Martin, N. Ortiz Gomez, and M. Vasile. Optimised Low-Thrust Mission to the Atira Asteroids. Advances in Space Research, Volume 59, Issue 7, 1 April 2017, pp. 1724-1739. doi: 10.1016/j.asr.2017.01.009

9. **M. Di Carlo**, J. M . Romero Martin, and M. Vasile. Automatic Trajectory Planning for Low-Thrust Active Removal Mission in Low-Earth Orbit. Advances in Space Research, Volume 59, Issue 5, 1 March 2017, pp. 1234-1258. doi: 10.1016/j.asr.2016.11.033

10. **M. Di Carlo**, D. Barbera, D. Conte, A. Mintus, J. M. Romero Martin, D. Budzyn, L. Teofili, S. Grys, J. Jamieson, C. Hay, T. Lund, N. Ikeda, R. Volpe and D. Fleming. HECATE - Human Exploration of Cis-lunar space via Assets Tele-operated from EML2. Acta Futura, December 2016, Vol. 10, p. 75-89. ISSN 2309-1940

Conference papers and presentations

1. C. Ortega Absil, L. Ricciardi, **M. Di Carlo**, C. Greco, R. Serra, M. Polnik, A. Vroom, A. Riccardi, E. Minisci and M. Vasile. GTOC9: Methods and results from the University of Strathclyde. On the generation and evolution of multiple debris removal missions. 26th International Symposium on Space Flight Dynamics (ISSFD), 3-9 June 2017, Matsuyama, Japan

2. **M. Di Carlo**, M. Vasile and S. Kemble. Optimised GTO-GEO Transfer using Low-Thrust Propulsion. 26th International Symposium on Space Flight Dynamics (ISSFD), 3-9 June 2017, Matsuyama, Japan

3. A. Vroom, **M. Di Carlo**, J. M. Romero Martin, and M. Vasile. Optimal Trajectory Planning for Multiple Asteroid Tour Mission by Means of an Incremental Bio-Inspired Tree Search Algorithm. 2016 IEEE Symposium Series on Computational Intelligence, 6-9 December 2016, Athens, Greece

4. **M. Di Carlo**, M. Vasile. Low-Thrust Tour of the Main Belt Asteroids. 2016 AIAA/AAS Astrodynamics Specialist Conference, 13-16 September 2016, Long Beach, CA

5. **M. Di Carlo**, L. Ricciardi, and M. Vasile. Multi-Objective Optimisation of Constellation Deployment using Low-Thrust Propulsion. 2016 AIAA/AAS Astrodynamics Specialist Conference, 13-16 September 2016, Long Beach, CA

6. D. Conte, D. Budzyn, H. Burgoyne, **M. Di Carlo**, D. Fries, M. Grulich, S. Heizmann, H. Jethani, M. Lapotre, T. Roos, E. Serrano Castillo, M. Sherrmann, R. Vieceli, L. Wilson and C. Wynard. Innovative Mars Global International Exploration (IMaGInE) Mission. 2016 AIAA/AAS Astrodynamics Specialist Conference, 13-16 September 2016, Long Beach, CA

7. **M. Di Carlo**, J. M. Romero Martin, and M. Vasile. CAMELOT - Computational Analytical Multi-fidElity Low-thrust Optimisation Toolbox. 6th International Conference on Astrodynamics Tools and Techniques (ICATT), 14-17 March 2016, Darmstadt, Germany

8. E. Fantino, R. Flores, A. Di Salvo, and **M. Di Carlo**. Analysis of Perturbations and Station-Keeping Requirements in Highly-Inclined Geosynchronous Orbits. International Symposium on Space Flight Dynamics, 19-23 October 2015, Munich, Germany

9. M. Vasile, **M. Di Carlo**. Efficient Solution of Min-Max Problems with a Combination of Surrogate Models and Inflationary Differential Evolution. International Conference on Evolutionary and Deterministic Methods for Design, Optimization and Control, EUROGEN 2015, 14-16 September, Glasgow, UK

10. D. Conte, **M. Di Carlo**, K. Ho, D. Spencer and M. Vasile. Earth-Mars Transfer through Moon Distant Retrograde Orbits. AIAA/AAS Astrodynamics Specialist Conference, 9-13 August 2015, Vail, CO

11. **M. Di Carlo**, M. Vasile, and E. Minisci. Multi-Population Adaptive Inflationary Differential Evolution Algorithm with Adaptive Local Restart. IEEE Congress on Evolutionary Computation, 25-28 May 2015, Sendai, Japan

12. **M. Di Carlo**, N. Ortiz Gomez, J. M. Romero Martin, C. Tardioli, F. Gachet, K. Kumar and M. Vasile. Optimised Low-Thrust Mission to the Atira Asteroids. 25th AAS/AIAA Space Flight Mechanics Meeting, 11-15 January 2015, Williamsburg, VA

13. **M. Di Carlo**, M. Vasile, and E. Minisci. Multi-Population Adaptive Inflationary Differential Evolution Algorithm. Workshop on Bioinspired Optimization Methods and their Applications, BIOMA 2014, 13 September 2014, Ljubljana, Slovenia

Technical reports

- RASC-AL (Revolutionary Aerospace System Concepts Academic Linkage) Report: IMaGInE (Innovative Mars Global International Exploration) Mission.
  Work submitted to NASA/NIA as part of the participation in the student competition RASC-AL (winning team).
  Joint work with The Pennsylvania State University (USA), California Institute of Technology (USA), Georgia Institute of Technology (USA), Technische Universitat Munchen (Germany), Universitat Stuttgart (Germany), University of Colorado Boulder (USA), Lulea University of Technology (Sweden), Università di Bologna (Italy), University of Illinois-Urbana Champaign (USA), Wroclaw Institute of Technology (Poland).

- ESA Moon Challenge Report: HECATE - Human Exploration of CisLunar Space via Assets Teleoperated from EML2.
  Report submitted to ESA and presented at the International Symposium on Moon 2020-2030, 15-16 December 2016, ESA/ESTEC, Noordwijk, The Netherlands, as part of the participation in the international student competition "ESA Moon Challenge" (winning team).
  Joint work with Pennsylvania State University (USA), Wroclaw Institute of Technology (Poland), University of Kyoto (Japan) and Università Roma La Sapienza (Italy).

- Caltech Space Challenge Report: L-dorado (Team Explorer).
  Work submitted and presented at the 2015 Caltech Space Challenge, California Institute of Technology, Pasadena, CA, USA.
  Joint work with California Institute of Technology (USA), Massachusetts Institute of Technology (USA), The Pennsylvania State University (USA), University of Illinois at Urbana-Champaign (USA), Georgia Institute of Technology (USA), Ecole Polytechnique (France), Ecole Polytechnique Federale de Lausanne (Switzerland), University of Colorado Boulder (USA), Università di Napoli Federico II (Italy).

Structure of the thesis

The thesis is divided into two parts. Part I describes the theoretical and methodological developments, and includes Chapters 1 to 7, while Part II describes applications of these methods to low-thrust missions. It is important to stress that the applications presented in Part II are, themselves, an original scientific contribution. Chapter 1 briefly introduces the low-thrust trajectory design and optimisation problem; the theoretical details are given in Appendix A and Appendix B. Chapter 2 collects and analyses analytical control laws, available in the literature, for the variation of specific orbital elements, using low-thrust propulsion. Analytical equations for the cost of the transfers and for the time variation of the orbital elements are also derived and presented, where not already present in the literature. Analytical laws that provide variation of the same orbital elements are compared against each other. Chapter 3 introduces novel analytical control laws for the simultaneous variation of semi-major axis, inclination and right ascension of the ascending node of circular orbits; the control laws are designed so as to exploit the combination of the second order zonal harmonic of the Earth's gravitational field, J_2, and low-thrust propulsion. Part of the content of Chapter 3 is published in [62]. Chapter 4 presents the analytical and semi-analytical equations, derived in terms of non-singular equinoctial elements, for the propagation of the Keplerian motion perturbed by zonal harmonics of the Earth's gravitational potential (J_2, J_3, J_4, J_5), atmospheric drag and third body gravitational perturbations. Analytical formulae for the effect of low-thrust acceleration following an inverse square law are also presented. Additional mathematical details, analytical equations and integrals are given in Appendix C. Part of the content of Chapter 4 and Appendix C is published in [64]. Chapter 5 describes the original transcription methods developed for this thesis and used to solve the low-thrust optimal control problem with a direct method. A comparison of the results given by the transcription methods, against those obtained by tools used at the Centre National d'Etudes Spatiales and at the European Space Agency, is also given. The transcription methods presented in Chapter 5 are published in [63–66]. In Chapter 6, preliminary studies and results on the generation of surrogate models for the creation of a cartography of cost and time of flight of low-thrust transfers are presented. Techniques for surrogate-based optimisation are also presented and tested. Finally, Chapter 7 presents a novel adaptive multi-population global optimisation algorithm, Multi Population Adaptive Inflationary Differential Evolution Algorithm (MP-AIDEA). Its performance is assessed on a

range of academic test functions and real-world optimisation problems against other global optimisation algorithms. Part of the content of Chapter 7 is published in [67] and is under review for publication in the journal "Soft Computing". In Part II, Chapters 8 and 9 discuss the applications of the methods developed in Part I to the design of two new space mission design problems: a mission to visit the Atira asteroids, a small group of 14 asteroids in the inner solar systems, and a mission to visit asteroids in the main belt. Both problems involve the solution of combinatorial problems, whose solution methods are also described. To the author's knowledge, no other study of low-thrust mission to the Atira asteroids are present in the literature. The study of the mission to the main asteroid belt considers a number of possible targets that is order of magnitudes bigger than in other works available in the literature; moreover, the study is also complemented by an analysis of the launch of the spacecraft to the main asteroids belt region. The results of the study of the missions to the Atira and main belt asteroids have been published in [63] and [65]. Chapters 10, 11 and 12 presents three new applications of low-thrust missions in Earth's orbit, published, respectively, in [62, 64] and [66]. In Chapter 10, a mission to deorbit multiple non-cooperative objects from LEO using a single low-thrust servicing spacecraft is presented. A surrogate model of the cost of low-thrust transfers is used to reduce the computational time associated with the solution of the combinatorial part of the problem. In Chapter 11, the analytical laws presented in Chapter 3 are used, in combination with a multi-objective algorithm, to optimise the deployment of a constellation of low-thrust spacecraft in MEO. Finally, in Chapter 12, the global optimisation of the low-thrust transfer from GTO to GEO is presented. The global solver used for this application is MP-AIDEA (Chapter 7). Chapter 13 summarises the main findings of this thesis and outlines some possible future works.

Part I

Theoretical and methodological developments

Chapter 1

Low-thrust trajectories design

This chapter presents some basic elements of design and optimisation of low-thrust trajectories. A summary of the main works available in the literature is also given. Each section includes a brief comment aimed at explaining how the work presented in this thesis is build upon the results already available in the literature and further extends and improves them. Section 1.1 presents an overview of existing low-thrust guidance control laws. In Section 1.2, methods to describe the motion of the spacecraft subject to continuous acceleration are presented. Section 1.3 presents the problem of the optimisation of low-thrust trajectories and its solution techniques while Section 1.4 describes local and global solution algorithms. Finally, Section 1.5 introduces the use of surrogate models for optimal low-thrust transfers.

1.1 Low-thrust guidance control laws and algorithms

Guidance schemes for low-thrust transfers provide a practical and quick tool to evaluate and design low-thrust trajectories. The advantage of the guidance laws lies, in fact, in their speed of computation, which can be orders of magnitude greater than the speed of a trajectory optimisation process. The solutions obtained are, however, non-optimal. They are nonetheless useful when a low-fidelity, quick estimation of the cost of a low-thrust transfer is required. In this case it would be impractical to solve an optimisation problem [78].

In the most simple cases, guidance laws define the control profile for the variation of a single orbital element. In the more complete formulations they define, instead, a control profile for the variation of all the orbital elements. Example of control laws for the variation of single or pair of orbital elements were given in [39], [158] and [160].

A guidance algorithm for the simultaneous variation of all the orbital elements is the Proximity Quotient guidance law, or Q-law, presented by Petropolous [155]. The author used a Lyapunov function to express how close the spacecraft is, during the transfer, to the target orbit; the thrust vector was then chosen to get closer to the target orbit as quickly as possible. A different method for the variation of all the orbital elements was introduced by Ruggiero in [182]. Ruggiero presented a method to blend optimal thrust directions, designed to provide the highest instantaneous rate of change of each orbital element. The method also introduced

a threshold on manuever efficiency to account for the fact that a specific thrust profile might not produce significant effects on some parts of the orbit.

A survey and analysis of guidance laws for the variation of single or pairs of orbital elements is presented in Chapter 2. Analytical equations are provided, where not available in the literature, for the computation of the cost of the transfer or for the variation in time, during the transfer, of the orbital elements. The aim is to provide a complete list of low-fidelity analytical equations for the quick evaluation of a variety of low-thrust transfers, and to analyse their range of applicability and their results. The guidance schemes in Chapter 2 consider the low-thrust acceleration to be the only perturbation to the Keplerian orbital motion. Novel analytical equations for low-thrust transfers under the effect of the perturbation due to the second order zonal harmonic of the Earth's gravitational potential are presented in Chapter 3. They provide a fast tool for the evaluation of higher-fidelity low-thrust transfers between circular inclined orbits with the Earth as the central body, exploiting the combination of natural perturbations and low-thrust acceleration.

1.2 Orbital motion under continuous acceleration

The motion equations of a spacecraft are given by a set of first-order differential equations:

$$\dot{\mathbf{X}} = \mathbf{h}\left(\mathbf{X}, \mathbf{u}, t\right) \ , \tag{1.1}$$

where $\mathbf{X} \in \mathbb{R}^{n_x}$ is the state of the spacecraft, $\mathbf{u} \in \mathbb{L}^{\infty}$ is the control ($\mathbf{u} = \epsilon \ \hat{\mathbf{u}}$, where $\epsilon = \|\mathbf{u}\|$ is the low-thrust acceleration magnitude) and t is the time. The vector $\mathbf{X}$ indicates any set of orbital elements or any six independent constants of the motion [204]. In Chapters 2 and 4, keplerian and equinoctial oribtal elements will be used, and Equations 1.1 will be expressed as the Gauss form of the variation of parameters equations. The description of the motion of the spacecraft is completed with a differential equation that expresses the time variation of the mass:

$$\dot{m} = -\frac{F}{I_{sp} g_0}. \tag{1.2}$$

In Equation 1.2, m is the mass of the spacecraft, F the thrust of the engine, equal to $F = m \ \epsilon$, I_{sp} the specific impulse of the engine, assumed constant throughout this thesis, and g_0 the gravitational attraction at sea level. The acceleration magnitude ϵ is upper bounded due to technological reasons: $0 \leq \epsilon \leq \epsilon_{max}$.

Because of the small magnitude of the acceleration ϵ provided by low-thrust propulsion systems, the transfers of spacecrafts subject to continuous low-thrust acceleration are characterised by long times of flight and many orbital revolutions. As a result, the numerical integration of Equations 1.2, even when $\mathbf{f} = 0$, requires computational times that might be unacceptable for preliminary estimations or when the model has to be evaluated several times, as in the optimisation of low-thrust trajectories. To overcome this problem, closed form solutions, averaging techniques or assumptions on the shape of the trajectory can be used.

Closed form solutions can be obtained under specific assumptions on the direction of the thrust vector. Tsien gave analytical solutions for the cases of radial or circumferential thrust [203] while Benney presented an analytical solution for the case of continuous tangential thrust [16]. Boltz presented an analytical solution to the problem of constant radial acceleration applied to circular orbits in the case of constant specific thrust acceleration (constant ratio between radial acceleration and varying acceleration of gravity) [24]. The analytical solution provides a description of the motion, as well as of the time of flight and of the approximate change in mass. The problem of constant radial acceleration was also revisited in [167] and [171]. In [25], Boltz presented an approximate analytical solution to the problem of continuous tangential thrust at constant specific thrust acceleration, applied to a spacecraft initially on circular orbit. Analytical solutions to the low-thrust accelerated motion were also proposed by Kechichian, who studied the zero-eccentricity-constrained orbit raising problem in the presence of Earth's shadow [104]. The assumption was that the low-thrust acceleration is applied only when the spacecraft is in sunlight, and that its direction (in-plane only) is switched once per orbit. Solutions were provided for two possible strategies, that differ depending on whether the pitch reorentation manuever is carried out inside or outside the shadow arc. In [105], Kechichian computed analytical solutions through an averaging technique for orbit raising with constant tangential acceleration and Earth's shadow. An averaging method for the analysis of continuous thrust was presented also by Petropolous for the escape from GTO [153]. Empirically selected thrust profiles were considered, and analytical integrals were obtained for the averaged variational equations. In [26], an analytical solution was presented for the motion of satellites under the effect of constant tangential acceleration, for orbits with generic eccentricity. The solution was obtained using perturbation theory and a non-singular variation of parameter formulation of the orbital dynamics. Colombo presented semi-analytical formulas for the case of continuous acceleration applied along the orbit track [45]. The Gauss' planetary equations were used to obtain the secular variation of the orbital elements while a trigonometric expansion was used for the periodic component.

The works discussed above derived analytical equations under specific assumptions for the thrust profiles. A more general solution was presented by Zuiani in [240] and [241]. Analytical solutions were presented for the motion of a spacecraft under constant low-thrust control acceleration and J_2 zonal harmonic perturbation. The analytical formulae presented by Zuiani are based on a first order expansion in the perturbing acceleration and are expressed in non-singular equinoctial elements. Formulae are presented for the case of constant tangential acceleration, constant acceleration in a radial-transverse-normal reference frame and constant inertial acceleration. Therefore, they allow one to model a generic direction for the thrust vector. The proposed equations are valid both for an osculating propagation of the orbital elements (with rectification after a few orbital revolutions) or for implementation in an averaged propagator.

The orbital motion of a spacecraft subject to continuous low-thrust acceleration can be described also using shape-based methods. Shape-based methods rely on the assumption that the shape of the trajectory is known a priori. The thrust profile that generates the assumed trajec-

tory is computed a posteriori. This may pose problems because the required thrust magnitude, to follow a specific shaped trajectory, may not be feasible for the actual spacecraft propulsion system. It may also be the case that the actual spacecraft have only constant thrust capability while modulated thrust is required for the spacecraft to travel the path of the shape [47]. The sub-optimal solutions obtained with the shaping methods can be used as estimates in preliminary mission design and as guides and initial guesses in optimisation. A survey of exact solutions to the planar equations of motion for a low-thrust spacecraft, using shaping methods, was presented in [157]. For the proposed shapes of trajectory, the velocity at any point and the thrust magnitude and direction are available analytically in terms of the initial conditions and free trajectory parameters. Applications of shape-based methods for the design of low-thrust trajectories were presented in [147, 156, 225]. Shape-based approach based on pseudo-equinoctial elements were presented in [60] and [210].

In this thesis, the analytical equations presented in [240, 241] are extended to include the effect of different orbital perturbations: third, fourth and fifth order zonal harmonic of to the Earth's gravitational potential, atmospheric drag and third body perturbation (Chapter 4). Moreover, an analytical solution for a thrust profile following an inverse square law is also presented. As a result, a higher fidelity analytical model is obtained for the description of the motion of the spacecraft under the effect of both low-thrust acceleration and natural perturbations. This model is then used in conjunction with optimisation algorithms for the design of optimal low-thrust trajectories.

1.3 Low-thrust trajectory optimisation

The definition of optimal low-thrust trajectories requires the solution of a continuous optimal control problem, formulated as:

$$\begin{aligned} \min_{\mathbf{u}} \; & J\left(\mathbf{X}, \mathbf{u}, t\right) \\ \text{s.t.} \quad & \dot{\mathbf{X}} = \mathbf{h}(\mathbf{X}, \mathbf{u}, \mathbf{p}, t) \\ & \mathbf{c}(\mathbf{X}, \mathbf{u}, \mathbf{p}, t) = 0 \\ & \boldsymbol{\psi}\left(\mathbf{X}(t_0), \mathbf{X}(t_f), t_0, t_f\right) = 0 \\ & t \in [t_0, t_f] \end{aligned} \tag{1.3}$$

where

- $\mathbf{p} \in \mathbb{R}^{n_p}$ is a vector of parameters
- $J\left(\mathbf{X}, \mathbf{u}, t\right)$ is the cost function, $J : \mathbb{R}^{n_x} \times \mathbb{R}^{n_u} \times [t_0, t_f] \to \mathbb{R}$
- $\mathbf{h}(\mathbf{X}, \mathbf{u}, \mathbf{p}, t)$ are n_x dynamic constraints, $\mathbf{h} : \mathbb{R}^{n_x} \times \mathbb{R}^{n_u} \times \mathbb{R}^{n_p} \times [t_0, t_f] \to \mathbb{R}^{n_x}$
- $\mathbf{c}(\mathbf{X}, \mathbf{u}, \mathbf{p}, t)$ are n_c algebraic equality constraints, $\mathbf{c} : \mathbb{R}^{n_x} \times \mathbb{R}^{n_u} \times \mathbb{R}^{n_p} \times [t_0, t_f] \to \mathbb{R}^{n_c}$
- $\boldsymbol{\psi}\left(\mathbf{X}(t_0), \mathbf{X}(t_f), t_0, t_f\right)$ are the boundary conditions, $\boldsymbol{\psi} : \mathbb{R}^{2n_x+2} \to \mathbb{R}^{n_\psi}$

Depending on the cost function J, three types of problems are defined:

- The problem of Lagrange: the objective function depends on the values of the states and controls from t_0 to t_f:
$$J = \int_{t_0}^{t_f} L\left(\mathbf{X}, \mathbf{u}, t\right) dt \ . \tag{1.4}$$
- The problem of Mayer: the objective function is a function of the final time and state:
$$J = \Phi\left(\mathbf{X}\left(t_f\right), t_f\right) \ . \tag{1.5}$$
- The problem of Bolza (the modern optimal control problem): a combination of the problem of Lagrange and Mayer:
$$J = \Phi\left(\mathbf{X}\left(t_f\right), t_f\right) + \int_{t_0}^{t_f} L\left(\mathbf{X}, \mathbf{u}, t\right) dt \ . \tag{1.6}$$

Let the focus be on the problem of Bolza. The augmented cost function is obtained adjoining the boundary constraints, dynamic and equality constraints using the Lagrangian multipliers $\boldsymbol{\nu}$, $\boldsymbol{\lambda}$ and $\boldsymbol{\mu}$:

$$\begin{aligned} J = &\Phi\left(\mathbf{X}\left(t_f\right), t_f\right) + \boldsymbol{\nu}^T \boldsymbol{\psi}\left(\mathbf{X}\left(t_0\right), \mathbf{X}\left(t_f\right), t_0, t_f\right) + \\ &+ \int_{t_0}^{t_f} \left[L\left(\mathbf{X}, \mathbf{u}, t\right) + \boldsymbol{\lambda}\left(t\right)^T \left(\mathbf{h}\left(\mathbf{X}, \mathbf{u}, \mathbf{p}, t\right) - \dot{\mathbf{X}} \right) + \boldsymbol{\mu}\left(t\right)^T \mathbf{c}\left(\mathbf{X}, \mathbf{u}, \mathbf{p}, t\right) \right] dt. \end{aligned} \tag{1.7}$$

In Equation 1.7, $\boldsymbol{\nu}$ are the Lagrangian multipliers for the boundary conditions, $\boldsymbol{\lambda}$ are the Lagrangian multipliers for the dynamic and $\boldsymbol{\mu}$ are the Lagrangian multipliers for the equality constraints. The integrand in Equation 1.7 can be re-arranged by introducing the Hamiltonian

$$\mathcal{H}\left(\mathbf{X}, \mathbf{u}, \boldsymbol{\lambda}, \boldsymbol{\mu}, t\right) = L\left(\mathbf{X}, \mathbf{u}, t\right) + \boldsymbol{\lambda}\left(t\right)^T \mathbf{h}\left(\mathbf{X}, \mathbf{u}, \mathbf{p}, t\right) + \boldsymbol{\mu}\left(t\right)^T \mathbf{c}\left(\mathbf{X}, \mathbf{u}, \mathbf{p}, t\right) \ , \tag{1.8}$$

so that the cost function can be expressed as:

$$J = \Phi\left(\mathbf{X}\left(t_f\right), t_f\right) + \boldsymbol{\nu}^T \boldsymbol{\psi}\left(\mathbf{X}\left(t_0\right), \mathbf{X}\left(t_f\right), t_0, t_f\right) + \int_{t_0}^{t_f} \left[\mathcal{H}\left(\mathbf{X}, \mathbf{u}, \boldsymbol{\lambda}, \boldsymbol{\mu}, t\right) - \boldsymbol{\lambda}\left(t\right)^T \dot{\mathbf{X}} \right] dt \ . \tag{1.9}$$

From Equation 1.9 the complete set of necessary conditions for optimality can be derived (see Appendix A). This set, also referred to as the Euler-Lagrange equations, constitutes the following differential-algebraic system:

$$\begin{aligned} &\dot{\mathbf{X}} = \mathbf{h}\left(\mathbf{X}, \mathbf{u}, \mathbf{p}, t\right) \\ &\dot{\boldsymbol{\lambda}}\left(t\right) = -\boldsymbol{H}_{\mathbf{X}}^T \\ &\boldsymbol{H}_{\mathbf{u}}^T = 0 \end{aligned} \tag{1.10}$$

In Equation 1.10, $\mathbf{H_X}$ is the row vector representing the partial derivatives of the Hamiltonian $\mathcal{H}$ with respect to $\mathbf{X}$, $\mathbf{H_X} = [\partial\mathcal{H}/\partial X_1,\ \ldots, \partial\mathcal{H}/\partial X_{n_x}]$, while $\mathbf{H_u}$ is the row vector representing the partial derivatives of the Hamiltonian $\mathcal{H}$ with respect to $\mathbf{u}$, $\mathbf{H_u} = [\partial\mathcal{H}/\partial u_1,\ \ldots, \partial\mathcal{H}/\partial u_{n_u}]$. The boundary conditions at t_0 and t_f are defined by:

$$\begin{aligned} &\boldsymbol{\psi}\left(\mathbf{X}\left(t_0\right), \mathbf{X}\left(t_f\right), t_0, t_f\right) = 0 \\ &\boldsymbol{\lambda}\left(t_f\right)^T = \left[\boldsymbol{\Phi}_{\mathbf{X}} + \boldsymbol{\nu}\left(t\right)^T \boldsymbol{\psi}_{\mathbf{X}}\right]_{t=tf} \\ &\left[\boldsymbol{\phi}_t + \boldsymbol{\nu}^T \boldsymbol{\psi}_t + \mathcal{H}\right]_{t=t_f} = 0\ . \end{aligned} \tag{1.11}$$

The problem defined by Equations 1.10 and 1.11 is a two-point boundary value problem (TPBVP), as some boundary conditions on the states are specified at the initial time and some boundary conditions on the states and adjoints are specified at the terminal time [48]. The last of Equations 1.10 is an application of Pontryagin maximum principle. It can in fact be expressed as:

$$\mathbf{u} = \arg\min_{\mathbf{u}\in\mathcal{U}} \mathcal{H}\left(\mathbf{X}, \mathbf{u}, \boldsymbol{\lambda}, \boldsymbol{\mu}, t\right)\ , \tag{1.12}$$

where $\mathcal{U}$ is the domain of the feasible controls. A more complete discussion of the optimal control problem is given in Appendix A and in [19, 36, 151].

For low-thrust trajectories applications, depending on the choice of the objective function J, different optimal control problems can be defined:

1. the fuel-optimal problem: the objective is the maximisation of the final mass of the spacecraft (minimisation of the propellant mass):

$$J = \int_{t_0}^{t_f} \epsilon(t)\ dt\ ; \tag{1.13}$$

2. the minimum time problem: the objective is the minimisation of the time of flight, expressed as

$$J = \int_{t_0}^{t_f} dt\ . \tag{1.14}$$

The boundary conditions on the state depend on the transfer type; for example, for a rendezvous, they are

$$\mathbf{r}(t_0) = \mathbf{r}_0,\ \mathbf{v}(t_0) = \mathbf{v}_0,\ m(t_0) = m_0 \tag{1.15}$$

at the initial time t_0, while the terminal conditions are

$$\mathbf{r}(t_f) = \mathbf{r}_f, \mathbf{v}(t_f) = \mathbf{v}_f, m(t_f) > m_p\ , \tag{1.16}$$

where m_p is the propellant mass. Solutions to the low-thrust trajectory optimal control problem can be obtained by indirect or direct methods, as discussed in the following sections.

1.3.1 Indirect methods

Indirect methods find a solution to the low-thrust optimal control problem by solving the differential-algebraic system of Equations 1.10 and 1.11. Finding a solution for these equations is not easy: the addition of the costate variables doubles the size of the dynamical system [48]. Moreover, the values of the initial costates are unknown and difficult to estimate, since they lack physical significance. Some methods to estimate the values of the initial costates have been proposed in [93]. For the fuel-minimum problem, a notable solution using indirect method was formulated by Lawden, in the so-called primer vector theory [124, 166, 183]. Expressing the low-thrust control vector as $\mathbf{u}(t) = \epsilon(t)\hat{\mathbf{u}}$, it is possible to find that the Hamiltonian $\mathcal{H}$ is minimised when the thrust direction $\hat{\mathbf{u}}(t)$ is aligned with the opposite to the adjoint to the velocity vector $\boldsymbol{\lambda}_v(t)$, that is $\hat{\mathbf{u}}(t) = -k\boldsymbol{\lambda}_v(t)$. The vector $\mathbf{p}_v = -\boldsymbol{\lambda}_v(t)$ is termed primer vector. The choice of the thrust acceleration magnitude ϵ that minimises $\mathcal{H}$ is then given by a bang-bang control law:

$$\epsilon = \begin{cases} \epsilon_{max} & \text{for } S_w > 0 \\ 0 & \text{for } S_w < 0 \, . \end{cases} \tag{1.17}$$

S_w is the switching function $S_w(t) = p_v - 1$, where p_v is the magnitude of $\mathbf{p}_v$. Thus, the thrust magnitude switches between its limiting values of 0 and $F_{max} = m\,\epsilon_{max}$.

Obtaining optimal bang-bang solutions is generally difficult, since the structure of the control is not known a priori and the convergence radius for the optimal solution is usually very small [18]. To overcome this problem, a perturbation parameter can be added to the objective function (Equation 1.13) and updated by a continuation procedure. An example of this solution method is presented in [18], where one of the proposed perturbed objective function includes an energy term:

$$J = \int_{t_0}^{t_f} \left[\epsilon(t) - k\,\epsilon(t)\,(1 - \epsilon(t))\right] dt \, . \tag{1.18}$$

The continuation approach starts by solving the perturbed problem with value of the perturbation parameter k equal to 1. Then the TPBVP is solved with a reduced value of the perturbation parameter, using the solution of the previous TPBVP as starting point. The process is repeated for decreasing values of k. In [18] this method is applied to solve a minimum-fuel low-thrust transfer from Earth to Venus.

Examples of indirect optimisation of low-thrust trajectories are presented in [172, 173]. Indirect solutions to the TPBVP are generally obtained using numerical methods. However, analytical solutions are available in some cases under particular simplifying assumption. A well known example is the solution to the minimum time problem of low-thrust transfers between circular inclined orbits, first formulated by Edelbaum [72] and then casted by Kechichian as a minimum time problem [106]. The simplifying assumption is that the orbit eccentricity remains zero during the entire transfer. More details about this solution are given in Section 2.2.2.

1.3.2 Direct methods

Direct methods transcribe the infinite dimensional continuous optimal control problem into a finite dimensional parameter optimisation problem, in which the parameters are the discrete representation of the states and controls time histories [48]. The solution is then obtained solving a non-linear programming (NLP) problem. The constrained nonlinear programming problem with equality and inequality constraints is expressed as:

$$\begin{aligned} \min_{\mathbf{x}\in\mathbb{X}} \ & \tilde{J}(\mathbf{x}) \\ \text{s.t.} \quad & \mathbf{c}(\mathbf{x}) = 0 \\ & \mathbf{g}(\mathbf{x}) \leq 0 \end{aligned} \tag{1.19}$$

where

- $\mathbb{X}$ is a subset of $\mathbb{R}^{n_x}$
- $\tilde{J}(\mathbf{x}) : \mathbb{X} \to \mathbb{R}$ is the scalar objective function
- $\mathbf{x} \in \mathbb{X}$ is the vector of n_x variables to optimise
- $\mathbf{c}(\mathbf{x}) : \mathbb{X} \to \mathbb{R}^{n_c}$ is the set of equality constraints
- $\mathbf{g}(\mathbf{x}) : \mathbb{X} \to \mathbb{R}^{n_g}$ is the set of inequality constraints

Problem 1.19 can be expressed in a compact form as

$$\min_{\mathbf{x}\in\mathcal{F}} \tilde{J}(\mathbf{x}) \tag{1.20}$$

where $\mathcal{F}$ is the feasible set.

Definition 1.3.1 (Feasible Set)**.** *The feasible set $\mathcal{F}$ is a subset of $\mathbb{X}$ that contains all feasible points:*

$$\mathcal{F} := \{\mathbf{x} \in \mathbb{X} : \mathbf{c}(\mathbf{x}) = 0, \mathbf{g}(\mathbf{x}) \leq 0\} \tag{1.21}$$

The complete formulation of the NLP problem and the necessary and sufficient conditions for optimality are given in Appendix B.

While generally easier to solve than indirect methods, direct methods present both advantages and disadvantages when compared to indirect techniques. Direct methods do not require to double the dimension of the system by adding costate variables, nor to find an appropriate initial guess for their value. Moreover, performance index, equality and inequality constraints can be easily altered to obtain different problem formulations, while for indirect methods a new performance index or a new set of constraints results in a new derivation of the TPBVP [113]. However, direct methods do not make use of the necessary conditions derived from the formulation of the optimal control problem and, therefore, their solution is not guaranteed to be an extremum of the problem [48]. The necessary conditions can be used,

when employing a direct method, to determine, a posteriori, whether the obtained solution satisfies them [47, 166].

The transcription of the optimal control problem into a parameter optimisation problem can be realised in different way, depending on the quantities that are parametrised:

- only the control variables are parametrised; this is referred to as control parametrisation;
- state and control variables are parametrised.

In the control parametrisation method, control is approximated by a linear combination of basis functions [128, 202]. One of the most used approach is to use piecewise-constant basis functions. The low-thrust control $\mathbf{u}$ on the control subinterval $[\tau_{k-1}, \tau_k)$ is approximated as [128]

$$\mathbf{u}(t) \approx \boldsymbol{\sigma}_k, \quad t \in [\tau_{k-1}, \tau_k), \quad k = 1, \ldots, l \tag{1.22}$$

where l is the number of control subintervals, and $\boldsymbol{\sigma}_k$ is the control on that subinterval. The decision variables are the control values $\boldsymbol{\sigma}_k$; the nodal points, or switching times, τ_k are usually pre-fixed and satisfy

$$t_0 = \tau_0 < \tau_1 < \ldots \tau_{k-1} < \tau_k < \cdots < \tau_{l-1} < \tau_l = t_f \ . \tag{1.23}$$

The control at any time $t \in [t_0, t_f]$ can therefore be approximated as

$$\mathbf{u}(t) \approx \sum_{k=1}^{l} \boldsymbol{\sigma}_k \mathcal{X}[\tau_{k-1}, \tau_k)(t) \ , \tag{1.24}$$

where $\mathcal{X}[\tau_{k-1}, \tau_k)(t)$ is defined as

$$\mathcal{X}[\tau_{k-1}, \tau_k)(t) = \begin{cases} 1 & \text{if } t \in [\tau_{k-1}, \tau_k), \\ 0 & \text{if } t \notin [\tau_{k-1}, \tau_k) \ . \end{cases} \tag{1.25}$$

This formulation can be easily extended to other examples of control parametrisation. For example, the control could be defined, on each subinterval, through linear interpolation of the parameters defined at the switching times. A direct method based on the linear interpolation of the control parameters is presented in Section 5.3 and Chapter 12 of this thesis.

In the more general case, both states and controls are parametrised in the implementation of the direct method. In this work, both control parametrisation and state and control parametrisations are used. The proposed direct transcription methods are presented in Chapter 5.

Three techniques are commonly used to solve direct optimisation problems: single shooting algorithms, multiple shooting algorithms and collocation. In this work, shooting techniques will be used. The single shooting method can be summarised as follows [20]:

1. Provide an initial guess for the solution vector $\mathbf{x}$. The expression for $\mathbf{x}$ depends on the formulation of the problem. For example, for the control parametrisation with piecewise-

constant basis functions and a-priori defined switching times presented above, $\mathbf{x} = [\boldsymbol{\sigma}_1, \boldsymbol{\sigma}_2, \ldots, \boldsymbol{\sigma}_l]^T$.

2. Propagate the system defined by Equations 1.2 using the chosen initial guess for $\mathbf{x}$.

3. Use a NLP problem to adjust $\mathbf{x}$ to satisfy the equality and inequality constraints $\mathbf{c}(\mathbf{x}) = 0$ and $\mathbf{g}(\mathbf{x}) \leq 0$, while minimising the chosen objective function $\tilde{J}$.

In the single shooting method the system's dynamic is propagated with a single integration from the initial time t_0 to the final time t_f. In the multiple shooting algorithm, instead, the trajectory is split into phases or segments. Using the same formulation introduced above, these segments can be identified by their initial and final times, τ_{k-1} and τ_k. The initial state vector for each segment $[\tau_{k-1}, \tau_k)$ is determined by the optimisation process, and is therefore treated as a decision variable [108]. Therefore the vector $\mathbf{x}$ now includes also the initial state vector $\mathbf{X}$ for each segment:

$$\mathbf{x} = [\mathbf{X}_0, \boldsymbol{\sigma}_1, \mathbf{X}_1, \boldsymbol{\sigma}_2, \ldots, \mathbf{X}_{k-2}, \boldsymbol{\sigma}_{k-1}, \mathbf{X}_{k-1}, \boldsymbol{\sigma}_k, \ldots, \mathbf{X}_{l-1}, \boldsymbol{\sigma}_l]^T \,. \tag{1.26}$$

For segment k, the state is propagated from τ_{k-1} to τ_k using the initial state $\mathbf{X}_{k-1}$. Denoting the result of this integration as $\hat{\mathbf{X}}_k$, the following constraints have to be satisfied to ensure that the segments join at the boundaries:

$$\mathbf{c}(\mathbf{x}) = \begin{bmatrix} \hat{\mathbf{X}}_1 - \mathbf{X}_1 \\ \hat{\mathbf{X}}_2 - \mathbf{X}_2 \\ \vdots \\ \hat{\mathbf{X}}_{k-1} - \mathbf{X}_{k-1} \\ \hat{\mathbf{X}}_k - \mathbf{X}_k \\ \vdots \\ \hat{\mathbf{X}}_{l-1} - \mathbf{X}_{l-1} \end{bmatrix} = \mathbf{0} \,. \tag{1.27}$$

The problem is solved, as with the single shooting algorithm, by an NLP problem solver. The dimension of the problem is higher for a multiple rather than single shooting technique. The Jacobian matrix associated to the problem is, however, sparse. The sparsity is a consequence of the multiple shooting formulation: variables early in the trajectory do not change constraints later in the trajectory [20]. The multiple shooting method is, moreover, more robust than the single shooting with respect to poor initial guesses [108].

In the collocation method the basic principle is to divide the transfer into segments that begin and end with nodes. The states and controls are represented by discrete values at the nodal points, and using an interpolating polynomial for points between two consecutive nodes. The equations of motion are enforced at the nodal points and at the center of each segment: the slopes of the polynomials are constrained to satisfy the differential equations of motion. The difference between the effective and estimated derivatives at coincident times (defects) constitutes the set of constraints of the NLP problem. The integration of the system dynamic is,

therefore, implicit. Collocation methods are presented in [20] and in [97] for applications to low-thrust orbital transfers.

A well known and widely used direct method for the design of low-thrust trajectory is the Sims and Flanagan method [188]. In this method the trajectory is divided into legs that begin and end at control nodes (control nodes might be associated to planets or small bodies, or can be free points in space). Each leg has a match point and the trajectory is propagated forward in time from the leg's earlier control node to the match point and backward from the leg's later control node to the match point. The low-thrust acceleration is modelled with a series of impulses. The variables to optimise are the states and mass of the spacecraft at each control node and the corresponding epochs. Constraints are imposed so that the states and mass of the spacecraft are continuous at the match points. The Sims-Flanagan method has been implemented in the software packages Gravity Assist Low-Thrust Local Optimization Program (GALLOP) [138] and Mission Analysis Low-Thrust Optimizer (MALTO) [189]. In [230] two improvements to the Sims-Flanagan method were introduced: the first consisted in the replacement of the impulses with continuous thrust, numerically propagated using Taylor integration; the second consisted in the introduction, among the optimisation variables, of the time mesh, through the use of the Sundman transformation, so that the segments can be automatically distributed more densely near the central body. In [211] a method was proposed to transcribe the optimal control problem into a NLP problem using Finite Elements in Time (FET). In the proposed approach, the time domain is decomposed into finite time elements, and on each time element the states and controls are parametrised using internal node values and appropriate polynomials. The Direct Finite Elements Transcription (DFET) method was applied to different trajectory design problems [206, 207] and implemented in the tool Direct Interplanetary Trajectory Analysis (DITAN) [17]. In [241] Zuiani presented a direct transcription method based on the decomposition of the trajectory into direct finite perturbative elements. Each finite element represents an arc of prescribed true longitude amplitude where the first-order perturbed Keplerian model presented in [240] is applied. To obtain the boundary points of the element, the perturbed motion is analytically propagated backward and forward from the midpoint of each arc. The arcs are then interconnected by imposing matching conditions at their boundaries. An application of the use of a direct method to solve low-thrust trajectories was presented by Kluever [115]. The author presented a method to compute minimum-time transfers by blending three extremal feedback control laws for the variation of semi-major axis, eccentricity and inclination. Each steering law is assigned a weight and the optimisation consists in finding the values for these weights. In particular, the weighting functions are parametrised using a linear interpolation through 21 nodes equally spaced in time. The motion of the spacecraft is modelled using equinoctial elements and orbital averaging techniques in which Guassian quadrature is used to evaluate the integrals of the variation of orbital elements over one period. The NLP problem is solved by gradient-based optimisation method. Proposed applications are, among others, the transfer from GTO to GEO. The same author also studied the GTO-GEO transfer with variable specific impulse [114]. In this case the costates time histories are parametrised by linear interpolation and the design varia-

bles of the NLP problem are the nodal values of the costates. The objective is the minimisation of the fuel mass and a local optimisation method is used to solve the problem.

The applications proposed in Part II of this thesis (Chapters 8 to 12) are solved using direct methods and the transcription techniques described in Chapter 5. Both local and global solution algorithms are considered to solve the proposed problems . An overview of local and global optimisation algorithms is given in the next section.

1.4 Solution algorithms

This section introduces a summary of existing methods for the solution of Problem 1.19. The following definitions of local and global minima are given:

Definition 1.4.1 (Local minimum.)**.** *A local minimum* $\mathbf{x}_{LM}$ *of the objective function* $\tilde{J} : \mathbb{X} \to \mathbb{R}$ *is a vector* $\mathbf{x}_{LM} \in \mathcal{F}$ *that satisfies:*

$$\exists \varepsilon > 0 : \tilde{J}(\mathbf{x}_{LM}) \leq \tilde{J}(\mathbf{x}) \ \forall \mathbf{x} \in \mathcal{F}, \ \|\mathbf{x} - \mathbf{x}_{LM}\| < \varepsilon \tag{1.28}$$

Definition 1.4.2 (Global minimum.)**.** *A global minimum* $\mathbf{x}_{GM}$ *of the objective function* $\tilde{J} : \mathbb{X} \to \mathbb{R}$ *is a vector* $\mathbf{x}_{GM} \in \mathcal{F}$ *that satisfies:*

$$\tilde{J}(\mathbf{x}_{GM}) \leq \tilde{J}(\mathbf{x}) \ \forall \mathbf{x} \in \mathcal{F} \tag{1.29}$$

1.4.1 Local algorithms

The methods traditionally used to optimise low-thrust trajectories are local methods. They are able to find a solution that is generally a local minimum, not the best solution [56, 205]. Moreover, they require an initial guess of the solution parameters that is not only hard to find but that also generally causes the optimiser to converge to an optimal trajectory close to the initial guess (that is rarely close to the global optimum) [56].

A variety of local algorithms exist for the solution of optimisation problems. For unconstrained problems, well known methods are, among others, gradient descent and Netwon's method [20]. In the case of constrained optimisation problem, Sequential Quadratic Programming (SQP) and Interior Point Methods (IPM) can be used (Appendix B). In this work the chosen local optimisation algorithm is the MATLAB[1] *fmincon* algorithm, that includes both SQP and IPM solvers.

1.4.2 Global algorithms

To overcome the limitations of the local optimisation methods, effective global optimisation techniques are required. Global optimisation methods have been used since the second half of the 1990s for the solution of optimal space trajectory design problems [214]. Commonly used global stochastic algorithms include evolutionary solvers such as Differential Evolution

[1] `https://uk.mathworks.com/products/matlab.html`

(DE) [163, 164], Genetic Algorithms (GA) [86] and Particle Swarm Optimisers (PSO) [71, 109], or algorithms based on multiple local search and gradient methods, such as Multistart (MS) and Monotonic Basin Hopping (MBH) [222]. An assessment of global optimisation methods for the solution of trajectory design problems has been presented in [68, 69]. The outcome of this studies shows that, compared to other solvers, DE provide good results on most of the problems.

Global techniques are commonly used for the optimisation of impulsive trajectories [208, 209, 213, 214]. In order to use global algorithms for the optimisation of low-thrust trajectories, quantities that must be described continuously, such as thrust magnitude or pointing time history, can be parametrised using, for example, polynomial equations in time [48]. Compared to local methods, global algorithms do not require an initial guess and are more likely to locate a global minimum than to be attracted to a local minimum [48]. Examples of applications of stochastic and deterministic global algorithms for the optimisation of low-thrust trajectories have been presented in [56, 61, 69, 154, 156, 174, 216, 218, 224, 231]. In [231], the Sims-Flanagan method (Subsection 1.3.2) was used for the optimisation of multi-gravity assist low-thrust trajectories using Multistart, MBH and Simulated Annealing. In [60], De Pascale and Vasile used a global optimisation method that blends an evolutionary algorithm with a deterministic domain decomposition technique in order to design low-thrust transfers with multiple gravity-assist maneuvers. In [216], the global optimisation of low-thrust transfers with gravity assists, using exponential sinusoid, was presented. Di Lizia presented the global optimisation of a low-thrust Earth-Mars transfer in [69]. The constraints term is included in the objective function by means of penalty terms and weighted sum. The azimuth and elevation angles during the transfer are modelled using a linear interpolation of their values corresponding to six points on the trajectory, uniformly distributed in time. Different global methods are used to solve the problem. Vavrina presented a combination of GA with a local optimisation tool for the design of low-thrust trajectories, GALLOP [218]. Each member of the population of the GA is sent to GALLOP to be locally optimised. Before optimisation in GALLOP, the individuals of the population are, generally, neither feasible nor locally optimal. GALLOP then refines and repairs each individual, allowing the included NLP solver to adjust the design variables towards feasible and locally optimal areas of the design space. Other applications of global methods to spacecraft trajectory optimisation were presented in [56, 154, 209].

Considering the good performances of DE over a wide variety of optimisation problems [59], including space problems, in [217] an hybridisation of DE with the restarting procedure of MBH was proposed. The resulting algorithm was called Inflationary Differential Evolution Algorithm (IDEA). Despite being a very efficient optimiser, DE has in fact questionable local search ability and work has been done in the literature to improve its local convergence by combining it with local optimisation strategies [169]. In [131, 217] it was moreover demonstrated that DE can converge to a fixed point, a level set or a hyperplane that does not contain the global minimum. The collapse of the population to a fixed point or a neighbourhood of a fixed point from which DE cannot escape was another motivation for the development of IDEA [217]. Further improvement of the algorithm was presented in [141], where a mecha-

nism to automatically adapt the main parameters of the DE was proposed.

In this thesis, the work presented in [217] and [141] is further extended to develop a multi-population solver capable of adapting the main parameters associated to the MBH hybridisation. The multi-population algorithm, called Multi-Population Adaptive Inflationary Differential Evolution Algorithm (MP-AIDEA), is presented in Chapter 7.

1.5 Surrogate models of low-thrust optimal transfers

Surrogate models, or metamodels, are widely used for the design and optimisation of many engineering applications. They replace the computationally expensive high fidelity simulations with a model constructed using few responses of such expensive simulations, and they can be used for surrogate-based optimisation applications [79]. Both direct and indirect methods for the solution of low-thrust optimal transfer are generally computationally expensive; therefore, surrogate models have the potential to make the evaluation and optimisation of low-thrust trajectories more efficient. In [139] the use of machine learning regression is proposed to estimate the final spacecraft mass after an optimal low-thrust transfer, for transfers between Near Earth Objects. In [96] a similar approach is used for the problem of optimal asteroid hops (short transfers not requiring multiple revolutions). In Chapter 6, a method to generate surrogate models of optimal low-thrust transfer is presented. The transcriptions methods described in Chapter 5 are used to generate the training points for the model. The method proposed lays the basis for an extensive use of off-line generated metamodels in conjunction, for example, with combinatorial search algorithm, as presented in Chapter 10. Moreover, the methods presented are a first step for the definition of a complete cartography of the ΔV and ToF of low-thrust transfers. The resulting cartography provides a computationally efficient tool for the evaluation of the cost of a transfer for any possible variation of the orbital elements. Another proposed application is the online generation of surrogate models, during the optimisation process. In this case the initial metamodel is computed using few sample points, and its accuracy is improved during the optimisation by sampling the space at appropriate points.

1.6 Summary

This chapter has provided the theoretical basis and bibliographical background for the multi-fidelity optimisation of low-thrust transfers. In the next chapters, the different topics that have been introduced in this chapter will be presented in more details and will be further extended. The first step is a survey and analysis of the analytical control laws for low-thrust transfers available in the literature, addressed in Chapter 2.

Chapter 2

Analysis of analytical control laws for low-thrust orbit transfer

Different analytical control laws for the variation of orbital elements using low-thrust propulsion are available in the literature. Some of them are optimal laws, many others are guidance laws that realise the transfer from some initial condition to some final condition, with no guarantee of optimality. The aim of this chapter is to collect these laws and to present a comprehensive analysis of their assumptions, equations and results. For many of the considered control laws, no analytical expressions for the variation of the orbital elements with time and for the cost of the transfer are given in the literature; analytical expressions for these quantities have been derived, whenever possible, and are presented in this chapter in the form of propositions. All the new analytical equations have been validated through comparison with the results of a numerical integration. The analyses on the considered control laws include the comparison of the ΔVs of laws that realise the same orbital transfer using different control profiles, and the study of the variation of the ΔV with the initial values of the orbital elements and their desired changes. In addition, for cases in which closed form solutions can be derived only under specific assumptions (e.g. $e = 0$), the error introduced by using the analytical expression also when the assumptions are violated ($e \neq 0$) is assessed. The chapter starts with a brief introduction of the basic theoretical concepts in Section 2.1. Then the laws for the variation of semi-major axis (Section 2.2), eccentricity (Section 2.3), inclination (Section 2.4), right ascension of the ascending node (Section 2.5) and argument of the periapsis (Section 2.6) are presented. The chapters ends with a summary of the analytical laws presented (Section 2.7).

2.1 Introduction

It is assumed that the spacecraft is subject to a low-thrust acceleration $\mathbf{u}$ that can be expressed in a radial-transverse-normal RTN reference frame (see [204]) as (see Figure 2.1)

$$\mathbf{u} = \begin{bmatrix} u_R \\ u_T \\ u_N \end{bmatrix} = \begin{bmatrix} \epsilon \cos\beta \sin\alpha \\ \epsilon \cos\beta \cos\alpha \\ \epsilon \sin\beta \end{bmatrix} . \tag{2.1}$$

In Equation 2.1 ϵ is the magnitude of the low-thrust acceleration, α is the azimuth angle and β is the elevation angle. The Gauss' equations, expressing the time variation of the classic orbital

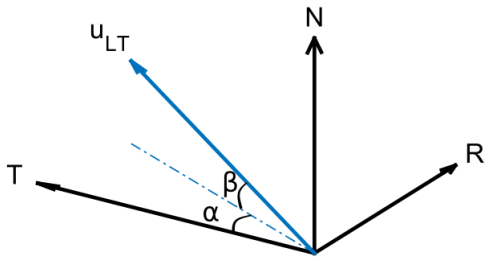

Figure 2.1: Low-thrust acceleration vector in a RTN reference frame and azimuth and elevation angles α and β.

elements due to the low-thrust acceleration $\mathbf{u}$ [13], are

$$\begin{aligned}
\frac{da}{dt} &= \frac{2a^2}{h}\epsilon\cos\beta\left[e\sin\theta\sin\alpha + \frac{p}{r}\cos\alpha\right], \\
\frac{de}{dt} &= \frac{\epsilon\cos\beta}{h}\left\{p\sin\theta\sin\alpha + [(p+r)\cos\theta + re]\cos\alpha\right\}, \\
\frac{di}{dt} &= \epsilon\frac{r}{h}\cos u\sin\beta, \\
\frac{d\Omega}{dt} &= \epsilon\frac{r}{h}\frac{\sin u}{\sin i}\sin\beta, \\
\frac{d\omega}{dt} &= \frac{1}{he}\epsilon\cos\beta\left[-p\cos\theta\sin\alpha + (p+r)\sin\theta\cos\alpha\right] - \frac{r\sin u\cos i}{h\sin i}\sin\beta, \\
\frac{d\theta}{dt} &= \frac{h}{r^2} + \frac{\epsilon}{eh}\cos\beta\left[p\cos\theta\sin\alpha - (p+r)\sin\theta\cos\alpha\right] \approx \frac{h}{r^2} .
\end{aligned} \tag{2.2}$$

In the previous equations, a is the semi-major axis, e the eccentricity, p the semilatus rectum, i the inclination, Ω the right ascension of the ascending node, ω the argument of the periapsis, θ the true anomaly, h the magnitude of the angular momentum, $h = \sqrt{\mu\, p}$, and u is the argument of latitude, $u = \omega + \theta$ [1].

[1] The argument of the latitude (scalar) u is not to be confused with the control vector $\mathbf{u}$, whose magnitude is denoted as ϵ.

The approximation in the last of Equations 2.2 derives from the assumption that the perturbing forces are small enough to produce a negligible effect on $d\theta/dt$, with respect to the term h/r^2, which is due to the Keplerian motion. The variation with time of the argument of latitude is [13]

$$\frac{du}{dt} = \frac{d\omega}{dt} + \frac{d\theta}{dt} = \frac{h}{r^2} - \frac{r \sin u \cos i}{h \sin i} \sin\beta \approx \frac{h}{r^2} \,. \tag{2.3}$$

The approximation in Equation 2.3 is based on the same assumptions for the approximation in the last of Equations 2.2. Another useful expression, used in the rest of the chapter, is the time variation of the eccentric anomaly E [39]:

$$\frac{dE}{dt} = \sqrt{\frac{\mu}{a}}\frac{1}{r} + \frac{1}{e \sin E}\left[\cos E \frac{de}{dt} - \frac{r}{a^2}\frac{da}{dt}\right] \approx \sqrt{\frac{\mu}{a}}\frac{1}{r} \,. \tag{2.4}$$

The approximation in Equation 2.4 holds when da/dt and de/dt are small [39]. In the rest of the chapter, it is in fact assumed, unless otherwise specified, that the perturbing forces are small enough to produce negligible variations in the orbital elements over one orbital period.

2.2 Variation of semi-major axis or combination of semi-major axis and other orbital elements

In this section, the thrust laws for the variation of the semi-major axis, or a combination of orbital elements including the semi-major axis, are presented.

2.2.1 Maximum instantaneous rate of change of semi-major axis

The thrust angles that provide the maximum instantaneous rate of change of the orbital elements can be obtained deriving the Gauss' equations with respect to α and β, as presented in [182]. In particular, for maximum variation of the semi-major axis [182]:

$$\frac{\partial}{\partial\alpha}\left(\frac{da}{dt}\right) = 0, \; \frac{\partial}{\partial\beta}\left(\frac{da}{dt}\right) = 0 \,. \tag{2.5}$$

The previous equations provide the well-known result that the rate of change of the semi-major axis is maximum for planar thrust ($\beta = 0$) and azimuth angle equal to the flight path angle γ [182]:

$$\alpha = \arctan\left(\frac{e \sin\theta}{1 + e\cos\theta}\right) = \gamma, \; \beta = 0 \,. \tag{2.6}$$

In particular, $\alpha = \gamma$ to increase the semi-major axis and $\alpha = \pi + \gamma$ to decrease the semi-major axis. Equations 2.5 and 2.6 are given in [182] while, to the author's best knowledge, the equations and derivations presented in the rest of this subsection are novel and have not been presented elsewhere. Using Equation 2.6 in the general case of non circular orbits, the time

variations of semi-major axis, eccentricity and argument of periapsis are

$$\begin{aligned}
\frac{da}{dt} &= \text{sgn}(\cos\alpha)\frac{2a^2\epsilon}{\sqrt{\mu a(1-e^2)}}\sqrt{1+e^2+2e\cos\theta}, \\
\frac{de}{dt} &= \text{sgn}(\cos\alpha)\frac{2\epsilon\sqrt{a(1-e^2)}}{\sqrt{\mu}}\frac{(e+\cos\theta)}{\sqrt{1+e^2+2e\cos\theta}}, \\
\frac{d\omega}{dt} &= \text{sgn}(\cos\alpha)\sqrt{\frac{p}{\mu}}\frac{\epsilon}{e}\frac{2\sin\theta}{\sqrt{1+e^2+2e\cos\theta}}\,.
\end{aligned} \tag{2.7}$$

Equations 2.7 are obtained using the Gauss' equations (Equations 2.2) and expressing $\sin\alpha$ and $\cos\alpha$ as

$$\begin{aligned}
\cos\alpha &= \text{sgn}(\cos\alpha)\frac{1+e\cos\theta}{\sqrt{1+e^2+2e\cos\theta}}, \\
\sin\alpha &= \text{sgn}(\cos\alpha)\frac{e\sin\theta}{\sqrt{1+e^2+2e\cos\theta}}\,.
\end{aligned} \tag{2.8}$$

The expressions for $\cos\alpha$ and $\sin\alpha$ in Equation 2.8 are obtained from Equation 2.6 and using $\cos(\arctan x) = 1/\sqrt{1+x^2}$ and $\sin(\arctan x) = x/\sqrt{1+x^2}$. The variations of a, e and ω with θ are

$$\begin{aligned}
\frac{da}{d\theta} &= \frac{da}{dt}\frac{dt}{d\theta} = \text{sgn}(\cos\alpha)\frac{2\epsilon}{\mu}a^3\left(1-e^2\right)\frac{\sqrt{1+e^2+2\,e\,\cos\theta}}{\left(1+e\,\cos\theta\right)^2}, \\
\frac{de}{d\theta} &= \frac{de}{dt}\frac{dt}{d\theta} = \text{sgn}(\cos\alpha)\frac{2\epsilon}{\mu}a^2\left(1-e^2\right)\frac{e+\cos\theta}{\left(1+e\,\cos\theta\right)^2\sqrt{1+e^2+2\,e\,cos\theta}}, \\
\frac{d\omega}{d\theta} &= \frac{d\omega}{dt}\frac{dt}{d\theta} = \text{sgn}(\cos\alpha)\frac{2\epsilon p^2}{e\mu}\frac{\sin\theta}{(1+e\cos\theta)^2\sqrt{1+e^2+2e\cos\theta}}\,.
\end{aligned} \tag{2.9}$$

The equations for e and ω can not be integrated separately from the equation in a because of the semi-major axis appearing in both $de/d\theta$ and $d\omega/d\theta$. An analytical approximation can, however, be obtained under the assumption that the variation of a over one orbital period is small, so that a can be kept constant. When this approximation holds, the mean variation of e during an orbital period can be computed using

$$\Delta e_{2\pi} = \int_0^{2\pi}\frac{de}{d\theta}d\theta\,. \tag{2.10}$$

The corresponding secular variation of e is

$$\overline{\frac{de}{dt}} = \frac{\Delta e_{2\pi}}{T}, \tag{2.11}$$

where T is the orbital period. Integration of Equations 2.9 gives $\Delta e_{2\pi} = \Delta\omega_{2\pi} = 0$, meaning that there is no variation of eccentricity or argument of periapsis during the transfer. The

equation for the semi-major axis gives instead

$$\Delta a_{2\pi} = \text{sgn}(\cos\alpha)\frac{2\epsilon a^3\left(1-e^2\right)}{\mu}f(e), \tag{2.12}$$

where

$$f(e) = \frac{2}{1-e}E_{Ic}\left(\frac{4e}{(1+e)^2}\right) + \frac{2}{1+e}F_{Ic}\left(\frac{4e}{(1+e)^2}\right) . \tag{2.13}$$

In Equation 2.13 F_{Ic} and E_{Ic} are, respectively, the complete elliptic integral of the first and second kind:

$$\begin{aligned} F_{Ic}(m) &= F_I\left(\frac{\pi}{2}, m\right) , \\ E_{Ic}(m) &= E_I\left(\frac{\pi}{2}, m\right) , \end{aligned} \tag{2.14}$$

and F_I and E_I are the elliptic integral of the first and second kind [13] (see Appendix C). The mean variation with time of the semi-major axis is

$$\overline{\frac{da}{dt}} = \frac{\Delta a_{2\pi}}{T} = \text{sgn}(\cos\alpha)\frac{\epsilon a^{3/2}}{\pi\sqrt{\mu}}(1-e^2)f(e) , \tag{2.15}$$

and depends on the eccentricity e. However, since the eccentricity does not change during the transfer, the variation of semi-major axis with time can be obtained integrating Equation 2.15 to obtain the expression given in Proposition 2.2.1.

Proposition 2.2.1. *The variation of the semi-major axis with time during a transfer with the control profile defined in Equation 2.6, and under the assumption that a does not change over one orbital period, is*

$$a(t) = \left[\frac{1}{a_0} + \left(\frac{\epsilon(1-e^2)f(e)}{2\pi\sqrt{\mu}}\right)^2 t^2 - sgn(\cos\alpha)\frac{\epsilon(1-e^2)f(e)}{\pi\sqrt{a_0\mu}}t\right]^{-1} . \tag{2.16}$$

Finally, the relationship for $a(t)$ given in Equation 2.16, allows one to compute the cost of the transfer, according to Proposition 2.2.2:

Proposition 2.2.2. *The cost of a transfer to change the semi-major axis from a_0 to a_f, obtained with the control profile defined in Equation 2.6, and under the assumption that a does not change over one orbital period, is*

$$\Delta V = \epsilon\, ToF = \frac{2\pi\left|\sqrt{\frac{\mu}{a_0}} - \sqrt{\frac{\mu}{a_f}}\right|}{(1-e^2)f(e)} . \tag{2.17}$$

In Equation 2.17, ToF is computed from Equation 2.16 using $a(ToF) = a_f$. It is important to stress that Equations 2.17 and 2.16 provide only an approximation to the ΔV and variation of a during the transfer, and that the approximation is incorrect when the variation of a over one orbital period, or the variation of eccentricity, can not be neglected. The validity of this assumption is illustrated hereafter for Earth's transfers and interplanetary transfers. Figure 2.2 shows the relative difference in ΔV obtained using analytical Equation 2.17 or computing the cost of the transfer by numerically integrating the Gauss' equations with Equation 2.6,

until the desired final semi-major axis is reached. The numerical integration of the equation of Gauss has been realised in MATLAB using *ode45*, a single step solver based on an explicit Runge-Kutta (4,5) formula, the Dormand-Prince pair. Different values of the initial semi-major axis, of the variation of semi-major axis and of the initial eccentricity are considered. Results show that the relative error is higher for higher values of the eccentricity but remains lower than 0.02 for Earth transfers with eccentricities up to 0.7.

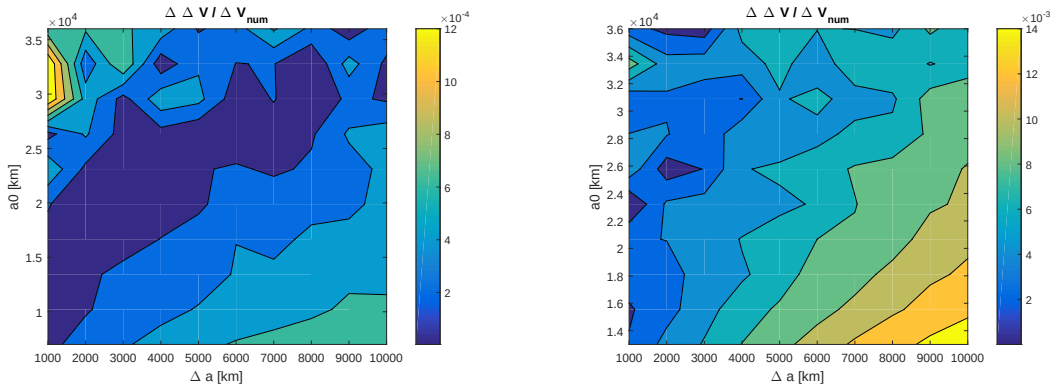

(a) $e_0 = 0.1$

(b) $e_0 = 0.5$

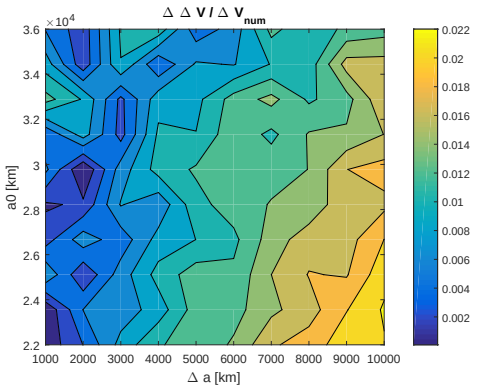

(c) $e_0 = 0.7$

Figure 2.2: Relative difference between numeric and analytical ΔV for Earth transfers, using the thrust law corresponding to the maximum instantanoues rate of change of the semimajor axis

Figure 2.3 shows the relative difference in ΔV for interplanetary transfers and three different values of the eccentricity. The error is bigger in these cases.

The analytical equation for the ΔV can, therefore, be used to approximate the cost of Earth transfers for small values of the low-thrust acceleration, while it gives non negligible errors in the case of interplanetary transfers; interplanetary transfers are, in fact, characterised by longer orbital periods, over which the value of the semi-major axis can not be assumed to remain constant. When the assumption of constant semi-major axis over one orbital period does not hold, no analytical solution exists to describe the motion of the spacecraft under the considered thrust profile.

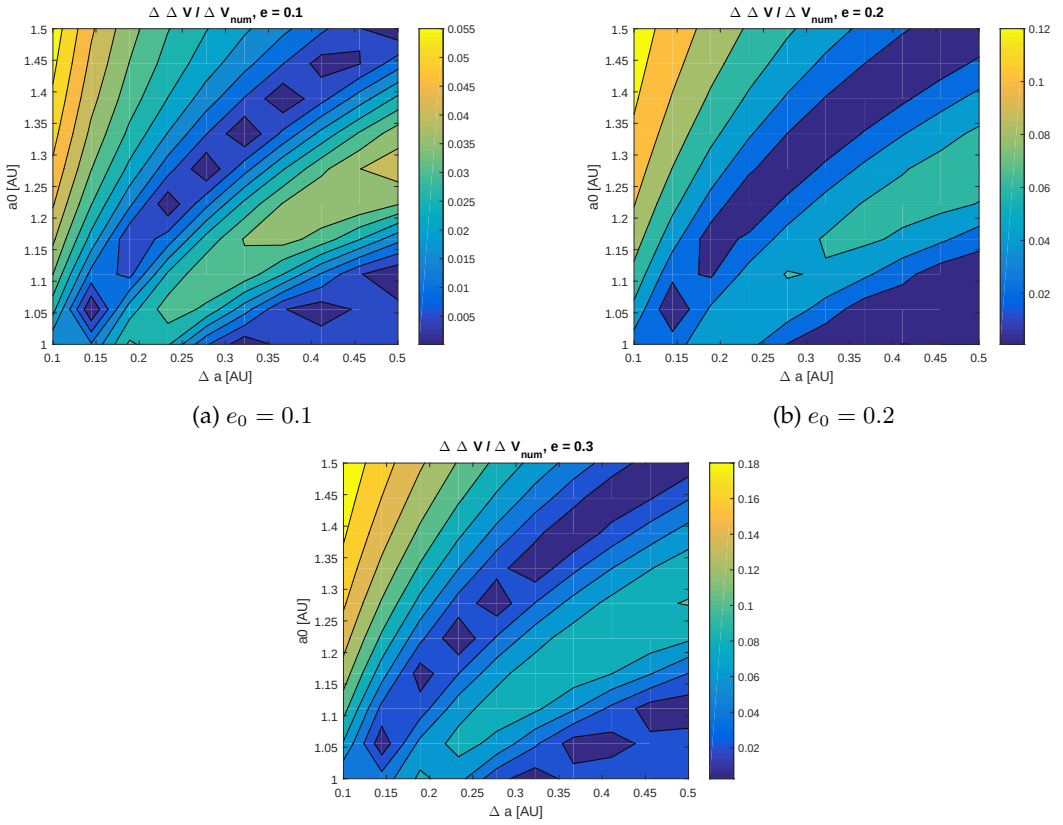

(a) $e_0 = 0.1$

(b) $e_0 = 0.2$

(c) $e_0 = 0.3$

Figure 2.3: Relative difference between numeric and analytical ΔV for interplanetary transfers, using the thrust law corresponding to the maximum instantanoues rate of change of the semimajor axis.

2.2.2 Combined variation of semi-major axis and inclination

This section presents the results of the well-known optimal transfer between circular orbits of different semi-major axis and inclination, first presented by Edelbaum [72] and then reformulated by Kechichian [106, 107]. The formulation presented here is based on the work of Kechichian [106], who modified the original formulation and substituted the set of two expressions for the inclination with a single expression valid throughout any desired transfer. Only the main equations are reported here. For the complete derivation and solution of the problem refer to [106, 107].

It is assumed that $\alpha = 0$ during the entire transfer, so that the low-thrust acceleration components are

$$u_R = 0 \ , \ u_T = \epsilon \cos\beta \ , \ u_N = \epsilon \sin\beta \ . \tag{2.18}$$

The equation of Gauss for the semi-major axis is therefore

$$\frac{da}{dt} = \epsilon \frac{2a^2}{h} \frac{p}{r} \cos\beta \ . \tag{2.19}$$

For circular orbits it becomes

$$\frac{da}{dt} = \frac{2a\epsilon\cos\beta}{v}\ , \tag{2.20}$$

where $v = \sqrt{\mu/a}$ is the velocity on a circular orbit of radius a. The equation for da/dt can therefore be substituted with an equation for dv/dt:

$$\frac{dv}{dt} = -\epsilon\cos\beta\ . \tag{2.21}$$

For the inclination, the average of di/dt over the angular position $u = \theta + \omega$ is computed. In the case of circular orbit, the average on u is

$$\overline{\frac{di}{dt}} = \frac{\Delta i_{2\pi}}{T}, \tag{2.22}$$

where $\Delta i_{2\pi}$ is obtained by integration of di/du from 0 to 2π, using

$$\frac{di}{du} = \frac{di}{dt}\frac{dt}{du} = \epsilon\frac{r}{h}\cos u\sin\beta\frac{r^2}{h}\ . \tag{2.23}$$

The angle β has constant magnitude over one orbital period but changes sign at $u = \pi/2$ and $u = 3\pi/2$; if an increase of inclination is sought, $\beta > 0$ for $-\pi/2 < u < \pi/2$ and $\beta < 0$ for $\pi/2 < u < 3\pi/2$:

$$\Delta i_{2\pi} = \frac{1}{2\pi}\int_0^{\pi/2}\left(\frac{di}{du}\right)_{\beta>0}d\mathrm{u} + \frac{1}{2\pi}\int_{\pi/2}^{3\pi/2}\left(\frac{di}{du}\right)_{\beta<0}d\mathrm{u} + \frac{1}{2\pi}\int_{3\pi/2}^{2\pi}\left(\frac{di}{du}\right)_{\beta>0}d\mathrm{u}. \tag{2.24}$$

Combining Equations 2.23 and 2.24 results in:

$$\overline{\frac{di}{dt}} = \frac{2\epsilon\sin\beta}{\pi v}. \tag{2.25}$$

The optimal control problem to be solved is a minimum time problem for the transfer from (v_0, i_0) to (v_f, i_f), defined by v and i as state variables, t as the independent variable and β as the control variable. The Hamiltonian associated to the minimum time problem is

$$\mathcal{H} = 1 + \lambda_i\left(\frac{2\varepsilon\sin\beta}{\pi v}\right) - \lambda_v\epsilon\cos\beta, \tag{2.26}$$

being $J = \int_{t_0}^{t_f} dt$ the performance index. The result of the optimal control problem gives the expression for the variation of the thrust angle β with time:

$$\beta(t) = \arctan\left(\frac{v_0\sin\beta_0}{v_0\cos\beta_0 - \epsilon\ t}\right), \tag{2.27}$$

where β_0 is defined as

$$\tan\beta_0 = \frac{\sin\left[\frac{\pi}{2}(i_f - i_0)\right]}{\frac{v_0}{v_f} - \cos\left[\frac{\pi}{2}\ (i_f - i_0)\right]}\ . \tag{2.28}$$

The expressions for the variation of the states v and i with the time are

$$v(t) = \sqrt{v_0^2 + \epsilon^2 t^2 - 2\,\epsilon\,t\,v_0 \cos\beta_0}\,, \tag{2.29}$$

$$i(t) = i_0 + \frac{2}{\pi}\left[\arctan\left(\frac{\epsilon\,t - v_0\cos\beta_0}{v_0\sin\beta_0}\right) + \frac{\pi}{2} - \beta_0\right]\,. \tag{2.30}$$

The ΔV required for the transfer is:

$$\Delta V = \sqrt{v_0^2 + v_f^2 - 2 v_0 v_f \cos\left[\frac{\pi}{2}\,(i_f - i_0)\right]} \tag{2.31}$$

Despite the out-of-plane thrust, the right ascension of the ascending node does not change during the transfer. The variation of the sign of β at $\pi/2$ and $3\pi/2$ and the $\sin u$ term in the equation for $d\Omega/dt$ are such that $\Delta\Omega_{2\pi} = 0$.

Figure 2.4 shows the ΔV required for the variation of a and i for different values of a_0, $\Delta a = a_f - a_0$ and Δi. Note that the transfer is more expensive at lower Δa, when $\Delta i \neq 0$, because of the increased cost required to change inclination at lower semi-major axis.

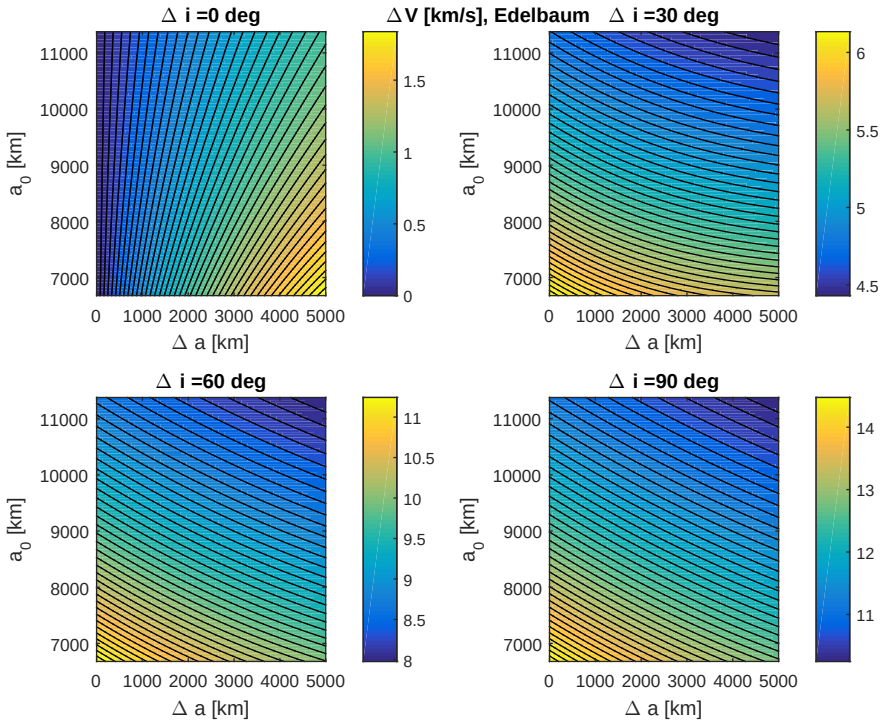

Figure 2.4: ΔV for the variation of a and i for different values of a_0, Δa and Δi.

In this type of transfer, with combined variation of semi-major axis and inclination, the semi-major axis could grow to very large values when a large inclination change takes place [107]. It is, however, possible to constraint a such that $a \leq a_{lim}$ during the transfer [107]. A

constraint is therefore added to the optimal control problem:

$$g(v, i, t) = v_{lim} - v \leq 0 \, , \tag{2.32}$$

where v_{lim} is the circular velocity corresponding to a_{lim}. From Equations 2.32 and 2.21:

$$\dot{g} = -\frac{dv}{dt} = \epsilon \cos\beta \, . \tag{2.33}$$

The augmented Hamiltonian is, therefore, in this case

$$\mathcal{H} = 1 + \lambda_i \left(\frac{2\epsilon \sin\beta}{\pi v} \right) - \lambda_v \epsilon \cos\beta + \mu\epsilon \cos\beta \, . \tag{2.34}$$

The details of the solution of the optimal control problem are given in [107] and are not reported here. Only the final results are given in the following. The solution is characterised by a sequence of unconstrained-constrained-unconstrained arcs. On the constrained arcs $v = v_{lim}$ and $\beta = \pi/2$; therefore a pure inclination change, with the inclination changing linearly with time, is obtained on the constrained arc. The entry and exit times to the constrained arc are defined as t_1 and t_2. The time t_1 and t_2 of entry and exit of the constrained arc are

$$\begin{aligned} t_1 &= \frac{v_0 \cos\beta_0}{\epsilon}, \\ t_2 &= \frac{\pi \, v_{lim}}{2\epsilon} \left[i_f - \frac{2}{\pi} \left(\frac{\pi}{2} - \beta_0 \right) - \frac{2}{\pi} \arctan\left(\frac{\sqrt{(v_f - v_{lim})\,(v_f + v_{lim})}}{v_{lim}} \right) \right] + \frac{v_0 \cos\beta_0}{\epsilon} \, . \end{aligned} \tag{2.35}$$

The variable β_0 is the initial value of the control β at the initial time t_0:

$$\sin\beta_0 = \frac{v_{lim}}{v_0} \, . \tag{2.36}$$

The time of flight $ToF = t_f$ of the transfer is

$$t_f = t_2 + \frac{\sqrt{(v_f - v_{lim})\,(v_f + v_{lim})}}{\epsilon} \, . \tag{2.37}$$

The evolutions of v, i and β as a function of time t in the interval $[0, t_1)$ are

$$\begin{aligned} v(t)_{t\in[0,t_1)} &= \sqrt{v_0^2 + \epsilon^2 t^2 - 2\epsilon \, t \, v_0 \, \cos\beta_0}, \\ i(t)_{t\in[0,t_1)} &= i_0 + \frac{2}{\pi} \left[\arctan\left(\frac{\epsilon t - v_0 \cos\beta_0}{v_0 \sin\beta_0} \right) + \frac{\pi}{2} - \beta_0 \right], \\ \beta(t)_{t\in[0,t_1)} &= \frac{v_{lim}}{v_0 \cos\beta_0 - \epsilon t} \, . \end{aligned} \tag{2.38}$$

The analytical expressions for v, i and β in the interval $[t_1, t_2]$ are

$$\begin{aligned} v(t)_{t\in[t_1,t_2]} &= v_{lim}, \\ i(t)_{t\in[t_1,t_2]} &= i_1 + \frac{2\epsilon}{\pi v_{lim}}\left(t - t_1\right), \\ \beta(t)_{t\in[t_1,t_2]} &= \frac{\pi}{2}, \end{aligned} \tag{2.39}$$

where i_1 is the inclination at time t_1

$$i_1 = i(t_1) = i_0 - \frac{2}{\pi}\beta_0 \,. \tag{2.40}$$

The variations of v, i and β in the interval from t_2 to t_f are

$$\begin{aligned} v(t)_{t\in[t_2,t_f]} &= \sqrt{v_{lim}^2 + \epsilon^2\left(t - t_2\right)^2}, \\ i(t)_{t\in[t_2,t_f]} &= i_0 + \frac{2}{\pi}\left(\frac{\pi}{2} - \beta_0\right) + \frac{2\epsilon}{\pi v_{lim}}\left(t_2 - \frac{v_0\cos\beta_0}{\epsilon}\right) + \frac{2}{\pi}\left[\arctan\left(\frac{\epsilon(t-t_2)}{v_{lim}}\right)\right], \\ \beta(t)_{t\in[t_2,t_f]} &= -\frac{v_{lim}}{\epsilon\left(t - t_2\right)} \,. \end{aligned} \tag{2.41}$$

The total ΔV is obtained from the summation of the ΔV for each phase. For the phases from t_0 to t_1 and from t_2 to t_f the ΔV can be obtained from Equation 2.31. For the phase from t_1 to t_2 the ΔV is given by:

$$\Delta V_{t_1,t_2} = \frac{(i_2 - i_1)\pi v_{lim}}{2} \,, \tag{2.42}$$

where i_2 is obtained from Equation 2.41 at $t = t_2$.

2.2.3 Combined variation of semi-major axis and right ascension

Analogously to the transfer presented in Section 2.2.2, it is possible to realise a transfer to change a and Ω, keeping i constant. The derivation for this type of transfer was presented in [107]. In this case the sign of the elevation angle has to be switched at $u = 0$ and $u = \pi$. This results in $\Delta i_{2\pi} = 0$, while the equation for the right ascension is

$$\Delta\Omega_{2\pi} = \frac{\epsilon\, a^2}{\mu \sin i}\left[\int_0^{\pi} \sin u \sin\beta d\mathrm{u} - \int_{\pi}^{2\pi} \sin u \sin\beta d\mathrm{u}\right] \,, \tag{2.43}$$

so that:

$$\overline{\frac{d\Omega}{dt}} = \frac{\Delta\Omega_{2\pi}}{T} = \frac{2\epsilon\sin\beta}{\pi V \sin i} \,. \tag{2.44}$$

The differential equations for the states v and Ω of the problem are, therefore, Equations 2.21 and 2.44. The Hamiltonian for the problem is

$$\mathcal{H} = 1 + \lambda_v\left(-\epsilon\cos\beta\right) + \lambda_\Omega \frac{2\epsilon\sin\beta}{\pi v \sin i} \,. \tag{2.45}$$

Details of the solution of the optimal control problem are given in [107]. The final results are reported hereafter. The elevation angle at the beginning of the transfer can be computed from:

$$\tan\beta_0 = \frac{\sin\left(\frac{\pi}{2}\sin i\Delta\Omega\right)}{\frac{v_0}{v_f} - \cos\left(\frac{\pi}{2}\sin i\Delta\Omega\right)}\,, \tag{2.46}$$

while during the transfer the evolution of β is given by Equation 2.27. The variation of Ω during the transfer is

$$\Omega(t) = \Omega_0 + \frac{2}{\pi\sin i}\left[\arctan\left(\frac{\epsilon t - v_0\cos\beta_0}{v_0\sin\beta_0}\right) + \frac{\pi}{2} - \beta_0\right], \tag{2.47}$$

while the variation of v is given by Equation 2.29. The analytical expression for the ΔV required to realise the transfer is

$$\Delta V = \sqrt{v_0^2 + v_f^2 - 2\,v_f\,v_0\cos\left(\frac{\pi}{2}\sin i\Delta\Omega\right)}\,. \tag{2.48}$$

Figures 2.5 and 2.6 show the ΔV required to change semi-major axis and right ascension for different values of Δa, $\Delta\Omega$, i and initial semi-major axis. The transfer requires higher ΔV when a_0 is lower. Note that when $i = 0$, Ω is not defined and the transfer reduces, therefore, to a variation of semi-major axis.

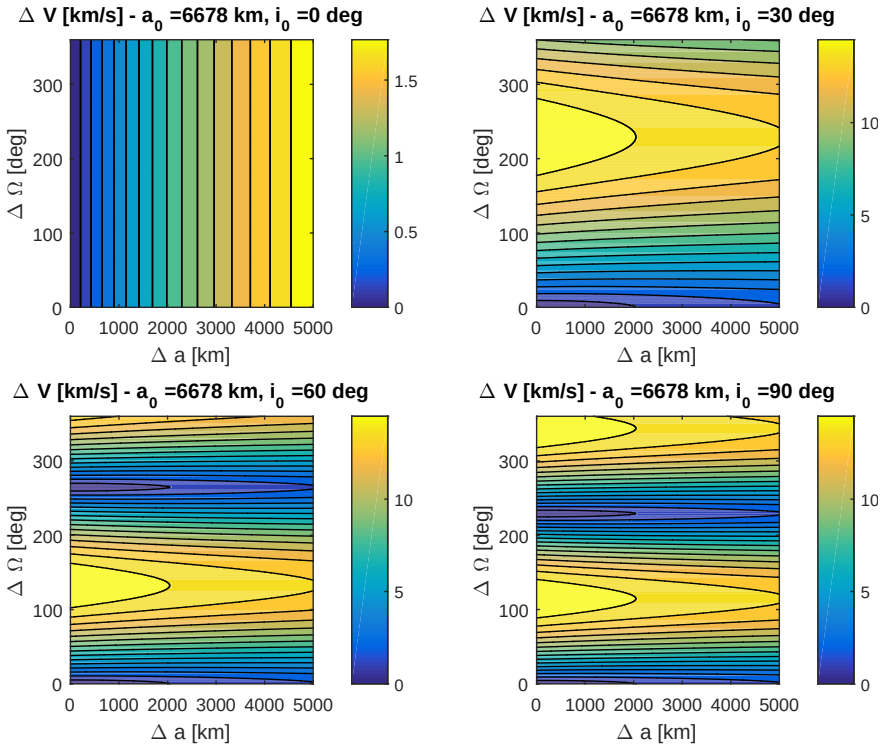

Figure 2.5: ΔV for the variation of a and Ω for different values of Δa, $\Delta\Omega$ and i and for initial semi-major axis equal to 6678 km.

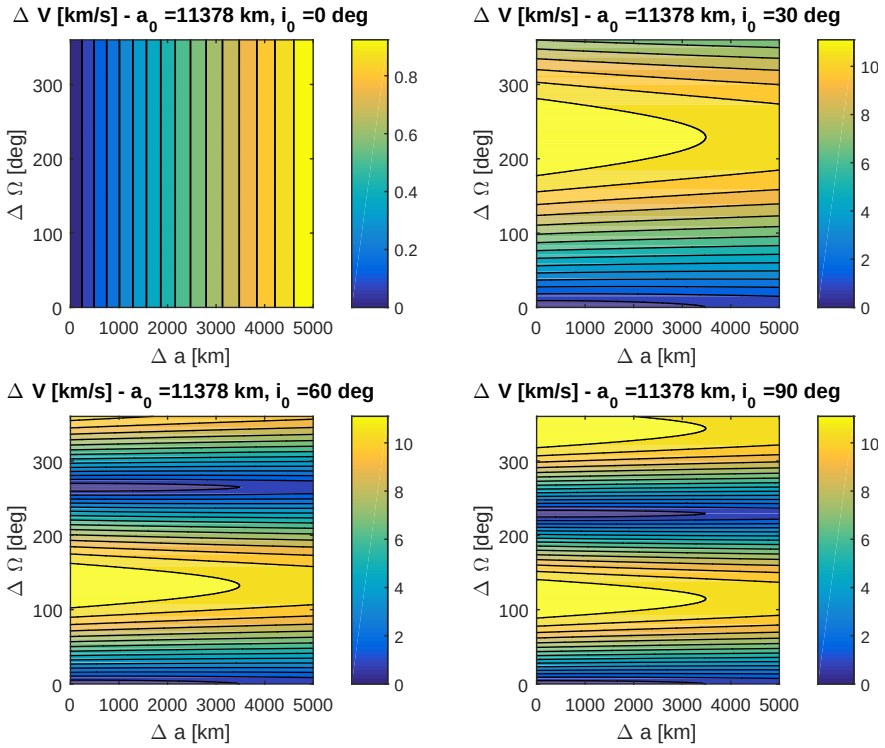

Figure 2.6: ΔV for the variation of a and Ω for different values of Δa, $\Delta\Omega$ and i and for initial semi-major axis equal to 11378 km.

2.2.4 Variation of semi-major axis without variation of eccentricity

In [39], a thrust profile that changes the semi-major axis of non circular orbits, without any variation in the eccentricity, was presented. In order to obtain this thrust profile, the expressions for the variation of the orbital elements with respect to the eccentric anomaly E, rather than the argument of the latitude u, are required. From the Gauss' equation for da/dt (Equation 2.2) it is possible to derive a relationship for da/dE:

$$\frac{da}{dE} = \frac{da}{dt}\frac{dt}{dE} = \frac{2a^{5/2}}{\mu\sqrt{p}}\left[u_R\, a\, e\sqrt{1-e^2}\sin E + u_T\, p\right] . \tag{2.49}$$

Similarly, it is possible to obtain the equations for the variation of the eccentricity with the eccentric anomaly,

$$\frac{de}{dE} = \frac{\sqrt{a\,p}}{\mu}\left[u_R\, a\,\sqrt{1-e^2}\sin E + u_T\, a\,\left(2\cos E - e - e\cos^2 E\right)\right] , \tag{2.50}$$

and, finally, for the argument of the periapsis:

$$\frac{d\omega}{dE} = \frac{a^2\sqrt{1-e^2}}{\mu e}\left\{-u_R\left(\cos E - e\right) + u_T\left[1+\frac{a}{p}\left(1-e\cos E\right)\right]\left(\sqrt{1-e^2}\sin E\right)\right\} + \\ - u_N\frac{a^2\cot i}{\mu\sqrt{1-e^2}}\left\{\sqrt{1-e^2}\cos\omega\sin E\left(1-e\cos E\right) + \sin\omega\left[-e+\cos E\left(1+e^2\right)-e\cos^2 E\right]\right\}\ . \tag{2.51}$$

The variation of a at constant e can be obtained with a radial acceleration that changes sign when $E = 0$ and $E = \pi$ [39]. Integration of the equation for de/dE from 0 to 2π gives, in this case [39] ,

$$\Delta e_{2\pi} = \frac{\sqrt{a\,p}}{\mu}\left[\left(\text{sgn}u_R\right)_{E=\pi/2}4\left|u_T\right|\sqrt{1-e^2} - 3\pi\, e\, u_T\ .\right] \tag{2.52}$$

In order to have zero variation of eccentricity the following relationship has to be satisfied:

$$\frac{|u_R|}{u_T} = \frac{3\pi}{4}\frac{e}{\sqrt{1-e^2}}\ . \tag{2.53}$$

Expressions for u_R and u_T can be obtained using Equation 2.53 and considering $\sqrt{u_R^2+u_T^2} = \epsilon$. The expressions for the angles α and β that satisfy Equation 2.53, not given in [39] and, to the author's best knowledge, not reported in the literature, are

$$\alpha = \left(\text{sgn}\sin E\right)_{E=\pi/2}\arctan\left(\frac{3\pi}{4}\frac{e}{\sqrt{1-e^2}}\right),\ \beta = 0\ . \tag{2.54}$$

By using the expression in Equation 2.53 to derive u_R, it is possible to obtain the equation for the secular variations of a, as reported also in [39]:

$$\overline{\frac{da}{dt}} = \frac{\Delta a_{2\pi}}{T} = \left[\frac{2}{\sqrt{\mu}}\sqrt{1-e^2} + \frac{3e^2}{\sqrt{\mu\left(1-e^2\right)}}\right]a^{3/2}\,u_T\ . \tag{2.55}$$

Analogously, it is possible to verify that:

$$\overline{\frac{de}{dt}} = 0\ . \tag{2.56}$$

The rest of this subsection reports equations that are not available in the literature and that are derived here for the first time. Integration of Equation 2.55 gives:

$$\sqrt{\frac{\mu}{a_0}} - \sqrt{\frac{\mu}{a(t)}} = \frac{1}{2}\left[\frac{2+e^2}{\sqrt{1-e^2}}\right]\,u_T\,t\ , \tag{2.57}$$

from which it is possible to obtain an analytical expression for the variation of a with time, given in Proposition 2.2.3:

Proposition 2.2.3. *The time variation of the semi-major axis during a transfer realised with the control profile defined in Equations 2.53 and 2.54 is:*

$$a(t) = a_0 \left[1 - \sqrt{\frac{a_0}{\mu}} \left(\frac{2+e^2}{2\sqrt{1-e^2}} \right) u_T t \right]^{-2} . \tag{2.58}$$

From the previous equation it is also possible to derive an analytical equation for the cost of the transfer:

Proposition 2.2.4. *The cost of a transfer to change the semi-major axis from a_0 to a_f, while keeping the eccentricity constant, using the control profile defined in Equations 2.53 and 2.54, is:*

$$\Delta V = u_T \, ToF = 2 \left| \sqrt{\frac{\mu}{a_0}} - \sqrt{\frac{\mu}{a_f}} \right| \left[\frac{\sqrt{1-e^2}}{2+e^2} \right] . \tag{2.59}$$

The proposed control law does not cause any variation of the argument of periapsis during the transfer: $\overline{d\omega/dt} = 0$.

2.2.5 Comparison of laws for the variations of semi-major axis

Figure 2.7 compares the cost required for the variation of a using the control laws presented in this section. Note that for $e = 0$, Equations 2.17, 2.31 (with $\Delta i = 0$), 2.48 (with $\Delta\Omega = 0$), and 2.59 are equivalent, therefore they provide the same ΔVs. On the contrary, there is a difference in ΔV when $e \neq 0$. Equations in Section 2.2.2 and 2.2.3 are valid only for $e = 0$, therefore are not included in this comparison. Figure 2.7 shows the difference in ΔV when using Equations 2.17 and 2.59; this difference increase with increasing eccentricity but is however limited to very small values.

2.3 Variation of eccentricity or combination of eccentricity and other orbital elements

In this section, the control laws for the variation of the eccentricity, or combinations of orbital elements including the eccentricity, are presented.

2.3.1 Maximum instantaneous rate of change of eccentricity

The maximum instantaneous rate of change of e is obtained using values of α and β computed from [182]

$$\frac{\partial}{\partial \alpha} \left(\frac{de}{dt} \right) = 0, \; \frac{\partial}{\partial \beta} \left(\frac{da}{dt} \right) = 0 . \tag{2.60}$$

The resulting azimuth and elevation angles are [158]

$$\alpha = \arctan \left(\frac{\sin\theta}{\cos\theta + \cos E} \right), \; \beta = 0 . \tag{2.61}$$

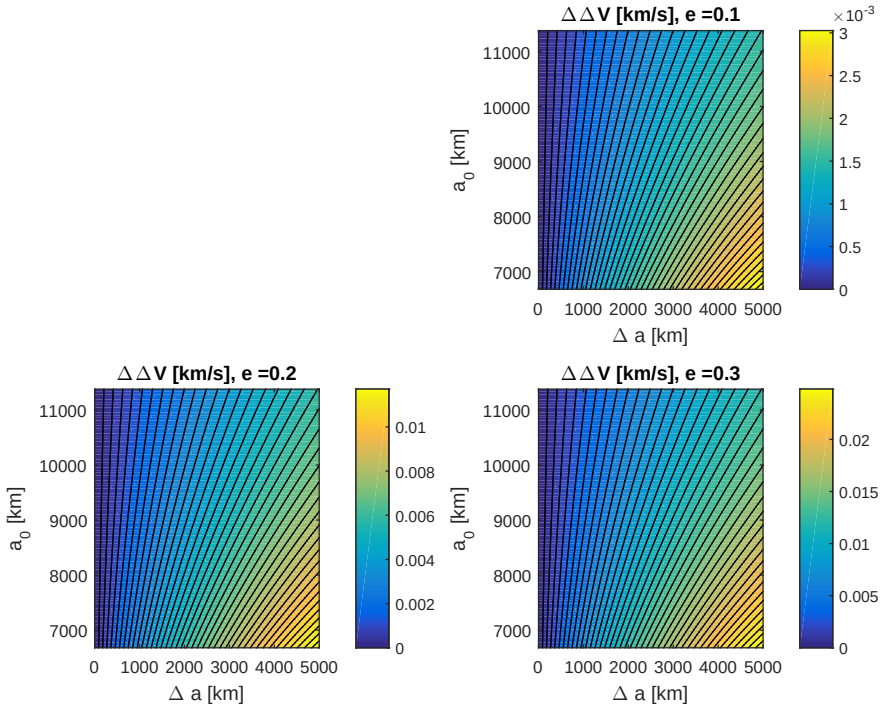

Figure 2.7: $\Delta\Delta V$ for the variation of a for different values of a_0, Δa and for $e \neq 0$ (difference between Equations 2.17 and 2.59 - the order of the difference is ΔV from Equation 2.17 minus ΔV from Equation 2.59).

The equations for the variation of the orbital elements can not be analytically integrated when using the control profile defined in Equation 2.61. Moreover, no analytical expression exists for the cost of the transfer.

2.3.2 Variation of eccentricity without variations of semi-major axis and argument of periapsis

In this section two different strategies are presented to obtain variation of eccentricity without variation of semi-major axis and argument of periapsis. The first one was presented by Pollard [160] and the second one by Burt [39].

Pollard

Pollard presented a strategy to change the eccentricity keeping the semi-major axis constant [160], using thrusting arcs centred at the periapsis and apoapsis of the orbit. For consistency with the rest of this chapter, the equations presented here have been derived for thrust continuously applied over the entire orbit and are, therefore, to be considered as a novel derivation. For more information about the thrusting strategy with thrust at periapsis and apoapsis refer

to [160]. The considered thrust pattern is perpendicular to the major axis of the orbit:

$$\alpha = \begin{cases} \theta & \text{if } e_f > e_0 \\ \pi + \theta & \text{if } e_f < e_0 \end{cases}, \beta = 0, \tag{2.62}$$

where e_0 is the initial eccentricity and e_f is the final eccentricity. Substituting these values for α and β in Equations 2.49 and 2.50 results in:

$$\begin{aligned} \frac{da}{dE} &= \text{sgn}(e_f - e_0)\frac{2\epsilon a^3\sqrt{1-e^2}}{\mu}\cos E, \\ \frac{de}{dE} &= \text{sgn}(e_f - e_0)\frac{\epsilon\, a\sqrt{ap}}{\mu}\left[\frac{-e\cos^3 E + (1+2e^2)\cos^2 E - 3e\cos E + 1}{1 - e\cos E}\right], \\ \frac{d\omega}{dE} &= \text{sgn}(e_f - e_0)\frac{\epsilon a^2}{\mu e}\left(\sin E\cos E - e\sin E\right) . \end{aligned} \tag{2.63}$$

The variations of semi-major axis and argument of periapsis over one orbital period are $\Delta a_{2\pi} = \Delta\omega_{2\pi} = 0$, while the secular variation of the eccentricity is

$$\overline{\frac{de}{dt}} = \text{sgn}(e_f - e_0)\frac{\Delta e_{2\pi}}{T} = \text{sgn}(e_f - e_0)\frac{3}{2}\epsilon\sqrt{\frac{p}{\mu}} . \tag{2.64}$$

The variation of eccentricity with time is reported in Proposition 2.3.1.

Proposition 2.3.1. *The variation of eccentricity with time, when using the control profile defined in Equation 2.62 to change the eccentricity without variations of the semi-major axis, is:*

$$e(t) = e_0 + sgn(e_f - e_0)\sin\left(\frac{3}{2}\sqrt{\frac{a}{\mu}}\epsilon\, t\right) . \tag{2.65}$$

Integration of Equation 2.65 from e_0 to e_f provides the ΔV required to realise the transfer:

Proposition 2.3.2. *The cost of the transfer to change the eccentricity from e_0 to e_f, using the control profile defined in Equation 2.62, is:*

$$\Delta V = \frac{2}{3}\sqrt{\frac{\mu}{a}}\left|\arcsin e_f - \arcsin e_0\right| . \tag{2.66}$$

Burt

In the work of Burt [39], it was proposed to change e, without variations of a and ω, using a transverse acceleration u_T reversed in sign when $E = \pm\pi/2$ (crossing of the minor axis) [39]. The corresponding thrust angles are, therefore

$$\alpha = \begin{cases} \begin{cases} 0 & \text{for } -\frac{\pi}{2} \le E < \frac{\pi}{2} \\ \pi & \text{for } \frac{\pi}{2} \le E < \frac{3\pi}{2} \end{cases} & \text{if } e_f > e_0 \\ \begin{cases} \pi & \text{for } -\frac{\pi}{2} \le E < \frac{\pi}{2} \\ 0 & \text{for } \frac{\pi}{2} \le E < \frac{3\pi}{2} \end{cases} & \text{if } e_f < e_0 \end{cases}, \quad \beta = 0 . \tag{2.67}$$

The variations of the orbital elements over one orbital period are

$$\begin{aligned} \Delta a_{2\pi} &= \Delta\omega_{2\pi} = 0, \\ \Delta e_{2\pi} &= \text{sgn}\,(e_f - e_0)\,\frac{8a^2\sqrt{1-e^2}\epsilon}{\mu}\,. \end{aligned} \tag{2.68}$$

It is possible to obtain an analytical expression for the variation of e with time. The secular rate of change is

$$\overline{\frac{de}{dt}} = \frac{\Delta e_{2\pi}}{T} = \text{sgn}\,(e_f - e_0)\,\frac{4}{\pi}\sqrt{\frac{a}{\mu}}\sqrt{1-e^2}\epsilon\,. \tag{2.69}$$

Integration of the previous expression results in:

$$e(t) = e_0 + \text{sgn}\,(e_f - e_0)\sin\left[\frac{4}{\pi}\sqrt{\frac{a}{\mu}}\epsilon\,t\right]\,. \tag{2.70}$$

The cost of the transfer, not explicitly reported in [39], can be analytically obtained from Proposition 2.3.3.

Proposition 2.3.3. *The cost of a transfer to change the eccentricity from e_0 to e_f, without variations of a and ω and using the control profile defined in Equation 2.67, is:*

$$\Delta V = \epsilon\, ToF = \frac{\pi}{4}\sqrt{\frac{\mu}{a}}\,|\arcsin e_f - \arcsin e_0|\,. \tag{2.71}$$

2.3.3 Combined variation of eccentricity and inclination without variation of other orbital elements

According to Pollard [160], the simultaneous variation of e and i can be obtained using:

$$\alpha = \begin{cases} \theta & \text{if } e_f > e_0 \\ \pi + \theta & \text{if } e_f < e_0 \end{cases}\quad,\quad \beta = \begin{cases} \text{sgn}\,(\Delta i)\,|\beta| & \text{if } -\frac{\pi}{2} \le E < \frac{\pi}{2} \\ -\text{sgn}\,(\Delta i)\,|\beta| & \text{if } \frac{\pi}{2} \le E < \frac{3\pi}{2} \end{cases}\,. \tag{2.72}$$

In [160], the equations for this transfer are derived for thrust applied on arcs centered at the periapsis and apoapsis of the orbit. In this thesis, instead, continuous thrust applied over the entire orbit is considered. The derivation of the following equations is therefore novel, but the final results are equivalent to the one presented in [160], if the two arcs have span angle equal to π. The equations for the secular variation of a, e and ω are derived from the results presented in the previous section, with the addition of the term $\cos\beta$ in the expressions for u_R and u_T and considering the addition of the term due to u_N in $\overline{d\omega/dt}$:

$$\begin{aligned} \overline{\frac{da}{dt}} &= 0, \\ \overline{\frac{de}{dt}} &= \frac{\Delta e_{2\pi}}{T} = \text{sgn}(e_f - e_0)\frac{3}{2}\epsilon\cos\beta\sqrt{\frac{p}{\mu}}, \\ \overline{\frac{d\omega}{dt}} &= -\sqrt{\frac{a}{\mu}}\frac{\epsilon\sin\beta\cot i\sin\omega}{\pi\sqrt{1-e^2}}2(1+e^2)\,. \end{aligned} \tag{2.73}$$

The variation of the inclination with the eccentric anomaly is

$$\frac{di}{dE} = \frac{\epsilon \sin\beta a^2}{\mu\sqrt{1-e^2}} \left\{ \cos E \left[-e + \cos E \left(1+e^2\right) - e\cos^2 E \right] - \sqrt{1-e^2}\sin\omega \sin E \left(-e\cos E\right) \right\} . \tag{2.74}$$

It is possible to derive the secular variation of i by integrating the previous expression from 0 to 2π, changing sign of β at the minor axis crossing:

$$\overline{\frac{di}{dt}} = \frac{\Delta i_{2\pi}}{T} = \frac{\epsilon \sin\beta}{\pi}\sqrt{\frac{a}{\mu}}\cos\omega \frac{2(1+e^2)}{\sqrt{1-e^2}} . \tag{2.75}$$

Combining the equations for the secular variations of eccentricity and inclination provides:

$$\overline{\frac{di}{de}} = \text{sgn}(e_f - e_0)\frac{4}{3\pi}\frac{1+e^2}{1-e^2}\tan\beta\cos\omega . \tag{2.76}$$

It is possible to integrate the previous equation from i_0 to i_f and from e_0 to e_f, under the assumption that ω and β are both constant. This is true when $\sin\omega = 0$ (see Equation 2.73 for $d\overline{\omega}/dt$), that is when $\omega = 0$ or $\omega = \pi$. The integration provides an expression for the value of β:

$$\tan\beta = \text{sgn}(e_f - e_0)\frac{3\pi}{4}\frac{i_f - i_0}{\cos\omega}\left[\log\frac{(1+e_f)(1-e_0)}{(1-e_f)(1+e_0)} - e_f + e_0\right]^{-1} . \tag{2.77}$$

The equation for the variation of the eccentricity with time is similar to Equation 2.65, but for the term in β:

$$e(t) = \sin\left(\arcsin e_0 + \text{sgn}(e_f - e_0)\frac{3}{2}\cos\beta\sqrt{\frac{a}{\mu}}\epsilon t\right) . \tag{2.78}$$

From $\overline{di/dt}$ is possible to find an expression for the variation of the inclination i with time, according to Proposition 2.3.4.

Proposition 2.3.4. *The variation of inclination with time, for a transfer to change the eccentricity from e_0 to e_f and to change the inclination from i_0 to i_f, using the control profile defined in Equations 2.72 and 2.77 is:*

$$\begin{aligned} i(t) =& i_0 + \frac{4}{3}\frac{\cos\omega\tan\beta}{\pi}\left[2\log\left(\frac{\cos\left(\frac{\arcsin e_0}{2}\right) - \sin\left(\frac{\arcsin e_0}{2}\right)}{\cos\left(\frac{\arcsin e_0}{2}\right) + \sin\left(\frac{\arcsin e_0}{2}\right)}\right) + e_0 + \right. \\ & \left. -2\log\left(g(e_0,\beta,\epsilon,a,t)\right) + \sin\left(\arcsin e_0 + \frac{3}{2}\cos\beta\epsilon\sqrt{\frac{a}{\mu}}t\right)\right] , \end{aligned} \tag{2.79}$$

where

$$g(e_0,\beta,\epsilon,a,t) = \frac{\cos\left[\frac{1}{4}\left(2\arcsin e_0 + 3\cos\beta\epsilon\sqrt{\frac{a}{\mu}}t\right)\right] - \sin\left[\frac{1}{4}\left(2\arcsin e_0 + 3\cos\beta\epsilon\sqrt{\frac{a}{\mu}}t\right)\right]}{\cos\left[\frac{1}{4}\left(2\arcsin e_0 + 3\cos\beta\epsilon\sqrt{\frac{a}{\mu}}t\right)\right] + \sin\left[\frac{1}{4}\left(2\arcsin e_0 + 3\cos\beta\epsilon\sqrt{\frac{a}{\mu}}t\right)\right]} . \tag{2.80}$$

Note that an analytic equation for $i(t)$, corresponding to Equation 2.79, was not derived in [160]. The cost of the transfer is similar to the one given in Equation 2.66, but for the term in

β:

Proposition 2.3.5. *The cost of a transfer to change the eccentricity from e_0 to e_f and to change the inclination from i_0 to i_f, using the control profile defined in Equations 2.72 and 2.77 is:*

$$\Delta V = \frac{2}{3}\sqrt{\frac{\mu}{a}}\frac{|\arcsin e_f - \arcsin e_0|}{\cos\beta} \,. \tag{2.81}$$

It has to be stressed that this control law and the corresponding transfer are valid only when there is a non-zero change of eccentricity, because $\beta = 0$ when $e_0 = e_f$. Therefore, this thrust profile can not be used to obtain a pure variation of inclination. Despite the presence of an out-of-plane component, this thrust profile causes no variation of the right ascension. The expression for the variation of the right ascension with the eccentric anomaly is [160]

$$\frac{d\Omega}{dE} = \frac{u_N a^2}{\mu}\frac{(1 - e\cos E)}{\sin i}\left[\sin E\cos\omega + \frac{(\cos E - e)}{\sqrt{1-e^2}}\sin\omega\right] \,. \tag{2.82}$$

Integration over one orbital period, with β changing sign at the minor axis crossing, results in $\Delta\Omega_{2\pi} = 0$.

2.3.4 Comparison of laws for the variation of e only

Figures 2.8 and 2.9 show the ΔV required for the variation of e without variation of semi-major axis. In particular, Figure 2.8 shows the ΔV relative to the thrust profile defined by Burt (Equation 2.71) and Figure 2.9 shows the ΔV relative to the thrust profile defined by Pollard (Equation 2.66). As shown, the cost is higher when the thrust profile defined by Burt is used. This is evident in Figure 2.10, where the difference is represented. It is also noted that the difference in ΔV decreases with increasing semi-major axis.

2.4 Variation of inclination

The maximum instantaneous variation of inclination is obtained using [182]

$$|\beta| = \frac{\pi}{2} \,. \tag{2.83}$$

Because of the term $\cos u$ in the Gauss' equation for di/dt, it follows that in order to obtain a non zero variation of inclination, β has to change sign at $u = \pi/2$ and $u = 3\pi/2$. Equation 2.83 can therefore be rewritten as

$$\beta = \text{sgn}\left(\cos u\right)\text{sgn}\left(i_f - i_0\right)\frac{\pi}{2} \,. \tag{2.84}$$

Because of the term in $\sin u$ in the equation for $d\Omega/dt$, this thrust profile causes no variation of right ascension. There is, however, a variation of ω due to β. No simple expression is available for the variation of ω and i with time when $e \neq 0$.

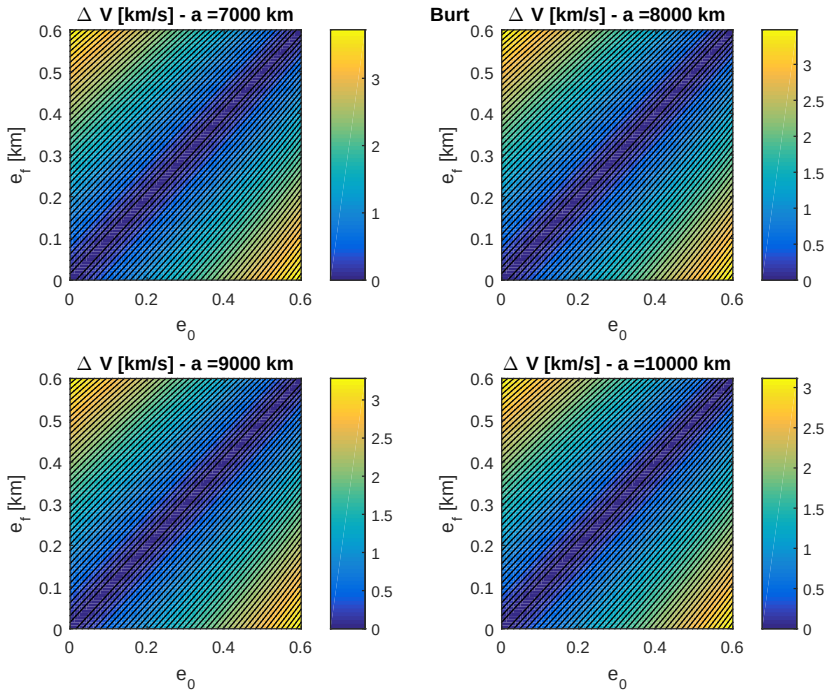

Figure 2.8: ΔV for the variation of e for different values of e_0, e_f and a - Burt.

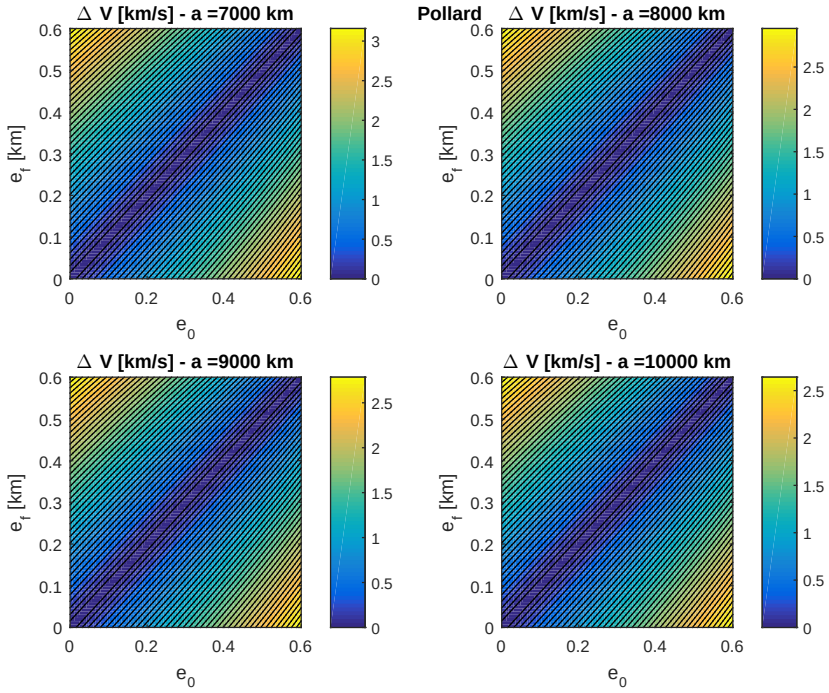

Figure 2.9: ΔV for the variation of e for different values of e_0, e_f and a - Pollard.

For $e = 0$, instead, it is possible to find analytical equations for the variation of the orbital elements and for the cost of the transfer. To the author's knowledge, the analytic equations

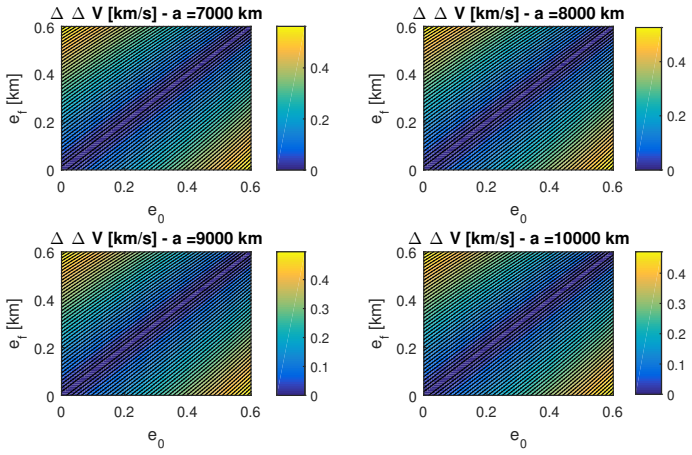

Figure 2.10: Difference in ΔV between Burt's and Pollard's laws for the variation of e for different values of e_0, e_f and a. The order of the difference is Burt minus Pollard.

derived hereafter are not present in the literature. The variation with time of the inclination is

$$\overline{\frac{di}{dt}} = \text{sgn}(i_f - i_0) 2 \frac{\epsilon}{\pi} \sqrt{\frac{a}{\mu}} \, . \tag{2.85}$$

Integration of Equation 2.85 gives the expression for the variation of the inclination with time.

Proposition 2.4.1. *The variation with time of the inclination for a transfer following the control profile defined in Equation 2.84 is*

$$i(t) = i_0 + sgn(i_f - i_0) \frac{2\epsilon}{\pi} \sqrt{\frac{a}{\mu}} t \, . \tag{2.86}$$

Proposition 2.4.2. *The cost of the transfer to change the inclination by Δi following the control profile defined in Equation 2.84 is given by:*

$$\Delta V = \frac{\pi}{2} \sqrt{\frac{\mu}{a}} \Delta i \, . \tag{2.87}$$

It is important to stress that the ΔV in Equation 2.87 is different from the one defined in Section 2.2.2 (Equation 2.31) when using $a_f = a_0$. The reason is that in this case $\beta = \pi/2$ during the entire transfer, while in Section 2.2.2 a variable profile for β is defined, such that the transfer can be realised in the minimum time. Moreoever, for the transfer defined in Section 2.2.2, even when $a_f = a_0$, a is not constant during the transfer. This is not the case here, where $a(t) = a_0 \ , \forall t \in [t_0, t_f]$. Figure 2.11 shows the ΔV necessary for a change of inclination at different values of semi-major axis when considering Equation 2.87 and Equation 2.31. The control profile defined in Section 2.2.2 gives lower ΔV.

The difference in the cost ΔV between these two thrusting strategies is shown in Figure 2.12

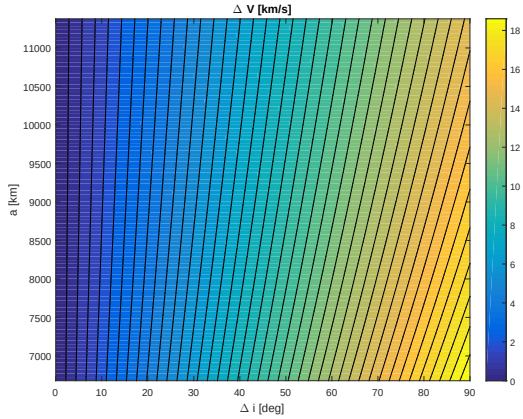

(a) Maximum instantaneous variation of i (Equation 2.87)

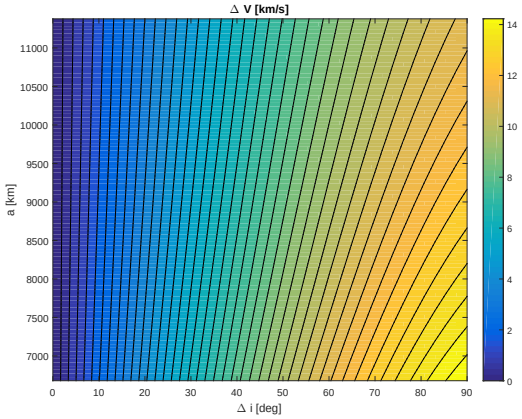

(b) Edelbaum's law for the combined variation of a and i (Equation 2.31)

Figure 2.11: ΔV for the variation of i for different values of a (Equations 2.87 and 2.31).

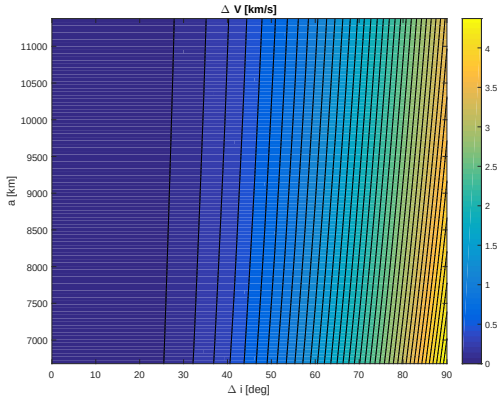

Figure 2.12: $\Delta\Delta V$ for the variation of i for different values of a (difference between ΔV from Equation 2.87 and ΔV from Equation 2.31).

2.5 Variation of right ascension of the ascending node

Considering the Gauss' equation for $d\Omega/dt$, the instantaneous maximum variation of Ω is obtained using

$$\beta = \text{sgn}(\Omega_f - \Omega_0)\text{sgn}\left(\sin u\right)\frac{\pi}{2}\,. \tag{2.88}$$

This control pattern does not cause variation of i. No analytical expressions are available for the time variation of Ω and ω under this control law, in the general case $e \neq 0$. Analytical equations are available when $e = 0$. In this case:

$$\overline{\frac{d\Omega}{dt}} = \text{sgn}(\Omega_f - \Omega_0)\frac{2\epsilon}{\pi}\sqrt{\frac{a}{\mu}}\frac{1}{\sin i}\,. \tag{2.89}$$

The expression for $\Omega(t)$, obtained from Equation 2.89, is given in Proposition 2.5.1.

Proposition 2.5.1. *The time variation of Ω for a transfer to change the right ascension from Ω_0 to Ω_f, using the control profile defined in Equation 2.88, is:*

$$\Omega(t) = \Omega_0 + sgn(\Omega_f - \Omega_0)\frac{2\epsilon}{\pi}\sqrt{\frac{a}{\mu}}\frac{1}{\sin i}t \,. \tag{2.90}$$

To the author's best knowledge, Equation 2.90 is not available in the literature. The cost of the transfer is [182]

$$\Delta V = \frac{\pi}{2}\sqrt{\frac{\mu}{a}}\Delta\Omega \sin i \,. \tag{2.91}$$

Figure 2.13 shows the ΔV necessary for a change of right ascension at different values of semi-major axis and inclination for a circular orbit. For a given $\Delta\Omega$, the cost is higher at higher inclinations and lower at higher values of the semi-major axis.

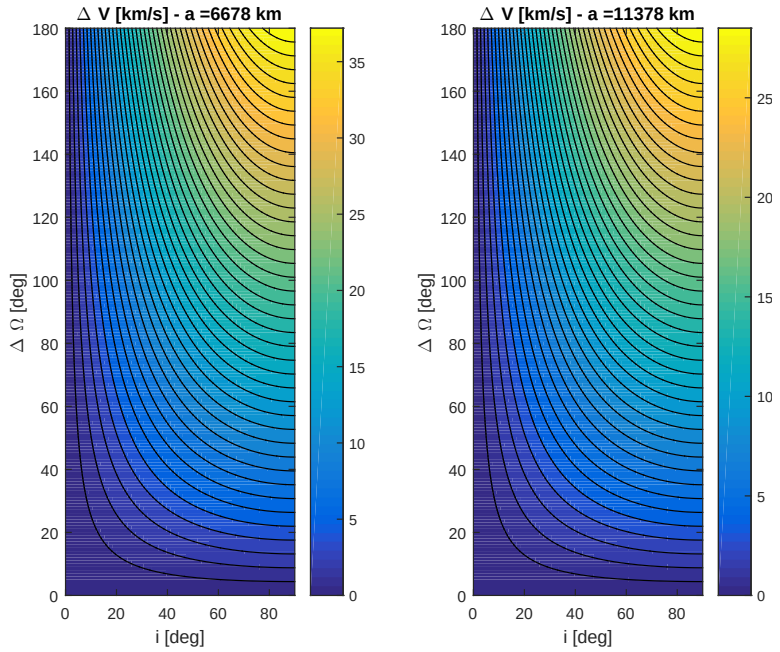

Figure 2.13: ΔV for the variation of Ω for different values of i and a, using the thrust profile for maximum instantaneous variation of Ω.

As a comparison, Figure 2.14 shows the ΔV for the same transfers, obtained using the thrust law given in Section 2.2.3, with $a_0 = a_f$. In this case the ΔV cost is lower.

2.6 Variation of argument of the periapsis

Different laws are available in the literature for the variation of the argument of periapsis. They are presented in this section.

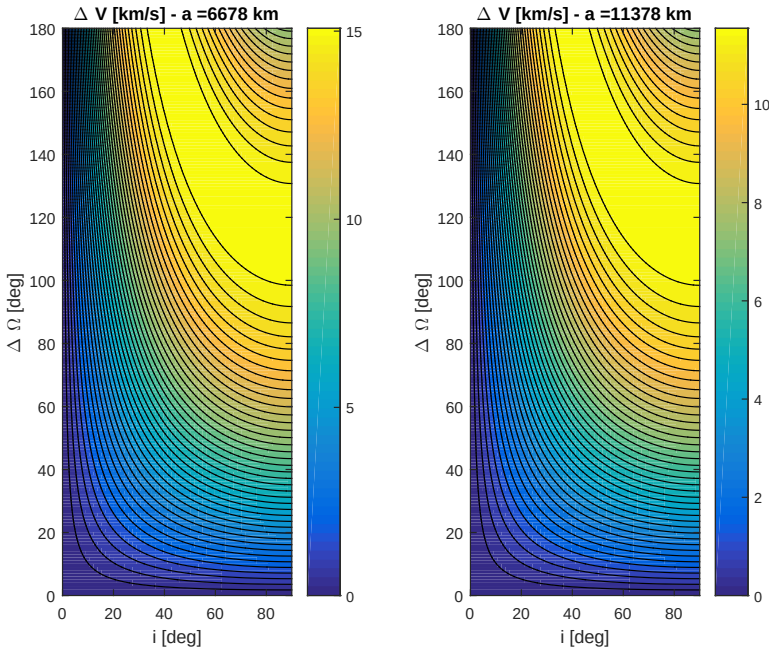

Figure 2.14: ΔV for the variation of Ω for different values of i and a - Section 2.2.3

2.6.1 Maximum instantaneous variation of argument of the periapsis

The thrust angles for the maximum instantaneous variation of ω can be found by deriving $d\omega/dt$ with respect to α and β.

In-plane acceleration

In [158], the case in which $u_N = 0$ was considered. Since β is not defined, the only equation to consider is, therefore,

$$\frac{d}{d\alpha}\frac{d\omega}{dt} = 0\,. \tag{2.92}$$

The following azimuth angle satisfies the previous equation [158, 182]

$$\alpha = \arctan\left(-\frac{1+e\cos\theta}{2+e\cos\theta}\cot\theta\right)\,. \tag{2.93}$$

No analytical equations for the cost of the transfer and the variation of orbital elements can be derived using this value of α.

In-plane and out-of-plane acceleration

If the change of argument of periapsis is realised by means of both in-plane and out-of-plane accelerations, the full set of equations to find the optimal values of α and β is

$$\frac{\partial}{\partial\alpha}\frac{d\omega}{dt} = 0,\ \frac{\partial}{\partial\beta}\frac{d\omega}{dt} = 0\,. \tag{2.94}$$

The equation for α gives the same value defined in Equation 2.93 while the elevation angle is [182]

$$\tan\beta = \frac{e\sin(\theta+\omega)\cot i}{(1+e\cos\theta)\sin(\alpha-\theta)-\sin\theta\cos\alpha} \,. \tag{2.95}$$

These expressions for α and β do not allow to derive analytical equations for the variation of the orbital elements and for the cost of the transfer.

2.6.2 Variation of argument of the periapsis without variation of semi-major axis and eccentricity

The next subsections present thrust profiles that cause changes in the argument of the periapsis while keeping the semi-major axis and eccentricity constant.

Transverse acceleration

It is possible to change ω, without variations of a and e, by using a thrust with non-zero component of the transverse component u_T, reversed in sign at the major axis crossing [39]. The following corresponding expressions for α and β are not reported in [39]:

$$\alpha,\beta = \begin{cases} \alpha = \begin{cases} 0 & \text{for } 0 \le E < \pi \\ \pi & \text{for } \pi \le E < 2\pi \end{cases}, \beta = 0 & \text{if } \mathrm{sgn}(\omega_f-\omega_0) > 0 \,, \\ \alpha = \begin{cases} \pi & \text{for } 0 \le E < \pi \\ 0 & \text{for } \pi \le E < 2\pi \end{cases}, \beta = 0 & \text{if } \mathrm{sgn}(\omega_f-\omega_0) < 0 \,. \end{cases} \tag{2.96}$$

If u_T is reversed in sign at the major axis crossing (that is, at $E = 0$ and $E = \pi$), Equations 2.49 and 2.50 give

$$\overline{\frac{da}{dt}} = \overline{\frac{de}{dt}} = 0 \,, \tag{2.97}$$

while, for the argument of periapsis [39]

$$\overline{\frac{d\omega}{dt}} = \mathrm{sgn}(\omega_f-\omega_0)\frac{2}{\pi}\sqrt{\frac{a}{\mu}}\frac{(2-e^2)}{e}\epsilon \,. \tag{2.98}$$

The following analytical expressions for the time variation of ω and for the cost of the transfer are not reported in [39] or, to the author's best knowledge, anywhere else in the literature. Integration of Equation 2.98 gives a linear variation of ω with time, as shown in Proposition :

Proposition 2.6.1. *The variation of ω with time, for a transfer to change the argument of periapsis from ω_0 to ω_f, keeping a and e constant, and following the control profile defined in Equation 2.96, is*

$$\omega(t) = \omega_0 + sgn(\omega_f-\omega_0)\frac{2}{\pi}\sqrt{\frac{a}{\mu}}\frac{(2-e^2)}{e}\epsilon\, t \,. \tag{2.99}$$

Proposition 2.6.2. *The cost required for a transfer to change the argument of periapsis from ω_0 to ω_f,*

keeping a and e constant, and following the control profile defined in Equation 2.96, is

$$\Delta V = \frac{\pi}{2}\sqrt{\frac{\mu}{a}}\frac{e}{(2-e^2)}\left|\omega_f - \omega_0\right| \ . \tag{2.100}$$

Radial acceleration

Another possible thrust profile that changes ω while keeping a and e constant is the unidirectional radial acceleration [39]:

$$\alpha = \begin{cases} \pi/2 & \text{if } \omega_f > \omega_0 \\ 3\pi/2 & \text{if } \omega_f < \omega_0 \end{cases} \ , \ \beta = 0 \ . \tag{2.101}$$

The secular variations of a and e are $\overline{da/dt} = \overline{de/dt} = 0$ while

$$\overline{\frac{d\omega}{dt}} = \text{sgn}(\omega_f - \omega_0)\sqrt{\frac{p}{\mu}}\epsilon \ . \tag{2.102}$$

The following analytical expressions for the time variation of ω and for the cost of the transfer, under the control law defined in Equation 2.101, are not reported in [39].

Proposition 2.6.3. *The variation with time of the argument of periapsis ω for a transfer to go from ω_0 to ω_f, with no variations of a and e, and using the control profile defined in Equation 2.101 is:*

$$\omega(t) = \omega_0 + sgn(\omega_f - \omega_0)\sqrt{\frac{p}{\mu}}\epsilon t \ . \tag{2.103}$$

Proposition 2.6.4. *The cost of a transfer to go from ω_0 to ω_f, with no variations of a and e, and using the control profile defined in Equation 2.101 is:*

$$\Delta V = \sqrt{\frac{\mu}{p}}\left|\omega_f - \omega_0\right| \ . \tag{2.104}$$

Acceleration parallel to the major axis of the ellipse

The last proposed thrusting strategy that changes ω without variations of a and e is identified in [160] as an in-plane acceleration parallel to the major axis of the ellipse:

$$\begin{aligned} u_R &= -\text{sgn}(\omega_f - \omega_0)\epsilon\frac{(\cos E - e)}{1 - e\cos E} = -\text{sgn}(\omega_f - \omega_0)\epsilon\cos\theta, \\ u_T &= \text{sgn}(\omega_f - \omega_0)\epsilon\frac{\sqrt{1-e^2}\sin E}{1 - e\cos E} = \text{sgn}(\omega_f - \omega_0)\epsilon\sin\theta, \\ u_N &= 0 \ . \end{aligned} \tag{2.105}$$

This results in the following azimuth and elevation angles:

$$\tan\alpha = -\cot\theta, \ \beta = 0 \ . \tag{2.106}$$

The derivation in [160] considers thrust applied at the periapsis and apoapsis of the orbit. In the following, in order to be consistent with the rest of the chapter, equations are derived for the case of thrust applied over the entire orbit. Using Equations 2.49 and 2.50 it is possible to find that, with this thrust profile, the secular variations of semi-major axis and eccentricity are

$$\overline{\frac{da}{dt}} = \overline{\frac{de}{dt}} = 0 \, . \tag{2.107}$$

The following holds for the argument of the periapsis (Equation 2.51):

$$\overline{\frac{d\omega}{dt}} = \text{sgn}(\omega_f - \omega_0) \frac{3\epsilon}{2e} \sqrt{\frac{p}{\mu}} \tag{2.108}$$

Equation 2.108 can be also obtained from the corresponding equation given in [160], considering two thrust arcs at periapsis and apoapsis, of amplitude π. The following equations for the time variation of ω and for the cost of the transfer are, instead, not reported in [160].

Proposition 2.6.5. *The time variation of ω for a transfer to go from ω_0 to ω_f, while keeping a and e constant, using the control profile of Equation 2.106, is:*

$$\omega(t) = \omega_0 + sgn(\omega_f - \omega_0) \frac{3\epsilon}{2e} \sqrt{\frac{p}{\mu}} t \, . \tag{2.109}$$

Proposition 2.6.6. *The cost of a transfer to go from ω_0 to ω_f, while keeping a and e constant, using the control profile of Equation 2.106, is:*

$$\Delta V = \frac{2e}{3} \sqrt{\frac{\mu}{p}} \left| \Delta\omega \right| \, . \tag{2.110}$$

2.6.3 Comparison of laws for the variation of argument of the periapsis

The following figures show the ΔV cost for the variation of ω for the control laws defined in Subsection 2.6.2, for different values of $\Delta\omega$, e and a. Figures 2.15 and 2.16 show the results for transverse and radial low-thrust acceleration, respectively, as proposed in [39]. Figure 2.17 presents instead the results for the case of low-thrust acceleration parallel to the major axis of the ellipse.

Results show that the law with acceleration parallel to the major axis of the ellipse is the most advantageous one in terms of ΔV, while the law with radial acceleration is the most expensive.

2.7 Summary

Table 2.1 summarises the control laws presented in this chapter for the orbit transfer from $(a_0, e_0, i_0, \Omega_0, \omega_0)$ to $(a_f, e_f, i_f, \Omega_f, \omega_f)$. For each control law, the number of the equations which give the thrust angles, the time evolution of the orbital elements and the ΔV are given. When an orbital element do not change during the transfer this is directly reported in

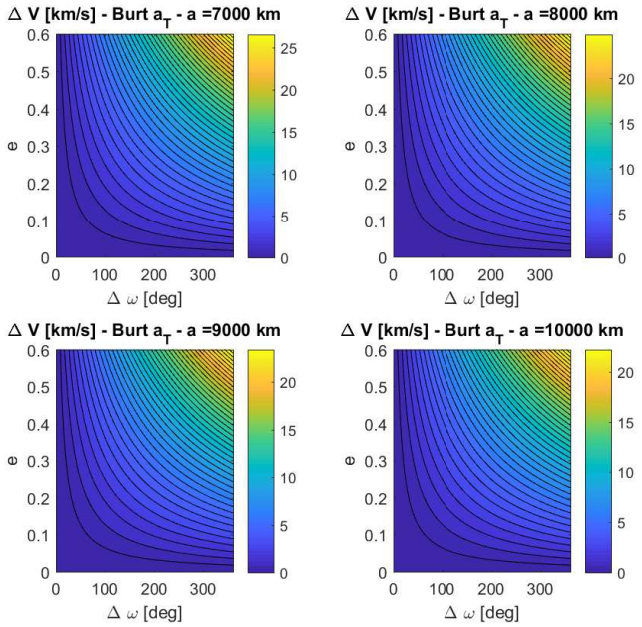

Figure 2.15: ΔV for the variation of ω at constant a and e for different values of $\Delta\omega$, e and a using transverse acceleration.

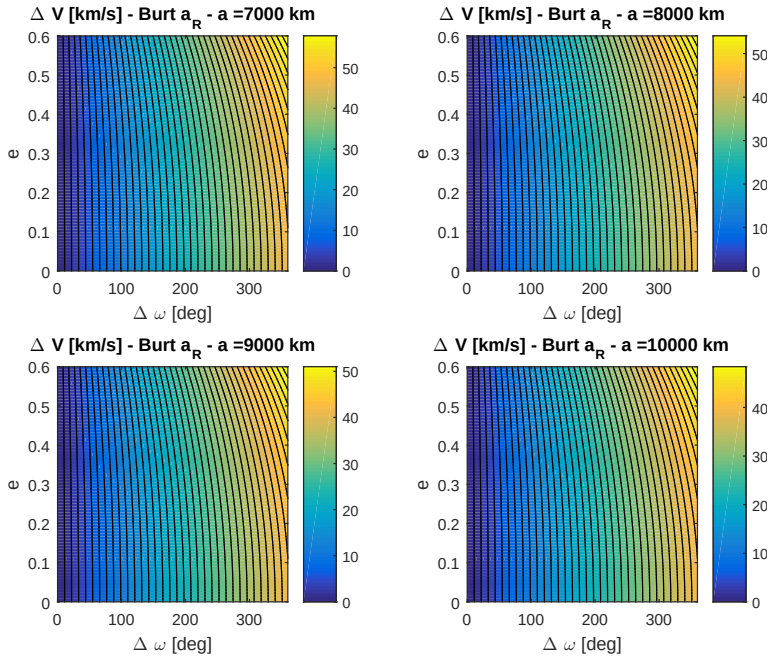

Figure 2.16: ΔV for the variation of ω at constant a and e for different values of $\Delta\omega$, e and a using radial acceleration.

the table giving its initial value. The last column gives the number of the section where the control law is described in details. N.A. stands for either not available or not applicable. Table

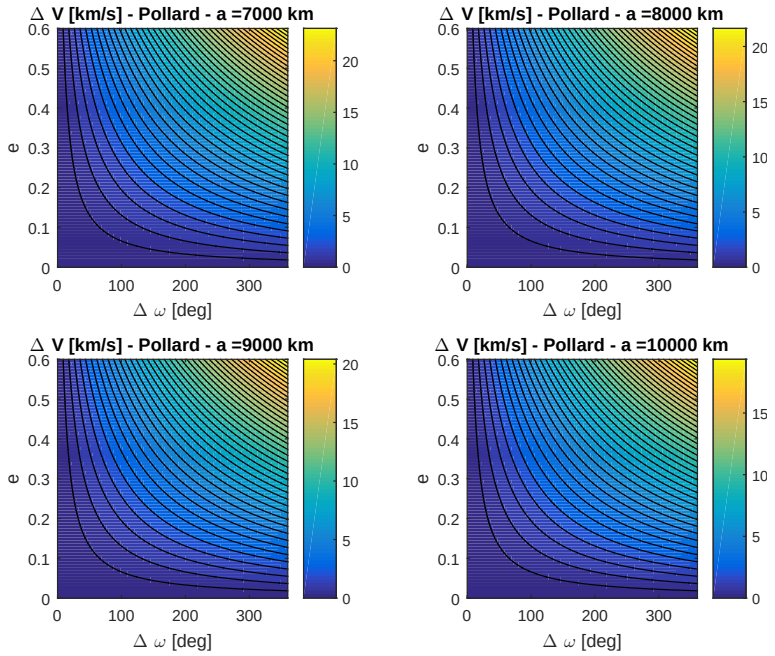

Figure 2.17: ΔV for the variation of ω at constant a and e for different values of $\Delta\omega$, e and a using acceleration parallel to the major axis of the ellipse.

2.2 shows, for each control law, if the control was obtained solving an optimal control problem (OCP) or computing the maximum instantanoues rate of change of the orbital elements. It shows, moreover, which orbital elements are to be changed and which ones stay constant during the transfer. The last column reports if new analytical equations were derived in this thesis.

The control laws presented in this chapter represent a low-fidelity tool for the estimation of the cost of low-thrust transfers and do not take into account the presence of perturbations to the Keplerian orbital motion of the spacecraft. Perturbations could however produce significant variations in the orbital elements' profile. The objective of the next chapter (Chapter 3) is to present novel laws for the fast estimation of the cost of a low-thrust transfer in Earth's orbit under the effect of geopotential perturbation.

Table 2.1: Summary of low-thrust control laws.

		α	β	$a(t)$	$e(t)$	$i(t)$	$\Omega(t)$	$\omega(t)$	ΔV	Section
	Semi-major axis									
1	Max variation a	2.6	2.6	N.A.	N.A.	i_0	Ω_0	N.A.	N.A.	2.2.1
2	Max variation a, $e = 0$	2.6	2.6	2.16	N.A.	i_0	Ω_0	N.A.	2.17	2.2.1
3	Δa, Δi, $e_0 = 0$	2.6	2.27	2.29	e_0	2.30	Ω_0	-	2.31	2.2.2
4	Δa, Δi, $e = 0$, $a \leq a_{lim}$	2.6	2.38-2.41	2.38-2.41	e_0	2.38-2.41	Ω_0	-		2.2.2
5	Δa, $\Delta\Omega$, $e = 0$	2.6	2.27	2.29	e_0	i_0	2.47	-	2.48	2.2.3
6	Δa, $\Delta e = \Delta\omega = 0$	2.54	2.54	2.58	e_0	i_0	Ω_0	ω_0	2.59	2.2.4
	Eccentricity									
7	Max variation e	2.61	2.61	N.A.	N.A.	i_0	Ω_0	N.A.		2.3.1
8	Δe, $\Delta a = \Delta\omega = 0$, Burt	2.67	2.67	a_0	2.70	i_0	Ω_0	ω_0	2.71	2.3.2
9	Δe, $\Delta a = \Delta\omega = 0$, Pollard	2.62	2.62	a_0	2.65	i_0	Ω_0	ω_0	2.66	2.3.2
10	Δe, Δi, $\Delta a = 0$	2.72	2.77	a_0	2.78	i_0	Ω_0	2.79	2.81	2.3.3
	Inclination									
11	Max variation i, $e \neq 0$	N.A.	2.84	a_0	e_0	N.A.	Ω_0	N.A.	N.A.	2.4
12	Max variation i, $e = 0$	N.A.	2.84	a_0	e_0	2.86	Ω_0	-	2.87	2.4
	Right ascension of the ascending node									
13	Max variation Ω, $e \neq 0$	N.A.	2.88	a_0	e_0	i_0	N.A.	N.A	N.A	2.5
14	Max variation Ω, $e = 0$	N.A.	2.88	a_0	e_0	i_0	2.90	-	2.91	2.5
	Argument of the periapsis									
15	Max variation ω, Petropolous [158]	2.93	0	N.A.	N.A.	i_0	Ω_0	N.A.	N.A.	2.6.1
16	Max variation ω, Ruggiero [182]	2.93	2.95	N.A.	N.A.	N.A.	N.A.	N.A.	N.A.	2.6.1
17	$\Delta\omega$, $\Delta a = \Delta e = 0$, Burt 1 [39]	2.96	2.96	a_0	e_0	i_0	Ω_0	2.99	2.100	2.6.2
18	$\Delta\omega$, $\Delta a = \Delta e = 0$, Burt 2 [39]	2.101	2.101	a_0	e_0	i_0	Ω_0	2.103	2.104	2.6.2
19	$\Delta\omega$, $\Delta a = \Delta e = 0$, Pollard [160]	2.106	2.106	a_0	e_0	i_0	Ω_0	2.109	2.110	2.6.2

Table 2.2: Taxonomy of analytical low-thrust control laws. OCP stands for Optimal Control Problem.

		OCP minimum time	Maximum instantaneous rate of change of OE	Other guidance law	Orbital elements to be changed					Orbital elements that stay constant					Include new derivations?
					a	e	i	Ω	ω	a	e	i	Ω	ω	
	Semi-major axis														
1	Max variation a, $e \neq 0$		■		■							■	■		
2	Max variation a, $e = 0$		■		■						■		■	■	■
3	Δa, Δi, $e_0 = 0$	■					■				■		■	■	
4	Δa, Δi, $e = 0$, $a \leq a_{lim}$	■					■				■	■		■	
5	Δa, $\Delta\Omega$, $e = 0$	■						■			■	■		■	
6	Δa, $\Delta e = \Delta\omega = 0$			■	■						■	■	■	■	■
	Eccentricity														
7	Max variation e		■			■						■	■		
8	Δe, $\Delta a = \Delta\omega = 0$, Burt			■		■					■		■	■	■
9	Δe, $\Delta a = \Delta\omega = 0$, Pollard			■		■	■				■		■	■	■
10	Δe, Δi, $\Delta a = 0$			■		■	■				■		■	■	■
	Inclination														
11	Max variation i, $e \neq 0$		■				■				■	■		■	
12	Max variation i, $e = 0$		■				■				■	■		■	■
	Right ascension of the ascending node														
13	Max variation Ω, $e \neq 0$		■					■			■	■	■		
14	Max variation Ω, $e = 0$		■					■			■	■	■		■
	Argument of the periapsis														
15	Max variation ω, Petropolous		■						■			■	■		
16	Max variation ω, Ruggiero		■						■			■			
17	$\Delta\omega$, $\Delta a = \Delta e = 0$, Burt 1			■					■		■	■	■	■	
18	$\Delta\omega$, $\Delta a = \Delta e = 0$, Burt 2			■					■		■	■	■	■	■
19	$\Delta\omega$, $\Delta a = \Delta e = 0$, Pollard			■					■		■	■	■	■	■

The content of this chapter was published in M. Di Carlo, L. A. Ricciardi, M. Vasile, "Multi-Objective Optimisation of Constellation Deployment using Low-Thrust Propulsion", 2016 AIAA/AAS Astrodynamics Specialist Conference, 13-16 September 2016, Long Beach, CA

Chapter 3

Analytical laws for the variation of a, i, Ω with J_2

The control laws for low-thrust transfers presented in the previous chapter do not consider perturbations to the Keplerian orbital motion. In this chapter, novel analytical control laws are derived for the solution of the TPBVP associated to the low-thrust transfer between inclined circular orbits, under the effect of the second order zonal harmonic of the Earth's gravitational potential, J_2. This perturbation causes secular variations in the right ascension of the ascending node, Ω. Analytical laws are also derived for the variations of the orbital elements with time and for the cost of the transfer. The chapter is structured as follow: the effect of the zonal harmonic perturbation and the considered TPBVP are briefly introduced in Section 3.1 while Sections 3.2 to 3.4 present three strategies for low-thrust transfers under J_2 perturbation. Section 3.5 compares the results of the three strategies and concludes the chapter. In Chapter 11, the novel laws presented here are used to compute the ΔV cost of low-thrust transfers from LEO to MEO.

3.1 Introduction

The proposed low-thrust transfers realise the simultaneous variation of semi-major axis, inclination and right ascension of circular orbits, in a given time of flight ToF. It is assumed that while the transfer takes place, the spacecraft is subject to the perturbing acceleration of the second order zonal harmonic of the Earth's gravitational potential, J_2. This causes a secular drift in the right ascension of the ascending node Ω, according to [204]:

$$\dot{\Omega}_{J_2} = -\frac{3}{2}\sqrt{\mu} J_2 R_\oplus^2 \cos i \, a^{-7/2} \,, \tag{3.1}$$

where $R_\oplus$ is the Earth's radius. The considered TPBVP can be expressed as follow

$$\begin{aligned} &\dot{\mathbf{x}} = \mathbf{h}\left(\mathbf{x}, \tilde{\mathbf{u}}, t\right) \\ &\mathbf{x}\left(t_0\right) = \mathbf{x}_0 \\ &\mathbf{x}\left(t_0 + ToF\right) = \mathbf{x}_f \\ &t \in [t_0, t_0 + ToF] \end{aligned} \tag{3.2}$$

The state $\mathbf{x}$ is:

$$\mathbf{x} = [a, i, \Omega]^T \ , \tag{3.3}$$

and the initial and final conditions are expressed as

$$\begin{aligned} &\mathbf{x}_0 = [a_0, i_0, \Omega_0]^T \\ &\mathbf{x}_f = [a_f, i_f, \Omega_f]^T = [a_0 + \Delta a, i_0 + \Delta i, \Omega_0 + \Delta\Omega]^T \end{aligned} \tag{3.4}$$

The control $\tilde{\mathbf{u}}$ depends on the considered solution method, presented in the next sections. The dynamic $\mathbf{h}$ is expressed by the Gauss' equations (Equations 2.2), for the case $e = 0$, and modified to include the term $d\Omega/dt$ given in Equation 3.1:

$$\mathbf{h}\left(\mathbf{x}, \tilde{\mathbf{u}}, t\right) = \begin{bmatrix} 2a^2/h \ \epsilon \cos\beta \cos\alpha, \\ \epsilon \ a/h \cos u \sin\beta, \\ \epsilon \frac{a}{h} \frac{\sin u}{\sin i} \sin\beta - \frac{3}{2}\sqrt{\mu} J_2 R_\oplus^2 \cos i \ a^{-7/2} \end{bmatrix} \tag{3.5}$$

The drift in Ω caused by J_2 can be exploited, in combination with the low-thrust propulsion, to obtain the desired variation of right ascension, $\Delta\Omega$. In particular, three possible low-thrust strategies are considered. They all assume that $a_0 < a_f$. The scenario for which these laws were specifically developed is, in fact, one in which a launcher leaves the spacecraft into an injection orbit of semi-major axis a_0; from the injection orbit, the spacecraft, using its low-thrust propulsion system, reaches its final operation orbit, at an altitude higher than the injection one (refer to Chapter 11). The three strategies are presented in detail in the following subsections; their applications to the problem of the deployment of satellite constellations is described in Chapter 11.

3.2 Strategy 1: $\Delta\Omega_{J_2}$ + $(\Delta a, \Delta i)$

For the first proposed strategy, the transfer from the initial to the final orbit is realised in two phases. During the first phase, denoted as $\Delta\Omega_{J_2}$, and characterised by a time of flight ToF_1, J_2 is exploited to obtain a given variation of right ascension. In the second phase, $(\Delta a, \Delta i)$, characterised by a time of flight ToF_2, the low-thrust acceleration is applied to change semi-major axis and inclination from their initial to their final values. In this phase, the low-thrust is applied on two thrust arcs of angular span $2\bar{\psi}$ and constant elevation angle $\bar{\beta}$. The variation of Ω (due to J_2 only) during the second phase is such that, starting from the value of Ω reached

at the end of phase 1, the final targeted right ascension can be obtained. The vector of controls for Strategy 1 is $\tilde{\mathbf{u}} = [\bar{\psi}, \bar{\beta}, ToF_1, ToF_2]^T$. The two phases of Strategy 1 are schematically represented in Figure 3.1.

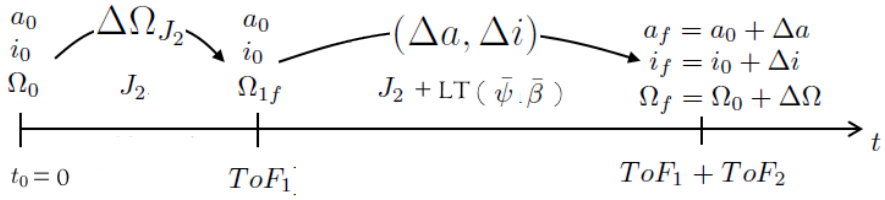

Figure 3.1: Representation of the two phases of Strategy 1. LT stands for low-thrust.

The following subsections describe the two phases in more detail and derive the system of four equations required to compute the four components of $\tilde{\mathbf{u}}$ that solve the TPBVP (Problem 3.2). Analytical equations for the variation of the orbital elements during the transfer and for the ΔV cost of the transfer are also provided.

First phase

During the first phase no operation of the low-thrust engine is required. The semi-major axis and inclination remain equal to their initial values, a_0 and i_0. This means that, under the assumption that $a_0 < a_f$, the effect of the drift of Ω due to J_2 is maximum, for the range of semi-major axis $[a_0, a_f]$ (Equation 3.1). The time of flight associated to this phase is identified as ToF_1. Since a_0 and i_0 are constant, Ω changes according to (Equation 3.1):

$$\Omega_1(t) = -\frac{3}{2}\sqrt{\mu} J_2 R_\oplus^2 \cos i_0 a_0^{-7/2} t \ , \ t \in [0, ToF_1] \ , \tag{3.6}$$

and $a_1(t) = a_0, \ i_1(t) = i_0 \ \forall t \in [0, ToF_1]$. The right ascension of the ascending node at the end of the first phase is identified as $\Omega_1(ToF_1) = \Omega_{1f}$. ToF_1 and Ω_{1f} satisfy the following relationship:

$$ToF_1 = \frac{\Omega_{1f} - \Omega_0}{\frac{3}{2}\sqrt{\mu} J_2 R_\oplus^2 \cos i_0 a_0^{-7/2}} \tag{3.7}$$

Second phase

The second phase is realised operating the low-thrust engine during two thrust arcs per orbital revolution. During this phase the semi-major axis and inclination change from their initial to their final values. Moreover, the variable drift of Ω due to J_2 is such that, at the end of the transfer, the right ascension will have changed from Ω_{1f} to Ω_f. Note that the variation of Ω takes place only because of J_2 and not because of the low-thrust acceleration (as explained later, see Equation 3.16). The time of flight of the second phase is ToF_2. The simultaneous variation of a and i in a given time of flight ToF_2 can be obtained with two tangential thrust

arcs of angular span $2\ \bar{\psi}$ (constant during the transfer), constant azimuth angle $\bar{\alpha} = 0$ and constant elevation angle $\bar{\beta}$, centred at the nodal points of the orbit, as shown in Figure 3.2.

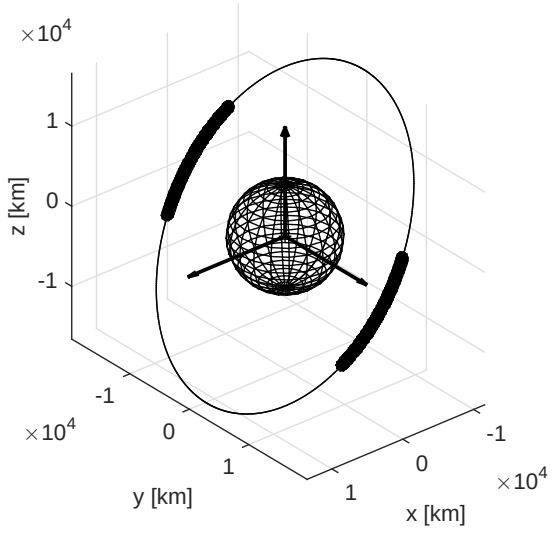

Figure 3.2: Strategy 1, phase 2: thrust arcs centred at the nodal points of the orbit.

The azimuth angle $\bar{\beta}$ has equal and opposite values on the two thrust arcs. The relevant equations for this transfer can be obtained from the Gauss' equations for the variation with time of the semi-major axis and inclination of circular orbits (Equation 2.2) and using $\alpha = 0$:

$$\begin{aligned} \frac{da}{dt} &= \frac{2a^2}{h}\varepsilon \cos\bar{\beta}, \\ \frac{di}{dt} &= \epsilon\frac{a}{h}\cos u \sin\bar{\beta}\ . \end{aligned} \tag{3.8}$$

The variations of a and i with the argument of the latitude u are (Equation 2.3)

$$\begin{aligned} \frac{da}{du} &= \frac{da}{dt}\frac{dt}{du} = \frac{2a^3}{\mu}\epsilon\cos\bar{\beta}, \\ \frac{di}{du} &= \frac{di}{dt}\frac{dt}{du} = \frac{\epsilon a^2 \sin\bar{\beta}\cos u}{\mu}\ . \end{aligned} \tag{3.9}$$

The secular variations of a and i are computed as follows:

$$\begin{aligned} \overline{\frac{da}{dt}} &= \frac{\Delta a_{2\pi}}{T} = \frac{1}{T}\left[\int_{-\bar{\psi}}^{\bar{\psi}}\frac{da}{du}d\mathrm{u} + \int_{\pi-\bar{\psi}}^{\pi+\bar{\psi}}\frac{da}{du}d\mathrm{u}\right] = \frac{4a^2\bar{\psi}\ \epsilon\cos\bar{\beta}}{\pi\sqrt{\mu a}}\ , \\ \overline{\frac{di}{dt}} &= \frac{1}{T}\left[\int_{-\psi}^{\bar{\psi}}\frac{di}{du}d\mathrm{u} + \int_{\pi-\bar{\psi}}^{\pi+\bar{\psi}}\frac{di}{du}d\mathrm{u}\right] = \frac{2\ \epsilon\ a\sin\bar{\beta}\sin\bar{\psi}}{\pi\sqrt{\mu a}}\ . \end{aligned} \tag{3.10}$$

In Equation 3.10 it is assumed that the variations of a and i in one revolution are negligible, so

that the integrands depend only on u. In order for a and i to reach their final values simultaneously, the following equation is integrated from a_0 to a_f and from i_0 to i_f:

$$\frac{\overline{da}}{di} = \frac{\overline{da}}{dt}\frac{\overline{dt}}{di} = \frac{2\,a\,\bar{\psi}\cos\bar{\beta}}{\sin\bar{\psi}\sin\bar{\beta}}\,. \tag{3.11}$$

The integration provides the constant elevation angle $\bar{\beta}$ required to realise the transfer from a_0 to a_f and from i_0 to i_f, as a function of $\bar{\psi}, a_0, a_f, i_0$ and i_f:

$$\tan\bar{\beta} = \frac{2\bar{\psi}\,(i_f - i_0)}{\sin\bar{\psi}\log(a_f/a_0)}\,. \tag{3.12}$$

Finally, the expressions for the variation of a and i with time, during the second phase $(\Delta a, \Delta i)$, are (Equations 3.10 and 3.11):

$$\begin{aligned} a_2(t) &= \mu\left[\frac{\mu}{a_0} + \left(\frac{2\,\epsilon\,\cos\bar{\beta}\,\bar{\psi}\,(t - ToF_1)}{\pi}\right)^2 - 2\sqrt{\frac{\mu}{a_0}}\left(\frac{2\,\epsilon\,\cos\bar{\beta}\,\bar{\psi}\,(t - ToF_1)}{\pi}\right)\right]^{-1}, \\ i_2(t) &= i_0 + \frac{\tan\bar{\beta}\sin\bar{\psi}}{2\,\bar{\psi}}\log\left(\frac{a_2(t)}{a_0}\right)\,, \end{aligned} \tag{3.13}$$

with $t \in [ToF_1, ToF_1 + ToF_2]$. From Equations 3.12 and 3.13, the time of flight of the second phase of the transfer can be expressed as a function of $\bar{\psi}$ and of the initial and final orbital elements:

$$ToF_2 = \frac{\pi}{2\,\epsilon\,\bar{\psi}}\left(\sqrt{\frac{\mu}{a_0}} - \sqrt{\frac{\mu}{a_f}}\right)\sqrt{1 + \frac{4\bar{\psi}^2\,(i_f - i_0)^2}{\sin^2\bar{\psi}\log^2(a_f/a_0)}}\,. \tag{3.14}$$

During the second phase of the transfer the right ascension changes because of J_2 and because of the variation of a and i with time. The variation of Ω with time is (Equations 2.2 and 3.1):

$$\frac{d\Omega}{dt} = \frac{\epsilon a(t)^2}{\mu}\frac{\sin u\sin\bar{\beta}}{\sin i(t)} - \frac{3}{2}\sqrt{\mu}J_2R_\oplus^2\cos i(t)a(t)^{-7/2}\,. \tag{3.15}$$

The first term in the previous equation cancels out when integrating in u over one revolution, because $\bar{\beta}$ has equal and opposite values on the two thrust arcs. The secular variation of the right ascension is, therefore, due only to J_2:

$$\frac{\overline{d\Omega}}{dt} = -\frac{3}{2}\sqrt{\mu}J_2R^2\cos i(t)a(t)^{-7/2}\,. \tag{3.16}$$

It is possible to write the expression of the variation of Ω with i as

$$\frac{\overline{d\Omega}}{di} = \frac{\overline{d\Omega}}{dt}\frac{\overline{dt}}{di} = -\frac{3\pi\mu J_2R_\oplus^2a^{-4}\cos i}{4\epsilon\cos\bar{\beta}\sin\bar{\psi}}\,. \tag{3.17}$$

Equation 3.17 can be integrated using the following expression for the variation of the semi-

major axis with time (obtained from Equation 3.13):

$$a(t) = a_0 \exp\left[\frac{2\,\bar{\psi}\,(i(t) - i_0)}{\tan\bar{\beta}\sin\bar{\psi}}\right] . \tag{3.18}$$

Substitution of the previous equation in $d\overline{\Omega/di}$ (Equation 3.17) and integration from Ω_{1f} to $\Omega(ToF_1 + ToF_2)$ and from i_0 to i_f results in

$$\Omega(ToF_1 + ToF_2) = \Omega_{1f} + \frac{k_1(\bar{\beta}, \bar{\psi})}{1 + k_2^2} k_3, \tag{3.19}$$

where

$$\begin{aligned} k_1(\bar{\beta}, \bar{\psi}) &= -\frac{3\pi\mu J_2 R_\oplus^2}{4\,a_0^4\,\epsilon\,\sin\bar{\beta}\sin\bar{\psi}} \exp\left[\frac{4\log(a_f/a_0) i_0}{(i_f - i_0)}\right], \\ k_2 &= \frac{4\log(a_f/a_0)}{(i_f - i_0)}, \\ k_3 &= \exp(k_2 i_f)(k_2\cos i_f + \sin i_f) - \exp(k_2 i_0)(k_2\cos i_0 + \sin i_0) , \end{aligned} \tag{3.20}$$

and it is required that $\Omega(ToF_1 + ToF_2) = \Omega_f$. Equation 3.20 becomes singular when $(i_f - i_0)$ is small. In the case $i_f = i_0$, an alternative, non-singular formulation is available. When $i_f = i_0$, $\bar{\beta} = 0$ and the expression for Ω_{2f} can be obtained integrating $d\Omega/da$ obtained from Equations 3.10 and 3.16:

$$\Omega(ToF_1 + ToF_2) = \Omega_{1f} + \frac{3}{32}\frac{\pi\mu J_2 R_\oplus^2 \cos i}{\varepsilon\psi}\left(\frac{1}{a_f^4} - \frac{1}{a_0^4}\right) . \tag{3.21}$$

The cost of the transfer can be computed analytically considering that the engine is on during a fraction of the orbital period equal to

$$\frac{4\bar{\psi}}{2\pi} 2\pi\sqrt{\frac{a^3}{\mu}}; \tag{3.22}$$

therefore

$$\frac{d\Delta V}{dt} = \frac{\epsilon\,\frac{4\bar{\psi}}{2\pi} 2\pi\sqrt{\frac{a^3}{\mu}}}{2\pi\sqrt{\frac{a^3}{\mu}}} = \frac{2\,\epsilon\,\bar{\psi}}{\pi} . \tag{3.23}$$

The final expression for the cost of the transfer is

$$\Delta V = \int_{ToF_1}^{(ToF_1+ToF_2)} \frac{d\Delta V}{dt} d\tau = \frac{2\,\epsilon\,\bar{\psi}\,ToF_2}{\pi} = \left(\sqrt{\frac{\mu}{a_0}} - \sqrt{\frac{\mu}{a_f}}\right)\sqrt{1 + \frac{4\bar{\psi}^2\,(i_f - i_0)^2}{\sin^2\bar{\psi}\log^2(a_f/a_0)}} . \tag{3.24}$$

Solution method

Given a total time of flight ToF to realise the transfer, the unknowns of the problems are the four components of the vector $\tilde{\mathbf{u}}$, that is $\bar{\beta}$, $\bar{\psi}$, ToF_1 and ToF_2. The problem can be solved

solving the system composed by the following set of equations (Equations 3.7, 3.12, 3.14 and 3.19):

$$\begin{aligned}
&\tan\bar{\beta} = \frac{2\bar{\psi}\,(i_f - i_0)}{\sin\bar{\psi}\log(a_f/a_0)} \\
&\Omega_f = \Omega_0 - \frac{3}{2}\sqrt{\mu}J_2R_\oplus^2\cos i_0 a_0^{-7/2}ToF_1 + \frac{k_1(\bar{\beta},\bar{\psi})}{1+k_2^2}k_3 \\
&ToF_2 = \frac{\pi}{2\,\epsilon\,\bar{\psi}}\left(\sqrt{\frac{\mu}{a_0}} - \sqrt{\frac{\mu}{a_f}}\right)\sqrt{1 + \frac{4\bar{\psi}^2\,(i_f - i_0)^2}{\sin^2\bar{\psi}\log^2(a_f/a_0)}} \\
&ToF_1 + ToF_2 = ToF
\end{aligned} \tag{3.25}$$

In particular, substituting the first of Equations 3.25 into the second, provides a non-linear equation in $\bar{\psi}$, that is solved using an algorithm based on a combination of bisection, secant, and inverse quadratic interpolation methods, implemented in the function *fzero* in Matlab. Once $\bar{\psi}$ is found, the rest of the Equations 3.25 allows one to find $\bar{\beta}, ToF_1$ and ToF_2. Figure 3.3 shows an example of transfer realised using Strategy 1, with time of flight of 600 days and low-thrust acceleration ϵ equal to $1.5\ 10^{-4}$ m/s^2. The variation of semi-major axis is from 10000 to 24200 km, the inclination changes from 51 to 56 deg and the right ascension changes from 0 deg to 150 deg. The relevant parameters of the solution for the low-thrust control are $\bar{\psi} = 67.02$ deg and $\bar{\beta} = 14.1$ deg. The times of flight of the two phases are $ToF_1 = 359.1$ days and $ToF_2 = 240.9$ days. The cost of the transfer is $\Delta V = 2.32$ km/s. Figure 3.3 shows that, during the first phase, the semi-major axis and inclination stay constant, while the right ascension changes because of J_2. In the second phase, the semi-major axis and inclination change from their initial to their final values and the variation of right ascension is such as to obtain, at the end of the transfer, and by means of J_2 only, the final desired value.

3.3 Strategy 2: $(\Delta a, \Delta i)$ + $\Delta\Omega_\beta$

Also in the second proposed low-thrust strategy the transfer is realised in two phases. The first phase, $(\Delta a, \Delta i)$, is similar to the second phase of Strategy 1. The low-thrust is applied on two thrust arcs of angular span $2\bar{\psi}_1$ and elevation angle $\bar{\beta}_1$, for a time of flight equal to ToF_1. In the second phase, of time of flight ToF_2 and referred to as $\Delta\Omega_\beta$, an out-of-plane control thrust is used to change Ω to its final value. During the second phase the low-thrust is applied on two thrust arcs of angular span $2\bar{\psi}_2$. The vector $\tilde{\mathbf{u}}$ associated to the TPBVP is now $\tilde{\mathbf{u}} = \left[\bar{\psi}_1, \bar{\beta}_1, \bar{\psi}_2, ToF_1, ToF_2\right]^T$. The two phases of Strategy 2 are schematically represented in Figure 3.4

The following subsections describe them in more detail. Analytical equations for the variation of the orbital elements during the transfer and for the ΔV of the transfer are also provided.

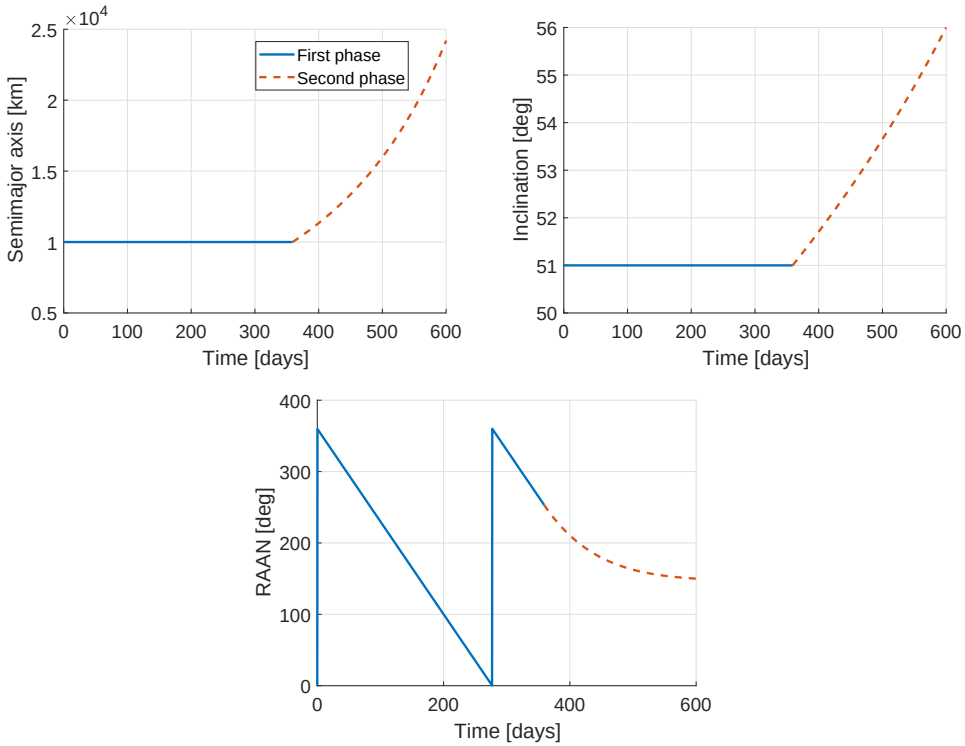

Figure 3.3: Variation of a, i and Ω during low-thrust transfer with Strategy 1.

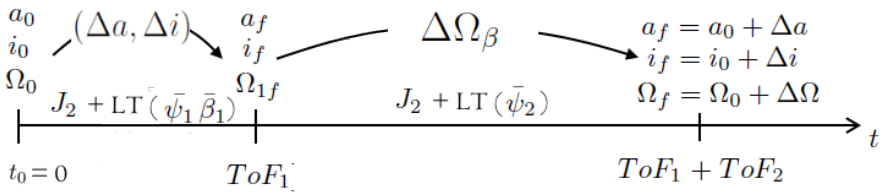

Figure 3.4: Representation of the two phases of Strategy 2. LT stands for low-thrust.

First phase

During the first phase, a and i are changed from their initial values, a_0 and i_0, to their final values, a_f and i_f, as described in Section 3.2. The engine is operated on two arcs per orbital revolution of amplitude 2 $\bar{\psi}_1$ and elevation angle $\bar{\beta}_1$. The time of flight of the first phase is denoted as ToF_1. The right ascension at the end of the first phase is computed from Equation 3.19 as:

$$\Omega_{1f} = \Omega_0 + \frac{k_1\left(\bar{\psi}_1, \bar{\beta}_1\right)}{1 + k_2^2} k_3 \,. \tag{3.26}$$

The cost, ΔV_1, is computed using Equation 3.24.

Second phase

During the second phase Ω is changed using out-of-plane thrust; two thrust arcs of angular span $2\bar{\psi}_2$ and elevation angle $\left|\bar{\beta}_2\right| = 90$ deg are applied at the apsidal points of the orbit, $u = 90$ and $u = 270$ deg, as shown in Figure 3.5.

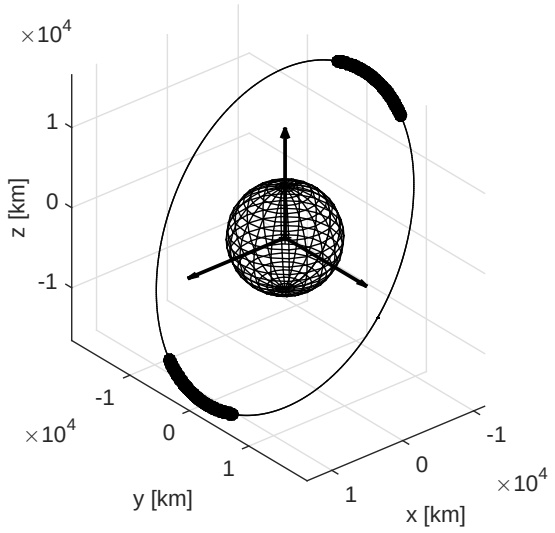

Figure 3.5: Strategy 2, phase 2: thrust arcs centred at the apsidal points of the orbit.

The sign of $\bar{\beta}$ is opposite on the two thrust arcs. Using the Gauss equation for Ω, Equations 2.2 and 2.3, it is possible to obtain the variation of Ω with the argument of the latitude, due to the low-thrust propulsion3:

$$\frac{d\Omega}{du} = \frac{\epsilon\, a^2 \sin u}{\mu \sin i} \sin\beta \,. \tag{3.27}$$

The variation of Ω in one orbital period, due to the low-thrust propulsion, is

$$\Delta\Omega_{2\pi}^{LT} = \int_{\frac{\pi}{2}-\bar{\psi}_2}^{\frac{\pi}{2}+\bar{\psi}_2} \frac{\epsilon\, a^2 \sin u}{\mu \sin i} \mathrm{du} - \int_{\frac{3\pi}{2}-\bar{\psi}_2}^{\frac{3\pi}{2}+\bar{\psi}_2} \frac{\epsilon\, a^2 \sin u}{\mu \sin i} \mathrm{du} = \frac{4\,\epsilon\, a^2 \sin\bar{\psi}_2}{\mu\ \sin i} \,. \tag{3.28}$$

During the second phase, the variation of Ω, due to both the out-of-plane thrust and J_2, is

$$\overline{\frac{d\Omega}{dt}} = \frac{2\,\epsilon \sin\bar{\psi}_2}{\pi \sin i_f} \sqrt{\frac{a_f}{\mu}} - \frac{3}{2}\sqrt{\mu} J_2 R_\oplus^2 \cos i_f\ a_f^{-7/2} \,. \tag{3.29}$$

The previous equation is obtained considering constant values of the semi-major axis and inclination. The semi-major axis does not change because $\left|\bar{\beta}\right| = 90$, while the variation of inclination is zero over one orbital period because the effect of the out-of-plane thrust on the

inclination is equal and opposite on the two thrust arcs. The variation with time of Ω is

$$\Omega_2(t) = \Omega_{1f} + \left(\frac{2\,\epsilon \sin \bar{\psi}_2}{\pi \sin i_f} \sqrt{\frac{a_f}{\mu}} - \frac{3}{2} \sqrt{\mu} J_2 R_\oplus^2 \cos i_f \; a_f^{-7/2} \right) (t - ToF_1) \,, \tag{3.30}$$

with $t \in [ToF_1, ToF_1 + ToF_2]$. The semi-amplitude of the thrust arcs can be computed from Equations 3.30 and 3.26 as:

$$\sin \bar{\psi}_2 = \left(\Omega_f - \Omega_{1f} + \frac{3}{2} \sqrt{\mu} J_2 R_\oplus^2 \cos i_f a_f^{-7/2} \, ToF_2 \right) \left(\frac{2\,\epsilon}{\pi \sin i_f} \sqrt{\frac{a_f}{\mu}} ToF_2 \right)^{-1} . \tag{3.31}$$

The cost associated to the variation of Ω can be computed analytically, following a procedure similar to the one presented in Section 3.2, as

$$\Delta V_2 = \frac{2\,\epsilon\,\bar{\psi}_2}{\pi} ToF_2, \tag{3.32}$$

where ToF_2 is derived from Equation 3.31. The total cost is $\Delta V = \Delta V_1 + \Delta V_2$.

Solution method

When the combined transfer $(\Delta a, \Delta i)$ + $\Delta\Omega_\beta$ has to be realised in a total time of flight ToF, the equations defined above are not in a sufficient number to solve the problem. There are indeed five unknowns ($\bar{\psi}_1$, $\bar{\beta}_1$, $\bar{\psi}_2$, ToF_1 and ToF_2) while the available equations are four (Equations 3.12, 3.14, 3.31 and $ToF_1 + ToF_2 = ToF$):

$$\begin{aligned}
&\tan \bar{\beta}_1 = \frac{2\bar{\psi}_1 \left(i_f - i_0\right)}{\sin \bar{\psi}_1 \log(a_f/a_0)} \\
&ToF_1 = \frac{\pi}{2\,\epsilon\,\bar{\psi}_1} \left(\sqrt{\frac{\mu}{a_0}} - \sqrt{\frac{\mu}{a_f}} \right) \sqrt{1 + \frac{4{\bar{\psi}_1}^2 \left(i_f - i_0\right)^2}{\sin^2 \bar{\psi}_1 \log^2(a_f/a_0)}} \\
&\sin \bar{\psi}_2 = \left(\Omega_f - \Omega_0 - \frac{k_1\left(\bar{\psi}_1, \bar{\beta}_1\right)}{1 + k_2^2} k_3 + \frac{3}{2} \sqrt{\mu} J_2 R_\oplus^2 \cos i_f a_f^{-7/2} \, ToF_2 \right) \left(\frac{2\,\epsilon}{\pi \sin i_f} \sqrt{\frac{a_f}{\mu}} ToF_2 \right)^{-1} \\
&ToF_1 + ToF_2 = ToF
\end{aligned} \tag{3.33}$$

It is possible, however, to define different arbitrary values of $ToF_1 < ToF$ and compute the corresponding values of $\bar{\psi}_1$, $\bar{\beta}_1$, $\bar{\psi}_2$ and ToF_2. In particular, it is possible to find a ToF_1 such that the ΔV of the transfer is the minimum possible value. An example of transfer realised with this strategy is shown in Figure 3.6. The initial and final orbital elements are those used for the example reported in Section 3.2. The minimum ΔV transfer is realised with $\Delta V = 2.31$ km/s and the parameters of the low-thrust control are $\bar{\psi}_1 = 33.75$ deg, $\bar{\beta}_1 = 11.82$ deg and $\bar{\psi}_2$ = 0.29 deg. The times of flight of the two phases are $ToF_1 = 474.07$ days and $ToF_2 = 125.93$. The variation of orbital elements is reported in Figure 3.6. During the first phase the semi-major axis and inclination change from their initial to their final values while the variation of right ascension is due only to J_2. Note how the drift of Ω is slower than in the example reported in

Figure 3.3. This is because the semi-major axis increases considerably during the first phase, thus reducing $d\Omega/dt$. In the second phase the semi-major axis and inclination remain constant while the right ascension changes because of the out-of-plane thrust. The minimum ΔV transfer corresponds to a small value of $\bar{\psi}_2$, meaning that the out-of-plane thrust, more expensive than the in-plane thrust, is applied on very short arcs.

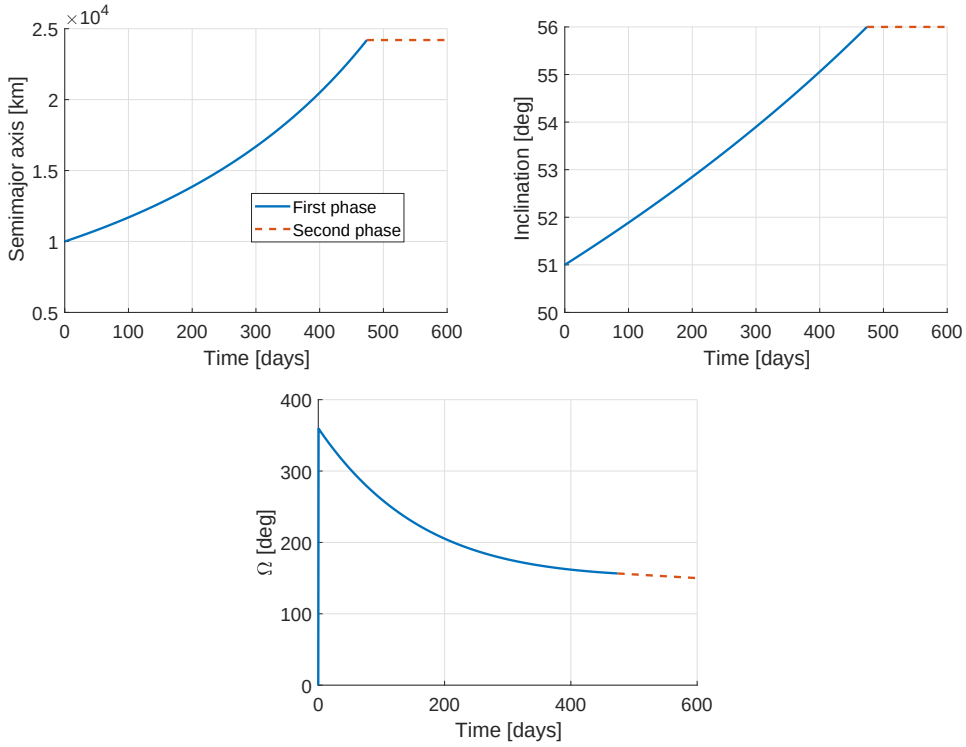

Figure 3.6: Variation of a, i and Ω during low-thrust transfer with Strategy 2.

The transfer shown in Figure 3.6 is the one characterised by the lowest value of ΔV. The ΔVs obtained for different values of ToF_1 are reported in Figure 3.7. Figure 3.8 shows the variation of right ascension during the transfer for two possible solutions: $ToF_1 = 474.07$ days and ToF_1 = 505 days. The higher ΔV obtained when $ToF_1 = 505$ days is due to the greater variation of Ω obtained with out-of-plane thrust during the second phase. $\bar{\psi}_2$ is indeed equal to 61.66 deg when $ToF_1 = 505$ days.

3.4 Strategy 3: $(\Delta a, \Delta\Omega_{J_2})$ + Δi

The low-thrust transfer using Strategy 3 is realised in two phases; the first one changes semi-major axis and right ascension, $(\Delta a, \Delta\Omega_{J_2})$, and the second one changes the inclination, Δi. The first phase makes use of low-thrust acceleration on two thrust arcs of semi-amplitude $\bar{\psi}_1$, for a time of flight ToF_1, while the second phase uses arcs of semi-amplitude $\bar{\psi}_2$ for a time of flight ToF_2. The vector of unknown variables is $\tilde{\mathbf{u}} = \left[\bar{\psi}_1, \bar{\psi}_2, ToF_1, ToF_2\right]^T$. The strategy is schematically shown in Figure 3.9. More details are given hereafter.

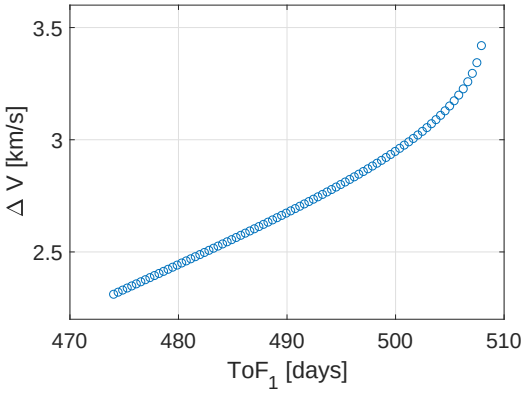

Figure 3.7: ΔVs for different values of ToF_1.

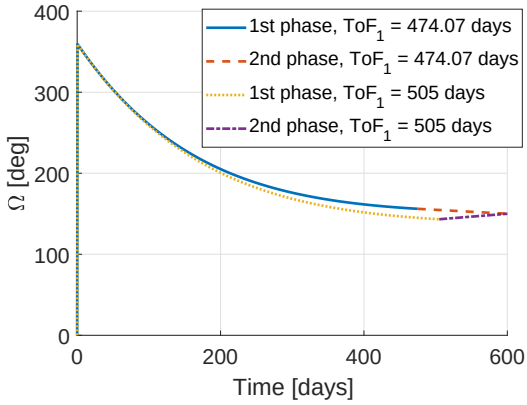

Figure 3.8: Variation of Ω during the transfer for $ToF_1 = 480$ days and ToF_1=505 days.

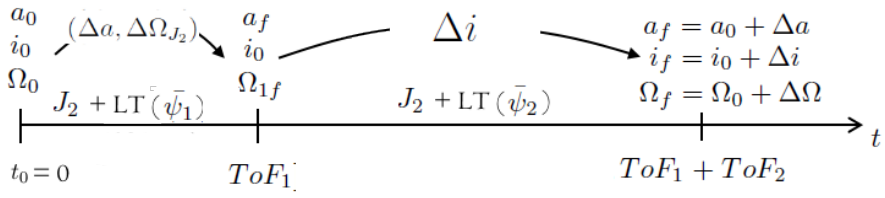

Figure 3.9: Representation of the two phases of Strategy 3. LT stands for low-thrust.

First phase

The transfer in the first phase of Strategy 3 is analogous to the transfer during the second phase of Strategy 1, with $\bar{\beta}_1 = 0$. During the first phase a tangential thrust is used to increase the semi-major axis from a_0 to a_f. The low-thrust engine is operated during two thrust arcs per revolution, of semi-amplitude $\bar{\psi}_1$. Considering Equation 3.14 with $\bar{\beta} = 0$, the time of flight for the first phase of the transfer is given by

$$ToF_1 = \frac{\pi}{2\,\epsilon\,\bar{\psi}_1}\left(\sqrt{\frac{\mu}{a_0}} - \sqrt{\frac{\mu}{a_f}}\right) . \tag{3.34}$$

The cost of this phase can be computed analytically using Equation 3.24 with $\bar{\beta} = 0$:

$$\Delta V_1 = \sqrt{\frac{\mu}{a_0}} - \sqrt{\frac{\mu}{a_f}} . \tag{3.35}$$

The right ascension at the end of the transfer is obtained by integrating $d\Omega/da$ obtained from the equations for $d\Omega/dt$ and da/dt with $i(t) = i_0$ (refer to Section 2.1). This results in:

$$\Omega_{1f} = \Omega_0 + \frac{3}{32}\frac{\mu J_2 R_\oplus^2 \cos i_0}{\epsilon\bar{\psi}_1}\left(\frac{1}{a_f^4} - \frac{1}{a_0^4}\right) . \tag{3.36}$$

Second phase

The transfer in the second phase of Strategy 3 is analogous to the transfer during the second phase of Strategy 1, with $\bar{\beta} = 90$ deg. The thrust is applied during two thrust arcs per revolution, of semi-amplitude $\bar{\psi}_2$, with elevation angle $\bar{\beta}_2 = 90$ deg. This causes the inclination to change from i_0 to i_f while the semi-major axis stays constant at a_f. The time required can be computed integrating the equation for di/dt (Equation 3.10) from i_0 to i_f, using $a = a_f$:

$$ToF_2 = \frac{\pi}{2\,\epsilon}\frac{i_f - i_0}{\sin\bar{\psi}_2}\sqrt{\frac{\mu}{a_f}}\ . \tag{3.37}$$

The cost of this phase is derived from Equations 3.37 and 3.23:

$$\Delta V_2 = \frac{\bar{\psi}_2}{\sin\bar{\psi}_2}\sqrt{\frac{\mu}{a_f}}\,(i_f - i_0)\ . \tag{3.38}$$

The variation of right ascension is obtained from Equation 3.17 with $a = a_f$:

$$\Omega_{2f} = \Omega_{1f} + \frac{3}{4}\frac{\pi\,\mu\,J_2\,R_\oplus^2}{\epsilon\,a_f^4\,\sin\bar{\psi}_2}\,(\sin i_0 - \sin i_f)\ . \tag{3.39}$$

Solution method

The equations presented in the previous subsections can be used to solve the problem in which the entire transfer has to be realised in a given time of flight ToF. The unknowns are $\bar{\psi}_1$, $\bar{\psi}_2$, ToF_1 and ToF_2, while the available equations are (Equations 3.34, 3.37, 3.39, 3.36):

$$\begin{aligned}
&ToF_1 = \frac{\pi}{2\,\epsilon\,\bar{\psi}_1}\left(\sqrt{\frac{\mu}{a_0}} - \sqrt{\frac{\mu}{a_f}}\right)\\
&ToF_2 = \frac{\pi}{2\,\epsilon}\frac{i_f - i_0}{\sin\bar{\psi}_2}\sqrt{\frac{\mu}{a_f}}\\
&\Omega_f = \Omega_0 + \frac{3}{32}\frac{\mu J_2 R_\oplus^2\cos i_0}{\epsilon\bar{\psi}_1}\left(\frac{1}{a_f^4} - \frac{1}{a_0^4}\right) + \frac{3}{4}\frac{\pi\,\mu\,J_2\,R_\oplus^2}{\epsilon\,a_f^4\,\sin\bar{\psi}_2}\,(\sin i_0 - \sin i_f)\\
&ToF_1 + ToF_2 = ToF
\end{aligned} \tag{3.40}$$

An example of transfer realised with this strategy is shown in Figure 3.10. The transfer requires $\Delta V = 2.6201$ km/s, $\bar{\psi}_1 = 34.21$ deg, $\bar{\psi}_2 = 17.56$ deg, $ToF_1 = 457.7$ days and $ToF_2 = 142.3$ days. There is no variation of inclination during the first phase, while during the second phase the semi-major axis stays constant and the inclination and right ascension change reaching their final values.

3.5 Comparison and summary

Figure 3.11 shows the variation of orbital elements during the example of transfer considered in the previous sections, for the three proposed strategies.

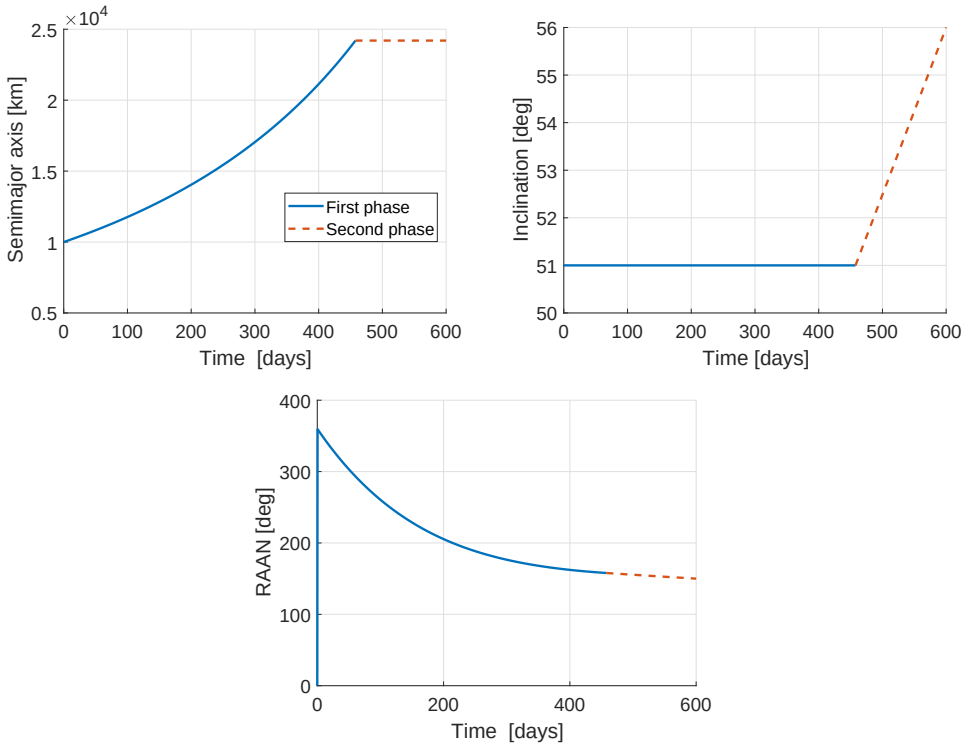

Figure 3.10: Variation of a, i and Ω during low-thrust transfer with strategy 3.

Figure 3.12 shows the ΔV required to realise the transfer defined in Subsection 3.2, for different values of the times of flight and using the three proposed strategies. For Strategy 2, for which a unique solution does not exist, the solutions plotted are the ones corresponding to the values of ToF_1 and ToF_2 providing the lowest value of the ΔV for that transfer. The fact that, for Strategy 2, ToF_1 and ToF_2 are chosen to minimise the ΔV, explains the noisy and non-asymptotically behaviour of the curve relative to Strategy 2 in Figure 3.12.

Results show that the first and second strategies are those giving the lowest ΔVs. In Chapter 11, where low-thrust transfers between circular inclined orbit are considered in order to study the deployment of satellite constellations, Strategy 1 is used. Strategy 1 provides, in fact, low ΔV while requiring the low-thrust system to operate only during one portion of the transfer.

The analytical laws presented in Chapter 2 and in this chapter represent a set of tools, of different levels of fidelity, for the preliminary estimation of the cost of low-thrust transfer. They assume that specific thrust profiles and specific orbital perturbations are present. In the more general case, however, any thrust profile, under any perturbation condition, could be applied to the considered spacecraft. In the next chapter, analytical and semi-analytical equations for the propagation of the motion of the spacecraft, subject to different low-thrust acceleration profiles and orbital perturbations, are presented.

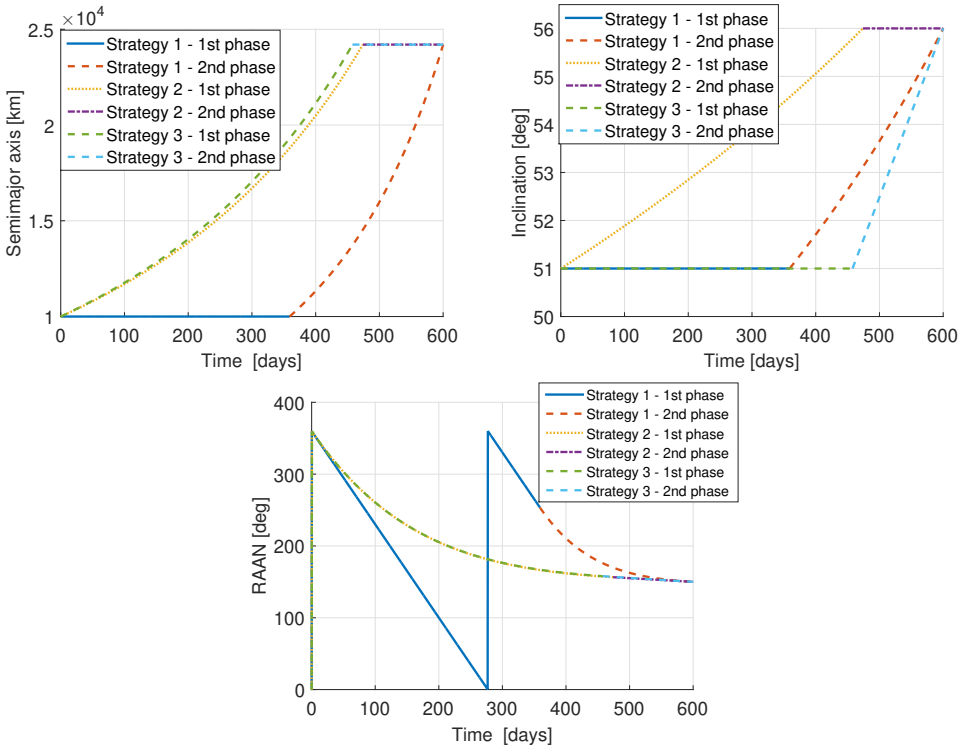

Figure 3.11: Variation of a, i and Ω during low-thrust transfer with strategies 1, 2 and 3.

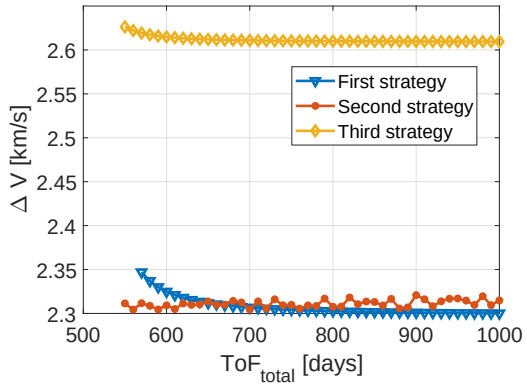

Figure 3.12: ΔVs for different values of ToF_{total}.

Chapter 4

Part of the content of this Chapter was published in M. Di Carlo, J. M. Romero Martin, M. Vasile, "Automatic trajectory planning for low-thrust active removal mission in low-earth orbit", Advances in Space Research, Volume 59, Issue 5, 1 March 2017, pp. 1234-1258

Analytical propagation via first-order expansions

This chapter presents analytical equations for the propagation of the motion of the spacecraft subject to low-thrust accelerations and orbital perturbations. The work described here is based on, and extends, the work presented by Zuiani in [239, 240]. Zuiani derived analytical equations for the motion of the spacecraft subject to constant tangential acceleration, constant acceleration in the radial-transverse-normal reference frame, constant acceleration in the inertial reference frame and orbital perturbations due to the second order zonal harmonic of the Earth's gravitational perturbation, J_2. Here the study is extended to consider a low-thrust profile following an inverse square law and to include perturbations due to the zonal harmonics J_3, J_4, J_5, the atmospheric drag and the third body gravitational perturbation. Analytical equations expressed in terms of non-singular equinoctial elements have been derived for J_3, J_4, J_5 and low-thrust acceleration changing as $1/r^2$. For the atmospheric drag, a new analytical solution is derived, based on a Chebyshev interpolation of the atmospheric density with respect to the altitude. The analytical equations for the third body gravitational perturbation have, instead, been obtained starting from formulae for the third-body potential already available in the literature. The theoretical background for the development of the analytical equations is presented in Section 4.1. Sections 4.2, 4.3, 4.4 and 4.5 present the mathematical derivation of the equations relative to the perturbations and thrust acceleration included in this work. Finally, Section 4.6 discusses the validation of the analytical propagation against the NASA open-source software GMAT.

4.1 Introduction

The analytical formulae presented in [239,240] describe the motion of the satellite by means of equinoctial elements, in order to avoid singularities when $i = 0$ or $e = 0$. The set of equinoctial

elements is [33]

$$\begin{aligned} &a, \\ &P_1 = e\sin(\Omega+\omega), \\ &P_2 = e\cos(\Omega+\omega), \\ &Q_1 = \tan\frac{i}{2}\sin\Omega, \\ &Q_2 = \tan\frac{i}{2}\cos\Omega, \\ &L, \end{aligned} \tag{4.1}$$

where $L = \Omega + \omega + \theta$ is the true longitude. The perturbing acceleration is expressed in a radial-transverse-normal reference frame RTN. In this chapter the notation is consistent with Zuiani, [240], who measured the in-plane angle of the perturbing acceleration from the radial direction, rather than from the transverse direction. In order to avoid confusion with the notation used in Chapter 2, in this chapter the in-plane thrust angle will be therefore identified as α', where $\alpha' = \pi/2 - \alpha$, with α defined as in Chapter 2 (see Figure 4.1).

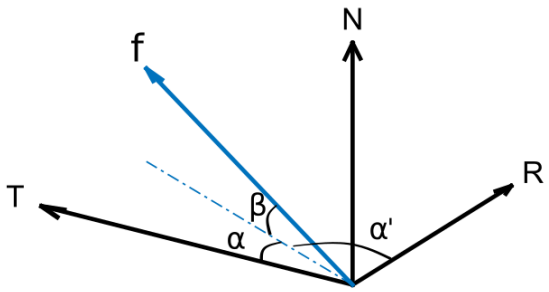

Figure 4.1: Perturbing acceleration in the RTN reference frame and representation of the angles α, α' and β.

Any perturbing acceleration to the Keplerian orbital motion (including low-thrust perturbation) is therefore expressed in the RTN frame as

$$\mathbf{f} = \begin{bmatrix} f_R \\ f_T \\ f_N \end{bmatrix} = \begin{bmatrix} \epsilon\cos\beta\cos\alpha' \\ \epsilon\cos\beta\sin\alpha' \\ \epsilon\sin\beta \end{bmatrix}. \tag{4.2}$$

The Gauss' planetary equations, expressed in terms of equinoctial elements, are [13]

$$\begin{aligned}
\frac{da}{dt} &= \frac{2}{B}\sqrt{\frac{a^3}{\mu}}\left[\left(P_2\sin L - P_1\cos L\right) f_R + \Phi(L) f_T\right], \\
\frac{dP_1}{dt} &= B\sqrt{\frac{a}{\mu}}\left[-f_R\cos L + \left(\frac{P_1+\sin L}{\Phi(L)} + \sin L\right) f_T - P_2\frac{Q_1\cos L - Q_2\sin L}{\Phi(L)} f_N\right], \\
\frac{dP_2}{dt} &= B\sqrt{\frac{a}{\mu}}\left[f_R\sin L + \left(\frac{P_2+\cos L}{\Phi(L)} + \cos L\right) f_T + P_1\frac{Q_1\cos L - Q_2\sin L}{\Phi(L)} f_N\right], \\
\frac{dQ_1}{dt} &= \frac{B}{2}\sqrt{\frac{a}{\mu}}\left(1+Q_1^2+Q_2^2\right)\frac{\sin L}{\Phi(L)} f_N, \\
\frac{dQ_2}{dt} &= \frac{B}{2}\sqrt{\frac{a}{\mu}}\left(1+Q_1^2+Q_2^2\right)\frac{\cos L}{\Phi(L)} f_N\,.
\end{aligned} \tag{4.3}$$

B and $\Phi(L)$ are defined as

$$B = \sqrt{1-e^2} = \sqrt{1-P_1^2-P_2^2}, \tag{4.4}$$

$$\Phi(L) = 1 + e\cos\theta = 1 + P_1\sin L + P_2\cos L\,. \tag{4.5}$$

The sixth Gauss' equation is obtained under the assumption that the perturbative acceleration is small compared to the local gravitational acceleration [241]:

$$\frac{dt}{dL} \approx \sqrt{\frac{a^3}{\mu}}\frac{B^3}{\Phi^2(L)}\,. \tag{4.6}$$

Combining Equations 4.3 and 4.6, the variations of the equinoctial elements with the true longitude can be expressed as:

$$\begin{aligned}
\frac{da}{dL} =& \frac{2a^3B^2}{\mu}\left[\frac{\left(P_2\sin L - P_1\cos L\right)}{\Phi^2(L)} f_R + \frac{1}{\Phi(L)} f_T\right], \\
\frac{dP_1}{dL} =& \frac{B^4a^2}{\mu}\left\{\left[-\frac{\cos L}{\Phi^2(L)} f_R + \left(\frac{P_1+\sin L}{\Phi^3(L)} + \frac{\sin L}{\Phi^2(L)}\right) f_T\right] - P_2\frac{Q_1\cos L - Q_2\sin L}{\Phi^3(L)} f_N\right\}, \\
\frac{dP_2}{dL} =& \frac{B^4a^2}{\mu}\left\{\left[\frac{\sin L}{\Phi^2(L)} f_R + \left(\frac{P_2+\cos L}{\Phi^3(L)} + \frac{\cos L}{\Phi^2(L)}\right) f_T\right] + P_1\frac{Q_1\cos L - Q_2\sin L}{\Phi^3(L)} f_N\right\}, \\
\frac{dQ_1}{dL} =& \frac{B^4a^2}{2\mu}\left(1+Q_1^2+Q_2^2\right)\frac{\sin L}{\Phi^3(L)} f_N, \\
\frac{dQ_2}{dL} =& \frac{B^4a^2}{2\mu}\left(1+Q_1^2+Q_2^2\right)\frac{\cos L}{\Phi^3(L)} f_N\,.
\end{aligned} \tag{4.7}$$

The motion of the satellite is described using an analytical solution to Equations 4.7, generated with the method of perturbations [204]. The idea at the basis of the method of perturbations is that small disturbing forces cause small deviations from the known solution to the unperturbed problem. The small perturbing forces can be associated with small parameters which characterise the magnitude of the disturbing forces. Introducing $\mathbf{X}$, the state of the spacecraft, expressed in terms of equinoctial elements, $\mathbf{X} = [a, P_1, P_2, Q_1, Q_2, L]^T$, and the variable

$\widetilde{\mathbf{X}} = [a, P_1, P_2, Q_1, Q_2]^T$, Equations 4.7 can be reformulated as in the method of perturbations:

$$\frac{d\widetilde{\mathbf{X}}}{dL} = \epsilon F\left(\widetilde{\mathbf{X}}, L, \alpha', \beta\right) . \tag{4.8}$$

The first-order approximation of the solution is

$$\widetilde{\mathbf{X}} \approx \widetilde{\mathbf{X}}_0 + \epsilon\widetilde{\mathbf{X}}_1 , \tag{4.9}$$

where

$$\widetilde{\mathbf{X}}_1 = \int_{L_0}^{L} F\left(\widetilde{\mathbf{X}}, \mathcal{L}, \alpha', \beta\right) d\mathcal{L} . \tag{4.10}$$

Analytical solutions to Equation 4.10 are derived in [240] and, in the rest of this chapter, for different perturbing accelerations. The resulting analytical equations can be used for the propagation of the osculating orbital elements, for propagation of few orbital revolutions. In this case, also the equation for the variation of time with the true longitude L (Equation 4.6) is propagated [240]. For the perturbations and low-thrust profile introduced in this work, however, no closed form solution is available for the time equation. Therefore, the expression for the time is integrated with a quadrature method, in agreement with [240]. For longer propagation times, an averaged propagation of the orbital elements is implemented; the variation of the equinoctial elements is, in this case, computed as

$$\widetilde{\mathbf{X}}(t) = \widetilde{\mathbf{X}}_0 + \int_{t_0}^{t} \dot{\widetilde{\mathbf{X}}}\left(\tau, \widetilde{\mathbf{X}}\left(\tau\right), \alpha', \beta\right) d\tau, \tag{4.11}$$

where

$$\dot{\widetilde{\mathbf{X}}} = \frac{\Delta\widetilde{\mathbf{X}}_{2\pi}}{T} . \tag{4.12}$$

In Equation 4.12, $\Delta\widetilde{\mathbf{X}}_{2\pi}$ is the variation of the orbital elements over one revolution, computed using the analytical formulae in Equation 4.10 with $L - L_0 = 2\pi$, and T is the orbital period. While the integrals in Equation 4.10 are computed analytically, the time integral in Equation 4.12 is computed numerically; the resulting averaged propagator is, therefore, a semi-analytical method. Analytical solutions are considered for the following accelerations and orbital perturbations:

- second zonal harmonic of the Earth's gravitational perturbation, J_2 (refer to [240]);
- third, fourth and fifth zonal harmonic of the Earth's gravitational perturbation, J_3, J_4, J_5 (Section 4.2);
- atmospheric drag (Section 4.3);
- solar radiation pressure, including eclipses (refer to [240]);
- third body gravitational perturbation (Section 4.4);
- constant tangential acceleration (refer to [240]);

- constant acceleration in a radial-transverse-normal reference frame (refer to [240]);
- acceleration with constant azimuth and elevation angles in a radial-transverse-normal reference frame, and with magnitude of the acceleration proportional to $1/r^2$, where r is the distance from the central body (Sun) (Section 4.5);
- constant acceleration in an inertial reference frame (refer to [240]).

It is assumed that, since the perturbing accelerations are small, it is possible to superimpose the analytical solutions relative to each perturbation [240].

4.2 J_3, J_4 and J_5 perturbations

The potential due to the zonal terms of the Earth's gravity field is [204]

$$U = \frac{Gm_\oplus}{r}\left[1 - \sum_{l=2}^{\infty} J_l \left(\frac{R_\oplus}{r}\right)^l \mathcal{P}_l\left(\sin\delta\right)\right] . \tag{4.13}$$

In Equation 4.13 r is the distance of the considered point from the center of mass of the Earth, δ is its declination, $m_\oplus$ is the mass of the Earth, $R_\oplus$ its radius and $\mathcal{P}_l$ are the Legendre polynomials of order l in $\sin\delta$ [4]:

$$\mathcal{P}_l(x) = \frac{1}{2^l l!}\frac{d^l}{dx^l}\left[\left(x^2-1\right)^l\right] . \tag{4.14}$$

The expression for the coordinate z, $z = r\sin\delta$, is used to substitute $\sin\delta = z/r$ in Equation 4.13. The perturbing acceleration due to J_l can be computed from the gradient of the associated potential U_{J_l} as:

$$\mathbf{f}_{J_l} = \nabla U_{J_l} = \frac{\partial U_{J_l}}{\partial r}\hat{\mathbf{i}}_R + \frac{\partial U_{J_l}}{\partial z}\hat{\mathbf{k}} , \tag{4.15}$$

where $\hat{\mathbf{i}}_R$ is the versor of the RTN reference frame and $\hat{\mathbf{k}}$ the z-component versor of the Earth Centred Inertial (ECI) reference frame [204]. The components of the perturbing acceleration due to J_l can be expressed, in the RTN reference frame, as:

$$\begin{aligned} f_{J_{l\,R}} &= \mathbf{f}_{J_l}\cdot\hat{\mathbf{i}}_R = \frac{\partial U_{J_n}}{\partial r} + \frac{\partial U_{J_l}}{\partial z}\hat{\mathbf{k}}\cdot\hat{\mathbf{i}}_R, \\ f_{J_{l\,T}} &= \mathbf{f}_{J_l}\cdot\hat{\mathbf{i}}_T = \frac{\partial U_{J_l}}{\partial z}\hat{\mathbf{k}}\cdot\hat{\mathbf{i}}_T, \\ f_{J_{l\,N}} &= \mathbf{f}_{J_l}\cdot\hat{\mathbf{i}}_N = \frac{\partial U_{J_l}}{\partial z}\hat{\mathbf{k}}\cdot\hat{\mathbf{i}}_N . \end{aligned} \tag{4.16}$$

The scalar products in the previous equations are

$$\begin{aligned} \hat{\mathbf{k}}\cdot\hat{\mathbf{i}}_R &= \sin i\sin u, \\ \hat{\mathbf{k}}\cdot\hat{\mathbf{i}}_T &= \sin i\cos u, \\ \hat{\mathbf{k}}\cdot\hat{\mathbf{i}}_N &= \cos i . \end{aligned} \tag{4.17}$$

The analytical equations for the variation of the equinoctial orbital elements under the effect of J_3, J_4 and J_5 perturbations are derived in the following subsections. While previous works have presented analytical solutions for the motion of a satellite subject to aspherical gravitational perturbations [34, 118], to the author's best knowledge, analytical equations in non-singular equinoctial elements are not present in the literature.

4.2.1 J_3 perturbation

The potential due to J_3 is

$$U_{J_3} = -J_3 \left(\frac{R_\oplus}{r}\right)^3 \mathcal{P}_3 \left(\sin\delta\right) = -\frac{\mu_\oplus}{r} J_3 \left(\frac{R_\oplus}{r}\right)^3 \left(\frac{5}{2}\frac{z^3}{r^3} - \frac{3}{2}\frac{z}{r}\right), \tag{4.18}$$

obtained using

$$\mathcal{P}_3 \left(x\right) = \frac{1}{2}\left(5x^3 - 3x\right) . \tag{4.19}$$

The derivatives of the potential with respect to r and z are

$$\frac{dU_{J_3}}{dr} = \frac{1}{2}\mu_\oplus J_3 \frac{R_\oplus^3}{r^5}\left(\frac{z^3}{r^3} - 15\frac{z}{r}\right), \tag{4.20}$$

$$\frac{dU_{J_3}}{dz} = \frac{3}{2}\mu_\oplus J_3 \frac{R_\oplus^3}{r^5}\left(1 - 5\frac{z^2}{r^2}\right) . \tag{4.21}$$

The components of the perturbing acceleration due to J_3 are:

$$\begin{aligned}
f_{J_{3R}} &= 2\mu_\oplus J_3 \frac{R_\oplus^3}{r^5} \sin i \sin u \left(5\sin^2 i \sin^2 u - 3\right), \\
f_{J_{3T}} &= \frac{3}{2}\mu_\oplus J_3 \frac{R_\oplus^3}{r^5} \sin i \cos u \left(1 - 5\frac{z^2}{r^2}\right), \\
f_{J_{3N}} &= \frac{3}{2}\mu_\oplus J_3 \frac{R_\oplus^3}{r^5} \cos i \left(1 - 5\frac{z^2}{r^2}\right) .
\end{aligned} \tag{4.22}$$

The terms in i and u in Equations 4.22 can be expressed in terms of the equinoctial elements. Moreover, using

$$r = \frac{a(1-e^2)}{1 + e\cos\theta} = \frac{aB^2}{\Phi(L)}, \tag{4.23}$$

it is possible to obtain the three components of the perturbing acceleration expressed in terms of equinoctial elements:

$$
\begin{aligned}
f_{J_{3_R}} &= 4\mu_\oplus J_3 R_\oplus^3 \frac{\Phi^5(L)}{a^5 B^{10}} \left(\frac{Q_2 \sin L - Q_1 \cos L}{S}\right) \left[\frac{20\left(Q_2 \sin L - Q_1 \cos L\right)^2}{S^2} - 3\right], \\
f_{J_{3_T}} &= 3\mu_\oplus J_3 R_\oplus^3 \frac{\Phi^5(L)}{a^5 B^{10}} \left(\frac{Q_2 \cos L + Q_1 \sin L}{S}\right) \left[1 - \frac{20\left(Q_2 \sin L - Q_1 \cos L\right)^2}{S^2}\right], \\
f_{J_{3_N}} &= \frac{3}{2}\mu_\oplus J_3 R_\oplus^3 \frac{\Phi^5(L)}{a^5 B^{10}} \frac{\left(1 - Q_1^2 - Q_2^2\right)}{S} \left[1 - \frac{20\left(Q_2 \sin L - Q_1 \cos L\right)^2}{S^2}\right],
\end{aligned}
\tag{4.24}
$$

where $S = 1 + Q_1^2 + Q_2^2$. The accelerations in Equations 4.24 are substituted in 4.7. After integration, the following expressions for the components of $\widetilde{\mathbf{X}}^{J_3} \approx \widetilde{\mathbf{X}}_0 + \epsilon_{J_3} \widetilde{\mathbf{X}}_1^{J_3}$ are obtained:

$$
\begin{aligned}
a^{J_3} &= a_0 + \epsilon_{J_3} \frac{a_0}{B_0^8 S_0^3} \left(8\, I_{J_3,a,1} + 6\, I_{J_3,a,2}\right), \\
P_1^{J_3} &= P_{10} + \epsilon_{J_3} \frac{1}{B_0^6 S_0^3} \left[I_{J_3,P_1} - \frac{3}{2} P_{20} \left(1 - Q_{10}^2 - Q_{20}^2\right) I_{J_3,P_1,P_2}\right], \\
P_2^{J_3} &= P_{20} + \epsilon_{J_3} \frac{1}{B_0^6 S_0^3} \left[I_{J_3,P_2} + \frac{3}{2} P_{10} \left(1 - Q_{10}^2 - Q_{20}^2\right) I_{J_3,P_1,P_2}\right], \\
Q_1^{J_3} &= Q_{10} + \epsilon_{J_3} \frac{3}{4\, B_0^6 S_0^2} \left(1 - Q_{10}^2 - Q_{20}^2\right) I_{J_3,Q_1}, \\
Q_2^{J_3} &= Q_{20} + \epsilon_{J_3} \frac{3}{4\, B_0^6 S_0^2} \left(1 - Q_{10}^2 - Q_{20}^2\right) I_{J_3,Q_2},
\end{aligned}
\tag{4.25}
$$

where $\epsilon_{J_3} = J_3 R_\oplus^3 a_0^{-3}$. The vector $\widetilde{\mathbf{X}}_0 = [a_0, P_{10}, P_{20}, Q_{10}, Q_{20}]^T$ is the set of initial equinoctial elements. The integrals $I_{J_3,a,1}, I_{J_3,a,2}, I_{J_3,P_1}, I_{J_3,P_2}, I_{J_3,P_1,P_2}, I_{J_3,Q_1}$ and I_{J_3,Q_2} in Equations 4.25 are reported in Appendix C. They are computed analytically using the software Wolfram Mathematica [1], and the results are then directly exported in MATLAB.

4.2.2 J_4 perturbation

The potential due to J_4 is expressed as

$$
U_{J_4} = \frac{\mu_\oplus J_4}{8} \frac{R_\oplus^4}{r^5} \left[35 \frac{z^4}{r^4} - 30 \frac{z^2}{r^2} + 3\right]. \tag{4.26}
$$

[1] https://www.wolfram.com/mathematica/

Following the same approach used for J_3, the components of the perturbing accelerations are

$$\begin{aligned}
f_{J_{4R}} &= \frac{\mu_\oplus J_4 R_\oplus^4}{8B^{12}a^6}\Phi(L)^6\left[\frac{2800}{S^4}\left(Q_2\sin L - Q_1\cos L\right)^4 - \frac{600}{S^2}\left(Q_2\sin L - Q_1\cos L\right)^2 + 15\right], \\
f_{J_{4T}} &= -\frac{\mu_\oplus J_4 R_\oplus^4}{S^2B^{12}a^6}\Phi^6(L)\left[\frac{280}{S^2}\left(Q_2\sin L - Q_1\cos L\right)^2 - 30\right]\left(Q_2\cos L + Q_1\sin L\right) \\
&\quad \left(Q_2\sin L - Q_1\cos L\right), \\
f_{J_{4N}} &= -\frac{\mu_\oplus J_4 R_\oplus^4}{S^2B^{12}a^6}\left(1 - Q_1^2 - Q_2^2\right)\Phi(L)^6\left[\frac{140}{S^2}\left(Q_2\sin L - Q_1\cos L\right)^2 - 15\right] \\
&\quad \left(Q_2\sin L - Q_1\cos L\right) \ .
\end{aligned} \tag{4.27}$$

The first-order variations of the equinoctial elements are

$$\begin{aligned}
a^{J_4} &= a_0 + \epsilon_{J_4}\frac{a_0}{B_0^{10}S_0^4}\left(\frac{I_{J_4,a,1}}{4} - 2I_{J_4,a,2}\right), \\
P_1^{J_4} &= P_{10} - \epsilon_{J_4}\frac{1}{B_0^8S_0^4}\left[I_{J_4,P_1} + P_{20}(1 - Q_{10}^2 - Q_{20}^2)I_{J_4,P_1,P_2}\right], \\
P_2^{J_4} &= P_{20} + \epsilon_{J_4}\frac{1}{B_0^8S_0^4}\left[I_{J_4,P_2} + P_{10}(1 - Q_{10}^2 - Q_{20}^2)I_{J_4,P_1,P_2}\right], \\
Q_1^{J_4} &= Q_{10} + \epsilon_{J_4}\frac{1}{2B_0^8S_0^3}\left(1 - Q_{10}^2 - Q_{20}^2\right)I_{J_4,Q1}, \\
Q_2^{J_4} &= Q_{20} + \epsilon_{J_4}\frac{1}{2B_0^8S_0^3}\left(1 - Q_{10}^2 - Q_{20}^2\right)I_{J_4,Q2},
\end{aligned} \tag{4.28}$$

where $\epsilon_{J_4} = J_4R_\oplus^4a_0^{-4}$ The integrals in Equations 4.28 are reported in Appendix C.

4.2.3 J_5 perturbation

The potential due to J_5 is

$$U_{J_5} = -\frac{\mu_\oplus J_5 R_\oplus^5}{8}\frac{z}{r^7}\left(63\frac{z^4}{r^4} - 70\frac{z^2}{r^2} + 15\right) \ . \tag{4.29}$$

The components of the corresponding perturbing acceleration are

$$
\begin{aligned}
f_{J_5\,R} &= \frac{\mu_\oplus J_5 R_\oplus^5}{2SB^{14}a^7}\Phi^7(L)\left(Q_2\sin L - Q_1\cos L\right)\left[\frac{3024}{S^4}\left(Q_2\sin L - Q_1\cos L\right)^4 + \right.\\
&\left. -\frac{840}{S^2}\left(Q_2\sin L - Q_1\cos L\right)^2 + 45\right],\\
f_{J_5\,T} &= -\frac{\mu_\oplus J_5 R_\oplus^5}{4SB^{14}a^7}\Phi^7(L)\left(Q_2\cos L + Q_1\sin L\right)\left[\frac{5040}{S^4}\left(Q_2\sin L - Q_1\cos L\right)^4 + \right.\\
&\left. -\frac{840}{S^2}\left(Q_2\sin L - Q_1\cos L\right)^2 + 15\right],\\
f_{J_5\,N} &= -\frac{\mu_\oplus J_5 R_\oplus^5}{8SB^{14}a^7}\Phi^7(L)\left(1 - Q_1^2 - Q_2^2\right)\left[\frac{5040}{S^4}\left(Q_2\sin L - Q_1\cos L\right)^4 + \right.\\
&\left. -\frac{840}{S^2}\left(Q_2\sin L - Q_1\cos L\right)^2 + 15\right].
\end{aligned}
\tag{4.30}
$$

The first-order variations of the equinoctial elements are

$$
\begin{aligned}
a^{J_5} &= a_0 + \frac{\epsilon_{J_5} a_0}{S_0^5 B_0^{12}} I_{J_5,a},\\
P_1^{J_5} &= P_{10} - \frac{\epsilon_{J_5}}{2S_0^5 B_0^{10}}\left[I_{J_5,P_1} - \frac{P_{20}}{4}\left(1 - Q_{10}^2 - Q_{20}^2\right) I_{J_5,P_1,P_2}\right],\\
P_2^{J_5} &= P_{20} - \frac{\epsilon_{J_5}}{2S_0^5 B_0^{10}}\left[I_{J_5,P_2} + \frac{P_{10}}{4}\left(1 - Q_{10}^2 - Q_{20}^2\right) I_{J_5,P_1,P_2}\right],\\
Q_1^{J_5} &= Q_{10} - \frac{\epsilon_{J_5}}{16B^{10}S_0^4}\left(1 - Q_{10}^2 - Q_{20}^2\right) I_{J_5,Q_1},\\
Q_2^{J_5} &= Q_{20} - \frac{\epsilon_{J_5}}{16B_0^{10}S_0^4}\left(1 - Q_{10}^2 - Q_{20}^2\right) I_{J_5,Q_2},
\end{aligned}
\tag{4.31}
$$

where $\epsilon_{J_5} = J_5 R_\oplus^5 a_0^{-5}$. The integrals in Equations 4.31 are reported in Appendix C.

4.3 Atmospheric drag

This section presents an analytical solution for the effect of the atmospheric drag perturbation. In the literature, one of the first analytical solutions to the motion of a satellite subject to atmospheric drag was developed by King-Hele and Cook [49–53, 111, 112]. The authors presented solutions for an exponential atmospheric density model under different simplifying assumptions (on the eccentricity of the orbit, symmetry of the atmosphere and on the scale height of the exponential model). The authors also extended their work to include day-to-night variation in the atmospheric density. In [21], a semi-analytical solution was presented for the TD88 density model [186], a model that takes into account also the effects of solar and geomagnetic activity. More recently, Martinusi developed analytical solutions in terms of non-singular equinoctial elements, first for constant atmospheric density (or circular orbits) [136] and later for an exponential atmospheric model [137]. To the author's best knowledge, the work of Martinusi, published after the method presented in this thesis was developed, is the only other analytical

solution expressed in terms of equinoctial elements existing in the literature.

The analytical solution presented in this work is based on a Chebyshev interpolation of the atmospheric density with respect to the altitude, in order to obtain integrals for which an analytical solution exists. The magnitude of the acceleration acting on a spacecraft due to the atmospheric drag perturbation is

$$f_{Drag} = \frac{1}{2}\rho\, C_D \frac{A}{m} v^2, \tag{4.32}$$

where ρ is the atmospheric density, C_D the drag coefficient and A the area of the spacecraft in the direction of the velocity. It is possible to express f_{Drag} as a function of the equinoctial elements by using the energy equation to write the square of the velocity as

$$v^2 = \frac{\mu_\oplus}{a}\left(\frac{2\Phi(L)}{B^2} - 1\right) . \tag{4.33}$$

f_{Drag} is, therefore,

$$f_{Drag} = \frac{1}{2}\rho\, C_D \frac{A}{m}\frac{\mu_\oplus}{a}\left(\frac{2\Phi(L)}{B^2} - 1\right) . \tag{4.34}$$

The drag acceleration is directed along the opposite direction of the velocity vector of the spacecraft and, therefore, its orientation in the radial-transverse-normal reference frame RTN is defined by the flight path angle γ as

$$\begin{cases} f_{Drag_R} = -f_{Drag}\sin\gamma, \\ f_{Drag_T} = -f_{Drag}\cos\gamma, \\ f_{Drag_N} = 0, \end{cases} \tag{4.35}$$

where γ is

$$\tan\gamma = \frac{e\sin\theta}{1 + e\cos\theta} . \tag{4.36}$$

The angle γ can be expressed in terms of the equinoctial elements

$$\begin{aligned} \sin\gamma &= \frac{P_2\sin L - P_1\cos L}{D(L)}, \\ \cos\gamma &= \frac{1 + P_1\sin L + P_2\cos L}{D(L)} , \end{aligned} \tag{4.37}$$

where $D(L) = \sqrt{1 + P_1^2 + P_2^2 + 2(P_2\cos L + P_1\sin L)}$. Thus, the three components of the acceleration due to the atmospheric drag, using Equations 4.34, 4.35 and 4.37, are

$$\begin{aligned} f_{Drag,R} &= \frac{1}{2}\rho\, C_D \frac{A}{m}\frac{\mu_\oplus}{a}\left(\frac{2\Phi(L)}{B^2} - 1\right)\frac{(P_2\sin L - P_1\cos L)}{D(L)}, \\ f_{Drag,T} &= \frac{1}{2}\rho\, C_D \frac{A}{m}\frac{\mu_\oplus}{a}\left(\frac{2\Phi(L)}{B^2} - 1\right)\frac{(1 + P_1\sin L + P_2\cos L)}{D(L)}, \\ f_{Drag,N} &= 0 . \end{aligned} \tag{4.38}$$

Substituting Equation 4.38 in Equations 4.7, analytical equations for the variations of the equinoctial elements can be obtained:

$$\begin{aligned}
a^{Drag} &= a_0 + a_0^2 C_D \frac{A}{m}\left(e_0^2 I_{Drag,1} + I_{Drag,2}\right), \\
P_1^{Drag} &= P_{10} + B_0^2 a_0 C_D \frac{A}{m}\left[\sin\left(\Omega_0+\omega_0\right)\left(eI_{Drag,3}+I_{Drag,5}\right) + \cos\left(\Omega_0+\omega_0\right) I_{Drag,4}\right], \\
P_2^{Drag} &= P_{20} + B_0^2 a_0 C_D \frac{A}{m}\left[\cos\left(\Omega_0+\omega_0\right)\left(eI_{Drag,3}+I_{Drag,5}\right) - \sin\left(\Omega_0+\omega_0\right) I_{Drag,4}\right], \\
Q_1^{Drag} &= Q_{10}, \\
Q_2^{Drag} &= Q_{20}\,.
\end{aligned} \tag{4.39}$$

The integrals $I_{Drag,1}$, $I_{Drag,2}$, $I_{Drag,3}$, $I_{Drag,4}$ and $I_{Drag,5}$ are

$$\begin{aligned}
I_{Drag,1} &= \int_{\theta_0}^{\theta} \frac{\sin^2\vartheta\sqrt{1+e^2+2e\cos\vartheta}}{(1+e\cos\vartheta)^2}\rho(\vartheta)d\vartheta, \\
I_{Drag,2} &= \int_{\theta_0}^{\theta} \sqrt{1+e^2+2e\cos\vartheta}\rho(\vartheta)d\vartheta, \\
I_{Drag,3} &= \int_{\theta_0}^{\theta} \frac{\sqrt{1+e^2+2e\cos\vartheta}}{(1+e\cos\vartheta)^2}\rho(\vartheta)d\vartheta, \\
I_{Drag,4} &= \int_{\theta_0}^{\theta} \frac{\sin\vartheta\sqrt{1+e^2+2e\cos\vartheta}}{(1+e\cos\vartheta)^2}\rho(\vartheta)d\vartheta, \\
I_{Drag,5} &= \int_{\theta_0}^{\theta} \frac{\cos\vartheta\sqrt{1+e^2+2e\cos\vartheta}}{(1+e\cos\vartheta)^2}\rho(\vartheta)d\vartheta\,.
\end{aligned} \tag{4.40}$$

A complete analytical solution is available when using an exponential atmospheric density model to compute ρ [204]. $\rho(\theta)$ is expressed as a Chebyshev polynomial interpolation with respect to the altitude above the Earth's surface $h_\oplus$ (see Appendix D and [84]):

$$\rho\left(\theta\right) = \sum_{j=0}^{N} c_j h_\oplus^j(\theta) = \sum_{j=0}^{N} c_j \left(\frac{p}{1+e\cos\theta} - R_\oplus\right)^j\,. \tag{4.41}$$

In the previous equation N is the order and c_j are the coefficients of the interpolation. In order to better approximate the exponential model, the altitude is segmented in different intervals, and on each one of them the atmospheric density is approximated by a Chebyshev interpolation with different coefficients c_j. The considered intervals of altitude are: from 110 to 125 km, from 125 to 150 km, from 150 to 250 km, from 250 to 350 km, from 350 to 500 km, from 500 to 700 km, from 700 to 1000 km, from 1000 to 2000 km, from 2000 to 3000 km, from 3000 to 4000 km and at altitude greater than 4000 km. The Chebyshev interpolation for each one of these altitude ranges is realised to order $N = 4$, obtaining:

$$\rho(\theta) = k_0 + k_1\left(\frac{1}{1+e\cos\theta}\right) + k_2\left(\frac{1}{1+e\cos\theta}\right)^2 + k_3\left(\frac{1}{1+e\cos\theta}\right)^3 + k_4\left(\frac{1}{1+e\cos\theta}\right)^4, \tag{4.42}$$

where

$$\begin{aligned} k_0 &= c_0 - c_1 R_\oplus + c_2 R_\oplus^2 - c_3 R_\oplus^3 + c_4 R_\oplus^4, \\ k_1 &= c_1 p - 2c_2 p R_\oplus + 3c_3 p R_\oplus^2 - 4c_4 p R_\oplus^3, \\ k_2 &= c_2 p^2 - 3c_3 p^2 R_\oplus + 6c_4 p^2 R_\oplus^2, \\ k_3 &= c_3 p^3 - 4c_4 p^3 R_\oplus, \\ k_4 &= c_4 p^4 \, . \end{aligned} \tag{4.43}$$

Substituting the previous expression for $\rho(\theta)$ in Equations 4.40 results in

$$I_{Drag,n} = \sum_{j=0}^{4} k_n I_{Drag,nj} \qquad n = 1, \dots 5 \, . \tag{4.44}$$

The integrals $I_{Drag,nj}$ and their analytical solutions are reported in Appendix C. The coefficients c_j, for each one of the ranges of altitudes specified above, are reported in Table 4.1. The density obtained using the given coefficients is expressed in kg/$DU_\oplus^3$, where $DU_\oplus = R_\oplus$.

Table 4.1: Coefficients of the Chebyshev expansion for the atmospheric density (Equation 4.41).

Altitude range [km]	c_0 [kg/$DU_\oplus^3$]	c_1 [kg/$DU_\oplus^4$]	c_2 [kg/$DU_\oplus^5$]	c_3 [kg/$DU_\oplus^6$]	c_4 [kg/$DU_\oplus^7$]
110-125	$1.8701\ 10^{16}$	$-3.5373\ 10^{15}$	$2.5063\ 10^{20}$	$-7.8776\ 10^{21}$	$9.2605\ 10^{22}$
125-150	$6.0998\ 10^{15}$	$-1.0877\ 10^{18}$	$7.2857\ 10^{19}$	$-2.1713\ 10^{21}$	$2.4286\ 10^{22}$
150-250	$3.4480\ 10^{13}$	$-3.9085\ 10^{15}$	$1.6716\ 10^{17}$	$-3.1870\ 10^{18}$	$2.2815\ 10^{19}$
250-350	$4.3292\ 10^{11}$	$-1.9432\ 10^{13}$	$2.0749\ 10^{14}$	$1.5029\ 10^{15}$	$-2.6172\ 10^{16}$
350-500	$2.6590\ 10^{11}$	$-1.4350\ 10^{13}$	$2.9393\ 10^{14}$	$-2.6984\ 10^{15}$	$9.3433\ 10^{15}$
500-700	$1.8558\ 10^{10}$	$-6.7202\ 10^{11}$	$9.1863\ 10^{12}$	$-5.6139\ 10^{13}$	$1.2909\ 10^{14}$
700-1000	$1.3690\ 10^{9}$	$-3.7062\ 10^{10}$	$3.7867\ 10^{11}$	$-1.7269\ 10^{12}$	$2.9621\ 10^{12}$
1000-2000	$1.2758\ 10^{7}$	$-1.7198\ 10^{8}$	$8.9247\ 10^{8}$	$-2.0969\ 10^{9}$	$1.8710\ 10^{9}$
2000-3000	$1.6982\ 10^{6}$	$-1.5222\ 10^{7}$	$5.1628\ 10^{7}$	$-7.8357\ 10^{7}$	$4.4830\ 10^{7}$
3000-4000	$1.3617\ 10^{5}$	$-9.0765\ 10^{5}$	$2.2785\ 10^{6}$	$-2.5511\ 10^{6}$	$1.0741\ 10^{6}$
>4000	0	0	0	0	0

4.3.1 Corrective terms for J_2 and Earth's flattening

Particular attention has to be paid when the propagation is realised over longer period of times and at lower altitudes. In this cases the coupling of J_2 and atmospheric drag requires a corrective term δr to the radial position [55]:

$$r' = r + \delta r \tag{4.45}$$

where r is the Keplerian distance:

$$r = \frac{p}{1 + e\cos\theta} \tag{4.46}$$

and δr is

$$\delta r = J_2 \frac{R_\oplus^2}{p} \left\{ \frac{1}{4} \sin^2 i \cos 2(\omega + \theta) - \left[\frac{1}{2} - \frac{3}{4} \sin^2 i \right] \left[1 + \frac{e \cos\theta}{1 + \sqrt{1 - e^2}} + \frac{2}{\sqrt{1 - e^2}} \frac{r}{a} \right] \right\} \quad (4.47)$$

The integrals reported in Appendix C do not take into account the corrective term δr. No analytical solution has been derived for the integrals with corrective term δr. When this has to be used, the integration is performed numerically.

To show the effect of the coupling term, a propagation of one year, considering J_2 and atmospheric drag is realised using the initial orbital elements defined in Table 4.2, describing a low altitude orbit.

Table 4.2: Initial orbital elements for one year propagation with J_2 and atmospheric drag.

a [km]	e	i [deg]	Ω [deg]	ω [deg]
6978.14	0.03	30	0	30

When the corrective term is not taken into account the averaged analytical propagation gives an error with respect to a numerical propagation, as shown in Figure 4.2. The numerical

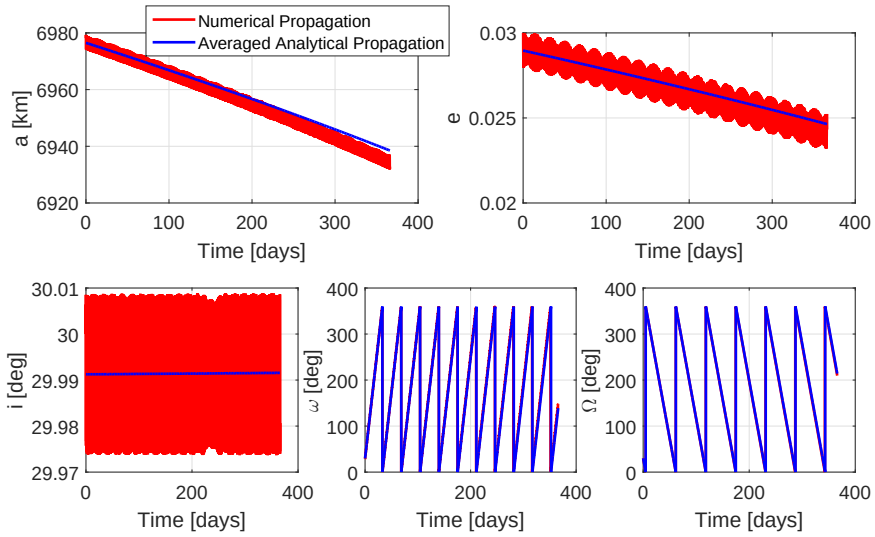

Figure 4.2: Comparison of averaged analytical and numerical propagation with J_2 and atmospheric drag without corrective term for the position.

propagation is realised by numeric integrations of Equations 4.3. When using the corrective term δr for r, however, the results of the averaged analytical propagation coincide with those of the numerical propagation, as shown in Figure 4.3. In this case, the averaged semi-analytical propagation is realised with numerical integration of the integrals defined in Equations 4.44. The numerical integration of these integrals slows down the averaged propagator by a factor of at least 6. The corrective term is, however, not necessary for higher altitude orbits, where the coupling between J_2 and atmospheric drag is negligible.

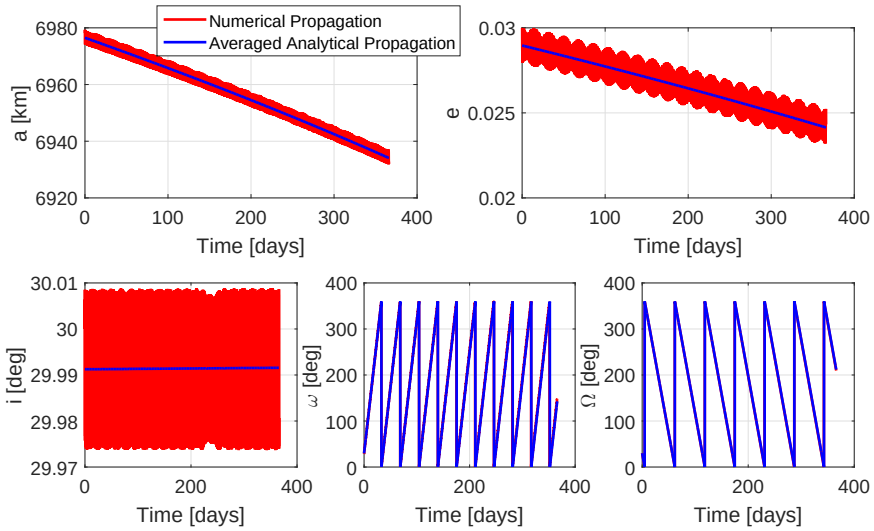

Figure 4.3: Comparison of averaged semi-analytical and numerical propagation with J_2 and atmospheric drag with corrective term for the position.

In the drag model described above, it is assumed that the Earth has a spherical shape and that therefore the altitude can be computed as $h_\oplus = r - R_\oplus$. In order to account for the Earth's surface flattening, the Earth's radius is expressed as [55]:

$$R_\oplus^{flat} = R_\oplus \left[1 - f_\oplus \sin^2 i \sin^2 (\omega + \theta)\right] \tag{4.48}$$

where $f_\oplus = 0.00335$ is the Earth flattening factor. The integrals reported in Appendix C do not take into account the Earth flattening. No analytical solution has been derived for the integrals with Earth flattening. When this has to be taken into consideration, the integration of the corresponding integrals is performed numerically.

4.4 Third body perturbation

The following derivation of the third body perturbation is based upon the work of Cefola [41]. Cefola presented equations describing the potential used to model the influence of third bodies, equations for the derivative of the potential with respect to the equinoctial elements and other relevant parameters, and the Lagrange planetary equations expressed in equinoctial elements and depending upon the derivative of the potential. In this work, the Lagrange planetary equations have been integrated analytically, using the expression for the derivatives of the potential presented by Cefola. This section introduces at first the main equation introduced in [41] and then presents the analytical equations for the equinoctial elements derived for this thesis.

The potential expressing the influence of the gravity of a third body (Sun, Moon or other

planets) on an Earth orbiting satellite is:

$$U^{3rd} = \sum_{j=2}^{\infty} U_j^{3rd} \tag{4.49}$$

where

$$U_j^{3rd} = \frac{\mu_{3rd}}{r_{3rd}} \left(\frac{r}{r_{3rd}} \right)^j \mathcal{P}_j \left(\cos \xi \right) \ . \tag{4.50}$$

In Equation 4.50, μ_{3rd} is the gravitational potential of the third body, r_{3rd} is the distance from the central body to the third body, r is the distance from the Earth to the satellite, P_j is the Legendre polynomial of order j and ξ is the angle between the vectors $\mathbf{r}_{3rd}$ and $\mathbf{r}$.

The equations for the variation with time of the equinoctial elements, due to the third body perturbation, are [41]:

$$\begin{aligned}
\frac{da}{dt} &= 0 \\
\frac{dP_1}{dt} &= \frac{1}{n\, a^2 B} \left[B^2 \frac{\partial \bar{U}^{3rd}}{\partial P_2} - P_2 \gamma_{3rd} \left(Q_1 \frac{\partial \bar{U}^{3rd}}{\partial \alpha_{3rd}} - Q_2 \frac{\partial \bar{U}^{3rd}}{\partial \beta_{3rd}} \right) \right] \\
\frac{dP_2}{dt} &= -\frac{1}{n\, a^2 B} \left[B^2 \frac{\partial \bar{U}^{3rd}}{\partial P_1} - P_1 \gamma_{3rd} \left(Q_1 \frac{\partial \bar{U}^{3rd}}{\partial \alpha_{3rd}} - Q_2 \frac{\partial \bar{U}^{3rd}}{\partial \beta_{3rd}} \right) \right] \\
\frac{dQ_1}{dt} &= \frac{S}{2\, n\, a^2 B} \gamma_{3rd} \frac{\partial \bar{U}^{3rd}}{\partial \beta_{3rd}} \\
\frac{dQ_2}{dt} &= \frac{S}{2\, n\, a^2 B} \gamma_{3rd} \frac{\partial \bar{U}^{3rd}}{\partial \alpha_{3rd}}
\end{aligned} \tag{4.51}$$

where $n = \sqrt{\mu_\oplus / a^3}$ is the spacecraft mean motion. The terms $\partial \bar{U}^{3rd}/\partial P_1$, $\partial \bar{U}^{3rd}/\partial P_2$, $\partial \bar{U}^{3rd}/\partial \alpha_{3rd}$ and $\partial \bar{U}^{3rd}/\partial \beta_{3rd}$ in Equation 4.51 are reported in [41] up to $j = 6$, where $\bar{U}^{3rd}$ is the potential averaged over one orbital period:

$$\bar{U}^{3rd} = \frac{1}{2\pi} \int_0^{2\pi} U^{3rd} d\vartheta \tag{4.52}$$

The angles α_{3rd}, β_{3rd} and γ_{3rd} are the three direction cosines of $\mathbf{r}_{3rd}$ relative to the equinoctial frame:

$$\begin{aligned}
\alpha_{3rd} &= \hat{\mathbf{f}} \cdot \hat{\mathbf{r}}_{3rd} \\
\beta_{3rd} &= \hat{\mathbf{g}} \cdot \hat{\mathbf{r}}_{3rd} \\
\gamma_{3rd} &= \hat{\mathbf{w}} \cdot \hat{\mathbf{r}}_{3rd}
\end{aligned} \tag{4.53}$$

where $\hat{\mathbf{f}}$, $\hat{\mathbf{g}}$ and $\hat{\mathbf{w}}$ are the versors of the equinoctial frame [57]. Using Equations 4.6 and 4.51, expressions for the variation of the equinoctial elements with respect to L can be found and,

after integration, the final results are:

$$\begin{aligned}
a^{3rd} &= a_0 \\
P_1^{3rd} &= P_{10} + \frac{B_0^2}{256\, r_{3rd}^4} \frac{\mu_{3rd}}{\mu_\oplus} k_{P_1} I_{3rd} \\
P_2^{3rd} &= P_{20} + \frac{B_0^2}{256\, r_{3rd}^4} \frac{\mu_{3rd}}{\mu_\oplus} k_{P_2} I_{3rd} \\
Q_1^{3rd} &= Q_{10} + \frac{B_0^2\, \gamma_{3rd}\, S_0}{512\, r_{3rd}^4} \frac{\mu_{3rd}}{\mu_\oplus} k_{Q_1} I_{3rd} \\
Q_2^{3rd} &= Q_{20} + \frac{B_0^2\, \gamma_{3rd}\, S_0}{512\, r_{3rd}^4} \frac{\mu_{3rd}}{\mu_\oplus} k_{Q_2} I_{3rd}
\end{aligned} \tag{4.54}$$

where

$$I_{3rd} = \left[-\frac{2}{B_0^3} \Lambda_0 \left(\mathcal{L} \right) - \frac{1}{P_{20} B_0^2} \frac{P_{10} + \left(P_{10}^2 + P_{20}^2 \right) \sin \mathcal{L}}{\Phi_0 \left(\mathcal{L} \right)} \right]_{L_0}^{L} \tag{4.55}$$

and

$$\Lambda_0(L) = \arctan \left\{ \frac{1}{B} \left[-P_{10} + (P_{20} - 1) \tan \left(\frac{L}{2} \right) \right] \right\} \tag{4.56}$$

The expressions for $k_{P_1}, k_{P_2}, k_{Q_1}$ and k_{Q_2} are too cumbersome to be reported in this thesis; they can be found at http://dx.doi.org/10.15129/354f9b2a-d1d5-4f51-9545-e963251f1e40. They were obtained using the software Mathematica; the results were directly exported from Mathematica to MATLAB. Due to the averaging process used to obtain $\bar{U}^{3rd}$, the averaged propagation results in a double average for the third-body effect (Equations 4.10 and 4.52).

4.5 Low-thrust acceleration following an inverse square law

For Solar Electric Propulsion (SEP) applications or solar sails, it is assumed that the low-thrust acceleration decreases as the distance from the Sun increases. This is modelled considering the following inverse square law expression for the magnitude of the low-thrust acceleration (Equation 2.1):

$$\epsilon = \tilde{\epsilon} / (r/\tilde{r})^2 \tag{4.57}$$

where $\tilde{\epsilon}$ is a reference low-thrust acceleration, obtained at a distance from the Sun equal to $\tilde{r}$. The distance of the spacecraft from the central body, r, can be expressed as [240]:

$$r = \frac{a\, B^2}{\Phi(L)} \,. \tag{4.58}$$

The low-thrust acceleration is therefore:

$$\mathbf{f} = \begin{bmatrix} f_R \\ f_T \\ f_N \end{bmatrix} = \tilde{\epsilon} \tilde{r}^2 \frac{\Phi(L)^2}{a^2 B^4} \begin{bmatrix} \cos\beta \cos\alpha' \\ \cos\beta \sin\alpha' \\ \sin\beta \end{bmatrix} \,. \tag{4.59}$$

Substituting Equations 4.57 and 2.1 into Equations 4.7 and integrating from L_0 to L with constant azimuth angle α' and elevation angle β results in

$$
\begin{aligned}
a^{RTN_{1/r^2}} &= a_0 + \tilde{\epsilon}\frac{2a_0\tilde{r}^2}{\mu B_0}\cos\beta\left[\left(P_{20}\cos\alpha' + P_{10}\sin\alpha'\right)\left(\cos L_0 - \cos L\right) - \right. \\
&\quad \left.\left(P_{10}\cos\alpha' - P_{20}\sin\alpha'\right)\left(\sin L - \sin L_0\right) + \sin\alpha'\left(L - L_0\right)\right] , \\
P_1^{RTN_{1/r^2}} &= P_{10} + \tilde{\epsilon}\frac{\tilde{r}^2}{\mu}\left[-\cos\alpha'\cos\beta\left(\sin L - \sin L_0\right) + \sin\alpha'\cos\beta\left(-\cos L + \cos L_0\right) + \right. \\
&\quad \left.\left(\sin\alpha'\cos\beta + P_{20}Q_{20}\sin\beta\right)I_{s1} - Q_{10}P_{20}\sin\beta I_{c1} + P_{10}\sin\alpha'\cos\beta I_{11}\right] , \\
P_2^{RTN_{1/r^2}} &= P_{20} + \tilde{\epsilon}\frac{\tilde{r}^2}{\mu}\left[\cos\alpha'\cos\beta\left(\cos L_0 - \cos L\right) + \sin\alpha'\cos\beta\left(\sin L - \sin L_0\right) + \right. \\
&\quad \left.\left(\sin\alpha'\cos\beta + P_{10}Q_{10}\sin\beta\right)I_{c1} - Q_{20}P_{10}\sin\beta I_{s1} + P_{20}\sin\alpha'\cos\beta I_{11}\right] , \\
Q_1^{RTN_{1/r^2}} &= Q_{10} + \tilde{\epsilon}\frac{\tilde{r}}{2\mu}\sin\beta S_0 I_{s1} , \\
Q_2^{RTN_{1/r^2}} &= Q_{20} + \tilde{\epsilon}\frac{\tilde{r}}{2\mu}\sin\beta S_0 I_{c1} .
\end{aligned}
\tag{4.60}
$$

The expression for I_{11} is reported in [240]. The integrals I_{s1} and I_{c1} are

$$
I_{s1} = \frac{P_{10}}{e_0^2}\left(L - L_0\right) - \frac{P_{20}}{e_0^2}\log\frac{\Phi(L)}{\Phi(L_0)} - \frac{P_{10}}{e_0^2}I_{11} , \tag{4.61}
$$

and

$$
I_{c1} = \frac{P_{20}}{e_0^2}\left(L - L_0\right) + \frac{P_{10}}{e_0^2}\log\frac{\Phi(L)}{\Phi(L_0)} - \frac{P_{20}}{e_0^2}I_{11} . \tag{4.62}
$$

If $e_0 \approx 0$, the following non-singular expressions are used:

$$
I_{s1} = \cos L_0 - \cos L , \quad I_{c1} = \sin L - \sin L_0 . \tag{4.63}
$$

4.6 Validation against GMAT and numerical propagation

The validation of the averaged semi-analytical propagator is realised comparing its results against those obtained with numerical integration of the Gauss' equations (Equations 4.3) and against the results of the NASA open-source software General Mission Analysis Tool (GMAT) [2]. While the averaged propagator provides the mean orbital elements of the orbit, GMAT gives as output a set of osculating orbital elements. In order to be able to compare the results, the initial osculating orbital elements, used to define the initial state of the orbit in GMAT, are converted into mean orbital elements. These are then used as initial conditions for the averaged propagator. Detailed equations for the conversion from mean to osculating orbital elements can be found in [118, 204]. The conversion takes into account the perturbation due to J_2. A more accurate conversion should consider an higher order and degree for the gravitational harmonic field and third body perturbations [92]. For a first approximation, however,

[2] `https://gmat.gsfc.nasa.gov/`

the use of J_2 only is deemed sufficiently accurate. The conversion from mean to osculating elements has been verified by comparison with the software CNES STELA[3], that implements a propagation both in osculating and mean orbital elements. The validation against GMAT is performed for the perturbations due to J_2, J_3, J_4 and J_5, the third body effect of Sun and Moon and solar radiation pressure. GMAT does not implement the exponential atmospheric density model considered in this work, therefore the atmospheric drag perturbation is not included when comparing the averaged propagator with GMAT. GMAT is used with the Runge Kutta 89 integrator with default values for the accuracy and step size.[4] For the validation of the effect of the atmospheric drag perturbation, the numerical integration of the equations of motion is performed instead. The numerical integration is performed using MATLAB *ode113*, a variable-step, variable-order Adams-Bashforth-Moulton predict-evaluate-correct-evaluate solver of order 13. Numerical integration is used also to validate the equations resulting from the low-thrust acceleration presented in Section 4.5. Different orbits are considered: Low Earth Orbit (LEO), Sun-Synchronous Orbit (SSO), Medium Earth Orbit (MEO), Geostationary Transfer Orbit (GTO), Geostationary Equatorial Orbit (GEO) and High Elliptic Orbit (HEO). The initial osculating orbital elements of the considered orbits are reported in Table 4.3.

Table 4.3: Initial osculating orbital element of the different orbits used for the validation of the semi-analytical propagator.

	a [km]	e	i [deg]	Ω [deg]	ω [deg]
LEO 1	7000	0	45	0	-
LEO 2	8000	0.15	0	-	0
SSO	7200	0.01	98.7183	0	0
MEO	29600	0	56	0	0
GTO	24505	0.725	7	0	0
GEO	42165	0	0	-	0
HEO	42165	0.4	63.4	0	270

A 1000 kg mass spacecraft with initial propagation date 21 March 2030, 00:00 is considered. The spacecraft reflectivity coefficient for the solar radiation pressure coefficient is set to $C_r = 1.3$ and the drag coefficient is set to $C_D = 2.2$. The area to mass ratios for solar radiation pressure and atmospheric drag are, respectively, 0.1 m^2/kg and 0.02 m^2/kg. A cylindrical shadow model is considered for the solar radiation pressure. For the low-thrust acceleration, the thrust is assumed to be 0.1 N at $\tilde{r} = R_\oplus$. The azimuth and elevation angles are set to $\alpha' = 90$ deg and $\beta = 30$ deg. The variations of the equinoctial elements, for propagations of one year starting from the initial orbits described in Table 4.3, are shown in the next subsections. The computational time required for a one year propagation of orbit LEO 1, considering perturbations due to J_2, J_3, J_4, J_5, Sun and Moon and solar radiation pressure with eclipses, using the semi-analytical propagator, is 1.2 % of the time required by GMAT on a system with Intel(R) Core(TM) i7-3770 CPU 3.40 GHz with 8GB RAM. The computational time of the propagation of orbit LEO1 with J_2 and atmospheric drag (exponential atmospheric model),

[3] https://logiciels.cnes.fr/en/content/stela

[4] http://gmat.sourceforge.net/doc/R2017a/html/Propagator.html

using the semi-analytical propagator, is 3.2 % of the time required by the numerical integration of the equations of Gauss and 1.4 % of the time required by GMAT (that implements a Jacchia-Roberts atmospheric density model).

4.6.1 LEO 1

This section presents the comparison of the results of the semi-analytical propagator with those of GMAT and of the numerical integration of the equations of Gauss, for orbit LEO 1 (Table 4.3). Figure 4.4 shows the results of the propagation considering J_2, J_3, J_4, J_5, Sun and Moon and solar radiation pressure with eclipses; the results of the semi-analytical propagator (in blue) are in agreement with those of GMAT (in red), thus demonstrating the validity of the method presented in Sections 4.2 and 4.4 and in [240]. Figure 4.5 shows the results of the propagation with J_2 and atmospheric drag perturbation. In this case the averaged semi-analytic propagator is compared to the numerical integration of the Gauss' equations. The agreement of the results demonstrate the validity of the equations developed in Section 4.3. Finally, Figure 4.6 presents the results of the propagation with low-thrust acceleration following an inverse square law $1/r^2$ (Section 4.5). In this case too the comparison is against a numerical integration of the Gauss' equations.

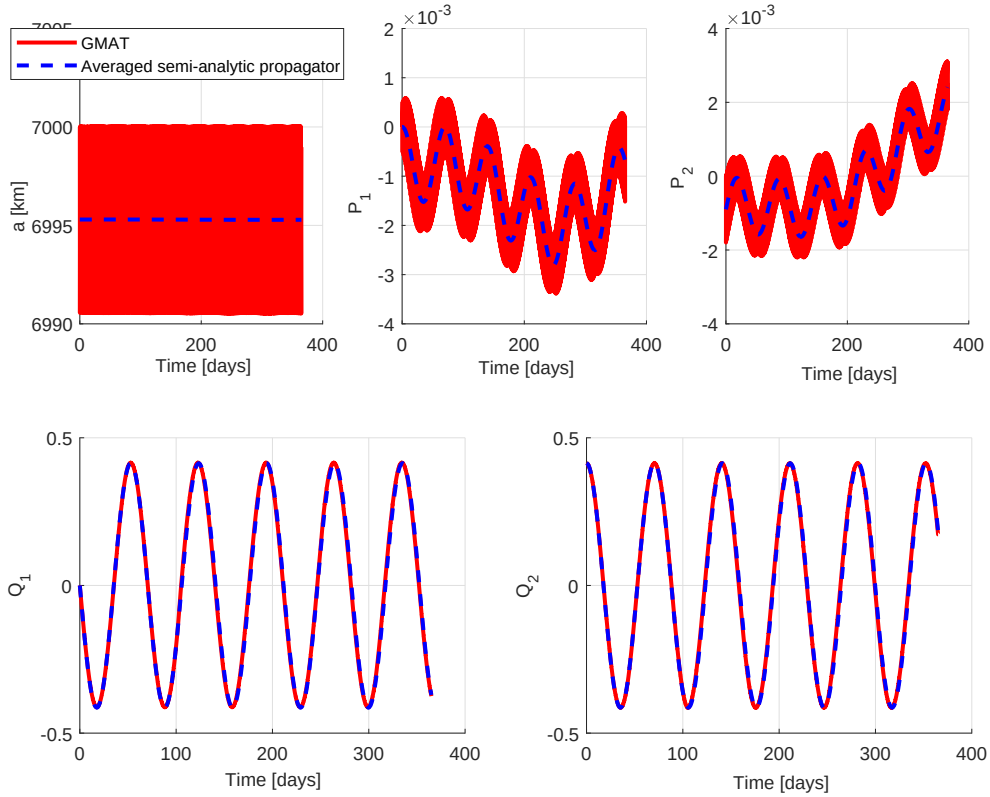

Figure 4.4: Validation against GMAT for orbit LEO 1: J_2 to J_5, Sun, Moon, SRP and eclipses.

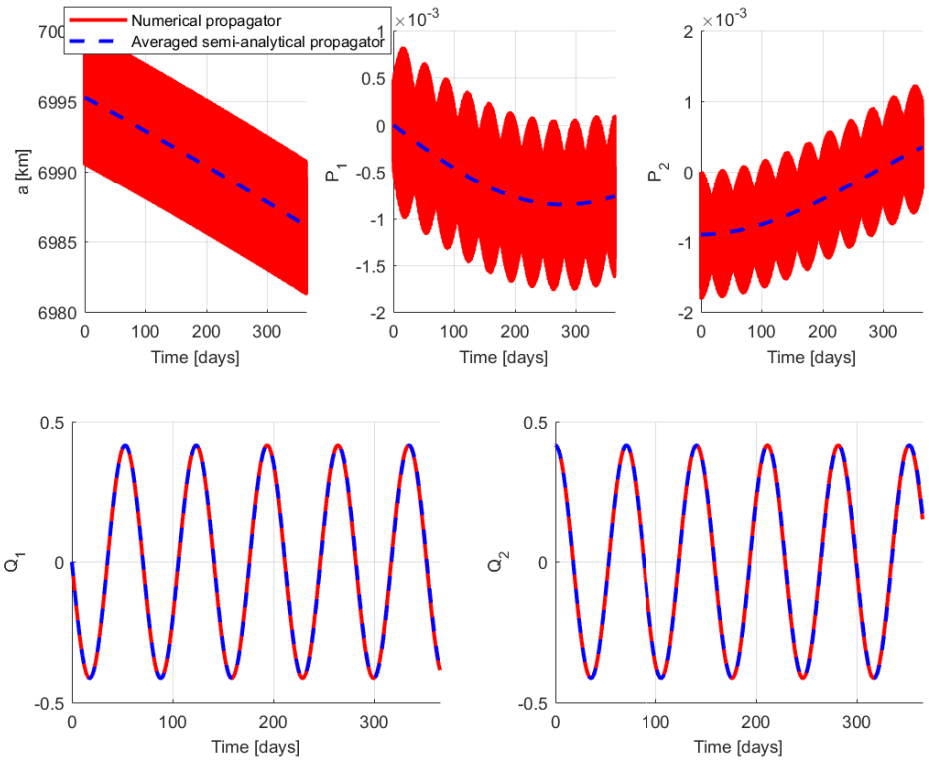

Figure 4.5: Validation against numerical propagation for orbit LEO 1: J_2 and drag.

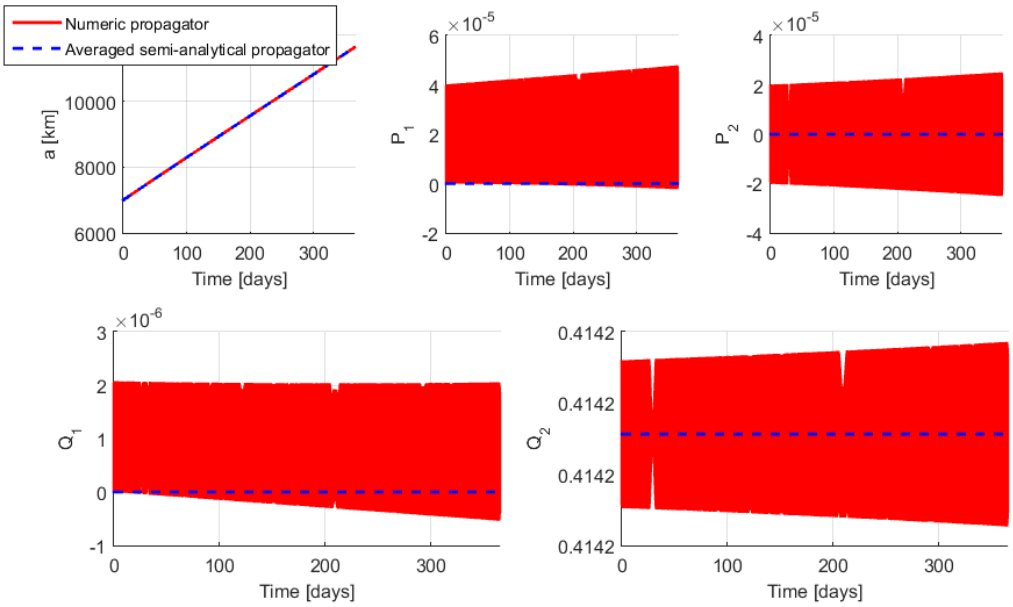

Figure 4.6: Validation against numerical propagation for orbit LEO 1: low-thrust acceleration (Section 4.5).

4.6.2 LEO 2

This section presents the comparison of the results of the semi-analytical propagator with those of GMAT and of the numerical integration of the equations of Gauss, for orbit LEO 2 (Table 4.3). Figure 4.7 shows the results of the propagation considering J_2, J_3, J_4, J_5, Sun and Moon and solar radiation pressure with eclipses; the results of the semi-analytical propagator, in blue, are in agreement with those of GMAT, in red, thus demonstrating the validity of the method presented in Sections 4.2, 4.4 and in [240]. Figure 4.8 shows the results of the propagation with J_2 and atmospheric drag perturbation. In this case, the averaged semi-analytic propagator is compared to the numerical integration of the Gauss' equations. The agreement of the results demonstrate the validity of the equations developed in Section 4.3. Finally, Figure 4.9 presents the results of the propagation with low-thrust acceleration following an inverse square law (Section 4.5). In this case too the comparison is against a numerical integration of the Gauss' equations and the results are in good agreement.

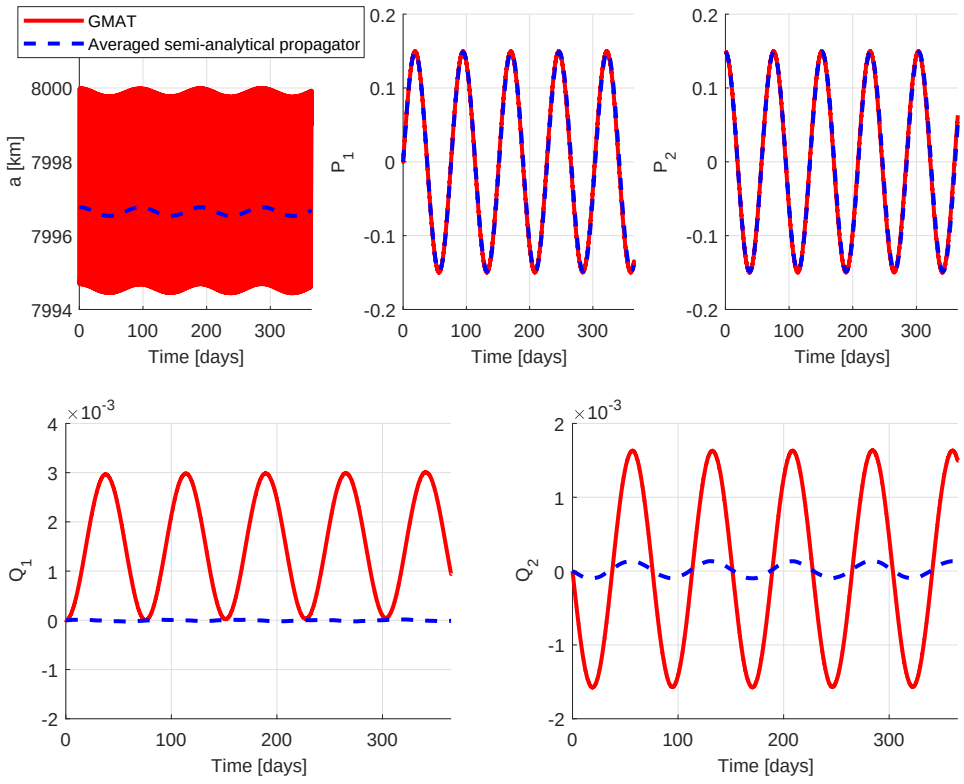

Figure 4.7: Validation against GMAT for orbit LEO 2: J_2 to J_5, Sun, Moon, SRP and eclipses.

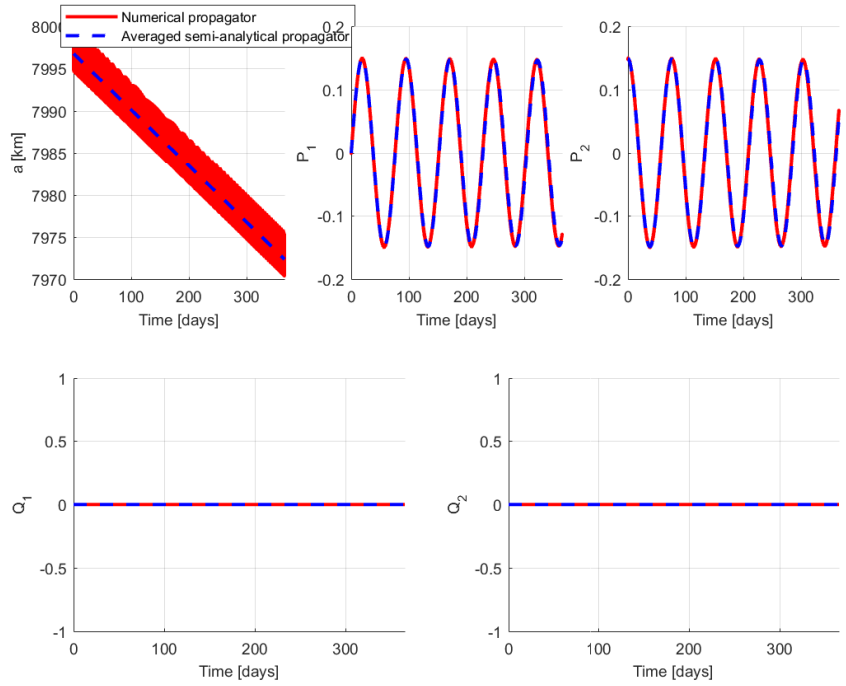

Figure 4.8: Validation against numerical propagation for orbit LEO 2: J_2 and atmospheric drag.

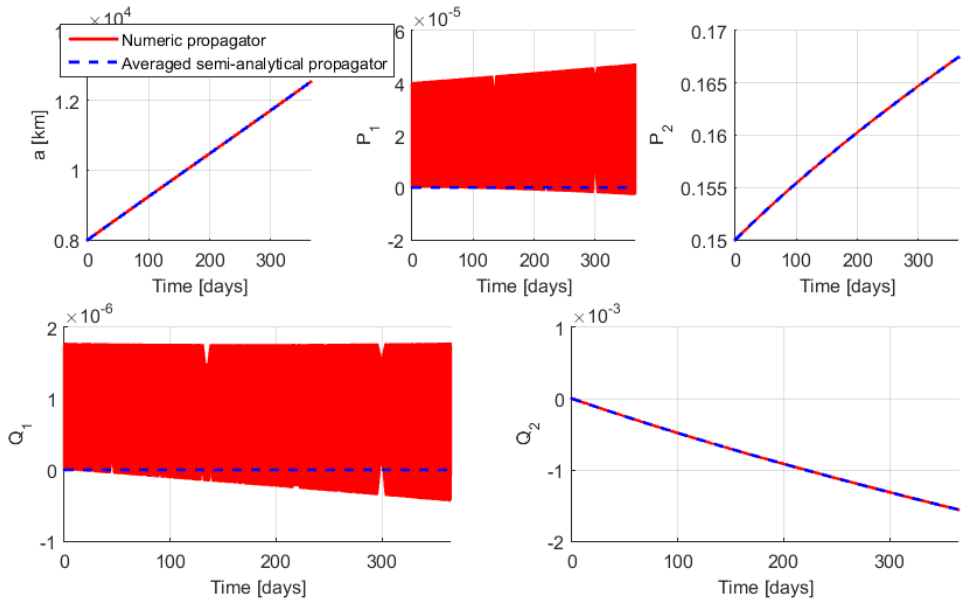

Figure 4.9: Validation against numerical propagation for orbit LEO 2: low-thrust acceleration (Section 4.5).

4.6.3 SSO

This section presents the comparison of the results of the semi-analytical propagator with those of GMAT and of the numerical integration of the equations of Gauss, for a SSO (Table 4.3). Figure 4.10 shows the results of the propagation with perturbations due to J_2, J_3, J_4, J_5, Sun and Moon and solar radiation pressure with eclipses; the results of the semi-analytical propagator, in blue, are in agreement with those of GMAT, in red, thus demonstrating the validity of the method presented in Sections 4.2, 4.4 and in [240]. Figure 4.11 shows the results of the propagation with J_2 and atmospheric drag perturbation. In this case the averaged propagator is compared to the numerical integration of the Gauss' equations. The agreement of the results demonstrate the validity of the equations developed in Section 4.3. Finally, Figure 4.12 presents the results of the propagation with low-thrust acceleration following an inverse square law $1/r^2$ (Section 4.5). In this case too the comparison is against a numerical integration of the Gauss' equations and the results are in good agreement.

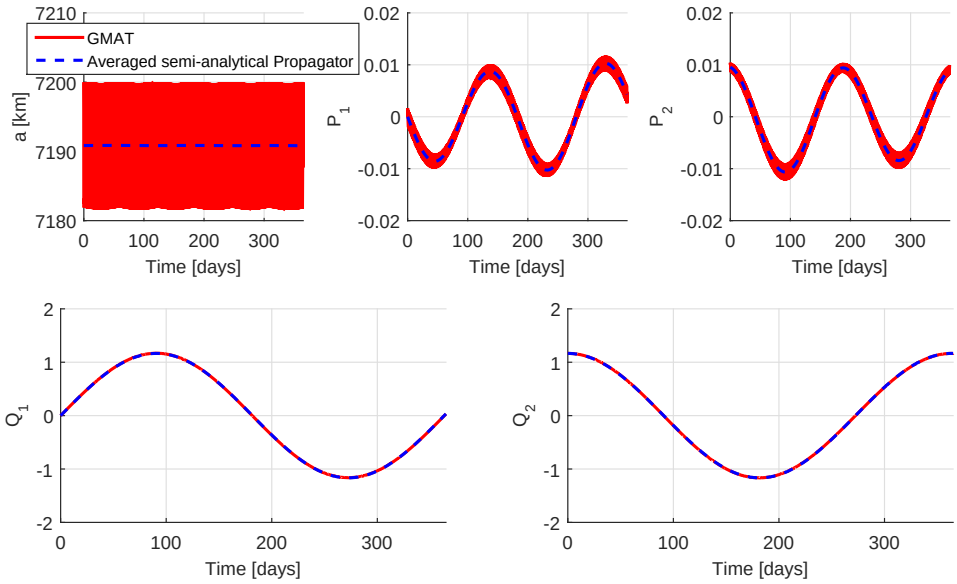

Figure 4.10: Validation against GMAT for SSO: J_2 to J_5, Sun, Moon, SRP and eclipses.

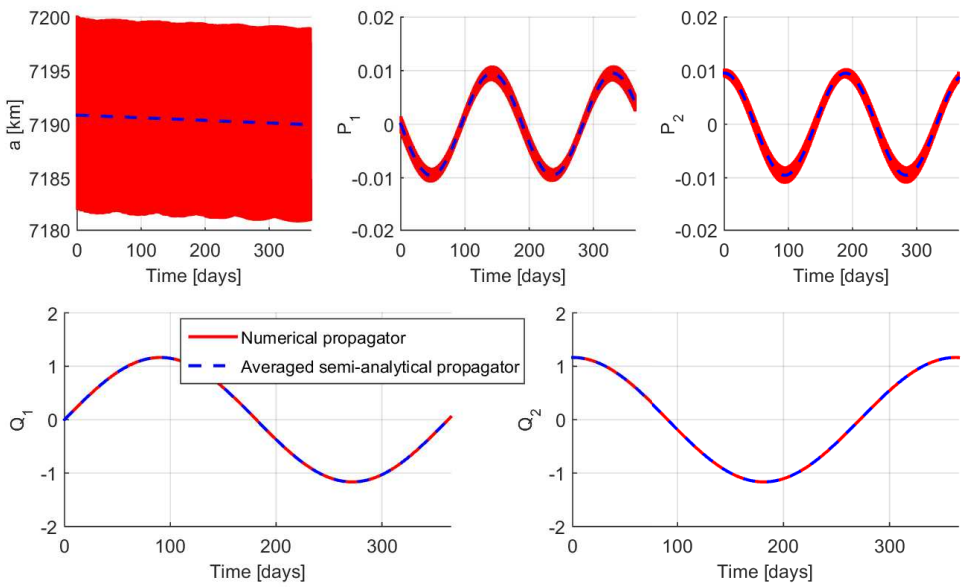

Figure 4.11: Validation against numerical propagation for orbit SSO: J_2 and atmospheric drag.

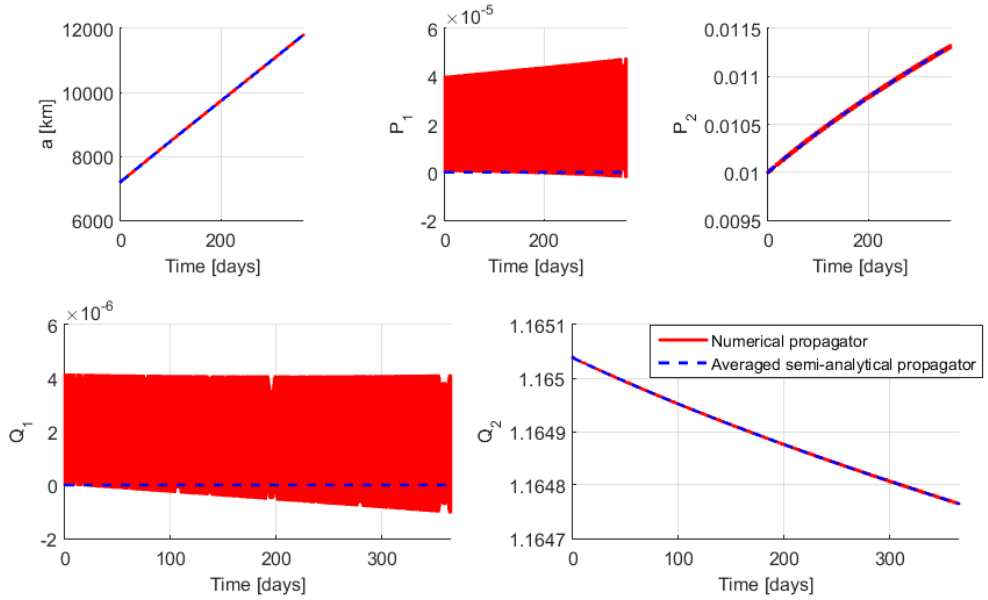

Figure 4.12: Validation against numerical propagation for orbit SSO: low-thrust acceleration (Section 4.5).

4.6.4 MEO

This section presents the comparison of the results of the averaged propagator with those of GMAT and of the numerical integration of the equations of Gauss for a MEO (Table 4.3). Figure 4.13 shows the results of a propagation with perturbations due to J_2, J_3, J_4, J_5, Sun and Moon and solar radiation pressure with eclipses. Results in Figure 4.13 show a 0.076 $\%$ relative error in the equinoctial parameter Q_2 at the end of the propagation. This is due to the fact that nutation and precession are not included in the semi-analytical averaged propagator, and this affects the acceleration of the gravitational perturbations. The gravitational accelerations of Section 4.2 are, in fact, expressed in an Earth-fixed reference frame, and should be transformed into an inertial reference frame before the propagation [145] . This will be the subject of future works, while in this thesis the accelerations in the Earth-fixed reference frame are directly used for integration of the spacecraft's motion. To explain how this affects the results of the propagator, Figure 4.14 shows that the same kind of error can be also seen when considering only the perturbation due to J_2. Figure 4.15 shows, instead, a comparison of the results produced by the semi-analytical propagator with those of the AGI software System Tool Kit (STK) using the "J_2 propagator"[5], that considers only the main secular effects of J_2. In this case the results are in agreement for Q_1 and Q_2, while a negligible numerical error, that does not cause any effect in the complete comparison of Figure 4.13, is evident for P_1 and P_2. To further demonstrate that the difference in Q_2 in Figure 4.13 is due only to the gravitational acceleration, Figures 4.16 and 4.17 show the comparison of results considering third body perturbations only (Sun and Moon) and solar radiation pressure. Neither the third body perturbations nor the solar radiation pressure show an error in Q_2. The comparison considering solar radiation pressure only (Figure 4.17) shows some small differences in Q_1, that does not cause any effect in the complete comparison of Figure 4.13 and that will be the subject of future further investigations.

The comparison of propagations including the atmospheric drag perturbation is not considered for orbit MEO, because of the negligible atmospheric density for this orbital regime.

Finally, Figure 4.18 presents the results of the propagation with low-thrust acceleration changing as $1/r^2$ (Section 4.5). The comparison is against a numerical integration of the Gauss' equations and the results are in good agreement.

[5]https://www.agi.com/products/engineering-tools

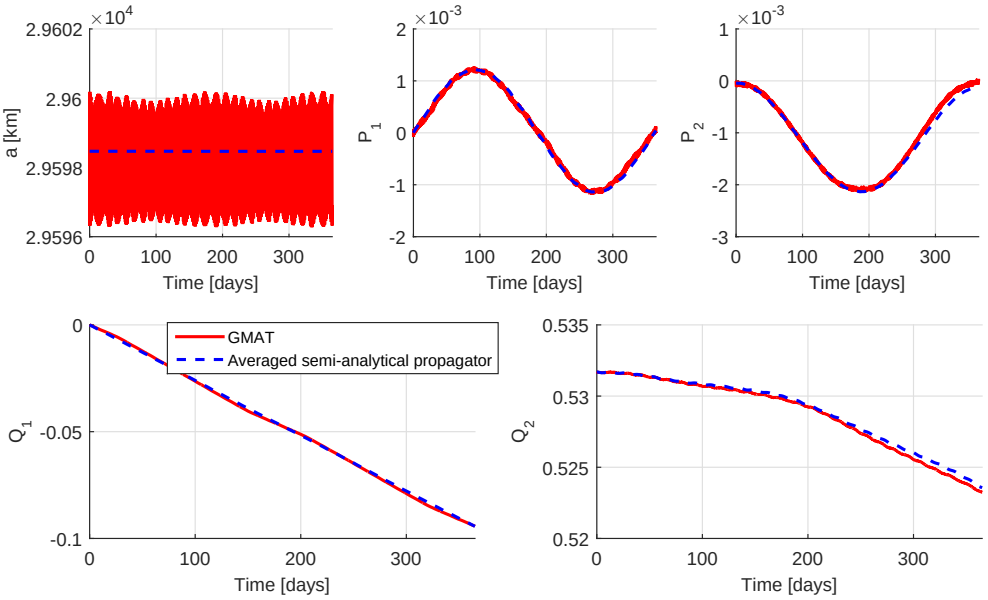

Figure 4.13: Validation against GMAT for MEO: J_2 to J_5, Sun, Moon, SRP and eclipses.

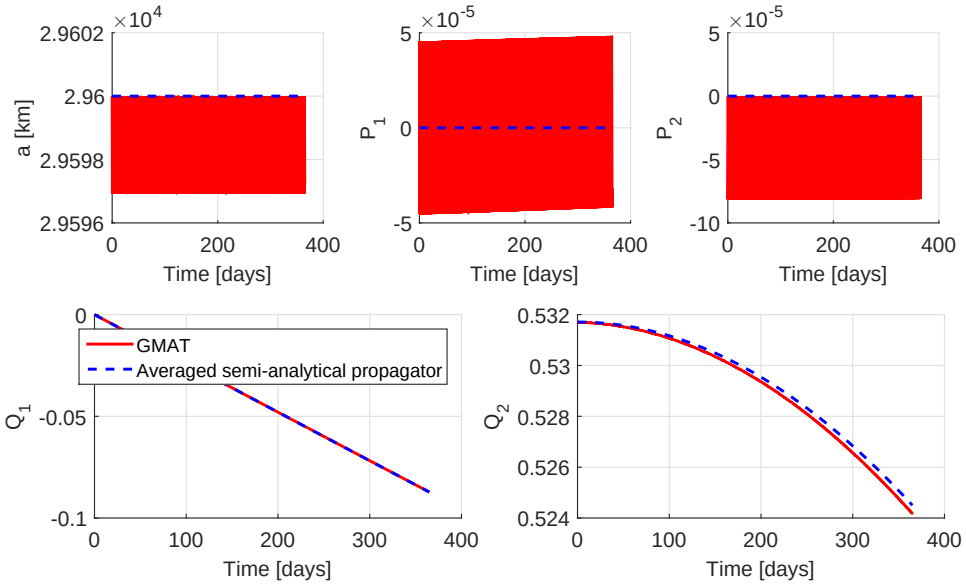

Figure 4.14: Validation against GMAT for MEO: J_2.

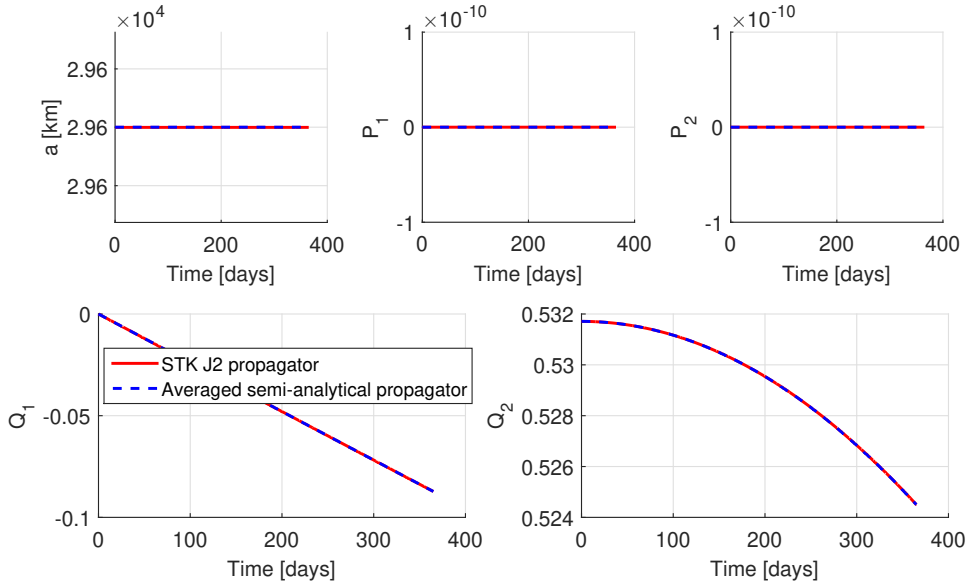

Figure 4.15: Validation against STK "J_2 propagator" for MEO.

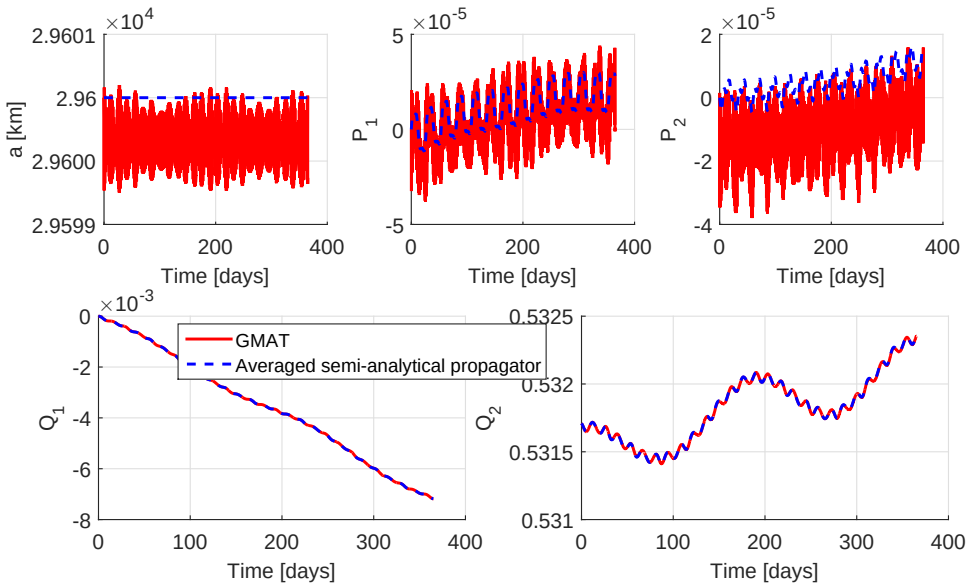

Figure 4.16: Validation against GMAT for MEO: Sun and Moon gravitational perturbations.

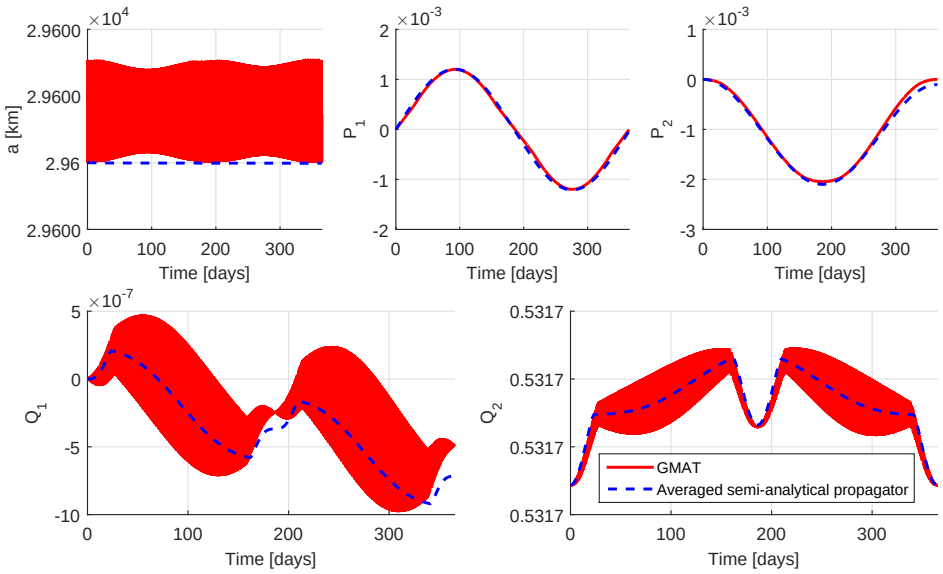

Figure 4.17: Validation against GMAT for MEO: SRP and eclipses.

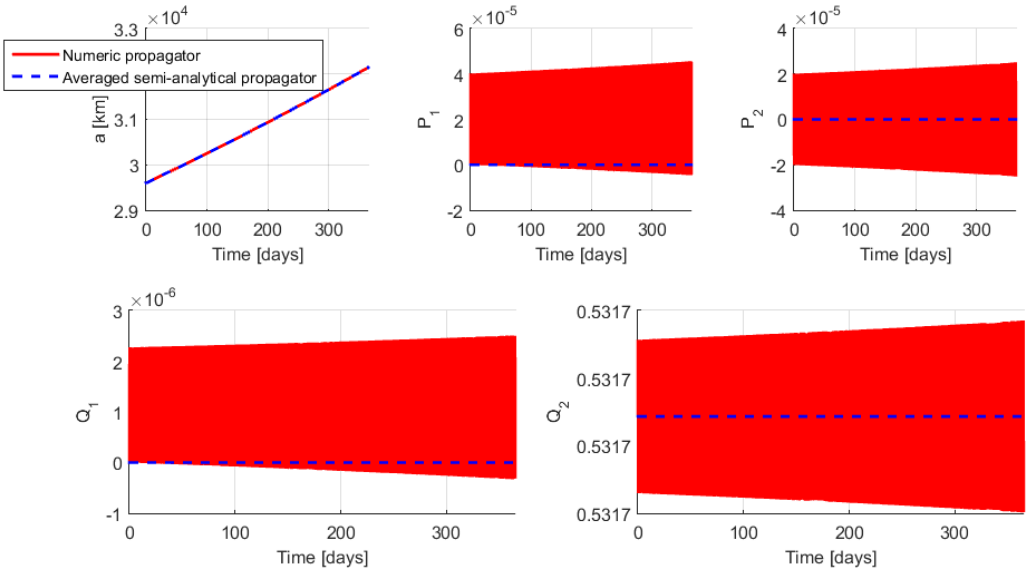

Figure 4.18: Validation against numerical propagation for orbit MEO: low-thrust acceleration (Section 4.5).

4.6.5 GTO

This section presents the comparison of the results of the semi-analytical propagator with those of GMAT and of the numerical integration of the equations of Gauss for a GTO (Table 4.3). Figure 4.19 shows the results of a propagation with perturbations due to J_2, J_3, J_4, J_5, Sun and Moon and solar radiation pressure with eclipses. Also in this case, as for the MEO test case (Subsection 4.6.5), results in Figure 4.19 show an error in the equinoctial parameter Q_1 at the end of the propagation. Figure 4.20 shows that the same kind of error can be seen also when considering only the perturbation due to J_2. Figure 4.21 shows, instead, a comparison of the results produced by the semi-analytical propagator with those of AGI STK using the "J_2 propagator", that considers only the main secular effects due to J_2. In this case the results of Q_1 and Q_2 are in agreement with those of STK.

The comparison with the atmospheric drag perturbation is not considered for orbit GTO, because of the negligible atmospheric density for this orbital regime.

Finally, Figure 4.22 presents the results of the propagation with low-thrust acceleration following the inverse square law $1/r^2$ (Section 4.5). The comparison is against a numerical integration of the Gauss' equations and the results are in good agreement.

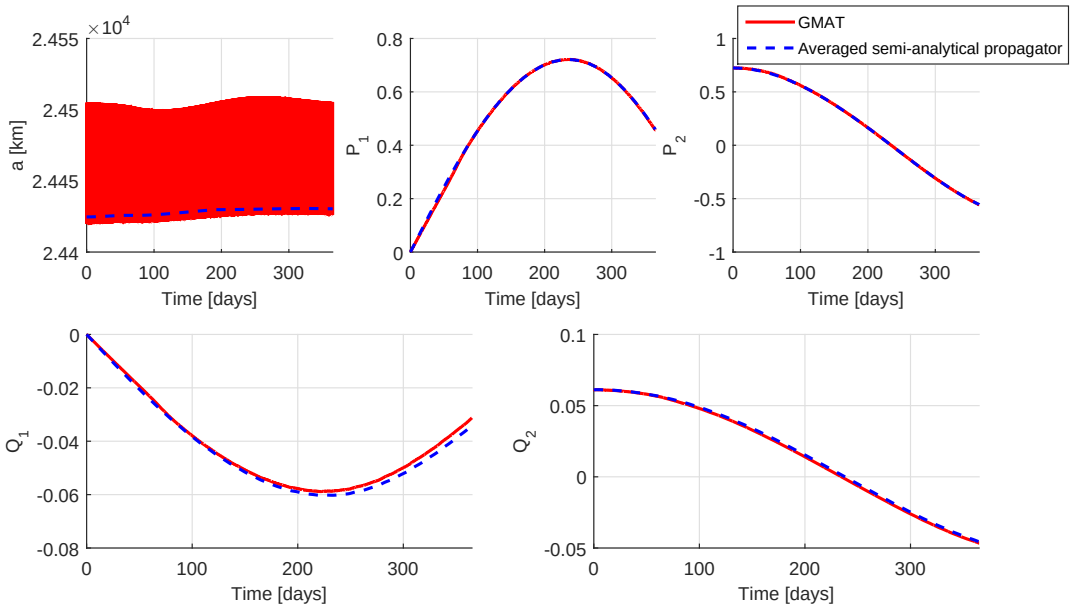

Figure 4.19: Validation against GMAT for GTO: J_2 to J_5, Sun, Moon, SRP and eclipses.

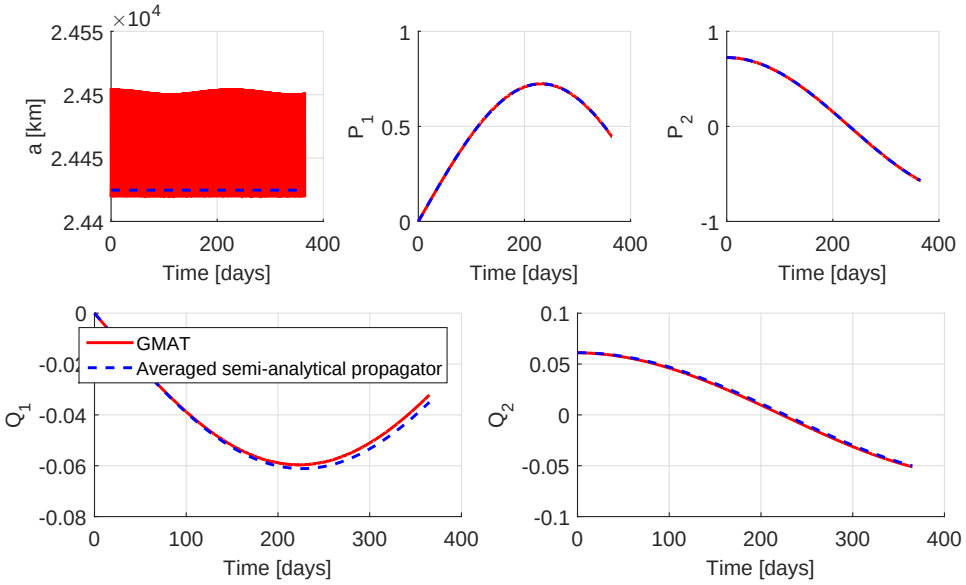

Figure 4.20: Validation against GMAT for GTO: J_2.

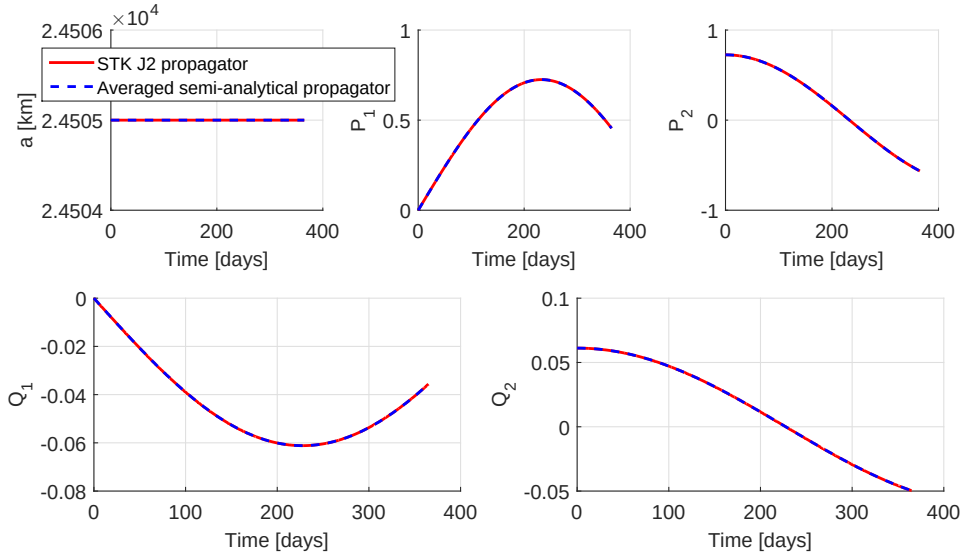

Figure 4.21: Validation against STK "J_2 propagator" for GTO.

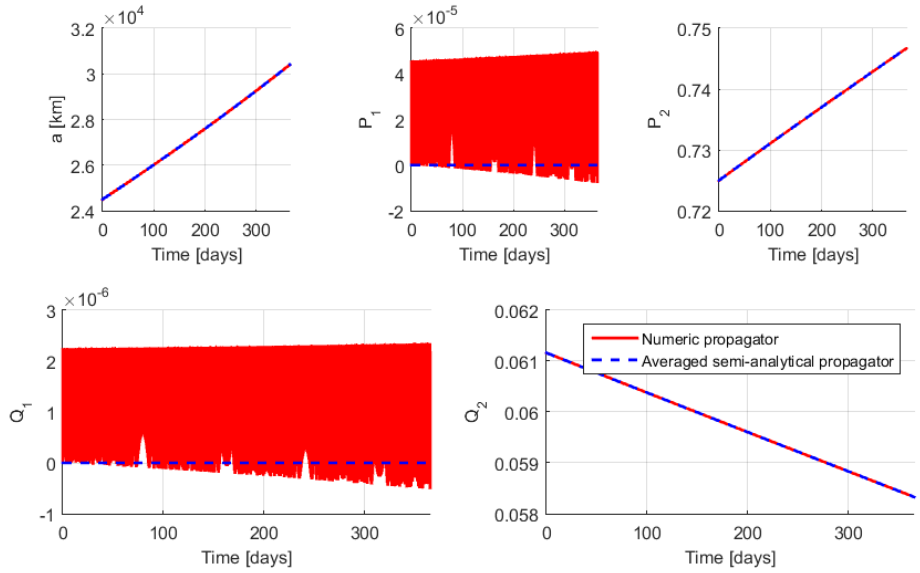

Figure 4.22: Validation against numerical propagation for orbit GTO: low-thrust acceleration (Section 4.5).

4.6.6 GEO

This section presents the comparison of the results of the semi-analytical propagator with those of GMAT and of the numerical integration of the equations of Gauss for a GEO (Table 4.3). Figure 4.23 shows the results of a propagation with perturbations due to J_2, J_3, J_4, J_5, Sun and Moon and solar radiation pressure with eclipses. Also in this case, as for the MEO and GTO test cases (Subsections 4.6.5 and 4.6.5), results in Figure 4.23 show an error in the equinoctial parameter Q_2 at the end of the propagation. Figure 4.24 shows that the same kind of error can be seen also when considering only the perturbation due to J_2. Figure 4.25 shows, instead, a comparison with the results of STK using the "J_2 propagator", that considers only the main secular effects due to J_2. In this case the results of Q_1 and Q_2 are in agreement with those of STK.

The comparison with the atmospheric drag perturbation is not considered for orbit GEO, because of the negligible atmospheric density for this orbital regime.

Finally, Figure 4.26 presents the results of the propagation with low-thrust acceleration following the inverse square law $1/r^2$ (Section 4.5). The comparison is against a numerical integration of the Gauss' equations and the results are in good agreement.

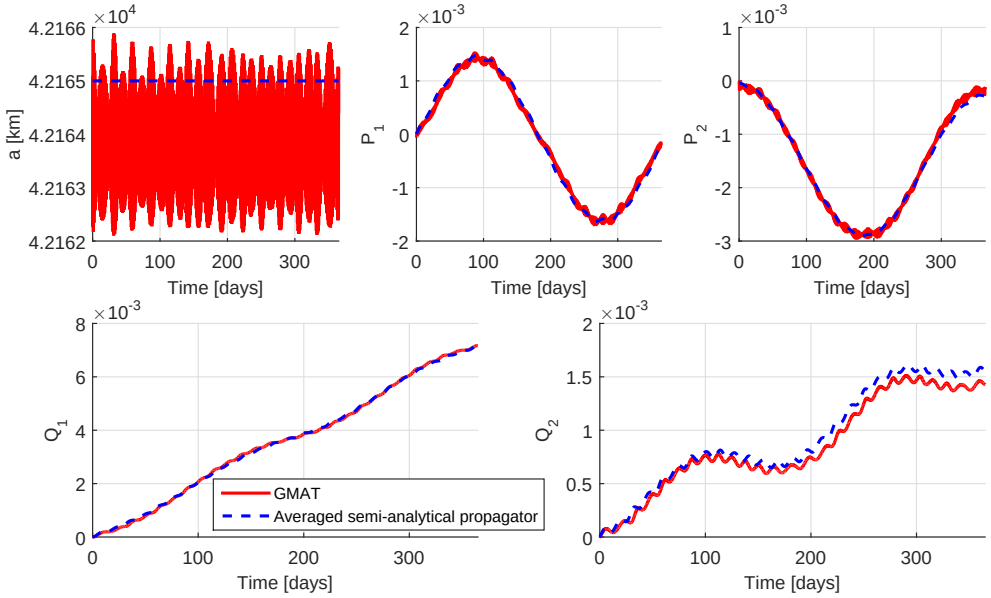

Figure 4.23: Validation against GMAT for GEO: J_2 to J_5, Sun, Moon, SRP and eclipses.

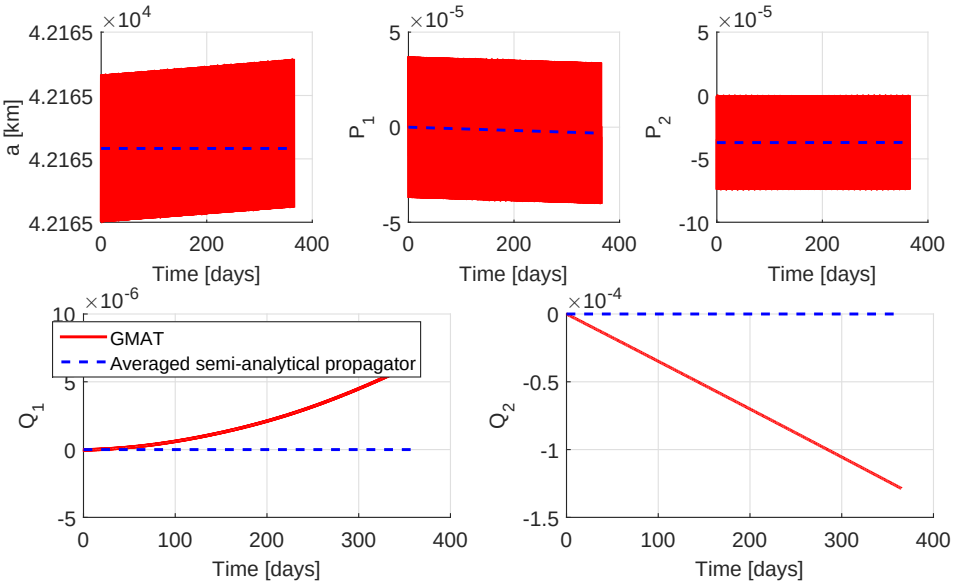

Figure 4.24: Validation against GMAT for GEO: J_2.

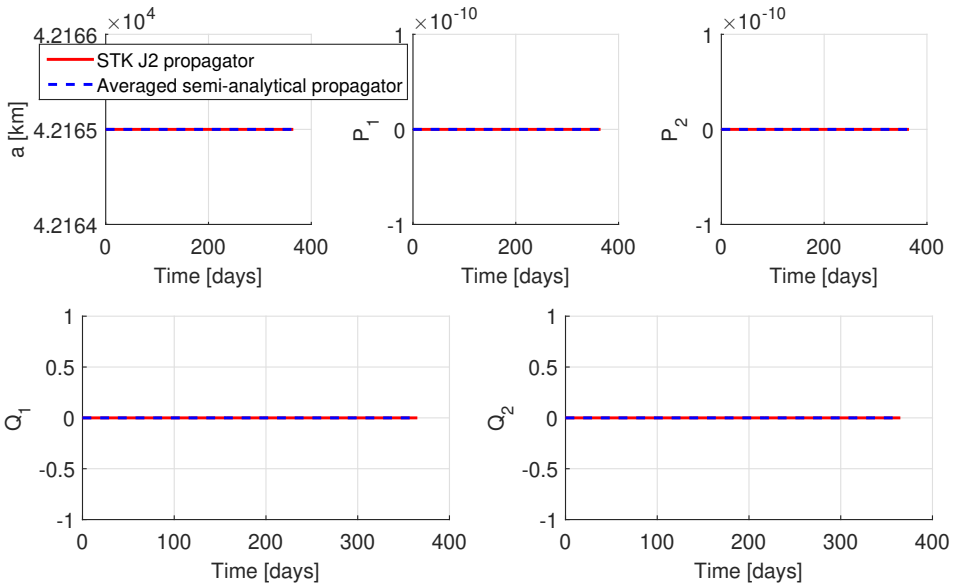

Figure 4.25: Validation against STK "J_2 propagator" for GEO.

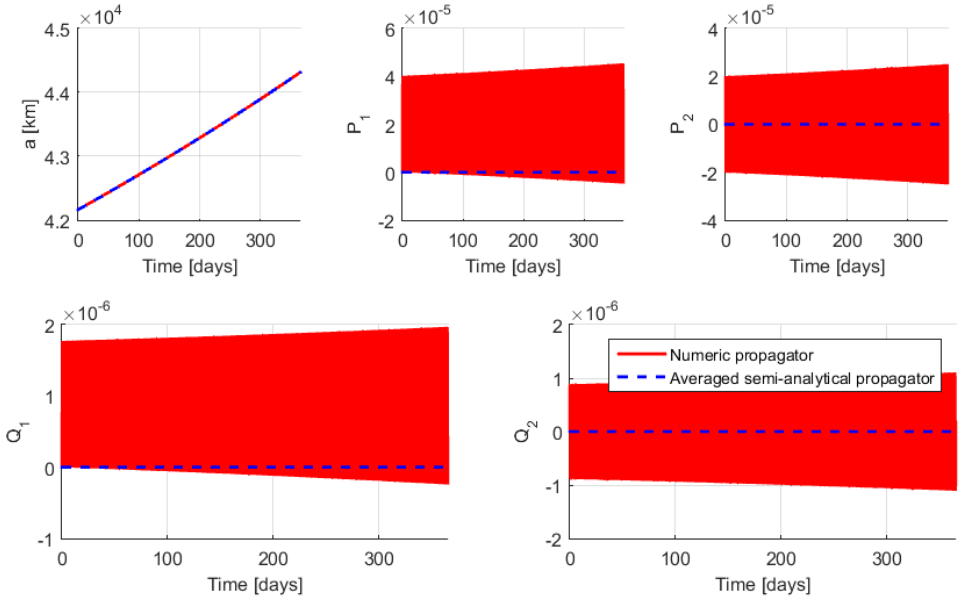

Figure 4.26: Validation against numerical propagation for GEO: low-thrust acceleration (Section 4.5).

4.6.7 HEO

This section presents the comparison of the results of the semi-analytical propagator with those of GMAT and of the numerical integration of the equations of Gauss for a HEO (Table 4.3). Figure 4.27 shows the results of a propagation with perturbations due to J_2, J_3, J_4, J_5, Sun and Moon and solar radiation pressure with eclipses. Also in this case, as for the MEO, GTO and GEO test cases, results in Figure 4.27 show an error in the equinoctial parameter Q_2 at the end of the propagation. Figure 4.28 shows that the same kind of error can be seen also when considering only the perturbation due to J_2. Figure 4.29 shows instead a comparison with the results of STK using the "J_2 propagator", that considers only the main secular effects due to J_2. In this case the results of Q_1 and Q_2 are in agreement with those of STK.

The comparison with the atmospheric drag perturbation is not considered for orbit HEO, because of the negligible atmospheric density for this orbital regime.

Finally, Figure 4.30 presents the results of the propagation with low-thrust acceleration changing as $1/r^2$ (Section 4.5). The comparison is against a numerical integration of the Gauss' equations and the results are in good agreement.

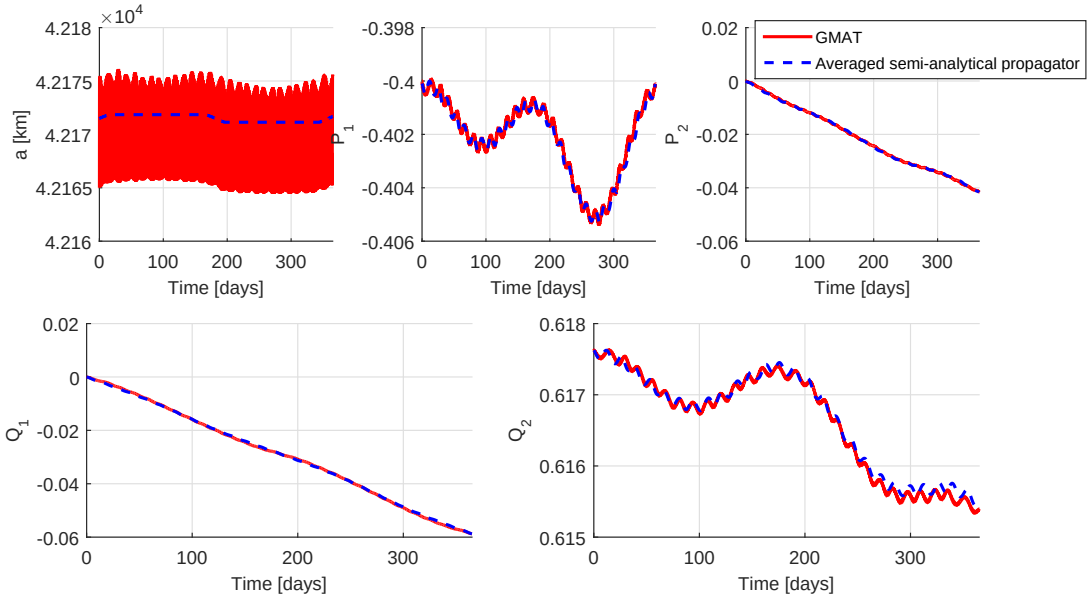

Figure 4.27: Validation against GMAT for HEO: J_2 to J_5, Sun, Moon, SRP and eclipses.

4.7 Conclusion

This chapter has presented analytical equations for the propagation of the motion of the spacecraft via first-order expansion. The analytical formulae are available for different low-thrust

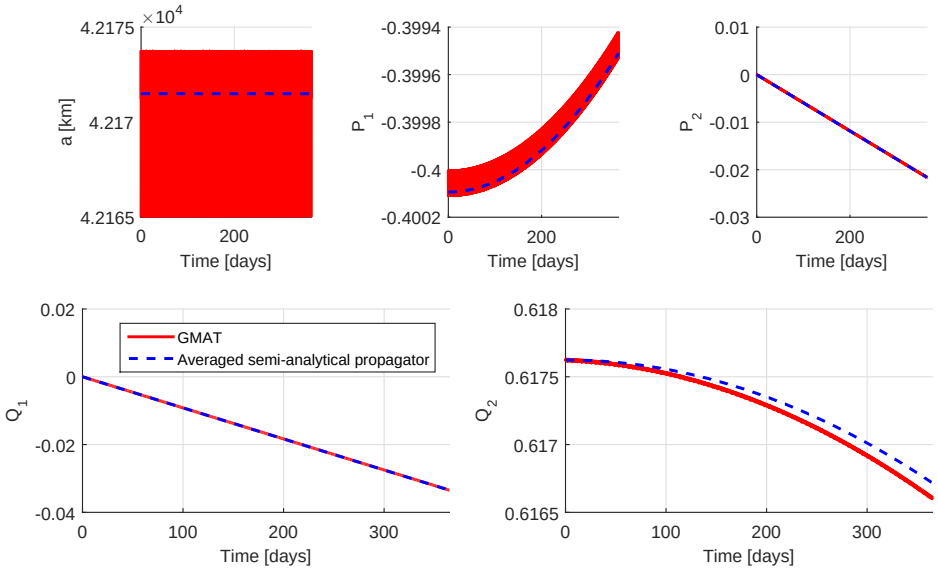

Figure 4.28: Validation against GMAT for HEO: J_2.

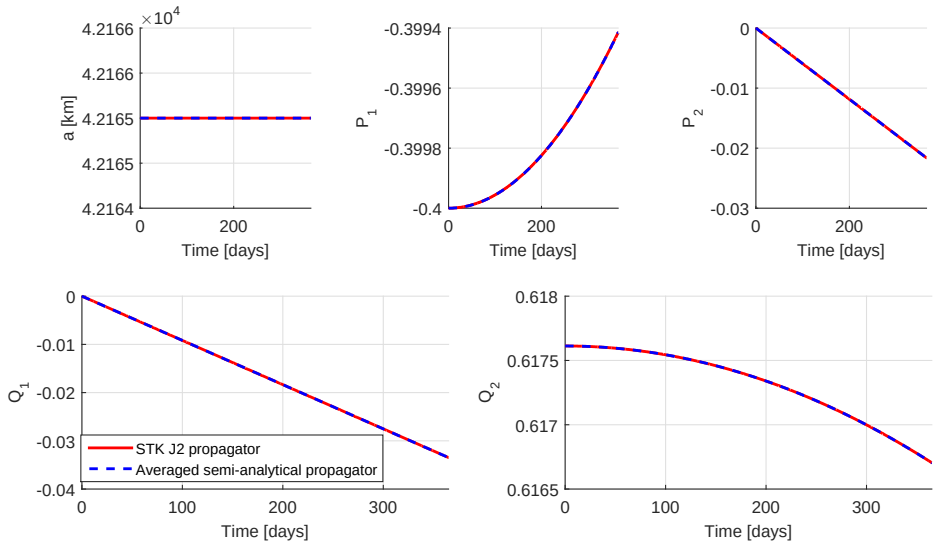

Figure 4.29: Validation against STK "J_2 propagator" for HEO.

profiles and orbital perturbations. The work presented in this chapter uses the equations presented in [240] as a starting point, and extends the results to include the perturbations of the zonal harmonics J_3, J_4 and J_5, atmospheric drag, Sun and Moon gravitational perturbations and low-thrust acceleration with magnitude following an inverse square law. The results of the averaged semi-analytical propagator have been assessed through comparison with those of the NASA open-source software GMAT and through comparison with numerical propagation of the Gauss' equations. The comparisons show a good agreement for all the perturbations

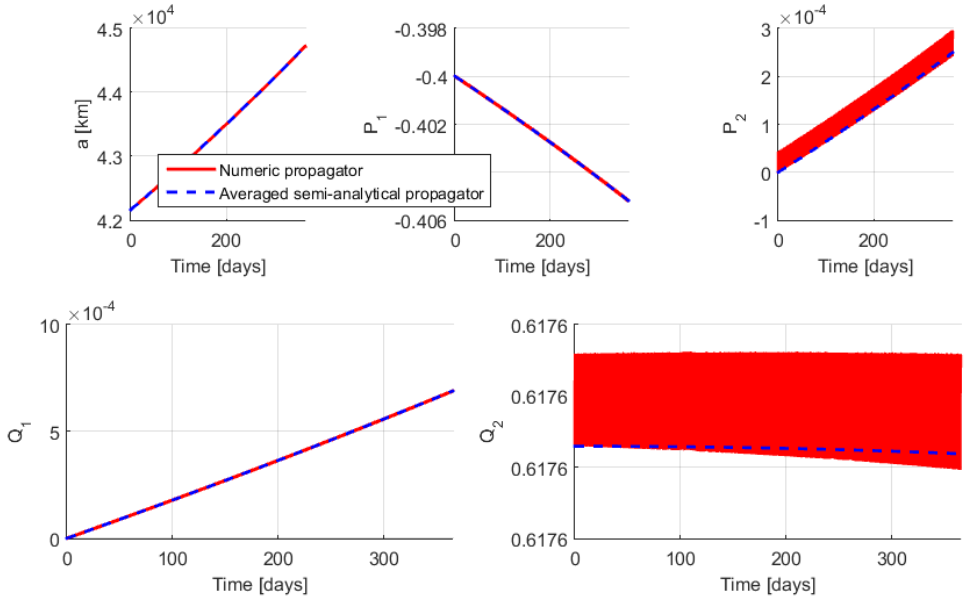

Figure 4.30: Validation against numerical propagation for orbit HEO: low-thrust acceleration (Section 4.5).

and accelerations in LEO and SSO, while in MEO, GTO, GEO and HEO an error is evident when considering the gravitational perturbation, due to the absence of the modelling of nutation and precession. This will be addressed in future works. Future works will also consider the second order term J_2^2 and a dynamical model for the atmospheric density, in order to take into account variations of the density due to the time and date of the year and to solar and geomagnetic activities.

The analytical equations presented in this chapter represent a computationally efficient tool to model the motion of the spacecraft, subject to low-thrust acceleration and orbital perturbations. The inclusion of orbital perturbations makes these equations suitable for higher fidelity representation of the motion of the spacecraft. Moreover, when used in conjunction with optimisation algorithms, the analytical equations can speed up the optimisation process, compared to the use of numerical solutions. The next chapter shows how a direct transcription of the optimal control problem, that makes use of the analytical model presented in this chapter, can be used to optimise low-thrust transfers.

Chapter 5

Transcription methods using first-order expansions

This chapter presents the low-thrust direct transcription methods developed and used in this thesis for the applications presented in Part II. Existing transcription methods for the low-thrust optimal control problem have been presented in Section 1.3.2. The transcriptions proposed in this chapter are based on the work of Zuiani [241] and have been developed with the aim of speeding up the convergence to the optimal solution and reducing the number of optimisation variables. The reduction of the number of optimisation variables is obtained by introducing assumptions on the structure of the low-thrust control profile.

The first proposed parametrisation divides the transfer into legs of predefined span angle; on each leg the low-thrust acceleration magnitude can assume any value in the range going from zero to the maximum acceleration. This method is presented in Section 5.1 and is referred to as Direct Transcription using Thrust Element of Variable Acceleration (DT-TEVA). Two additional proposed transcription methods are based on an alternation of coast and thrust legs; the low-thrust acceleration applied on the thrust leg is the maximum that can be provided by the engine. The position of the thrust legs on the orbit can be either optimised (Section 5.2) or can be fixed a-priori (thrust legs at periapsis and apoapsis of the orbit, as in [240], Section 5.3). The first method is referred to as Direct Transcription using Coast and Thrust Elements of Constant Acceleration (DT-CTECA) while the second is referred to as Direct Transcription using Thrust Elements at Periapsis and Apoapsis (DT-TEPA). Both DT-CTECA and DT-TEVA implement a constant control on each thrust element; this type of control can be more easily applied to a low-thrust spacecraft, both on-board and from the ground, than a variable control. The validation of the transcription methods is reported in Section 5.4. The validation is against an indirect method developed at the Centre National d'Etudes Spatiale and two low-thrust softwares developed at the European Space Operation Centre. A comparison against the direct Sims and Flanagan method, for the original formulation proposed by Zuiani, was already presented in [241].

5.1 Direct Transcription using Thrust Elements of Variable Acceleration (DT-TEVA)

The Direct Transcription using Thrust Elements of Variable Acceleration (DT-TEVA) is based on the work presented in [241]. In [241], the transfer is split into a sequence of thrust elements, with the state of the spacecraft propagated forward from the mid-point of each element to the final point of that element, and backward from the mid-point to the initial point. Differently from the formulation of Zuiani, in DT-TEVA the forward and backward propagation are substituted by a single forward propagation from the initial to the final point of each element. This reduces the computational time with respect to the original formulation, since a single propagation, rather than two, has to be performed for each element. The acceleration value is allowed to assume, on each element, any value from zero to its maximum allowed value; coast arcs are, therefore, obtained when the value of the acceleration goes to zero. This section presents the direct transcription, using DT-TEVA, of the minimum propellant problem for a fixed time transfer. The departure (initial) and arrival (final) states are represented by the vectors of equinoctial parameters $\mathbf{X}_0 = [a_0, P_{1,0}, P_{2,0}, Q_{1,0}, Q_{2,0}, L_0]^T$ and $\mathbf{X}_f = [a_f, P_{1,f}, P_{2,f}, Q_{1,f}, Q_{2,f}, L_f]^T$. The transfer is split into n_{LT} legs, where n_{LT} is computed from the desired length of each leg, ΔL, as $n_{LT} = \lfloor (L_f - L_0)/\Delta L \rfloor$. The true longitudes of the nodes that segment the transfer are computed as

$$L_s = L_{s-1} + \Delta L \quad s = 1, \ldots, n_{LT} \,. \tag{5.1}$$

On each leg, the low-thrust acceleration vector, $[u_{LT_R}, u_{LT_T}, u_{LT_N}]^T$ is expressed in a local radial-transverse-normal RTN reference frame as in Equation 2.1 and using the definition of α' given in Chapter 4 (Equation 4.2):

$$\mathbf{u}_{LT,s} = \begin{Bmatrix} u_{LT_R} \\ u_{LT_T} \\ u_{LT_N} \end{Bmatrix}_s = \begin{Bmatrix} \epsilon \cos\alpha'_s \cos\beta_s \\ \epsilon \sin\alpha'_s \cos\beta_s \\ \epsilon \sin\beta_s \end{Bmatrix} . \tag{5.2}$$

The trajectory is analytically propagated forward from the departure point $\mathbf{X}_0$ to a mid-point, and backward from the end point $\mathbf{X}_f$ to the mid-point (Figure 5.1), using the asymptotic expansion solutions presented in Chapter 4.

On each thrust leg, the magnitude of the acceleration can assume any value in the range $[0, \epsilon_{max}]$, where ϵ_{max} is the maximum acceleration provided by the engine. Each s-th leg is, therefore, represented by the vector $\widetilde{\mathbf{X}}_s = [a_s, P_{1,s}, P_{2,s}, Q_{1,s}, Q_{2,s}]^T$ and by magnitude, azimuth and elevation of the low-thrust acceleration. For the proposed multiple shooting formulation, the vector of variables to optimise, $\mathbf{x} \in \mathbb{R}^{n_x}$, where $n_x = 3n_{LT} + 5\ (n_{LT} - 1)$, is:

$$\mathbf{x} = \left[\epsilon_1, \alpha'_1, \beta_1, \tilde{\mathbf{X}}_1, \epsilon_2, \alpha'_2, \beta_2, \tilde{\mathbf{X}}_2, \ldots, \epsilon_{n_{LT}}, \alpha'_{n_{LT}}, \beta_{n_{LT}}, \tilde{\mathbf{X}}_{n_{LT}}\right]^T . \tag{5.3}$$

The optimisation problem is formulated as a non-linear programming problem whose ob-

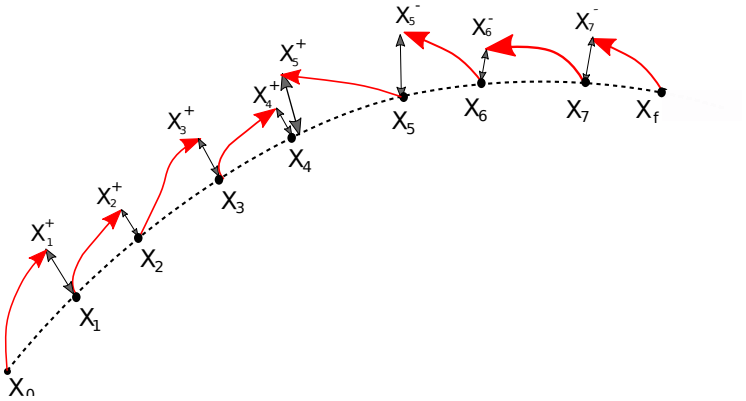

Figure 5.1: Segmentation of the trajectory into thrust legs of variable acceleration.

jective is the minimisation of the total ΔV:

$$\begin{aligned} \min_{\mathbf{x}\in\mathbb{R}^{n_x}} \quad & J(\mathbf{x}) = \Delta V \\ \text{s.t.} \quad & \mathbf{g}(\mathbf{x}) \leq 0 \\ & \mathbf{c}\left(\mathbf{x}\right) = 0 \\ & \mathbf{x}^L \leq \mathbf{x} \leq \mathbf{x}^U \ . \end{aligned} \tag{5.4}$$

If the low-thrust acceleration is modelled with a constant value ϵ_s on each arc, then $\Delta V = \sum_{s=1}^{n_{LT}} \epsilon_s \Delta t_s\left(\mathbf{x}\right)$ where $\Delta t_s\left(\mathbf{x}\right)$ is the time length of each thrust leg. The $n_c = 5\ n_{LT} + 1$ non-linear equality constraints are the matching constraints at the nodes of a multiple-shooting method (Equation 1.27), plus a constraint on the total time of flight:

$$\mathbf{c}\left(\mathbf{x}\right) = \left[\begin{array}{c} \begin{cases} \widetilde{\mathbf{X}}_s^+ - \widetilde{\mathbf{X}}_s & s = 1, \ldots, n_{LT}/2 \\ \widetilde{\mathbf{X}}_s^- - \widetilde{\mathbf{X}}_s & s = n_{LT}/2, \ldots, n_{LT} - 1 \end{cases} \\ \sum_{s=1}^{n_{LT}} \Delta t_s - ToF \end{array} \right] . \tag{5.5}$$

The plus and minus signs in the constraints equations (Equation 5.5) indicate, respectively, the forward integration leg and the backward integration leg. ToF is the total time of flight of the transfer. The other elements in Equation 5.5 are (refer to Equation 4.9)

$$\begin{cases} \widetilde{\mathbf{X}}_s^+ = \widetilde{\mathbf{X}}_{s-1} + \epsilon \widetilde{\mathbf{X}}_1 |_{L_{s-1}}^{L_s} & s = 1, \ldots, n_{LT}/2 \\ \widetilde{\mathbf{X}}_{s-1}^- = \widetilde{\mathbf{X}}_s + \epsilon \widetilde{\mathbf{X}}_1 |_{L_s}^{L_{s-1}} & s = n_{LT}/2, \ldots, n_{LT} \\ \widetilde{\mathbf{X}}_{nLT}^- = \widetilde{\mathbf{X}}_f + \epsilon \widetilde{\mathbf{X}}_1 |_{L_f}^{L_{nLT}} & \end{cases} \tag{5.6}$$

where $\mathbf{X}_1 |_{L_a}^{L_b} = \int_{L_a}^{L_b} F\left(\mathbf{X}, \mathcal{L}, \alpha, \beta\right) d\mathcal{L}$.

The inequality constraint vector is $\mathbf{g}(\mathbf{x}) = \emptyset$. The lower and upper boundaries are

$$\begin{aligned}\mathbf{x}^L &= [0, -\pi,\ -\pi/2,\ 0.9\min(a_0, a_f),\ -1,\ -1,\ -\tan\left[1.1\max(i_0, i_f)/2\right],\ -\tan\left[1.1\max(i_0, i_f)/2\right],\ \ldots]^T,\\ \mathbf{x}^U &= [\epsilon_{max}, \pi,\ \pi/2,\ 1.1\max(a_0, a_f),\ 1,\ 1,\ \tan\left[1.1\max(i_0, i_f)/2\right],\ \tan\left[1.1\max(i_0, i_f)/2\right],\ \ldots]^T.\end{aligned} \tag{5.7}$$

The initial guess for the solution vector is obtained considering the following values for the angles of the low-thrust acceleration:

$$\alpha'^{IG}_s = \begin{cases}\pi/2 & \text{if } a_f \geq a_0\\ -\pi/2 & \text{if } a_f < a_0\end{cases},\ \beta^{IG}_s = 0\,. \tag{5.8}$$

The initial guesses for the nodal points $\widetilde{\mathbf{X}}_s$ of the multiple shooting methods are defined by the following relationships, where $s = 1, \ldots, n_{LT}$:

$$\begin{aligned}\widetilde{\mathbf{X}}^{IG}_s = \Bigg[&a_0 + \frac{a_f - a_0}{n_{LT}-1}(s-1),\ P_{1,dep} + \frac{P_{1,f} - P_{1,0}}{n_{LT}-1}(s-1),\ P_{2,0} + \frac{P_{2,f} - P_{2,0}}{n_{LT}-1}(s-1),\\ &Q_{1,0} + \frac{Q_{1,f} - Q_{1,0}}{n_{LT}-1}(s-1),\ Q_{2,0} + \frac{Q_{2,f} - Q_{2,0}}{n_{LT}-1}(s-1)\Bigg]^T\end{aligned} \tag{5.9}$$

An example of trajectory resulting from this definition for the initial guess of the nodal points of the multiple-shooting method is shown in Figure 5.2.

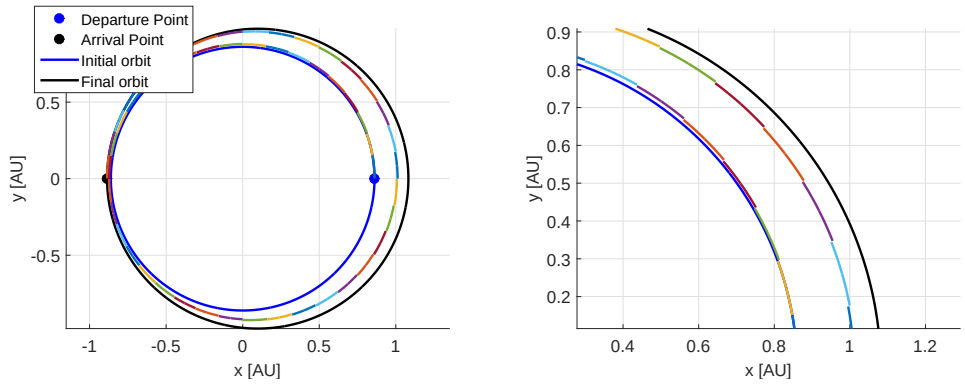

Figure 5.2: Trajectory resulting from the initial guess for the solution of the NLP problem. Enlargement on the right shows that the matching conditions at the nodes are not satisfied.

Problem 5.4 is solved with MATLAB *fmincon*, using either the SQP or IPM algorithms (Appendix B). In order to speed up the solution of the problem, the Jacobian of the constraints $\mathbf{c}(\mathbf{x})$ and of the objective function are computed by finite difference and given as input to *fmincon*.

5.2 Direct Transcription using Coast and Thrust Elements of Constant Acceleration (DT-CTECA)

The transcription method presented in this section is still based on the segmentation into elements proposed in [241], but introduces a novel alternation of coast and thrust elements. Differently from DT-TEVA, for which the angular length of each element was fixed, in DT-CTECA the angular length of the elements can assume any value in the considered range. Thrust elements can, therefore, disappear, if their angular lengths collapse to zero. The low-thrust acceleration on the thrust elements is considered to be equal to the maximum possible value, while in DT-TEVA the acceleration was allowed to assume any value from zero to the maximum value. In particular, in DT-CTECA, the transfer from $\mathbf{X}_0$ to $\mathbf{X}_f$ is split into a predefined sequence of n_{LT} finite coast and thrust legs. Each s-th leg is represented by the vector $\mathbf{X}_s = [a_s, P_{1,s}, P_{2,s}, Q_{1,s}, Q_{2,s}, L_s]^T$, plus, in case of thrust arc, by the low-thrust acceleration vector, $[u_{LT_R}, u_{LT_T}, u_{LT_N}]^T$. The trajectory is analytically propagated forward from the departure point $\mathbf{X}_0$ to a mid-point, and backward from the end point $\mathbf{X}_f$ (Figure 5.3) to the mid-point. The motion is assumed purely Keplerian along coast legs, while thrust legs are analytically propagated using the asymptotic expansion solutions presented in Chapter 4. Each leg begins and ends at an ON/OFF control node, where ON nodes define the switching point from a coast to a thrust leg and OFF nodes define the switching point from a thrust to a coast leg. Therefore, thrust legs are defined by a set of orbital elements at an ON node, $\mathbf{X}_s^{ON}$, and coast legs are defined by a set of orbital elements at an OFF node, $\mathbf{X}_s^{OFF}$.

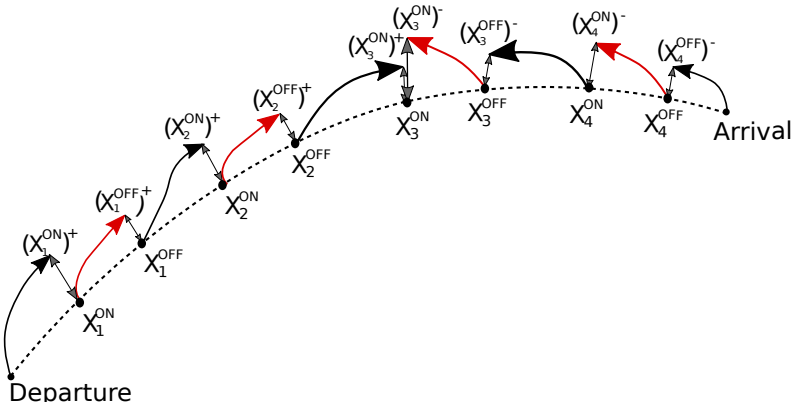

Figure 5.3: Segmentation of the trajectory into coast legs (black) and thrust legs (red).

The mass of the spacecraft is conservatively kept constant over each transfer arc and updated at the end of the transfer according to the propellant mass spent to realise that transfer. In this proposed multiple-shooting approach, the optimisable vector for the transfer is defined by the azimuth and elevation angles α'_s and β_s, for each thrust leg, and by the equinoctial elements at each ON and OFF point; the $n_x = 14\, n_{LT}$ variables are:

$$\mathbf{x} = [\alpha'_1, \beta_1, \mathbf{X}_1^{ON}, \mathbf{X}_1^{OFF}, \alpha'_2, \beta_2, \mathbf{X}_2^{ON}, \mathbf{X}_2^{OFF}, \ldots, \alpha'_{n_{LT}}, \beta_{n_{LT}}, \mathbf{X}_{n_{LT}}^{ON}, \mathbf{X}_{n_{LT}}^{OFF}]^T \,. \tag{5.10}$$

The optimisation problem is formulated as a non-linear programming problem, as in Section 5.1. The $n_c = 5(2\ n_{LT} + 1) + 1$ non-linear equality constraints $\mathbf{c}(\mathbf{x}) = 0$ are the matching constraints of a multiple-shooting method (Equation 1.27), and in this case they take the form:

$$\begin{cases} \left(\widetilde{\mathbf{X}}_s^{ON}\right)^+ - \widetilde{\mathbf{X}}_s^{ON} = 0 & \text{for } s = 1, \ldots, n_{LT}/2 \\ \left(\widetilde{\mathbf{X}}_s^{OFF}\right)^+ - \widetilde{\mathbf{X}}_s^{OFF} = 0 & \text{for } s = 1, \ldots, n_{LT}/2 \\ \left(\widetilde{\mathbf{X}}_s^{ON}\right)^- - \widetilde{\mathbf{X}}_s^{ON} = 0 & \text{for } s = n_{LT}/2+1, \ldots, n_{LT} \\ \left(\widetilde{\mathbf{X}}_s^{OFF}\right)^- - \widetilde{\mathbf{X}}_s^{OFF} = 0 & \text{for } s = n_{LT}/2+1, \ldots, n_{LT} \\ \left(\widetilde{\mathbf{X}}_{nLT/2+1}^{ON}\right)^+ - \left(\widetilde{\mathbf{X}}_{nLT/2+1}^{ON}\right)^- = 0 & \\ \sum_{s=1}^{n_{LT}} \Delta t_s - ToF = 0 & \end{cases} \tag{5.11}$$

The elements in Equation 5.11 are (refer to Equation 4.9)

$$\begin{cases} \left(\widetilde{\mathbf{X}}_1^{ON}\right)^+ = \widetilde{\mathbf{X}}_0 + \epsilon\widetilde{\mathbf{X}}_1|_{L_0}^{L_1^{ON}} & \\ \left(\widetilde{\mathbf{X}}_s^{ON}\right)^+ = \widetilde{\mathbf{X}}_{s-1}^{OFF} + \epsilon\widetilde{\mathbf{X}}_1|_{L_{s-1}^{OFF}}^{L_s^{ON}} & \text{for } s = 2, \ldots, n_{LT}/2 \\ \left(\widetilde{\mathbf{X}}_s^{OFF}\right)^+ = \widetilde{\mathbf{X}}_s^{ON} + \epsilon\widetilde{\mathbf{X}}_1|_{L_s^{ON}}^{L_s^{OFF}} & \text{for } s = 1, \ldots, n_{LT}/2 \\ \left(\widetilde{\mathbf{X}}_s^{ON}\right)^- = \widetilde{\mathbf{X}}_s^{OFF} + \epsilon\widetilde{\mathbf{X}}_1|_{L_s^{OFF}}^{L_s^{ON}} & \text{for } s = n_{LT}/2+1, \ldots, n_{LT} \\ \left(\widetilde{\mathbf{X}}_s^{OFF}\right)^- = \widetilde{\mathbf{X}}_{s+1}^{ON} + \epsilon\widetilde{\mathbf{X}}_1|_{L_{s+1}^{ON}}^{L_s^{OFF}} & \text{for } s = n_{LT}/2+1, \ldots, n_{LT}-1 \\ \left(\widetilde{\mathbf{X}}_{nLT}^{OFF}\right)^- = \widetilde{\mathbf{X}}_f + \epsilon\widetilde{\mathbf{X}}_1|_{L_f}^{L_{nLT}^{OFF}} & \end{cases} \tag{5.12}$$

The linear inequality constraints are

$$\mathbf{g}(\mathbf{x}) = \begin{bmatrix} L_0 - L_1^{ON} \\ L_1^{ON} - L_1^{OFF} \\ L_1^{OFF} - L_2^{ON} \\ \vdots \\ L_{n_{LT}}^{ON} - L_{n_{LT}}^{OFF} \\ L_{n_{LT}}^{OFF} - L_f \end{bmatrix}. \tag{5.13}$$

The lower and upper boundaries are

$$\begin{aligned} \mathbf{x}^L &= [-\pi,\ -\pi/2,\ 0.9\min(a_0, a_f),\ -1,\ -1,\ -\tan[1.1\max(i_0, i_f)/2],\ -\tan[1.1\max(i_0, i_f)/2], \\ &\ L_0,\ \ldots]^T, \\ \mathbf{x}^U &= [\pi,\ \pi/2,\ 1.1\max(a_0, a_f),\ 1,\ 1,\ \tan[1.1\max(i_0, i_f)/2],\ \tan[1.1\max(i_0, i_f)/2],\ L_f,\ \ldots]^T. \end{aligned} \tag{5.14}$$

The initial guess for α and β, in Equation 5.10, are chosen according to Equation 5.8. The initial

guesses for the state vectors $\mathbf{X}_s^{ON}$ and $\mathbf{X}_s^{OFF}$ are

$$\begin{aligned}
\mathbf{X}_s^{ON} = \Bigg[& a_0 + \frac{a_f - a_0}{2n_{LT}+1}(1+2\,(s-1)),\ P_{1,dep} + \frac{P_{1,f} - P_{1,0}}{2n_{LT}+1}(1+2\,(s-1)), \\
& P_{2,0} + \frac{P_{2,f} - P_{2,0}}{2n_{LT}+1}(1+2\,(s-1)),\ Q_{1,0} + \frac{Q_{1,f} - Q_{1,0}}{2n_{LT}+1}(1+2\,(s-1)), \\
& Q_{2,0} + \frac{Q_{2,f} - Q_{2,0}}{2n_{LT}+1}(1+2\,(s-1)),\ L_0 + \frac{L_f - L_0}{2n_{LT}+1}(1+2\,(s-1)) \Bigg]^T \\
\mathbf{X}_s^{OFF} = \Bigg[& a_0 + \frac{a_f - a_0}{2n_{LT}+1}2s,\ P_{1,dep} + \frac{P_{1,f} - P_{1,0}}{2n_{LT}+1}2s,\ P_{2,0} + \frac{P_{2,f} - P_{2,0}}{2n_{LT}+1}2s, \\
& Q_{1,0} + \frac{Q_{1,f} - Q_{1,0}}{2n_{LT}+1}2s,\ Q_{2,0} + \frac{Q_{2,f} - Q_{2,0}}{2n_{LT}+1}2s,\ L_0 + \frac{L_f - L_0}{2n_{LT}+1}2s \Bigg]^T
\end{aligned} \tag{5.15}$$

When necessary, in order to facilitate convergence of the NLP problem to a solution, a continuation method (refer to [18,29]) over the modulus of the thrust is implemented. An application of the continuation method is presented in Chapter 8 and Section 8.7.3. In the continuation method, at each step, the acceleration ϵ' of the low-thrust engine is described in terms of the nominal acceleration ϵ and the number of steps K of the continuation method as:

$$\epsilon' = \epsilon(K+1-k),\ k = 1, \ldots, K\ . \tag{5.16}$$

At the first step, $k = 1$, the NLP problem is solved using an acceleration equal to $\epsilon' = K\ \epsilon$, that is an acceleration K times higher than the nominal one. This normally facilitates converge to a solution. The resulting solution is then taken as initial guess for the solution of the problem corresponding to $k = 2$, when the level of acceleration is $\epsilon' = (K-1)\ \epsilon$. The process is repeated until a solution for $k = K$, that is $\epsilon' = \epsilon$, is obtained.

The NLP problem is solved using the MATLAB *fmincon* algorithm. In order to speed up the solution of the NLP problem, the elements of the Jacobian of $\mathbf{c}\,(\mathbf{x})$ are computed analytically, when possible, or by finite differences, and given as input to *fmincon*. This considerably speed up the computation. Figure 5.4 shows, in fact, the sparsity of the Jacobian of $\mathbf{c}\,(\mathbf{x})$ for an example with $n_{LT} = 12$; only few non-zero elements exist.

5.3 Direct Transcription using Thrust Elements at Periapsis and Apoapsis (DT-TEPA)

In the last proposed formulation, the low-thrust acceleration is applied only during thrust legs at the periapsis and apopsis of the transfer orbit. The direction of the thrust is kept constant on each thrust arc. This formulation is referred to as Direct Transcription using Thrust Elements at Periapsis and Apoapsis (DT-TEPA) and is based on the work presented in Zuiani et al. [240]. In this thesis, the work of Zuiani is used as a starting point for the introduction of additional optimisable variables. An application of the original transcription method and of its extension to include additional variables is presented in Chapters 10 and 12. In the original version of

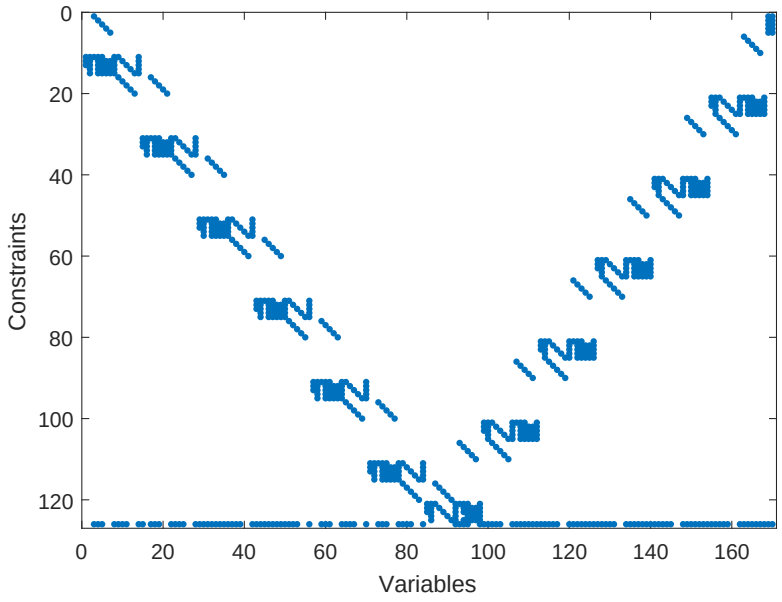

Figure 5.4: Sparsity of the Jacobian matrix of the constraints.

this transcription method, as it was presented by Zuiani, the parameters defining the thrust profile are ΔL_p and ΔL_a, the angles representing the span of the thrust legs, and the azimuth and elevation angle at periapsis and apoapsis, α'_p, α'_a, β_p and β_a. The control parameters are discretised during the transfer by considering k_{LT} nodes to model the variation of ΔL_p, ΔL_a, α'_p, α'_a, β_p and β_a from $t = 0$ to $t = ToF$. A linear interpolation is then used to define the value of the control parameters at any time during the transfer. The vector $\mathbf{x} \in \mathbb{R}^{n_x}$ of parameters to optimise, with $n_x = 6\ k_{LT}$, is:

$$\begin{aligned}\mathbf{x} = [&\Delta L_{p1},\ \Delta L_{p2},\ \dots\ \Delta L_{pk_{LT}},\ \Delta L_{a1},\ \Delta L_{a2},\ \dots\ \Delta L_{ak_{LT}}, \alpha'_{p1},\ \alpha'_{p2},\ \dots\ \alpha'_{pk_{LT}},\\ &\alpha'_{a1},\ \alpha'_{a2},\ \dots\ \alpha'_{ak_{LT}},\ \beta_{p1},\ \beta_{p2},\ \dots,\ \beta_{pk},\ \beta_{a1},\ \beta_{a2},\ \dots\ \beta_{ak_{LT}}]^T\end{aligned} . \tag{5.17}$$

The state of the spacecraft is propagated using the averaged analytical propagator described in Chapter 4. The optimisation problem consists in the minimisation of the ΔV required to realise the transfer while constraining the final orbital elements at the end of the transfer to coincide with those of the final orbit. The non-linear constrained optimisation problem is formulated as in Equation 5.4. The equality constraints $\mathbf{c}(\mathbf{x})$ impose the matching of the final orbital elements with the targeted ones (see, for example, Chapter 12 and Equation 12.4). With reference to Equations 4.11 and 4.12, this can be expressed as:

$$\mathbf{c}(\widetilde{\mathbf{x}}) = \widetilde{\mathbf{X}}_0 + \int_{t_0}^{t_0+ToF} \dot{\widetilde{\mathbf{X}}}(\mathbf{x})\, d\tau - \widetilde{\mathbf{X}}_f\ . \tag{5.18}$$

The inequality constraints depend on the considered problem; one of the constraints is expressed as

$$g_j\left(\mathbf{x}\right) = \max\left(|\Delta L_p(t)|+|\Delta L_a(t)|\right) - 2\pi\ , \tag{5.19}$$

so that the sum of the span angle of the two thrust legs does not exceed one orbital revolution. The other inequality constraints depend on the considered problem (see, for example, Chapter 12 and Equation 12.5). As regards $\mathbf{x}^L$ and $\mathbf{x}^U$, values have to be such that ΔL_p, ΔL_a and α' are in the range $[0, 2\pi]$ while β is in the range $[-\pi/2, \pi/2]$.

The proposed control parametrisation with thrust legs at periapsis and apoapsis can be modified to account for two additional thrust legs during the orbit. This introduces additional optimisation variables, and is novel with respect to the original work presented in [240]. The additional thrust legs are characterised by length ΔL_{pa} (thrust arc between periapsis and apoapsis) and ΔL_{ap} (thrust arc between apoapsis and periapsis). The angular distance between any two arcs is constrained to be:

$$\frac{2\pi - \Delta L_p - \Delta L_{pa} - \Delta L_a - \Delta L_{ap}}{4} \tag{5.20}$$

The elevation angles on the two additional arcs can be chosen so as to cause a specific and desired varation of orbital elements, for example of the inclination, as in Chapter 12. The control parameters are, in this case, $n_x = 12\ k_{LT}$:

$$\begin{aligned}\mathbf{x} = [&\Delta L_{p1},\ \Delta L_{p2},\ \ldots\ \Delta L_{pk},\ \Delta L_{a1},\ \Delta L_{a2},\ \ldots\ \Delta L_{ak},\ \Delta L_{pa1},\ \Delta L_{pa2},\ \ldots\ \Delta L_{pak},\\ &\Delta L_{ap1},\ \Delta L_{ap2},\ \ldots\ \Delta L_{apk}, \alpha'_{p1},\ \alpha'_{p2},\ \ldots\ \alpha'_{pk},\ \alpha'_{a1},\ \alpha'_{a2},\ \ldots\ \alpha'_{ak},\ \alpha'_{pa1},\ \alpha'_{pa2},\ \ldots\ \alpha'_{pak},\\ &\alpha'_{ap1},\ \alpha'_{ap2},\ \ldots\ \alpha'_{apk},\ \beta_{p1},\ \beta_{p2},\ \ldots,\ \beta_{pk},\ \beta_{a1},\ \beta_{a2},\ \ldots\ \beta_{ak},\ \beta_{pa1},\ \beta_{pa2},\ \ldots\ \beta_{pak},\\ &\beta_{ap1},\ \beta_{ap2},\ \ldots\ \beta_{apk}]^T\ .\end{aligned} \tag{5.21}$$

One of the inequality constraint $g_j(\mathbf{x})$ has now to be formulated as:

$$g_j\left(\mathbf{x}\right) = \max\left(\|\Delta L_p(t)\|+\|\Delta L_a(t)\|+\|\Delta L_{pa}(t)\|+\|\Delta L_{ap}(t)\|\right) - 2\pi \tag{5.22}$$

5.4 Comparison and validation

In this section, DT-TEVA, DT-CTECA and DT-TEPA are validated against other low-thrust trajectory optimisation methods.

5.4.1 DT-TEVA and DT-CTECA

This section presents a comparison and validation of the transcription methods DT-TEVA and DT-CTECA described in Sections 5.1 and 5.2. The test case is a transfer from Earth to asteroid Apophis, and the results are compared to those of the tool "Electric Transfer Optimisation with Planetocentric and Heliocentric Phases", ETOPH, of the Centre National d'Études Spatiales

(CNES). ETOPH is a tool for indirect optimisation of electric propelled trajectories [18,76]. A validation against the direct method of Sims and Flanagan was performed for the original formulation of Zuiani in [241]. It is assumed that the spacecraft is subject to an acceleration that follows an inverse square law; therefore, the analytical model presented in Section 4.5 is used. In this case the objective function is

$$\Delta V = \int \epsilon \, dt = \int \frac{F(t)}{m(t)} dt = \int \frac{\tilde{F}\,\tilde{r}^2}{r(t)^2\, m(t)} dt \, . \tag{5.23}$$

It is conservatively assumed that m stays constant during the transfer; moreover, using Equation 4.6, the integral in time is transformed into an integral in the true longitude:

$$\Delta V = \int \frac{\tilde{F}}{\tilde{r}^2} r(t)^2 \, m dt = \int \frac{\tilde{F}\,\tilde{r}^2}{r(t)^2\, m} \sqrt{\frac{a^3}{\mu}} \frac{B^3}{\Phi(L)^2} dL \, . \tag{5.24}$$

By expressing r as a function of L (Equation 4.58), the ΔV of the transfer can be computed as:

$$\Delta V = \int \frac{\tilde{F}\,\tilde{r}^2}{m} \sqrt{\frac{a^3}{\mu}} \frac{B^3}{\Phi(L)^2} \frac{\Phi(L)^2}{a^2 B^4} dL \approx \frac{\tilde{F}\,\tilde{r}^2}{m} \frac{1}{\sqrt{\mu\, a} B} \Delta L \, . \tag{5.25}$$

The data for the transfer are reported in Table 5.1, where $\tilde{F}$ is the thrust provided by the engine at $\tilde{r} = 1$ AU, and v_∞ is the magnitude of the $\mathbf{v}_\infty$ vector at departure. The orbital elements of the Apophis asteroid are taken from the JPL Small-Body Database Browser [1].

Table 5.1: Data for transfer from Earth to asteroid Apophis.

Departure	Arrival	v_∞ [km/s]	m_0 [kg]	$\tilde{F}$ [mN]	I_{sp} [s]
22/10/2026	11/07/2028	3.34	644.3	53	3080

For this problem, the vector $\mathbf{x}$ of parameters to optimise (Equations 5.3 and 5.10), includes also the azimuth and declination of the vector $\mathbf{v}_\infty$ at departure. The results given by the transcription methods DT-TEVA and DT-CTECA, presented in Sections 5.2 and 5.1, and by ETOPH, are summarised in Table 5.2. The initial guesses for DT-TEVA and DT-CTECA are generated according to the methods described in Sections 5.1 and 5.2.

Table 5.2: Comparison of result of transfer optimisation using the direct transcription methods DT-TEVA, DT-CTECA or the indirect method CNES ETOPH.

	ΔV [km/s]	Propellant mass [kg]
ETOPH	2.1499	44.30
DT-TEVA	2.2985	47.24
DT-CTECA	2.2898	47.07

The results of the transcription methods DT-TEVA and DT-CTECA compare well with the ones given by ETOPH. In particular, DT-TEVA and DT-CTECA give, as expected, conservatively higher values for the cost of the transfer. The reasons for this are the reduced number

[1] https://ssd.jpl.nasa.gov/sbdb.cgi#top)

degrees of freedom in the implementation of the problem in DT-TEVA and DT-CTECA, and the fact that the control on each thrust element is constant; ETOPH solves, instead, the necessary conditions for optimality. DT-CTECA considers a number of thrust arcs equal to $n_{LT} = 16$ for the 628 days transfer. The number of dimensions of the problem is $14n_{LT} + 2 = 226$. The additional two variables, with respect to the value of n_x given in Section 5.2, are the azimuth and declination of the vector $\mathbf{v}_\infty$ at departure. The trajectory for the transfer is shown in Figure 5.5a, while Figure 5.5b shows the control profile.

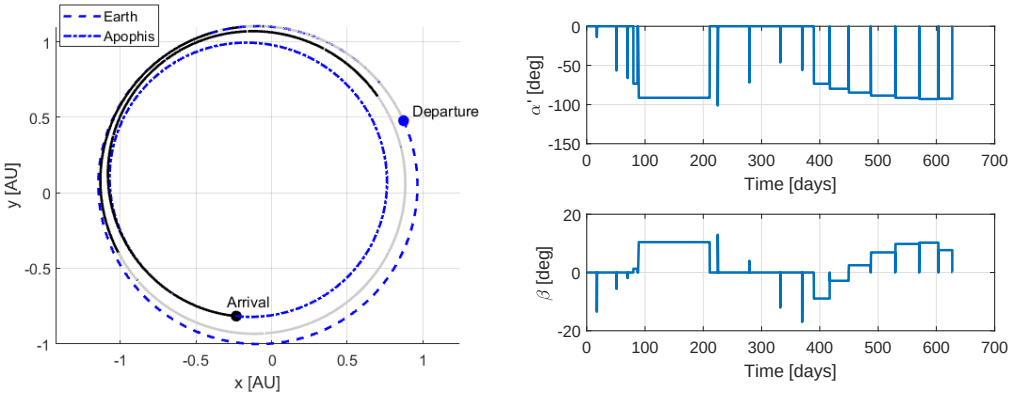

(a) Trajectory. Coast arcs are in gray, thrust arcs are in black.

(b) Control profile: azimuth angle α' and elevation angle β during the transfer.

Figure 5.5: Trajectory and control profile for the optimal transfer from Earth to Apophis using segmentation of the trajectory into coast and thrust legs (DT-CTECA).

It is possible to see that 7 of the 16 thrust arcs collapse to very small values of the arc length. This is due to the fact that the initial guess of the NLP problem spreads the thrust arcs uniformly from the departure to the arrival point. The optimal optimal solution is instead characterised by many thrust arcs located on the second part of the transfer. The collapsed arcs are characterised by a value of the arc length that is of the same order of magnitude of the tolerance of the NLP solver. The thrust arcs characterised by a negligible angular length would not be implemented in the actual control law of the spacecraft. The solver MATLAB *fmincon*, used to solve the NLP problem with interior-point method, performs 301 functions evaluation for each iteration (a function evaluation is a single call to the analytical propagator). Each function evaluation requires $2\ 10^{-4}$ seconds on a system with Intel(R) Core(TM) i7-3770 CPU 3.40 GHz wit 8BG RAM. The total number of function evaluations is 254345. When using *fmincon* with SQP, the problem converges to a slightly higher ΔV of 2.2951 km/s, but with a reduced number of function evaluations, equal to 52675.

The transcription method with segmentation into thrust legs of variable acceleration, DT-TEVA, uses $n_{LT} = 80$ legs of ≈ 7 deg span angle. The number of dimensions of the problem is $3n_{LT}+5(n_{LT}-1)+2 = 637$. The additional two variables, with respect to the value of n_x given in Section 5.1, are the azimuth and declination of the vector $\mathbf{v}_\infty$ at departure. The resulting trajectory and control profile are presented in Figure 5.6. Figure 5.6b shows that the control profile found by DT-TEVA is very similar to the one of DT-CTECA (Figure 5.5b). In Figure

5.6b, the values of α and β have no physical meaning when $\epsilon = 0$ (the engine is off). The times when the engine is on are approximately the same for both DT-TEVA and DT-CTECA. When using DT-TEVA, the solver MATLAB *fmincon* performs 712 functions evaluation for each iteration. The total number of function evaluations is 262728; using SQP the problem converges to a much higher ΔV of 2.8745 km/s. The number of constraints, for this problem, is 401. The interior point method is regarded as more efficient than SQP when dealing with a high number of constraints. There is, therefore, a 5% reduction in the number of function evaluations when using DT-CTECA rather than DT-TEVA, with an IPM solver, and a reduction of approximately 80% when using DT-CTECA with SQP, with a slight increase of the ΔV. The number of dimensions of the problem for DT-TEVA is higher than the number of dimensions for DT-CTECA. Results show that DT-CTECA, a lower-fidelity method that uses a reduced number of variables, is able to converge to a lower value of the ΔV, with reduced computational time. The control profile is, moreover, comparable to the one of the higher-fidelity method DT-TEVA.

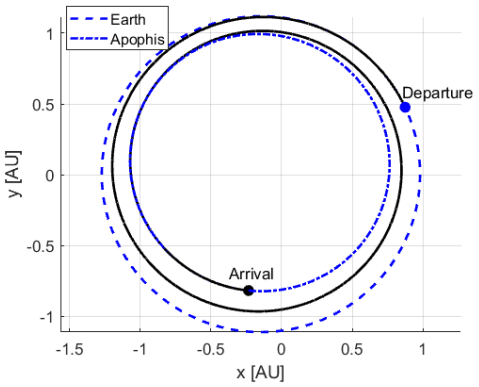

(a) Trajectory.

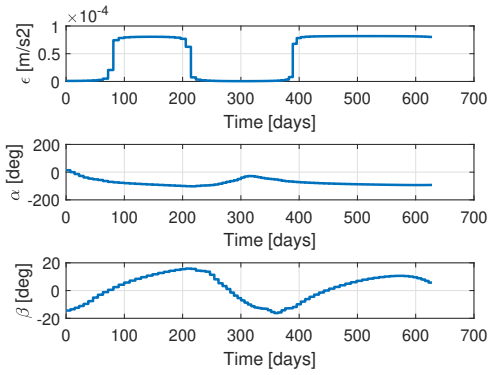

(b) Control profile: acceleration ϵ, azimuth angle α' and elevation angle β during the transfer.

Figure 5.6: Trajectory and control profile for the optimal transfer from Earth to Apophis using segmentation of the trajectory into coast and thrust legs (DT-TEVA).

5.4.2 DT-TEPA

The results provided by DT-TEPA were compared to those of two low-thrust softwares developed at the European Space Operation Centre (private communication): LATOP, an implementation of the Q-law, and MULTOP, an indirect method that makes use of orbit averaging and smoothing of the switching function . The considered test case is the GTO-GEO transfer without perturbation presented in Chapter 12. The best result obtained by DT-TEPA, using MATLAB *fmincon*, is $\Delta V = 1.5672$ km/s. LATOP and MULTOP return, respectively, 1.557 km/s and 1.5493 km/s. Therefore, the maximum difference is 17.9 m/s.

5.5 Summary

In this chapter three direct transcription methods for the optimisation of low-thrust trajectories have been presented. The results provided by two of them, DT-TEVA and DT-CTECA, have been validated in this chapter through comparison with the results of an indirect optimisation method developed at CNES. Because of the reduced number of optimisation variables, the assumptions of a constant control and the approximation in the integration, the solutions provided by the proposed transcription methods are suboptimal, and give a conservative estimation of the cost of the transfer. Results have shown, however, that the differences of ΔVs, with respect to the optimal solution of an indirect methods, are contained. The validation of DT-TEPA has shown that the results provided by this transcription method are comparable to those of two low-thrust software developed by ESA.

The application of these transcription methods to solve low-thrust optimisation problems is presented in Part II of this dissertation. In the next chapter, DT-TEVA will be used to generate the response of the training points of a surrogate model for low-thrust transfers.

Part of the content of this chapter was presented at the Seventh International Meeting on Celestial Mechanics (CelMec), 3-9 September 2017, San Martino al Cimino, Viterbo, Italy

Chapter 6

Preliminary study of surrogate-based optimal low-thrust transfers

This chapter presents some preliminary methods and results on the use of surrogate models for the evaluation of optimal low-thrust transfers. The surrogate models of low-thrust transfers are used when high-fidelity estimations are required, and therefore the analytical laws presented in Chapter 2 and 3 can not be used. The optimisation process of low-thrust trajectories, using higher fidelity models, can require long computational times. This is caused both by the high computational cost of a single function evaluation and by the fact that global algorithms generally require several thousands of function evaluations in order to locate the global minimum. By using surrogate models, the computational burden can be greatly reduced. Surrogate models provide, in fact, a fast approximation of high fidelity models. The resulting analytical function allows one to quickly evaluate quantities of interest (for example, the ΔV of the low-thrust transfer) from some input design parameters (the initial and final orbital elements for the considered transfer). Surrogate models can, therefore, be used to create a cartography of the cost of generic low-thrust transfers from any initial to any final orbit. This possible use of surrogate models will be referred to, in the following, as "offline". A different idea is at the basis of "online" surrogate models. "Online" surrogate models are used when the focus is on the convergence to the minimum of the problem, rather than on the precise representation of the high-fidelity function in the entire domain. The "online" surrogate model is built and updated as the optimisation proceeds.

This chapter is structured as follows: Section 6.1 introduces the main ideas behind the definition of surrogate models for low-thrust transfers, and presents the two proposed approaches ("offline" and "online" surrogate models). It also gives an overview of the methods available in the literature for the creation of surrogate models, with a focus on the interpolating Kriging model. Section 6.2 describes the method used for the "offline" generation of surrogate models for optimal low-thrust transfers, showing applications to transfers in Earth's and interplane-

tary space. The "online" surrogate models, which is an application to low-thrust transfers of a work already available in the literature (maximisation of the expected improvement), is presented in Appendix E. Section 6.3 concludes the chapter. An application on the use of surrogate models for low-thrust transfer is also proposed in Chapter 10.

6.1 Introduction

Surrogate models are widely used for the design and optimisation of many engineering problems. They replace the computationally expensive high fidelity simulations with a model created using few responses of such expensive simulations. In this chapter, surrogate models are used to evaluate and optimise low-thrust transfers. In particular, two possible applications are proposed: an "offline" and an "online" method to generate surrogate models.

In the offline surrogate model (Section 6.2) the aim is to generate an accurate response surface for the definition of the ΔV and ToF for the optimal transfer from an initial to a final orbit. The parameters of the surrogate model are the initial and final orbital elements.

In the online surrogate model (Section E.2), the aim is instead to locate the minimum of the ΔV cost for a given low-thrust transfer. The response surface is generated with few training points and the concept of expected improvement is used to locate the minimum. The online surrogate models are presented in Appendix E.

Different surrogate modelling techniques exist. They include, among others, polynomial models, radial basis functions, artificial neural networks and Kriging method [79, 85]. The surrogate model used in this study is a Kriging surrogate model. In particular, the MATLAB toolbox Design and Analysis of Computer Experiments (DACE) is used [132]. The use of neural network was also investigated, using the MATLAB Neural Network Toolbox. The Kriging method was selected because of its interpolating nature at the training points, because it gives an estimation of the error, and because its parameters were found to be easier to set than those of the neural network.

The first step in the construction of a Kriging surrogate model is to consider a set of n_{tr} training points $\mathcal{TP} = [\mathbf{x}_1, \mathbf{x}_2, \ldots, \mathbf{x}_{n_{tr}}]^T$, with $\mathbf{x}_i \in \mathbb{R}^d$, where d is the dimension of the problem, and the corresponding observed values $\mathbf{y} = [y_1, y_2, \ldots, y_{n_{tr}}]^T$. The Kriging predictor at a point $\mathbf{x}$ can be written as the sum of a regression model $\mathbf{f}_K$ and a random function (stochastic process) $z_K(\mathbf{x})$ [132]:

$$\hat{y}(\mathbf{x}) = \mathbf{f}_K^T(\mathbf{x})\,\boldsymbol{\beta}_K^* + z_K(\mathbf{x}) \ . \tag{6.1}$$

The coefficients in $\boldsymbol{\beta}_K$ are regression parameters while $\mathbf{f}_K$ includes p_K chosen functions. The random process $z_K(\mathbf{x})$ has zero mean and covariance:

$$\mathrm{E}\left[z_K(\mathbf{x}_i)\, z_K(\mathbf{x}_j)\right] = \sigma^2 \mathcal{R}(\theta, \mathbf{x}_i, \mathbf{x}_j) \ . \tag{6.2}$$

The correlation $\mathcal{R}$ is given in Equation 6.5. More in detail, the Kriging predictor is:

$$\hat{y}(\mathbf{x}) = {\mathbf{f}_K}^T(\mathbf{x})\,\boldsymbol{\beta}_K^* + {\mathbf{r}_K(\mathbf{x})}^T R^{-1}\left(\mathbf{y} - F_K \boldsymbol{\beta}_K^*\right) \tag{6.3}$$

In the previous equation:

- $\mathbf{f}_K(\mathbf{x}) = [f_{K,1}(\mathbf{x}), f_{K,2}(\mathbf{x}), \dots f_{K,p_K}(\mathbf{x})]^T$ is a set of p_K functions, where p_K depends on the considered regression model, according to the following:
  - Constant regression model: $p_K = 1$ and $f_{K,1}(\mathbf{x}) = 1$;
  - Linear regression model: $p_K = (d+1)$ and $f_{K,1}(\mathbf{x}) = 1$, $f_{K,2}(\mathbf{x}) = x_1$, ..., $f_{K,d+1}(\mathbf{x}) = x_d$;
  - Quadratic regression model: $p_K = 1/2(d+1)(d+2)$ and $\mathbf{f}_K(\mathbf{x})$ according to Equations (2.23) in [132].
- F_K is the n_{tr}xp_f matrix $F_K = \left[\mathbf{f}_K(\mathbf{x_1})^T, \mathbf{f}_K(\mathbf{x_2})^T, \dots, \mathbf{f}_K(\mathbf{x_{n_{tr}}})^T\right]^T$
- R is the n_{tr}xn_{tr} matrix of correlations between training points; the ij element of the matrix is:
$$R_{ij} = \mathcal{R}(\theta, \mathbf{x}_i, \mathbf{x}_j) \tag{6.4}$$
and
$$\mathcal{R}(\theta, \mathbf{x}_i, \mathbf{x}_j) = \prod_{l=1}^{d} \mathcal{R}_l(\theta, \mathbf{x}_{il}, \mathbf{x}_{jl}) \ . \tag{6.5}$$
A commonly used expression for $\mathcal{R}_l(\theta, \mathbf{x}_{il}, \mathbf{x}_{jl})$ is:
$$\mathcal{R}_l(\theta, \mathbf{x}_{il}, \mathbf{x}_{jl}) = \exp(-\theta_k |x_{il} - x_{jl}|) \ . \tag{6.6}$$
- $\mathbf{r}_K(\mathbf{x})^T$ is the vector of correlation between the considered point $\mathbf{x}$ and the training points $\mathcal{TP}$:
$$\mathbf{r}_K(\mathbf{x}) = [\mathcal{R}(\theta, \mathbf{x}_1, \mathbf{x}), \mathcal{R}(\theta, \mathbf{x}_2, \mathbf{x}), \dots, \mathcal{R}(\theta, \mathbf{x}_{n_{tr}}, \mathbf{x})]^T \ . \tag{6.7}$$
- $\boldsymbol{\beta}_K^*$ is the vector of regression parameters, given by $\boldsymbol{\beta}_K^* = \left(F_K^T R^{-1} F_K\right)^{-1} F_K^T R^{-1} \mathbf{y}$

For a fixed set of training points the variables $\boldsymbol{\beta}_K^*$, R, $\mathbf{y}$ and F_K are fixed. They are obtained by minimising the difference between the observations $\mathbf{y}$ and the predicted values at the training points $\mathcal{TP}$. For every new $\mathbf{x}$ only $\mathbf{f}_K(\mathbf{x})$ and $\mathbf{r}_K(\mathbf{x})$ have to be computed to get the Kriging predictor [132]. The Kriging surrogate model gives also an estimate of the error of the predictor. The error is zero at the sample points, since Kriging is an interpolating model. The mean squared error at a generic point $\mathbf{x}$ is instead [132]:

$$\text{MSE}[\hat{y}(\mathbf{x})] = s^2(\mathbf{x}) = \sigma^2 \left[1 + \mathbf{U}^T \left(F_K^T R^{-1} F_K\right)^{-1} \mathbf{U} - \mathbf{r}_K^T R^{-1} \mathbf{r}_K\right] \ , \tag{6.8}$$

where $\mathbf{U} = F_K^T R^{-1} \mathbf{r}_K - \mathbf{f}_K$ and σ^2 is given by

$$\sigma^2 = \frac{1}{n_{tr}} (\mathbf{y} - F_K \boldsymbol{\beta}_K^*)^T R^{-1} (\mathbf{y} - F_K \boldsymbol{\beta}_K^*) \ . \tag{6.9}$$

In this study $p_K = 2$ and spherical correlation functions are used.

6.2 Offline generation of surrogate models

The aim of the offline generated surrogate model is to obtain a quick function for the cost and time of flight of a low-thrust transfer from an initial orbit $\mathcal{OE}_0 = \{a_0, e_0, i_0, \Omega_0, \omega_0, \theta_0\}^T$ to a final orbit $\mathcal{OE}_f = \{a_f, e_f, i_f, \Omega_f, \omega_f, \theta_f\}^T$. The following relationships are sought:

$$\Delta V = f_{\Delta V}(a_0, a_f, e_0, e_f, i_0, i_f, \Delta\Omega, \Delta\omega, \theta_0, \theta_f) \,, \tag{6.10}$$

$$ToF = f_{ToF}(a_0, a_f, e_0, e_f, i_0, i_f, \Delta\Omega, \Delta\omega, \theta_0, \theta_f) \,, \tag{6.11}$$

where $\Delta\Omega = \Omega_f - \Omega_0$ and $\Delta\omega = \omega_f - \omega_0$. The values of the initial and final argument of periapsis and right ascension of the ascending node can be substituted by the differences in their values, since different initial values of ω_0 and Ω_0 cause only a rotation of the considered orbit. In practical applications, an accurate surrogate model in the 10 dimensions of Equations 6.10 and 6.11 is difficult to obtain; this is due to the high number of training points required in order to have an adequate sampling of a high dimensional space, and to the difficulties for the surrogate method to handle a large number of training points and accurately describe the model. The problem of obtaining enough information to predict a design landscape in a hyper-cube of increasing dimensions is also referred to as *curse of dimensionality* [79]: if a certain level of accuracy is achieved by sampling a one-variable space in k locations, to achieve the same sample density in a d-dimensional space, d^k observations are required [80]. For this work it is therefore chosen to create a cartography of ΔV and ToF by patching together surrogate models corresponding to fixed values of some of the input parameters, and obtained on smaller intervals of the design space.

6.2.1 Transfer model

To generate the points for the training of the surrogate model, the transcription method DT-TEVA presented in Section 5.1 is used. All transfers have a free time of transfer, therefore the last constraint in Equation 5.5 is not considered. The length of the thrust arcs is $\Delta L = 10$ deg. Two NLP problems are solved, using the following two values for the initial guess of the acceleration on each thrust arc: $\epsilon^{IG} = 1$ $(\epsilon_{max} - 0.01\epsilon_{max})$ and $\epsilon^{IG} = 0.1(\epsilon_{max} - 0.01\epsilon_{\max})$. The term $-0.01\epsilon_{max}$ is added to ϵ_{max} to avoid, in the first case, a value of the acceleration located at the border of the search space. Among the two solutions of the two NLP problems, the one characterised by lower ToF and lower ΔV is used to generate the surrogate model. The motivation behind the choice to solve two NLP problems, using two different initial guesses, is illustrated schematically in Figure 6.1, for a case where $d = 1$ and $n_{tr} = 7$. For each training point, different initial guesses might converge to different local minima, and as a result, the surrogate model responses might be different, as shown schematically in the top left and top right figures of Figure 6.1. Figure 6.1c shows instead, in black, the response generated considering the minimum value between the two solutions at each training point.

An increasing accurate response surface can be obtained by solving more than two NLP problems for different initial guesses. For this thesis, solving two NLP problems is deemed

sufficient as a preliminary study. The generation of surrogate models using solutions of more than two NLP problems will be the subject of future works.

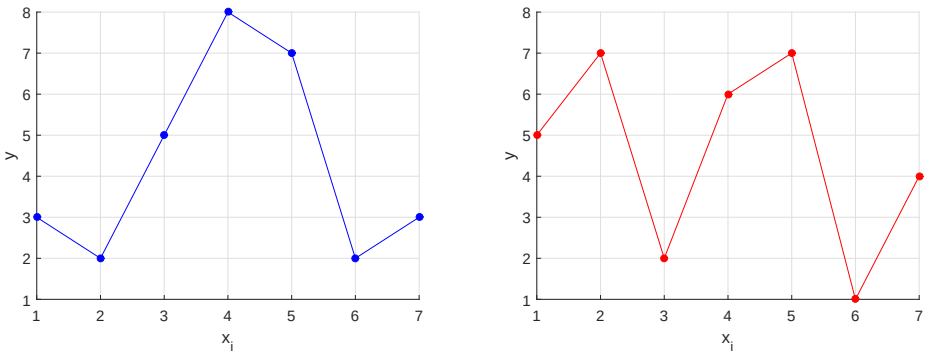

(a) Response obtained using solutions of initial guess 1.

(b) Response obtained using solutions of initial guess 2.

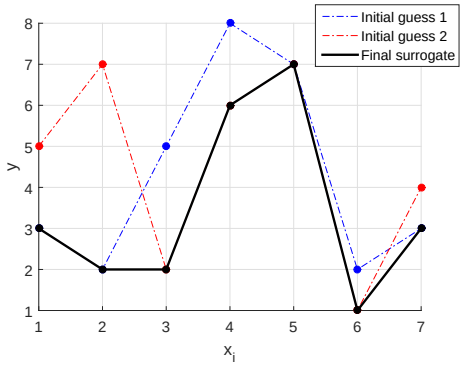

(c) Response obtained using solutions of initial guess 1, 2 and minimum results between 1 and 2.

Figure 6.1: Schematical representation of the different surrogate models obtained using results from two NLP problems, solved with different initial guesses.

6.2.2 Correspondence between Earth's and interplanetary transfers

Surrogate models for optimal low-thrust transfers are considered both for Earth's and interplanetary applications. In this section it is demonstrated that there is a correspondence between transfers with the Earth as central body and transfers with the Sun as central body, so that the same ΔVs and time of flights, expressed in appropriate distance and time units, can be considered for corresponding transfers. This allows one to compute transfers only for one of the two regions of space (e.g. interplanetary space), and translate the results to the other region (e.g. Earth's space). The correspondence is valid for transfers in regions with the same levels of gravitational acceleration. In the following this concept is explained in more details.

The distance and time units traditionally used for Earth's and interplanetary applications are summarised in Table 6.1.

Using the distance and time units reported in Table 6.1, however, results in the fact that

Table 6.1: Distance and time units for Earth and interplanetary transfers.

	Distance	Time
Earth	$\text{DU}_\oplus = 6\,378.136$ km	$\text{TU}_\oplus = 806.78$ s
Interplanetary	$\text{DU}_\odot = 149\,597\,870.691$ km	$\text{TU}_\odot = 58.13$ days

transfers in regions with equal gravitational acceleration, do not have also equal adimensional ΔV and time of flight. This is illustrated with an example. Table 6.2 reports the distance from Earth and Sun, respectively $r_\oplus$ and $r_\odot$, where the gravitational attraction, due solely to Earth and Sun, is equal to, respectively, $a_{g1} = 7.9993\ 10^{-6}$ km/s^2 and to $a_{g2} = 6.1245\ 10^{-6}$ km/s^2.

Table 6.2: Distance from Earth and Sun where the gravitational acceleration values a_{g1} and a_{g2} are obtained.

	$a_{g1} = 7.9993\ 10^{-6}$ km/s^2	$a_{g2} = 6.1245\ 10^{-6}$ km/s^2
Earth's	$r_{\oplus 1} = 2.23\ 10^5$ km = 35 $\text{DU}_\oplus$	$r_{\oplus 2} = 2.55\ 10^5$ km= 40 $\text{DU}_\oplus$
Interplanetary	$r_{\odot 1} = 0.8610\ \text{DU}_\odot$	$r_{\odot 2} = 0.9840\ \text{DU}_\odot$

Let us now consider a transfer in Earth's orbit, denoted by $\mathfrak{T}_\oplus$, and characterised by the following variation of orbital elements:

$$\{a_0 = r_{\oplus 1}, e_0 = i_0 = L_0 = 0\} \rightarrow \{a_f = r_{\oplus 2}, e_f = i_f = 0, L_f = \pi\}\ . \tag{6.12}$$

Let $\mathfrak{T}_\odot$ be instead the following transfer in interplanetary space:

$$\{a_0 = r_{\odot 1}, e_0 = i_0 = L_0 = 0\} \rightarrow \{a_f = r_{\odot 2}, e_f = i_f = 0, L_f = 0\}\ . \tag{6.13}$$

The costs and times of flight of transfers $\mathfrak{T}_\oplus$ and $\mathfrak{T}_\odot$ are reported in Table 6.3. The transcription strategy used to obtain these results has been presented in Chapter 5 (refer also to Section 6.2.1).

Table 6.3: ΔVs and ToFs for $\mathfrak{T}_\oplus$ and $\mathfrak{T}_\odot$.

$\mathfrak{T}_\oplus$		$\mathfrak{T}_\odot$	
ΔV [km/s]	ΔV [$\text{DU}_\oplus/\text{TU}_\oplus$]	ΔV [km/s]	ΔV [$\text{DU}_\odot/\text{TU}_\odot$]
0.0862	0.0109	2.0703	0.0695
ToF [days]	ToF [$\text{TU}_\oplus$]	ToF [days]	ToF [$\text{TU}_\odot$]
20.13	$2.1558\ 10^3$	483.34	8.3148

It is possible to see that neither the cost ΔV nor the time of flight ToF have equal values for the two transfers, when the distance and time units $DU_\oplus$, $TU_\oplus$, $DU_\odot$ and $TU_\odot$ are considered.

Let us now define a new set of distance and time units, for Earth and interplanetary transfers, denoted by $\text{DU}'_\oplus$ and $\text{TU}'_\oplus$ for Earth's transfers and $\text{DU}'_\odot$ and $\text{TU}'_\odot$ for interplanetary transfers. It is required that the level of acceleration, expressed in these units, is correspon-

dent, that is:

$$\frac{DU'_{\oplus}}{{TU'_{\oplus}}^2} = \frac{DU'_{\odot}}{{TU'_{\odot}}^2} \,. \tag{6.14}$$

By choosing

$$\begin{aligned} DU'_{\oplus} &= DU_{\oplus} \,, \\ TU'_{\oplus} &= TU_{\oplus} \,, \end{aligned} \tag{6.15}$$

then $DU'_{\odot}$ and $TU'_{\odot}$ can be defined using Equation 6.14 and imposing that the corresponding gravitational parameter is equal to 1:

$$\frac{{DU'_{\odot}}^3}{{TU'_{\odot}}^2} = 1 \,. \tag{6.16}$$

Using Equations 6.14, 6.15 and 6.16, the new distance and time units can be obtained. They are reported in Table 6.4.

Table 6.4: New distance and time units for Earth's and interplanetary transfers.

	Distance	Time
Earth's	$\text{DU}'_{\oplus} = 6\,378.136$ km	$\text{TU}'_{\oplus} = 806.78$ s
Interplanetary	$\text{DU}'_{\odot} = 3\,680\,137.56$ km	$\text{TU}'_{\odot} = 19\,379.39$ s

For the transfers $\mathfrak{T}_{\oplus}$ and $\mathfrak{T}_{\odot}$ proposed above, the ΔVs and ToFs, expressed in $\text{DU}_{\oplus}{}'$, $\text{TU}_{\oplus}{}'$,$\text{DU}_{\odot}{}'$ and $\text{TU}_{\odot}{}'$, are reported in Table 6.5.

Table 6.5: ΔVs and ToF for $\mathfrak{T}_{\oplus}$ and $\mathfrak{T}_{\odot}$ expressed in $\text{DU}_{\oplus}{}'$, $\text{TU}_{\oplus}{}'$,$\text{DU}_{\odot}{}'$ and $\text{TU}_{\odot}{}'$.

$\mathfrak{T}_{\oplus}$		$\mathfrak{T}_{\odot}$	
ΔV [km/s]	ΔV [$\text{DU}_{\oplus}{}'/\text{TU}_{\oplus}{}'$]	ΔV [km/s]	ΔV [$\text{DU}_{\odot}{}'/\text{TU}_{\odot}{}'$]
0.0862	0.0109	2.0703	0.0109
ToF [days]	ToF [$\text{TU}_{\oplus}{}'$]	ToF [days]	ToF [$\text{TU}_{\odot}{}'$]
20.13	$2.15\ 10^3$	483.34	$2.15\ 10^3$

Table 6.5 shows that there is correspondence both in terms of ΔV and ToF between $\mathcal{T}_{\oplus}$ and $\mathcal{T}_{\odot}$ when considering the distance and time unit $DU'_{\oplus}$, $TU'_{\oplus}$, $DU'_{\odot}$ and $TU'_{\odot}$. This correspondence is valid not only for the example of transfer presented here, but for any transfer between regions of corresponding gravitational attraction. These units will be therefore used, in the following sections, for the generation of surrogate models.

6.2.3 Training points

Different sampling plans can be used when generating surrogate models. Sampling plans include, among others, uniform sampling, latin hypercube, van der Corput sequences and Halton sequences [80,123]. In this work, the points are generated with a rectangular grid. The

number of training points for the generation of the surrogate model is defined as $n_{tr} = k^d$, where d is the dimension of the problem. Considering that the region of interest is a box defined by $\mathbf{x}^L$ and $\mathbf{x}^U$, the j-th component of the i-th design sites is defined as:

$$\mathbf{x}_{i,j} = \mathbf{x}_{i,j}^L + k_j \frac{\mathbf{x}_{i,j}^U - \mathbf{x}_{i,j}^L}{k} \; k_j = 0, 1, \ldots, k \tag{6.17}$$

6.2.4 Prediction metrics

The surrogate model is validated by evaluating its response at N_{test} test points, generated by latin-hypercube sampling in the considered box defined by $\mathbf{x}^L$ and $\mathbf{x}^U$. The test points are generate with a latin hypercube sampling method using MATLAB *lhsdesign*; the real value of the expensive model at the test points is then evaluated and compared with the result given by the Kriging model. In particular, three prediction metrics are considered:

- Correlation coefficient.
$$R\left(\mathbf{y}, \hat{\mathbf{y}}\right) = \frac{\operatorname{cov}\left(\mathbf{y}, \hat{\mathbf{y}}\right)}{\sigma\left(\mathbf{y}\right)\sigma\left(\hat{\mathbf{y}}\right)} \tag{6.18}$$

- Root mean square error (RMSE). The RMSE is computed as:
$$RMSE = \sqrt{\frac{\sum_{j=1}^{N_{test}} \left(y_j - \hat{y}_j\right)^2}{N_{test}}} \tag{6.19}$$
A good prediction gives low RMSE.

- Maximum error. The maximum error is the maximum absolute error at the test points. A low maximum error indicate a good prediction.

6.2.5 Tests in $d = 2$

In this section, surrogate models for cases where $d = 2$ are shown. In particular, transfers to change only the semi-major axis or only the eccentricity are considered.

Transfers with change of semi-major axis

This test case consider the creation of a surrogate model for the cost and time of flight of transfers with a change of semi-major axis of circular orbits, $e_0 = e_f = 0$. The other parameters are $i_0 = i_f = 0$, $L_0 = 0$ and $L_f = \pi$. The region of interest is defined by the initial and final values of the semi-major axis, in this case $\mathbf{x}^L = [0.86,\ 0.86]^T$ AU and $\mathbf{x}^U = [1.1,\ 1.1]^T$ AU. Note that transfers in this region correspond to transfers in the region $a \in [2.2296,\ 2.8519]\ 10^5$ km for Earth's transfers. In order to obtain corresponding ΔVs for Earth's transfers, the cost presented in this section must be converted from km/s into $DU'_{\odot}/TU'_{\odot}$ (refer to Table 6.4). The obtained value is then converted from $DU'_{\oplus}/TU'_{\oplus}$ to km/s. The training points are defined in this region using the method described in Subection 6.2.3 and $k = 6$. The transfer model presented in Subection 6.2.1 is then used to obtain the value of the function at the training

points and the Kriging model described in Section 6.1 is utilised to fit a response surface. The response surfaces for ΔV and ToF are shown in Figure 6.2, where the blue points are the 36 training points and the red points are the $N_{test} = 100$ test points.

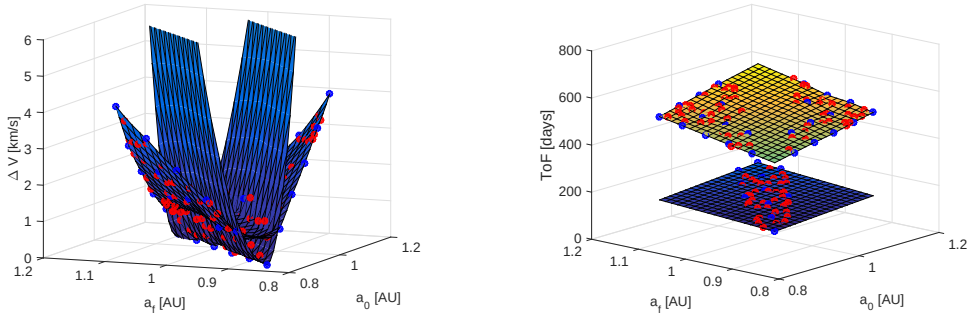

(a) ΔV (b) ToF

Figure 6.2: Surrogate models for transfers with change of semi-major axis, $d = 2, k = 6$. The blue points are the training points, the red points are the test sites.

Figure 6.2b clearly shows that two ranges of times of flight are possible. In particular, transfers with small variation of semi-major axis, that is, transfers around the diagonal defined by $a_f = a_0$, can be realised with 0 revolutions (times of flight lower than 220 days). All the other transfers require at least one orbital revolution (times of flight greater than 450 days). Two surrogate models are therefore generated, both for ToF and ΔV. The surrogate model relative to the 0 revolution solutions is denoted by $\mathcal{S}_{0rev}$ and is created using the set of training points characterised by 0 revolution, $\mathcal{TP}_{0rev}$, while $\mathcal{S}_{1rev}$ is created using the training points characterised by 1 revolution, $\mathcal{TP}_{1rev}$.

A test point is evaluated using $\mathcal{S}_{0rev}$ or $\mathcal{S}_{1rev}$, depending on its position with respect to the training points, as explained in the following and as shown in Figure 6.3. In particular, a test point surrounded by four training points of the set $\mathcal{TP}_{0rev}$ will be evaluated using $\mathcal{S}_{0rev}$ (Figure 6.3c). Viceversa, a test point surrounded by four training points of the set $\mathcal{TP}_{1rev}$ will be evaluated using $\mathcal{S}_{1rev}$ (Figure 6.3b). If a test point is surrounded by four training points that belong in part to $\mathcal{TP}_{0rev}$ and in part to $\mathcal{TP}_{1rev}$ (Figure 6.3d), then it is not possible to decide which model should be used. The test point is therefore identified as uncertain, both $\mathcal{S}_{0rev}$ and $\mathcal{S}_{1rev}$ are used to evaluate it, and the model that provides the lower ΔV is used for that point.

In this case, 66 out of 100 test points are identified as uncertain. This means that the ΔV corresponding to these points is the minimum ΔV between the cost of the 0 revolution transfer and the 1 revolution transfer. Generally, this means that the points are assumed to correspond to transfers realised with 1 orbital revolution, even when that transfer would be feasible also with 0 orbital revolution (a lower ΔV is generally associated to longer times of flight). The user should check, if interested, to see if solutions of lower time of flight (and 0 orbital revolution) exist. Out of the 66 uncertain points, 11 points correspond, indeed, to transfers that are thought to be possible only with 1 revolution while, in reality, they could be realised in a shorter time of flight with 0 revolution. This is illustrated in Figure 6.4, where the relationship between the

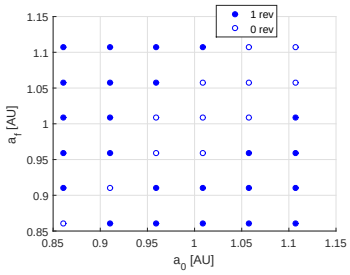

(a) Training points and number of revolutions associated to their solutions.

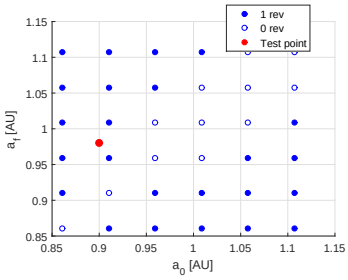

(b) Test point surrounded by 4 training points belonging to TP_{1rev}: use S_{1rev}.

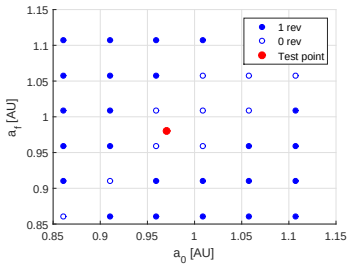

(c) Test point surrounded by 4 training points belonging to TP_{0rev}: use S_{0rev}.

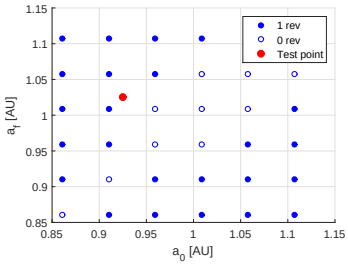

(d) Test point surrounded by 3 training points belonging to TP_{1rev} and 1 belonging to TP_{0rev}: uncertainty.

Figure 6.3: Schematic representation of how to choose the surrogate model to use to evaluate a test point.

real function values at the test point (abscissa) and the function value estimated from Kriging (ordinate), is shown for both ΔV and ToF. For a perfect estimation of the function by the surrogate model, the points in the figure should be aligned on the $y = x$ line.

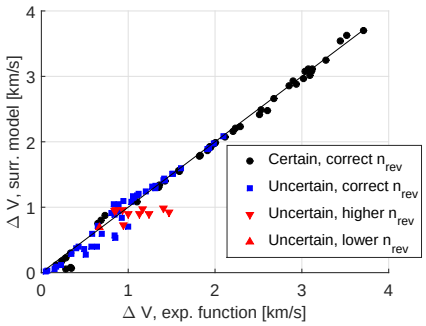

(a) ΔV

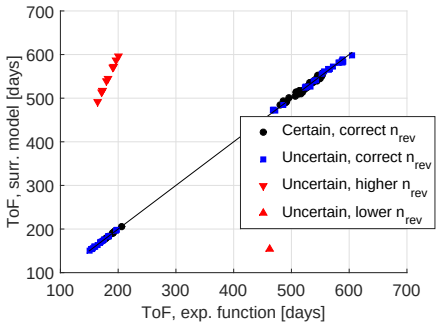

(b) ToF

Figure 6.4: Relationship between real function value and estimated function value from surrogate model for transfers with variations of semi-major axis, $d = 2$ and $k = 6$. Black dots represent points evaluated with the correct model. Blue squares and red triangles represent uncertain points.

The black dots in Figure 6.4 represent points evaluated using the correct model (either $\mathcal{S}_{0rev}$ or $\mathcal{S}_{1rev}$), because the test points are in a situation like the ones in Figure 6.3b or 6.3c. Blue

squares and red triangles correspond, instead, to a situation like the one in Figure 6.3d. In this case, the model providing the lower ΔV is used, that is $\mathcal{S}_{1rev}$. For the 54 blue squares this corresponds, indeed, to the real situation; the transfers can not be realised with 0 revolution. For the 11 downward triangles, instead, the transfer could be possible also with 0 revolution, at a lower ToF. There is, finally, one point, for which the minimum ΔV is obtained using $\mathcal{S}_{0rev}$ rather than $\mathcal{S}_{1rev}$ (upward red triangle). This is a particular behaviour found only in this case, and likely due to the particular shape of the response surfaces of the two surrogate models, that are very close to each other, and intersect for low values of ΔV (Figure 6.2).

Even if 11 points are evaluated using the surrogate model corresponding to the higher number of revolution, the results obtained are not wrong, but simply relative to a different solution for that transfer. The fact that many points appear to be outside the diagonal in Figure 6.4 is not a sign that the surrogate model is incorrect, but simply that the abscissa of those points corresponds to a 0 revolution solution, while the ordinate corresponds to a 1 revolution solution. To show the validity of the results, those 11 points are re-evaluated with the real expensive model for a number of revolution equal to 1, so that both the abscissa and ordinate values are relative to 1-revolution solutions. The results are shown in Figure 6.5.

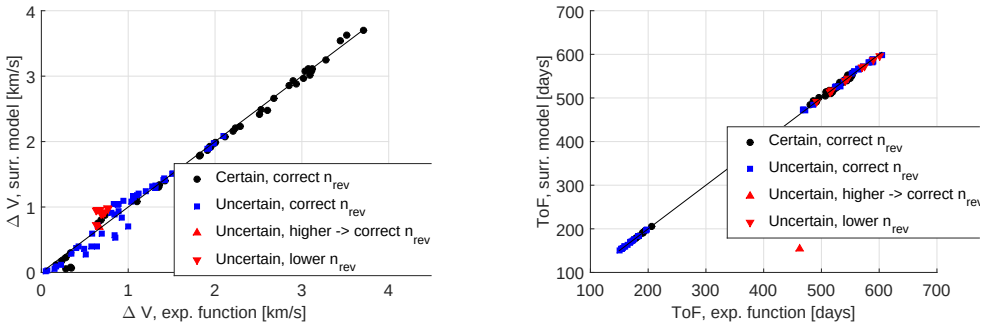

(a) ΔV (b) ToF

Figure 6.5: Relationship between real function value and estimated function value from surrogate model for transfers with variations of semi-major axis, $d = 2, k = 6$. Abscissa and ordinate values correspond to solutions with the same number of revolutions.

It is possible to see that now the results given by the surrogate model on the test points are in agreement with the results of the real model, except for one point for which the time of flight is underestimated.

Increasing the number of design sites can create a more accurate representation of the model, that can avoid the presence of such points. This is shown in the following, for k increased from 6 to 10, that is, using 100 rather than 36 training points. Figure 6.6 reports the response surface and the relationship between real and estimated values of the function at the 100 test points. The plots in Figure 6.6 can be compared to those in Figures 6.2, 6.4 and 6.5.

Table 6.6 summarises the prediction metrics for the $k = 6$ and the $k = 10$ test cases, and it shows the improvement in the results obtained with an increasing number of training points.

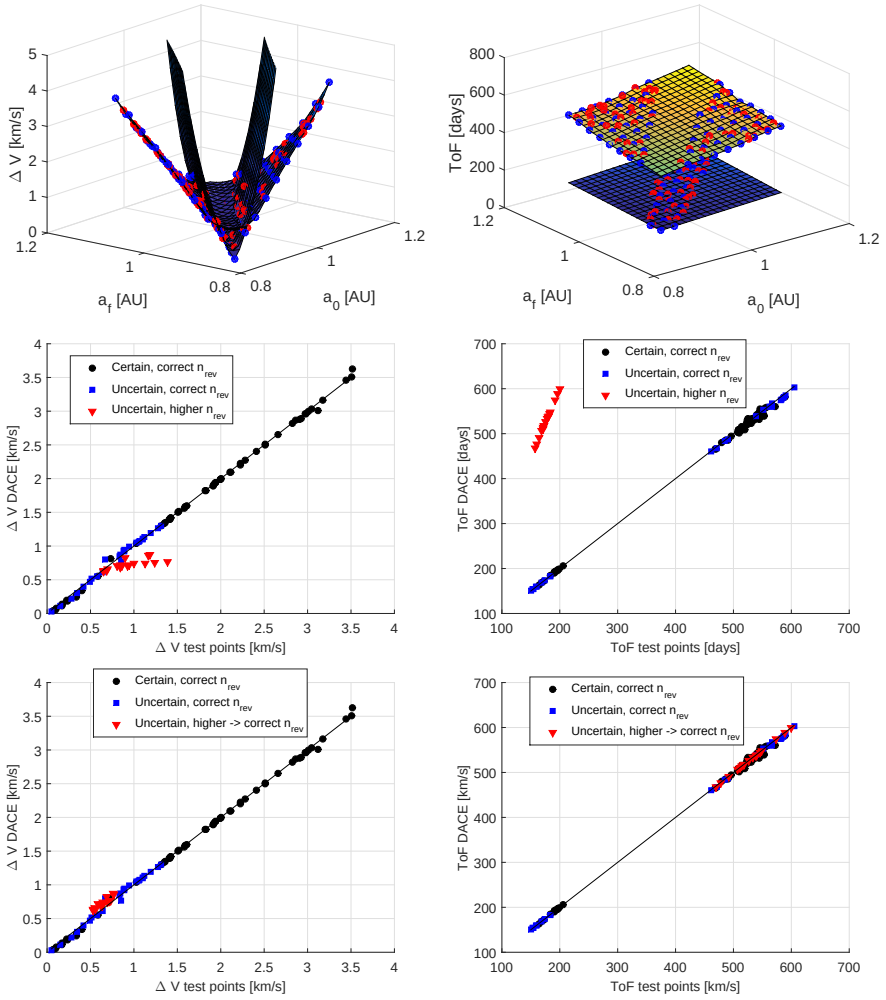

Figure 6.6: Response surface and results obtained using 100 training points for transfers with variation of semi-major axis, $d = 2$ and $k = 10$.

Table 6.6: Prediction metrics for transfers with variation of semi-major axis: $k = 6$ and $k = 10$.

	$k = 6$			$k = 10$		
	R	RMSE	Max error	R	RMSE	Max error
ΔV	0.99	0.0125 km/s	0.33 km/s	0.99	0.005 km/s	0.14 km/s
ToF	0.98	3.1 days	308 days	0.99	0.44 days	13.42 days

Transfers with change of eccentricity

A second example characterised by $d = 2$ is presented hereafter. In this case the surrogate model is relative to transfers characterised by a change of semi-major axis from 0.86 AU to 0.98 AU, $i_0 = i_f = 0$, $\bar{\omega}_0 = \theta_0 = \theta_f = 0$, $\bar{\omega}_f = \pi$, and e_0 and e_f in the range defined by $\mathbf{x}^L = [0,\ 0]^T$ and $\mathbf{x}^U = [0.1,\ 0.1]^T$. The parameter $\bar{\omega}$ is the longitude of the periapsis, used for elliptical equatorial orbits to define the angle of the eccentricity vector with respect to the x

axis of the reference frame. The results obtained in this case for $k = 6$ are presented in Figure 6.7.

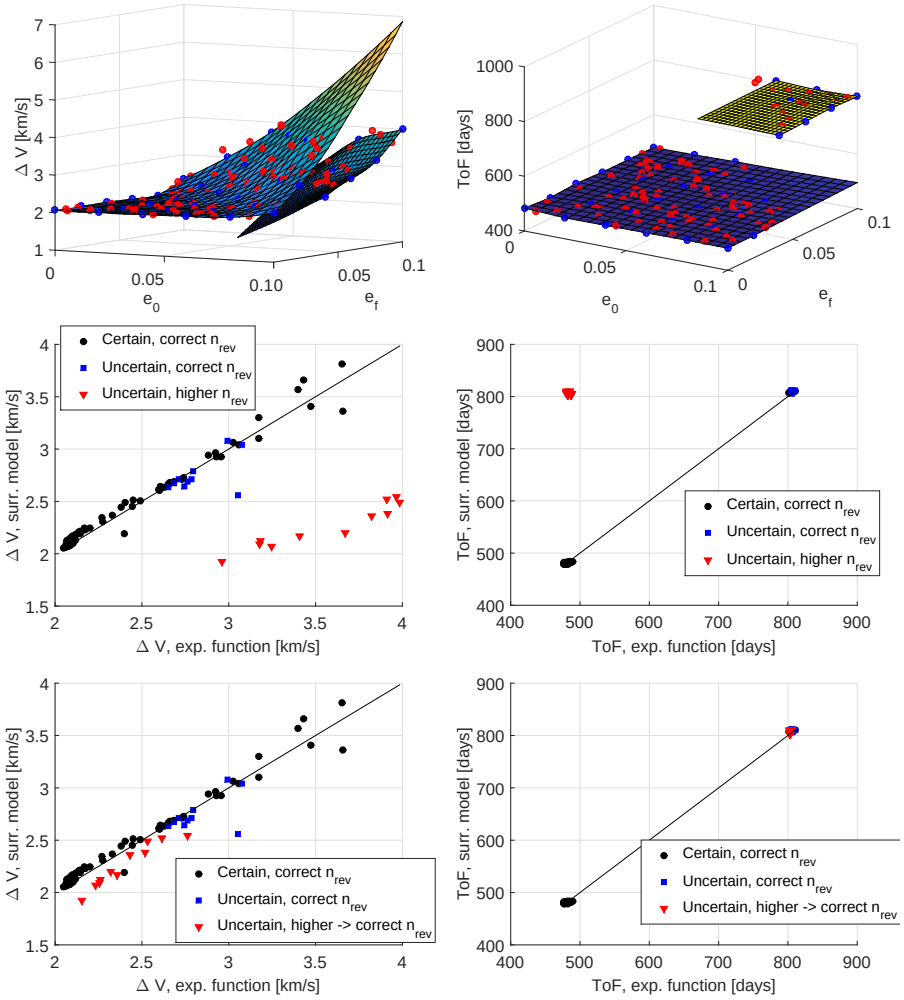

Figure 6.7: Relationship between real function value and estimated function value from surrogate model, for transfers with variation of eccentricity and $k = 6$. Black dots represent points evaluated with the correct model. Blue square and red triangles represent uncertain points.

Two surrogate models are created for the cost of the transfer, and two for the time of flight. Transfers characterised by higher values of e_0 and e_f require indeed 2 revolutions ($ToF > 800$ days) while transfers characterised by lower values of e_0 and e_f require 1 orbital revolution ($ToF < 500$ days).

For 21 points out of 100 test points there is uncertainty regarding which one of the two surrogate models should be used. For 11 out of 21 of these points, the surrogate model corresponding to 2 revolutions is used, while a solution would have been possible also for 1 orbital revolution (red triangles). The bottom of Figure 6.7 shows the relationship between real and estimated values when using 2 revolutions also for the real expensive model. Figure 6.8 shows,

instead, the results obtained when using $k = 10$, that correspond to 100 training points. It is possible to see how the results improve with an increasing number of training points. This is also shown in Table 6.7, where the final performance metrics are summarised.

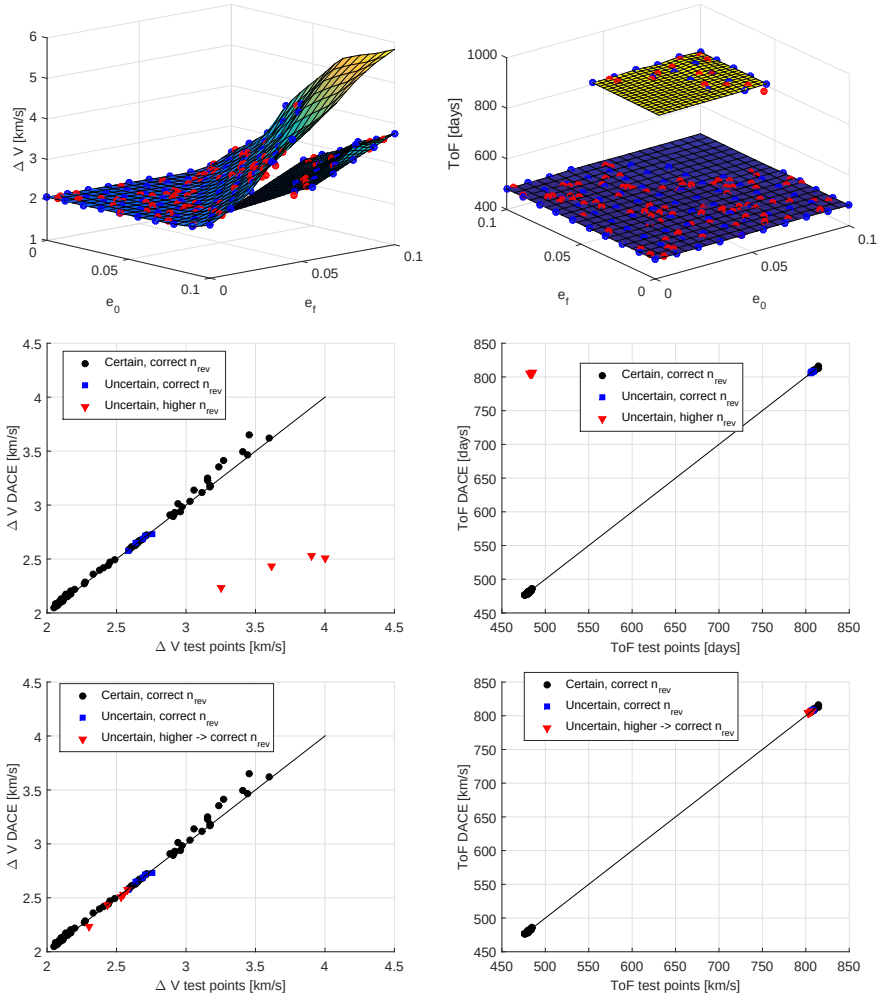

Figure 6.8: Response surface and results obtained using 100 training points for transfers with change of eccentricity.

Table 6.7: Prediction metrics: $k = 6$ and $k = 10$ for transfers with change of eccentricity.

	$k = 6$			$k = 10$		
	R	RMSE	Max error	R	RMSE	Max error
ΔV	0.97	0.009 km/s	0.49 km/s	0.99	0.0035 km/s	0.19 km/s
ToF	0.99	0.25 days	7.46 days	1	0.06 days	2.13 days

6.2.6 Cartography in $d = 4$

Having shown two $d = 2$ examples in the previous sections, here some preliminary results on the generation of a $d = 4$ cartography of ΔV and ToF are presented. The transfers are characterised by variations of both semi-major axis and eccentricity. The region of interest is defined by the lower and upper bounds for the initial and final semi-major axis and eccentricity: $\mathbf{x}^L = [0.86 \text{ AU}, \ 0.86 \text{ AU}, \ 0, \ 0]^T$ and $\mathbf{x}^U = [1.1 \text{ AU}, \ 1.1 \text{ AU}, \ 0.1, \ 0.1]^T$. The other orbital elements are $i_0 = i_f = \bar{\omega}_0 = \theta_0 = \theta_f = 0$, and $\bar{\omega}_f = \pi$. In this case the number of test points is $N_{test} = 500$. In order to assess the number of revolutions, and therefore the surrogate model to be used for the evaluation of the test points, 16 surrounding points have to be considered, rather than 4 (the number of surrounding training points for each test point is in fact 2^d). If all the 16 surrounding points of the considered test point are characterised by the same number of revolutions, then the number of revolution for the test point is uniquely defined. Otherwise, the lower ΔV is considered but a flag that shows that the test point is uncertain is set to 1. Results are presented in Figure 6.9 for $k = 6$.

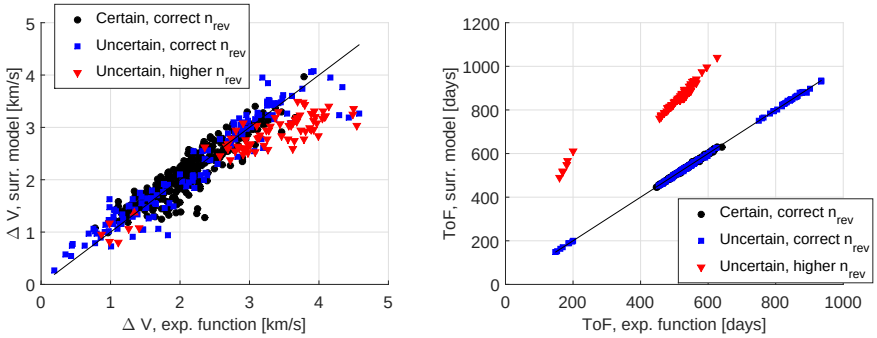

Figure 6.9: Relationship between real function value and estimated function value from surrogate model, $d = 4, k = 6$.

Out of 500 test points, 219 are uncertain points (red triangles and blue squares). In particular, the red triangles represent points corresponding to transfers that are estimated with an higher number of revolution when using the surrogate model. If the same number of revolution is used both for the real expensive function and the cheap surrogate model function, the results shown in Figure 6.10 are obtained. In this case, rather than re-evaluating the real expensive function with a higher number of revolutions, it was chosen to re-evaluate the surrogate model, since the evaluation of the surrogate model is faster than the evaluation of the expensive real function.

If k is increased from 6 to 8, the results shown in Figure 6.11 can be obtained. In this case the number of uncertain points is reduced from 219 to 151. The presence of more training points makes it easier, in fact, to choose which surrogate model to use for the test points.

Table 6.8 summarises the final performance metrics. In this case, only small improvements are obtained when using $k = 8$ rather than $k = 6$, suggesting that $k = 10$ or higher, or additional measures, should be taken in order to further improve the results.

In order to improve the results, alternative methods to the one presented above are used to

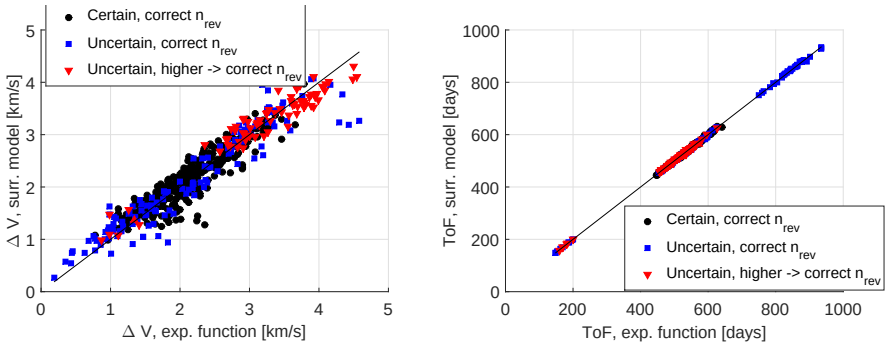

Figure 6.10: Relationship between real function value and estimated function value from surrogate model, $d = 4, k = 6$. Abscissa and ordinate values correspond to solutions with the same number of revolutions.

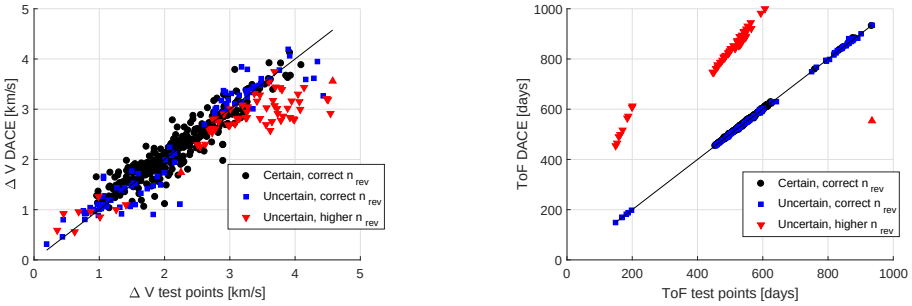

(a) ΔV - different number of revolutions on ascissa and ordinate for the red triangles.

(b) ToF - different number of revolutions on ascissa and ordinate for the red triangles.

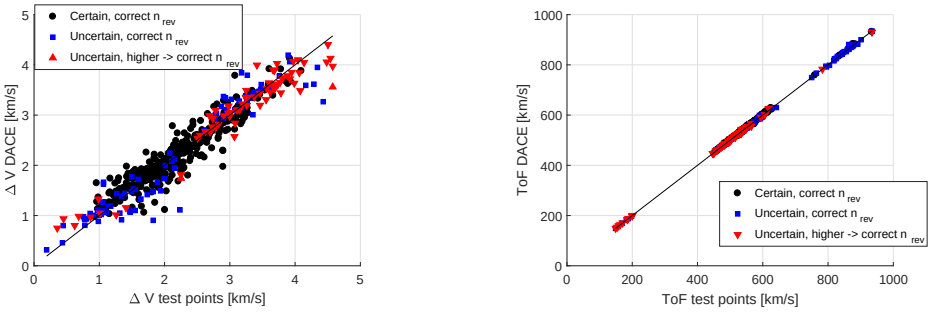

(c) ΔV - same number of revolutions on ascissa and ordinate for the red triangles.

(d) ToF - same number of revolutions on ascissa and ordinate for the red triangles.

Figure 6.11: Results for transfers with variation of semi-major axis and eccentricity, $d = 4, k = 8$.

Table 6.8: Prediction metrics: $k = 6$ and $k = 8$.

	$k = 6$			$k = 8$		
	R	RMSE	Max error	R	RMSE	Max error
ΔV	0.9533	0.0116 km/s	1.3102 km/s	0.9579	0.0110 km/s	1.1647 km/s
ToF	0.9997	0.1176 days	11.8772 days	0.9997	0.1156 days	17.6668 days

obtain the response of the training points and to generate and test the surrogate model. The main differences with respect to the approach presented in the previous sections are summarised in the following:

- Training points: transcription method.
  The solution of the low-thrust optimisation problem corresponding to each training point is obtained using DT-CTECA, rather than DT-TEVA (Chapter 5). DT-CTECA generally requires, in fact, a lower number of function evaluations to locate a minimum of the problem.

- Training points: number of NLP problems.
  The number of NLP problems solved for each training point is 8, rather than 2. As before, the response for each training point is given by the solution of the NLP problem that returns the minimum ΔV solution. The 8 NLP problems are obtained from the 8 possible combinations of settings resulting from the use of different solvers, number of thrust arcs, and type of initial guess, according to:

  - Solvers:
    1. MATLAB *fmincon-sqp*
    2. MATLAB *fmincon-interior-point*
  - Number n_{LT} of thrust arcs per orbital revolution (refer to Section 5.2):
    1. 4 thrust arcs
    2. 6 thrust arcs
  - Type of initial guess for the thrust arcs:
    1. Initial guess according to Equation 5.15
    2. Initial guess for $\mathbf{X}_s^{ON}$ according to Equation 5.15 and initial guess for $\mathbf{X}_s^{OFF}$ according to (different from Equation 5.15 for the last term in the true longitude):

$$\mathbf{X}_s^{OFF} = \left[a_0 + \frac{a_f - a_0}{2n_{LT}+1}2s,\ P_{1,dep} + \frac{P_{1,f} - P_{1,0}}{2n_{LT}+1}2s,\ P_{2,0} + \frac{P_{2,f} - P_{2,0}}{2n_{LT}+1}2s, \right.$$
$$\left. Q_{1,0} + \frac{Q_{1,f} - Q_{1,0}}{2n_{LT}+1}2s,\ Q_{2,0} + \frac{Q_{2,f} - Q_{2,0}}{2n_{LT}+1}2s,\ L_0 + \frac{L_f - L_0}{2n_{LT}+1}s \right]^T \tag{6.20}$$

- Training points: sampling plan.
  The training points, that were previously disposed on a regular grid (Section 6.2.3), are now generated in the design space using a Halton sequence [99].

- Training points: number of orbital revolutions.
  In the approach presented so far, the solution of each NLP problem was attempted with 0 revolution, and the number of revolutions was increased until a solution was found, for the considered NLP problem, with the lowest possible number of revolutions. Now, instead, each NLP problem is solved for 0, 1, 2 and 3 orbital revolutions, and results

are stored for each of these cases. For each training point $\mathbf{x}_i$, where $i = 1, \ldots, n_{tr}$, the following responses are, therefore, available: $\mathbf{y}_i = \left[y_i^{0rev}, y_i^{1rev}, y_i^{2rev}, y_i^{3rev}\right]^T$. As an example, the response y_i^{2rev} corresponds to the best solution obtained considering the 8 possible settings for the NLP problem and 2 orbital revolutions. Note that a given low-thrust transfer might not be possible when the number of orbital revolution is not sufficiently high. When this happens, this is recorded by assigning a not-a-number value to the response y. Different surrogate models are then built for the 0, 1, 2 and 3 orbital revolution cases, as described in the next point.

- Local (rather than global) surrogate model.
  For each test point $\mathbf{x}$, the predictor is obtained from a surrogate model generated using the q training points that are closest to the test point, rather than the entire set of training points. That is, given the set $\mathcal{TP} = [\mathbf{x}_1, \mathbf{x}_2, \ldots, \mathbf{x}_{n_{tr}}]^T$ of 4096 training point, only a subset $\mathcal{TP}_q \subset \mathcal{TP}$ is used to generate the Kriging predictor. In particular, if the predictor for the test point $\mathbf{x}$ is sought, for a transfer with 2 orbital revolution, then the subset $\mathcal{TP}_q$ is the set of the q training points closest to the considered test point $\mathbf{x}$, and the subset of responses $\mathbf{y}_s \subset \mathbf{y}$ includes the corresponding responses for 2 orbital revolutions.

- Test.
  The method presented in Section 6.2.5 for the estimation of the number of revolutions required to realise a transfer is no longer used. A new method is used instead. To explain how the new method work, let us assume that the interest is in estimating the predictor for a test point $\mathbf{x}$ for a transfer with 1 orbital revolution. For the considered test point, the distance is computed from the test point to the training points that return feasible solutions for 1 orbital revolution. These distances are then sorted, and if the closest distances are too high, then the test point corresponds to a transfer that can not be realised with 1 orbital revolution. If, on the contrary, there are training points sufficiently close to the test points that return feasible solutions using 1 orbital revolution, then the transfer corresponding to the test point can be realised with 1 orbital revolution. Due to these changes, testing the surrogate model does not require evaluating additional test points. Each training point is, in fact, also used as a test point, with the remaining 4095 training points used to find the q points closest to the test point.

Table 6.9 summarises the main changes implemented.

Tables 6.10, 6.11 and 6.12 shows the correlation coefficient, RMSE and maximum error for ΔV and ToF, using different values of q and for transfers with 0, 1, 2 or 3 orbital revolutions. The 4096 training points are used as test points only if a feasible solution is available, for each point, at the considered number of orbital revolutions.

Comparing the results in Tables 6.10, 6.11 and 6.12 with those in Table 6.8 for the case $k = 6$ shows that the implemented changes improve the results of the surrogate model for the ΔV, but present some additional difficulties for the ToF. Figures 6.12 show the relationship between the real and predicted ΔV and ToF for different number of orbital revolutions and the case $q = 25$. Figures 6.12 have to be compared to Figures 6.11(c) and (d), rather than

Table 6.9: Summary of the main changes in the generation of the training points and of the surrogate models.

TRAINING	SURROGATE	TEST
Transcription method: DT-TEVA → DT-CTECA **Number of NLP problems:** 2 → 8 **Sampling plan:** Regular grid → Halton sequence **Number of orbital revolutions:** Lowest possible → $\{0, 1, 2, 3\}$	**Surrogate model:** Global → Local	**Test points:** Create new → Use training points

Table 6.10: Correlation coefficient R.

	$n_{rev} = 0$		$n_{rev} = 1$		$n_{rev} = 2$		$n_{rev} = 3$	
	ΔV	ToF	ΔV	ToF	ΔV	ToF	ΔV	ToF
18	0.8785	0.9999	0.9956	0.9906	0.9982	0.9583	0.9985	0.9781
25	0.9648	1	0.9979	0.9963	0.9993	0.9854	0.9994	0.9904
30	0.9648	1	0.9981	0.9969	0.9993	0.9878	0.9995	0.9921
35	0.9690	1	0.9982	0.9972	0.9994	0.9889	0.9995	0.9929
40	0.9695	1	0.9981	0.9973	0.9994	0.9899	0.9995	0.9935
45	0.9696	1	0.9981	0.9974	0.9994	0.9903	0.9995	0.9938
50	0.9711	1	0.9982	0.9975	0.9994	0.9902	0.9995	0.9938

Table 6.11: RMSE for ΔV [km/s] and ToF [days].

	$n_{rev} = 0$		$n_{rev} = 1$		$n_{rev} = 2$		$n_{rev} = 3$	
	ΔV	ToF	ΔV	ToF	ΔV	ToF	ΔV	ToF
18	0.0066	0.0155	0.0015	0.1722	0.0012	0.5276	0.0011	0.5307
25	0.0035	0.0098	0.0011	0.1075	7.6071e-4	0.3062	6.8241e-4	0.3488
30	0.0034	0.0098	0.0010	0.0977	7.2817e-4	0.2793	6.5548e-4	0.3152
35	0.0033	0.0089	0.0010	0.0932	7.0210e-4	0.2664	6.3641e-4	0.2988
40	0.0033	0.0089	0.0010	0.0913	7.0944e-4	0.2542	6.5052e-4	0.2876
45	0.0033	0.0089	0.0010	0.0897	7.0692e-4	0.2496	6.4317e-4	0.2803
50	0.0032	0.0090	9.9486e-4	0.0884	6.9859e-4	0.2503	6.3035e-4	0.2798

Table 6.12: Maximum error for ΔV [km/s] and ToF [days].

	$n_{rev} = 0$		$n_{rev} = 1$		$n_{rev} = 2$		$n_{rev} = 3$	
	ΔV	ToF	ΔV	ToF	ΔV	ToF	ΔV	ToF
18	2.4797	2.5231	1.5950	127.7139	1.6040	780.3684	1.6111	439.9439
25	0.4543	1.6433	0.4163	51.6281	0.5178	205.6832	0.3416	231.8511
30	0.4534	0.8729	0.4734	52.4306	0.4958	157.5851	0.4782	302.9125
35	0.4175	0.7816	0.4119	48.8919	0.4779	146.3438	0.2925	295.2766
40	0.4721	0.8631	0.4188	47.4915	0.5138	136.1991	0.3498	294.3573
45	0.4734	0.7966	0.4721	46.2902	0.4323	137.6128	0.3114	277.8918
50	0.4627	0.8182	0.4496	48.6461	0.4833	137.7736	0.3047	281.5035

Figures 6.11(a) and (b). For each test point, in fact, a local surrogate model for a certain number of orbital revolution is evaluated only if the transfer corresponding to that test point can be realised with that number of orbital revolutions.

Figures 6.13 show, for each test point (on the x axis) the distance to the closest feasible training point (on the y axis), for the considered number of orbital revolution. If the test point is feasible for that number of orbital revolution, than it is represented by a blue dot. Otherwise, a red dot is used. Results show that the distance to the closest feasible training point is a valid indication for the feasibility of a transfer with a given number of orbital revolutions. When the distance to the closest feasible point is higher than a given threshold, the transfer for that point can not be realised with the considered number of orbital revolution. Future studies will be dedicated to the definition of a method for the assessment of the threshold distance that separates feasibility from non feasibility.

6.3 Conclusions and future work

This chapter has presented some preliminary methods and results on the use of surrogate models for low-thrust transfers.

Since the study is only at a preliminary stage, many directions for development can be proposed for its improvement. The first one would be to extend the analysis of the offline surrogate model to higher dimensions ($d > 4$).

In the proposed implementation of the offline surrogate-based method, moreover, the ToF is an output of the model. This means that the model can not be applied to fixed time transfers, that is, to cases where the ToF is an input to the problem, rather than an output. The development of surrogate models of fixed time transfers presents, in fact, some additional difficulties. When the ToF is one of the input parameter of the model, for a given variation of orbital elements the transfer could be infeasible for some values of the ToF (for example, when the ToF is not big enough to allow for a certain variation of orbital elements). This means that it would be necessary to deal with regions of infeasibility. To identify if a test point falls within a region of feasibility or within a region of infeasibility, convex hull could be defined. However, this presents some difficulties when d is high; moreover, regions of transition from feasible to infeasible space (and vice versa) should be modelled. These topics and possible improvements will be the subject of future works.

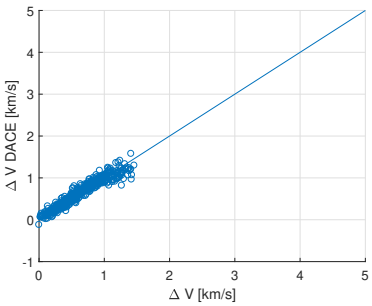

(a) ΔV - $n_{rev} = 0$.

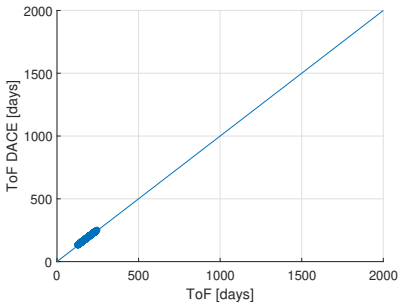

(b) ToF - $n_{rev} = 0$.

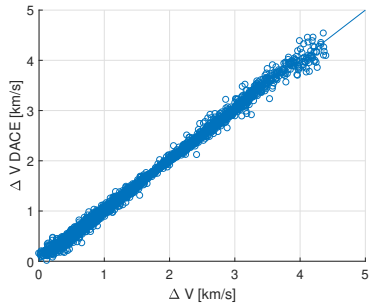

(c) ΔV - $n_{rev} = 1$.

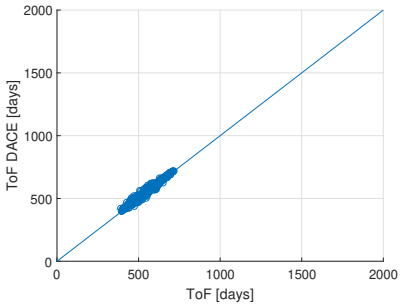

(d) ToF - $n_{rev} = 1$.

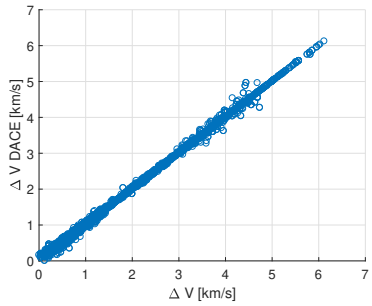

(e) ΔV - $n_{rev} = 2$.

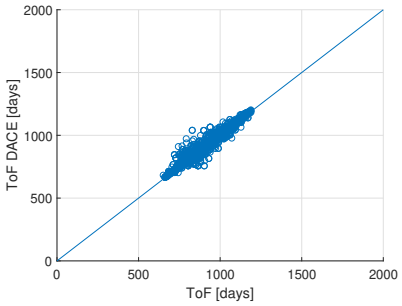

(f) ToF - $n_{rev} = 2$.

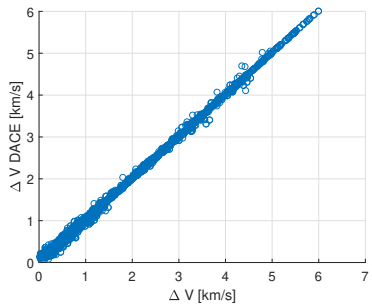

(g) ΔV - $n_{rev} = 3$.

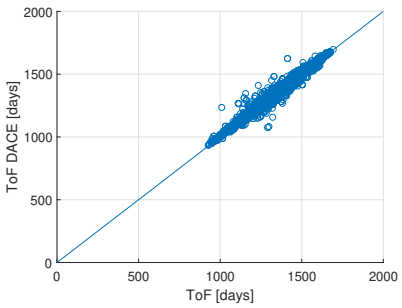

(h) ToF - $n_{rev} = 3$.

Figure 6.12: Results for transfers with variation of semi-major axis and eccentricity, $d = 4$, different number of revolutions n_{rev}, implementing the changes summarised in Table 6.9.

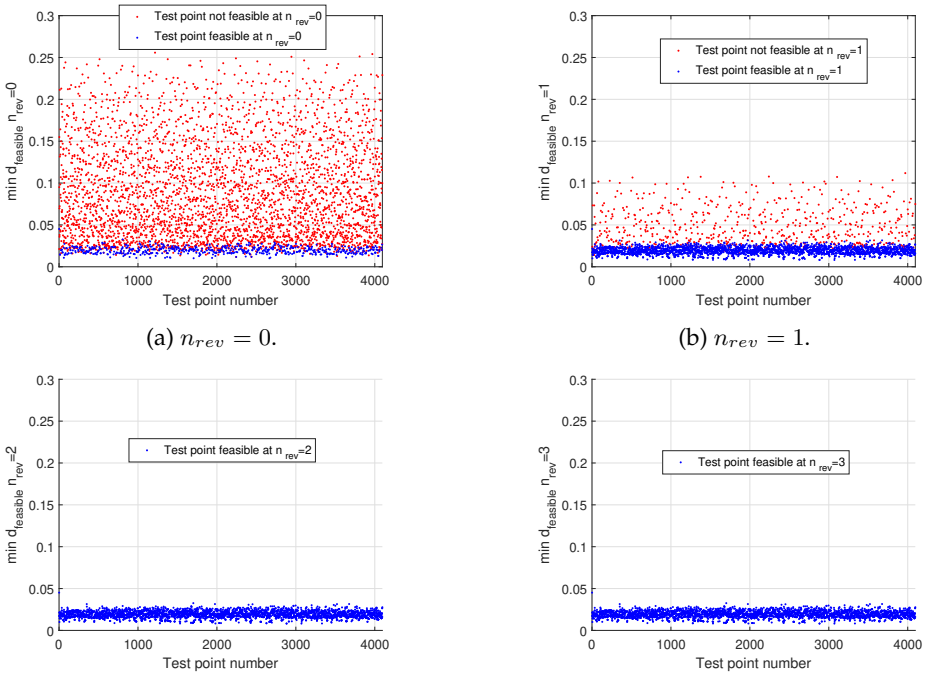

(a) $n_{rev} = 0$.

(b) $n_{rev} = 1$.

(c) $n_{rev} = 2$.

(d) $n_{rev} = 3$.

Figure 6.13: Distance between each test point (on the x axis) and the closest training point with feasible transfer at the considered number of orbital revolution. If the transfer is feasible for the considered test point, the distance is represented with a blue dot. Otherwise a red dot is used.

Chapter 7

The content of this chapter is under review for publication in the journal Soft Computing and part of its content was published in M. Di Carlo, M. Vasile, E. Minisci "Multi-Population Adaptive Inflationary Differential Evolution Algorithm with Adaptive Local Restart", IEEE Congress on Evolutionary Computation, 25-28 May 2015, Sendai, Japan

Multi Population Adaptive Inflationary Differential Evolution Algorithm

This chapter presents the global evolutionary algorithm Multi-Population Adaptive Inflationary Differential Evolution Algorithm (MP-AIDEA). MP-AIDEA is the multi-population version of Inflationary Differential Evolution Algorithm (IDEA), an algorithm which combines basic Differential Evolution (DE) with some of the restart and local search mechanisms of Monotonic Basin Hopping (MBH).

In the adaptive version presented here, the DE and MBH parameters are automatically adapted. The proposed algorithm implements a simple but effective mechanism to avoid multiple detections of the same local minima. The novel mechanism allows the algorithm to decide whether to start or not a local search.

The algorithm has been extensively tested over more than fifty test functions from the Competitions of the Congress on Evolutionary Computation (CEC), CEC 2005, CEC 2011 and CEC 2014, and compared against the algorithms participating in those competitions. For each test function this chapter reports best, worst, median, mean and standard deviation values of the best minimum found by the algorithm. Comparisons with other algorithms participating in the CEC competitions are presented in terms of relative ranking, Wilcoxon tests and success rates. For completeness, the chapter presents also the single population adaptive IDEA, that can adapt only CR and F, and shows that this simpler version can outperform the multi-population one if the radius of the restart bubble and the number of restarts are properly chosen. However, the choice of these parameter requires a computationally expensive pre-tuning process. The multi-population version MP-AIDEA automatically adapts the parameters during the optimisation process.

The chapter starts with a brief introduction of DE and IDEA and with a statement of the problem to solve in Section 7.1; the basic principles and fundamental theoretical developments of IDEA are briefly introduced in Section 7.2. The adaptation mechanisms are presented, to-

gether with the resulting adaptive multi-population version of IDEA, MP-AIDEA, in Section 7.4. The test cases are presented in Section 7.5 and the results are presented in Sections 7.5.1. Finally, the results of all the comparative tests are presented in Sections 7.5.2, 7.5.3 and 7.5.4. The notation of this chapter is independent from the notation of the rest of this thesis. Therefore, the definition of the Greek and Roman Symbols in the Nomenclature list at the beginning of this thesis does not apply to this chapter.

7.1 Introduction and problem statement

The algorithm IDEA is based on the hybridisation of DE with the restarting procedure of Monotonic Basin Hopping (MBH) [223]; it implements both a local restart in the neighborhood of a local minimum and a global restart in the whole search space. IDEA was shown to give better results than a simple DE but its performance is dependent upon the parameters controlling both the DE and MBH heuristics [217]. These parameters are the crossover probability CR, the differential weight F, the radius of the local restart bubble δ_{local} and the number of local restarts n_{LR}, whose best settings are problem dependent. Different adaptive mechanisms for adjusting CR and F during the search process can be found in the literature, [31, 130, 150], though no approach has been proposed so far to adapt δ_{local} and n_{LR}. In this work a simple mechanism to adapt CR and F within a single population and a multi-population strategy to adapt δ_{local} and n_{LR} is proposed.

The following class of global minimisation problems with box constraints is considered:

$$\min_{\mathbf{x}\in B} f(\mathbf{x}) \tag{7.1}$$

with $f : B \subseteq \mathbb{R}^{n_D} \to \mathbb{R}$, n_D the number of dimensions and the box B defined by the upper and lower boundaries $\mathbf{x}^L \leq \mathbf{x} \leq \mathbf{x}^U$. In the following, a gradient based local search algorithm will be used, therefore it is further required that $f \in C^2(B)$.

7.2 Inflationary Differential Evolution

This section briefly recalls the working principles of Inflationary Differential Evolution and presents the parameters that the algorithm adapts. Following the notation introduced in [217], the DE process is expressed as a discrete dynamical system. The governing equation, for the i-th individual at generation k, is expressed as:

$$\mathbf{x}_{i,k+1} = \mathbf{x}_{i,k} + S(\mathbf{x}_{i,k} + \mathbf{u}_{i,k}, \mathbf{x}_{i,k})\mathbf{u}_{i,k} \tag{7.2}$$

where S is the selection function, given in Equation 7.6, and $\mathbf{u}_{i,k}$ is ~~with~~ the trial vector, expressed as:

$$\mathbf{u}_{i,k} = \mathbf{e}\left[G\,\mathbf{x}_{r_1,k} + (1-G)\mathbf{x}_{i,k} + F(\mathbf{x}_{r_2,k} - \mathbf{x}_{r_3,k}) + (1-G)F(\mathbf{x}_{best,k} - \mathbf{x}_{i,k})\right] \tag{7.3}$$

where G can be either 0 or 1 (with $G = 1$ corresponding to the DE strategy DE/*rand* and $G = 0$ corresponding to the DE strategy DE/*current-to-best* [165]). In Equation (7.3), r_1, r_2 and r_3 are integer numbers randomly chosen in the population, and $\mathbf{e}$ is a mask containing random numbers of 0 and 1 according to:

$$e_t = \begin{cases} 1 \Rightarrow U \leq CR \\ 0 \Rightarrow U > CR \end{cases} \qquad t = 1, \ldots, n_D \tag{7.4}$$

U is a random number taken from a random uniform distribution $[0, 1]$. The product between $\mathbf{e}$ and $[G\mathbf{x}_{r_1,k} + (1-G)\mathbf{x}_{i,k} + F(\mathbf{x}_{r_2,k} - \mathbf{x}_{r_3,k}) + (1-G)F(\mathbf{x}_{best,k} - \mathbf{x}_{i,k})]$ in Equation (7.3) has to be intended component-wise. In this work, given $u_{h,i,k}$, the *h-th* component of the trial vector $\mathbf{u}_{i,k}$, the following correction is applied to satisfy the box constraints [238]:

$$u_{t,i,k} = \begin{cases} \left(x_{t,i,k} + x_t^L\right)/2, & \text{if } u_{t,i,k} < x_t^L \\ \left(x_{t,i,k} + x_t^U\right)/2, & \text{if } u_{t,i,k} > x_t^U \end{cases} \tag{7.5}$$

The selection function S is defined as:

$$S(\mathbf{x}_{i,k} + \mathbf{u}_{i,k}, \mathbf{x}_{i,k}) = \begin{cases} 1 \text{ if } f(\mathbf{x}_{i,k} + \mathbf{u}_{i,k}) < f(\mathbf{x}_{i,k}) \\ 0 \text{ otherwise} \end{cases} \tag{7.6}$$

In the general case in which the indices r_1, r_2 and r_3 can assume any value, in [217] it was demonstrated that the population can converge to a fixed point different from a local minimum or to a level set. Furthermore, in [131] it was demonstrated that DE can converge to a hyperplane that does not contain the global minimum. Finally, consider the following proposition.

Proposition 7.2.1. *Consider the subset $\Psi = \{\mathbf{x} \in B : f(\mathbf{x}) \leq \bar{f}\}$ and the superset ϕ such that:*

1. $\Psi \subset \phi$
2. $\mathbf{x}_{i,k+1} \in \phi, \forall i$
3. $\forall \mathbf{x} \in \phi \setminus \Psi, f(\mathbf{x}) > \bar{f}$

then if the population at iteration k is entirely contained in Ψ it cannot escape from Ψ at any future iteration.

Proof. The proof descends from the definition of S. Suppose that a candidate individual $\mathbf{x}_{i,k+1}$ was generated by map (7.2) then, because of point 3 of the proposition, it would be rejected by the selection operator. □

Therefore, when the population contracts within a ball $B_c \subseteq \Psi$ of radius ρ_l, DE can only converge to a point or a subset within B_c. We call ρ_l the contraction limit, in the following.

In Inflationary Differential Evolution, the DE heuristics is iterated until the population reaches the contraction limit. A local search is then started from the best individual in the population $\mathbf{x}_{best}$, the corresponding local minimum $\mathbf{x}_{LM}$ is saved in an archive of local minima

A and the population is restarted in a bubble B_R of radius δ_{local} around the local minimum $\mathbf{x}_{LM}$. This mechanisms is borrowed from the basic logic underneath Monotonic Basin Hopping [223]. To assess if the contraction condition is satisfied, the maximum distance between all possible combinations of individuals of the population at generation k, $\rho^{(k)}$, is computed:

$$\rho^{(k)} = \max\left(||\mathbf{x}_{i,k} - \mathbf{x}_{l,k}||\right) \quad i,l = 1,\ldots,N_{pop} \tag{7.7}$$

where N_{pop} is the number of individuals in the population. The contraction is verified when $\rho^{(k)} \leq \bar{\rho}\rho_{max}$, where $\rho_{max} = \arg\max_k \rho^{(k)}$ is the maximum value of ρ ever recorded until generation k and $\bar{\rho}$ is one of the parameters of the algorithm, the contraction threshold. This contraction criterion is consistent with Proposition 7.2.1 under the assumption that $\rho_l = \bar{\rho}\rho_{max}$.

After a number n_{LR} of such local restarts, without any improvement of the current best solution, the archive A collects all the local minima found so far. At this point the population is restarted globally in the search space so that every individual is initially at a distance $\sqrt{n_D}\delta_{global}$ from the centres of the clusters of the local minima in A. During local restarts the most important information is preserved in the local minimum. The assumption is that the basin of attraction of that local minimum has already been explored and that exploration led to the convergence of the population to B_c. When the population is restarted globally the essential information, all the local minima, is stored in the archive A. Here the assumption is that IDEA has completely explored a funnel structure resulting in a cluster of minima.

These restart procedure were proven to be very effective in a series of difficult real problems in which the landscape presents multiple funnels (see [217] for additional details).

The complete Inflationary Differential Evolution process with trial vector (Equation 7.3) is governed by the following key parameters: N_{pop}, CR and F, G, $\bar{\rho}$, δ_{local}, n_{LR}, δ_{global}. From experience, δ_{global} is not a critical parameter in most of the cases while CR, F, δ_{local} and n_{LR} play a significant role and are not always easy to define. The parameters CR and F are applied to update each individual in a population while δ_{local} and n_{LR} are applied to restart the whole population. Therefore, two adaptation mechanisms are proposed, one for CR and F and one for δ_{local} and n_{LR}. In particular, the adaptation mechanisms of CR, F and δ_{local} are such as to result in the definition of numerical values for these parameters, to be used by the algorithm. On the contrary, the use of n_{LR} is replaced by a mechanism that allows the algorithm to decide when to perform a local or global restart, so that the definition of a numerical value for n_{LR} is not required anymore.

7.3 Adaptation mechanisms

Because of the very nature of CR and F, δ_{local} and n_{LR}, the automatic adaptation of CR and F requires only the evaluation of the success of each candidate increment $\mathbf{u}_{i,k}$. On the other hand, the adaptation of δ_{local} and n_{LR} requires the evaluation of the success of the restart of an entire population. Therefore, it is proposed to extend the working principle of Inflationary Differential Evolution by evolving n_{pop} populations in parallel, where n_{pop} is defined a priori.

Each population adapts its own values of CR and F. A stigmergic approach is used in

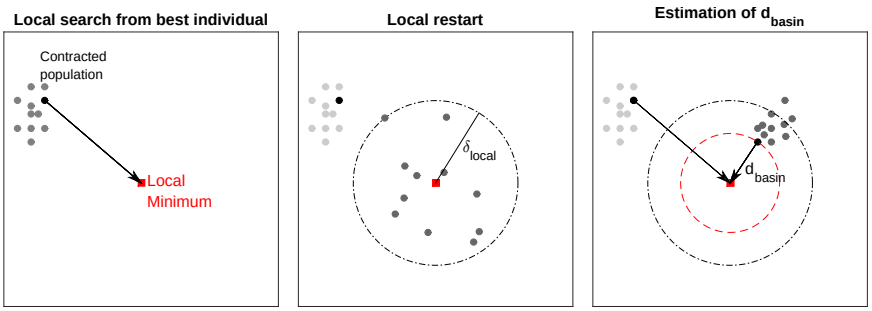

Figure 7.1: Identification of the basin of attraction of local minimum $\mathbf{x}_{LM}$

which the CR and F of each individual are drawn from a joint probability distribution, over a set of possible values of CR and F, that evolves with the population.

All populations are then concurrently adapting δ_{local} and the number of local restarts. More specifically, the adaptation mechanism of the local restart bubble evolves a probability distribution function over a range of possible values of δ_{local}. Each population draws values from that probability distribution and at each local restart increases the probability associated to the value of δ_{local} that led to a transition from one local minimum to another. The range of δ_{local} is also adapted by taking the mean and the minimum distance among the local minima in A.

The number of local restarts, instead, is dictated by the contraction of a population within the basin of attraction of an already identified local minimum. Given a local minimum $\mathbf{x}_{LM} \in A$ and a list of $n_{best,LM}$ best individuals from which a local search converged to $\mathbf{x}_{LM}$, the size of the basin of attraction of $\mathbf{x}_{LM}$ is defined as

$$d_{basin,LM} = \min_j ||\mathbf{x}_{best,j} - \mathbf{x}_{LM}||, \quad j \in 1, ..., n_{best,LM} \tag{7.8}$$

Each local minimum $\mathbf{x}_{LM}$ in A, therefore, is associated to a particular $d_{basin,LM}$. Figure 7.1 illustrates this mechanism. Once $d_{basin,LM}$ is estimated, every time the condition $\rho_m^{(k)} \leq \bar{\rho}\rho_{m,max}$ is satisfied for population m, if the best individual $\mathbf{x}_{best,m}$ is at a distance lower than $d_{basin,LM}$ from $\mathbf{x}_{LM}$, then no local restart is performed but the population is restarted globally in the search space. The number $n_{best,LM}$ is set to 4 in this implementation.

The overall algorithm, called Multi-Population Adaptive Inflationary Differential Evolutionary Algorithm (MP-AIDEA) is described in more detail in the following section.

7.4 Multi-Population Adaptive Inflationary Differential Evolution

MP-AIDEA is described in Algorithm 1. Let n_{pop} be the number of populations and m the index identifying each population. With reference to Algorithm 1, after initialisation of main parameters and functionalities (Algorithm 1, line 1), MP-AIDEA starts by running n_{pop} Differential Evolutions in parallel, one per population (Algorithm 1, line 3). During each evolution

Algorithm 1 MP-AIDEA

1: Initialisation (Section 7.4.1, Algorithm 2)
2: **for** $m \in [1, \ldots, n_{pop}]$ **do**
3: Run Differential Evolution with adaptive CR and F until contraction to B_c (Section 7.4.2, Algorithms 3 and 4)
4: **end for**
5: **for** $m \in [1, \ldots, n_{pop}]$ **do**
6: $\mathbf{x}_{best,m} = argmin_{\mathbf{x}_{m,i} \in P_m} f(\mathbf{x}_{m,i})$
7: **if** $(\forall \mathbf{x}_{LM} \ : \ [\|\mathbf{x}_{best,m} - \mathbf{x}_{LM}\| > d_{basin,LM}$ **or** $i_{LM} < n_{best,LM}])$ **or** $A = \emptyset$ **then**
8: Run local search and find local minimum $\mathbf{x}_{min,m}^{(s_m)}$
9: $s_m = s_m + 1$
10: **if** $\exists \ \mathbf{x}_{LM} \ : \ \|\mathbf{x}_{min,m}^{(s_m)} - \mathbf{x}_{LM}\| \leq \varepsilon\Delta$ **then**
11: $i_{LM} = i_{LM} + 1$
12: $d_{basin,LM} = \min[d_{basin,LM}, ||\mathbf{x}_{best,m} - \mathbf{x}_{LM}||]$
13: $LR_m = 1$
14: **else**
15: $\mathbf{x}_{LM} \leftarrow \mathbf{x}_{min,m}^{(s_m)}$
16: Store local minima $\mathbf{x}_{LM}$ in A, compute $d_{basin,LM} = \|\mathbf{x}_{best,m} - \mathbf{x}_{LM}\|$
17: $LR_m = 1$
18: **end if**
19: **else**
20: $LR_m = 0$
21: **end if**
22: **end for**
23: Update distribution of δ_{local} (Algorithm 6)
24: Restart populations with Algorithm 7 using LR_m, δ_{local} and δ_{global}
25: If total number of function evaluations is lower than maximum number of function evaluations, goto (2)

process, the parameters F and CR are automatically adapted following the approach presented in Section 7.4.2. When a population m contracts within a ball B_c of radius $\bar{\rho}\ \rho_{m,max}$, the evolution of that population is stopped. Once all the populations have contracted, the relative position of the best individual of each population, $\mathbf{x}_{best,m}$ with respect to the local minima in A, $\mathbf{x}_{LM}$, is assessed (Algorithm 1, line 7). This step makes use of all the minima found by all populations and, therefore, it has to be regarded as an information sharing mechanism among populations. If the best individual of population m is not within the basin of attraction of any previously detected local minimum (that is, $\forall LM \ : \ \|\mathbf{x}_{best,m} - \mathbf{x}_{LM}\| > d_{basin,LM}$) then a local search is run (Algorithm 1, line 8) and the resulting local minimum is stored in the archive A (Algorithm 1, line 16). The flag for the local restart, LR_m, is set to 1. On the contrary, if the best individual of population m is inside the basin of attraction of a previously detected local minimum, the local search is not performed and LR_m is set to 0 (Algorithm 1, line 20).

Before running a local or a global restart (Algorithm 1, line 24), the probability distribution associated to δ_{local} and its range are updated (Algorithm 1, line 23). After restarting the population, if the number of maximum function evaluations is not exceeded, the process restarts from line 2 in Algorithm 1. Each part of Algorithm 1 is explained in more details hereafter.

7.4.1 Initialisation

The steps for the initialisation of MP-AIDEA are presented in Algorithm 2. MP-AIDEA starts with the initialisation of n_{pop} populations, with N_{pop} individuals each, in the search space B. The number of function evaluations for each population is set to zero, $n_{feval,m} = 0$ and $\bar{\rho}$, δ_{global}, are initialised to the values specified by the user. The counter of the number of local search per population, s_m, is set to 0.

Algorithm 2 MP-AIDEA: initialisation

1: Set values for n_{pop}, N_{pop}, $\bar{\rho}$, δ_{global}, ε, $s_m = 0 \; \forall m \in [1, \ldots, n_{pop}]$
2: Set $n_{feval,m} = 0$ and $k_m = 1$ (generation number) for each populations $m \in [1, \ldots, n_{pop}]$
3: Initialize population P_m with individuals $\mathbf{x}_{m,i} \; \forall m \in [1, \ldots, n_{pop}]$ and $\forall i \in [1, \ldots, N_{pop}]$
4: Compute $\Delta = \|\mathbf{x}^U - \mathbf{x}^L\|$ where $\mathbf{x}^L$ and $\mathbf{x}^U$ are the lower and upper boundaries of the search space

7.4.2 Differential Evolution and the adaptation of CR and F

For each population m a DE process is run (Algorithm 3, line 6), using Equations 7.2 to 7.6. The parameter G, in Equation 7.3, assumes values equal to 0 or 1 with probability 0.5. During the advancement from parents to offspring, each individual of the population is associated to a different value of CR and F, drawn from a distribution $\mathbf{CRF}_m^{(k_m)}$ (Algorithm 3, lines 1, 2, 3). $\mathbf{CRF}_m^{(k_m=1)}$ is initialised as a uniform distribution with $(n_D+1)^2$ points in the space $CR \in [0.1, 0.99]$ and $F \in [-0.5, 1]$ (Algorithm 3, line 1). A Gaussian kernel is then allocated to each node and a probability density function is built by Parzen approach [141]. The values of CR and F to be associated to the individuals of the population are drawn from this distribution (Algorithm 3, line 4). A change value dd linked to each kernel is initialised to zero (Algorithm 3, line 3) and is used during the advancement of the population from parents to children to adapt CR and F (Algorithm 3, line 8). The adaptation of CR and F is summarised in Algorithm 4 and described in the following.

For each individual i of each population m the adaptation mechanism for CR and F is started only if the child is characterised by an objective function value lower than the parent's one, that is $f(\mathbf{x}_{m,i}^{(k_m+1)}) < f(\mathbf{x}_{m,i}^{(k_m)})$ (Algorithm 4, line 1). If this condition is verified, the difference in objective function between parent and child at subsequent generation, $df_{m,i}^{(k_m+1)} = |f(\mathbf{x}_{m,i}^{(k_m+1)}) - f(\mathbf{x}_{m,i}^{(k_m)})|$, is computed (Algorithm 4, line 2). Then the sorted elements of $\mathbf{CRF}_m^{(k_m)}$ are sequentially evaluated; the q-th value of CR in $\mathbf{CRF}_m^{(k_m)}$ is identified as $\mathbf{CRF}_{m,q,1}^{(k_m)}$ and the q-th value of F is identified as $\mathbf{CRF}_{m,q,2}^{(k_m)}$. The first time that $dd_{m,q}^{(k_m)}$ (the dd value associated to the q-th row of $\mathbf{CRF}_m^{(k_m)}$) is lower than $df_{m,i}^{(k_m+1)}$ (Algorithm 4, line 4), the differential weight $F_{m,i}^{(k_m)}$ used for the individual $\mathbf{x}_{m,i}^{(k_m)}$ substitutes $\mathbf{CRF}_{m,q,2}^{(k_m)}$ and $df_{m,i}^{(k_m+1)}$ substitutes $dd_{m,q}^{(k_m)}$ (Algorithm 4, lines 5 and 6). This is because $F_{m,i}^{(k_m)}$ produced a bigger decrease in the objective function than $\mathbf{CRF}_{m,q,2}^{(k_m)}$ (as shown by $df_{m,i}^{(k_m+1)} > dd_{m,q}^{(k_m)}$). For CR, the value associated to $\mathbf{x}_{m,i}^{(k_m)}$ substitutes $\mathbf{CRF}_{m,q,1}^{(k_m)}$ (Algorithm 4, line 8) only if $df_{m,i}^{(k_m+1)}$ is greater than a given value CRC (Algorithm 4, line 7), [141].

Algorithm 3 Differential Evolution with adaptive CR and F

1: Regular meshes $\mathbf{CR}$ and $\mathbf{F}$ with $(n_D+1)^2$ points (n_D is the dimensionality of the problem) in the space $CR \in [0.1, 0.99] \times F \in [-0.5, 1]$ are created
2: Initialize $\mathbf{CRF}_m^{(k_m=1)}$ with points of the mesh: $\mathbf{CRF}_{m,q,1}^{(k_m=1)} \leftarrow \mathbf{CR}_q$ and $\mathbf{CRF}_{m,q,2}^{(k_m=1)} \leftarrow \mathbf{F}_q$ for all $q \in [1, \ldots, (n_D+1)^2]$
3: Associate to each row of $\mathbf{CRF}_m^{(k_m=1)}$ an element $dd_{m,q}^{(k_m=1)} = 0$ for all $q \in [1, \ldots, (n_D+1)^2]$
4: Sample $\mathbf{CR}_m^{(k_m)}$ and $\mathbf{F}_m^{(k_m)}$ from a bi-variate distribution on the two dimensional lattice defined by the rows of $\mathbf{CRF}_m^{(k_m=1)}$
5: **for** $i \in [1, \ldots, N_{pop}]$ **do**
6: $\quad \mathbf{x}_{m,i}^{(k_m+1)} \leftarrow \mathrm{DE}\left(\mathbf{x}_{m,i}^{(k_m)}, \mathbf{CR}_m^{(k_m)}, \mathbf{F}_m^{(k_m)}\right)$
7: $\quad n_{feval,m} = n_{feval,m} + 1$
8: $\quad$ Update $\mathbf{CRF}_m^{(k_m)}$ (Algorithm 4)
9: **end for**
10: $k_m = k_m + 1$
11: Row sort $\mathbf{CRF}_m^{(k_m+1)}$ in terms of $dd_m^{(k_m+1)}$ values
12: Compute $\rho_m^{(k_m)} = \max(||\mathbf{x}_{m,i}^{(k_m)} - \mathbf{x}_{m,l}^{(k_m)}||)\ \forall \mathbf{x}_{m,i}^{(k_m)}, \mathbf{x}_{m,l}^{(k_m)} \in P_m^{(k_m)}$
13: Until $\rho_m^{(k_m)} \leq \bar{\rho} \cdot \rho_{m,max}$,
where $\rho_{m,max} = \max\left[\rho_m^{(k_m=1)}, \rho_m^{(k_m=2)}, \ldots \rho_m^{(k_m)}\right]$, or $k_m < 10D$, goto (4)

Algorithm 4 Updating the joint distribution $\mathbf{CRF}$

if $f(\mathbf{x}_{m,i}^{(k_m+1)}) < f(\mathbf{x}_{m,i}^{(k_m)})$ **then**
$\quad$ Compute $df_{m,i}^{(k_m+1)} = ||f(\mathbf{x}_{m,i}^{(k_m+1)}) - f(\mathbf{x}_{m,i}^{(k_m)})||\ \forall i \in [1, \ldots, n_{pop}]$
$\quad$ **for** $q \in [1, \ldots, (n_D+1)^2]$ **do**
$\quad\quad$ **if** $dd_{m,q} < df_{m,i}^{(k_m+1)}$ **then**
$\quad\quad\quad \mathbf{CRF}_{m,q,2}^{(k_m)} \leftarrow F_{m,i}^{(k_m)}$
$\quad\quad\quad dd_{m,q}^{(k_m)} \leftarrow df_{m,i}^{(k_m+1)}$
$\quad\quad\quad$ **if** $df_{m,i}^{(k_m+1)} > CRC$ **then**
$\quad\quad\quad\quad \mathbf{CRF}_{m,q,1}^{(k_m)} \leftarrow CR_{m,i}^{(k_m)}$
$\quad\quad\quad$ **end if**
$\quad\quad$ **end if**
$\quad$ **end for**
end if

The DE stops according to the contraction condition presented in Section 7.2. In order to prevent an excessive use of resources when the population partitions, a fail safe criterion was introduced that stops the DE after $10D$ generations (Algorithm 3, line 13).

7.4.3 Local search and restart mechanisms

After the evolution of all populations has stopped, MP-AIDEA checks if the best individual of each population is inside the basin of attraction of any previously detected local minimum (see Algorithm 1, line 7). If that is not the case, a local search is performed from the best individual and the population is locally restarted within a hypercube with edge equal to $2\delta_{local}$ around

the detected local minimum; otherwise, no local search is performed and the population is restarted globally in the whole search space (Algorithm 1, line 24). Prior to the implementation of the restart mechanisms, MP-AIDEA updates the estimation of the size of the basin of attraction of each minimum, the archive A (see Algorithm 1, lines 5 to 22) and the distribution over the possible values of $2\delta_{local}$ (see Algorithm 1, line 23). In the following the identification of the basin of attraction, the estimation of δ_{local} and the two restart mechanisms are described in more details.

Identification of the basin of attraction

In order to mitigate the possibility of running multiple local searches that converge to already discovered local minima, MP-AIDEA estimates for each local minimum in A the radius of the basin of attraction of that local minimum. The radius of the basin of attraction is here defined as the distance $d_{basin,LM}$ from a given local minimum $\mathbf{x}_{LM}$ such that if the best individual in the population m, $\mathbf{x}_{best,m}$, is at a distance from $\mathbf{x}_{LM}$ lower than $d_{basin,LM}$, a local search starting from $\mathbf{x}_{best,m}$ would converge to $\mathbf{x}_{LM}$.

The radius $d_{basin,LM}$ is estimated with the simple procedure in Algorithm 1, lines 7 to 19. Once the evolution of all populations has stopped, the distance $\|\mathbf{x}_{best,m} - \mathbf{x}_{LM}\|$ of the best individual, in each population, with respect to all the minima in A is calculated and compared to the $d_{basin,LM}$ associated to each local minimum in A; initially all $d_{basin,LM}$ are set to 0. If the distance $\|\mathbf{x}_{best,m} - \mathbf{x}_{LM}\|$ is grater than $d_{basin,LM}$ a local search is started from $\mathbf{x}_{best,m}$. If the resulting local minimum $\mathbf{x}_{min,m}^{(s_m)}$ already belongs to A, the counter i_{LM} is updated and the new estimate of the basin of attraction of $\mathbf{x}_{LM}$ becomes $d_{basin,LM} = \min[d_{basin,LM}, \|\mathbf{x}_{best,m} - \mathbf{x}_{LM}\|]$. $\mathbf{x}_{min,m}^{(s_m)}$ belongs to A if $\exists\ \mathbf{x}_{LM} \in A\ :\ \|\mathbf{x}_{min,m}^{(s_m)} - \mathbf{x}_{LM}\| \leq \varepsilon\Delta$. ε is set to 10^{-3}. If i_{LM} exceeds a given maximum value and $\|\mathbf{x}_{best,m} - \mathbf{x}_{LM}\| < d_{basin,LM}\ \forall\ LM$ no local search and no local restart are performed. The counter i_{LM} is initialised to 1 for every new local minimum and keeps track of the number of times a local minimum is discovered.

Adaptation of δ_{local}

When a population m is locally restarted, individuals are generated by taking a random sample, with Latin Hypercube, within a hypercube with edge equal to $2\delta_{local,m}$. The dimension $\delta_{local,m}$ is drawn from a probability distribution that is progressively updated at every restart. We use a kernel approach with kernels centered in the elements of a vector $\mathbf{B}$ (see Algorithm 6) containing a range of possible values of $\delta_{local,m}$. The vector $\mathbf{B}$ is initialised, with the procedure presented in Algorithm 5, when all populations perform a local search for the first time and at every global restart. During initialisation the distance between all the local minima in the archive A is computed (Algorithm 5, line 1) and $\mathbf{B}$ is initialised with values spanning the interval between the minimum and the mean distance among minima (Algorithm 5, lines 2-3). The mean values instead of the max is used to limit the size of the restart bubble and speed up convergence under the assumption that a local restart needs to lead to the local exploration of the search space. In the experimental tests it will be shown that this working assumption is

generally verified and $\delta_{local,m}$ tends to converge to small values. Then, a second vector $\mathbf{dd}_b$, with the same number of components of $\mathbf{B}$, is initialised to zero (Algorithm 5, line 4).

During the update phase of $\delta_{local,m}$, MP-AIDEA uses the index s_m to keep track of the number of times population m performed a local search and calculates the difference p_m between two subsequent local minima (see Algorithm 6, line 5). The value p_m is then compared to the elements in $\mathbf{dd}_b$ and when $dd_{b,q} < p_m$ then $\delta_{local,m}$ replaces B_q, and p_m replaces $dd_{b,q}$ (Algorithm 6, lines 7-10). In other words, if the $\delta_{local,m}$ used to restart population m led to a local minimum $\mathbf{x}_{min,m}^{(s_m)}$ different from $\mathbf{x}_{min,m}^{(s_m-1)}$, the local minimum previously identified by the same population, the probability of sampling $\delta_{local,m}$ is increased.

Algorithm 5 Initialise $\mathbf{B}$

1: Compute d_{minMIN} and $d_{minMEAN}$
2: Create 1-dimensional regular grid with $(n_D + 1)$ points in the interval $[d_{minMIN}, d_{minMEAN}]$
3: Initialise $\mathbf{B}$ with points of the grid
4: Initialise vector $\mathbf{dd}_b$ associated to $\mathbf{B}$ with element $dd_{b,q} = 0$ for all $q \in [1, \ldots, (n_D + 1)]$

Algorithm 6 Update the distribution of δ_{local}

1: **if** All populations did local search for the 1st time **then**
2: Create vector $\mathbf{B}$ using Algorithm 5
3: **end if**
4: **for** $m \in [1, \ldots, n_{pop}]$ **do**
5: Compute $p_m = ||\mathbf{x}_{min,m}^{(s_m)} - \mathbf{x}_{min,m}^{(s_m-1)}||$
6: **for** $q \in [1, \ldots, n_D + 1]$ **do**
7: **if** $\mathbf{dd}_{b,q} < p_m$ **then**
8: $\mathbf{B}_q \leftarrow \delta_{local,m}$
9: $\mathbf{dd}_{b,q} \leftarrow p_m$
10: **end if**
11: **end for**
12: **end for**
13: Row sort $\mathbf{B}$ according to $\mathbf{dd}_b$ values

Algorithm 7 MP-AIDEA: local and global restart

1: **for** $m \in [1, \ldots, n_{pop}]$ **do**
2: **if** $LR_m = 1$ **then**
3: Sample $\delta_{local,m}$ from the kernel distribution over the values in $\mathbf{B}$
4: L.R.: Initialise population P_m in a hypercube centred in $\mathbf{x}_{min,m}^{(s_m)}$with edge $2\delta_{local,m}$ for all $m \in \{1, \ldots, n_{pop}\}$
5: **else**
6: Cluster local minima in A and compute cluster baricentres $\mathbf{x}_c$
7: G.R.: Initialise population $P_m = \{\mathbf{x}_{m,i} : \ ||\mathbf{x}_{m,i} - \mathbf{x}_c|| > \ \sqrt{n_D}\delta_{global}, \forall i \in \{1, \ldots, N_{pop}\}\}$
8: Initialise vector $\mathbf{B}$ using Algorithm 5
9: **end if**
10: **end for**

Local and global restart

After the identification of the basin of attraction and the update of the value of δ_{local} populations undergo a restart process in which a new population is generated either by sampling a neighborhood of a local minimum (local restart) or by sampling the whole search space (global restart). The two restart procedures are described in Algorithm 7.

The local restart procedure takes the latest identified local minimum $\mathbf{x}_{min,m}^{(s_m)}$ of population m and restart the population with Latin Hypercube sampling in a box centred in $\mathbf{x}_{min,m}^{(s_m)}$ with edge length $2\delta_{local,m}$.

The global restart procedure identifies clusters of local minima with a Fuzzy C-Mean algorithm [22], computes the centre of each cluster and initialises population m so that each individual is at distance at least $\sqrt{n_D}\delta_{global}$ from each of the centres of the clusters (Algorithm 7, lines 6 and 7).

At each local and global restart, the **CRF** matrix is re-initialised while the vector **B** is initialised only after every global restart. The motivation for re-initialising **CRF** at every restart is twofold: on one hand different values of CR and F might be optimal in different parts of the search space, on the other hand convergence to the optimal value of CR and F is not always guaranteed. In search spaces with uniform and homogeneous structures restarting **CRF** and **B** might lead to an overhead on the computational cost, therefore in future implementations the possibility of retaining **CRF** and **B** across the restart process will be tested.

7.4.4 Computational complexity

The computational complexity of MP-AIDEA is defined by the three main sets of operations:

- *Local search.* The local search uses the MATLAB *fmincon* function which implements an SQP scheme with Broyden-Fletcher-Goldfarb-Shanno (BFGS) estimation of the Hessian matrix. Since the matrix is generally dense, its decomposition is $\mathcal{O}(n_D^3)$.

- *Adaptation of* **CR and F**. The adaptation of CR and F for each individual in each population is the other expensive bit of the algorithm and is $\mathcal{O}(n_{pop}N_{pop}n_D^2)$ (see line 2 in Algorithm 1, line 8 in Algorithm 3 and line 3 in Algorithm 4). As a comparison, the computational complexity of the standard DE is $\mathcal{O}\left(N_{pop}\right)$.

- *Restart mechanisms.* The cost of the local restart procedure is limited to the generation of $n_{pop}N_{pop}$ individuals, while the global restart has a cost associated also to clustering, which is $\mathcal{O} = (n_{LM}^2 n_D n_{iter})$ [22], where n_{iter} is the number of iterations for the clustering, and one associated to the verification that the new population is far from the clusters, which is $\mathcal{O}(n_{pop}n_{LM})$ (see line 7 of Algorithm 7).

Overall when $n_{pop}N_{pop} < n_D$ the dominant algorithmic cost is the local search while the adaptation of CR and F becomes more expensive for large and numerous populations. Since in the experimental test cases we will use $n_{pop} = 4$ and $N_{pop} = n_D$ the overall algorithmic complexity remains $\mathcal{O}(n_D^3)$.

7.5 Experimental performance analysis

The effectiveness of MP-AIDEA is tested on a benchmark composed of three test sets. The three test sets are made of functions taken from three past competitions of the Congress on Evolutionary Computation (CEC). 20 functions from CEC 2005 [197], 9 real world problems from CEC 2011 [58] and 22 functions from CEC 2014 [127] are considered, for a total of 51 different problems. The list of functions used in each test set is reported in Tables 7.1, 7.2 and 7.3. They include both academic test functions and real world optimisation problems. Since the interest is in solving the problem defined in Equation 7.1, all functions selected for this benchmark are continuous and differentiable

Four different metrics are used to evaluate MP-AIDEA against the algorithms that participated in the three CEC competitions:

- Metric 1: Best, worst, median, mean and standard deviation of the best result over a given number of independent runs of the algorithm.
- Metric 2: Ranking against the other algorithms using the same ranking approach proposed in the CEC 2011 competition.
- Metric 3: Wilcoxon test. This is used to compare MP-AIDEA to the algorithm participating in the CEC 2011 and CEC 2014 competitions and for which the source code is available online.
- Metric 4: Success rate. This is used to compare MP-AIDEA to the algorithm participating in the CEC 2011 and CEC 2014 competition and for which the source code is available online.

The settings of MP-AIDEA were maintained constant for all problems within a particular test set and were changed going from one test set to another. This is in line with the way all the other algorithms competed.

The ranking of the algorithms participating in every competition was adjusted to account only for their performance on the selected subset of differentiable functions.

It will be shown that all metrics lead to similar conclusions: MP-AIDEA ranks among the first four algorithms, if not first, in all three test sets and for all dimensions. It will be also shown that MP-AIDEA can detect previously undiscovered minima on some particularly difficult functions.

The current implementation of MP-AIDEA can be found open source at `https://github.com/strath-ace/smart-o2c` together with the benchmark of test cases.

7.5.1 Test sets

This section briefly describes each test set, the settings of MP-AIDEA and metric 1 for all test sets.

Table 7.1: Functions of the CEC 2005 test set.

	Unimodal Functions
1	Shifted Sphere Function
2	Shifted Schwefel's Problem
3	Shifted Rotated High Conditioned Elliptic Function
5	Schwefel's Problem with Global Optimum on Bounds
	Multimodal Functions
6	Shifted Rosenbrock's function
7	Shifted Rotated Griewank's Function without Bounds
8	Shifted Rotated Ackley's Function with Global Optimum on Bounds
9	Shifted Rastrigin's Function
10	Shifted Rotated Rastrigin's Function
11	Shifted Rotated Weierstrass Function
12	Schwefel's Problem
13	Expanded Extended Griewank's plus Rosenbrock Function
14	Shifted Rotated Expanded Scaffer's
	Hybrid Composition Functions
15	Hybrid Composition Function
16	Rotated Hybrid Composition Function
18	Rotated Hybrid Composition Function
19	Rotated Hybrid Composition Function with Narrow Basin for the Global Opt.
20	Rotated Hybrid Composition Function with the Global Optimum on the Bounds
21	Rotated Hybrid Composition Function
22	Rotated Hybrid Composition Function with High Condition Number Matrix

Table 7.2: Functions of the CEC 2011 test set.

1	Parameter Estimation for Frequency-Modulated Sound Waves (n_D=6)
2	Lennard-Jones Potential Problem (n_D=30)
3	The Bifunctional Catalyst Blend Optimal Control Problem (n_D=1)
5	Tersoff Potential for model Si(B) (n_D=30)
6	Tersoff Potential for model Si(C) (n_D=30)
7	Spread Spectrum Radar Polyphase Code Design (D=20)
10	Circular Antenna Array Design Problem (n_D=12)
12	Messenger: Spacecraft Trajectory Optimisation Problem (n_D=26)
13	Cassini 2: Spacecraft Trajectory Optimisation Problem (n_D=22)

CEC 2005 test set

Following the rules of the CEC 2005 competition, MP-AIDEA was used to solve the problems in the CEC 2005 test set in dimension $n_D = 10$, 30 and 50, with a maximum number of function evaluation equal to $n_{feval,max} = 10000\ n_D$. The experiments were repeated for a total of $n_{runs} = 25$ independent runs for each function [197]. Functions 4, 17, 24 and 25 of the CEC 2005 competition were not included in the test set because non-differentiable.

The number of populations in MP-AIDEA was set to $n_{pop} = 4$ and the number of individuals in each population was set to $N_{pop} = n_D$. The contraction limit was set to $\bar{\rho} = 0.2$ and the

Table 7.3: Functions of the CEC 2014 test set.

Unimodal Functions	
1	Rotated High Conditioned Elliptic Function
2	Rotated Bent Cigar Function
3	Rotated Discus Function
Multimodal Functions	
4	Shifted and Rotated Rosenbrock's Function
5	Shifted and Rotated Ackley's Function
7	Shifted and Rotated Griewank's Function
8	Shifted Rastrigin's Function
9	Shifted and Rotated Rastrigin's Function
10	Shifted Schwefel's Function
11	Shifted and Rotated Schwefel's Function
13	Shifted and Rotated HappyCat Function
14	Shifted and Rotated HGBat Function
15	Shifted and Rotated Expanded Griewank's plus Rosenbrock's Function
16	Shifted and Rotated Expanded Scaffer's F6 Function
Hybrid Function	
17	Hybrid Function 1
18	Hybrid Function 2
20	Hybrid Function 4
21	Hybrid Function 5
Composition Function	
23	Composition Function 1
24	Composition Function 2
25	Composition Function 3
28	Composition Function 6

global restart distance was set to $\delta_{global} = 0.1$. In line with the metrics presented at the CEC 2005 competition, Tables 7.4 and 7.5 reports the difference, in the objective value, between the result obtained with MP-AIDEA and the known global minimum.

Table 7.6 reports the best objective function error values obtained by all the algorithms participating in the CEC 2005 competition and MP-AIDEA for functions 13 and 16 and $n_D = 10$. According to the CEC 2005 specifications, the accuracy level for the detection of the global minimum is 10^{-2} for these functions. MP-AIDEA is able to identify the global minimum of both functions 13 and 16. Previously only EvLib [15] succeeded in identifying the global minimum of function 13 and no other algorithm participating in the competition managed to find the global minimum of function 16.

CEC 2011 test set

Following the rules of the CEC 2011 competition [58], MP-AIDEA was run for $n_{feval,max} = 150000$ function evaluations on the CEC2011 test set. The experiments were repeated for $n_{runs} = 25$ independent runs. Test functions with equality and inequality constraints were

Table 7.4: Objective functions errors of the CEC 2005 test set in dimension 10D and 30D.

	Best	Worst	Median	Mean	Std
10D					
1	0.00e+00	0.00e+00	0.00e+00	0.00e+00	0.00e+00
2	0.00e+00	1.14e-13	0.00e+00	0.00e+00	4.34e-14
3	0.00e+00	0.00e+00	0.00e+00	0.00e+00	0.00e+00
5	5.60e-06	1.70e-04	6.17e-05	6.59e-05	4.36e-05
6	3.04e-10	2.33e-09	1.80e-09	1.60e-09	6.06e-10
7	4.83e-13	1.48e-02	1.02e-10	1.97e-03	4.21e-03
8	2.00e+01	2.00e+01	2.00e+01	2.00e+01	6.65e-10
9	0.00e+00	9.95e-01	0.00e+00	3.98e-02	1.99e-01
10	0.00e+00	3.98e+00	1.99e+00	1.79e+00	1.04e+00
11	3.29e+00	5.88e+00	5.31e+00	4.71e+00	6.18e-01
12	0.00e+00	1.19e-12	5.68e-14	1.71e-13	2.79e-13
13	9.87e-03	5.31e-01	2.66e-01	2.40e-01	1.58e-01
14	3.32e-01	3.52e+00	2.13e+00	2.11e+00	6.70e-01
15	0.00e+00	4.00e+02	2.84e-14	2.98e+01	8.14e+01
16	0.00e+00	1.15e+02	1.00e+02	9.53e+01	2.25e+01
18	3.00e+02	9.00e+02	8.00e+02	7.18e+02	2.43e+02
19	3.00e+02	9.06e+02	8.00e+02	7.45e+02	2.03e+02
20	3.00e+02	9.38e+02	8.00e+02	6.83e+02	2.46e+02
21	3.00e+02	8.00e+02	3.00e+02	4.20e+02	1.50e+02
22	3.00e+02	8.01e+02	7.54e+02	6.53e+02	2.01e+02
30D					
1	0.00e+00	0.00e+00	0.00e+00	0.00e+00	0.00e+00
2	0.00e+00	2.27e-13	1.14e-13	5.68e-14	6.46e-14
3	0.00e+00	0.00e+00	0.00e+00	0.00e+00	0.00e+00
5	1.81e-01	1.52e+00	4.58e-01	5.13e-01	2.97e-01
6	5.81e-10	4.07e+00	8.25e-03	3.45e-01	8.95e-01
7	4.26e-13	1.79e-11	2.64e-12	4.58e-12	4.86e-12
8	2.00e+01	2.00e+01	2.00e+01	2.00e+01	9.26e-13
9	0.00e+00	5.97e+00	2.21e+00	2.40e+00	1.49e+00
10	1.99e+01	4.78e+01	3.18e+01	3.05e+01	7.16e+00
11	1.57e+01	2.69e+01	2.09e+01	2.12e+01	2.99e+00
12	8.24e-12	5.89e+02	1.05e+01	1.22e+02	2.06e+02
13	8.88e-01	2.66e+00	1.64e+00	1.60e+00	4.44e-01
14	1.10e+01	1.26e+01	1.17e+01	1.17e+01	3.77e-01
15	2.27e+01	4.00e+02	4.00e+02	3.15e+02	1.37e+02
16	4.16e+01	6.85e+01	5.68e+01	5.69e+01	6.99e+00
18	8.00e+02	9.11e+02	9.09e+02	8.87e+02	4.43e+01
19	8.00e+02	9.12e+02	9.06e+02	8.73e+02	5.14e+01
20	8.00e+02	9.13e+02	9.07e+02	8.78e+02	4.99e+01
21	5.00e+02	5.00e+02	5.00e+02	5.00e+02	4.91e-11
22	8.78e+02	9.22e+02	9.10e+02	9.06e+02	1.04e+01

Table 7.5: Objective functions errors of the CEC 2005 test set in dimension 50D.

	Best	Worst	Median	Mean	Std
1	0.00e+00	0.00e+00	0.00e+00	0.00e+00	0.00e+00
2	5.68e-14	5.68e-13	1.14e-13	5.68e-14	1.45e-13
3	0.00e+00	0.00e+00	0.00e+00	0.00e+00	0.00e+00
5	8.28e-01	1.97e+01	2.52e+00	4.25e+00	4.82e+00
6	3.80e-10	3.11e+01	2.58e+01	2.27e+01	8.82e+00
7	6.11e-12	2.25e-07	8.05e-11	1.00e-08	4.50e-08
8	2.00e+01	2.00e+01	2.00e+01	2.00e+01	2.00e-12
9	4.97e+00	1.29e+01	7.96e+00	8.41e+00	2.14e+00
10	5.47e+01	1.01e+02	7.66e+01	7.61e+01	1.17e+01
11	3.62e+01	5.94e+01	4.57e+01	4.64e+01	6.50e+00
12	4.80e+01	9.37e+03	8.07e+02	1.24e+03	1.84e+03
13	2.87e+00	5.00e+00	3.96e+00	3.89e+00	6.35e-01
14	2.04e+01	2.19e+01	2.12e+01	2.12e+01	4.13e-01
15	2.57e+01	4.00e+02	2.88e+02	3.08e+02	1.00e+02
16	5.10e+01	7.65e+01	6.08e+01	6.25e+01	6.96e+00
18	3.04e+02	9.34e+02	9.24e+02	8.65e+02	1.30e+02
19	8.00e+02	9.34e+02	9.25e+02	8.92e+02	5.85e+01
20	3.00e+02	9.65e+02	9.13e+02	8.52e+02	1.32e+02
21	5.00e+02	5.00e+02	5.00e+02	5.00e+02	7.65e-08
22	9.20e+02	9.70e+02	9.48e+02	9.50e+02	1.31e+01

Table 7.6: CEC 2005 best objective function error values for Functions 13 and 16, $n_D = 10$. ([67] © 2015 IEEE)

Algorithm	Function 13	Function 16
BLX-GL50 [83]	3.70e-01	7.20e+01
BLX-MA [143]	3.80e-01	9.00e+01
CoEVO [161]	4.70e-01	1.20e+02
DE (Ronkonnen) [178]	4.60e-01	1.50e+02
DE (Bui) [37]	2.70e-01	1.00e+02
DMS-L-PSO [126]	2.50e-01	5.20e+01
EDA [235]	1.60e+00	1.30e+02
ES [54]	7.90e-01	9.70e+01
EvLiv [15]	9.90e-03	1.20e+02
flexGA [7]	4.20e-02	1.10e+02
G-CMA-ES [9]	4.10e-01	7.90e+01
K-PCX [191]	3.30e-01	8.80e+01
L-CMA-ES [10]	1.90e-01	6.10e+01
L-SaDE [168]	1.20e-01	8.60e+01
SPC-PNX [11]	3.50e-01	9.10e+01
MP-AIDEA	**9.87e-03**	**0.00e+00**

not included in the tests. The number of populations n_{pop} was set to 4 and the number of individuals in each population was set to $N_{pop} = 30$ regardless of the dimensionality of the problem. The contraction limit and the global restart distance were set respectively to $\bar{\rho} = 0.2$ and $\delta_{global} = 0.1$. Table 7.7 reports the best, worst, median, mean objective function found

by MP-AIDEA and the associated standard deviation. The table also reports, in the second column and for each function, the best value found during the competition by the competing algorithms [8, 12, 73, 74, 94, 117, 122, 133, 135, 176, 184, 190, 227]. The reference to the algorithm providing to the best result is given. When more than one algorithm was able to locate the best result, only the winning algorithm of the competition, GA-MPC [74], is reported.

Table 7.7: Objective functions of the CEC 2011 test set.

	Other alg.	MPAIDEA				
	Best	Best	Worst	Median	Mean	Std
1	0 [74]	9.30e-19	1.09e+01	6.67e-15	8.44e-01	2.92e+00
2	-2.84e+01 [74]	-2.84e+01	-2.71e+01	-2.76e+01	-2.79e+01	4.74e-01
3	1.15e-05 [74]	1.15e-05	1.15e-05	1.15e-05	1.15e-05	5.83e-17
5	-3.69e+01 [190]	-3.68e+01	-3.45e+01	-3.60e+01	-3.61e+01	7.40e-01
6	-3.68e+01 [176]	-2.92e+01	-2.30e+01	-2.74e+01	-2.72e+01	2.32e+00
7	5.00e-01 [74]	5.00e-01	7.13e-01	5.00e-01	5.31e-01	5.30e-02
10	-2.18e+01 [74]	-2.18e+01	-2.14e+01	-2.16e+01	-2.16e+01	1.42e-01
12	6.78e+00 [94]	6.88e+00	1.51e+01	1.22e+01	1.15e+01	2.53e+00
13	8.39e+00 [74]	8.71e+00	1.98e+01	1.43e+01	1.34e+01	3.10e+00

CEC 2014 test set

In line with the rules of the CEC 2014 competition [127], MP-AIDEA was applied to the solution of the functions in the CEC 2014 test set in dimension $n_D = 10$, 30, 50 and 100, with maximum number of function evaluations $n_{feval,max} = 10000 n_D$. The experiments were repeated for $n_{runs} = 51$ independent runs. Non-differentiable functions 6, 12, 19, 22, 26, 27, 29 and 30 were not included in the test set (see Table 7.3). The number of populations was set to $n_{pop} = 4$ and the number of individuals in each population was set to $N_{pop} = n_D$. The contraction limit and the global restart distance were set respectively to $\bar{\rho} = 0.2$ and $\delta_{global} = 0.1$. Tables 7.8 and 7.9 report the difference between the objective value found by MP-AIDEA and the known global minimum. In agreement with the guidelines of the competition error values smaller than 10^{-8} are reported as zero [127]. Table 7.10 reports the best objective function errors values obtained by all the algorithms participating in the competition and MP-AIDEA for functions 9, 10, 11 and 15 in 10 dimensions. MP-AIDEA finds the global minimum of function 11, unlike all the other competing algorithms, and gives good results for the other functions.

7.5.2 Ranking

In this section MP-AIDEA is ranked against a group of algorithms participating in each CEC competition. The rankings include those algorithms that reported their results in a paper and MP-AIDEA with two different settings:

- $n_{pop} = 4$ and $N_{pop} = n_D$. This settings will be indicated as "MP-AIDEA" in the following and corresponds to the settings that was used to generate the results in Section 7.5.1.

Table 7.8: Objective functions errors of the CEC 2014 test set in dimension 10D and 30D.

	Best	Worst	Median	Mean	Std
10D					
1	0.00e+00	0.00e+00	0.00e+00	0.00e+00	0.00e+00
2	0.00e+00	0.00e+00	0.00e+00	0.00e+00	0.00e+00
3	0.00e+00	0.00e+00	0.00e+00	0.00e+00	0.00e+00
4	0.00e+00	4.34e+00	0.00e+00	8.50e-02	6.07e-01
5	2.85e-06	2.00e+01	1.31e-05	1.84e+00	5.38e+00
7	0.00e+00	1.23e-02	0.00e+00	2.51e-03	4.02e-03
8	0.00e+00	9.95e-01	0.00e+00	1.37e-01	3.46e-01
9	0.00e+00	3.98e+00	1.99e+00	1.87e+00	9.26e-01
10	0.00e+00	1.19e+02	1.87e-01	9.33e+00	2.79e+01
11	0.00e+00	2.95e+02	3.67e+01	8.82e+01	8.69e+01
13	3.83e-02	1.09e-01	6.52e-02	6.98e-02	1.69e-02
14	1.06e-02	6.40e-02	2.23e-02	2.48e-02	1.03e-02
15	1.97e-02	4.54e-01	3.25e-01	3.10e-01	9.14e-02
16	2.07e-01	2.53e+00	1.42e+00	1.38e+00	5.15e-01
17	0.00e+00	1.43e+02	6.18e+00	2.85e+01	4.53e+01
18	4.90e-03	3.05e+00	6.56e-02	4.29e-01	6.15e-01
20	5.85e-03	2.89e+00	2.23e-01	4.67e-01	5.69e-01
21	1.44e-02	5.87e+01	4.97e-01	4.09e+00	1.39e+01
23	3.29e+02	3.29e+02	3.29e+02	3.29e+02	3.05e-12
24	1.00e+02	1.11e+02	1.06e+02	1.05e+02	3.61e+00
25	1.00e+02	1.19e+02	1.00e+02	1.03e+02	5.07e+00
28	1.01e+02	4.81e+02	3.57e+02	3.47e+02	6.58e+01
30D					
1	0.00e+00	0.00e+00	0.00e+00	0.00e+00	6.88e-14
2	0.00e+00	0.00e+00	0.00e+00	0.00e+00	4.16e-13
3	0.00e+00	0.00e+00	0.00e+00	0.00e+00	2.13e-14
4	0.00e+00	0.00e+00	0.00e+00	0.00e+00	3.64e-13
5	2.00e+01	2.00e+01	2.00e+01	2.00e+01	3.19e-04
7	0.00e+00	0.00e+00	0.00e+00	0.00e+00	1.59e-13
8	0.00e+00	3.98e+00	1.99e+00	2.24e+00	1.14e+00
9	1.09e+01	3.28e+01	2.19e+01	2.26e+01	5.54e+00
10	3.69e+00	1.25e+02	1.07e+01	1.83e+01	3.09e+01
11	6.94e+02	2.34e+03	1.55e+03	1.56e+03	3.70e+02
13	1.25e-01	2.56e-01	1.91e-01	1.91e-01	3.23e-02
14	1.06e-01	2.19e-01	1.47e-01	1.54e-01	2.23e-02
15	1.36e+00	2.98e+00	2.00e+00	2.05e+00	4.06e-01
16	8.40e+00	1.12e+01	1.00e+01	1.00e+01	6.53e-01
17	1.56e+02	9.22e+02	5.21e+02	5.13e+02	1.79e+02
18	1.23e+01	4.70e+01	2.63e+01	2.73e+01	9.35e+00
20	4.29e+00	2.85e+01	1.56e+01	1.57e+01	5.78e+00
21	7.57e+00	5.36e+02	2.38e+02	2.31e+02	9.89e+01
23	3.15e+02	3.15e+02	3.15e+02	3.15e+02	1.35e-10
24	2.00e+02	2.26e+02	2.22e+02	2.19e+02	8.81e+00
25	2.00e+02	2.04e+02	2.03e+02	2.03e+02	6.52e-01
28	6.31e+02	8.56e+02	7.93e+02	7.74e+02	6.20e+01

Table 7.9: Objective functions errors of the CEC 2014 test set in dimension 50D and 100D.

	Best	Worst	Median	Mean	Std
50D					
1	0.00e+00	0.00e+00	0.00e+00	0.00e+00	0.00e+00
2	0.00e+00	0.00e+00	0.00e+00	0.00e+00	0.00e+00
3	0.00e+00	0.00e+00	0.00e+00	0.00e+00	0.00e+00
4	0.00e+00	0.00e+00	0.00e+00	0.00e+00	0.00e+00
5	2.00e+01	2.00e+01	2.00e+01	2.00e+01	2.40e-05
7	0.00e+00	0.00e+00	0.00e+00	0.00e+00	6.58e-13
8	2.98e+00	1.09e+01	7.96e+00	7.67e+00	1.84e+00
9	3.68e+01	8.76e+01	5.77e+01	5.83e+01	1.06e+01
10	6.58e+00	2.49e+02	1.75e+01	5.22e+01	6.41e+01
11	2.21e+03	4.86e+03	3.96e+03	3.85e+03	5.21e+02
13	2.07e-01	3.83e-01	3.01e-01	3.08e-01	4.51e-02
14	1.68e-01	2.68e-01	2.32e-01	2.32e-01	2.48e-02
15	3.38e+00	6.31e+00	4.94e+00	4.93e+00	6.68e-01
16	1.78e+01	2.07e+01	1.91e+01	1.91e+01	6.20e-01
17	5.72e+02	1.70e+03	1.07e+03	1.05e+03	2.65e+02
18	4.12e+01	1.40e+02	7.31e+01	7.04e+01	2.07e+01
20	5.10e+01	1.88e+02	9.97e+01	1.02e+02	2.84e+01
21	3.71e+02	1.07e+03	7.79e+02	7.63e+02	1.53e+02
23	3.44e+02	3.44e+02	3.44e+02	3.44e+02	9.45e-08
24	2.52e+02	2.71e+02	2.54e+02	2.56e+02	3.89e+00
25	2.00e+02	2.10e+02	2.07e+02	2.07e+02	1.51e+00
28	1.02e+03	1.25e+03	1.16e+03	1.15e+03	5.45e+01
100D					
1	0.00e+00	0.00e+00	0.00e+00	0.00e+00	0.00e+00
2	0.00e+00	0.00e+00	0.00e+00	0.00e+00	0.00e+00
3	0.00e+00	0.00e+00	0.00e+00	0.00e+00	3.75e-12
4	0.00e+00	3.99e+00	9.32e-12	3.13e-01	1.08e+00
5	2.00e+01	2.00e+01	2.00e+01	2.00e+01	6.35e-06
7	0.00e+00	0.00e+00	0.00e+00	0.00e+00	0.00e+00
8	1.59e+01	4.28e+01	3.08e+01	2.98e+01	5.26e+00
9	1.44e+02	2.10e+02	1.78e+02	1.76e+02	1.83e+01
10	1.29e+02	1.08e+03	4.92e+02	5.24e+02	2.34e+02
11	8.36e+03	1.13e+04	9.92e+03	9.91e+03	6.78e+02
13	3.12e-01	5.14e-01	4.44e-01	4.37e-01	4.11e-02
14	2.58e-01	3.56e-01	3.01e-01	3.04e-01	2.19e-02
15	1.02e+01	2.27e+01	1.63e+01	1.63e+01	2.41e+00
16	3.92e+01	4.35e+01	4.17e+01	4.17e+01	7.96e-01
17	2.09e+03	3.69e+03	2.73e+03	2.78e+03	4.29e+02
18	1.57e+02	2.63e+02	2.09e+02	2.10e+02	3.09e+01
20	2.67e+02	5.98e+02	4.25e+02	4.21e+02	8.30e+01
21	8.88e+02	2.15e+03	1.51e+03	1.53e+03	3.00e+02
23	3.48e+02	3.48e+02	3.48e+02	3.48e+02	1.39e-03
24	3.63e+02	3.80e+02	3.69e+02	3.70e+02	3.25e+00
25	2.00e+02	2.54e+02	2.00e+02	2.14e+02	1.99e+01
28	1.70e+03	2.46e+03	2.23e+03	2.15e+03	2.11e+02

Table 7.10: CEC 2014 best objective function error values for Functions 9, 10, 11 and 15, $n_D = 10$. ([67] © 2015 IEEE)

Algorithm	Func. 9	Func. 10	Func. 11	Func. 15
b3e3pbest [38]	2.60e+00	0.00e+00	9.50e+01	5.70e-01
CMLSP [43]	0.00e+00	2.50e-01	3.60e+00	4.50e-01
DE-b6e6rl [159]	2.50e+00	0.00e+00	3.60e+01	4.90e-01
FCDE [125]	8.00e+00	3.10e-01	1.40e+02	6.50e-01
FERDE [170]	3.00e+00	0.00e+00	3.80e-01	3.50e-01
FWA-DM [234]	2.00e+00	9.10e-13	4.00e+01	3.20e-01
GaAPADE [134]	1.90e+00	2.40e-02	2.40e+00	3.80e-01
L-SHADE [198]	2.20e-03	0.00e+00	3.90e-01	2.10e-01
MVMO [77]	9.90e-01	6.20e-02	3.40e+00	2.10e-01
NRGA [233]	9.90e-01	3.70e+00	1.90e+01	3.70e-01
OptBees [70]	2.00e+00	3.50e+00	1.30e+02	6.30e-01
POBL-ADE [101]	1.00e+00	2.20e+01	3.60e+00	1.70e-01
rmalschma [144]	9.90e-01	6.20e-02	1.90e-01	3.10e-01
RSDE [229]	2.00e+00	3.50e+00	1.90e+01	3.60e-01
SOO [162]	9.00e+00	1.30e+02	3.50e+02	4.40e-01
SOO-BOBYQA [162]	9.00e+00	1.30e+02	3.50e+02	4.20e-01
UMOEAs [75]	9.90e-01	6.20e-02	3.50e+00	3.20e-01
MP-AIDEA	**0.00e+00**	**0.00e+00**	**0.00e+00**	**1.97e-02**

- $n_{pop} = 1$, $N_{pop} = 4n_D$; MP-AIDEA adapts CR and F but uses fixed values for δ_{local} and n_{LR}. In particular, $n_{LR} = 10$ and δ_{local} = 0.1, unless otherwise specified. This settings will be indicated as "MP-AIDEA, $n_{pop} = 1$" in the following.

The ranking method follows the rules of the CEC 2011 competition [196]. All algorithms are ranked on the basis of the best and mean values of the objective function obtained over a certain number of runs. The following procedure is used to obtain the ranking:

- for each function, algorithms are ranked according to the best objective value;
- for each function, algorithms are ranked according to the mean objective value;
- the ranking for the best and mean objective values of a particular algorithm are added up over all the problems to get the absolute ranking.

In the following the rankings obtained for the CEC 2005, CEC 2011 and CEC 2014 test sets are presented.

CEC 2005 test set

The rankings obtained for $n_D = 10$, $n_D = 30$ and $n_D = 50$ are reported in Table 7.11. Only the competing algorithms that reported in their paper also the results obtained for the hybrid functions of the CEC 2005 competition (Table 7.1) are considered. Results show that, for $n_D = 10$ and $n_D = 30$, MP-AIDEA with adaptation of δ_{local} and n_{LR} is ranked first, while for $n_D = 50$ results are better when using MP-AIDEA with non-adapted $\delta_{local} = 0.1$ and $n_{LR} = 10$. In any case, both settings outperform the winning algorithm of the competition CEC 2005.

Table 7.11: CEC 2005 algorithms ranking. ([67] © 2015 IEEE)

Rank	$n_D = 10$	$n_D = 30$	$n_D = 50$
1	**MP-AIDEA**	**MP-AIDEA**	**MP-AIDEA**, $n_{pop} = 1$
2	**MP-AIDEA**, $n_{pop} = 1$	**MP-AIDEA**, $n_{pop} = 1$	**MP-AIDEA**
3	G-CMA-ES [9]	G-CMA-ES	G-CMA-ES
4	L-SaDE [168]	L-CMA-ES	L-CMA-ES
5	DMS-L-PSO [126]	K-PCX	flexGA
6	L-CMA-ES [10]	BLX-GL50	
7	BLX-GL50 [83]	SPC-PNX	
8	DE (Ronkonnen) [178]	DE (Ronkonnen)	
9	SPC-PNX [11]	DE (Bui)	
10	EvLiv [15]	flexGA	
11	EDA [235]	CoEVO	
12	K-PCX [191]	EDA	
13	BLX-MA [143]		
14	DE (Bui) [37]		
15	CoEVO [161]		
16	flexGA [7]		
17	ES [54]		

CEC 2011 test set

The results obtained on the CEC 2011 test set are reported in Table 7.12. MP-AIDEA ranks first if problem 13 (the Cassini 2 Spacecraft Trajectory Optimisation Problem) is excluded from the test set and second if it is included. The reason for this can be found in Figure 7.2. Figure 7.2 shows the convergence profile of the best solutions found by MP-AIDEA and GA-MPC, the winning algorithm of the competition, on function 13 for an increasing number of function evaluations (greater than the limit prescribed by the CEC 2011 competition). The results for GA-MPC are obtained using the code available online[1].

On this test problem, GA-MPC converges very rapidly to a local minimum but then stagnates. On the contrary, MP-AIDEA has a slower convergence for the first 200,000 function evaluations but then progressively finds better and better minima as the number of function evaluations increases. This demonstrates that in a realistic scenario in which function evaluations are not arbitrarily limited, MP-AIDEA would provide better results than the algorithm that won the competition.

Results in Table 7.12 shows that MP-AIDEA with adaptation of δ_{local} and n_{LR} performs better than MP-AIDEA with fixed values of δ_{local} and n_{LR}. The adaptation history of δ_{local} is shown in Figure 7.3 for each of the four populations on test functions 12 and 13 and for 600,000 function evaluations.

[1] http://www3.ntu.edu.sg/home/epnsugan/index_files/CEC11-RWP/CEC11-RWP.htm

Table 7.12: CEC 2011 algorithms ranking. ([67] © 2015 IEEE)

Rank	with Function 13	without Function 13
1	GA-MPC [74]	**MP-AIDEA**
3	**MP-AIDEA**	GA-MPC
4	SAMODE [73]	EA-DE-MA
5	EA-DE-MA [190]	SAMODE
6	WI-DE [94]	WI-DE
7	Adap. DE 171 [8]	**MP-AIDEA**, $n_{pop} = 1$
8	**MP-AIDEA**, $n_{pop} = 1$	ED-DE
10	DE-Λ [176]	DE-Λ
11	ED-DE [227]	Adapt. DE 171
12	DE-RHC [122]	DE-RHC
13	RGA [184]	RGA
14	Mod-DE-LS [135]	Mod-DE-LS
15	mSBX-GA [12]	mSBX-GA
16	ENSML-DE [133]	CDASA
17	CDASA [117]	ENSML-DE

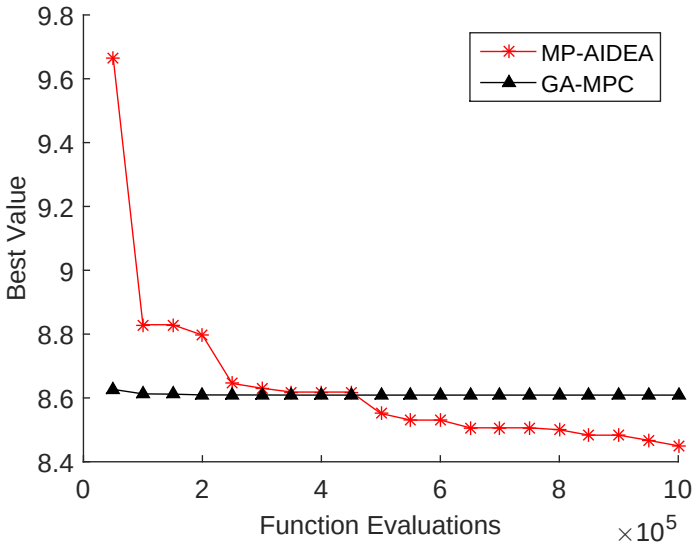

Figure 7.2: Best values of MP-AIDEA and GA-MPC for Function 13, CEC2011. ([67] © 2015 IEEE)

CEC 2014 test set

The ranking results for the CEC 2014 test set are reported in Table 7.13. MP-AIDEA with one population is tested in this case with both $\delta_{local} = 0.1$ and $\delta_{local} = 0.3$. For $n_D = 10$ the results of MP-AIDEA with adaptation of δ_{local} and n_{LR} are better than those of MP-AIDEA with fixed values of δ_{local} and n_{LR}, for both $\delta_{local} = 0.1$ and $\delta_{local} = 0.3$. In the other cases MP-AIDEA with fixed values of δ_{local} and n_{LR} outperforms MP-AIDEA with adaptation of δ_{local} and n_{LR} when $\delta_{local} = 0.1$ but not when $\delta_{local} = 0.3$. These results show the strong influence

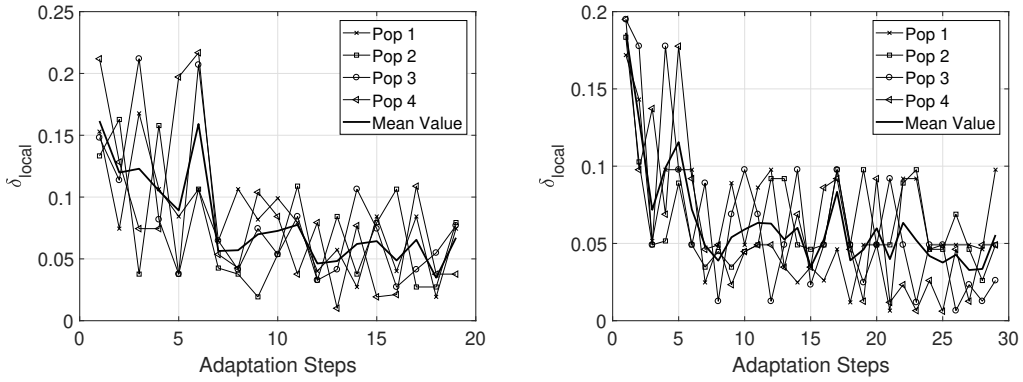

Figure 7.3: δ_{local} for the four populations of MP-AIDEA for Functions 12 (left) and 13 (right), CEC 2011.

of this parameter on the results obtained by MP-AIDEA. The adaptation history of δ_{local} for test functions 9, 17 and 25 at $n_D = 30$ and 300,000 functions evaluations is shown in Figure 7.4.

These figures show how the adaptation of δ_{local} is effective when a sufficient number of adaptation steps can be performed within the limit of the maximum number of function evaluation (300,000 in this case). For function 25, for example, the adaptation steps are only 7, while they are 11 for function 17 and 18 for function 9. In these two cases δ_{local} converges to 0.1 and 0.04, respectively.

The performance of MP-AIDEA for the 30D functions of the CEC 2014 test set is further investigated to test the dependence of the results upon the two non-adapted parameters, $\bar{\rho}$ and δ_{global}. Table 7.14 shows the raking obtained when varying $\bar{\rho}$ and δ_{global}.

Case B of Table 7.14 shows the ranking obtained when using $\bar{\rho} = 0.3$ instead than $\bar{\rho} = 0.2$. Comparing the results in Table 7.14 with those in Table 7.13 it is possible to see that MP-AIDEA performs better using $\bar{\rho} = 0.3$ rather than $\bar{\rho} = 0.2$, moving from the fourth to the third position in the ranking. At the same time there is no significant dependence upon the value of δ_{global}, as shown by Cases C and D in Table 7.14, where δ_{global} is changed from its nominal value of 0.1 to 0.2 and 0.3.

7.5.3 Wilcoxon test

The Wilcoxon rank sum test is a nonparametric test for two populations when samples are independent. In this case the two populations of samples are, for each problem, the n_{runs} values of the objective function obtained by MP-AIDEA and by another algorithms participating in the CEC 2011 and CEC 2014 competitions. No test is performed for the CEC2005 test set, since for no one of the algorithms participating in the CEC 2005 competition the code is available online.

The Wilcoxon test is realised using the MATLAB function *ranksum*. *ranksum* tests the null hypothesis that data from two entries z_1 and z_2 are samples from continuous distributions with equal medians. Results from *ranksum* are presented in the following as values of p and

Table 7.13: CEC 2014 algorithms ranking. ([67] © 2015 IEEE)

Rank	$n_D = 10$	$n_D = 30$
1	UMOEAs [75]	L-SHADE
2	**MP-AIDEA**	UMOEAs
3	L-SHADE [198]	GaPADE
4	MVMO [77]	**MP-AIDEA** $n_{pop} = 1, \delta_{local} = 0.1$
5	**MP-AIDEA,** $n_{pop} = 1, \delta_{local} = 0.1$	**MP-AIDEA**
6	DE-b6e6rl [159]	CMLSP
7	rmalschma [144]	**MP-AIDEA** $n_{pop} = 1, \delta_{local} = 0.3$
8	**MP-AIDEA,** $n_{pop} = 1, \delta_{local} = 0.3$	rmalshcma
9	GaAPADE [134]	MVMO
10	FERDE [170]	DE-b6e6rl
11	CMLSP [43]	b3e3pbest
12	b3e3pbest [38]	FERDE
13	RSDE [229]	RSDE
14	FWA-DE [234]	FWA-DE
15	POBL-ADE [101]	POBL-ADE
16	OptBees [70]	OptBees
17	SOO-BOBYQA [162]	SOO-BOBYQA
18	FCDE [125]	NRGA
19	NRGA [233]	FCDE
20	SOO [162]	SOO

Rank	$n_D = 50$	$n_D = 100$
1	**MP-AIDEA** $n_{pop} = 1, \delta_{local} = 0.1$	**MP-AIDEA** $n_{pop} = 1, \delta_{local} = 0.1$
2	UMOEAs	UMOEAs
3	MVMO	L-SHADE
4	**MP-AIDEA**	**MP-AIDEA**
5	L-SHADE	rmalshcma
6	**MP-AIDEA** $n_{pop} = 1, \delta_{local} = 0.3$	**MP-AIDEA** $n_{pop} = 1, \delta_{local} = 0.3$
7	rmalshcma	POBL-ADE
8	b3e3pbest	b3e3pbest
9	FERDE	OptBees
10	DE-b6e6rl	DE-b6e6rl
11	RSDE	RSDE
12	POBL-ADE	FWA-DE
13	OptBees	
14	FWA-DE	
15	SOO	

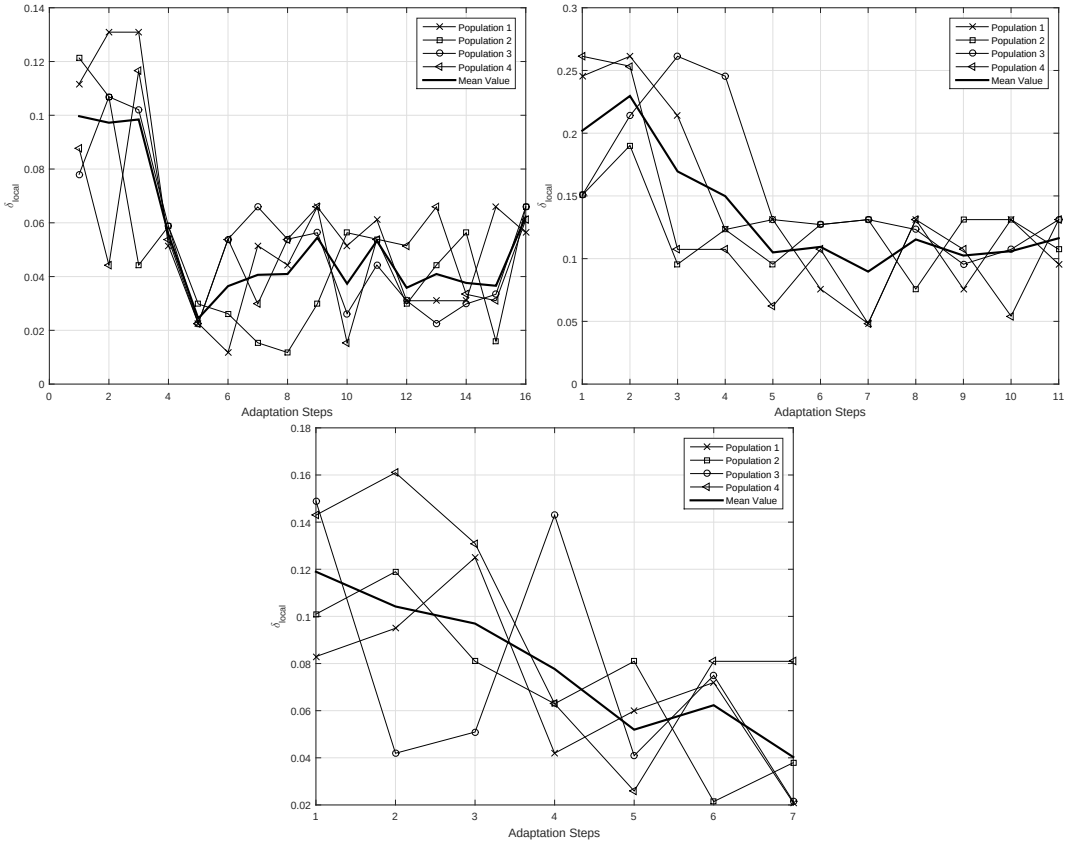

Figure 7.4: δ_{local} for the four populations of MP-AIDEA for Functions 9 (top left), 17 (top right) and 25 (bottom), $n_D = 30$, CEC 2014.

h. p, ranging from 0 to 1, is the probability of observing a test statistic as or more extreme than the observed value under the null hypothesis. h is a logical value, where $h = 1$ indicates rejection of the null hypothesis at the $100\alpha\%$ significance level while $h = 0$ indicates a failure to reject the null hypothesis at the $100\alpha\%$ significance level, where α is 0.05. When $h = 1$, the null hypothesis that distributions z_1 and z_2 have equal medians is rejected, and additional test are conducted to assess which one of the two distributions has lower median. In order to do so, three types of tests are realised using *ranksum* for the two distributions z_1 and z_2:

- Two-sided hypothesis test: the alternative hypothesis states that z_1 and z_2 have different medians. Two distributions with equal medians will give as results $p_B = 1$ and $h_B = 0$ (failure to reject the null hypothesis that z_1 and z_2 have equal medians), while two distributions with different medians will give as results $p_B = 0$ and $h_B = 1$ (rejection of the null hypothesis that z_1 and z_2 have equal medians). If the two-sided hypothesis test finds that the two distributions have equal medians ($p_B = 1$ and $h_B = 0$), no further test is conducted. Otherwise the left-tailed and right-tailed hypothesis test are conducted.

- Left-tailed hypothesis test: the alternative hypothesis states that the median of z_1 is lower than the median of z_2. If z_1 has median greater than the median of z_2, results will be

Table 7.14: CEC 2014 algorithms ranking, 30D, $\bar{\rho} = 0.1$ and $\bar{\rho} = 0.3$. ([67] © 2015 IEEE)

	Case A	Case B	Case C	Case D
Rank	$\bar{\rho} = 0.1$ $\delta_{global} = 0.1$	$\bar{\rho} = 0.3$ $\delta_{global} = 0.1$	$\bar{\rho} = 0.2$ $\delta_{global} = 0.2$	$\bar{\rho} = 0.2$ $\delta_{global} = 0.3$
1	L-SHADE	L-SHADE	L-SHADE	L-SHADE
2	UMOEAs	UMOEAs	UMOEAs	UMOEAs
3	GaAPADE	**MP-AIDEA**	GaAPADE	GaAPADE
4	**MP-AIDEA**	GaAPADE	**MP-AIDEA**	**MP-AIDEA**
5	CMLSP	CMLSP	CMLSP	CMLSP
6	rmalshcma	rmalschma	rmalshcma	rmalshcma
7	MVMO	MVMO	MVMO	MVMO
8	DE-b6e6rl	DE-b6e6rl	DE-b6e6rl	DE-b6e6rl
9	b3e3pbest	b3e3pbest	b3e3pbest	b3e3pbest
10	FERDE	FERDE	FERDE	FERDE
11	RSDE	RSDE	RSDE	RSDE
12	FWA-DE	FWA-DE	FWA-DE	FWA-DE
13	POBL-ADE	POBL-ADE	POBL-ADE	POBL-ADE
14	OptBees	OptBees	OptBees	OptBees
15	SOO-BOBYQA	SOO-BOBYQA	SOO-BOBYQA	SOO-BOBYQA
16	NRGA	NRGA	NRGA	NRGA
17	FCDE	FCDE	FCDE	FCDE
18	SOO	SOO	SOO	SOO

$p_L = 1$ and $h_L = 0$ (failure to reject the hypothesis that z_1 has median greater than z_2) while if z_1 has median lower than z_2 results will be $p_L = 0$ and $h_L = 1$ (rejection of the hypothesis that z_1 has median greater than z_2).

- Right-tailed hypothesis test: the alternative hypothesis states that the median of z_1 is greater than the median of z_2. If z_1 has median lower than the median of z_2, results will be $p_R = 1$ and $h_R = 0$ (failure to reject the hypothesis that z_1 has median lower than z_2) while if z_1 has median greater than z_2 results will be $p_R = 0$ and $h_R = 1$ (rejection of the hypothesis that z_1 has median lower than z_2).

If z_1 is the distribution of results of MP-AIDEA and z_2 the distribution of results given by another algorithm, the possible results obtained from the *ranksum* tests are summarised in Table 7.15.

Table 7.15: Wilcoxon test: possible outcomes.

MATLAB *ranksum* option	both		left		right	
	h_B	p_B	h_L	p_L	h_R	p_R
Case 1: equal medians	0	1	-	-	-	-
Case 2: median of MP-AIDEA is greater	1	0	0	1	1	0
Case 3: median of MP-AIDEA is lower	1	0	1	0	0	1

Case 1 in Table 7.15 ($h_B = 0$) represents a situation in which the distribution of results from

MP-AIDEA and a competing algorithm have equal median (failure to reject the hypothesis that z_1 has median lower than z_2). Case 2 (h_B=1, h_L=0 and h_R=1) represents a situation in which the median of MP-AIDEA is greater than the median of the other algorithm (rejection of the null hypothesis that z_1 and z_2 have equal medians, failure to reject the hypothesis that z_1 has median greater than z_2, rejection of the hypothesis that z_1 has median lower than z_2). Case 3 (h_B=1, h_L=1 and h_R=0) represents instead a situation in which the median of MP-AIDEA is lower than the median of the other algorithm (rejection of the null hypothesis that z_1 and z_2 have equal medians, rejection of the hypothesis that z_1 has median greater than z_2, failure to reject the hypothesis that z_1 has median lower than z_2). In the following, test functions with results corresponding to cases 1 and 3 are shown in bold (MP-AIDEA has median equal or lower than the competing algorithm). For case 3 results with $p_B < 5 \cdot 10^{-2}$, $p_L < 5 \cdot 10^{-2}$ and $p_R > 9.5 \cdot 10^{-1}$ are considered significant. Analogously, the competing algorithm has median lower than MP-AIDEA if $p_B < 5 \cdot 10^{-2}$, $p_L > 9.5 \cdot 10^{-1}$ and $p_R < 5 \cdot 10^{-2}$.

CEC 2011 test set

For the CEC 2011 test set the comparison is limited against the two top algorithms, GA-MPC and DE-Λ, for which the code is available online [1, 2]. The outcome of the Wilcoxon test for the comparison of MP-AIDEA against GA-MPC, the winning algorithm of the CEC2011 competition, can be found in Table 7.16 for all the functions in the test set in Table 7.2.

Table 7.16: Outcome of the Wilcoxon test on the CEC 2011 test set: MP-AIDEA vs. GA-MPC.

	both		left		right		
Func.	h	p	h	p	h	p	Result type (Table 7.15)
1	1	1.28e-04	0	1.00e+00	1	6.40e-05	Case 2
2	**1**	**1.43e-04**	**1**	**7.14e-05**	**0**	**1.00e+00**	**Case 3**
3	1	1.10e-05	0	1.00e+00	1	5.49e-06	Case 2
5	**1**	**5.12e-06**	**1**	**2.56e-06**	**0**	**1.00e+00**	**Case 3**
6	**1**	**4.78e-02**	**1**	**2.39e-02**	**0**	**9.77e-01**	**Case 3**
7	**1**	**3.01e-09**	**1**	**1.50e-09**	**0**	**1.00e+00**	**Case 3**
10	0	3.62e-01	0	8.24e-01	0	1.81e-01	Not significant
12	0	4.85e-01	0	2.42e-01	0	7.64e-01	Not significant
13	1	4.61e-03	0	9.98e-01	1	2.31e-03	Case 2

The comparison of MP-AIDEA with GA-MPC shows that the median of MP-AIDEA is lower than the median of GA-MPC (Case 3) for functions 2, 5, 6 and 7, while it is higher (Case 2) for functions 1, 3 and 13. Results for functions 10 and 12 are not significant enough to obtain a clear indication.

The outcome of the Wilcoxon test for the comparison of MP-AIDEA with DE-Λ is reported in Table 7.17.

The comparison of MP-AIDEA with DE-Λ (Table 7.17) shows that the median of MP-AIDEA is lower than the median of DE-Λ for functions 3, 5, 6, 10, 12 and 13. Results for the remaining functions 1, 2 and 7 are not significant enough to obtain a clear indication.

Table 7.17: Outcome of the Wilcoxon test on the CEC 2011 test set: MP-AIDEA vs. DE-Λ.

	both		left		right		
Func	h	p	h	p	h	p	Result type (Table 7.15)
1	0	7.58e-02	0	9.64e-01	1	3.79e-02	Not significant
2	0	4.72e-01	0	2.36e-01	0	7.70e-01	Not significant
3	**1**	**9.73e-11**	**1**	**4.86e-11**	**0**	**1.00e+00**	**Case 3**
5	**1**	**8.52e-08**	**1**	**4.26e-08**	**0**	**1.00e+00**	**Case 3**
6	**1**	**1.41e-09**	**1**	**7.07e-10**	**0**	**1.00e+00**	**Case 3**
7	0	5.05e-02	1	2.52e-02	0	9.76e-01	Not significant
10	**1**	**1.18e-07**	**1**	**5.89e-08**	**0**	**1.00e+00**	**Case 3**
12	**1**	**2.57e-09**	**1**	**1.29e-09**	**0**	**1.00e+00**	**Case 3**
13	**1**	**2.04e-03**	**1**	**1.02e-03**	**0**	**9.99e-01**	**Case 3**

Table 7.18 summarises the outcome of the Wilcoxon tests for the CEC 2011 test set. The table reports the number of functions for which the median of MP-AIDEA is lower, equal or higher than the median of the competing algorithm. The results in Table 7.18 show that MP-AIDEA clearly outperforms DE-Λ and has median lower than GA-MPC for 4 test functions.

Table 7.18: Summary of Wilcoxon Test Results, CEC 2011 test set: MP-AIDEA vs. GA-MPC and DE-Λ. The table reports the number of functions for which the median of MP-AIDEA is equal (Case 1), higher (Case 2) or lower (Case 3) than the median of the competing algorithm.

	GA-MPC	DE-Λ
Case 1: equal medians	0	0
Case 2: median of MP-AIDEA is greater	3	0
Case 3: median of MP-AIDEA is lower	4	6
Not significant	2	3

CEC 2014 test set

Codes for the algorithms UMOEAs, CLMSP, L-SHADE and MVMO are avilable online [3]. Wilcoxon test results for the comparison of MP-AIDEA with these algorithms at 10, 30, 50 and 100 dimensions are reported in Appendix F.

A summary of the results is given in Table 7.19. Table 7.19 shows the number of function for which Case 1, 2 or 3 in Table 7.15 are verified and the number of functions for which the results are not significant enough to judge, for n_D equal to 10, 30, 50 and 100.

For $n_D = 10$, the median of MP-AIDEA is lower than the one of UMOEAs in 11 cases, while in 3 cases the medians are equal and in 4 cases the median of UMOEAs is lower than the median of MP-AIDEA. In 4 cases (functions 10, 17, 20 and 21) the results are not significant enough to judge. For $n_D = 30$ and $n_D = 100$ the median of MP-AIDEA is lower than the median of UMOEAs in 9 cases and the median of UMOEAs is lower than the one of MP-AIDEA for other 9 functions. For 4 functions the results are not significant enough to obtain a clear indication. The median of MP-AIDEA is lower than the one of UMOEAs in 11 cases for

Table 7.19: Summary of Wilcoxon test results, CEC 2014. The table reports the number of functions for which the median of MP-AIDEA is equal (Case 1), higher (Case 2) or lower (Case 3) than the median of the competing algorithm.

	UMOEAs			
	$n_D = 10$	$n_D = 30$	$n_D = 50$	$n_D = 100$
Case 1	3	0	0	0
Case 2	4	9	7	9
Case 3	11	9	11	9
Not significant	4	4	4	4
	L-SHADE			
	$n_D = 10$	$n_D = 30$	$n_D = 50$	$n_D = 100$
Case 1	3	0	0	0
Case 2	8	17	13	10
Case 3	9	5	8	9
Not significant	2	0	1	3
	MVMO			
	$n_D = 10$	$n_D = 30$	$n_D = 50$	$n_D = 100$
Case 1	0	0	0	0
Case 2	3	7	11	9
Case 3	13	10	8	10
Not significant	6	5	3	3
	CMLSP			
	$n_D = 10$	$n_D = 30$	$n_D = 50$	$n_D = 100$
Case 1	0	0	0	0
Case 2	1	9	2	2
Case 3	21	13	20	20
Not significant	0	0	0	0

$n_D = 50$.

As regards the comparison with L-SHADE, MP-AIDEA has lower median for a number of functions greater than L-SHADE only for $n_D = 10$ (9 functions).

In all dimension but $n_D = 50$, the number of functions for which the median of MP-AIDEA is lower than the median of MVMO is greater than the number of functions for which the median of MVMO is lower than the median of MP-AIDEA.

In all the cases MP-AIDEA has median lower than CMLSP for the majority of the tested functions.

Summarizing, results of the Wilcoxon test show that MP-AIDEA clearly outperforms CMLSP for all the values of n_D, gives similar or slighlty better results than UMOEAs and MVMO while is outperformed by L-SHADE for $n_D = 30$, $n_D = 50$ and $n_D = 100$.

7.5.4 Success rate

In this section the success rate of MP-AIDEA and of the top performing algorithms is presented for the test sets CEC 2011 and CEC 2014. No algorithm participating in the CEC 2005 is included in the comparison due to the lack of availability of the source code.

The computation of the success rate SR is reported in Algorithm 5 for a generic algorithm AG and a generic problem min_f [217]; n_{runs} is the number of times AG is applied to solve min_f. In Algorithm 5, $\bar{\mathbf{x}}(AG, i)$ denotes the lowest minimum observed during the i-th run of the algorithm AG. The quantity f_{global} is the known global minimum of the function and tol_f is a prescribed tolerance with respect to f_{global}. The index j_{sr} represents the number of times algorithm AG generates values lower or equal than $f_{global} + tol_f$. For each test set, the total number of functions for which each of the tested algorithms has the best success rate is also reported.

Algorithm 8 Calculation of the success rate

1: Apply AG to min_f for n_{runs} times and set $j_{sr} = 0$
2: **for** $i \in [1, \dots n_{runs}]$ **do**
3: Compute $\delta_f = \| f_{global} - f(\bar{\mathbf{x}}(AG, i)) \|$
4: **if** $\delta_f < tol_f$ **then**
5: $j_{sr} = j_{sr} + 1$
6: **end if**
7: **end for**
8: $SR = j_{sr}/n_{runs}$

CEC 2011 test set

For the calculation of the success rate on the test set CEC 2011 the following algorithms are considered: MP-AIDEA with 4 populations (MP-AIDEA), adaptive δ_{local} and local restart; MP-AIDEA with one population, $n_{LR} = 10$ and $\delta_{local} = 0.1$ (MP-AIDEA*); GA-MPC; DE-Λ. Table 7.20 shows the obtained values of SR and the value of tol_f used for each function and shows that MP-AIDEA outperforms all the other algorithms on most of the functions. The result against GA-MPC would be even better if a higher number of function evaluation was considered, as explained in section 7.5.2.

CEC 2014 test set

For the comparison on the test set CEC 2014 the following algorithms are considered: MP-AIDEA, MP-AIDEA*, UMOEAs, CLMSP, L-SHADE and MVMO [3]. The values of the success rates for all tested algorithms are shown in Tables from 7.21 to 7.24, together with the associated values of tol_f. The total number of problems for which an algorithm yields the best success rate is also reported.

For all dimensions MP-AIDEA compares very well against the other algorithms. In low dimension the full adaptive settings is the most competitive while as the number of dimensions increases the single population version with $\delta_{local} = 0.1$ results the most successful algorithm.

Table 7.20: Success rate: CEC2011 test set. Highest success rates for each function are shown in bold and their total is reported at the bottom of the table. MP-AIDEA* represents MP-AIDEA with settings $n_{pop} = 1$, $\delta_{local} = 0.1$ and $n_{LR} = 10$.

	tol_f	MP-AIDEA	MP-AIDEA*	GA-MPC	DE-Λ
1	1.0e-01	**0.92**	0.48	0.80	0.64
2	1.0e-01	**0.40**	0.20	0.12	**0.40**
3	1.0e-06	**1.00**	**1.00**	**1.00**	**1.00**
5	1.0e-01	**0.44**	0.20	0.16	0.04
6	1.0e+01	0.76	0.76	**0.84**	0.00
7	1.0e-01	**0.92**	0.64	0.04	0.72
10	1.0e-01	**0.36**	0.16	0.24	0.00
12	2.0e+00	**0.24**	0.00	0.20	0.00
13	1.0e+00	0.16	0.04	**0.52**	0.00
Total		7	1	3	2

These results are in line with the results in Section 7.5.2 and confirm the position of MP-AIDEA in the ranking.

7.6 Conclusions

This chapter has presented MP-AIDEA, an adaptive version of Inflationary Differential Evolution, which automatically adapts the two key parameters of Differential Evolution, CR, F, the size of the restart bubble δ_{local} and the number of local restarts n_{LR}. The adaptation of the number of local restarts is implemented through a mechanism that mitigates the possibility to detect the same local minimum multiple times. This mechanism allows MP-AIDEA to automatically identify when to switch from a local to a global restart of the population.

MP-AIDEA was tested on a total of 51 problems, taken from three CEC competitions, grouped in three test sets (named CEC 205, CEC 2011 and CEC 2014) and compared against 53 algorithms that participated in those three competitions. Four different metrics were presented to assess the performance of MP-AIDEA. Results demonstrated that MP-AIDEA ranks first in the CEC 2005, outperforming all the other algorithms for all problem dimensionalities. On the CEC 2011 test set, MP-AIDEA ranks second, after GA-MPC, if the number of function evaluations is restricted to the one prescribed by the competition. However, it was demonstrated that, in problem 13, an increase of the number of function evaluations does not provide any improvement of the objective value returned by GA-MPC but greatly improves the result of MP-AIDEA. It was noted, in fact, that GA-MPC has a fast convergence but then tends to stagnate. On the contrary, the convergence profile of MP-AIDEA is slower but, thanks to the restart mechanism, achieves better objective values. In this test set, in particular, the adaptation of the local restart neighborhood was shown to be effective providing competitive results compared to the settings of MP-AIDEA with a single population and predefined values of δ_{local} and number of restarts. This is confirmed by the Wilcoxon test, and the success rate.

On the test set CEC 2014, results are not equally satisfactory for all dimensions. MP-AIDEA

Table 7.21: Success rate: CEC 2014, 10D. Highest success rates for each function are shown in bold. and their total is reported at the bottom of the table for each value of n_D. MP-AIDEA* represents MP-AIDEA with settings $n_{pop} = 1$ and $\delta_{local} = 0.1$.

	tol_f	MP-AIDEA	MP-AIDEA*	UMOEAs	L-SHADE	MVMO	CMLSP
$n_D = 10$							
1	1.0e-06	**1.00**	**1.00**	**1.00**	**1.00**	0.00	0.00
2	1.0e-06	**1.00**	**1.00**	**1.00**	**1.00**	**1.00**	0.00
3	1.0e-06	**1.00**	**1.00**	**1.00**	**1.00**	**1.00**	0.00
4	1.0e-01	**0.98**	0.78	0.51	0.18	0.67	0.53
5	1.0e-01	**0.75**	0.33	0.06	0.04	0.12	0.00
7	1.0e-02	0.98	0.92	**1.00**	0.90	0.39	0.16
8	1.0e-01	0.86	**1.00**	0.98	**1.00**	**1.00**	0.00
9	1.0e+00	**0.37**	0.20	0.27	0.06	0.14	0.00
10	1.0e-01	0.33	0.00	0.18	**0.98**	0.00	0.00
11	1.0e+00	**0.06**	**0.06**	0.00	0.00	0.00	0.00
13	1.0e-01	0.92	0.53	**1.00**	**1.00**	**1.00**	0.24
14	1.0e-01	**1.00**	**1.00**	0.55	0.84	0.69	0.06
15	1.0e-01	**0.04**	0.00	0.00	0.00	0.00	0.00
16	1.0e+00	0.24	0.20	0.14	**0.29**	0.16	0.00
17	1.0e+01	0.53	0.45	0.37	**0.98**	0.57	0.10
18	1.0e+00	0.71	0.39	0.45	**0.96**	0.33	0.18
20	1.0e+00	0.78	0.98	0.88	**1.00**	0.96	0.18
21	1.0e+01	0.92	0.98	0.90	**1.00**	0.92	0.63
23	2.0e+02	0.00	0.00	0.00	0.00	0.00	0.00
24	2.0e+02	**1.00**	**1.00**	**1.00**	**1.00**	**1.00**	**1.00**
25	2.0e+02	**1.00**	0.98	0.86	0.75	0.96	0.96
28	2.0e+02	**0.06**	0.00	0.04	0.00	0.00	0.02
Total		12	7	6	12	5	1

Table 7.22: Success rate: CEC 2014, 30D. Highest success rates for each function are shown in bold. and their total is reported at the bottom of the table for each value of n_D. MP-AIDEA* represents MP-AIDEA with settings $n_{pop} = 1$ and $\delta_{local} = 0.1$.

	tol_f	MP-AIDEA	MP-AIDEA*	UMOEAs	L-SHADE	MVMO	CMLSP
$n_D = 30$							
1	1.0e-06	**1.00**	**1.00**	0.96	**1.00**	0.00	0.00
2	1.0e-06	**1.00**	**1.00**	**1.00**	**1.00**	0.18	0.00
3	1.0e-06	**1.00**	**1.00**	**1.00**	**1.00**	0.02	0.00
4	1.0e-06	**1.00**	**1.00**	0.86	**1.00**	**1.00**	0.00
5	2.0e+01	**1.00**	**1.00**	0.37	0.00	**1.00**	0.00
7	1.0e-04	**1.00**	**1.00**	**1.00**	**1.00**	0.73	0.86
8	1.0e-01	0.04	**1.00**	0.10	**1.00**	**1.00**	0.00
9	1.0e+01	0.00	0.04	0.47	**0.94**	0.00	0.02
10	1.0e-01	0.00	0.98	0.00	**1.00**	0.00	0.00
11	1.0e+03	0.08	**0.22**	**0.22**	0.12	0.02	0.00
13	1.0e-01	0.00	0.67	**0.92**	0.12	0.00	0.00
14	2.0e-01	**0.96**	0.53	0.41	0.12	0.76	0.00
15	2.0e+00	**0.47**	0.39	0.04	0.24	0.10	0.00
16	1.0e+01	0.47	0.65	0.14	**1.00**	0.61	0.00
17	5.0e+02	0.47	0.94	0.00	**1.00**	0.98	**1.00**
18	2.0e+01	0.25	0.33	0.43	**1.00**	0.75	0.75
20	2.0e+01	0.76	**1.00**	0.90	**1.00**	0.96	**1.00**
21	1.0e+01	0.02	**0.98**	0.00	0.25	0.04	0.04
23	2.0e+02	0.00	0.00	0.00	0.00	0.00	0.00
24	2.2e+02	0.18	**0.76**	0.04	0.00	0.00	0.41
25	2.0e+02	0.00	0.00	0.00	0.00	0.00	0.00
28	7.0e+02	0.20	0.10	0.04	0.00	0.00	**0.63**
Total		8	11	5	12	3	3

Table 7.23: Success rate: CEC 2014, 50D. Highest success rates for each function are shown in bold and their total is reported at the bottom of the table for each value of n_D. MP-AIDEA* represents MP-AIDEA with settings $n_{pop} = 1$ and $\delta_{local} = 0.1$.

	tol_f	MP-AIDEA	MP-AIDEA*	UMOEAs	L-SHADE	MVMO	CMLSP
$n_D = 50$							
1	1.0e-06	**1.00**	**1.00**	**1.00**	0.00	0.00	0.00
2	1.0e-06	**1.00**	**1.00**	**1.00**	**1.00**	0.00	0.00
3	1.0e-06	**1.00**	**1.00**	0.80	**1.00**	0.00	0.00
4	1.0e-06	**1.00**	**1.00**	0.18	0.00	0.98	0.00
5	2.0e+01	**1.00**	**1.00**	0.35	0.00	**1.00**	0.00
7	1.0e-04	**1.00**	**1.00**	**1.00**	**1.00**	0.41	0.00
8	5.0e+00	0.18	**1.00**	0.51	**1.00**	0.94	0.00
9	5.0e+01	0.18	0.69	**1.00**	**1.00**	0.10	0.00
10	1.0e+01	0.12	0.98	0.16	**1.00**	0.10	0.00
11	3.0e+03	0.06	**0.78**	0.10	0.16	0.12	0.00
13	3.0e-01	0.49	0.65	**1.00**	**1.00**	0.94	0.20
14	2.0e-01	**0.10**	0.04	0.02	0.00	0.08	0.00
15	5.0e+00	0.57	**0.94**	0.14	0.39	0.49	0.00
16	1.8e+01	0.02	0.16	0.06	**1.00**	0.08	0.00
17	1.0e+03	0.41	**0.98**	0.00	0.12	0.88	0.04
18	1.0e+02	0.94	**0.96**	0.45	0.63	**0.96**	0.22
20	1.0e+02	0.51	0.96	0.63	**1.00**	**1.00**	**1.00**
21	1.0e+03	0.96	**1.00**	0.10	**1.00**	**1.00**	0.22
23	3.4e+02	0.00	0.00	0.00	0.00	0.00	0.00
24	2.6e+02	**0.90**	**0.90**	0.02	0.00	0.86	0.00
25	2.1e+02	0.02	**0.18**	0.02	0.12	0.08	0.02
28	1.1e+03	0.20	**0.37**	0.04	0.27	0.00	0.33
Total		8	15	5	10	4	1

Table 7.24: Success rate: CEC 2014, 100D. Highest success rates for each function are shown in bold and their total is reported at the bottom of the table for each value of n_D. MP-AIDEA* represents MP-AIDEA with settings $n_{pop} = 1$ and $\delta_{local} = 0.1$.

	tol_f	MP-AIDEA	MP-AIDEA*	UMOEAs	L-SHADE	MVMO	CMLSP
$n_D = 100$							
1	1.0e-06	**1.00**	**1.00**	**1.00**	0.00	0.00	0.00
2	1.0e-06	**1.00**	**1.00**	**1.00**	**1.00**	0.00	0.00
3	1.0e-06	**1.00**	**1.00**	0.41	1.00	0.00	0.00
4	1.0e-06	**0.92**	0.78	0.00	0.00	0.35	0.00
5	2.0e+01	**1.00**	**1.00**	0.63	0.00	**1.00**	0.00
7	1.0e-04	**1.00**	**1.00**	**1.00**	**1.00**	0.82	0.00
8	5.0e+00	0.00	0.98	0.00	**1.00**	0.04	0.00
9	2.0e+02	0.88	**1.00**	**1.00**	**1.00**	0.61	0.00
10	5.0e+02	0.51	**1.00**	0.20	**1.00**	0.08	0.00
11	1.0e+04	0.55	**1.00**	0.59	0.06	0.57	0.00
13	4.0e-01	0.16	0.12	**1.00**	**1.00**	**1.00**	0.00
14	3.0e-01	0.45	0.16	**1.00**	**1.00**	**1.00**	0.90
15	2.0e+01	0.92	**1.00**	**1.00**	**1.00**	0.90	0.00
16	4.0e+01	0.02	0.12	0.00	**0.96**	0.00	0.00
17	3.0e+03	0.67	**0.84**	0.00	0.04	0.39	0.00
18	2.0e+02	0.41	**1.00**	0.00	0.10	**1.00**	0.00
20	3.0e+02	0.08	0.98	0.37	**1.00**	**1.00**	**1.00**
21	1.0e+03	0.02	**0.98**	0.00	0.00	0.18	0.00
23	3.7e+02	**1.00**	**1.00**	**1.00**	**1.00**	**1.00**	0.98
24	3.7e+02	0.57	0.04	0.00	0.00	**0.98**	0.00
25	2.5e+02	0.96	**1.00**	**1.00**	**1.00**	0.22	**1.00**
28	2.0e+03	**0.27**	**0.27**	0.00	0.00	0.00	0.04
Total		7	15	9	12	7	2

is in the top three algorithms except in dimension 30. When the number of populations is reduced to one and $\delta_{local} = 1$, MP-AIDEA outperforms all other algorithms in dimension 50 and 100.

One part of the problem is the extra effort required by the multi-population adaptive algorithm to identify the correct value of δ_{local}. However, another part of the problem was found in the contraction limit. This is in line with the theoretical findings in [131], where it was found that DE can converge to a level set in the general case. Furthermore, it was noted that the populations can naturally partition and form clusters that independently converge to separate points. This slow rate of convergence affects the restart and local search mechanisms and the associated adaptation machinery. Since the current implementation uses a synchronous restart and adaptation of δ_{local} and n_{LR}, the number of restarts might be limited by the fact that the evolution of all populations has to come to a stop before any of them can be restarted. Future work will be dedicated to improve these aspects of the algorithm.

The development of the single objective global optimiser MP-AIDEA is the last step in the definition of tools and methodologies to be used for the multi-fidelity global optimisation of low-thrust trajectories. The methods and techniques presented in Part I of the dissertation will now be applied to interplanetary and Earth's mission design in Part II.

Part II

Applications

The content of this chapter was published in M. Di Carlo, J. M. Romero Martin, N. Ortiz Gomes, M. Vasile, "Optimised low-thrust mission to the Atira asterois", Advances in Space Research, Volume 59, Issue 7, 1 April 2017, pp. 1724-1739

Chapter 8

Low-thrust mission to the Atira asteroids

In this chapter, a small, low-cost, electric propelled mission to visit the known Atira asteroids and to discover new Near Earth Asteroids (NEA) is presented. The trajectory is optimised to maximise the number of visited asteroids of the Atira group, with minimum propellant consumption. During the tour of the Atira asteroids an opportunistic NEA discovery campaign is proposed to increase knowledge of the asteroid population. The mission ends with a transfer to an orbit with perihelion equal to Venus's orbit radius. This orbit represents a vantage point to monitor and detect asteroids in the inner part of the Solar System and provide early warning in the case of a potential impact. The analytical formulae presented in Chapter 4, the transcription method presented in Chapter 5 and the global solver MP-AIDEA (Chapter 7) are used to design this mission.

The chapter is structured as follows. Section 8.1 introduces the problem and present the main information about the Atira asteroids. Section 8.2 presents an overview of the mission design process. The methods used to find the sequence of visited asteroids and optimise the associated low-thrust trajectory are described in Sections 8.3 and 8.4, including different strategies to achieve the final surveillance orbit. The study of the launch and orbit injection strategy is presented in Section 8.5; the study of the visibility analysis of inner-Earth asteroids is described in Section 8.6 and the results are presented in Section 8.7. Some conclusions are given in Section 8.8.

8.1 The Atira asteroids

Atira asteroids are recently-discovered celestial bodies characterised by orbits lying completely inside the heliocentric orbit of the Earth. The study of these objects is difficult due to the limitations of ground-based observations: objects can only be detected when the Sun is not in the field of view of the telescope. However, many asteroids are expected to exist in the inner region of the solar system, many of which could pose a significant threat to our planet. Atira

asteroids are NEAs with both perihelion and aphelion within the orbit of the Earth (aphelion $Q < 0.983$ AU), also called Inner-Earth Objects (IEOs). The first Atira object was discovered in 2003 and, as of March 2016, sixteen asteroids are counted in this group (see Table 8.1)[1]. However, many more objects are expected to exist in the same region of the solar system. To date, over eleven thousand NEAs have been identified, the majority of which are characterized by semi-major axis greater than 1 AU, as shown in Figure 8.1, where the distribution of the known NEAs is shown in the a-e and a-i planes, with the Atira asteroids represented by triangular markers.

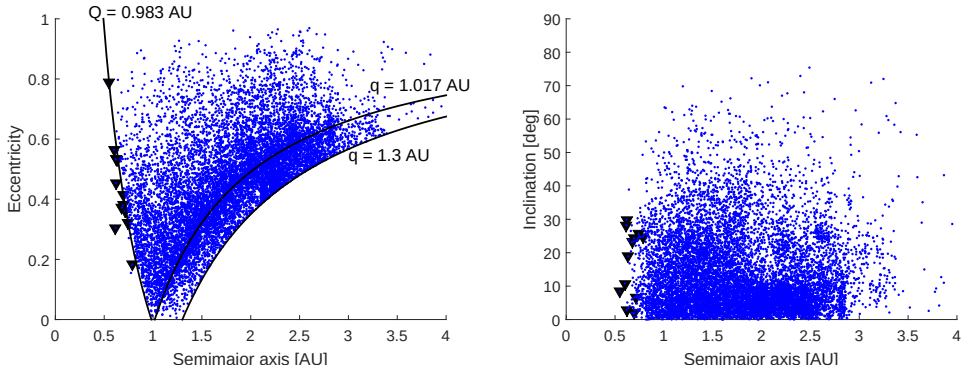

Figure 8.1: NEAs distribution in the a-e and a-i planes; black triangles indicate Atira asteroids.

Inner solar system asteroids are indeed difficult to discover and track because Earth-bound telescopes have difficulties detecting asteroids when the Sun is in the field of view. For this reason these asteroids could represent a hazard for our planet. The object that exploded in an air burst over Chelyabinsk, in Russia, in February 2013, injuring more than 1,000 people, approached, undetected, from the Sun direction.

In recent years, successful electric propelled missions such as Deep Space 1 [175], Hayabusa [103]) and Dawn [32] have demonstrated the possibility to successfully survey or even land on asteroids in our solar system. However, to date no mission has targeted inner solar system asteroids, including members of the Atira group.

8.2 Mission design overview

The encounters with the Atira asteroids are realised through a series of fly-by's at the nodal points of the orbits of the asteroids. The mission design process is divided into three phases:

1. Sequence Finder: identification of the optimal sequence of asteroids to visit, departure and arrival dates using an impulsive Lambert model for the transfers (Section 8.3).

2. Additional Optimisation: refinement of the optimal solution found at the previous step using MP-AIDEA (Chapter 7, Section 8.3.1).

[1]JPL Small-Body Database Search Engine - `http://ssd.jpl.nasa.gov/sbdb_query.cgi`

Table 8.1: Orbital elements of the known Atira asteroids: t_p is the time of passage at perihelion. The asteroids shown in bold are the ones known when the study started and therefore the ones considered in this work.

Object ID	a [AU]	e	i [deg]	Ω [deg]	ω [deg]	t_p [ET]
1998 DK36	0.69	0.42	2.02	151.46	180.04	1998-Jun-07.3
2003 CP20	0.74	0.32	25.62	103.92	252.93	2014-Dec-24.0
2004 XZ130	0.62	0.45	2.95	211.41	5.16	2014-Nov-27.6
2004 JG6	0.64	0.53	18.94	37.04	352.98	2014-Sep-13.3
2005 TG45	0.68	0.37	23.33	273.46	230.42	2014-Dec-29.0
2006 WE4	0.78	0.18	24.77	311.04	318.62	2014-Nov-07.5
2007 EB26	0.55	0.79	8.49	63.22	236.71	2007-Apr-30.2
2008 EA32	0.62	0.30	28.27	100.97	181.85	2015-Feb-17.4
2008 UL90	0.69	0.38	24.31	81.17	183.61	2014-Dec-09.9
2010 XB11	0.62	0.53	29.88	96.32	202.48	2015-Feb-14.2
2012 VE46	0.71	0.36	6.67	8.95	190.36	2014-Dec-03.8
2013 JX28	0.60	0.56	10.76	39.97	354.88	2014-Dec-31.8
2013 TQ5	0.77	0.16	16.38	286.77	247.32	2014-Oct-12.5
2014 FO47	0.75	0.27	19.18	358.68	347.41	2015-Mar-07.8
2015 DR215	0.67	0.47	4.10	315.05	42.17	2015-Dec-17.2
2015 ME131	0.80	0.19	28.88	314.36	164.03	2015-Oct-26.7

3. Low-Thrust Trajectory Optimisation: translation of the optimal impulsive solution found at the previous step into a low-thrust optimal trajectory using the transcription method presented in Section 5.2 (Section 8.4).

After the last fly-by the spacecraft is injected into a reduced perihelion surveillance orbit using the electric propulsion system (Section 8.4). The baseline trajectory solution is then used to analyse the feasibility of a low-cost launch opportunity (Section 8.5).

Given that the main objective is to maximise the number of visited asteroids with the minimum propellant mass, the trajectory is not optimised for the discovery campaign. On the contrary a visibility analysis is carried out in order to assess the number of asteroids that could potentially be observed along the baseline trajectory derived from point 3 here above (Section 8.6).

8.3 Sequence finder

The definition of the optimal sequence of asteroids and departure and arrival dates at the nodes of the asteroids, requires the solution of a combinatorial optimisation problem. This problem is solved using an algorithm called "Lambert problem to Target Asteroids at Nodal points" (LambTAN). LambTAN is inspired to the general branch-and-prune techniques and in particular the incremental pruning techniques proposed in [14] and [215]. Complete trajectories are incrementally constructed by adding one transfer arc at a time following a tree structure in which each branch is a possible partial sequence of asteroids. Partial transfers are pruned out if one or more criteria are not met (for example, the ΔV of an arc is greater than a

given maximum value).

The asteroids are assumed to move on Keplerian orbits as a solution of a two-body Sun-asteroid problem. The trajectories are composed of sequences of conic arcs linked together through discrete, instantaneous events. Each conic arc is the solution of a Lambert problem, which is solved to compute the ΔV required for the spacecraft to hop from one asteroid to another. Asteroids are met at their nodal points to avoid expensive inclination change manoeuvres. At every hop the spacecraft is transferred to a new heliocentric orbit. For the following hop a new set of departure conditions are identified along the current heliocentric orbit, within a minimum and maximum value for the time of flight to reach the nodal point of the next asteroid. As an example, Figure 8.2 shows several Lambert arcs reaching a given asteroids from different departure points on the Earth's orbit.

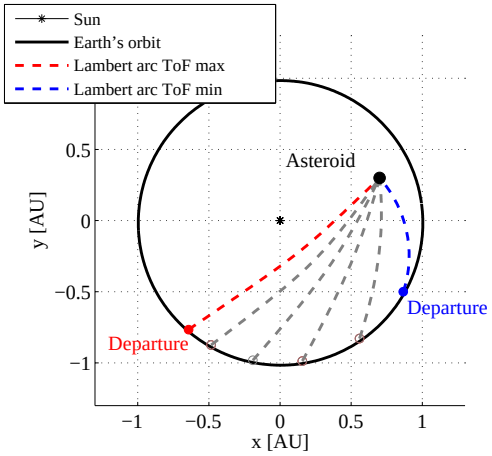

Figure 8.2: Lambert arcs for Earth-to-asteroid transfer example. The asteroid fly-by occurs at the nodal point. Subsequent asteroid-to-asteroid transfers are computed in analogous fashion.

The search space is pruned in order to exclude non-feasible solutions for the low-thrust optimisation as well as considering constraints for the maximum local departure ΔV, the minimum and maximum time of flights and the minimum perihelion. More details about the algorithm LambTAN can be found in Appendix G. By representing with N_A the number of visited asteroids, the complete solution vector provided by LambTAN is

$$\mathbf{x}_{LambTAN} = [T_1, ToF_1, A_1, T_2, ToF_2, A_2, \ldots, T_{N_A}, ToF_{N_A}, A_{N_A}]^T, \tag{8.1}$$

where, for the first transfer, T_1 is the departure time, ToF_1 is the time of flight for the Lambert arc and A_1 is the target asteroid.

8.3.1 Additional optimisation

The optimisation analysis previously described results in many solutions, each one characterised by a specific set of variables (number of asteroid visited, asteroids sequence, departure

dates, time of flights). The solutions obtained are ranked in order to identify the ones with maximum sequence length and lowest ΔV. The first ranked solutions is then further optimised by means of the single population adaptive version of MP-AIDEA (Chapter 7). The optimisation executed using MP-AIDEA is realised in order to improve the departure dates found by LambTAN, leading to a reduced ΔV for the transfers. In order to do so, a time window of $\pm\mathfrak{T}$ days is allocated around each departure date T_i found by LambTAN and MP-AIDEA is run to find, in this search space, departure dates leading to a reduced value of the total ΔV. The values of the times of flight are derived from the requirement to encounter the asteroids at one of their nodes and, thus, are not optimised further. Considering the solution vector provided by LambTAN (Equation 8.1), the lower and upper boundaries, $\mathbf{x}^L$ and $\mathbf{x}^U$ of the search space for MP-AIDEA are defined as

$$\begin{aligned} \mathbf{x}^L &= [T_1 - \mathfrak{T}, T_2 - \mathfrak{T}, \ldots, T_{N_A} - \mathfrak{T}]^T \,, \\ \mathbf{x}^U &= [T_1 + \mathfrak{T}, T_2 + \mathfrak{T}, \ldots, T_{N_A} + \mathfrak{T}]^T. \end{aligned} \tag{8.2}$$

8.4 Low-thrust trajectory optimisation

The outcome of the sequence finder and optimisation with MP-AIDEA is a sequence of transfer arcs characterised by a departure state vector, an end state vector, a transfer time and a departure ΔV. The low-thrust optimisation process determines, for each transfer arc, an optimal control history, for the low-thrust engine of the spacecraft, to depart from the initial state vector and achieve the desired end position and velocity in the given transfer time. The problem is solved using the transcription method DT-CTECA presented in Section 5.2, with the analytical model for the motion of the spacecraft subject to constant low-thrust acceleration in the RTN reference frame presented in Chapter 4. For the trajectories considered in this study, the angle β is set to zero, since the transfers are all on the ecliptic plane. The azimuth angles α'_s are instead optimisation variables, while the modulus ϵ of the acceleration depends only on the mass of the spacecraft. The mass of the spacecraft is conservatively kept constant over each transfer arc and updated at the end of the transfer according to the propellant mass spent to realise that transfer. The corresponding non-linear programming problem is solved using MATLAB *fmincon* with sequential quadratic programming algorithm.

In order to facilitate convergence of the NLP problem, a continuation method is implemented (see Section 5.2).

8.4.1 Transfer to the surveillance orbit

After the fly-by with the last asteroid in the sequence identified by LambTAN, the spacecraft is moved to an orbit with reduced perihelion, equal to 0.725 AU, in order to continue its observation of NEAs. Three strategies are considered for this transfer: 1) a low-thrust spiral, 2) a low-thrust transfer exploiting resonances with the Earth, 3) a low-thrust transfer exploiting one Earth's gravity assist. The design of these possibilities is briefly described in the following.

1. *Low-thrust spiral*. The optimisation problem is analogous to the one previously described but without the constraint on the transfer time in Equation 5.5.

2. *Low-thrust and Earth's Resonances*. The spiral is timed to take advantage of the gravity perturbation of the Earth to change the perihelion of the orbit. The Earth can perturb the orbit of the spacecraft when the Earth is in the vicinity of the aphelion of the orbit of the spacecraft at the same time that the spacecraft is at the aphelion [193]. In particular, if the Earth is ahead of the spacecraft the perihelion will be increased, while if the Earth is behind the spacecraft the perihelion will be decreased [91,179]. For this study a reduction of perihelion is sought.

3. *Low-thrust and Earth's swing-by*. The low-thrust engine is used to inject the spacecraft, after the last fly-by, into a trajectory that encounters the Earth, so that a gravity assist that reduces the perihelion can be realised. The gravity assist is modeled with the linked conic approximation proposed in [209]. The trajectory optimisation problem is modified including the time of the swing-by of the Earth, T_{GA}, and the radius of the perigee of the hyperbola at the Earth, r_p^{GA}. The solution vector (Equation 5.10) becomes:

$$\mathbf{x}^{GA} = [\alpha'_1, \mathbf{X}_1^{ON}, \mathbf{X}_1^{OFF}, \alpha'_2, \mathbf{X}_2^{ON}, \mathbf{X}_2^{OFF}, \ldots, \alpha'_{n_{LT}}, \mathbf{X}_{n_{LT}}^{ON}, \mathbf{X}_{n_{LT}}^{OFF}, T_{GA}, r_p^{GA}]^T \ . \quad (8.3)$$

   Since the arrival state vector is not known a priori, the backward propagation is not implemented in this case. The non-linear programming problem is solved minimising the propellant consumption subject to the constraints given in Equation 5.5, only for the forward propagation leg, plus the following two additional constraints:

   - the orbit of the spacecraft after the gravity assist with the Earth has perihelion equal to 0.725 AU;
   - the encounter with the Earth takes place after a coast arc with minimum duration of 30 days to minimise the risks during critical phases of the mission.

8.5 Launch and orbit injection

The mission proposed aims at achieving the desired scientific objectives with a small spacecraft and a low-cost launch opportunity. In order to meet this expectation the launch and orbit injection strategy needs to be carefully considered. Two options are analysed; injecting the spacecraft into an escape trajectory with the right velocity at the Earth to reach the first asteroid with no low-thrust manoeuvres or injecting the spacecraft into an escape trajectory that provides zero relative velocity with respect to the Earth and then using the low-thrust engine to reach the first asteroid. The former strategy provided the best results in terms of total ΔV and launch cost and will be described in the following.

The assumption is that the launcher places the spacecraft on a Geostationary Transfer Orbit (GTO), with orbital elements a_{GTO}, e_{GTO}, i_{GTO} and ω_{GTO}, and provides an re-ignitable upper stage. The heliocentric velocity of the spacecraft on its departure from Earth, $\mathbf{v}_{initial}$, is

obtained from the solution provided by the LambTAN algorithm. The relative velocity vector with respect to Earth at the departure is simply $\mathbf{v}_\infty = \mathbf{v}_{initial} - \mathbf{v}_\oplus$, where $\mathbf{v}_\oplus$ is the velocity of the Earth expressed in the heliocentric reference frame. The vector $\mathbf{v}_\infty$ is then transformed from the heliocentric to the planetocentric reference frame in order to obtain its declination δ, required to compute the inclination i of the hyperbolic orbit, according to [192]:

$$\sin i = \frac{\sin \delta}{\sin (\omega_{GTO} + \theta)}, \tag{8.4}$$

where θ is the true anomaly corresponding to the asymptotic direction [108]. The angle θ can be computed using the following equations:

$$a_{hyp} = -\frac{\mu_\oplus}{\|\mathbf{v}_\infty\|^2} , \tag{8.5}$$

$$e_{hyp} = 1 - \left(\frac{a_{GTO}(1 - e_{GTO})}{a_{hyp}} \right) , \tag{8.6}$$

and

$$\theta = \arccos \left(-\frac{1}{e_{hyp}} \right) . \tag{8.7}$$

The computed values of δ and θ could be such that using them together with ω_{GTO} in Equation (8.4) would give $\sin i > 1$. In this case, since δ is defined by the geometry of the initial velocity, a change of i and ω is required to insert the spacecraft into the appropriate hyperbolic orbit. It is therefore assumed that the upper stage can provide multiple manoeuvres to change i and ω. In the following, a two manoeuvre injection strategy is considered:

1. the first manoeuvre, executed at the ascending node of the GTO orbit, change the inclination from i_{GTO} to $i_{inj} = i_{GTO} + \Delta i$;
2. the second manoeuvre is executed at an appropriate position along the GTO orbit with inclination i_{inj} so that the injection into the hyperbolic orbit, with an appropriate value of ω_{inj}, can be obtained.

The values of i_{inj} and ω_{inj} corresponding to the lowest ΔV for the two manoeuvres are computed using the following procedure:

- the true anomaly of the point where the second manoeuvre takes place is $(2\pi - \omega_{GTO} + \omega_{inj})$ (Figure 8.3). Using this value of true anomaly, the position and velocity of the spacecraft at the point along the orbit where the hyperbolic injection manoeuvre is executed are computed, for each value of $\omega_{inj} \in [0, 2\pi]$, using

$$r_{inj} = \frac{a_{GTO}(1 - e_{GTO}^2)}{1 + e_{GTO} \cos (2\pi - \omega_{GTO} + \omega_{inj})} \tag{8.8}$$

and

$$v_{inj} = \sqrt{\frac{\mu_\oplus}{a_{GTO}(1 - e_{GTO}^2)}} \sqrt{1 + e_{GTO}^2 + 2e_{GTO} \cos (2\pi - \omega_{GTO} + \omega_{inj})} ; \tag{8.9}$$

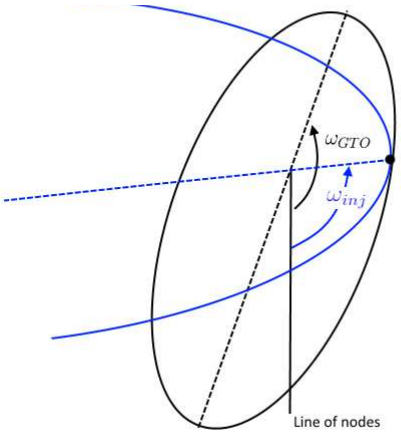

Figure 8.3: Orbit geometry for the second manuever: the GTO with inclination i_{inj} is in black, the hyperbolic orbit is in blue.

- the eccentricity of the hyperbola is computed, for each value of $\omega_{inj} \in [0, 2\pi]$, using

$$e_{hyp} = 1 - \frac{r_{inj}}{a_{hyp}} , \tag{8.10}$$

  with a_{hyp} from Equation 8.5;

- values of θ are computed using Equation 8.7;

- the inclination i_{inj} is computed using δ from Equation 8.4 and θ resulting from the previous step for every value of $\omega_{inj} \in [0, 2\pi]$;

- the ΔV required to perform the variation of inclination with the first manoeuvre is computed as

$$\Delta V_i = 2 v_{asc} \sin\left(\frac{\Delta i}{2}\right) , \tag{8.11}$$

  where $\Delta i = i_{inj} - i_{GTO}$ and v_{asc} is the velocity at the ascending node of the orbit:

$$v_{asc} = \sqrt{\frac{\mu_\oplus}{a_{GTO}(1 - e_{GTO}^2)}} \sqrt{1 + e_{GTO}^2 + 2 e_{GTO} \cos\left(2\pi - \omega_{GTO}\right)} \tag{8.12}$$

- the variation of velocity required to perform the second manoeuvre and inject the spacecraft into the hyperbolic orbit is computed as:

$$\Delta V_{inj} = \sqrt{v_{hyp}^2 + v_{inj}^2 - 2 v_{hyp} v_{inj} \cos \gamma_{inj}} \tag{8.13}$$

  where v_{hyp} is the velocity at the perigee on the hyperbolic orbit:

$$v_{hyp} = \sqrt{\frac{2\mu_\oplus}{r_{inj}} + \|\mathbf{v}_\infty\|^2} ; \tag{8.14}$$

γ_{inj} is the flight path angle at the point of the manoeuvre:

$$\tan \gamma_{inj} = \frac{e_{GTO} \sin (2\pi - \omega_{GTO} + \omega_{inj})}{1 + e_{GTO} \cos (2\pi - \omega_{GTO} + \omega_{inj})} ; \tag{8.15}$$

- finally, the total variation of velocity is:

$$\Delta V_{total} = \Delta V_i + \Delta V_{inj} . \tag{8.16}$$

The values of i_{inj} and ω_{inj} leading to the lower value of ΔV_{total} are used to realise the two manoeuvres to inject the spacecraft into its hyperbolic orbit.

8.6 Visibility analysis

During the transfer from one asteroid to another, observations of the inner part of the solar system can be carried out with appropriate instrumentation placed on-board of the spacecraft, in order to detect new NEAs. The observations are carried out also during the transfer to and on the surveillance orbit. This analysis provides insight into the likelihood of observing new NEAs based on the current population. The instrument that has been selected for this mission is the same one used for the Canadian microsatellite NEOSSat, launched in 2003. This instrument has a limiting relative magnitude V of 19.5 with an exposure time of 100 seconds [226].

8.6.1 Near Earth Asteroids population

The expected number and size of the asteroids potentially observable during the mission lifetime are derived from the available catalogue of known NEAs. The database of known NEAs is taken from the JPL Small-Body Database Search Engine[2].

Approximately 9,000 NEAs are currently known; however, the working assumption is that more than 10^6 objects with absolute magnitude lower than $H = 26$ exist. This assumption is in agreement with the NEA population estimate by Harris [95] and is used to evaluate the quality of the proposed survey. In line with the work of Greenstreet et al. [87] the further assumption that the existing population is composed of 30.1% of Amors asteroids, 63.3% of Apollo asteroids, 5% of Atens asteroids and 1.6% of Inner Earth Objects is introduced. With these two assumptions in mind, a synthetic population is generated by re-sampling the joint distribution of the orbital elements of the known NEAs. The existing population is then added to the synthetic one for consistency. The orbital elements of the synthetic and true populations are defined at a given epoch and the orbits of all the asteroids are then propagated forward in time for the duration of the mission. To generate the synthetic population, a total of 1,430,600 IEOs, Atens, Apollos and Amors are generated by re-sampling the existing joint distribution. Then, from the obtained synthetic population 22,890 IEOs, 71,531 Atens and 905,579 Apollos

[2]JPL Small-Body Database Search Engine - `http://ssd.jpl.nasa.gov/sbdb$_$query.cgi$#$x`

are selected, so that the sum is 10^6 NEAs and the number of objects in each group respect the percentages given by Greenstreet.

The absolute magnitude H of the asteroids of the synthetic populations is obtained considering the cumulative distribution [195]:

$$N(< H) = 10^{-3.88+0.39H} \ . \tag{8.17}$$

The probability density function of the absolute magnitude H, f_H, is computed by normalising Equation 8.17 as follows:

$$f_H = \frac{1}{C_H} \cdot 10^{-3.88+0.39H} \ , \tag{8.18}$$

where C_H is given by:

$$C_H = \int_{H(N=1)}^{H(N=10^6)} 10^{-3.88+0.39H} dH \ , \tag{8.19}$$

so that f_H can be expressed as:

$$f_H = 8.98\ 10^{-7} \cdot 10^{-3.88+0.39H} \ . \tag{8.20}$$

The slope parameter G of the asteroids of the population has been modelled considering a distribution with mean value and standard deviation as proposed in [219]. In order to obtain statistically significant results, 100 different synthetic populations of 10^6 IEOs, Atens and Apollos asteroids are generated and an independent visibility analysis is run for each population.

8.6.2 Observation constraints

In order for the on-board camera to detect an asteroid, the following three constraints have to be met:

- the asteroid has to be within the Field of View (FOV) of the camera;
- the asteroid relative magnitude V with respect to the camera has to be below the camera detection threshold;
- the phase angle ϕ Sun-asteroid-spacecraft (Figure 8.4) has to be below a certain threshold.

The first two constraints are linked to the field of view of the camera and its limiting magnitude detection capability. The third constraint takes into account the necessary illumination conditions for the asteroid to be observed by the spacecraft. The best illumination conditions take place when $\phi = 0$, that is when the spacecraft is between the Sun and the asteroid. The asteroid relative magnitude V is given by [195]

$$V = 5\log_{10}(r_{ast-\odot}\ r_{ast-SC}) + H - 2.5\log_{10}((1-G)\lambda_1 + G\lambda_2) \ , \tag{8.21}$$

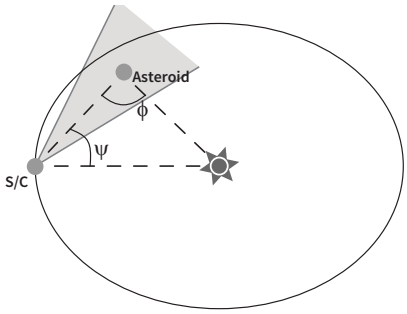

Figure 8.4: Camera pointing towards the inner part of the spacecraft trajectory. The angle ψ is used to define the pointing direction of the camera (Section 8.7.5).

where

$$\begin{aligned} \lambda_1 &= \exp(-(3.33\tan(\frac{\phi}{2}))^{0.63}) \ , \\ \lambda_2 &= \exp(-(1.87\tan(\frac{\phi}{2}))^{1.22}) \ . \end{aligned} \tag{8.22}$$

In the previous equations $r_{ast-\odot}$ is the distance between the asteroid and the Sun in AU, r_{ast-SC} is the distance between the asteroid and the spacecraft in AU, ϕ is the phase angle between the position vector asteroid-Sun and the position vector asteroid-spacecraft and G is the slope parameter of the asteroid. The diameter of the NEAs is related to the absolute magnitude according to [199]

$$D = \frac{1329}{\sqrt{p_v}} 10^{-0.2H} \ , \tag{8.23}$$

where D is the diameter in km and p_v is the albedo of the asteroid.

8.7 Results

In this section the results obtained using the methods described in the previous sections are presented.

8.7.1 Sequence finder

The parameters used for the LambTAN solver are summarised hereafter and in Table 8.2 (refer to Appendix G):

- the set of considered asteroids, $\mathcal{A}$, comprises the first twelve asteroids from Table 8.1 (shown in bold in Table 8.1);
- the maximum mission time is 10 years, with initial epoch 01 January 2020 and final epoch 01 January 2030;

- the minimum and maximum times of flight for each transfer are 30 and 365 days, with steps of 10 days;
- the maximum departure ΔV for the Lambert transfer, ΔV_{max}, is 3 km/s for departures from Earth and 1.5 km/s for departures from other orbits;
- the minimum perihelion q_{min} for the Lambert transfer is 0.31 AU;
- the considered low-thrust acceleration ϵ is 10^{-4} m/s^2 (corresponding to a 700 kg spacecraft with thrust equal to 0.07 N, Section 8.7.3) and the parameter C for the translation of the impulsive transfer into a low-thrust transfer (Appendix G) is set to 2. This value was obtained from a preliminary experimental test campaign where each transfer generated by LambTAN was re-optimised with the low-thrust solver.

Table 8.2: LambTAN simulation parameters (refer to Table G.1).

$\mathcal{A}$	Asteroid in bold in Table 8.1
T_0	01/01/2020
T_{end}	01/01/2030
ToF_{max}	365 days
ToF_{min}	30 days
ToF_{step}	10 days
ΔV_{MaxDep}	3 km/s from Earth
	1.5 km/s from transfer orbits
q_{min}	0.31 AU
ϵ	10^{-4} m/s^2
C	2

LambTAN finds 133,761 solutions, with longest solutions characterised by six fly-bys; in Figure 8.5 the total ΔV required for all the solutions of four, five or six asteroids fly-by's are presented.

Since many of the solutions are characterised by the same sequences of asteroids but different departure dates, a filtering process is applied to identify solutions targeting different asteroids. After the filtering, fourteen solutions with different sequence of asteroids, visiting six asteroids, and fifty-seven different solutions visiting five asteroids are found. The best solution found by LambTAN, that is, the one characterised by the maximum number of asteroids visited and the lowest total ΔV, has six fly-bys based on the following sequence: Earth - 2013 JX28 - 2006 WE4 - 2004 JG6 - 2012 VE46 - 2004 XZ130 - 2008 UL90 with a total ΔV cost of 3.77 km/s and a transfer time of about 8.4 years, as summarised in Table 8.3.

Considering a typical chemical propulsion specific impulse of $I_{sp} = 321$ s and a spacecraft dry mass of approximately 595 kg at the end of the six fly-bys (as found in Table 8.5), realising the six fly-by's with a chemical engine would require 1377.36 kg of propellant.

The positions of the targeted nodal points are shown in Figure 8.6 in the x - y plane of a heliocentric inertial reference frame.

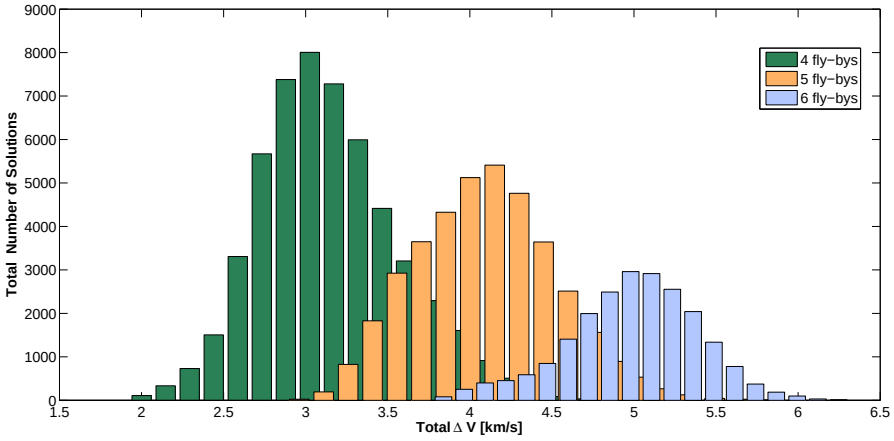

Figure 8.5: Solution distribution.

Table 8.3: Best solution obtained with six visited asteroids using LambTAN.

	Asteroid	Departure date	ToF [days]	Arrival date	ΔV [km/s]	m_p [kg]
	2013 JX28	2020/09/29	205	2021/04/22	0.87	476.54
	2006 WE4	2022/05/14	215	2022/12/15	0.86	357.79
	2004 JG6	2023/06/14	235	2024/02/04	0.61	200.60
	2012 VE46	2024/09/11	265	2025/06/03	0.36	101.37
	2004 XZ130	2026/09/15	205	2027/04/08	0.73	173.15
	2008 UL90	2028/07/31	195	2029/02/11	0.34	67.91
TOT.					3.77	1377.36

8.7.2 Refinement of the best solution

The best solution identified by LambTAN is further optimised using MP-AIDEA (Chapter 7 and Section 8.3.1). For the additional optimisation a local window of $\mathfrak{T} = 10$ days is allocated around the previous defined departure dates in order to identify new departures dates leading to an improved result in term of total ΔV. The semi-amplitude of the local window is 10 days because of the value chosen for ToF_{step} in LambTAN. The maximum number of function evaluations for MP-AIDEA is 2000. The settings of the parameters of the single population version of MP-AIDEA are $\delta_{local} = 0.1$ and $n_{LR} = 10$ [141]. The results are reported in Table 8.4, showing a reduction of 0.16 km/s in the total ΔV and of 103.76 kg in the propellant consumption with respect to the results presented in Table 8.3. This solution and the results shown in Table 8.4 have been used for the optimisation of the low-thrust trajectory.

8.7.3 Low-thrust trajectory optimisation

For the low-thrust optimisation the initial nominal low-thrust acceleration is set to 10^{-4}m/s^2, equivalent to a thrust $F = 0.07$ N applied to a 700 kg spacecraft. The specific impulse consi-

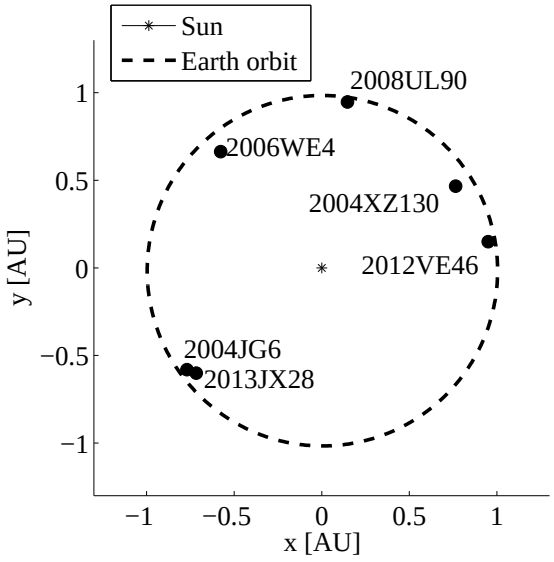

Figure 8.6: Targeted nodal points of the visited asteroids.

Table 8.4: Further optimisation of the best solution obtained with six visited asteroids using MP-AIDEA.

	Asteroid	Departure date	ToF [days]	Arrival date	ΔV [km/s]	m_p [kg]
	2013 JX28	2020/09/20	214.5329	2021/04/22	0.95	487.06
	2006 WE4	2022/05/24	205	2022/12/15	0.69	272.10
	2004 JG6	2023/06/12	236.2514	2024/02/04	0.61	195.56
	2012 VE46	2024/09/05	270.6114	2025/06/03	0.34	93.62
	2004 XZ130	2026/09/18	201.5318	2027/04/08	0.72	167.80
	2008 UL90	2028/08/10	185.0003	2029/02/11	0.29	57.46
TOT.					3.61	1273.60

dered is $I_{sp} = 3000$ s. The number of thrust legs for each transfer can vary between $n_{LT} = 2$ and $n_{LT} = 8$ and the initial acceleration for the continuation method varies between 1 and 25 times the nominal acceleration, that is, K goes from 1 to 25. The final solution for each transfer is the one obtained with the number of thrust arc n_{LT} and the initial acceleration value for the continuation method that provide the lower ΔV. Following the strategy described in Section 8.7.4, the spacecraft is injected into an interplanetary orbit that meets the first asteroid without any thrust leg. After the first fly-by the engine is switched on to achieve the remaining five fly-by's. The resulting low-thrust trajectory is reported in Table 8.5 and shown in Figure 8.7, where the thrust arcs are in black and the coast arcs are in gray.

Transfer to the surveillance orbit

The transfer to the surveillance orbit using only a low-thrust spiral is reported in Table 8.6 and Figure 8.8.

Table 8.5: Summary of the simulation results for the low-thrust trajectory.

	Asteroid	Time Engine On [days]	m_0 [kg]	m_f [kg]	ΔV [km/s]
	2013 JX28	0	700	700	-
	2006 WE4	129.05	700	673.45	1.12
	2004 JG6	152.57	673.45	642.07	1.37
	2012 VE46	41.77	642.07	633.47	0.40
	2004 XZ130	158.40	633.47	600.89	1.51
	2008 UL90	30.04	600.89	594.17	0.30
TOTAL					4.70

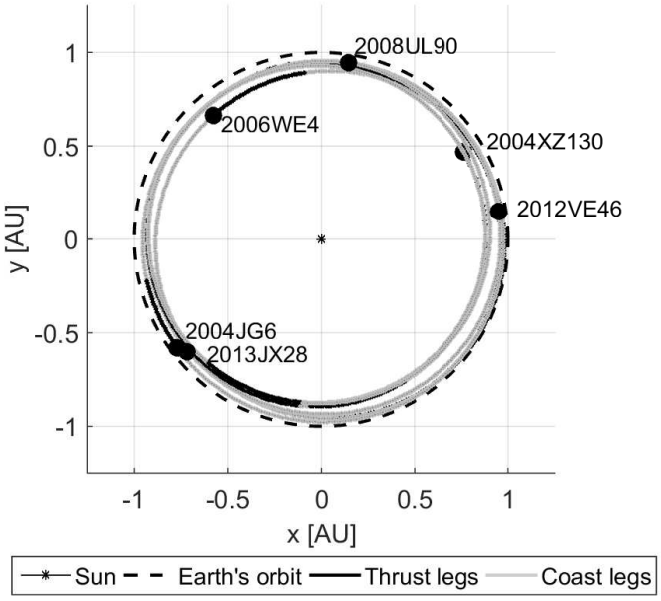

Figure 8.7: Low-thrust trajectory to visit six Atira asteroids at their nodal points. Coast legs are shown in gray and thrust legs in black.

Table 8.6: Summary of transfer to surveillance orbit after final fly-by using a low-thrust spiral.

Departure date	ToF [days]	Engine on [days]	Arrival date	m_0 [kg]	m_f [kg]	ΔV [km/s]
2029/02/11	421.78	176.83	2030/04/09	594.17	557.80	1.79

The total ΔV for this option is:

$$\Delta V_{fly-by} + \Delta V_{parking-orbit} = (4.70 + 1.79)\,\text{km/s} = 6.49\,\text{km/s}. \tag{8.24}$$

In this case the low-thrust engine enables the entire mission to be achieved with approximately 145 kg of propellant, so that a spacecraft with a dry mass of 555 kg (Table 8.6) can be brought to the final surveillance orbit starting from a launch mass of 700 kg. This is a remarkable

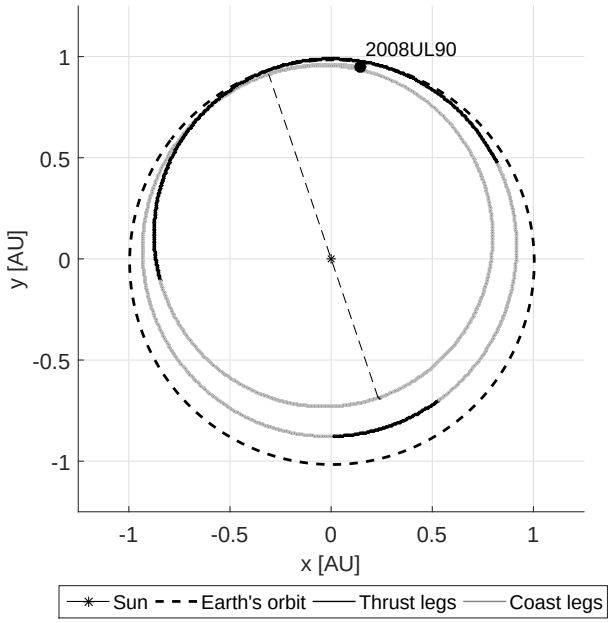

Figure 8.8: Transfer to parking orbit using electric propulsion.

improvement over the propellant mass required for a chemical propulsion system (Table 8.4). The semi-major axis variation and the thrust angle profile during the trajectory are reported in Figure 8.9, together with a 0/1 flag representing the Off/On conditions of the engine. The fly-bys are indicated by the vertical lines.

A reduction of the ΔV required to lower the perihelion is theoretically achievable by exploiting multiple shallow swing-by's of the Earth (see strategy 2 in Section 8.4). However, after the last fly-by the orbit of the spacecraft has a perihelion equal to 0.8755 AU and an aphelion equal to 0.9633 AU. In this configuration the maximum variation of perihelion is limited to 0.0012 AU per revolution of the spacecraft, which implies a very slow transfer to the target surveillance orbit. The use of the Earth resonances has, therefore, not been considered further in this study.

The transfer to the surveillance orbit using one swing-by of the Earth, instead, takes 564.91 days. The minimum altitude from the Earth during the swing-by is 535.37 km and the total ΔV to achieve the surveillance orbit is 1.27 km/s, against the 1.79 km/s required for a direct low-thrust spiral. The transfer is shown in Figure 8.10, where thrust arcs are in black and coast arcs in gray. The coast leg before the encounter with the Earth lasts 63.78 days. Details of the transfer are given in Table 8.7.

Table 8.7: Summary of transfer to surveillance orbit with gravity assist of the Earth.

Departure date	ToF [days]	Engine on [days]	Arrival date	m_0 [kg]	m_f [kg]	ΔV [km/s]
2029/02/11	564.91	125.24	2030/08/29	594.17	568.41	1.27

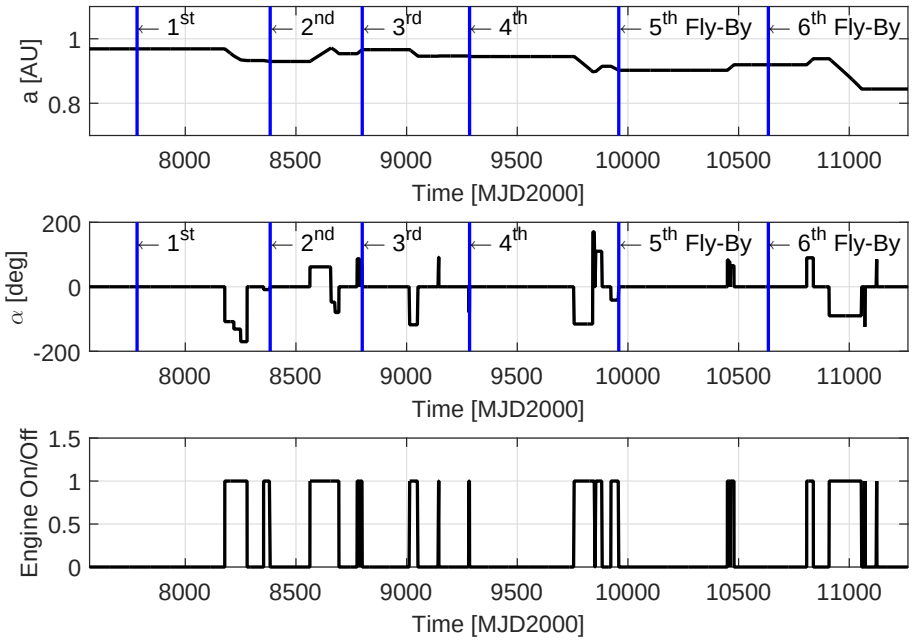

Figure 8.9: Semi-major axis, thrust angle α', and switching function profiles for low-thrust trajectory.

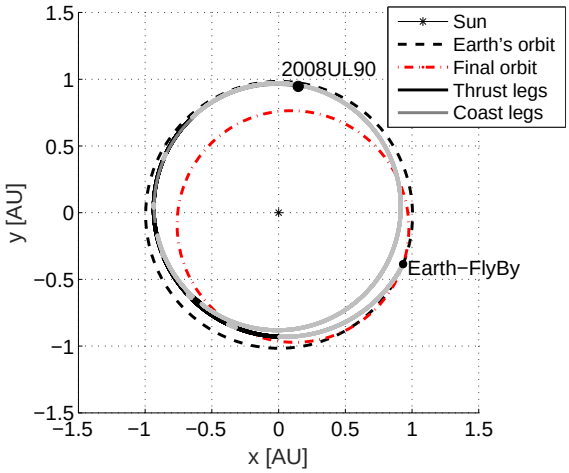

Figure 8.10: Transfer to parking orbit realised with gravity assist from the Earth.

8.7.4 Launch and orbit injection

In this section it is demonstrated that the launch and orbit injection strategy proposed in Section 8.5 can be realised with the Indian Space Research Organisation GSLV-D6 (Geosyn-

chronous Satellite Launch Vehicle)[3], provided that a restartable upper stage is available. The GSLV-D6 places the spacecraft on a GTO with the following orbital elements :

Altitude of perigee	$h_{\oplus p,GTO} = 170$ km
Altitude of apogee	$h_{\oplus a,GTO} = 35,975$ km
Inclination	$i_{GTO} = 19$ deg
Argument of perigee	$\omega_{GTO} = 178$ deg

The heliocentric velocity of the spacecraft at departure from Earth and its geocentric declination are computed with the equations given in Section 8.5, resulting in $\|\mathbf{v}_\infty\| = 0.65$ km/s and $\delta = -23.26$ deg.

If a manoeuvre to inject the spacecraft into the hyperbolic orbit was to be realised at the perigee of the GTO orbit, the following orbital parameters, computed using Equations 8.5 to 8.7, would be obtained for the hyperbolic orbit: $a_{hyp} = -9.41 \cdot 10^5$ km, $e_{hyp} = 1.007$ and $\theta = 173.22$ deg. However, for these values of δ and θ and using $\omega_{GTO} = 178$ deg, Equation 8.4 yields $\sin i > 1$. Since δ is defined by the geometry of the initial velocity, a change of i and ω is required to insert the spacecraft into the appropriate hyperbolic orbit, as described in Section 8.5. The admissible values of i_{inj} for the considered values of δ and for $\omega_{inj} \in [0, 2\pi]$ are shown in Figure 8.11a. The ΔV required for the change of inclination (first manoeuvre) for different values of i_{inj} is shown in Figure 8.11b while the ΔV for the injection into the hyperbolic orbit is shown in Figure 8.12a. Finally, the total ΔV is shown in Figure 8.12b.

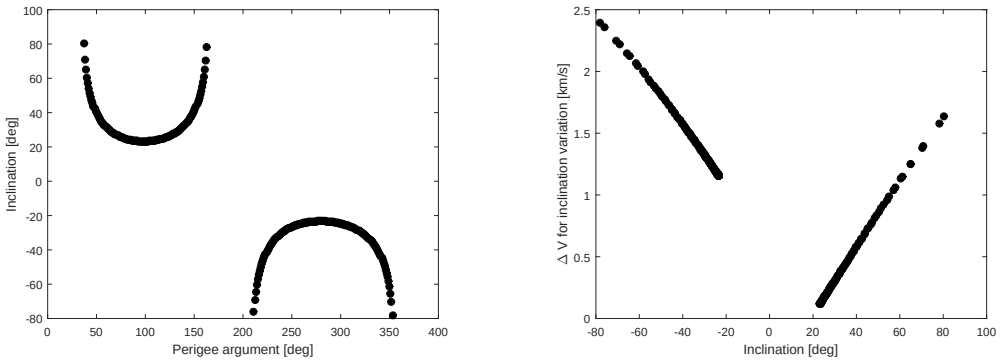

(a) (b)

Figure 8.11: (a): values of i_{inj} for different values of ω_{inj} allowing injection into the hyperbolic orbit. (b): ΔV for the variation of inclination from i_{GTO} to i_{inj} for different values of i_{inj} (on the x axis).

The minimum of ΔV_{total} is found for $\omega_{inj} = 158$ deg and $i_{inj} = 54.98$ deg. The inclination change requires $\Delta V = 0.99$ km/s. The perigee variation and injection into hyperbolic orbit requires a further $\Delta V = 1.74$ km/s, for a total velocity variation equal to $\Delta V = 2.73$ km/s.

[3]Indian Space Research Organisation - `http://www.isro.gov.in/launcher/gslv-d6`

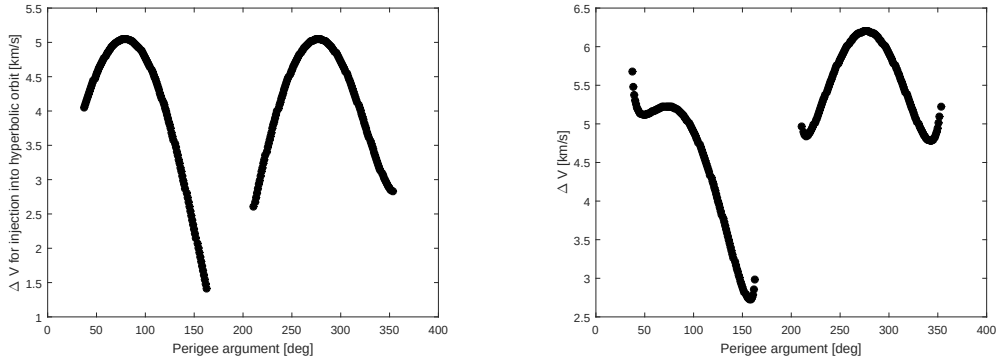

(a) (b)

Figure 8.12: (a): ΔV for the injection into the hyperbolic orbit for different values of ω_{inj} (on the x axis). (b): Total ΔV required to realize the two manoeuvres for the injection into the hyperbolic orbit for different values of ω_{inj} (on the x axis).

Considering a mass of the spacecraft of 700 kg and an upper stage with a dry mass of 300 kg and an I_{sp} of 400 s, the propellant required to inject the spacecraft into the hyperbolic orbit from the initial GTO orbit is 1004 kg and, therefore, the total launch mass is:

$$m_{SC} + m_{U/S} + m_p = (700 + 300 + 1004) \text{ kg} = 2004 \text{ kg}. \tag{8.25}$$

It is important to stress that the value of $I_{sp} = 400$ s for the specific impulse of the upper stage is different from the value of the specific impulse of the chemical engine defined in Section 8.7.1 ($I_{sp} = 321$ s), because it refers to a different engine.

The dry mass and propellant mass of the upper stage corresponds to a propellant mass fraction equal to 0.77. Based on the launch history and on future planned missions, GSLV-D6 has an upper limit of 2330 kg in GTO. It would thus accommodate the spacecraft and upper stage leaving a mass margin of 326 kg.

8.7.5 Visibility analysis

The number and type of asteroids that can be potentially detected over the mission lifetime are estimated by running 100 visibility simulations each with a different synthetic populations of 10^6 IEO, Atens and Apollos. The constraints chosen for the observations are:

- observations are only carried out when the low-thrust engine is off, at intervals of 5 days;
- the angle ψ (angle Sun-spacecraft-asteroid) is set to 45 degrees so that the camera does not point directly towards the Sun;
- the declination of the camera is zero degrees as the maximum population of asteroids is close to the ecliptic;
- the limiting relative magnitude of the camera is 19.5 and its FOV is 12 deg;

- the phase angle ϕ (angle Sun-asteroid-spacecraft) has to be lower than 120 degrees.

For the simulations a mean albedo of 0.154 is considered. Figure 8.13 shows a schematic representation of the geometry of observation. The blue arrow represents the direction of the instrument, oriented toward the inner part of the orbit; the red arrow is the spacecraft's velocity vector. The dots represent the asteroids detected during the observation.

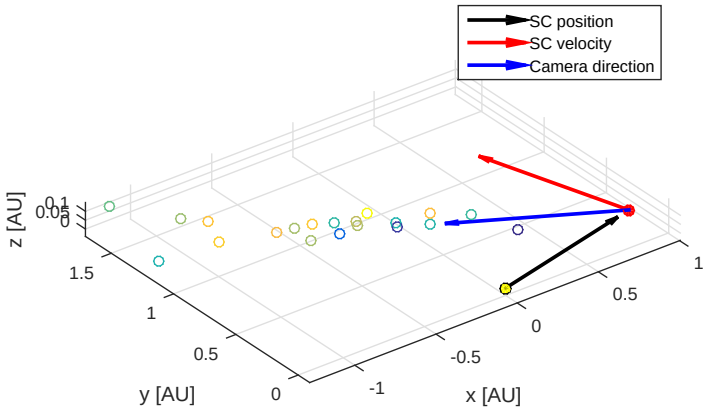

Figure 8.13: Representation of the asteroids observation.

Figure 8.14 shows the distribution of objects, in the $a-e$ plane, for the known and synthetic populations of IEOs, Atens and Apollo.

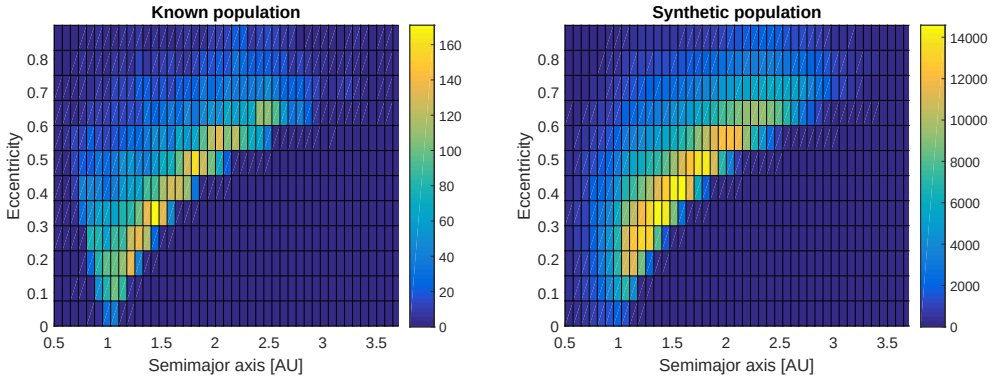

Figure 8.14: Distribution, in the $a-e$ plane, of the known and synthetic populations of IEOs, Atens and Apollos

Table 8.8 shows the results of the 100 simulations for the observations made by the spacecraft over the entire mission time, considering both the synthetic and known NEAs population. The table reports the number of unique Atira, Aten and Apollo asteroids (no repetition of the same asteroids between one observation and the next) observed during the entire mission. Also the diameters of the observed asteroids in each group are presented. Out of the observed NEAs reported in Table 8.8, 3 Atira, 32 Aten and 108 Apollo belong to the known NEAs population.

Table 8.8: Results of the visibility analysis using the synthetic and known populations of NEAs.

	Min	Mean	Max
Number observed Atira	26	39	60
Number observed Aten	77	96	120
Number observed Apollo	329	364	405
	Min	Mean	Max
Diameter observed Atira [km]	0.0989	0.9864	8.1168
Diameter observed Aten [km]	0.0814	1.1568	8.4291
Diameter observed Apollo [km]	0.0637	1.5946	8.5027

The distribution of the diameter of the observed NEAs is shown, for diameter smaller than 10 km, in Figure 8.15.

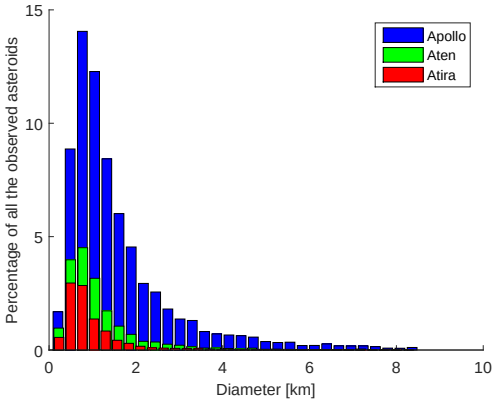

Figure 8.15: Distribution of the diameter of the observed objects for diameter between 0 and 10 km.

Results show that a mean value of 39 IEOs could be detected during the mission lifetime. The mission would also allow to observe, on average, 96 Atens and 364 Apollos. The distribution of the diameter of the observed asteroids of the synthetic populations (Figure 8.15) shows that most of the observed asteroids have diameter lower than 2 km. In particular, 32 objects with diameter lower than 0.5 km can be observed.

8.8 Conclusions

This chapter has presented a multiple-asteroid tour to visit the Atira asteroids using low-thrust propulsion, while conducting observations of the inner region of the solar system in order to possibly detect new NEAs. Hundreds of sequence of asteroid are found by a deterministic branch and prune procedure considering impulsive transfers for different departure and encounter dates and assuming fly-by of the asteroids at their nodal points. The best solution

found with this simple procedure is first refined using the single population version of MP-AIDEA and then translated into an optimised low-thrust transfer. It has to be noted that the approach proposed in this chapter does not provide an optimal solution in the optimal control sense but a feasible solution with a conservative estimation of the propellant cost. A further improvement is, therefore, expected by relaxing some of the terminal constraints and solving a more accurate optimal control problem. Results show that six asteroids of the Atira group can be visited through fly-by's over a period of approximately 8.4 years, with a small compact 700 kg spacecraft launched by a GSLV-D6. Results demonstrate that the tour of the Atira asteroids offers two additional opportunities. After the last asteroid the spacecraft can be placed, with a swing-by of the Earth, on a surveillance orbit with perihelion at Venus. This orbit offers a vantage point to observe and monitor the asteroids in the inner solar system. Furthermore, during the whole mission lifetime an asteroid survey campaign, using a small and compact instrument, can potentially discover on average 364 additional Near Earth Asteroids out of which 39 could belong to the IEO group.

The database of objects considered for this study included 12 asteroids. In the next chapter the design of a low-thrust mission to the main asteroid belt is proposed. When considering the main asteroid belt, the number of potential targets is orders of magnitude higher than the the number of asteroids in the Atira group. The approach used to solve the combinatorial problem, in the next chapter, will therefore be different from the one proposed in this chapter, since the evaluation of all the possible combinations of asteroids is not possible when the number of objects in the database is large. Moreover, different pruning methods and different strategies to move to the region of interest in the solar system are introduced.

The content of this chapter was published in M. Di Carlo, M. Vasile, J. Dunlop "Low-thrust tour of the main belt asteroids", Advances in Space Research, Accepted/In Press

Chapter 9

Low-thrust mission to the main belt asteroids

This chapter presents some results on a possible tour of the main asteroid belt using solar electric propulsion, where the length of the tour is constrained by the total mission time and the desirable launch capability. Two scenarii are considered: in the first scenario the database of target objects includes scientifically interesting bodies and tries to find the longest sequence of objects in a given time and ΔV budgets; in the second scenario, more than 100,000 objects are added to the previous database and the aim is to find the longest sequence of asteroids that contains also some (more than 0) scientifically interesting targets. Note that the number of possible targets is in this case about one order of magnitude larger than the one of previous GTOC competitions. The analysis proceeds, as in the first scenario, with the study of all optimal sequences that are achievable with a given time limit and ΔV budget.

In order to limit the total mission time and propellant cost, the strategy proposed is to initially transfer the spacecraft to an elliptical orbit with perihelion at (or near) the Earth and aphelion at the main belt and then adjust the trajectory to fly-by the largest number of objects. Each asteroid is expected to be visited with one single fly-by only.

The resulting combinatorial problem is solved with a combination of two simple pruning techniques. The first pruning is on the Minimum Orbit Interception Distance between the initial orbit and the asteroids in the database. After this first pruning a deterministic branch and prune algorithm is applied to a binary tree that incrementally constructs the optimal sequence of targets. Finally, the best solution is re-optimised with electric propulsion.

The direct transcription method presented in Chapter 5 and the asymptotic analytical solutions to the accelerated Keplerian motion (Chapter 4) are used to transcribe the optimal control problem that defines the optimal control profile of the engine. With the same transcription approach, also the transfer from the Earth to the first orbit traversing the main belt is optimised.

The attention is limited to transfer options that do not include swing-by's of the planets of the inner solar system; this reduces the complexity of the mission and remove the constraints on the launch window time. The transfer from the Earth to the main belt is, instead, concei-

ved to exploit at best the use of the launcher and the electric propulsion system. The launch feasibility, using two possible launchers, is also studied.

The chapter is structured as follows: Section 9.1 gives a description of the main belt of asteroids and presents previous analysis for missions aimed at visiting its asteroids. The proposed solution method to define a mission to the main belt is presented in Section 9.2. The results are then presented in Sections 9.3 and 9.4. Section 9.5 concludes this chapter.

9.1 The asteroids main belt

The main belt houses the majority of the asteroids in the solar system. It extends from 2.1 AU to 4 AU [142] and is estimated to contain several million asteroids, ranging in size from few millimeters to the 959 km diameter of Ceres [140]. Although larger asteroid are observable from Earth and are easy to identify, the classification of smaller objects still remains an open problem. Furthermore, there is an interest in the characterisation of the larger ones to better understand their composition and evolution from the primordial stages of the solar system till now. Key information on the composition of objects in the main belt can only be obtained from space-based spectroscopy and close encounter analyses. A mission that could visit at least ten objects will double the number of asteroids visited to date. However, designing a mission to characterise that many asteroids in the main belt is not an easy task. The main difficulty is to identify long sequences of asteroids that can be visited in a given time and with limited ΔV. The number of known objects exceeds 641,933[1] and the number of possible combinations of encounter is unmanageable.

The mission currently targeting objects in the main belt, Dawn[2], is visiting only two protoplanets using low-thrust propulsion. After visiting Vesta in 2011-2013, Dawn is now exploring the dwarf planet Ceres.

Previous works on the design of asteroid tours divide the design process into different steps [148]: the first step consists in the definition of a shortlist of potential targets, based on their orbital elements, dimensions or scientific characteristics. In the second step a sequence of target objects is selected using some form of global optimisation [6], in combination with reduced models that provide a quick estimation of the cost of the transfer. The last step is the optimisation of the sequence with a local optimisation method. An impulsive mission to visit asteroids in the main belt is presented in [185]: the objective of the proposed mission is to fly-by 10 or more asteroids in 7 years in the timeframe 2029-2030, using a Soyuz launch and gravity assist from Mars. The search of the combinatorial problem, solved by a branch and bound exploration, is driven by the assumption that all asteroid's fly-bys occur at the asteroid Minimum Orbital Intersection Distance (MOID) point. The use of gravity assist to reach the main belt is studied in [44], where the results of an analysis of accessibility for 200 asteroids in the main belt with diameter greater than 100 km are presented. The global minimum of the cost of the transfer to these asteroids, using gravity assists with Mars or Earth, is evaluated. Results

[1] http://ssd.jpl.nasa.gov/sbdb_query.cgi#x
[2] http://dawn.jpl.nasa.gov/

show that Mars is the most useful gravity-assist body and that dual gravity assists with Mars are the best type of trajectories to reach mid or outer belt asteroids and high-inclination ones. The low-thrust transfer to one of the considered asteroids, Flora, is presented. The problem is solved with indirect methods and homotopic approach. In [187] a study of the accessibility of more than 600,000 main belt asteroids is presented, considering rendezvous realised through globally optimal two-impulse or Mars gravity-assist transfers. The accessibility is modelled using a Gaussian Process Regression using 820 training points for the two-impulse case and 1620 training points for the Mars gravity-assist case. Results confirm that the ΔV requirement is reduced for transfers to the main belt that use Mars gravity assist. Mars' gravity assists to reach the main belt are also proposed in [232]. The transfer from a near-Earth asteroid to a main belt asteroid, using low-thrust propulsion and multiple gravity assists, is studied. Based on an analysis of the Tisserand graph, the Earth-Mars-Mars gravity assists sequence is found to be the best option to reach the main belt. A global solver is then used to obtain the event dates for the gravity assists and the deep space manuevers, using an impulsive model for the transfers. Finally, the optimal control problem for the design of low-thrust trajectories is solved using an indirect method and homotopic approach.

In recent times, the problem of visiting multiple asteroids has been part of the objective of some Global Trajectory Optimisation Competitions (GTOC)[3]. In particular, in GTOC4 the problem is to identify the maximum number of asteroids' fly-bys from a given list of 1438 objects, considering a rendezvous with the last asteroid in the sequence and a total mission time of ten years. GTOC5 also proposes a mission to Near Eearth Asteroids, considering a database of 7073 objects, while GTOC7 presents a multi-spacecraft exploration of the asteroid belt and a database of 16256 potential targets. For GTOC4, the first ranking team found a solution visiting 44 asteroids [88]. They solved the discrete part of the problem (the identification of the optimal sequence of asteroids to visit) using dynamic programming, performing the construction of the solution vector step by step and optimising time and mass consumption at each step. The trajectory is approximated with a solution of the Lambert problem. In [121], an algorithm called HDDP (Hybrid Differential Dynamic Programming) is used, a variant of the classical Differential Dynamic Programming technique. The multi-phase formulation of HDDP is used by splitting the trajectory into several portions connected by the fly-bys at the asteroids. The initial guess is obtained from a ballistic Lambert solution that provides the asteroid sequence. The solution is characterised by 24 fly-bys and 1 rendezvous.

This chapter presents some results on a possible tour of the main asteroid belt using solar electric propulsion where the length of the tour is constrained by the total mission time and the desirable launch capability.

9.2 Mission design overiew

In this work two databases of objects in the main belt are considered. The first database (Database 1) includes a selection of 424 objects of particular scientific interest ("CASTAway" propo-

[3] https://sophia.estec.esa.int/gtoc_portal/

sal's PI, personal communication[4]). These are, among others, active objects (main belt comets, mass losing asteroids), objects of extreme sizes (both small and big) and extreme shapes, fast rotators, binaries or triples and asteroid pairs. The second database (Database 2) is composed of 101,993 objects [185]. The distribution of semi-major axis a, eccentricity e and inclination i of the objects of the two databases is shown in Figures 9.1 and 9.2, where the curve $q = Q_{Mars}$ identifies the values of a and e such that the perihelion q is equal to the aphelion of Mars Q_{Mars}, while $Q = q_{Jup}$ identifies the values of a and e such that the aphelion Q is equal to the perihelion of Jupiter. Note that, although the complete Database 2 contains also asteroids with perihelion at Jupiter, in this analysis the attention is restricted to asteroids that are part of the main belt.

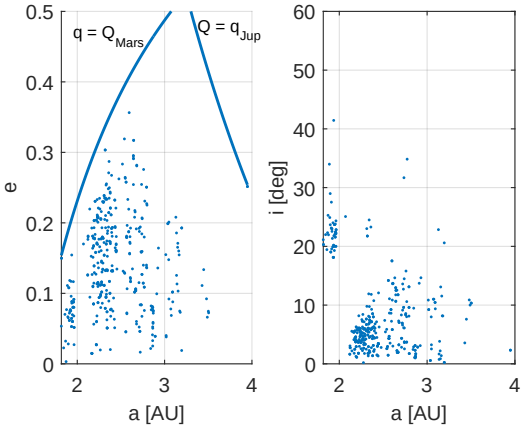

Figure 9.1: a-e and a-i distribution of the selected objects in the main belt for Database 1.

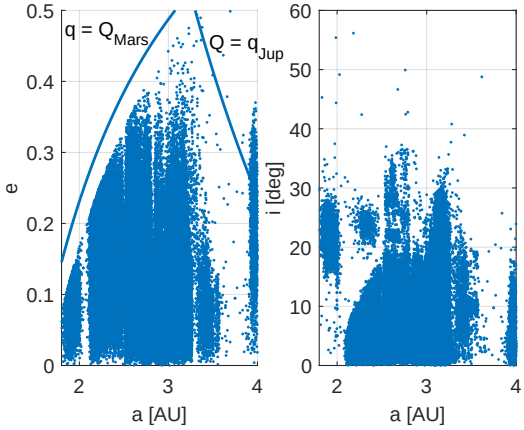

Figure 9.2: a-e and a-i distribution of the selected objects in the main belt for Database 2.

The design of the mission is divided in five steps. These are briefly introduced in the following and described in more details in the next subsections:

1. analysis of the MOID between different possible initial orbits of the spacecraft traversing the main belt and the orbits of all the asteroids in the database (Subsection 9.2.1);

2. study of the sequence of asteroids to visit using the results obtained from the computation of the MOID and a model with impulsive transfer between asteroids (Subsection 9.2.2);

3. optimisation of the parameters of the initial orbit in the main belt, of the times of the impulsive maneuvers and of the times of the encounters with the asteroids to reduce the ΔV associated to the mission (Subsection 9.2.3);

4. study of the transfer from the Earth to the main belt (Subsection 9.2.4) and of the launch of the spacecraft;

[4] https://sites.google.com/site/castawaymission/

5. optimisation of the low-thrust transfer to the main belt and of the tour of the selected sequence of asteroids (Subsection 9.2.5).

The tour of the main belt is assumed to start on the 01/01/2030 with a maximum duration of 5 years. Note that other dates around the 01/01/2030 were analysed but only the results for the 01/01/2030 are presented, as they are the most significant (Section 9.4.2).

9.2.1 Minimum Orbit Intersection Distance

In order to identify the initial orbit of the spacecraft and shortlist the asteroids to encounter, the Minimum Orbit Intersection Distance (MOID) [89, 90] between all the asteroids in the database and different possible initial orbits of the spacecraft is computed. The MOID is defined as a measure for the distance between the orbits of two objects. The computation of the MOID is realised using the Fortran code publicly available online from the Department of Mathematics of the University of Pisa, Italy[5]. The computation of the MOID returns, for each pair spacecraft's orbit-asteroids's orbit, the minimum, maximum and saddle points of the distance between the two orbits. These critical points are identified by the true anomalies θ_{ast}^{MOID} and θ_{sc}^{MOID} of the two objects on their orbit and by the distance between them at the critical points, d. In this study only points with $d < 0.01$ AU are considered. The computation of the MOID does not consider, however, the positions that the asteroids and spacecraft occupy on their orbits [28]. This means that an encounter between spacecraft and asteroid can not actually take place if the two bodies are not, at the same time, at θ_{ast}^{MOID} and θ_{sc}^{MOID}. In order to check which encounters at the MOID can be actually be realised, the following phasing analysis is applied:

- for each couple spacecraft's orbit - asteroid's orbit with $d <$ 0.01 AU, the times when the asteroid is at θ_{ast}^{MOID} are computed, starting from the initial date 01/01/2030, $t_0 = 10957.5$ MJD2000. These times, that repeat at intervals equal to the orbital period of the asteroid, are identified as T_{ast}^{MOID};
- different initial mean anomalies M_0 in the range $[0, 360)$ deg, at steps of 1 deg, are considered for the spacecraft on its orbit, with initial date t_0;
- Kepler equation is solved to obtain the true anomaly of the spacecraft at T_{sc}^{MOID}, $\theta_{sc}(T_{ast}^{MOID})$, starting from M_0 at t_0. If the following condition is satisfied

$$|\theta_{sc}(T_{ast}^{MOID}) - \theta_{sc}^{MOID}| < \delta \,, \tag{9.1}$$

  then the encounter between asteroid and spacecraft, at distance $d <$0.01 AU, actually takes place at time T_{ast}^{MOID}. δ is an appropriate small angle.

9.2.2 Study of the possible sequences of asteroids

At the end of the process defined in the previous subsection, for each value of M_0 (angular position of the spacecraft on the initial orbit at time t_0), a list of asteroids that encounter the

[5] http://adams.dm.unipi.it/~gronchi/HOMEPAGE/research.html

spacecraft at distance lower than 0.01 AU is available. The next step consists in computing the ΔV required to fly-by these objects. The cost of the transfer between one asteroid and the next is computed with a Lambert solver [204]. The total cost is given by the sum of all the ΔV_j, $\Delta V = \sum_j \Delta V_j$. Encountering each asteroid in the sequence could be however too expensive in terms of ΔV. This study, therefore, tries to identify a subset of objects, in the list of asteroids, that can be visited with a cost lower than a maximum allowable total ΔV_{max}. In order to do so, for a sequence of n asteroids, a vector $\mathbf{b}$ of length N_a composed of 0's and 1's is defined to identify which asteroids are encountered (1) and which ones are not (0). As a result, 2^{N_a} sequences, each characterised by a different number of visited asteroids and different values of ΔV, are available and need to be evaluated. An enumerative approach to evaluate all the 2^{N_a} possibilities is not practical when N_a is large. Thus, a deterministic Branch and Prune Approach (BPA) is applied. The BPA incrementally builds a binary tree in which each level corresponds to one of the N_a components in $\mathbf{b}$ and each branch is a sequence. At each level each branch is divided in two sub-branches, one with leaf with value 1 and one with leaf with value 0. Then each partial branch is evaluated. If the ΔV associated to the partial branch exceeds a given threshold the whole branch is discarded. A graphical representation of the binary tree and of its working mechanism is given in Figures 9.3 and 9.4.

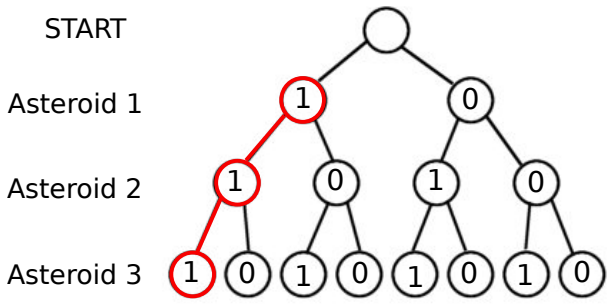

Figure 9.3: Representation of the binary tree. Branches with ΔV higher than threshold (example, in red in the figure) are discarded.

After this process, for each value of M_0 on the initial orbit, the vector $\mathbf{b}$ is translated into a list of N asteroids $\mathcal{A} = \{A_1, A_2, A_3, \dots A_N\}$, with $N \leq N_a$ and $\Delta V \leq \Delta V_{max}$. The initial orbit of the spacecraft is defined by means of its orbital elements $\mathcal{OE} = \{a, e, i, \Omega, \omega, M_0, t_0\}$, where M_0 is the mean anomaly at time t_0. The dates of the encounters are defined as $\mathcal{T} = \{T_1, T_2, \cdots T_N\}$.

9.2.3 Optimisation of the sequence of asteroids

The solution found at the previous step assumes that the encounters with the asteroids take place when they are at their critical true anomalies, θ_{ast}^{MOID}, starting from an initial orbit identified by $\mathcal{OE}$. A better solution might however exist and could be found by changing some of the parameters of the initial orbit $\mathcal{OE}$ (the initial mean anomaly M_0, the semi-major and eccen-

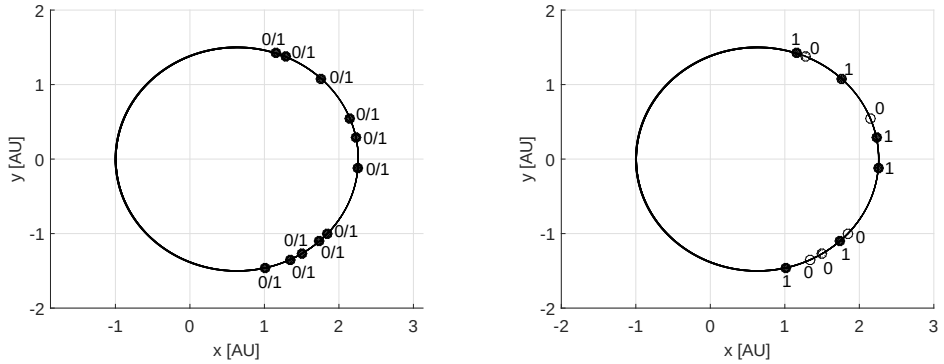

Figure 9.4: Identification of the sequence of asteroids to visit using the binary tree. Each asteroid in the sequence can be assigned a value equal to 0 or 1 (left); only asteroids with associated value of 1 are visited (right).

tricity a and e and the argument of perihelion ω) or by changing the dates of encounters with the asteroids $\mathcal{T}$, that is by encountering the asteroids not exactly at θ_{ast}^{MOID}. In order to find a better solution, a continuous global optimisation problem is solved, in which the objective is the minimisation of the total ΔV. The upper and lower bounderies for the global optimisation problem are defined by the vectors $\mathbf{x}^L$ and $\mathbf{x}^U$:

$$\mathbf{x}^L = [M_0 - \Delta M_0, a - \Delta a, e - \Delta e, \omega - \Delta\omega, T_1 - \Delta T_1, T_2 - \Delta T_2, \dots T_n - \Delta T_n]^T, \tag{9.2}$$

$$\mathbf{x}^U = [M_0 + \Delta M_0, a + \Delta a, e + \Delta e, \omega + \Delta\omega, T_1 + \Delta T_1, T_2 + \Delta T_2, \dots T_n + \Delta T_n]^T . \tag{9.3}$$

The global search is realised using the global optimiser MP-AIDEA (Chapter 7).

9.2.4 Transfer from the Earth to the main belt

This section describes the transfer strategy from the Earth to the first orbit in the main belt, $\mathcal{OE} = \{a, e, i, \Omega, \omega, M_0, t_0\}$. The transfer is realised by injecting the spacecraft into an intermediate phasing orbit, characterised by orbital elements $\mathcal{OE}_{int} = \{a_{int}, e_{int}, i, \Omega, \omega, 0, T_L\}$ and orbital period T_{int}. T_L is the date of the launch of the spacecraft and the corresponding mean anomaly is zero because, at launch, the spacecraft is at the perihelion of the interplanetary orbit (Earth). The ΔV required for the launch, ΔV_L, is computed using

$$\Delta V_L = \sqrt{2\frac{\mu_\odot}{r_\oplus} - \frac{\mu_\odot}{a_{int}}} - \sqrt{\frac{\mu_\odot}{r_\oplus}}\,, \tag{9.4}$$

where $\mu_\odot$ is the Sun's planetary constant and $r_\oplus$ is the Sun-Earth distance. The spacecraft remains on the intermediate phasing orbit for an integer number n_{rev} of revolutions. After n_{rev} revolutions, when the spacecraft is at the perihelion $r_\oplus$ of the intermediate phasing orbit,

ΔV_M is applied to reach the final orbit of semi-major axis a:

$$\Delta V_M = \sqrt{2\frac{\mu_\odot}{r_\oplus} - \frac{\mu_\odot}{a}} - \sqrt{2\frac{\mu_\odot}{r_\oplus} - \frac{\mu_\odot}{a_{int}}} \,. \tag{9.5}$$

The spacecraft moves then for a time

$$\Delta T = \frac{M_0 - M_p}{n} \tag{9.6}$$

on the orbit $\mathcal{OE}$. In the previous equation M_0 is the mean anomaly on the first orbit in the main belt at t_0, $M_p = 0$ deg is the mean anomaly at perihelion and n is the mean motion of the orbit $\mathcal{OE}$. For every value of n_{rev}, T_{int} has to be such that at the computed time of the launch, T_L,

$$T_L = t_0 - \Delta T - n_{rev} T_{int} \,, \tag{9.7}$$

the Earth is at the perihelion of $\mathcal{OE}$. This allows one to identify the value of T_{int}, and, therefore, the intermediate phasing orbit $\mathcal{OE}_{int}$, for every $\mathcal{OE}$ and n_{rev}.

The method described above provides an impulsive solution for the transfer from Earth to $\mathcal{OE}$ based on the assumption that the spacecraft is injected by the launcher or an upper stage into $\mathcal{OE}_{int}$. When the actual launch capabilities are considered the ΔV required to inject the spacecraft into the orbit $\mathcal{OE}_{int}$, by means of an escape hyperbola characterised by $V_\infty = \Delta V_L$, is the sum of two contributions:

$$\Delta V_{total} = \Delta V_i(i_{inj}, \omega_{inj}) + \Delta V_{inj}(i_{inj}, \omega_{inj}) \,, \tag{9.8}$$

where $\Delta V_i(i_{inj}, \omega_{inj})$ and $\Delta V_{inj}(i_{inj}, \omega_{inj})$ are, respectively, the ΔV required to change inclination from the orbit where the launcher is injecting the spacecraft to the escape hyperbola and the ΔV required to reach the required escape velocity. These ΔV's are a function of i_{inj} and ω_{inj}, the inclination and argument of the pericentre of the escape hyperbola. The calculation of these two ΔV's follows the approach presented in Chapter 8, Section 8.5. No consideration is done about the right ascension of the asymptote because any required right ascension of departure may be achieved by changing the time of day at which the spacecraft is launched [108]. Once ΔV_{total} has been found, the dry and propellant masses of the upper stage, $m_{dry}^{U/S}$ and $m_p^{U/S}$, can be computed as

$$\begin{aligned} &\frac{m_p^{U/S}}{m_p^{U/S} + m_{dry}^{U/S}} = k \,, \\ &m_0 + m_{dry}^{U/S} = \left(m_{dry}^{U/S} + m_p^{U/S} + m_0\right) \exp\left(-\frac{\Delta V_{total}}{I_{sp}^{U/S} g_0}\right) \,, \end{aligned} \tag{9.9}$$

where k and $I_{sp}^{U/S}$ are the propellant mass fraction and specific impulse of the upper stage and m_0 is the initial wet mass of the low-thrust spacecraft. Here it is assumed that the launcher injects the spacecraft in a Geostationay-Transfer Orbit (GTO). The total payload mass that the

launcher has to inject into GTO is, therefore, $m_{pl} = m_0 + m_p^{U/S} + m_{dry}^{U/S}$.

9.2.5 Low-thrust optimisation

The low-thrust optimisation process determines, for each transfer leg found using the process outlined in the previous sections, an optimal control history, for the low-thrust engine, to depart from one asteroid and reach the following asteroid in the sequence at a given time. The same process is applied also to optimise the transfer from Earth to $\mathcal{OE}$. The direct transcription method presented in Section 5.2 and the analytical model of Chapter 4 (constant low-thrust acceleration in the RTN reference frame) are used. The initial mass of the spacecraft at launch m_0 is set to a predefined value of 1000 kg. Note, however, that this assumption does not limit the validity of the results as any other initial mass at launch m_0' can be used, provided that the thrust magnitude is scaled by the ratio m_0'/m_0. For the trajectories considered in this study, the angle β is set to zero, since the transfers are all on the ecliptic plane and require no change of inclination (Section 9.3 and 9.4). This is a consequence of the assumptions and methods described in Section 9.2: the fly-bys of the asteroids take place at the MOID points of the spacecraft's heliocentric elliptic orbit and asteroids' orbits.

9.3 Results Database 1

The first search for optimal tours considers the asteroids in the database of scientific interesting asteroids (Database 1). This section presents the results of the scan of all possible sequences, with estimated cost lower than $\Delta V_{max} = 1$ km/s, and the low-thrust optimisation of the most promising solution.

9.3.1 Minimum Orbit Intersection Distance

The MOID is computed between all the asteroids in the database and different orbits of the spacecraft identified by the orbital elements in Table 9.1. In particular, the aphelion r_a is sampled at steps of 0.2 AU, and the inclination i and the argument of periapsis ω are sampled at steps of 5 deg. The spacecraft orbits are elliptical, with perihelion r_p at the Earth and aphelion r_a in a given range of distances from the Sun.

Table 9.1: Orbital elements of the different possible initial orbits of the spacecraft used for the computation of the MOID with the asteroids of Database 1.

r_p [AU]	r_a [AU]	i [deg]	Ω [deg]	ω [deg]
1	[1.8, 4]	[0, 30]	0	[0, 360]

Figure 9.5 shows, for the considered values of r_a, ω and i, the number of asteroids with $d < 0.01$ AU with respect to the orbit of the spacecraft. Results show that the maximum of this number increases with decreasing inclination. As the inclination increases a dependence on

the argument of the perihelion of the orbit become also evident and large regions where the number of asteroids with $d < 0.01$ AU is zero appear.

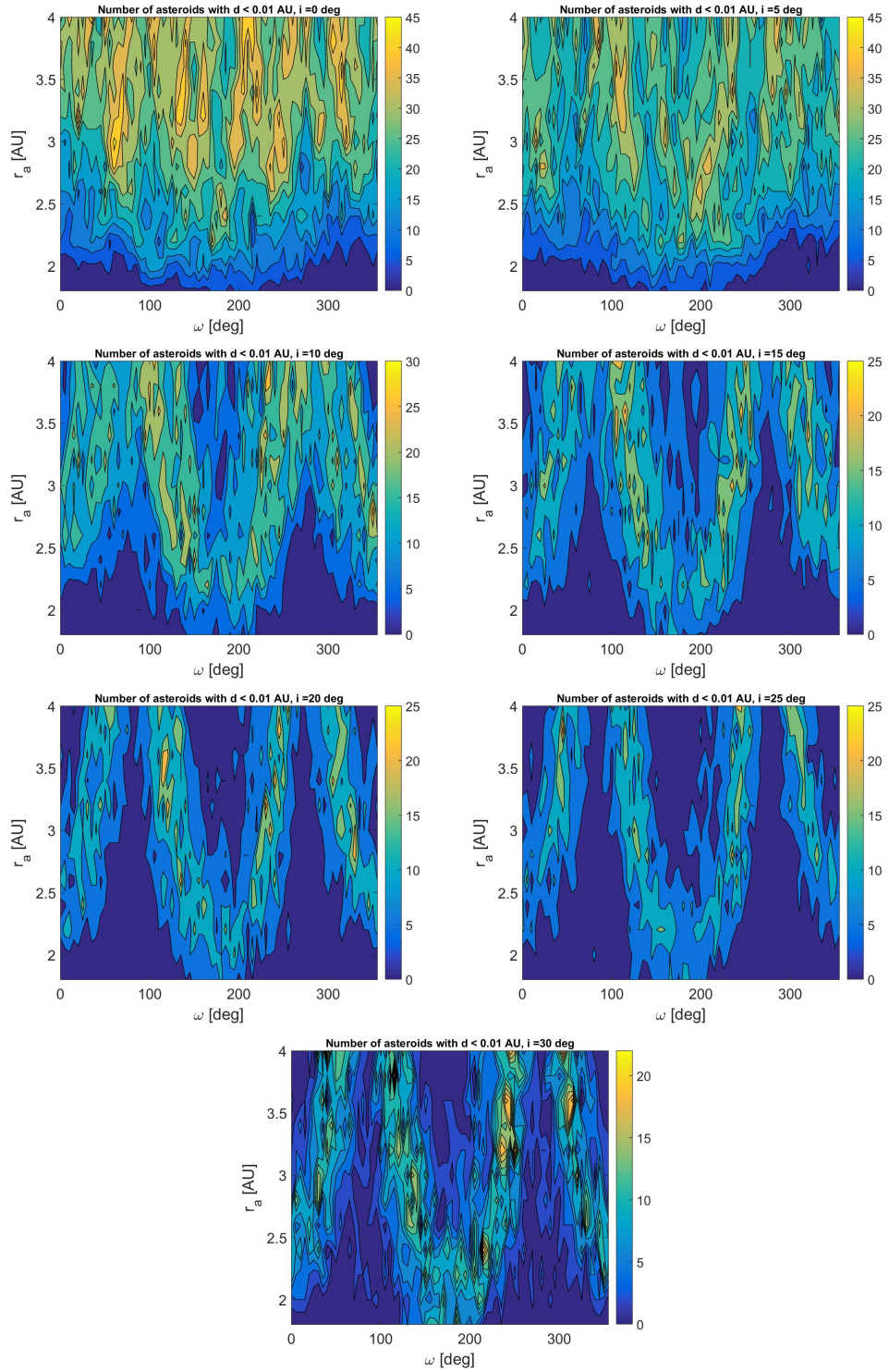

Figure 9.5: Number of asteroids in Database 1 with $d < 0.01$ AU for different initial orbits of the spacecraft.

The number of asteroids shown in Figure 9.5 does not account for the position of asteroids and spacecraft on their orbits. Once the phasing process presented in Subsection 9.2.1 is applied, the number of possible asteroids to encounter with $d < 0.01$ is further reduced. In particular, after phasing, two orbits characterised by the highest number of encounters with the asteroids in Database 1 can be identified. The orbital elements of these two orbits (O1 and O2) are given in Table 9.2.

Table 9.2: Orbits providing the highest number of encounters with asteroids in Database 1.

	a [AU]	e	i [deg]	Ω [deg]	ω [deg]
O1	2.2	0.5455	0	0	220
O2	2.3	0.5652	0	0	315

The number of possible encounters for different values of M_0 from 0 to 359 deg, for the orbits defined in Table 9.2, is shown in Figure 9.6. Results show that the maximum number of asteroids that it is possible to visit in 5 years is 8. The cost associated to the mission has however to be computed to verify that it is below the limit value of $\Delta V_{max} = 1$ km/s.

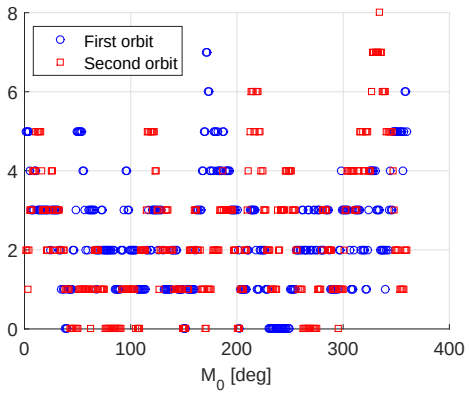

Figure 9.6: Number of asteroids with $d < 0.01$ and phasing condition (Equation 9.1) satisfied.

9.3.2 Study of the possible sequence of asteroids

Figures 9.7 and 9.8 show the ΔV required for the tour of the asteroids in Database 1, as a function of the number N of objects visited, for the two orbits defined in Table 9.2 and $\Delta V_{max} = 1$ km/s. The figures collect the results obtained for all the possible values of M_0 from 0 to 359 deg, at steps of 1 deg. Results show that, within the limit of $\Delta V_{max} = 1$ km/s, the maximum number of asteroids that is possible to visit is $N = 3$ for O1 and $N = 4$ for O2. The total computation time to obtain these results, for all the values of M_0 ranging from 0 to 359 deg, is 1 second on a Intel(R) Core(TM) i7-3770 CPU 3.4 GHz and 8 GB RAM using MATLAB R2015a. The length n of the binary vector $\mathbf{b}$ ranges from 1 to 8, depending on M_0.

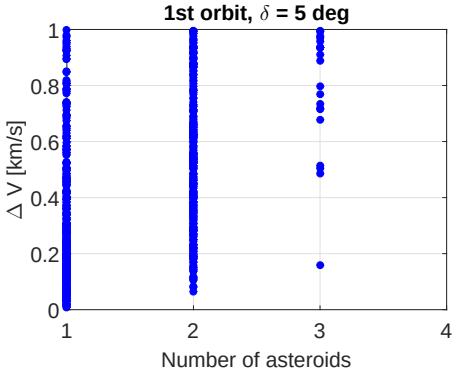

Figure 9.7: Relation between ΔV and number of visited asteroids for the orbit O1 for $\Delta V_{max} = 1$ km/s.

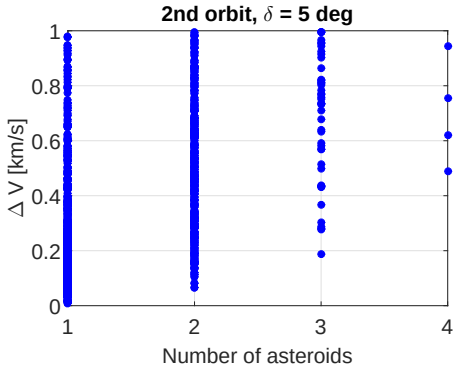

Figure 9.8: Relation between ΔV and number of visited asteroids for the orbit O2 for $\Delta V_{max} = 1$ km/s.

Results in Figures 9.7 and 9.8 are obtained using $\delta = 5$ deg. The sensitivity of the results on the value of δ is presented in Table 9.3, where the total number of solutions N_{TOT} and the number of solutions with 3 or 4 visited asteroids, N_3 and N_4, are presented for different values of δ. Results show that the total number of solutions N_{TOT} and the number of solutions with 3 or 4 visited asteroids decrease with δ.

Table 9.3: Sensitivity of the number of solutions to δ.

	O1		O2	
δ [deg]	N_{TOT}	N_3	N_{TOT}	N_4
5	1058	20	1532	4
1	528	4	700	0
0.5	324	2	428	0
0.25	172	1	198	0

9.3.3 Optimisation of the sequence of asteroids

The best solutions in Figures 9.7 and 9.8, that is, the solutions with highest number of asteroids and lowest ΔV, are optimised with MP-AIDEA. The lower and upper boundaries $\mathbf{x}^L$ and $\mathbf{x}^U$ used for the optimisation with MP-AIDEA are defined by Equations 9.2 and 9.3 and the values reported in Table 9.4. The intervals Δa, Δe and $\Delta\omega$ are given as a function of the nominal values, a, e and ω. MP-AIDEA is run for 50,000 function evaluations and the optimisation is repeated 25 times. The best solution obtained at the end of this process is then considered.

Table 9.5 shows the best optimised ΔV_{opt}, together with the number of visited asteroids N, the angle δ and the initial ΔV before the optimisation with MP-AIDEA.

The solution selected for the low-thrust optimisation is the one associated to orbit 2 (O2) in Table 9.2, as it allows to encounters 4 rather than 3 asteroids of Database 1. Details of the

Table 9.4: Parameters for the definition of $\mathbf{x}^U$ and $\mathbf{x}^L$.

ΔM_0 [deg]	Δa	Δe	$\Delta \omega$	ΔT_i [days]
1	0.01 a	0.01 e	0.01 ω	10

Table 9.5: Optimisation of the ΔV of the longest sequence of asteroids for the two orbits defined in Table 9.2.

Orbit	N	δ [deg]	ΔV [km/s]	ΔV_{opt} [km/s]
O1	3	5	0.1580	0.1024
O2	4	5	0.4881	0.3057

transfer are given in Table 9.6 and in Figure 9.9. The initial orbit in the main belt is characterised by orbital elements $\mathcal{OE}_1 = \{a = 2.2945\,\text{AU}, e = 0.5652, i = 0\,\text{deg}, \Omega = 0\,\text{deg}, \omega = 315.2038\,\text{deg}, M_0 = 214.8032\,\text{deg}, t_0 = 10958.5\,\text{MJD2000}\}$. The first visited asteroid, 2006 UJ47, is a fast rotator, characterised by a rotation period of 0.64 h. The other three asteroids in Table 9.6 are asteroids pairs. Asteroids pairs are defined as asteroids that had a very small relative velocity at some point in the past, in the order of m/s[6]. They may represent former binary asteroids or the result of collisional break-up of a parent asteroid.

Table 9.6: Selected solution for the main belt tour for Database 1.

	Targeted Asteroid	Dep. Date	Optimised Dep. Date	ToF [days]	Opt. ToF [days]	ΔV [m/s]	Opt. ΔV [m/s]
	2006 UJ47	01/01/2030	01/01/2030	294.25	294.02	80.34	67.58
	2007 UV	22/10/2030	22/10/2030	363.64	364.22	147.52	105.63
	2005 YN176	20/10/2031	21/10/2031	207.00	206.78	137.87	132.44
	Ockeghem	14/05/2032	15/05/2032	694.30	689.37	122.39	0.0004
TOT.						488.12	305.67

9.3.4 Transfer from the Earth to the main belt

The tour in Table 9.6 satisfies the 5 year requirement. The attempt now is to realise the launch and transfer to orbit $\mathcal{OE}_1$ in less than 5 years so that the mission time is less than 10 years. Two possibilities exist for the transfer from the Earth to the selected orbit $\mathcal{OE}_1$, with time of transfer shorter than 5 years. The details of these options are given in Table 9.7 and the orbits are shown in Figures 9.10 and 9.11. In Table 9.7 the times T_L and T_M when ΔV_L and ΔV_M are applied, the corresponding ΔV and the orbital elements of the intermediate phasing orbit are given.

[6] http://www.johnstonsarchive.net/astro/asteroidpairs.html

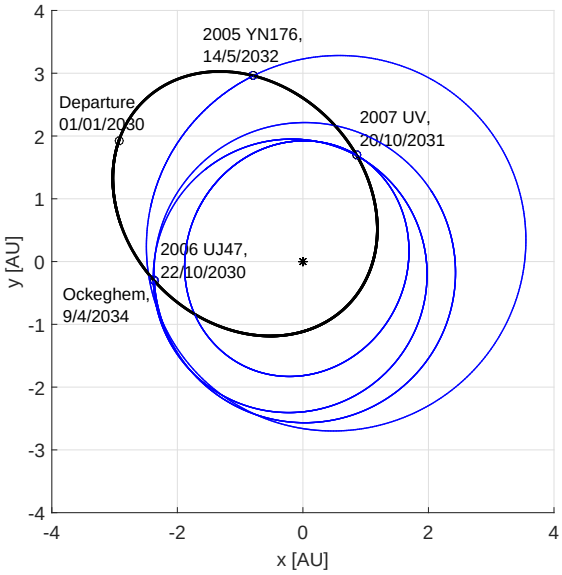

Figure 9.9: Selected solution for the main belt tour for Database 1.

Table 9.7: Transfers to the orbit characterised by orbital elements $\mathcal{OE}_1$ with transfer time shorter than 5 years.

	T_L	ΔV_L [km/s]	a_{int} [AU]	e_{int}	n_{rev}	T_M	ΔV_M [km/s]	ΔT [days]
T1	06/08/2026	2.4879	1.2107	0.1740	1	05/12/2027	4.9785	757.44
T2	06/08/2025	5.8463	1.7577	0.4311	1	05/12/2027	1.6202	757.44

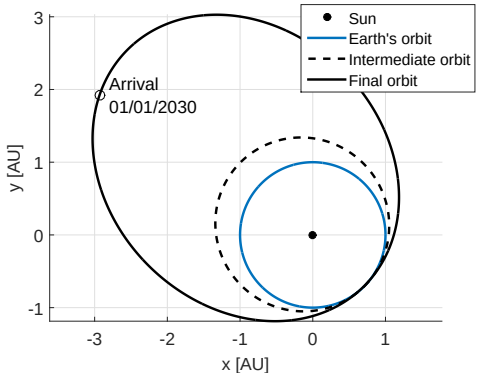

Figure 9.10: Transfer T1 to the orbit characterised by orbital elements $\mathcal{OE}_1$.

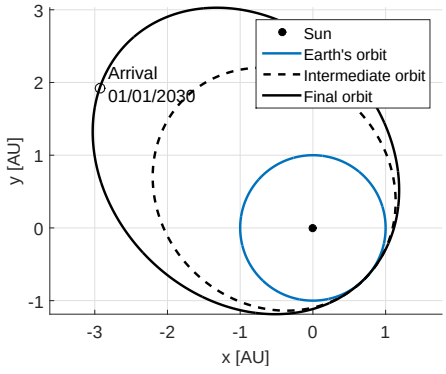

Figure 9.11: Transfer T2 to the orbit characterised by orbital elements $\mathcal{OE}_1$.

The launch for the two options T1 and T2 defined in Table 9.7 is investigated for two types of launchers: the Indian Space Research Organisation GSLV-D6 (Geosynchronous Satellite

Launch Vehicle)[7] and the European Space Agency Soyuz[8]. The GTO parameters of the GLSV and Soyuz launchers are summarised in Table 9.8, together with their maximum payload mass in GTO, m_{GTO}. The quantities $h_{\oplus p,GTO}$ and $h_{\oplus a,GTO}$ are the perigee altitude and apogee altitude of the GTO orbit.

Table 9.8: Orbital elements and payload mass in GTO: GLSV and Soyuz.

	$h_{\oplus p,GTO}$ [km]	$h_{\oplus a,GTO}$ [km]	i_{GTO} [deg]	ω_{GTO}[deg]	m_{GTO} [kg]
GLSV	170	35975	19	178	2330
Soyuz	250	35943	6	178	3250

Results for the two transfer options T1 and T2 and for the two launchers, obtained following the method described in Section 9.2.4, are shown in Figures 9.12 to 9.14.

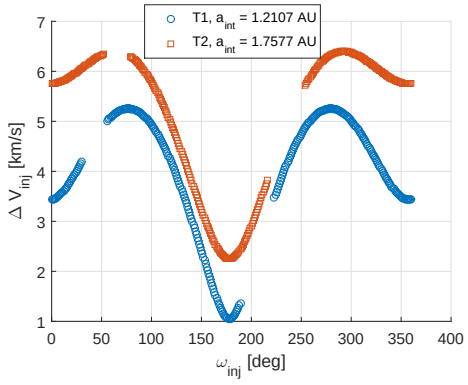

Figure 9.12: Variation of ΔV_{inj} with the argument of perigee of the hyperbolic orbit for the two transfer options considered.

Figure 9.12 shows the ΔV necessary for the injection into the hyperbolic orbit from the GTO, ΔV_{inj}. Notice that ΔV_{inj} depends only on ω_{inj}. Figure 9.13 presents the ΔV necessary for the inclination change from the inclination of the GTO to the appropriate inclination of the hyperbolic orbit. ΔV_i depends on both the considered intermediate phasing orbit (T1 or T2) and on the launcher chosen, since the GTO of GLSV and Soyuz have different inclinations. Finally, the total ΔV_{total}, given by the sum of ΔV_{inj} and ΔV_i, is presented in Figure 9.14. The minimum ΔV results are summarised in Table 9.9, that reports the inclination and argument of perigee of the injection hyperbolic orbit, the ΔV's, the propellant mass and dry mass of the upper stage, $m_p^{U/S}$ and $m_{dry}^{U/S}$, the total payload mass in GTO, m_{pl}, and the launcher mass margin. The assumed initial wet mass of the spacecraft is $m_0 = 1000$ kg and the considered upper stage has $I_{sp}^{U/S} = 400$ s and propellant mass fraction $k = 0.77$. Results show that, for this mass of the spacecraft, the injection into T1 could be realised using GLSV, while for T2 a Soyuz launch would be required. It is worth to recall that the reference value of m_0 chosen

[7] Indian Space Research Organisation - `http://www.isro.gov.in/launcher/gslv-d6`
[8] Arianespace - `http://www.arianespace.com/vehicle/soyuz/`

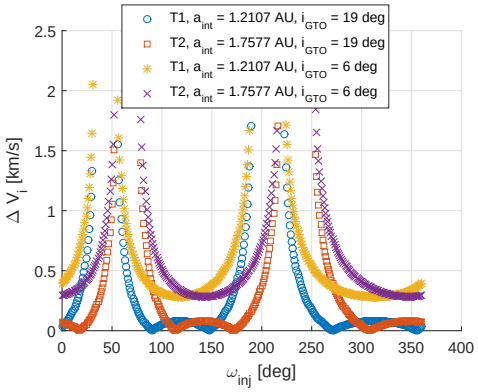

Figure 9.13: Variation of ΔV_i with the argument of perigee of the hyperbolic orbit for the two transfer options and the two launchers considered.

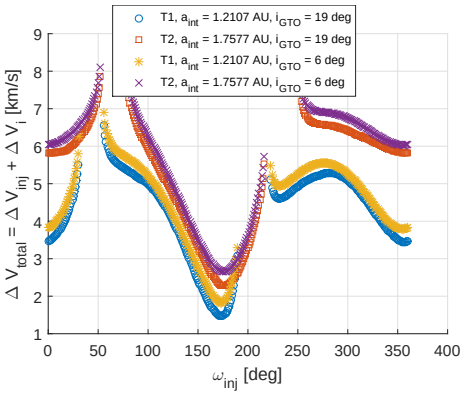

Figure 9.14: Variation of ΔV_{total} with the argument of perigee of the hyperbolic orbit for the two transfer options and the two launchers considered.

in this study can be changed without the need to redesign the tour and the transfer, provided that the thrust is rescaled accordingly (Section 9.3.5). The mass margins shown in Table 9.9 give indication about the values of m_0 that is possible to consider for each launch option and each launcher. For example, option T1, using Soyuz, would allow to increase the mass of the spacecraft, since the mass margin is 1311.04 kg. On the contrary, a launch with option T2 and GLSV would require a smaller spacecraft than the proposed 1000 kg.

Table 9.9: Launch and injection into intermediate phasing orbit (Database 1).

	i_{inj} [deg]	ω_{inj} [deg]	ΔV_i [km/s]	ΔV_{inj} [km/s]	ΔV_{total} [km/s]	m_{dry}^{US} [kg]	m_p^{US} [kg]	m_{pl} [kg]	Margin [kg]
T1, GLSV	31.42	173	0.34	1.12	1.47	156.89	525.26	1682.16	647.84
T2, GLSV	19.89	176	0.02	2.26	2.28	308.46	1032.67	2341.14	-11.14
T1, Soyuz	31.28	173	0.70	1.13	1.83	215.96	722.99	1938.96	1311.04
T2, Soyuz	19.84	176	0.38	2.27	2.65	407.03	1362.66	2769.69	480.31

9.3.5 Low-thrust optimisation

The electric engine considered in this study has thrust magnitude $F = 0.15$ N and specific impulse $I_{sp} = 3000$ s. The initial mass of the spacecraft at launch is assumed to be $m_0 = 1000$ kg. This corresponds to a low-thrust acceleration equal to $1.5\ 10^{-4}$m/s^2. Results for different initial mass of the spacecraft can be obtained by scaling the results presented here, under the assumption that the thrust level increases with the mass of the spacecraft, so that the acceleration is always $1.5\ 10^{-4}$m/s^2. The low-thrust ΔV required to realise the transfer to $\mathcal{OE}_1$ and the tour of the asteroids are shown in Table 9.10, together with the propellant consumption m_p and the initial and final masses, m_0 and m_f, for the two phases of the mission (transfer to $\mathcal{OE}_1$ and tour of the asteroids). Both the possible transfer options defined in Table 9.7 are considered. The low-thrust trajectories for the transfer phases T1 and T2 are shown in Figures

9.15 and 9.16, with coast arcs in gray and thrust arcs in black. The low-thrust trajectory for the tour phase corresponding to T1 is shown in Figures 9.17 while Figures 9.18 and 9.19 show the variation of a and e along the trajectory. Transfer option T2 allows for a higher final spacecraft mass (912.82 kg rather than 845.09 kg) but the transfer time is one year longer (Table 9.7) and the ΔV required for the injection into orbit is higher (Table 9.9). The time required to compute an optimal low-thrust asteroid-to-asteroid transfer is 1.5 seconds on an Intel(R) Core(TM) i7-3770 CPU 3.4GHz with 8GB RAM and the code implemented in MATLAB R2015a. The transfer from Earth to $\mathcal{OE}_1$, which is characterised by a longer time of flight and more transfer arcs, requires 3 second.

Table 9.10: ΔV and propellant consumption for the low-thrust transfer to $\mathcal{OE}_2$ and for the asteroids tour of Database 1.

	Transfer to $\mathcal{OE}_1$				Asteroids tour			
	m_0 [kg]	ΔV [kg]	m_p [kg]	m_f [kg]	m_0 [kg]	ΔV [km/s]	m_p [kg]	m_f [kg]
T1	1000	4.0604	129	871	871	0.8881	25.91	845.09
T2	1000	1.9582	64.43	935.57	935.57	0.7236	22.75	912.82

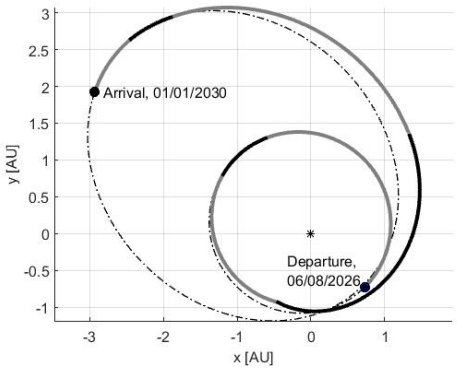

Figure 9.15: Low-thrust transfer trajectory to $\mathcal{OE}_1$, option T1.

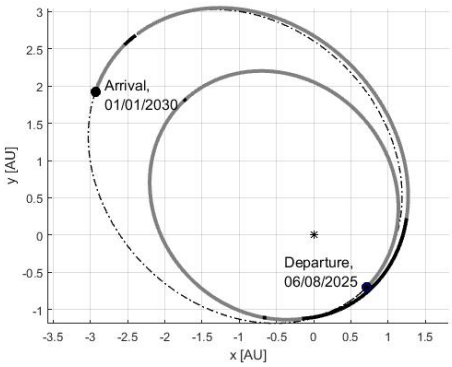

Figure 9.16: Low-thrust transfer trajectory to $\mathcal{OE}_1$, option T2.

9.4 Results Database 1 + 2

Results from Section 9.3 show that the maximum number of scientifically interesting asteroids that can be visited is four. The main belt, however, houses more than 641,933 objects; with such a large number of objects, additional asteroids of reduced scientific interest might be visited while travelling between two asteroids in Database 1. In order to study this scenario, the two Databases 1 and 2 were combined and new sequences were generated. This section presents the results of this analysis.

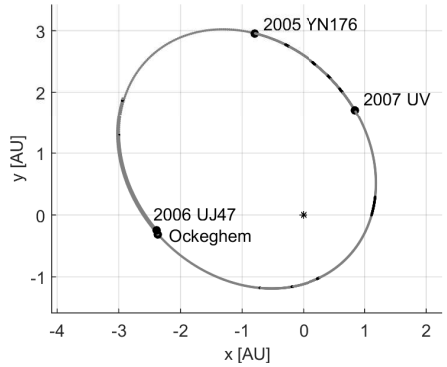

Figure 9.17: Low-thrust trajectory for the tour of the asteroids of Database 1. Thrust arcs are in black, coast arcs are in gray.

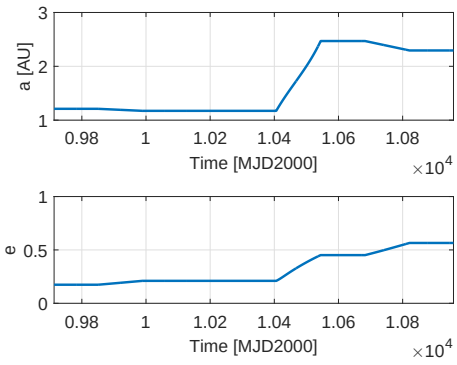

Figure 9.18: Variation of semi-major axis and eccentricity during the low-thrust transfer to $\mathcal{OE}_1$.

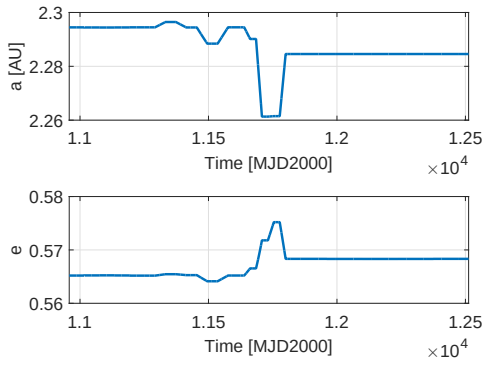

Figure 9.19: Variation of semi-major axis and eccentricity during the low-thrust tour of the asteroids of Database 1.

9.4.1 Minimum Orbit Intersection Distance

As before, the MOID is computed between all the asteroids in the combined database and different orbits of the spacecraft identified by the orbital elements in Table 9.11. The aphelion r_a is sampled at steps of 0.05 AU and $\bar{\omega}$ is sampled at steps of 10 deg.

Table 9.11: Orbital elements of the different possible initial orbits of the spacecraft used for the computation of the MOID.

r_p [AU]	r_a [AU]	i [deg]	Ω [deg]	$\overline{\omega}$ [deg]
1	[1.86, 2.46]	0	0	[0, 360]

Figure 9.20 shows, for each analysed value of the aphelion r_a and for different values of the longitude of periapsis $\overline{\omega}$, the number of asteroids with $d < 0.01$ AU with respect to the orbit of the spacecraft. As before, the higher the aphelion the greater the number of asteroids

with $d < 0.01$ AU. This is true in the range of r_a considered in this study. The phasing process presented in Subsection 9.2.1 is then applied to further reduce the shortlist. Figure 9.21 shows the number of asteroids that respect the condition in Equation 9.1, for different values of M_0 and for the value of $\overline{\omega}$ giving the maximum number of asteroids with $d < 0.01$ AU; $\delta = 1$ in this case. The number of asteroids with $d < 0.01$ AU and phasing condition satisfied can be as high as 82, when $r_a = 2.46$ AU. However, only transfers with a total ΔV lower than ΔV_{max} are considered. The sequence of asteroids that satisfy $\Delta V < \Delta V_{max}$ are presented in the next section.

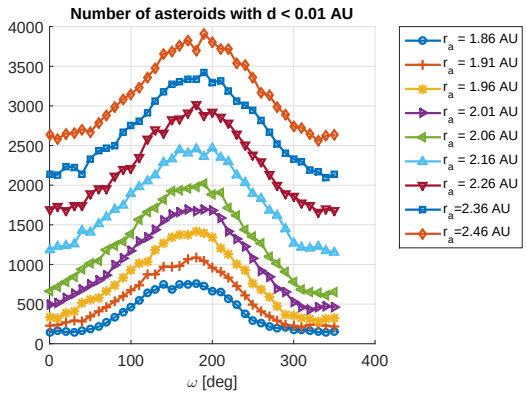

Figure 9.20: Number of asteroids with $d < 0.01$ AU for different initial orbit of the spacecraft, identified by their aphelion radius r_a.

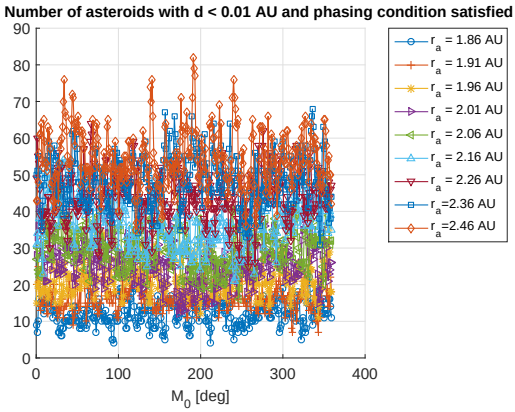

Figure 9.21: Number of asteroids with $d < 0.01$ AU and phasing condition for asteroids encounter (Equation 9.1) satisfied.

9.4.2 Study of the possible sequences of asteroids

Figure 9.22 shows the ΔV required for the tour of the asteroids, as a function of the number N of visited objects. The initial orbit of the spacecraft has $r_a = 1.86$ AU and $\omega = 180$ deg and the maximum mission cost is $\Delta V_{max} = 1$ km/s. Different values of the angle δ are considered, from $\delta = 0.1$ deg to $\delta = 1$ deg. The values of δ used in this section are different from the one used in Section 9.3. The dimension of the considered database of asteroids ($\sim$ 100,000 vs. $\sim$ 400) results in unmanageable computational time and amount of data generated when δ is larger than the value used here. Figure 9.22 collects the results for all the possible values of M_0 from 1 to 359 deg, at steps of 1 deg and, for each value of N, only the first 1000 best solutions (the ones with lower ΔV) are shown.

Results from Figure 9.22 show that higher values of δ allows one to find solutions with a longer list of asteroids, while still satisfying the condition $\Delta V < \Delta V_{max}$. The maximum value of N is indeed 4 for $\delta = 0.1$ deg and $N = 7$ for $\delta = 1$ deg. Figure 9.23 shows the relation between ΔV and number of visited asteroids for orbits with different values of r_a, as defined in Table 9.11, and different values of δ. The value of ω for each orbit is the one that allows one to visit the maximum possible number of asteroids for that r_a. As r_a increases, the maximum

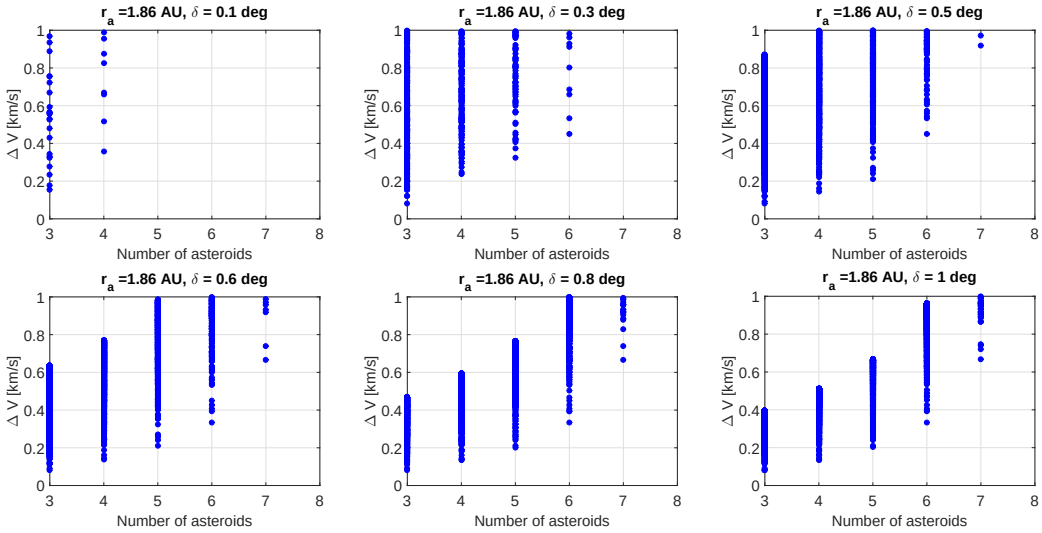

Figure 9.22: Relation between ΔV and number of visited asteroids for orbit with $r_a = 1.86$ AU and different values of δ.

number of asteroids that can be visited increases from 8, for r_a = 1.86 AU, to 11 for $r_a = 2.46$ AU and the ΔV associated to a given number of asteroids N decreases.

Figure 9.23 shows that the maximum number of visited asteroids, $N = 11$, can be obtained using an orbit with $r_a = 2.26$ AU or $r_a = 2.46$ AU. For $r_a = 2.26$ AU and $\delta = 0.5$ deg, the binary vector **b**, composed of 0's and 1's, has a length that depends on the value of M_0 (M_0 ranges from 1 to 359 deg). The minimum length of **b** is $n = 4$ and the maximum length is $n = 31$. The BPA has, therefore, to handle a maximum of 2^{31} sequences (Section 9.2.2). The total computation time, for all the values of M_0 ranging from 1 to 359 deg, is 82 minutes on a Intel(R) Core(TM) i7-3770 CPU 3.4 GHz and 8 GB RAM using MATLAB R2015a. In the following the solution characterised by $r_a = 2.26$ AU is analysed in more detail. Figure 9.24 shows the maximum number of asteroids that is possible to visit with maximum tour cost $\Delta V_{max} = 1$ km/s for different initial dates from December 2029 to January 2030 and $r_a = 2.26$ AU. The best results are obtained with initial date 01/01/2030, the one chosen for this study.

Since MP-AIDEA can reduce the ΔV cost of the mission, for $r_a = 2.26$ AU the binary tree for the generation of the possible sequences of asteroids is run also considering $\Delta V_{max} = 2$ km/s. The aim is to obtain, after optimisation, $\Delta V_{opt} < 1$ km/s with $N \geq 11$.

Results show that, within the limit of $\Delta V_{max} = 2$ km/s, the maximum number of asteroids that can be visited is N =14. However, by inspecting all the sequences, one can see that:

- for $N = 14$, only two different sequences are identified. They do not include any of the scientifically interesting asteroids in Database 1;
- for $N = 13$, 262 possible sequences are found, none of which include asteroids from Database 1;
- for $N = 12$, 5764 sequences are found, 29 of which included 1 or 2 asteroids from Data-

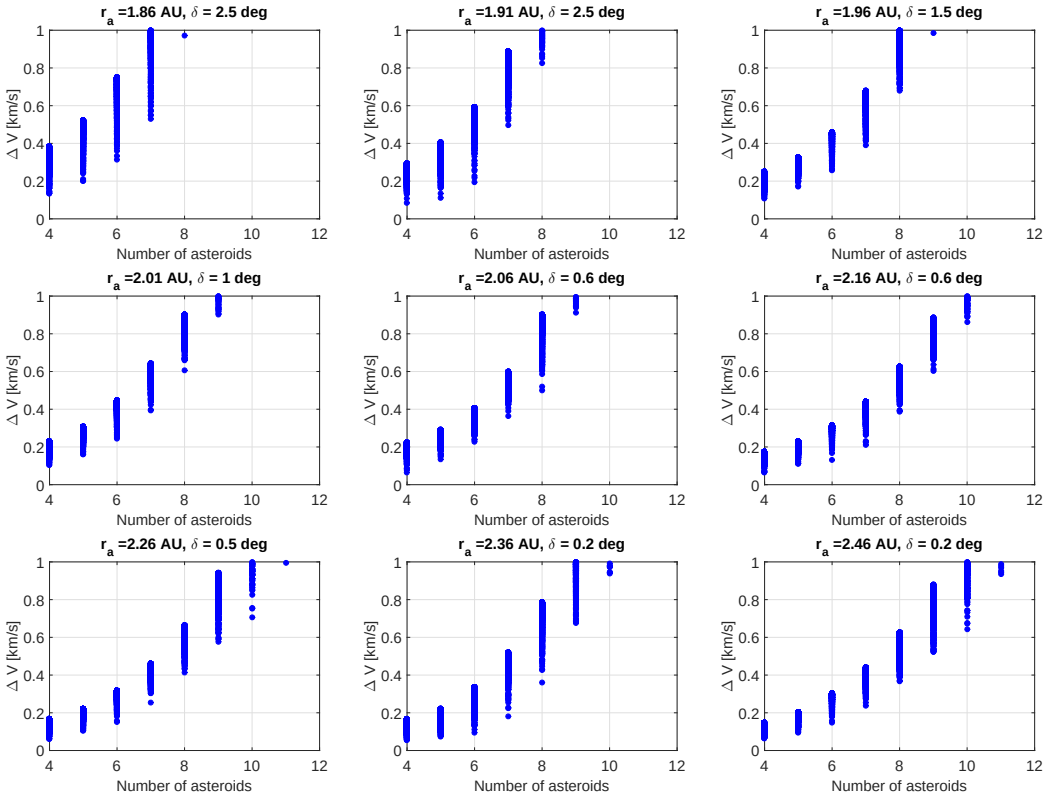

Figure 9.23: Relation between ΔV and number of visited asteroids for orbits with different r_a and for different values of δ.

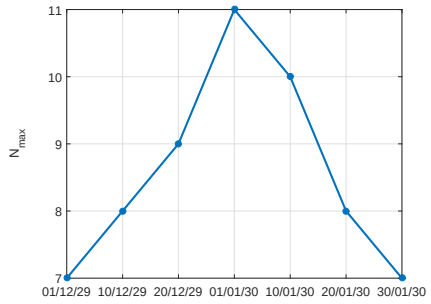

Figure 9.24: Maximum number of visited asteroids for $\Delta V_{max} = 1$ km/s and different initial date for the tour (dates in dd/mm/yy).

base 1. Among the 29 solutions with asteroids from Database 1, the one with lowest cost and two scientifically interesting asteroids has a $\Delta V = 1.7574$ km/s;

- for $N = 11$, 84606 possible sequences are found, out of which 2109 include 1 or 2 asteroids from Database 1. The solution with lowest ΔV and 2 scientifically interesting asteroids has a cost of 1.1865 km/s.

9.4.3 Optimisation of the sequence of asteroids

The solutions with $N = 11$ and $N = 12$ that include 2 asteroids from Database 1 and with lowest ΔV are further optimised using MP-AIDEA. The settings of the optimisation problem and the boundaries of the search space are the same ones used for Database 1. After optimisation, the solution characterised by $N = 12$ and $\Delta V = 1.7574$ km/s gives an optimised cost of $\Delta V_{opt} = 1.3$ km/s. The solution characterised by $N = 11$ and $\Delta V = 1.1865$ gives $\Delta V_{opt} = 0.7613$ km/s. Since in this case $\Delta V < 1$ km/s, this solution is the one selected for further analysis. Details of the asteroids visited, times of encounters and ΔV are given in Table 9.12, while a graphical representation is given in Figure 9.25 and Figure 9.26.

The scientifically interesting asteroids are represented in bold in Table 9.12. Both 2003 QS31 and 2110 Moore-Sitterly are asteroid pairs.

Table 9.12: Selected solution for the main belt tour for Database 1+2. Interesting asteroids from Database 1 are shown in bold.

Targeted Asteroid	Dep. Date	Optimised Dep. Date	ToF [days]	Opt. ToF [days]	ΔV [m/s]	Opt. ΔV [m/s]
2012 DW5	1/1/2030	1/1/2030	78.77	81.37	80.42	62.64
2005 QM95	20/3/2030	23/3/2030	148.27	145.02	240.41	16.12
2007 UJ78	16/8/2030	15/8/2030	119.12	119.92	216.58	113.86
2003 QS31	13/12/2030	13/12/2030	392.10	392.35	101.55	108.34
2001 QY152	9/1/2032	9/1/2032	105.36	105.25	51.17	37.07
2009 HL17	23/4/2032	23/4/2032	92.23	92.34	90.53	73.30
2005 SF9	24/7/2032	25/7/2032	143.38	143.43	94.41	74.04
Moore-Sitterly	15/12/2032	15/12/2032	409.26	409.08	35.33	13.92
2000 QL	28/1/2034	28/1/2034	64.72	64.88	106.24	107.09
2000 YU15	3/4/2034	3/4/2034	264.52	264.27	147.52	123.63
2000 VT44	23/12/2034	23/12/2034	59.97	59.82	22.40	31.28
					1186.55	761.28

The initial orbit of the spacecraft in the main belt has optimised orbital elements $\mathcal{OE}_{1+2} = \{a = 1.6299$ AU, $e = 0.3826$, $i = 0$ deg, $\Omega = 0$ deg, $\omega = 180.3330$ deg, $M_0 = 102.36$ deg, $t_0 = 10958.5$ MJD2000$\}$.

9.4.4 Transfer from the Earth to the main belt

Two possibilities exist for the transfer to the orbit $\mathcal{OE}_{1+2}$ with time of flight shorter than 5 years. These are presented in Table 9.13 and Figures 9.27 and 9.28.

Following the method described in Section 9.2.4, results for the two transfer options T1 and T2 and for the two launchers are shown in Figures 9.29 to 9.31.

The minimum ΔV results are summarised in Table 9.14. Both GSLV and Soyuz can be used to inject the spacecraft and upper stage into GTO, with Soyuz allowing for a larger mass margin.

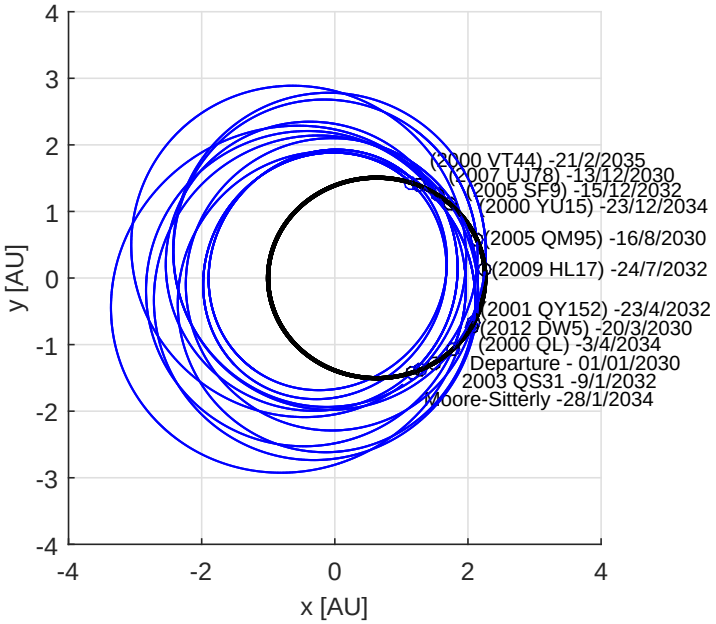

Figure 9.25: Selected solution for the main belt tour for Database 1+2.

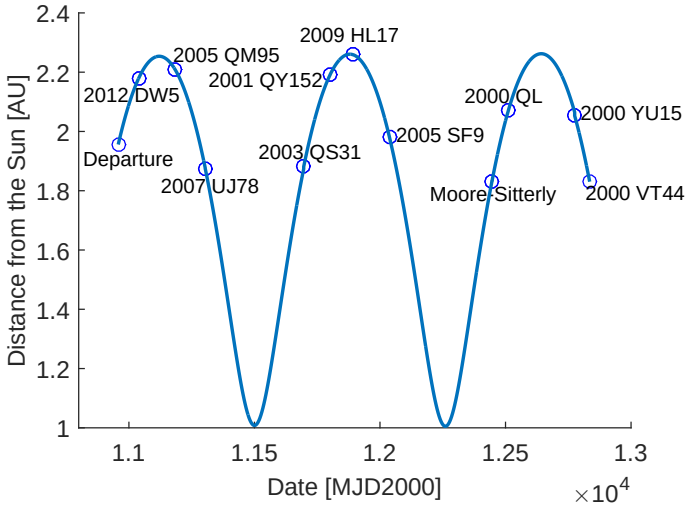

Figure 9.26: Distance of the spacecraft from the Sun for the selected solution for the main belt tour for Database 1+2.

9.4.5 Low-thrust optimisation

The ΔV required to realise the low-thrust transfer to $\mathcal{OE}_{1+2}$ and the tour of the asteroids is shown in Table 9.15, together with the propellant consumption m_p and the initial and final mass, m_0 and m_f, for the two phases of the mission (transfer to $\mathcal{OE}_1$ and tour of the asteroids). Both the possible transfer options defined in Table 9.13 are evaluated.

Table 9.13: Transfers to the orbit characterised by orbital elements $\mathcal{OE}_{1+2}$ with transfer time shorter than 5 years.

	T_L	ΔV_L [km/s]	a_{int} [AU]	e_{int}	n_{rev}	T_M	ΔV_M [km/s]	ΔT [days]
T1	21/03/2028	1.5935	1.1234	0.1099	1	29/05/2029	3.6929	216.09
T2	21/03/2026	3.7491	1.3653	0.2676	2	29/05/2029	1.5374	216.09

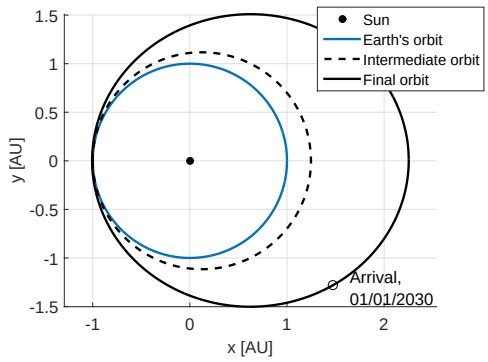

Figure 9.27: Orbits for transfer option T1 from Earth to orbit $\mathcal{OE}_{1+2}$.

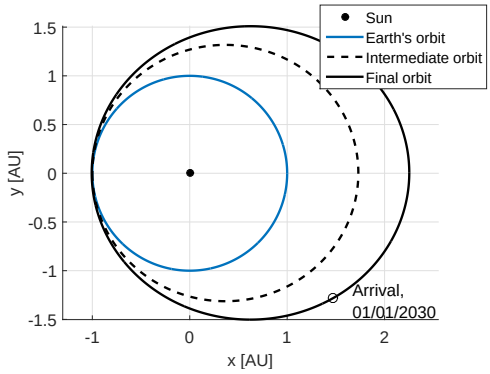

Figure 9.28: Orbits for transfer option T2 from Earth to orbit $\mathcal{OE}_{1+2}$.

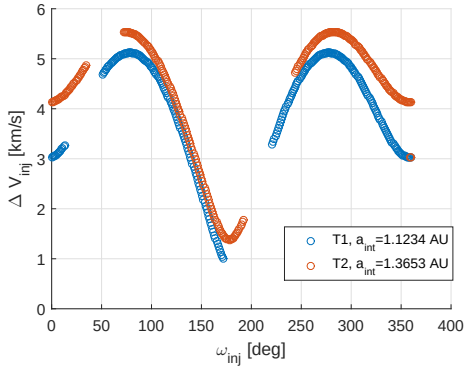

Figure 9.29: Variation of ΔV_{inj} with the argument of perigee of the hyperbolic orbit for the two transfer options considered.

The low-thrust trajectories for the transfer phases T1 and T2 are shown in Figure 9.32 and 9.33. The low-thrust trajectory for the asteroid tour phase of option T1 and the corresponding variation of a and e are shown in Figure 9.34 and Figures 9.35 and 9.36. Table 9.15 shows that transfer option T2 results in a higher final mass of the spacecraft (875.40 kg) than option T1. Option T2 has also a lower ΔV_{total} than T1 (Table 9.14), but the transfer time is 2 years longer (Table 9.13).

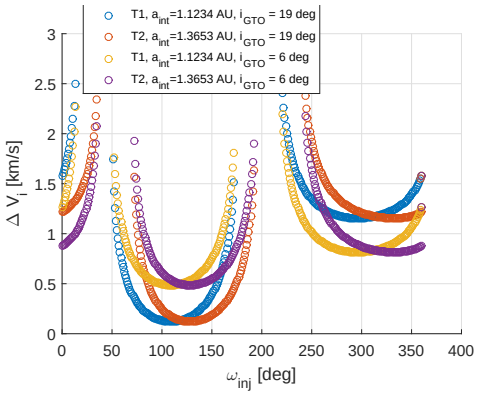

Figure 9.30: Variation of ΔV_i with the argument of perigee of the hyperbolic orbit for the two transfer options and the two launchers considered.

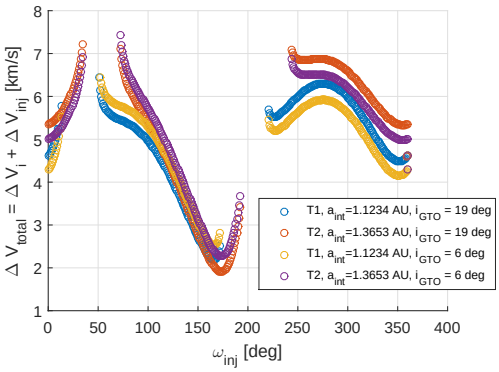

Figure 9.31: Variation of ΔV_{total} with the argument of perigee of the hyperbolic orbit for the two transfer options and the two launchers considered.

Table 9.14: Injection into intermediate phasing orbit (Database 1+2).

	i_{inj} [deg]	ω_{inj} [deg]	ΔV_i [km/s]	ΔV_{inj} [km/s]	ΔV_{total} [km/s]	m_{dry}^{US} [kg]	m_p^{US} [kg]	m_{pl} [kg]	Margin [kg]
T1, GLSV	51.94	166	0.91	1.29	2.20	290.10	971.21	2261.31	68.69
T2, GLSV	35.93	173	0.47	1.44	1.91	230.82	772.74	2003.56	326.44
T1, Soyuz	51.73	166	1.25	1.29	2.54	374.21	1252.77	2626.98	623.02
T2, Soyuz	35.78	173	0.83	1.44	2.27	305.99	1024.42	2330.42	919.58

Table 9.15: ΔV and propellant consumption for the low-thrust transfer to $\mathcal{OE}_{1+2}$ and tour of Database 1+2.

	Transfer to $\mathcal{OE}_{1+2}$				Asteroids tour			
	m_0 [kg]	ΔV [km/s]	m_p [kg]	m_f [kg]	m_0 [kg]	ΔV [km/s]	m_p [kg]	m_f [kg]
T1	1000	4.1345	131.19	868.81	868.81	2.9132	81.96	786.85
T2	1000	1.4541	48.25	951.75	951.75	2.4584	76.35	875.40

9.5 Conclusions

This chapter has presented some preliminary results for a possible low-thrust tour of the main belt, considering an heliocentric elliptical orbit for the spacecraft, with perihelion at the Earth and aphelion in the main belt region. The analysis on the database of targets of particular scientific interest shows that, with a threshold of 1 km/s on the preliminary estimation of the ΔV for the tour of the main belt, 4 scientific interesting asteroids can be visited in about 5 years. Combining the database of scientifically interesting asteroid with one composed by more than 100,000 objects, gives a solution with 11 visited asteroids, among which 2 are asteroid pairs. The low-thrust transfer from Earth to the main belt and the low-thrust tour of the asteroids can be realised, under the specified assumption, with approximately 212 kg of propellant and

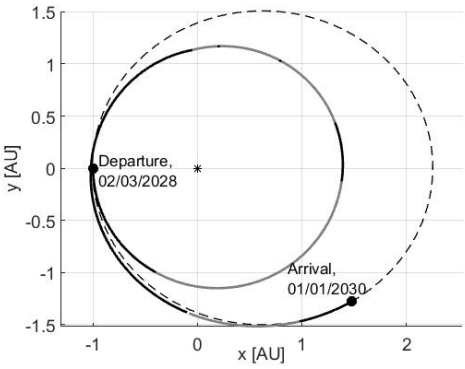

Figure 9.32: Low-thrust transfer trajectory to $\mathcal{OE}_{1+2}$, option T1. Thrust arcs are in black and coast arcs are in gray.

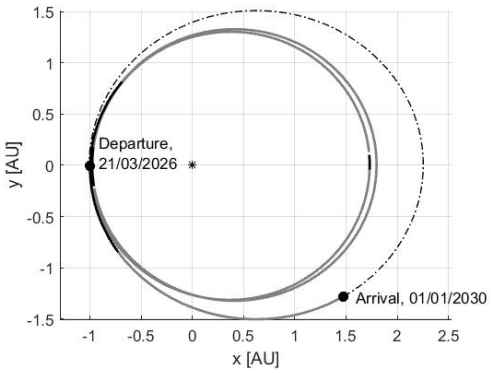

Figure 9.33: Low-thrust transfer trajectory to $\mathcal{OE}_{1+2}$, option T2. Thrust arcs are in black and coast arcs are in gray.

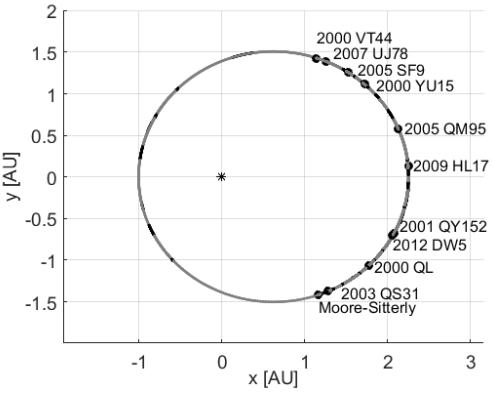

Figure 9.34: Low-thrust trajectory for the tour of the asteroids of Database 1+2. Thrust arcs are in black and coast arcs are in gray.

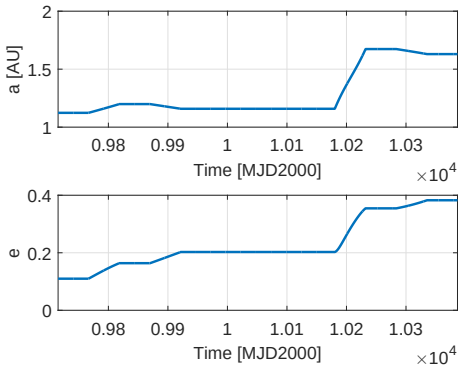

Figure 9.35: Variation of semi-major axis and eccentricity during the low-thrust transfer to $\mathcal{OE}_{1+2}$.

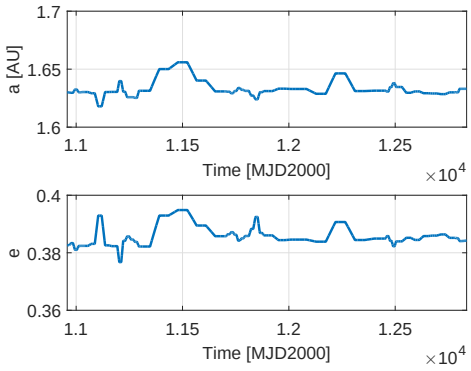

Figure 9.36: Variation of semi-major axis and eccentricity during the low-thrust tour of the selected objects of Database 1+2.

a mission time of less than 7 years. The GLSV launcher can be used to inject the spacecraft into space, with a mass margin of 68 kg. Higher mass margins are possible when allowing for longer transfer times to the main belt or when using the Soyuz launcher.

It is noted that by increasing the δ tolerance on the phasing and relaxing the constraint on the estimated ΔV even longer sequences might be possible with an optimised ΔV that might make the mission possible with larger launchers. Furthermore, the launch and transfer strategy in this preliminary analysis do not include any swing-by. More alternative solutions are, therefore, to be expected. This will be the object of a future study.

This chapter and Chapter 8 have presented applications of the tools developed in Part I to interplanetary missions. Chapters 10, 11 and 12 will present applications to missions in LEO, MEO and GEO.

The content of this chapter was published in M. Di Carlo, J. M. Romero Martin, M. Vasile, "Automatic trajectory planning for low-thrust active removal mission in Low-Earth Orbit", Advances in Space Research, Volume 59, Issue 5, 1 March 2017, pp. 1234-1258

Chapter 10

Removal of non-cooperative objects from LEO using low-thrust spacecraft

In this chapter, a low-thrust mission to de-orbit up to 10 non-cooperative objects per year from the region within 800 and 1400 km altitude in Low Earth Orbit (LEO) is proposed. The underlying idea is to use a single low-thrust servicing spacecraft to de-orbit several objects applying two different approaches. The first strategy is analogous to the Traveling Salesman Problem: the servicing spacecraft rendezvous with multiple objects in order to physically attach a de-orbiting kit that reduces the perigee of the orbit. The second strategy is analogous to the Vehicle Routing Problem: the servicing spacecraft rendezvous and docks with an object, spirals it down to a lower altitude orbit, undocks, and then spirals up to the next target.

In order to maximise the number of de-orbited objects with minimum propellant consumption, an optimal sequence of targets is identified using a bio-inspired incremental automatic planning and scheduling discrete optimisation algorithm, which uses a surrogate model of the optimal cost of the transfers (Chapter 6) The optimisation of the transfers is realised using a direct transcription method (Chapter 5) based on the analytical solution of the perturbed Keplerian motion presented in Chapter 4, taking into account the perturbations deriving from the J_2 gravitational effect and the atmospheric drag.

The chapter is structured as follows. The space debris problem is presented in Section 10.1. Section 10.2 gives a description of the considered active debris removal strategies; the targets selection method is addressed in Section 10.3. The discrete decision making algorithm for the object sequence selection and the low-thrust transfer model are described in Section 10.4 and 10.5. Results are presented in Section 10.7. Section 10.6 describe how the mission is defined and Section 10.8 concludes the chapter.

10.1 The space debris problem

Since the beginning of the space era, humankind have put into orbit over 10,000 objects [180]. Only 6% of these are active satellite while the rest are space debris [180]. The growth of the space debris population represents a collision threat for satellite and manned spacecraft in Earth orbit. Recent studies have concluded that regions within Low Earth Orbit (LEO) have already reached a critical density of objects which will eventually lead to a cascading process known as the Kessler syndrome [110]. It is expected for the LEO debris population to increase by approximately 30% in the next 200 years [98,180]. The Inter-Agency Space Debris Coordination Committee has issued guidelines to mitigate the growth of space debris [46]. However, it has been proven that compliance with these recommendations will not stop the exponential growth. In [129] it is indeed proved that, under the assumption that no spacecrafts are launched after December 2005, the debris population would still grow, driven by collision in the 900-1000 km altitude range. The active removal of five to ten large objects per year is required to stabilise the population [129]. Since in a no-further-release scenario collisions are the only reason for the growth of debris population, and since collision probability is a function of the object's cross section area, large objects are the main candidates for active removal [220]. Different methods have been proposed for removal of debris in LEO. These methods can be contact-less method, such as the Ion-Beam Shepherd [27], lasers and solar concentrator [212], or based on a physical contact with the spacecraft using throw-net, harpoon [228], clap or robotic arm. Mainly, the objective of the contact methods is to bring the space debris into a disposal or a re-entry orbit together with the servicing spacecraft. However, the robotic arm method can be used to attach a de-orbit device on the space debris, and then, the disposal of the debris will be performed in a controlled manner using the de-orbit kit [120].

Different scenarios for the active removal of space debris have been proposed in the literature. A mission for the removal of debris from Sun-synchronous orbit is presented in [40]. A servicing spacecraft carrying a number of de-orbiting devices is used to remove 35 objects from this region in 7 years. The spacecraft uses chemical propellant and is serviced 7 times during the mission time in order to be resupplied with propellant and more de-orbiting devices. In [30] a study is presented in which different scenarios are considered for chemical or electric propelled servicing spacecraft and for the use of de-orbit kits device or direct transfer of the objects on a disposal orbit. The targets are identified using a priority criterion based on the probability of a catastrophic collision and on the objects' masses. The sequence of targets to be removed is then computed using a brute-force approach in which each possible permutation is simulated. In [152] desirable targets, based upon the probabilistic likelihood of objects contributing to the debris field, are identified. Both impulsive and low-thrust missions are studied, with a limit total available ΔV assigned to them. ΔV analysis for transfer between object is mainly based on the change in the right ascension of the ascending node and no optimisation or identification of target sequence is performed. An automated procedure to generate route plans for an active debris removal campaign based on Ant Colony Optimization (ACO) combined with auction and bidding processes is presented in [194]. The heuristic of the ACO is

similar to the Physarum algorithm presented in this chapter. In [194] the problem is formulated as a typical multi-vehicle routing problem employing ACO to create preliminary encounter tours and to determine the total number of spacecrafts required to complete mitigation tasks. Auction and bidding process are used to coordinate the operation of the debris-mitigating satellites for both pre-mission planning and real-time adjustments to baseline designs. Finally, in [149], space debris on Sun-synchronous orbits are considered. A Lambert's problem with J_2 perturbation is used to compute the cost of all the debris-to-debris transfers and a branch-and-prune algorithm is used to construct the target sequence. The transfers between objects in the sequence is then optimised using an indirect method for the low-thrust transfers. The considered propulsion system has a thrust amplitude ranging from 0.5 N to 10 N for a 1000 kg spacecraft.

This chapter proposes two strategies to automatically plan active debris removal missions in which a single servicing spacecraft, equipped with an electric engine, removes multiple objects from LEO. The underlying optimal control problem defining the transfer between pairs of objects is solved with the approach based on asymptotic analytical solutions of the Keplerian motion under constant acceleration presented in Chapter 4 and using surrogate models for the evaluation of the cost of the transfer in order to reduce the computational burden of the combinatorial algorithm (Chapter 6).

10.2 Active debris removal strategies

Two strategies to actively remove objects from LEO are proposed and studied. These two strategies are here called the De-orbiting Travelling Salesman Problem (TSP) and the De-orbiting Vehicle Routing Problem (VRP). The De-orbiting TSP is analogous to the classic Travelling Salesman Problem: a servicing spacecraft (chaser) rendezvous with multiple objects (targets) in order to physically attach a de-orbiting system that reduces the altitude of the perigee of the orbit of the target down to 300 km. The De-orbiting TSP is analogous to the standard TSP in that the servicing spacecraft has to visit every city (every target). However, differently from the standard TSP, it is not required for the servicing spacecraft to return to the starting place at the end of the tour. This difference does not change the definition of the problem proposed in this study.

The De-orbiting VRP is analogous to the classic Vehicle Routing Problem: a servicing spacecraft rendezvous with an object, grabs it and spirals down to a circular disposal orbit with an altitude of 300 km. Once this orbit is reached, the chaser disengages with the target and moves to the next target. The disposal orbit can be seen as the depot of a typical VRP. In this case too, differently from the standard VRP, the chaser does not terminate its tour at the depot. This difference has no effect on the problem proposed here. Figure 10.1 illustrates the different mission phases of the two proposed strategies.

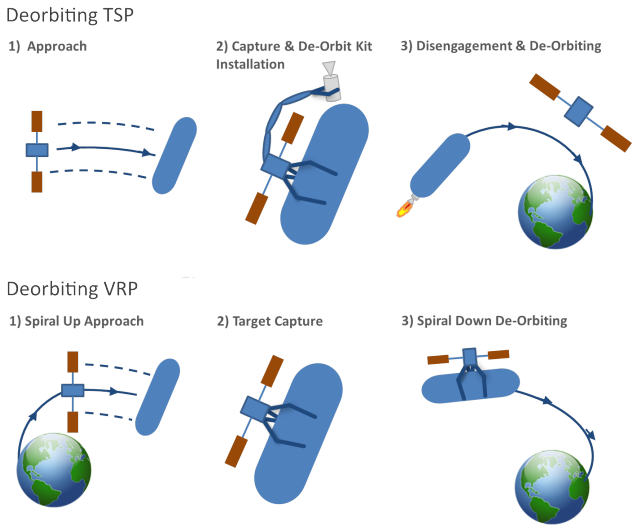

Figure 10.1: Mission phases of the two studied ADR strategies.

10.3 Target selection

A catalogue of the current objects in LEO is regularly maintained by the North American Aerospace Defence Command (NORAD). Each object in the catalogue is identified by its Two-Line Elements (TLE) set, defining its orbital parameters at a given epoch. For this work, TLE of all objects characterized by perigee altitude $h_{\oplus,p} \geq 800$ km and apogee altitude $h_{\oplus,a} \leq 1400$ km are taken from *space-track.org*. In order to target objects more likely to cause collision, only TLE characterized by Radar Cross Section (RCS) > 1 are considered. The Radar Cross Section is a measure of how detectable is an object with a radar; object with RCS > 1 m^2 are classified as large. Up to 721 objects characterized by $h_{\oplus,p} \geq 800$ km, $h_{\oplus,a} \leq 1400$ and RCS > 1 m^2 are found; their distribution in term of semi-major axis vs. inclination and semi-major axis vs. right ascension of the ascending node, Ω, is shown in Figure 10.2.

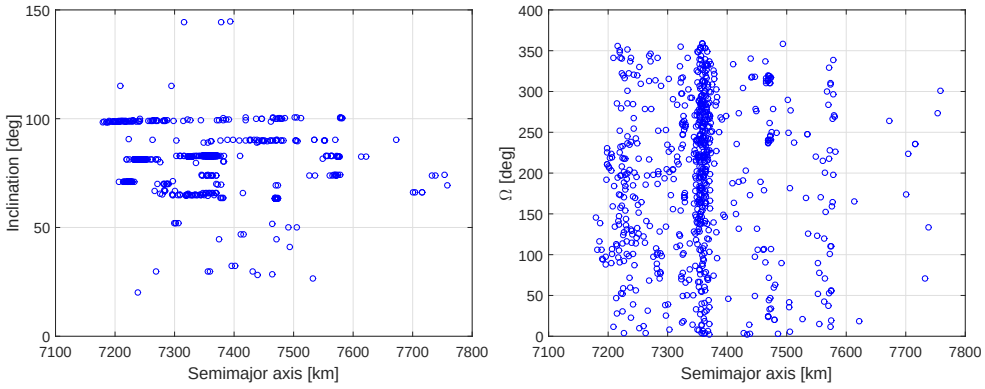

Figure 10.2: Semi-major axis, inclination and right ascension of objects in LEO characterized by $h_{\oplus,p} \geq 800$ km, $h_{\oplus,a} \leq 1400$ and RCS$\geq$1 m^2.

The potential 721 target objects are then further selected based on two main criteria: the right ascension of the ascending node drift due to the second zonal harmonic of the gravity, J_2, and the Criticality of Spacecraft Index (CSI) [181]. Figure 10.2 shows that Ω is widely spread. Low-thrust maneuvers to change the right ascension are particularly expensive and require long time when compared to maneuvers to change other orbital elements. Ruggiero et al. showed that changing 1 degree of right ascension requires 10 days when using optimal thrust angle for the change of Ω [182]. In this paper the change of Ω is performed by taking advantage of the natural rate of nodal regression due to J_2 and its dependence on altitude. Transferring the spacecraft to lower or higher altitude changes the rate of Ω relative to the initial orbit so that a shift in Ω can be realised [160]. The variation of Ω of the servicing spacecraft depends on its altitude and inclination i according to Equation 3.1. The effect of a change of semi-major axis on the variation of Ω is greater when the inclination is smaller, because of the $\cos i$ term in Equation 3.1.

A further classification of objects with low inclination is realised based on the Criticality of Spacecraft Index (CSI). The Criticality of Spacecraft Index expresses the environmental criticality of objects in Low Earth Orbit taking into account the physical characteristics of a given object, its orbit and the environment where this is located [181]. The CSI is not computed for the selected objects; instead, the location of these objects, in the inclination-perigee/apogee space, is compared against the location, in the same space, of the most critical objects reported in the work of Rossi [181]. Figure 10.3 shows the perigee and the apogee altitudes of the 721 objects characterised by $h_{\oplus,p} > 800$ km and $h_{\oplus,a}$ <1400 km as a function of the inclination. It can be compared with Figure 8 in [181] to see that the 25 circled objects in Figure 10.3 are in the same region as the 100 most critical objects in terms of CSI. These 25 objects are the ones selected for this study. Their orbital elements at epoch t_0 = 30 May 2015 are reported in Table 10.1 and shown in Figure 10.4.

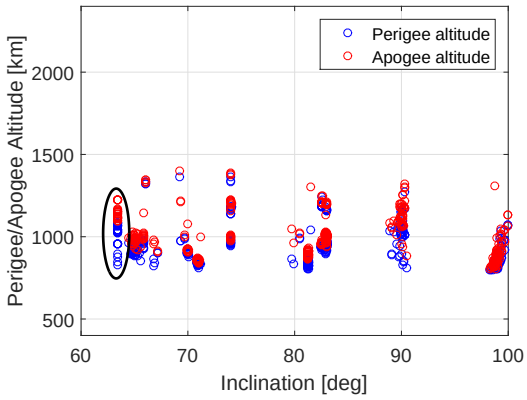

Figure 10.3: Perigee and apogee altitude of objects in LEO with $h_{\oplus,p} > 800$ km, $h_{\oplus,a} < 1400$ and RCS>1.

Table 10.1: List of selected objects The eccentric anomaly E is given at the epoch $t_0 = 30$ May 2015..

	ID	a [km]	e	i [deg]	Ω [deg]	ω [deg]	E [deg]
1	39012	7468.3502	0.0083	63.3824	237.3044	0.8990	359.2169
2	39016	7471.1909	0.0097	63.3825	240.6863	6.5523	353.6732
3	39015	7472.5431	0.0095	63.3828	246.1591	5.6338	354.5722
4	39011	7468.3501	0.0083	63.3835	237.2911	0.9268	359.1897
5	39013	7468.3457	0.0083	63.3851	236.4881	0.7138	359.3978
6	40113	7472.7134	0.0037	63.4023	316.5715	13.7191	346.4819
7	40110	7468.3365	0.0030	63.4026	313.7710	3.4835	356.6392
8	40114	7474.0679	0.0035	63.4027	317.0490	12.1346	348.0508
9	40111	7468.3378	0.0030	63.4036	313.9539	3.3535	356.7684
10	36417	7468.8627	0.0178	63.4045	319.3205	1.2414	136.7021
11	40109	7468.3382	0.0030	63.4048	313.0739	3.0576	357.0626
12	36418	7469.6579	0.0177	63.4050	318.8647	0.8968	90.3057
13	36415	7468.3664	0.0181	63.4057	313.6971	1.5540	358.6008
14	36413	7468.3637	0.0180	63.4064	315.3091	1.5248	358.6278
15	36414	7468.3642	0.0180	63.4079	313.8604	1.2339	358.9091
16	40340	7468.3186	0.0010	63.4084	240.6788	293.4985	66.5005
17	40343	7471.8760	0.0020	63.4093	245.3040	3.4906	356.6256
18	40342	7473.2452	0.0019	63.4096	240.8979	359.1859	0.9133
19	40339	7468.3132	0.0010	63.4097	239.8082	294.9368	65.0721
20	40338	7468.3152	0.0010	63.4108	239.8075	293.4250	66.5729
21	39243	7471.6919	0.0076	63.4150	32.8672	11.6594	348.6165
22	39240	7468.3470	0.0065	63.4154	24.7900	3.7401	356.4085
23	39244	7473.0697	0.0075	63.4156	33.7082	10.7899	349.4691
24	39239	7468.3482	0.0065	63.4158	24.7599	3.6762	356.4729
25	39241	7468.3452	0.0065	63.4170	23.8973	3.3104	356.8339

10.4 Incremental planning and scheduling algorithm

The utilised automatic planning and scheduling algorithm has been developed at the University of Strathclyde and is based on a single objective discrete optimisation algorithm which takes inspiration from the biology of the single cell slime mold Physarum Polycephalum. General information about the Physarum algorithm can be found in [5, 146, 200, 201]. Detailed information about the algorithm used for this study are in [64, 221].

10.4.1 Problem formulation

As introduced in Sec. 10.2, the two proposed ADR strategies are analogous to the typical TSP and VRP. In the TSP the goal is to minimise the total path length to visit every town/node once and only once. In the Deorbiting analogous, the goal is to minimise the total ΔV to execute all servicing tasks only one. In contrast to the regular TSP, where the cost of each arc connecting

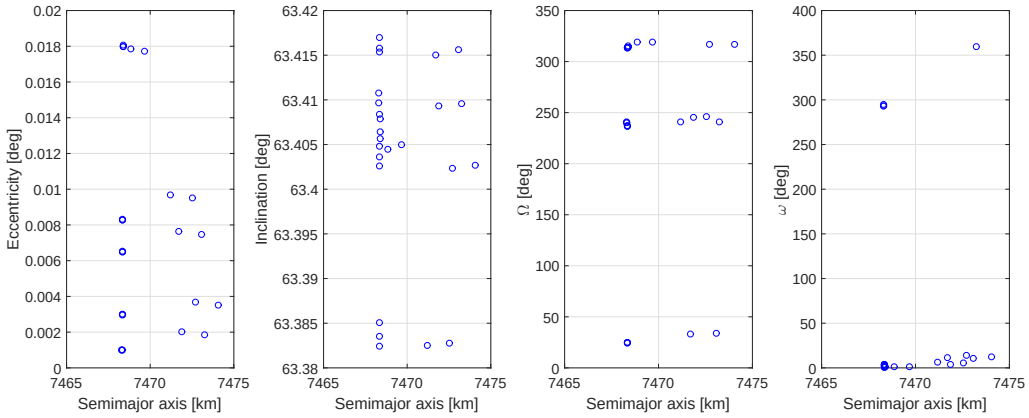

Figure 10.4: Orbital elements of the selected objects.

two nodes is constant, in the ADR case, the cost of the arc depends on the mass of the chaser, which varies with time. In fact, the mass of the servicing spacecraft depends on the propellant mass, that is progressively consumed to rendezvous with all the satellites, and on the number of de-orbit kits, that are progressively used to perform de-orbiting. The ADR analogous has other key distinctive features:

- Only n_T tasks among S_s are performed, where S_s is the set of targets to be serviced. n_T depends on the number of de-orbit kits available on-board the chaser.
- There is a constraints on the transfers time (ToF) between tasks so that $ToF \in [ToF_{min}, ToF_{max}]$.
- There is a waiting time at each target. This waiting time is the time required to performed the servicing, $t_{servicing}$.

The Deorbiting VRP is equivalent to the classic VRP, where after each service, the vehicle (the chaser in our case) has to return to the depot (the disposal orbit) before proceeding to the next service. Similar to the TSP, the goal of the VRP is to minimise the total distance covered and to conduct every task once and only once. The following features have been added to the ADR analogous:

- There is a global duration constraint on the total mission time, $t_{mission} < T_{max}$.
- There is a local duration constraint on the transfers time between tasks so that $ToF \in [ToF_{min}, ToF_{max}]$.

The decision graph of the Physarum algorithm is incrementally grown by the virtual agents where each node of the graph represents a decision. Each of the nodes are connected by arcs, and these arcs have an associated cost, evaluated making use of the model presented in Sec. 10.5. This cost is the ΔV associated to the transfer between each pair of targets.

Both for the TSP and VRP problems, the Physarum algorithm evaluate the cost of the low-thrust transfer between satellites using a surrogate model, rather than the actual low-thrust

model. This is justified by the combinatorial complexity of the problem and by the computational time required by the computation of the low-thrust transfer. To justify this method, an estimation of the total number of required operations and of the corresponding computational time, using the low-thrust model, is given in the following. Considering the set of 25 possible targets, the number of combinations of target-to-target transfer arcs can be computed using the formula $n!/(n-k)!$, where n=25 and k is the number of objects of the subset. In this case $k = 2$, giving a total number of 600 different transfer arcs. Considering a time of flight for the transfer from 1 to 180 days and a time step of 0.25 days, the total number of possible time of flights for each transfer arc is 716. Therefore, the total number of transfer arcs that should be computed is 600*716 = 429600. Hence, assuming that the low-thrust solver takes on average 25 sec to compute a transfer arc on an Intel(R) Core(TM) i7-3770 CPU 3.4GHz and 8GB RAM, the total computational time required to perform an exhaustive assessment of the search space is approximately 1243 days. Therefore, in order to reduce the computational time required by the Physarum in the evaluation of the cost of the transfer arcs, a surrogate model of the low-thrust transfers is used (Sec. 10.5.6). The evaluation of the surrogate model has an almost instantaneous computational time cost, resulting in a considerable reduction on the computational time.

10.5 Low-thrust transfer model

In this section the method used to compute the ΔV required to assess the cost of the transfer for the De-orbiting TSP and the De-orbiting VRP is described.

10.5.1 Debris dynamical model

The mean elements at epoch t_0 of each target are taken from the TLE catalog [100] and are propagated forward in time considering only the J_2 effect, since drag is not relevant at the considered altitude. The effect of drag is neglected also for the transfer between two targets in the De-orbiting TSP but is taken into account in the de-orbiting and orbit raising of the De-orbiting VRP. Neglecting the atmospheric drag for the propagation of the orbits of the target objects is justified by the small variations of a and e, due to drag, over a time interval of two years. Figure 10.5 shows, in this respect, the absolute difference between the semi-major axis and eccentricity after two years of propagation (a_{2y} and e_{2y}) and the initial semi major axis and eccentricity (a_0 and e_0), for each one of the 25 selected objects.

For each possible target, therefore, a, e and i are assumed to be constant, while Ω and ω change according to [204]:

$$\Omega(t) = \Omega(t_0) - \frac{3}{2}\bar{n}J_2\left(\frac{R_\oplus}{p}\right)^2 \cos i(t-t_0)\,, \tag{10.1}$$

$$\omega(t) = \omega(t_0) + \frac{3}{2}\bar{n}J_2\left(2 - \frac{5}{2}\sin^2 i\right)^2 (t-t_0)\,, \tag{10.2}$$

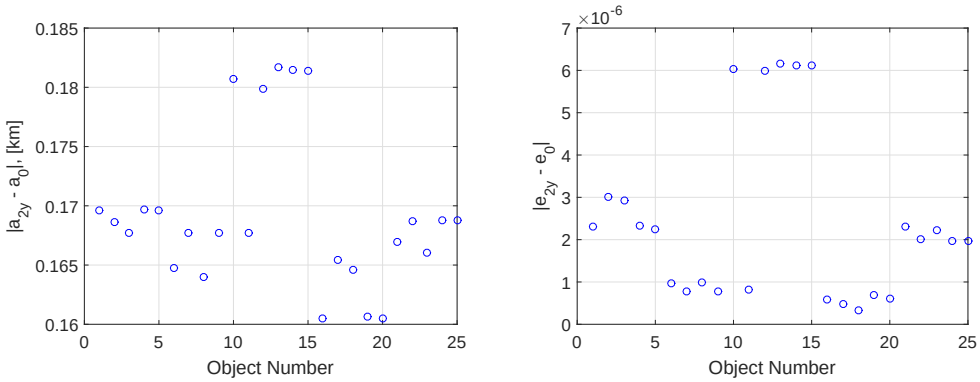

Figure 10.5: Variation of semi-major axis and eccentricity of the target objects during a time period of two years.

where

$$\bar{n} = n\left[1 + \frac{3}{2}J_2\left(\frac{R_\oplus}{p}\right)^2\sqrt{1-e^2}\left(1 - \frac{3}{2}\sin^2 i\right)\right] . \tag{10.3}$$

10.5.2 Time independence of the transfers

The rate of change of Ω and ω due to J_2 is different for each selected target object and depends on their orbital elements. During the transfer from any object A to any object B, realised in a time of flight ToF, the chaser has to correct Ω and ω by an amount:

$$\Delta\Omega(t_0, ToF) = \Omega_B(t_0 + ToF) - \Omega_A(t_0) , \tag{10.4}$$

$$\Delta\omega(t_0, ToF) = \omega_B(t_0 + ToF) - \omega_A(t_0) , \tag{10.5}$$

The different rates of change of Ω and ω for the two objects A and B result in different values of $\Delta\Omega$ and $\Delta\omega$ when transferring from one object to another at different epochs. This means that, for $t_1 \neq t_0$,

$$\Delta\Omega(t_0, ToF) \neq \Delta\Omega(t_1, ToF) , \tag{10.6}$$

and

$$\Delta\omega(t_0, ToF) \neq \Delta\omega(t_1, ToF) . \tag{10.7}$$

As a consequence, transfers realised at different starting epochs, would be characterised by different ΔV's. Consider now each combination of two objects A and B and the quantities:

$$\Delta\Omega_{AB}(t_0, T_{1y}) = [\Omega_A(t_0 + T_{1y}) - \Omega_B(t_0 + T_{1y})] - [\Omega_A(t_0) - \Omega_B(t_0)] , \tag{10.8}$$

$$\Delta\omega_{AB}(t_0, T_{1y}) = [\omega_A(t_0 + T_{1y}) - \omega_B(t_0 + T_{1y})] - [\omega_A(t_0) - \omega_B(t_0)] , \tag{10.9}$$

where t_0 is a given epoch and $T_{1y} = 1$ year. The quantities on the right hand side of Equations 10.8 and 10.9 are shown in Figure 10.6 for all the 600 combinations of transfers resulting from the 25 selected objects.

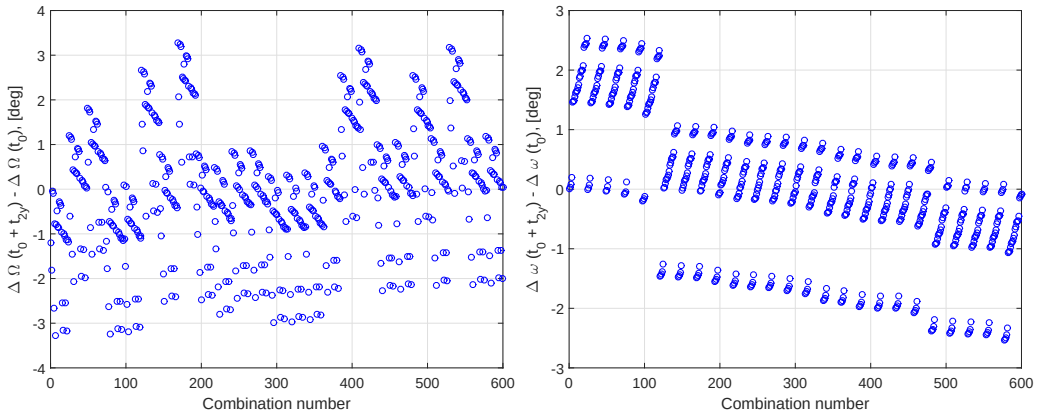

Figure 10.6: $\Delta\Omega_{AB}(t_0, T_{1y})$ and $\Delta\omega_{AB}(t_0, T_{1y})$ for the 600 combinations of transfers resulting from the 25 selected objects.

Figures 10.6 show that the differences in $\Delta\Omega$ are limited to less than 3.28 deg over one year and those of ω are limited to less than 2.53 degrees over the same period of time. To further investigate this, using the transfer model described in Section 10.5.3, the ΔV required to realise the following two transfers are computed:

- $a_A = 7470$ km $\rightarrow a_B = a_A$
- $e_A = 0 \rightarrow e_B = e_A$
- $i_A = 63$ deg $\rightarrow i_B = i_A$
- $\Omega_A(t_0) \rightarrow \Omega_B(t_0 + ToF)$

and

- $a_A = 7470$ km $\rightarrow a_B = a_A$
- $e_A = 0 \rightarrow e_B = e_A$
- $i_A = 63$ deg $\rightarrow i_B = i_A$
- $\Omega_A(t_0 + T_{1y}) \rightarrow \Omega_B(t_0 + T_{1y} + ToF)$

The worst possible transfer is considered, that is the one corresponding to:

$$[\Omega_B(t_0 + T_{1y}) - \Omega_A(t_0 + T_{1y})] - [\Omega_B(t_0) - \Omega_A(t_0)] = 3.28 \text{ deg} . \tag{10.10}$$

Figure 10.7 shows the difference between the ΔV's required to realise the two transfers defined above. The difference in ΔV is plotted against the ToF for the transfer.

The difference in the ΔV's required to realise transfers with different values of $\Delta\omega$ are expected to be lower than those in Figure 10.5 given the smaller values of the difference in $\Delta\omega$. Given the result in Figure 10.7 the time independence assumption is applied to the calculation of all the transfers in the remainder of this chapter. This assumption allows one to represent the ΔV only as a function of the mass of the target and the ToF (see Section 10.5.6).

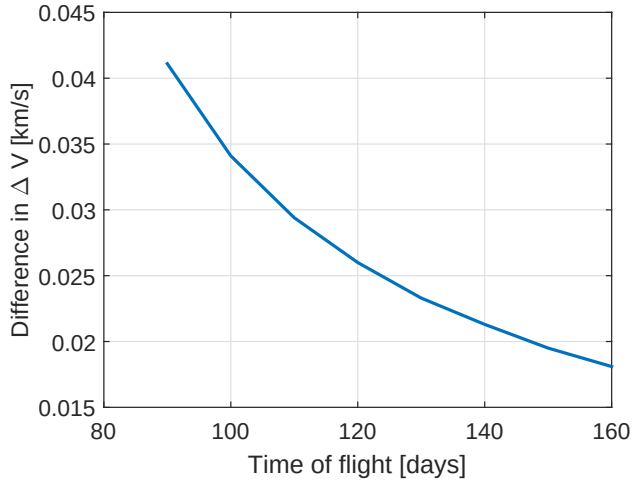

Figure 10.7: Difference in ΔV for transfers computed at different epochs (t_0 or $t_0 + T_{1y}$).

10.5.3 Transfer model

In this work the interest is in low-thrust transfer where a, e, i, Ω and ω undergo a variation. The analytical laws defined in Chapter 3, for the variation of a, i and Ω only, are, therefore, not appropriate for this study. An higher-fidelity and computationally more expensive model was devised and is presented hereafter.

The state $\mathbf{X}$ of the spacecraft is modeled using non-singular equinoctial elements, as in Chapter 4. The transfers between objects are optimised in order to reduce the total propellant consumption, or ΔV. The acceleration $\mathbf{u}_{LT}$ exerted by the thruster on the spacecraft is expressed in the spacecraft body-fixed radial-transverse-normal reference frame as in Equation 4.2 in Chapter 4 [240]. The low-thrust control parametrisation is based on the transcription presented in Section 5.3. Each orbit revolution of the servicing spacecraft is divided into four sectors: two thrust arcs (at perigee and apogee) and two coast arcs. In order to consider situations in which thrusting at perigee and apogee could not be the optimal choice, an additional decision parameter that produces a shift along the orbit of the center of the perigee thrust is added to the vector of variables to optimise defined in Equation 5.21. The additional variable is η, an angle defining the shift of the first thrust arc (perigee thrust arc) with respect to the perigee.

On each thrust arc, the state of the servicing spacecraft is propagated using the averaged analytical solution of the perturbed Keplerian motion (Chapter 4, Equation 4.11) with J_2 and atmospheric drag perturbation. As an example, Figure 10.8 shows the comparison of numerical and averaged analytical propagation for a propagation of 4 months considering perturbations due to J_2, atmospheric drag and continuous negative tangential acceleration due to a thrust of 0.1 N applied to a 3000 kg spacecraft with initial orbital elements defined in Table 10.2. For the atmospheric drag, the drag coefficient C_D is set to 2.2 and the area to mass ratio of the spacecraft is assumed to be $A/m = 10^{-2}\text{m}^2/\text{kg}$. The numerical propagation is realized using MATLAB *ode113* with integration of the equations of Gauss. The proposed propagation

is an example of the de-orbiting phase of the De-orbiting VRP. The results of the averaged analytical propagator are in agreement with those of the numerical propagation.

Table 10.2: Initial orbital elements for propagation with J_2, atmospheric drag and negative tangential acceleration.

a [km]	e	i [deg]	Ω [deg]	ω [deg]
7470	0.01	63.43	10	10

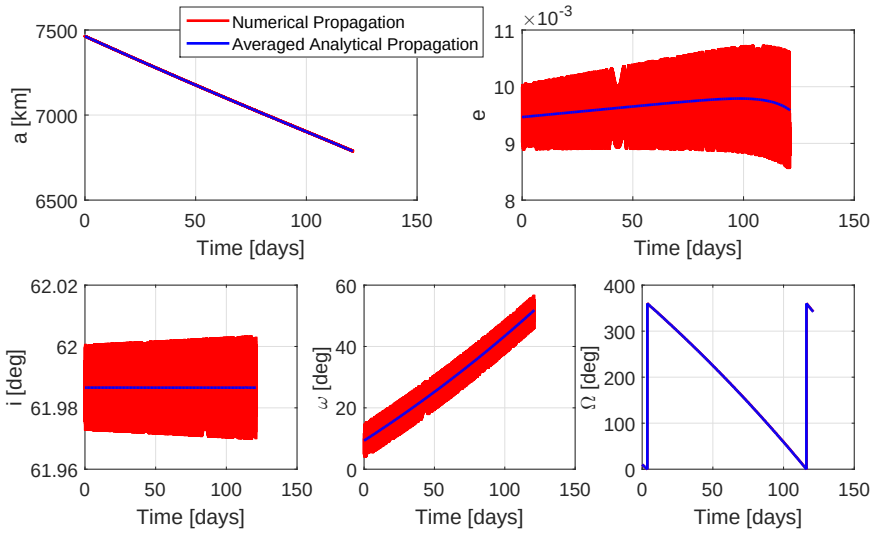

Figure 10.8: Comparison of averaged analytical and numerical propagation using J_2, atmospheric drag and continuous low-thrust negative tangential. acceleration.

For the purpose of this study, valid results are obtained without the corrective term for the J_2-drag coupling described in Section 4.3.1. This is shown indeed in Figure 10.8, where the corrective term is not used. It is possible to neglect the corrective term because of the rapid de-orbit of the satellite due to the presence of the low-thrust acceleration, meaning that the coupling effect of J_2 and atmospheric drag is not felt by the satellite. Therefore the expression for the analytical integrals reported in Appendix 4, that do not include the corrective term δr, can be used.

10.5.4 Rendezvous strategy

The rendezvous of the chaser with the target object requires imposing a terminal constraint on all the six orbital elements. For a transfer realised in a given time of flight, ToF, the optimisation problems consists in minimising the ΔV required to realise the transfer subject to the

terminal constraints

$$\mathbf{c} = \begin{bmatrix} a_C - a_T \\ e_C - e_T \\ i_C - i_T \\ \Omega_C(t_0 + ToF) - \Omega_T(t_0 + ToF) \\ \omega_C(t_0 + ToF) - \omega_T(t_0 + ToF) \\ \theta_C(t_0 + ToF) - \theta_T(t_0 + ToF) \end{bmatrix} = \mathbf{0} \, , \tag{10.11}$$

where t_0 is the departure time and the subscripts C and T denote the chaser servicing spacecraft and the target, respectively. The method proposed to satisfy the constraints in Equation 10.11 takes advantage of the natural rate of nodal regression and its dependence on the altitude [160]. The total transfer, characterised by a time of flight ToF, is divided into different phases. In the first phase, an optimisation problem is solved in order to satisfy the terminal constraints on e, i and ω, while minimising the propellant consumption in a time $ToF_{e,i,\omega}$. The second phase is realised in a time of flight $ToF_{a,\Omega} = ToF - ToF_{e,i,\omega}$ and its aim is to correct a and Ω, while keeping the terminal value of i and e and ω constant. It has to be noted that ω is not expected to change much during the transfer because of the inclination of the targets, which is close to the critical value of 63.43 deg. In order to achieve the final desired a and Ω the following strategy, that takes advantage of the natural nodal regression and its dependence on altitude, is used [42]:

- An optimisation problem is solved in order to minimise the ΔV required to move the spacecraft, in a time of flight T_{t1}, from the orbit attained at time $ToF_{e,i,\omega}$ to an appropriate parking orbit with semi-major axis a_w, while constraining e to be equal to the target's eccentricity e_T. Since this transfer is realised with in-plane thrust only ($\beta = 0$), no change of inclination will take place and therefore no constraint on i is required.
- The spacecraft remains on the parking orbit for an appropriate time $T_{w,\Omega}$.
- An optimisation problem is solved in order to minimise the ΔV required to move the spacecraft, in a time of flight T_{t2}, from the parking orbit to the final orbit with semi-major axis a_T, while constraining e and ω to be equal to e_T and $\omega_T(t_0 + ToF_{e,i,\omega} + T_{t1} + T_{w,\Omega} + T_{t2})$. Since this transfer is realised with in-plane thrust only ($\beta = 0$), no change of inclination will take place and therefore no constraint on i is required. At the end of this transfer the following condition is satisfied:

$$\Omega_C(t_0 + ToF_{e,i,\omega} + ToF_{a,\Omega}) = \Omega_T(t_0 + ToF_{e,i,\omega} + ToF_{a,\Omega}) \, , \tag{10.12}$$

  where $ToF_{a,\Omega}$ corresponds to the sum of transfer times and waiting time:

$$T_{t1} + T_{w,\Omega} + T_{t2} = ToF_{a,\Omega} = ToF - ToF_{e,i,\omega} \tag{10.13}$$

This strategy requires the computation of four parameters: T_{t1}, a_w, $T_{w,\Omega}$ and T_{t2}. Hence, four equations are required to solve the problem. The first one derives directly from the available time, Equations 10.13. The second equations is derived from Edelbaum theory for the required

ΔV for a transfer between circular orbits, described in Section 2.2.2, [72]. This equation applies here because of the small eccentricity of the orbits of the targets. By denoting the semi-major axis of the chaser at the end of the first phase with $a_{C(e,i,\omega)}$, the time to realise the transfer to the parking orbit can be computed as the ratio between the required ΔV and the spacecraft acceleration,

$$T_{t1} = \frac{k\sqrt{V_{C(e,i,\omega)}^2 + V_w^2 - 2V_{C(e,i,\omega)}V_w}}{\epsilon} , \tag{10.14}$$

where $V_{C(e,i,\omega)}$ is the circular velocity on the orbit of radius $a_{C(e,i,\omega)}$ and V_w is the circular velocity on an orbit of radius a_w. The quantity ϵ is the acceleration of the electric engine and the factor $k = 1.5$ is used to accommodate the extra time required to satisfy the constraints on e and ω. Similarly:

$$T_{t2} = \frac{k\sqrt{V_T^2 + V_w^2 - 2V_T V_w}}{\epsilon} , \tag{10.15}$$

where now V_T is the velocity on a circular orbit of radius equal to the semi-major axis of the target object. The forth equation is the matching condition on Ω at the end of the transfer:

$$\Omega_T(t_0) + \dot{\Omega}_T \cdot (T_{t1} + T_{t2} + T_{w,\Omega}) = \Omega_C(t_0) + \dot{\Omega}_{t1}T_{t1} + \dot{\Omega}_w T_{w,\Omega} + \dot{\Omega}_{t2}T_{t2} . \tag{10.16}$$

In Equation 10.16 $\dot{\Omega}_T$ is the drift of the right ascension of the target orbit and $\dot{\Omega}_{t1}$ and $\dot{\Omega}_{t2}$ are the drifts of the right ascensions of the transfers to and from the parking orbit. The drift $\dot{\Omega}$ changes during these two transfers because of the variation of semi-major axis but it can be approximated to be constant by using a mean semi-major axis $a_{t1} = \left(a_{C(e,i,\omega)} + a_w\right)/2$ for the transfer to the parking orbit and a mean semimajor axis $a_{t2} = (a_w + a_T)/2$ for the transfer from the parking orbit to the target orbit. Equations 10.13 to 10.16 allow to compute T_{t1}, a_w, $T_{w,\Omega}$ and T_{t2} required for the change of Ω.

Orbital phasing

One underlying assumption in the estimation of the ΔV is that the transfer requires a long spiral in which the variation of orbital elements over a complete revolution is small. This assumption is similar to the one made in Chapter 2, where it is assumed that the orbital elements stay constant over one orbital period. In this case, the orbital elements over the first revolution of the spiral will be very similar to the orbital elements of the departure orbit. Likewise, the orbital elements over the last revolution of the spiral will be very similar to the orbital elements of the target orbit. Furthermore, the initial and final true anomalies can change by at most 2π, which corresponds to equal or less than the orbital period of the departure, or target, orbit. Hence, a change of initial or final phase angle to match the initial and terminal conditions will have little effect on the overall spiral and thus on the total ΔV. An example is reported hereafter to show that the variation in ΔV when changing the departure true anomaly and reducing the time of flight by less than one orbital period is negligible. Let us consider the transfer from object 39012 to object 39016, realised with a time of flight of 44 days. Table 10.3 shows the ΔV required for the transfer, for different initial masses of the spacecraft and the three cases: (1)

$t_w = 0$, $ToF = 44$ days; (2) $t_w = 40$ min, $ToF = 44$ days; (3) $t_w = 43$ min, $ToF = 44$ days - 43 min, where t_w is a waiting time on the departure orbit, before starting the transfer, that causes a change of the initial phase angle.

Table 10.3: ΔV required for the transfer from object 39012 to object 39016 for different initial masses of the spacecraft, departure times and times of flight.

m [kg]	ToF = 44 days $t_w = 0$ min	ToF = 44 days $t_w = 40$ min	ToF = 44 days - 43 min $t_w = 43$ min
800	0.0836	0.0836	0.0838
1000	0.0856	0.0856	0.0858
1200	0.0886	0.0886	0.0858
1400	0.0947	0.0947	0.0931
1600	0.1110	0.1110	0.1101

Given its negligible effect on the ΔV and ToF, the phasing will not be considered when estimating the cost of the transfers.

10.5.5 Problem transcription

For the De-orbiting TSP strategy, the chaser rendezvous with each object using the strategy described in Section 10.5.4. During the optimisation process the drag perturbation is not included in the analytical propagator because the effect of the drag is negligible at the considered altitudes. As an example of the De-orbiting TSP, Figures 10.9 show the variation of orbital elements during the transfer from object 40342 to object 40338, realised in 42 days.

For the De-orbiting VRP, the following transfer model is assumed. Considering a situation in which the chaser has already realised rendezvous and docking with one of the target objects, the total transfer from one target to another consists in the following phases:

- The chaser de-orbits the target object by applying a constant negative tangential thrust over all its orbit, until it reaches a perigee of 300 km altitude. Once this disposal orbit has been reached, the servicing spacecraft disengages with the target.
- The chaser increases its semi-major axis by applying a constant positive tangential thrust, until it reaches the semi-major axis of the next target object
- The chaser rendezvous with the next target object using the strategy described in Section 10.5.4

The de-orbiting and orbit raising phases are computed using the averaged analytical propagator described in Chapter 4 and considering both J_2 and drag perturbations. As an example, Figure 10.10 shows the variation of perigee altitude of the chaser (grabbing object 36413 during the de-orbiting phase) and the subsequent orbit raising phase. The total time required is 180 days. The shorter orbit raising time is due to the fact that, when the perigee reaches 300 km, the servicing spacecraft disposes of the target. The orbit raising phase is, therefore, realised with a lower mass, resulting in an increased acceleration. Figure 10.10 shows also the variation

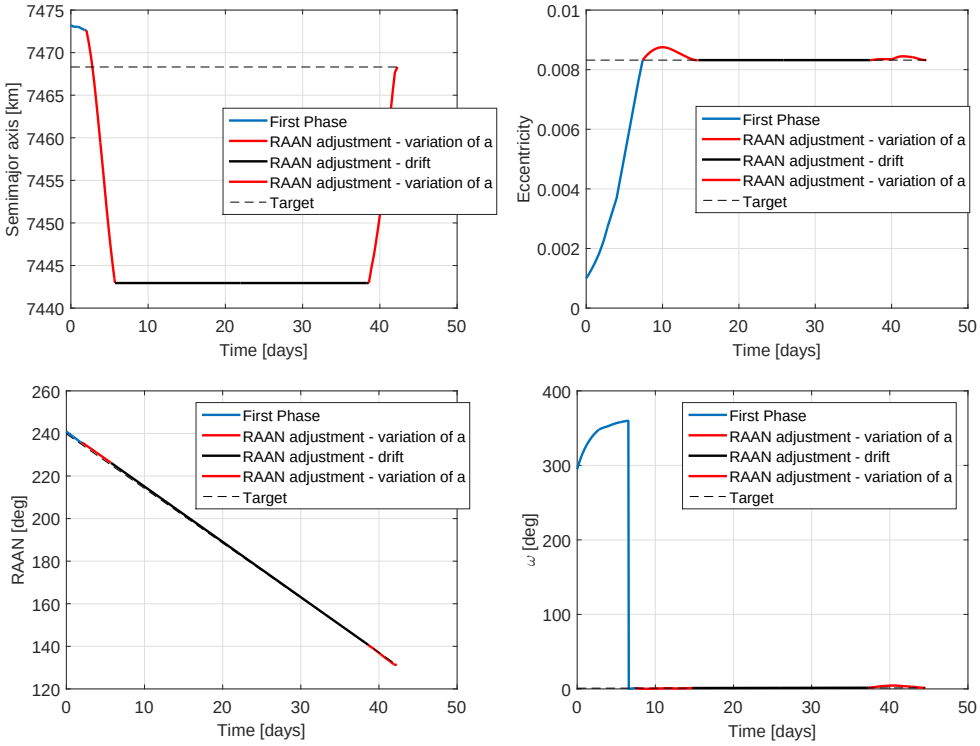

Figure 10.9: Orbital element variation of the chaser and of the target object 40338 during the transfer from spacecraft 40342 to 40338.

of Ω of the servicing spacecraft during the de-orbit and orbit raising phases and the variation of right ascension of the next target object, 39011. The right ascension of the two objects at the end of the orbit raising phase is very close, resulting in a reduced transfer time to the target object.

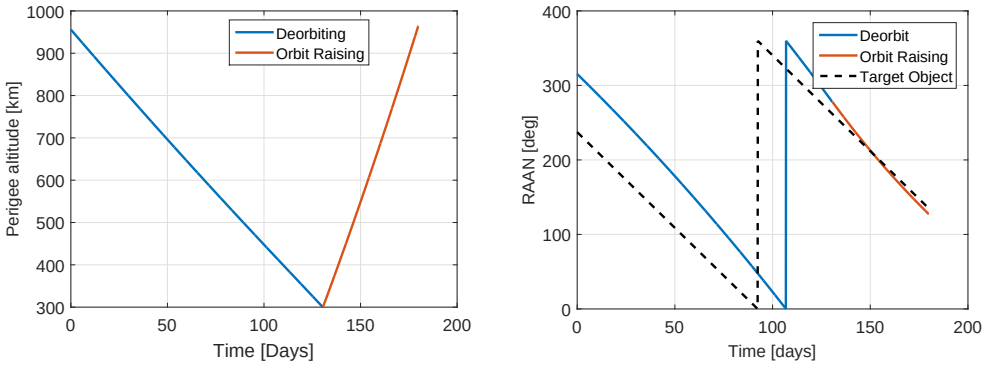

Figure 10.10: Variation of the perigee altitude for the servicing spacecraft during de-orbit of object 36413 and orbit raising to the semi-major axis of target object 39011.

10.5.6 Optimisation method

A direct method based on a single-shooting, direct collocation method is used (refer to Section 5.3). The MATLAB *fmincon-sqp* algorithm is used to solve the problem. Four nodes and linear interpolation are used to model the variation of the control variables in the optimisation of the first transfer of the rendezvous strategy when e, i and ω are modified; that is, with reference to Section 5.3, $k_{LT} = 4$. From four to eight nodes ($k_{LT} \in [4, 8]$) are used for the optimisation of the transfer to and from the parking orbit in order to adjust Ω.

Low-thrust transfer surrogate model

In order to reduce the computational burden in the process of the identification of the optimal sequence of targets, a surrogate model of the low-thrust transfer model is used by the Physarum algorithm to evaluate the cost to link two nodes (Section 10.4) [239].

The surrogate is generated before the optimisation using a database of pre-computed transfers between pairs of departure and target orbits. The surrogate model provides the value of the ΔV for a given combination of mass of the spacecraft and time of flight, that is $\Delta V = \Delta V(m, ToF)$. For this study, the MATLAB Toolbox DACE (Design and Analysis of Computer Experiment) has been used to construct a Kriging-based surrogate of the ΔV (Section 6.1) [132]. Each surrogate model is generated using 48 training points disposed on a regular grid. Figure 10.11 shows the surrogate model for the transfer from object 36414 to object 36417.

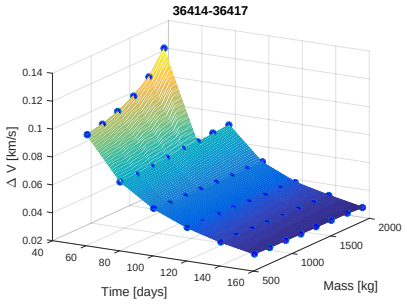

Figure 10.11: Surrogate model for the computation of ΔV for the transfer 36414-36417.

10.6 Mission definition

For this study, an electric propulsion engine providing 0.1 N of thrust and characterised by a specific impulse I_{sp} of 1600 s is considered. The wet mass of the servicing spacecraft, without the mass of the de-orbiting kits, is 1000 kg. Each serviced target is assumed to have a mass of 2000 kg [1]. For the De-orbiting TSP, 10 de-orbit kits of 175 kg are assumed to be on board the servicing spacecraft, resulting in a total initial mass of 2750 kg. The mass of 175 kg has

[1] http://astronautix.com/c/changzheng4c.html

been estimated considering the propellant required to reduce the perigee of the orbit of all the considered targets to 300 km. Assuming that the de-orbiting kit is activated at the apogee of the orbit of the target, the ΔV_{DK} required to reduce the perigee altitude to $h_{\oplus,pD} = 300$ km is

$$\Delta V_{DK} = \sqrt{2\frac{\mu_\oplus}{r_a} - \frac{\mu_\oplus}{a}} - \sqrt{2\frac{\mu_\oplus}{r_a} - \frac{\mu_\oplus}{a_D}}\,, \tag{10.17}$$

where a is the semi-major axis of the satellite to be de-orbited (Table 10.1), r_a is its apogee radius and $a_D = (r_a + r_{pD})/2$, where $r_{pD} = h_{\oplus,pD} + R_\oplus$. Assuming a specific impulse of the de-orbiting kit of $I_{sp} = 303.5$ s [236] and a structural mass fraction equal to 0.2 (to include also the mass of the attaching mechanism of the de-orbit kit), the higher mass of de-orbit kit for all the objects in Table 10.1 is 175 kg. It is assumed that at 300 km the effect of the drag is relevant enough to cause the re-entry of the object. For the objects in Table 10.1, a perigee altitude of 300 km causes the object to re-enter naturally in a time that goes from a minimum of 541 days to a maximum of 654 days. Introducing a lower altitude, corresponding, for example, to a controlled re-entry is also possible and would simply increase the mass of all the de-orbiting kits without affecting the overall strategy. A 175 kg drop is therefore modelled after each transfer to simulate the attachment of the de-orbit kit to the target. The propellant mass resulting from the transfer is also subtracted from the current mass. The settings and parameters for the Physarum algorithms are defined in [64]. Here, only the main relevant parameters of the problem are given: the set of targets $S_s = \{S_1, S_2, \ldots, S_{N_P}\}$ (Table 10.1), the mission start epoch, t_{start}, the maximum mission time, T_{max}, the lower and upper boundaries on the time of flight, ToF_{min} and ToF_{max}, for each leg connecting two targets i and j, the time spent at the target to dock and install the de-orbiting kit, $t_{servicing}$, and the maximum allowed change of velocity ΔV_{max}. Another important parameter is the maximum number of function calls, $Feval_{max}$, where a function call corresponds to the evaluation of one arc. The values of these parameters are reported in Table 10.4.

Table 10.4: Setting parameters

$Feval_{max}$	1×10^5
S_s	All elements in Table 10.1
t_{start}	30 May 2015
T_{max}	365 days
ToF_{min}	1 day
ToF_{max}	60 days for the De-orbiting TSP 185 days for the De-orbiting VRP
$t_{servicing}$	7 days
ΔV_{max}	2.0 km/s

10.7 Results

This section presents the results obtained for each of the two proposed ADR strategies. For each one of the two strategies, the Physarum solver is run on 25 different instances of the

optimisation problem. Each instance uses one of the 25 targets in Table 10.1 as the starting point of the sequence of targeted objects. Each optimisation is repeated 50 times, given the stochastic nature of the Physarum solver.

10.7.1 De-orbiting TSP

Figure 10.12 shows the results obtained when considering different possible initial targets for the 50 runs of the Physarum solver. The x-axis shows the NORAD ID of the first target in the sequence and the y-axis the total ΔV (left) and time of flight, ToF, (right) required for the entire mission. Each dot corresponds to one of the 50 solutions.

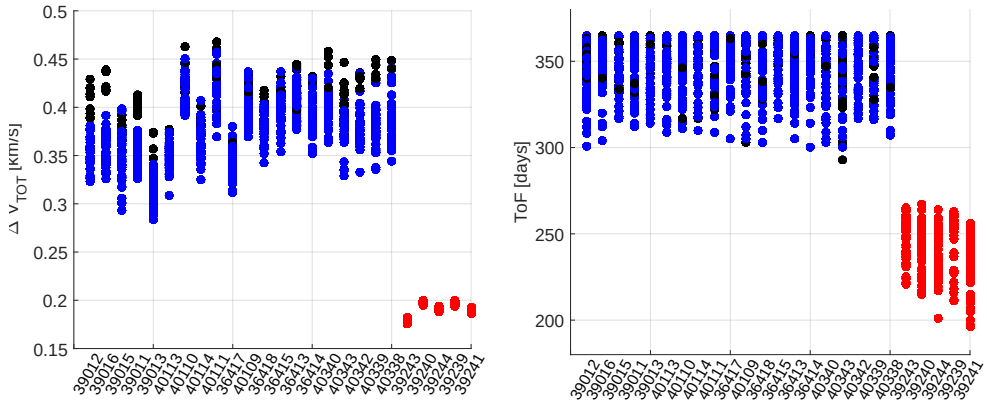

Figure 10.12: ΔV and ToF of 50 runs of the Physarum solver for the De-orbiting TSP, using different initial objects (as shown on the x axis). Black dots represent solution with 10 de-orbited objects, blue dots solutions with 9 de-orbited objects and red dots solutions with 5 de-orbited objects.

Figure 10.12 shows that the solver finds solutions with 10 or 9 de-orbited objects in most of the cases but can find only sequences with a maximum of 5 de-orbited objects if the first object is 39243, 39240, 39244, 39239 or 39241. This is due to the value of the right ascension of these objects, extremely different from the right ascension of the others (see Table 10.1). This means that a transfer from these targets to any other target in Table 10.1 requires longer times of flight.

The solution characterised by the maximum number of visited objects (10) and lower ΔV is reported in Table 10.5. Ten objects, identified in Table 10.5 by their NORAD ID, can be removed in less than one year. The mass m_0 is the mass at the beginning of each transfer and m_f is the mass at the end of each transfer. ToF represents the time of flight required to realise each transfer. The total time of the mission, considering a servicing time of 7 days for each object, is 365 days.

Information about the variability of the results obtained by the Physarum solver are given in Table 10.6. The first column shows the target used as root for the generation of the tree; the second column shows the maximum number of de-orbited targets starting from that root; the third column reports the number of runs (out of the 50) that return a number of de-orbited

Table 10.5: Sequence of satellite for De-orbiting TSP.

	Dep. Object	Arr. Object	ΔV [km/s]	ToF [days]	m_0 [kg]	m_f [kg]
1	39013	39011	0.010	51.00	2575.00	2398.35
2	39011	39012	0.004	10.00	2398.35	2222.81
3	39012	39016	0.093	27.00	2222.81	2034.60
4	39016	40342	0.044	31.00	2034.60	1853.95
5	40342	40340	0.013	32.00	1853.95	1677.44
6	40340	40339	0.024	43.00	1677.44	1499.85
7	40339	40338	0.003	2.00	1499.85	1324.58
8	40338	40343	0.114	52.00	1324.58	1139.98
9	40343	39015	0.042	54.00	1139.98	961.90
Total	-	-	0.3470	302	-	-

targets equal to the maximum number in column two; column four reports the number of unique sequences among the solutions with number of de-orbited targets equal to the maximum number; ΔV_{min} is the minimum cost of the solutions with maximum number of de-orbited targets and the last column reports the number of solutions with same sequence of visited targets as the one characterised by ΔV_{min}. The result relative to Table 10.5 is shown in bold. The sequence of targets reported in Table 10.5 is found 2 times by the Physarum solver, once with ΔV equal to 0.3470 km/s and total time of flight of 365 days (Table 10.5) and once with a ΔV of 0.3730 km/s and 334 days of time of flight.

The average run time per generation of the optimiser on one TSP instance using 40 agents is 2 minutes on an Intel(R) Core(TM) i7-3770 CPU 3.4GHz with 8GB RAM with the code implemented in MATLAB.

10.7.2 De-orbiting VRP

Figure 10.13 shows the results obtained when considering different possible initial targets for the De-orbiting VRP and 50 runs of the solver. The x-axis shows the NORAD ID of the first target in the sequence and the y-axis the total ΔV and time of flight required for the entire mission.

The solution characterised by the maximum number of de-orbited targets and lower ΔV for the De-orbiting VRP ADR is reported in Table 10.7. In this Table ToF represents the time required to de-orbit the initial target, raise the orbit to the semi-major axis of the next target and then adjust all the other orbital elements.

The de-orbiting of a target from the selected altitude region and the subsequent orbit raising to the next target takes a considerable amount of time, making this strategy not viable to remove 5 to 10 targets per year. These results are in agreement with the work presented in [220], where it is found that 5 objects per year can not be actively de-orbited by grabbing and moving them to a given disposal orbit. Information about the variability of the results obtained with the Physarum solver are given in Table 10.8. The results relative to Table 10.7 are shown in bold. In this case the Physarum solver finds 5 solutions with sequence equal to

Table 10.6: Analysis of the results given by the Physarum solver for the De-orbiting TSP.

Root	Max. num. objects	Num. sol. max. num. objects	Unique seq. max. obj.	ΔV_{min} [km/s]	Num. sol. same seq. ΔV_{min}
39012	10	9/50	4	0.3889	5
39016	10	5/50	3	0.4163	3
39015	10	10/50	6	0.3666	1
39011	10	9/50	3	0.3920	5
39013	**10**	**4/50**	**3**	**0.3470**	**2**
40113	10	2/50	2	0.3719	1
40110	10	6/50	4	0.4050	3
40114	10	6/50	4	0.3720	2
40111	10	7/50	5	0.3992	3
36417	10	2/50	2	0.3639	1
40109	10	8/50	6	0.4065	1
36418	10	5/50	4	0.3956	1
36415	10	5/50	3	0.4037	1
36413	10	5/50	4	0.3969	2
36414	10	7/50	4	0.3943	1
40340	10	4/50	3	0.4200	2
40343	10	21/50	9	0.3724	4
40342	10	5/50	3	0.4190	3
40339	10	6/50	4	0.4282	2
40338	10	3/50	2	0.4255	2
39243	5	50/50	1	0.1755	50
39240	5	50/50	2	0.1951	34
39244	5	50/50	3	0.1882	26
39239	5	50/50	2	0.1939	31
39241	5	50/50	2	0.1865	42

the one reported in Table 10.8.

For the De-orbiting VRP the run time is dependent upon the target used as root of the decision graph. The maximum run time per generation for 40 agents is 11 minutes on an Intel(R) Core(TM) i7-3770 CPU 3.4GHz with 8GB RAM with the code implemented in MATLAB.

10.8 Conclusions

This chapter has presented two low-thrust Active Debris Removal strategies: De-orbiting TSP and VRP. In the De-orbiting TSP strategy a servicing spacecraft, equipped with a low-thrust propulsion engine, attaches a de-orbit device to each target to be removed; in the De-orbiting VRP strategy the servicing spacecraft grab the targets and de-orbit them using low-thrust propulsion. Targets in LEO with altitude in the 800-1400 km range are considered in this analysis.

In order to find the optimal sequence of targets to be serviced (with the objective of maximising the number of de-orbited objects and minimising the propellant consumption), an incremental planning and scheduling optimisation algorithm is used. In order to reduce the computational burden, the planning and scheduling algorithm is used in conjunction with the

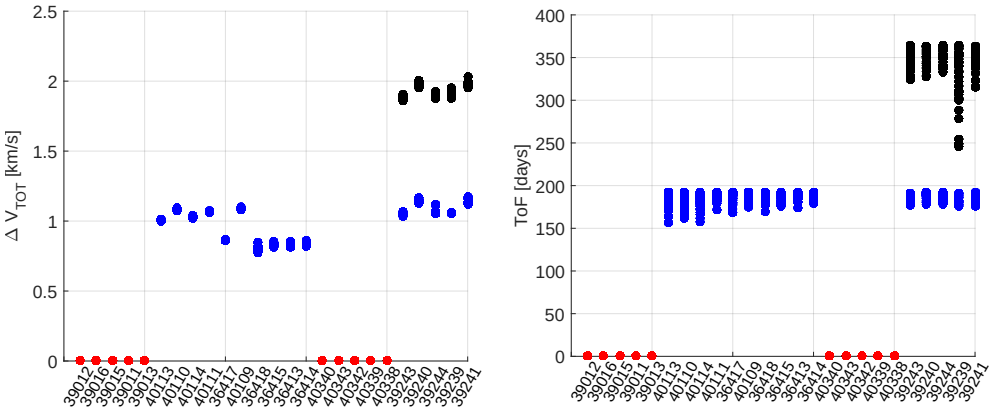

Figure 10.13: ΔV of 50 runs of the Physarum solver for the De-orbiting VRP, with different initial object in the sequence (as shown on the x axis). Black dots represent solution with 3 serviced objects, blue dots solutions with 2 serviced objects and red dots represents solution with 1 serviced objects.

Table 10.7: Sequence of satellite for the De-orbiting VRP strategy.

	Dep. Object	Arr. Object	ΔV [km/s]	ToF [days]	m_0[kg]	m_f[kg]
1	39243	36413	1.049	163.00	3000.00	2888.62
2	36413	39015	0.809	183.00	2888.62	2801.66
Total	-	-	1.8571	353	-	-

use of a surrogate model of the low-thrust transfer model.

This planning approach provides, per run, 1600 solutions in approximately 80 minutes for the De-orbiting TSP and in a maximum time of 7 hours for the De-orbiting VRP. On the De-orbiting TSP, out of the 1600 solutions, the planner can consistently find sequences with 10 objects, together with a large number of sequences with 9 objects or less. For the De-orbiting VRP, solutions fulfilling the one year constraint are limited to 3 targets.

Results have shown that the De-orbiting TSP strategy is the most effective ADR method, given the time constraint of 1 year for the mission time. Up to 10 targets per year can be removed with this strategy. On the contrary, the time required by the De-orbiting VRP strategy to de-orbit one single target makes it an infeasible option. This is in agreement with what found in [220]. Moreover, the De-orbiting TSP strategy is also less risky because the servicing spacecraft spends a shorter time in contact with the non-cooperative target and is not subjected to the perturbations experienced during the de-orbiting phase.

To be noted that the De-orbiting TSP strategy analysed in this work considers identical de-orbiting kits for each satellite and a cost function that does not depend on the mass of the de-orbiting kit. If the mass of the de-orbiting kit was included in the cost function the planner would yield also the optimal distribution of de-orbiting kits for a given scenario. This will be the subject of a future investigation.

Table 10.8: Information about the variability of the results of the Physarum solver for the Spiral De-orbiting VRP strategy.

Root	Max. num. objects	Num. sol. max. num. objects	Unique seq. max. obj.	ΔV_{min} [km/s]	Num. sol. same seq. ΔV_{min}
39012	1	50/50	1	-	-
39016	1	50/50	1	-	-
39015	1	50/50	1	-	-
39011	1	50/50	1	-	-
39013	1	50/50	1	-	-
40113	2	50/50	1	1.0026	50
40110	2	50/50	3	1.0710	48
40114	2	50/50	1	1.0219	50
40111	2	50/50	2	1.0592	34
36417	2	50/50	3	0.8581	12
40109	2	50/50	4	1.0837	42
36418	2	50/50	2	0.7748	48
36415	2	50/50	2	0.8172	39
36413	2	50/50	3	0.8118	36
36414	2	50/50	4	0.8190	21
40340	1	50/50	1	-	-
40343	1	50/50	1	-	-
40342	1	50/50	1	-	-
40339	1	50/50	1	-	-
40338	1	50/50	1	-	-
39243	**3**	**29/50**	**9**	**1.8571**	**5**
39240	3	26/50	4	1.9513	5
39244	3	26/50	7	1.8766	13
39239	3	41/50	4	1.8753	17
39241	3	28/50	8	1.9513	5

This chapter has applied the methodologies presented in Chapters 4 and 5 to the design of a mission in LEO. In the next chapter a concept to deploy the satellite of a constellation in MEO, using the novel laws presented in Chapter 3, will be described.

The content of this chapter was published in M. Di Carlo, L. A. Ricciardi, M. Vasile, "Multi-Objective Optimisation of Constellation Deployment using Low-Thrust Propulsion", 2016 AIAA/AAS Astrodynamics Specialist Conference, 13-16 September 2016, Long Beach, CA

Chapter 11

Constellation deployment

In this chapter an analysis of the deployment of future constellations using a combination of low-thrust propulsion and natural dynamics is presented. The deployment of the constellation is formulated as a multi-objective optimisation problem that aims at minimising the maximum transfer ΔV and the launch cost and maximise, at the same time, the pay-off given by the service provided by the constellation. The ΔV cost of the transfers is computed using the analytical equations presented in Chapter 3. The study considers the case of a typical constellation with 27 satellites in Medium Earth Orbit (MEO) and the use of only two launchers, one of which can carry a single satellite. It will be demonstrated that some strategies and deployment sequences are dominant and provide the best trade-off between peak transfer ΔV and monetary pay-off.

This chapter is structured as follows. Section 11.1 gives an introduction to the constellation and constellation deployment problem. Section 11.2 describes the configuration of the considered constellation, while Section 11.3 presents the method adopted to define the deployment sequence and Section 11.4 presents the considered launchers. The low-thrust and multi-objective techniques are described in Sections 11.5 and 11.6; Section 11.7 presents the results and Section 11.8 concludes the chapter.

11.1 Introduction and motivations

Satellite constellations are used for a wide range of applications and are deployed in different orbital regime around the Earth, according to their purpose. Navigation systems such as the Global Positioning System (GPS)[1], the Russian Glonass[2] and the Chinese BeiDou[3] are based on satellite constellations in MEO. The European Space Agency is currently launching its own navigation system, Galileo [4], in MEO. Telecommunication services are provided by constella-

[1] http://www.gps.gov/
[2] https://www.glonass-iac.ru/en/
[3] http://en.beidou.gov.cn/
[4] http://www.esa.int/Our_Activities/Navigation/Galileo/What_is_Galileo

tions in LEO, such as Globalstar[5] and Iridium[6]. Constellations are present in Sun-Synchronous Orbits for Earth Observation purposes (A-Train[7]) and in Geosynchronous High-Elliptic Orbit (HEO) for communications service to high-latitude regions (Sirius[8]). More constellation services are going to be launched in the near future: as an example, OneWeb[9] plans to put 720 small satellites in LEO starting in 2018 to provide broadband services.

This trend demands for an efficient satellite constellation launch and deployment strategy. As the number of satellites in orbit around the Earth increases it is also paramount to devise an appropriate de-orbiting strategy for the spacecraft at the end of the constellation lifetime. The aim is to avoid what happened on February 10, 2009, when an inactive Russian communications satellite, Cosmos 2251, collided with one of the satellite of the Iridium constellation, producing almost 2,000 pieces of debris. It is therefore desirable to equip future constellations with a propulsion system with sufficient propellant to de-orbit at the end of life or move to a safe graveyard orbit, such as an electric propulsion system.

The aim of the study presented in this chapter is in finding an optimal deployment sequence (which satellite is allocated to which slot), optimal launch sequence (which satellites are launched with which launcher) and optimal transfer strategy (which low-thrust trajectory is required to achieve the required slot) that can provide maximum pay-off, minimum launch cost and minimise the mass of propellant. The first objective defines the monetary gain provided by the service delivered by the constellation. The earlier the satellites in the constellation start providing their service the higher is the pay-off. The last objective, the propellant mass, is dictating the sizing of the propulsion system and the mass allocated to the deployment sequence.

The deployment sequence is a complex combinatorial problem that is here addressed with a simple deterministic greedy incremental algorithm that provides fast, though suboptimal, solutions. A separate combinatorial problem, equivalent to a bin packing problem, is solved to identify all the possible launch sequences assuming only two launchers are available. The solution of this second combinatorial problem provides the cost of the launch sequence. Finally the transfer strategy is optimised with a memetic evolutionary algorithm, called MACS2 (Multi-Agent Collaborative Search) that maximises the pay-off and minimises the maximum ΔV of the transfer. The ΔV costs of the transfers are calculated with the transfer strategy presented in Chapter 3.

11.2 Configuration of the constellation

The constellation considered in this study is a Walker Delta 56°:27/3/1 constellation in MEO [81]. In the notation $i : t/p/f$, used to describe Walker Delta constellation, i represents the inclination of the orbit, t the total number of satellites, p the number of planes and f is the rela-

[5] https://www.globalstar.com/en/
[6] https://www.iridium.com/
[7] https://atrain.nasa.gov/
[8] http://www.siriusxm.com/
[9] http://oneweb.world/

tive spacing between satellites in adjacent planes. The semi-major axis of the orbits is $a_{MEO} =$ 24200 km and the right ascension of the ascending node of the three planes are equally spaced of 120 deg. It is assumed that the only perturbation acting on the satellites is due to the second order zonal harmonic of the geopotential, J_2. This perturbation causes the right ascension of the orbital plane to drift at a rate given by Equation 3.1. A graphical representation of the considered constellation is given in Figure 11.1, where the axis are in Earth-radii.

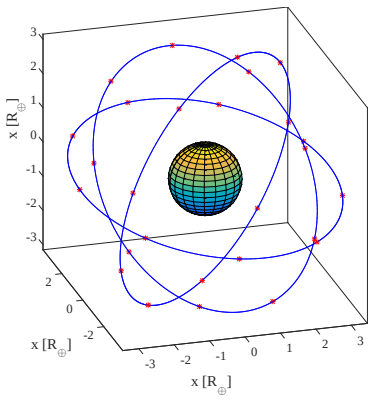

Figure 11.1: Walker Delta 56°:27/3/1 constellation.

11.3 Deployment sequence

In this section the method adopted to define the deployment sequence is described. The deployment sequence allows to define which satellite is allocated to which slot and the order with which these slots should be filled. The desired coverage strategy is the one that maximises the rate at which the constellation reaches its fully deployed coverage, i.e. that delays as much as possible eventual partial overlaps of coverage. To avoid dealing with a rather complex geometric problem involving the intersection of several spherical caps, the problem is tackled using an analogy: each satellite is considered to be an electrically charged particle that could be collocated in one of the available slots. By using this analogy, the desired coverage strategy translates into the strategy that minimises the integral over time of the energy of the whole system, assuming that the time interval between the collocation of each subsequent satellite is constant. A brute force analysis of all the possibilities for 27 satellites would require considering 27! combinations ($\approx 10^{28}$); in order to solve the problem a greedy tree-search approach is used instead [62]. With this approach, an initial position for the first satellite is chosen. Then, the integral over time of the energy resulting from the addition of one satellite is computed for all possible remaining positions, and all combinations with the same minimum are stored. With this approach, at each stage, a locally optimal choice is made, in an attempt to find the global optimum. This is repeated, stage by stage, for all promising combinations until all the satellites are collocated, and is also repeated for every possible choice for the initial satellite. This greedy approach does not guarantees to find the global optimal solution but provides

good solutions in a reasonable amount of time. Due to the symmetries present in the problem, multiple equivalent optimal solutions are possible, but only one is considered in the following [62]. The optimal satellite deployment sequence obtained is shown in Figure 11.2, where the abscissa indicates the ID of the satellite and the ordinate the plane (from 1 to 3) of arrival of the satellite.

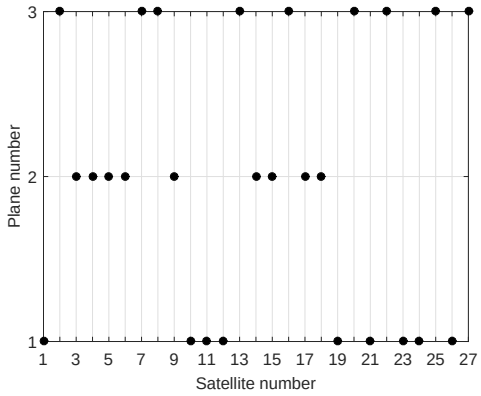

Figure 11.2: Representation of the optimal sequence of satellite deployment.

11.4 Launchers

For this study, two European launchers are considered: Vega[10] and Ariane 5[11]. For each launcher, models relating payload mass, target inclination and semi-major axis are developed from available data as simple second order bivariate polynomials. Figures 11.3 and 11.4 show the resulting surface for the two launchers.

It is assumed that the mass of each spacecraft is 700 kg. Due to fairing limitations, it is assumed that Vega can carry one satellite in orbit, while Ariane can carry four satellites of the constellation. With this assumption, and for a constellation of 27 satellites, 7 possible combinations of Ariane and Vega launches allow the deployment of the entire constellation. The total cost of the launches differs for the seven possibilities. Assuming a cost per launch of 32 million Euro for Vega and 200 million Euro for Ariane, the total cost reported in Table 11.1 can be obtained. The table also reports, for each combination, the total number of possible launch sequences.

Table 11.1 shows that two limit value exist for the cost of the launches. The minimum cost is obtained when all the launches are realised using Vega (option 1). The maximum cost is obtained when 6 launches are realised with Ariane and 3 with Vega (option 7). Assuming a rate of one launch per year, option 1 would require 27 years while option 7 would require 9 years, so there is a clear trade-off between total cost of the launches and total deployment time

[10] http://www.arianespace.com/wp-content/uploads/2015/09/Vega-Users-Manual_Issue-04_April-2014.pdf

[11] http://www.arianespace.com/wp-content/uploads/2015/09/Ariane5_users_manual_Issue5_July2011.pdf

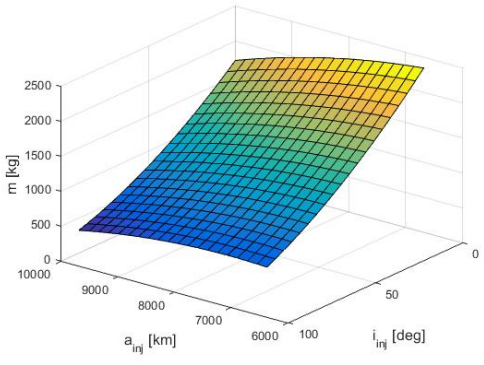

Figure 11.3: Relationship between mass and injection semi-major axis and inclination for Vega.

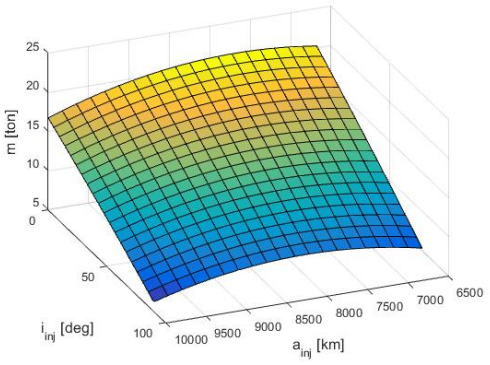

Figure 11.4: Relationship between mass and injection semi-major axis and inclination for Ariane 5.

Table 11.1: Combinations, launch sequences and total cost of Vega and Ariane launches for the deployment of a constellation of 27 satellites

	1	2	3	4	5	6	7
Number Ariane launches	0	1	2	3	4	5	6
Number Vega launches	27	23	19	15	11	7	3
Possible launch sequences	1	24	210	816	1365	792	84
Total cost [M €]	864	936	1008	1080	1152	1224	1296

(which relates to a reduced pay-off). [12] Due to the very large total number of possible launch sequences for the 7 deployment strategies (each of which would be followed by the solution of a bi-objective optimisation problem for the minimisation of the ΔV and the maximisation of pay-off), only a systematic study of the two limit cases was performed in the rest of the study.

11.5 Low-thrust transfer

Low-thrust strategies for the transfer between circular inclined orbits under the effect of J_2 are presented in Chapter 3. In this work the strategy presented in Section 3.4, providing the lower ΔV, is used for the transfer from the launcher injection orbit to the operational orbit in the MEO region.

[12] For the Vega launcher, the frequency of launches could be increased to more than one launch per year. An increase in the frequency of launches of Vega would result in a different value of the profit generated by each satellite. As a consequence, the results would be different from the ones presented in Section 11.7, since the multi-objective optimiser would have to optimise a different profit function. However, the solution method would remain the same.

11.6 Multi-objective deployment optimisation

The objectives of the optimisation of the constellation deployment are the minimisation of the maximum ΔV of all the low-thrust transfer, the maximisation of the profit of the constellation and the minimisation of the cost of the launches. As regards the cost of the launches, the two extreme cases in Table 11.1 are considered. The objectives considered in the following are therefore:

- minimisation of the maximum ΔV of the low-thrust transfers;
- maximisation of the profit P obtained from the deployment of the constellation. Each satellite is assumed to generate profit from the moment it reaches its final orbit, denoted as $T^i_{LAUNCH} + ToF^i$, up to an an end date defined as 5 years after the date of the last launch, T^{27}_{LAUNCH}:

$$P = \left[T^{27}_{LAUNCH} + 5 \text{ years} - \left(T^i_{LAUNCH} + ToF^i\right)\right] \dot{P} \tag{11.1}$$

  The adimensional profit rate $\dot{P}$ considered in this work is of one unit per day.

The multi-objective problem is solved using the memetic multi-objective optimiser Multi Agent Collaborative Search (MACS2) [177], a tool developed at the University of Strathclyde. Multi-Agent Collaborative Search is a meta-heuristic that combines local and global search heuristics. The vector of optimisable parameters $\mathbf{x}$, that is handled by MACS2, includes, for each satellite launched, the semi-major axis of the injection orbit, a_{inj}, the inclination of the injection orbit, i_{inj}, the right ascension of the ascending node of the injection orbit, Ω_{inj} and the time of flight from the injection to the operational orbit, ToF:

$$\mathbf{x} = [a^1_{inj}, i^1_{inj}, \Omega^1_{inj}, ToF^1, a^2_{inj}, i^2_{inj}, \Omega^2_{inj}, ToF^2, \ldots, a^{27}_{inj}, i^{27}_{inj}, \Omega^{27}_{inj}, ToF^{27}]^T \, . \tag{11.2}$$

When four satellites are launched with Ariane, the time of flights of the four satellites are constrained such that the sequence of deployment defined in Section 11.3 is still satisfied. The final semi-major axis and inclination of the arrival orbit are a_{MEO} and i_{MEO}. The right ascension of the arrival orbits is computed from Equation 3.1, based on the arrival time of the satellite on the selected orbit. The boundaries for the parameters to optimise are

$$\begin{aligned} &6878 \text{ km} \leq a_{inj} \leq 9378 \text{ km} \, , \\ &0 \text{ deg} \leq i_{inj} \leq 50 \text{ deg} \, , \\ &0 \text{ deg} \leq \Omega_{inj} \leq \ 360 \text{ deg} \, , \\ &300 \text{ days} \leq ToF \leq 1500 \text{ days} \, . \end{aligned} \tag{11.3}$$

The selected values of admissible a_{inj} have been chosen in order to avoid regions where the effect of the drag is not negligible ($a < 6878$ km) and regions where the drift of Ω due to J_2 is not very significant ($a > 9378$ km). Likewise the range of inclinations is restricted to exploit

the natural dynamics for the change of Ω. The considered value of the acceleration for the low-thrust transfer is 1.20510^{-4}m/s^2.

11.7 Results

This section presents the results obtained for the two selected cases in Table 11.1: maximum launch cost with minimum launch time, minimum launch cost with maximum launch time.

11.7.1 Maximum launch cost with minimum launch time

Option 7 in Table 11.1 identifies the solution with minimum launch times (9 years, in the assumption of 1 launch per year) but maximum cost for the launches (1296 million euros). The total cost of the 9 launches is fixed but different combinations of sequences of Ariane and Vega launches exist for that cost. In particular, 84 possible combinations of launches can be identified; some of these combinations are presented in Table 11.2, where "V" stands for launch with Vega and "A" for launch with Ariane.

Table 11.2: Possible combinations of Ariane and Vega launches for solution with deployment of the constellation in 9 launches.

Comb. \ Launch	1	2	3	4	5	6	7	8	9
1	V	V	V	A	A	A	A	A	A
2	V	V	A	V	A	A	A	A	A
⋮									
78	A	A	A	A	V	A	V	V	A
⋮									
81	A	A	A	A	A	V	V	V	A
82	A	A	A	A	A	V	V	A	V
83	A	A	A	A	A	V	A	V	V
84	A	A	A	A	A	A	V	V	V

Each combination defined in Table 11.2 generates a Pareto set in the plane ΔV_{max}-Profit. The 84 Pareto sets obtained are shown in Figure 11.5, with different color for each combination. A single Pareto set can be obtained by considering the non-dominated solution of the 84 combinations. This is shown in Figure 11.6, along with a number identifying the sequence of Vega and Ariane launchers (Table 11.2).

Results in Figure 11.6 show that only four combinations of launches give non-dominated results. These are combinations 78, 81, 82 and 84. The sequence of launchers for these four cases can be found in Table 11.2. The solutions of combination 84 are characterised by higher profit and higher maximum ΔV while the solutions of combination 78 are characterised by lower profit and lower maximum ΔV.

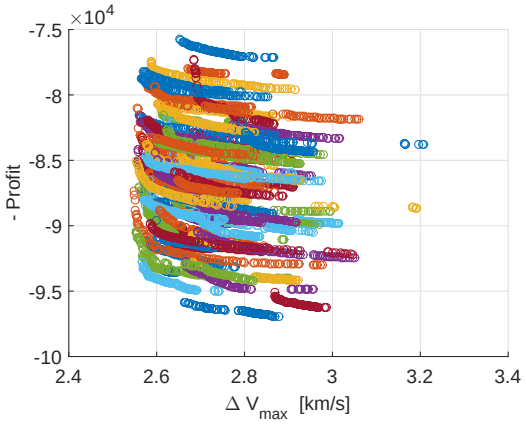

Figure 11.5: Pareto sets of the 84 combinations of launches corresponding to option 7 in Table 11.1.

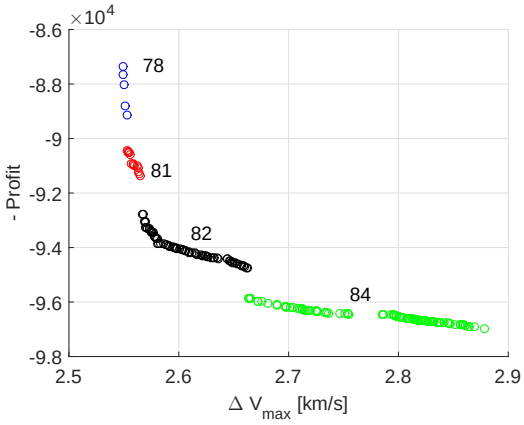

Figure 11.6: Non-dominated solutions resulting from the combinations of the 84 Pareto sets in Figure 11.5

Details of the two extreme solutions of the Pareto set are presented in Tables 11.3 and 11.4. Each table shows the number of the plane where each satellite is launched, the year of the launch, the name of the launcher, the time of flight and ΔV associated to the low-thrust transfer, the parameters of the injection orbit and the right ascension of the final orbit.

The times of flight in Table 11.3 are averagely higher than the times of flight in Table 11.4. Higher times of flight results in lower ΔV but also lower pay-off from the constellation, since the final time of full deployment of the constellation is shifted in time.

The optimal injection orbits are in both cases characterised by a value of the inclination i_{inj} close to the upper limit of 50 deg. This is due to the fact that changes of inclination are expensive in term of ΔV and require long times of flight and are therefore penalised both in term of ΔV_{max} and profit.

11.7.2 Minimum launch cost with maximum launch time

Option 1 in Table 11.1 identifies the solution with maximum launch times (27 years, under the assumption of 1 launch per year) but minimum total cost for the launches (864 million Euro). In this case only one combination exist for the 27 launches with Vega. The resulting Pareto front is shown in Figure 11.7.

The higher profit with respect to the case of maximum launch cost and minimum launch time is due to the fact that the profit is computed based on the time required for the full deployment of the constellation. In this case the deployment takes 27 years, plus the time of flight of the last satellite, while it was 9 years in the previous case. Table 11.5 shows details of the solution with higher maximum ΔV and higher profit. The higher values of ΔV are due to the limited launch capabilities of Vega with respect to Ariane. The inclination of the injection orbit is indeed lower than in Tables 11.3 and 11.4.

Table 11.3: Solution with minimum maximum ΔV and lower profit (combination of launches 78).

Plane ID	Year	Launcher	ToF [days]	ΔV [km/s]	a_{inj} [km]	i_{inj} [deg]	Ω_{inj} [deg]	Ω_{MEO} [deg]
1	1	Ariane	624.47	2.53	9378.00	49.93	0.00	327.30
3	1	Ariane	625.47	2.54	9378.00	49.93	0.00	207.25
2	1	Ariane	637.20	2.55	9378.00	49.93	0.00	86.63
2	1	Ariane	638.20	2.55	9378.00	49.93	0.00	86.58
2	2	Ariane	519.19	2.55	9378.00	50.00	157.03	73.68
2	2	Ariane	520.19	2.55	9378.00	50.00	157.03	73.63
3	2	Ariane	521.19	2.53	9378.00	50.00	157.03	193.58
3	2	Ariane	522.19	2.53	9378.00	50.00	157.03	193.53
2	3	Ariane	484.95	2.54	9378.00	50.00	0.00	56.35
1	3	Ariane	500.58	2.55	9378.00	50.00	0.00	295.53
1	3	Ariane	501.58	2.55	9378.00	50.00	0.00	295.48
1	3	Ariane	502.58	2.55	9378.00	50.00	0.00	295.43
3	4	Ariane	838.05	2.53	9377.98	50.00	70.56	138.73
2	4	Ariane	839.09	2.53	9377.98	50.00	70.56	18.67
2	4	Ariane	840.09	2.53	9377.98	50.00	70.56	18.62
3	4	Ariane	841.09	2.53	9377.98	50.00	70.56	138.57
2	5	Vega	448.68	2.55	9378.00	50.00	0.00	19.99
2	6	Ariane	655.91	2.54	9378.00	49.92	226.14	350.01
1	6	Ariane	656.91	2.53	9378.00	49.92	226.14	229.96
3	6	Ariane	657.91	2.53	9378.00	49.92	226.14	109.91
1	6	Ariane	658.91	2.53	9378.00	49.92	226.14	229.86
3	7	Vega	412.90	2.55	9378.00	50.00	21.06	103.61
1	8	Vega	579.87	2.55	9378.00	49.99	7.71	195.74
1	9	Ariane	677.39	2.53	9374.53	49.96	199.03	171.50
3	9	Ariane	678.40	2.53	9374.53	49.96	199.03	51.45
1	9	Ariane	679.40	2.53	9374.53	49.96	199.03	171.40
3	9	Ariane	680.40	2.53	9374.53	49.96	199.03	51.35

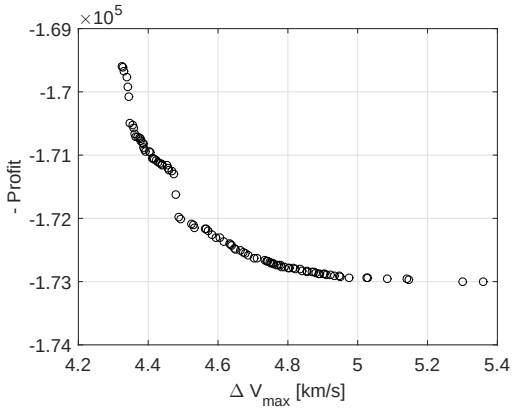

Figure 11.7: Pareto set corresponding to option 1 in Table 11.1.

11.8 Conclusions

This chapter has presented the study of the deployment of a constellation of 27 satellites on 3 planes in MEO using low-thrust propulsion and two possible launchers, Ariane and Vega. A sub-optimal but effective sequence is defined for the launches of the satellite, to allocate each

Table 11.4: Solution with higher maximum ΔV and higher profit (combination of launches 84).

Plane ID	Year	Launcher	ToF [days]	ΔV [km/s]	a_{inj} [km]	i_{inj} [deg]	Ω_{inj} [deg]	Ω_{MEO} [deg]
1	1	Ariane	434.47	2.87	8623.69	50.00	146.72	337.25
3	1	Ariane	435.47	2.82	8623.69	50.00	146.72	217.19
2	1	Ariane	436.47	2.83	8623.69	50.00	146.72	97.14
2	1	Ariane	437.47	2.83	8623.69	50.00	146.72	97.09
2	2	Ariane	405.06	2.85	8719.53	49.68	177.65	79.66
2	2	Ariane	406.06	2.85	8719.53	49.68	177.65	79.61
3	2	Ariane	407.06	2.80	8719.53	49.68	177.65	199.56
3	2	Ariane	408.06	2.80	8719.53	49.68	177.65	199.50
2	3	Ariane	452.77	2.84	8594.14	50.00	92.03	58.03
1	3	Ariane	453.77	2.86	8594.14	50.00	92.03	297.98
1	3	Ariane	454.77	2.86	8594.14	50.00	92.03	297.93
1	3	Ariane	455.77	2.86	8594.14	50.00	92.03	297.88
3	4	Ariane	420.57	2.83	8685.03	49.46	178.91	160.59
2	4	Ariane	421.57	2.88	8685.03	49.46	178.91	40.54
2	4	Ariane	422.57	2.87	8685.03	49.46	178.91	40.49
3	4	Ariane	423.57	2.82	8685.03	49.46	178.91	160.44
2	5	Ariane	501.19	2.84	9294.10	46.04	221.98	17.24
2	5	Ariane	502.19	2.84	9294.10	46.04	221.98	17.19
1	5	Ariane	503.19	2.69	9294.10	46.04	221.98	257.14
3	5	Ariane	504.19	2.73	9294.10	46.04	221.98	137.09
1	6	Ariane	388.98	2.82	8666.91	49.99	189.51	243.99
3	6	Ariane	389.98	2.86	8666.91	49.99	189.51	123.94
1	6	Ariane	390.98	2.81	8666.91	49.99	189.51	243.89
1	6	Ariane	391.98	2.81	8666.91	49.99	189.51	243.83
3	7	Vega	363.79	2.83	8728.84	49.95	104.34	106.18
1	8	Vega	362.44	2.88	8821.09	48.11	186.58	207.13
3	9	Vega	333.83	2.84	8787.84	49.48	10.25	69.50

satellite to a specific slot of the constellation. Two launch options (maximum launch time with minimum launch cost and minimum launch time with maximum launch cost) are studied. The transfer from injection to operation orbit is realised with low-thrust trajectories that exploit the natural perturbations due to the Earth's gravitational potential. Pareto sets are generated to show the relationship between the pay-off of the constellation and the the mass of propellant required for the most expensive low-thrust transfer from injection to operational orbit. Results show that only four combinations of sequence of launches constitute the points of the non-dominated Pareto set for the case of minimum launch time with maximum launch cost. In this case the launch of the constellation can be realised in 9 years, with increase in the pay-off that could be obtained with small variations of the maximum ΔV. The extreme case of maximum launch time (27 years) with minimum launch cost is also studied. In this case the sequence of launches is fixed and only one Pareto set exists.

While this chapter has focused on transfers to the MEO region, in the next chapter, a low-thrust transfer from GTO to GEO will be presented. The transfer will be optimised with local and global optimisation algorithms, rather than multi-objective tools.

Table 11.5: Solution with higher maximum ΔV and higher profit for launches with Vega only.

Plane ID	Year	Launcher	ToF [days]	ΔV [km/s]	a_{inj} [km]	i_{inj} [deg]	Ω_{inj} [deg]	Ω_{MEO} [deg]
1	1	Vega	479.96	4.10	8056.69	35.19	202.69	334.87
3	2	Vega	538.48	5.10	7674.50	27.23	158.37	192.67
2	3	Vega	434.60	4.21	7922.37	35.85	196.60	58.99
2	4	Vega	534.96	4.49	8091.04	33.18	118.76	34.60
2	5	Vega	461.75	3.75	8338.37	38.84	245.55	19.31
2	6	Vega	623.39	4.79	8101.14	26.79	149.88	351.72
3	7	Vega	618.04	4.95	8154.60	26.34	254.89	92.87
3	8	Vega	592.09	5.16	8139.59	26.36	190.83	75.10
2	9	Vega	551.55	4.65	8116.09	28.58	247.00	298.09
1	10	Vega	562.23	4.84	7893.93	28.91	244.28	158.41
1	11	Vega	505.64	4.95	7458.27	30.74	141.15	142.24
1	12	Vega	385.42	3.59	7822.33	42.63	173.26	129.41
3	13	Vega	515.57	4.81	8554.87	28.90	192.58	343.47
2	14	Vega	462.22	4.01	8039.53	37.85	121.40	207.13
2	15	Vega	509.53	4.88	8045.47	29.79	103.71	185.53
3	16	Vega	556.41	4.12	8920.56	29.71	106.02	283.95
2	17	Vega	573.93	4.95	8221.12	26.17	127.12	143.90
2	18	Vega	576.23	4.85	8092.05	28.47	224.02	124.65
1	19	Vega	471.27	4.57	8154.85	32.28	176.69	351.02
3	20	Vega	550.67	4.70	8592.51	29.14	156.64	207.74
1	21	Vega	551.40	4.94	8370.21	25.38	160.31	308.57
3	22	Vega	639.89	4.83	8471.34	24.20	208.49	164.81
1	23	Vega	573.90	4.95	7973.60	25.48	207.63	269.14
1	24	Vega	508.33	4.31	8094.43	32.24	134.14	253.44
3	25	Vega	609.78	5.36	8417.44	22.98	132.38	109.00
1	26	Vega	557.36	4.83	8334.08	28.74	221.32	212.62
3	27	Vega	426.53	4.04	8274.67	36.45	177.77	80.34

The content of this chapter was published in M. Di Carlo, M. Vasile, "Optimised GTO-GEO transfer using low thrust propulsion", 26th International Symposium on Space Flight Dynamics, ISSFD, 3-9 June 2017, Matsuyama, Japan

Chapter 12

Low-thrust GTO-GEO transfer

This chapter proposes a global optimisation of the low-thrust transfers from GTO to GEO, including different types of perturbation. The trajectory transcription method makes use of the analytical solution of the perturbed Keplerian motion presented in Chapter 4, together with a simple direct collocation of the thrust arcs (Chapter 5). Different strategies to explore the set of local minima of the low-thrust GTO to GEO transfer problem are presented and a number of locally optimal solutions are studied. The algorithm MP-AIDEA (Chapter 7) is used to globally explore the search space, so that no user-defined initial guess is required to start the global optimisation process. The chapter is structured as follow: the description of the problem is given in Section 12.1; the optimal transfer is studied with no perturbations in Section 12.2 and with the perturbations due to Earth's oblateness, drag and Sun gravitational attraction in Section 12.3; Section 12.4 concludes the chapter.

12.1 The GTO-GEO global optimisation problem

This chapter is concerned with the global optimisation of transfers from GTO to GEO with initial and final orbital parameters defined in Table 12.1.

Table 12.1: GTO and GEO orbital elements.

	a [km]	e	i [deg]	Ω [deg]	ω [deg]
GTO	24505	0.725	7	0	0
GEO	42165	0	0	-	-

The nominal time of flight for the transfer is $ToF = 225$ days. The spacecraft has initial mass $m_0 = 2000$ kg and engine characterised by thrust $F = 0.5$ N and specific impulse $I_{sp} = 2000$ s. The thrust vector is defined by its magnitude ϵ and by its azimuth and elevation angles, α' and β, in a RTN reference frame, as in Equation 4.2. Initially the thrust is applied along two arcs per orbital revolution, at the perigee and apogee of each orbit, as described in Section 5.3. In the absence of perturbations and for the initial orbital elements given in Table 12.1,

arcs centered at perigee and apogee represents ideal positions along the orbit to change semi-major axis, eccentricity and inclination. Considering the Gauss' equations expressing the time variation of semi-major axis and eccentricity due to perturbations (Equation 2.2), it is possible to define the point of the orbit providing the maximum rate of change of a and e by computing

$$\frac{\partial}{\partial\theta}\frac{da}{dt} = 0, \quad \frac{\partial}{\partial\theta}\frac{de}{dt} = 0, \tag{12.1}$$

where θ is the true anomaly. The previous equations give $\theta_a = 0$ for the maximum rate of change of the semi-major axis and $\theta_e = \pi$ for the maximum rate of change of the eccentricity, showing indeed that thrusting arcs centered at perigee and apogee provide the maximum instantaneous variation of semi-major axis and eccentricity. Following a similar analysis, the point of the orbit providing the maximum rate of change of i is at true anomaly θ_i given by [182]

$$\sin(\theta_i + \omega) = -e\sin\omega\,. \tag{12.2}$$

Figure 12.1 shows θ_i as a function of ω ranging from 0 to 2π. Due to the $\arcsin$ term in Equation 12.2, the optimal position to change i is at θ_i and $\theta_i + \pi$.

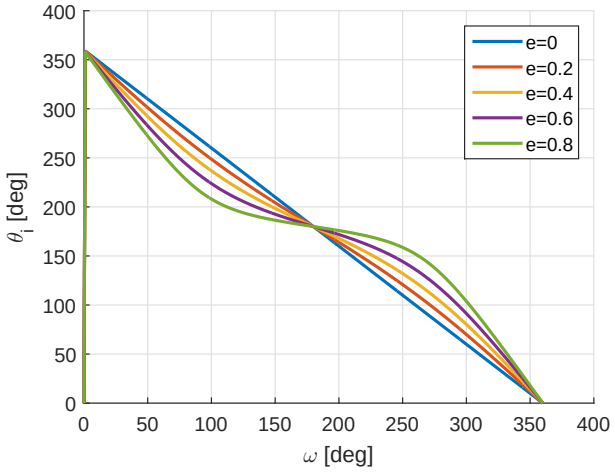

Figure 12.1: θ_i providing the maximum rate of change of i as a function of ω and for different values of e.

Figure 12.1 shows that when $\omega = 0$ and no perturbations causes ω to change, the perigee and apogee centered thrust arcs are ideal positions to change the inclination. However when ω changes or its initial value is not 0 or π, the positions along the orbit providing the maximum instantaneous rate of change of inclination are no more at perigee and apogee. For example, by considering the Gauss' equation for the inclination, in the limit case in which $\omega = 90$ deg and $\omega = 270$ deg, thrust applied at $\theta = 0$ and $\theta = 180$ deg results in zero variation of the inclination. In these cases two additional thrust arcs are added, for each revolution. This will be explained in Section 12.3. For the case without perturbation and with initial orbital elements defined in Table 12.1, two thrust arcs are considered. The length of the perigee arc is defined by the angle

ΔL_p and the length of the apogee arc is ΔL_a, as in Section 5.3. The azimuth angles on the two thrust arcs is not optimised but it follows one of the following four strategies:

1. tangential thrust on both perigee and apogee thrust arc;
2. tangential thrust at perigee, $\alpha' = \pi/2$ at apogee [116];
3. $\alpha' = \pi/2$ at perigee, tangential thrust at apogee;
4. $\alpha' = \pi/2$ on both perigee and apogee thrust arc [116].

$k_{LT} = 4$ nodes are used to model, using a linear interpolation, the variation of the control parameters from $t = 0$ to $t = ToF$. This is shown schematically in Figure 12.2 for ΔL_p.

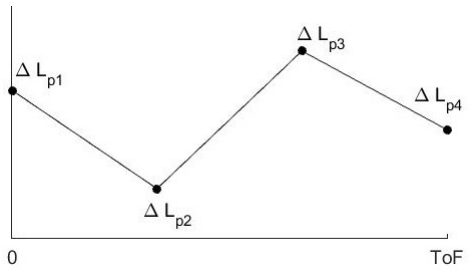

Figure 12.2: Variation of ΔL_p during the transfer from $t = 0$ to $t = ToF$.

The vector of parameters to optimise described in Equation 5.21 is defined, therefore, by $4\ k_{LT} = 16$ variables

$$\mathbf{x} = [\Delta L_{p1}\ \Delta L_{p2}\ \Delta L_{p3}\ \Delta L_{p4}\ \Delta L_{a1}\ \Delta L_{a2}\ \Delta L_{a3}\ \Delta L_{a4}\ \beta_{p1}\ \beta_{p2}\ \beta_{p3}\ \beta_{p4}\ \beta_{a1}\ \beta_{a2}\ \beta_{a3}\ \beta_{a4}]^T\ . \tag{12.3}$$

The equality constraints $\mathbf{c}\,(\mathbf{x})$ for this problem are

$$\begin{aligned} c_1\,(\mathbf{x}) &= a\,(\mathbf{x}, ToF)\,[1 - e\,(\mathbf{x}, ToF)] - a_{GEO}\ , \\ c_2\,(\mathbf{x}) &= a\,(\mathbf{x}, ToF)\,[1 + e\,(\mathbf{x}, ToF)] - a_{GEO}\ , \\ c_3\,(\mathbf{x}) &= 10\left[\sqrt{Q_1(\mathbf{x}, ToF)^2 + Q_2(\mathbf{x}, ToF)^2} - \tan\left(\frac{i_{GEO}}{2}\right)\right]\ , \end{aligned} \tag{12.4}$$

where $a(\mathbf{x}, ToF)$, $e(\mathbf{x}, ToF)$ are the semi-major axis and eccentricity at the end of the transfer and $Q_1\,(\mathbf{x}, ToF)$ and $Q_2\,(\mathbf{x}, ToF)$ are the third and fourth equinoctial elements at the end of the transfer. a_{GEO} and i_{GEO} are the semi-major axis and inclination of the target GEO (Table 12.1). The constraint on the final inclination is multiplied by 10 in order to match more precisely the final inclination of the GEO. The inequality constraints $\mathbf{g}\,(\mathbf{x})$ are

$$\begin{aligned} g_1\,(\mathbf{x}) &= R_\oplus - \min\,[a(\mathbf{x}, t)(1 - e(\mathbf{x}, t))]\ , \\ g_2\,(\mathbf{x}) &= \max\,(|\Delta L_p(\mathbf{x}, t)| + |\Delta L_a(\mathbf{x}, t)|) - 2\pi\ . \end{aligned} \tag{12.5}$$

They impose that the minimum perigee radius during the transfer is higher than the Earth's radius, $R_\oplus$, and that the maximum sum of perigee and apogee thrust arc length is lower than 2π. The lower and upper boundaries vectors are

$$\begin{aligned} &x_j^L = -2\pi,\ x_j^U = 2\pi,\ \ j = 1, \ldots, 8\ , \\ &x_j^L = -\pi/2,\ x_j^U = \pi/2,\ j = 9, \ldots, 16\ . \end{aligned} \tag{12.6}$$

The global optimisation algorithm MP-AIDEA is not formulated to explicitly manage equality or inequality constraints. The constrained problem presented in Equation 5.4 is therefore transformed into an unconstrained problem, applying a penalty method. The fitness function J' is expressed as a combination of the objective function J defined in Equation 5.4 and penalty constraints:

$$J'(\mathbf{x}) = J(\mathbf{x}) + w_1 \left[(\mathbf{g}(\mathbf{x}) > 0) \cdot |\mathbf{g}(\mathbf{x})|\right]^2 + w_2 |\mathbf{c}(\mathbf{x})|^2\ . \tag{12.7}$$

w_1 and w_2 are appropriate weight coefficients. The local search in MP-AIDEA is performed with MATLAB *fmincon-sqp*. During the local search, the equality and inequality constraints $\mathbf{c}(\mathbf{x})$ and $\mathbf{g}(\mathbf{x})$ are automatically handled by *fmincon*. The penalty of the objective function is, therefore, used only in the DE exploration part of MP-AIDEA. MP-AIDEA collects in an archive the local minima found during the exploration. It gives therefore the possibility to evaluate different possible solution to the GTO-GEO transfer problem, each one corresponding to a different local minimum.

12.2 GTO-GEO transfer without perturbations

In this section the optimisation of the GTO-GEO transfer, without perturbations, is presented. At first, local solutions to the problem are found using different initial guesses, based on a pre-defined structure for the initial guess vector $\mathbf{x}^{IG}$ [240]. The NLP problem presented in Equation 5.4 is solved using MATLAB *fmincon-sqp*. MP-AIDEA is then used to globally explore the whole search space, using the fitness function defined in Equation 12.7. For the local optimisation method, the vector of initial guess is

$$\begin{aligned} \mathbf{x}^{IG} = [&\Delta L_{p,1}^{IG}\ \Delta L_{p,2}^{IG}\ \Delta L_{p,3}^{IG}\ \Delta L_{p,4}^{IG}\ \Delta L_{a,1}^{IG}\ \Delta L_{a,2}^{IG}\ \Delta L_{a,3}^{IG}\ \Delta L_{a,4}^{IG} \\ &\beta_{p,1}^{IG}\ \beta_{p,2}^{IG}\ \beta_{p,3}^{IG}\ \beta_{p,4}^{IG}\ \beta_{a,1}^{IG}\ \beta_{a,2}^{IG}\ \beta_{a,3}^{IG}\ \beta_{a,4}^{IG}]^T\ . \end{aligned} \tag{12.8}$$

The initial guess is constructed using values of $\Delta L_{a,s}^{IG}$ linearly spaced from 0 to $\Delta L_{a,4}^{IG}$:

$$\Delta L_{a,s}^{IG} = \frac{\Delta L_{a,4}^{IG}}{3}(s-1), \quad s = 1, \ldots, 4\ . \tag{12.9}$$

The initial guess of the length of the perigee thrust arcs corresponding to the first three nodes is

$$\Delta L_{p,1}^{IG} = \Delta L_{p,2}^{IG} = \Delta L_{p,3}^{IG} = 0\ , \tag{12.10}$$

while $\Delta L_{p4}^{IG} \neq 0$. The initial guess for the elevation angles is

$$\beta_{p,s}^{IG} = \beta_{a,s}^{IG} = 0, \quad s = 1, \ldots, 4\,. \tag{12.11}$$

Using Equations 12.9, 12.10 and 12.11, the vector of initial guess $\mathbf{x}^{IG}$ of Equation 12.8 can be defined using only two parameters, $\Delta L_{p,4}^{IG}$ and $\Delta L_{a,4}^{IG}$:

$$\mathbf{x}^{IG} = [0 \;\; 0 \;\; 0 \;\; -\Delta L_{p,4}^{IG} \;\; 0 \;\; \frac{\Delta L_{a,4}^{IG}}{3} \;\; \frac{2\,\Delta L_{a,4}^{IG}}{3} \;\; \Delta L_{a,4}^{IG} \;\; 0 \;\; 0 \;\; 0 \;\; 0 \;\; 0 \;\; 0 \;\; 0 \;\; 0]^T\,. \tag{12.12}$$

Note that $\Delta L_s < 0$ correspond to thrust applied in the negative tangential direction. Different values of $|\Delta L_{p,4}^{IG}|$ and $|\Delta L_{a,4}^{IG}|$ have been considered, in the range $[0, 180]$ deg, at interval of 20 degrees, resulting in a total of 100 local optimisation problems for the 4 thrusting strategies defined in Section 12.1.

The results are shown in Figure 12.3. The NLP problem is solved with SQP and IPM algorithms. The solutions shown in Fig. 12.3 are the ones relative to the solver that returned the lower ΔV. SQP returned the lower ΔV solution in the 75% of the cases. When using the IPM solver, zero values in Eq. (12.12) are replaced by 1e-3, in order to avoid shift of the initial guess when this is at the boundaries of the search space. The red points represent the minimum ΔV.

Results show that in all the cases, higher ΔV solutions are obtained at low values of $\Delta L_{a,4}^{IG}$. For all the points that converged, the solutions are all different from each other, showing that the problem is characterised by a high number of local minima.

The minimum ΔV solutions are summarised in Table 12.2 and show that the best results are given by Strategy 2 and Strategy 4.

Table 12.2: Minimum ΔV solution for GTO-GEO transfer with no perturbations.

Strategy	1	2	3	4
ΔV [km/s]	1.6173	1.5672	1.6129	1.5687

The results presented above are obtained solving a local minimisation problem and using a predefined specific expression for the initial guess. Each solution is therefore likely to be a local minima of the problem and might be strongly dependent on the choice of the initial guess. In the following, the results found using the global optimisation algorithm MP-AIDEA are presented. MP-AIDEA is run with 1 population of 16 individuals (dimension of the problem) and for a total of $1.5\ 10^5$ function evaluations; 25 independent runs are considered in order to obtain statistically significant results. The results are shown in Figure 12.4, for the four considered thrusting strategies. For each strategy, the minimum ΔV for each one of the 25 runs of MP-AIDEA is represented. Three possible values of w_1 and w_2 are considered: 1, 10 and 100. The results of the local optimisation method (Table 12.2) are represented by the black lines.

Results show that the local optimisation method outperforms MP-AIDEA when the initial guess vector is close to the solution of the problem (Strategy 1 and 3) while the results of

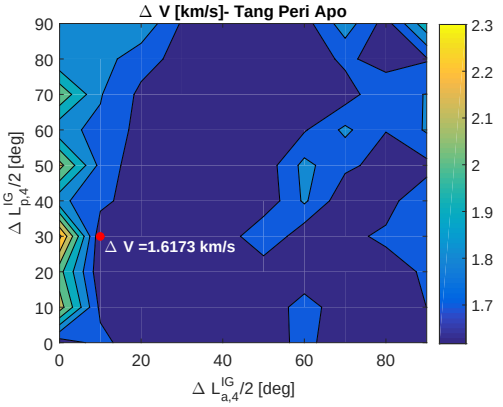

(a) Tangential thrust at perigee and apogee.

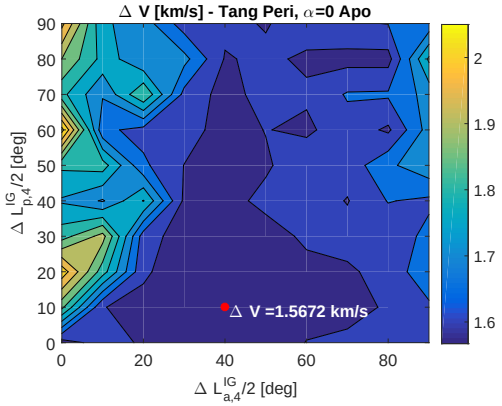

(b) Tangential thrust at perigee, $\alpha = 0$ at apogee.

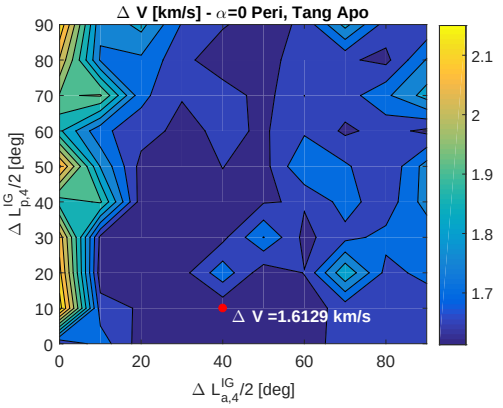

(c) $\alpha = 0$ at perigee, tangential thrust at apogee.

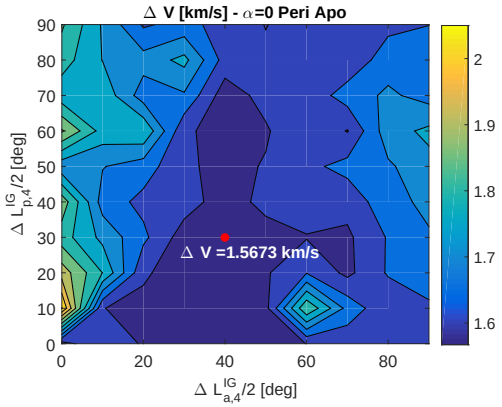

(d) $\alpha = 0$ at perigee and apogee.

Figure 12.3: ΔV for different values of ΔL_{a4}^{IG} and ΔL_{p4}^{IG} using SQP and IPMs solver. The minimum ΔV solution is identified by a red dot.

Strategy 2 and 4 show that in these cases the global search capabilites of MP-AIDEA are able to locate better solutions than those found by the local optimisation method. The minimum, maximum and mean values of the 25 runs, for each strategy, are reported in Table 12.3.

Table 12.3: ΔV [km/s] - Results of MP-AIDEA.

	Strategy 1			Strategy 2			Strategy 3			Strategy 4		
$w_1 = w_2$	1	10	100	1	10	100	1	10	100	1	10	100
Min	1.6558	1.6473	1.7046	**1.5644**	1.5646	1.5648	1.6626	1.6747	1.6833	1.5646	1.5650	**1.5645**
Mean	1.7263	1.7129	1.7580	1.5668	1.5673	1.5685	1.7144	1.7342	1.7538	1.5665	1.5675	1.5673
Max	1.8497	1.8683	1.8551	1.5728	1.5746	1.5763	1.8424	1.8223	1.8715	1.5691	1.5758	1.5710

The minimum ΔV solutions are obtained using Strategy 2 and $w = 1$ and Strategy 4 and $w = 100$ (results in bold in Table 12.3). The variation of orbital elements and the control parameters during the transfer for these two cases are shown in Figures 12.5 and 12.6. r_p and r_a in Figure 12.5 are the perigee and apogee radius.

Figure 12.7 shows the x-y view of the trajectory for Strategy 4. To make the plot more readable, only few orbital revolutions are represented. The thrust arcs are represented by

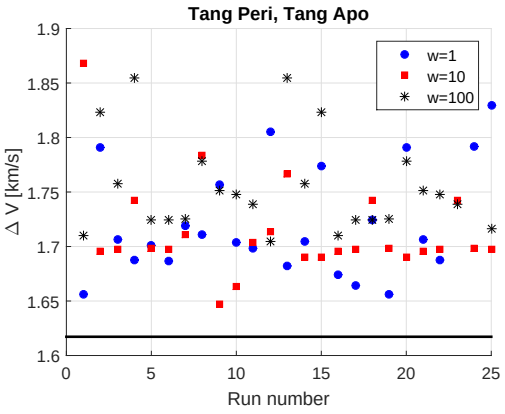

(a) Tangential thrust at perigee and apogee.

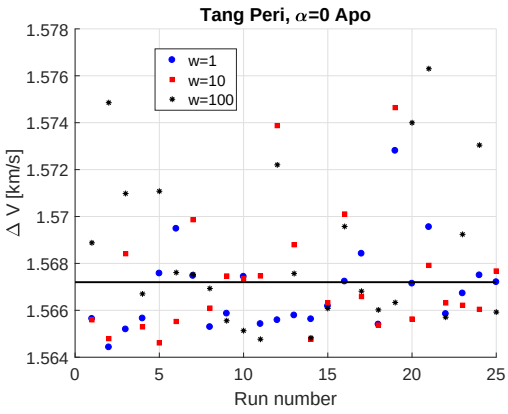

(b) Tangential thrust at perigee, $\alpha = 0$ at apogee.

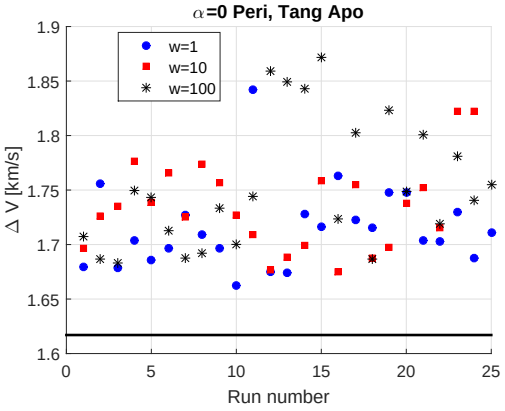

(c) $\alpha = 0$ at perigee, tangential thrust at apogee.

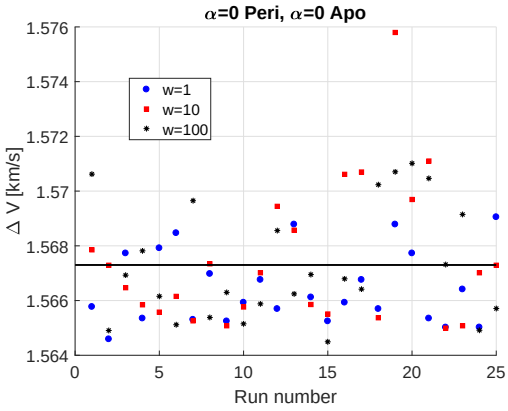

(d) $\alpha = 0$ at perigee and apogee.

Figure 12.4: Minimum ΔV of 25 runs of MP-AIDEA.

thick black lines.

Each one of the 25 runs of MP-AIDEA provides different solutions to the GTO-GEO transfer problem. As an example, Figure 12.8 shows the solutions characterised by $\Delta V < 1.7$ km/s found by a single run of MP-AIDEA using Strategy 4 and $w = 100$. Each solution correspond to different control history and orbital elements variation to realise the GTO-GEO transfer. In particular in this case 233 solutions are found with $\Delta V < 1.7$ km/s, among which 120 with $\Delta V < 1.65$ km/s and 21 with $\Delta V < 1.6$ km/s. The orbital elements variation and control history of the 21 solutions with $\Delta V < 1.6$ km/s are shown in Figures 12.9 and 12.10. A single run of MP-AIDEA can therefore find many local optima and many possible solutions to the problem.

12.3 GTO-GEO transfer with perturbations

The results presented in the previous section do not consider perturbations to the motion of the spacecraft. In this section the perturbations due to Earth's potential, drag and third body

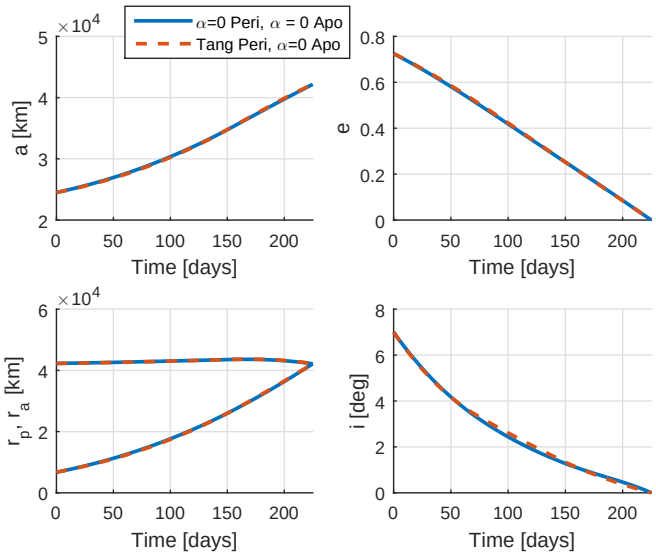

Figure 12.5: GTO-GEO transfer without perturbations - Minimum ΔV solutions from Table 12.3. Orbital elements variation.

are taken into account. Only strategy 4, that together with strategy 2 provided the best results in the case without perturbations, is considered.

12.3.1 Earth's gravitation perturbations

This section starts presenting the results that justify the need to add two thrust arcs to the control profile when perturbations that change ω are present, as anticipated in Section 12.1. Let us consider the minimum ΔV solution of Section 12.2, given by MP-AIDEA using strategy 4 and $\omega_0 = 0$. This solution is used as initial guess for the local optimisation of the GTO-GEO transfer with the addition of the perturbation due to second zonal harmonic of the aspheric Earth's potential, J_2. The orbital elements and control history are shown in Figure 12.12 and 12.13. The cost of the transfer is $\Delta V = 1.7347$ km/s.

Figure 12.13 shows that there is an increase of inclination during the transfer from $t = 25$ days to $t = 68$ days. The reason for this behavior is explained in the following. At t = 25 days the argument of perigee (that changes both because of J_2 and because of the low-thrust acceleration) goes from $\omega < \pi/2$ to $\omega > \pi/2$. The Gauss' equation for the time variation of the inclination depends on the term $\sin\beta\cos(\omega + \theta)$; this means that in order to have a continuous reduction of inclination with thrust applied on perigee ($\theta = 0$) and apogee ($\theta = \pi$) centered thrust arcs, β_a should be $\beta_a > 0$ when $\omega < \pi/2$ and $\beta_a < 0$ when $\omega > \pi/2$. Therefore, an instantaneous variation in the sign of β_a should take place at $t = 25$ days. Due to the type of control parametrisation and number of nodes used, the variation in the sign of β_a takes place however at t = 68 days, rather than 25 days (Figure 12.13). This explains the increase in inclination from 25 to 68 days from the start of the transfer. At $t = 68$ days the inclination starts to decrease again. This behaviour shows that the control parametrisation

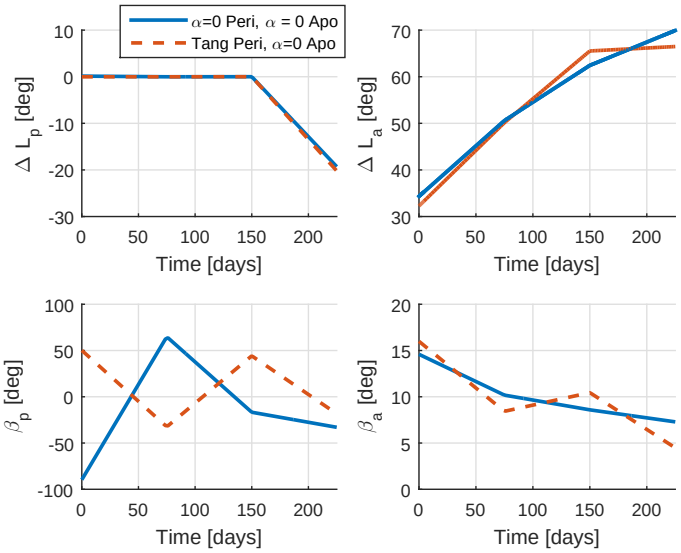

Figure 12.6: GTO-GEO transfer without perturbations - Minimum ΔV solutions from Table 12.3. Control history.

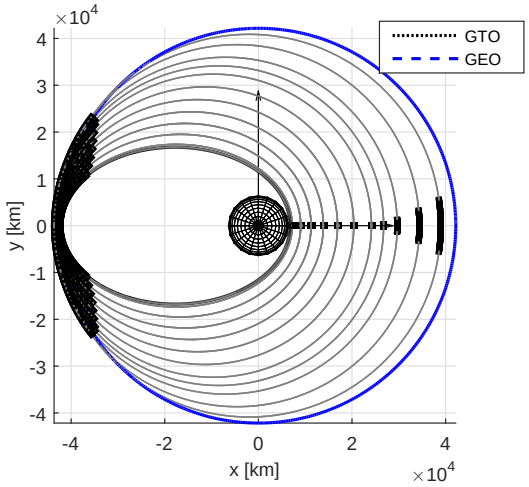

Figure 12.7: Minimum ΔV GTO-GEO transfer - Strategy 4.

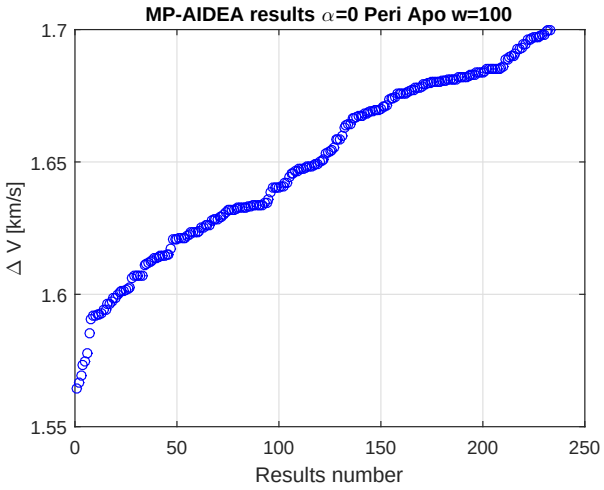

Figure 12.8: MP-AIDEA: solutions with ΔV <1.7 km/s using Strategy 4.

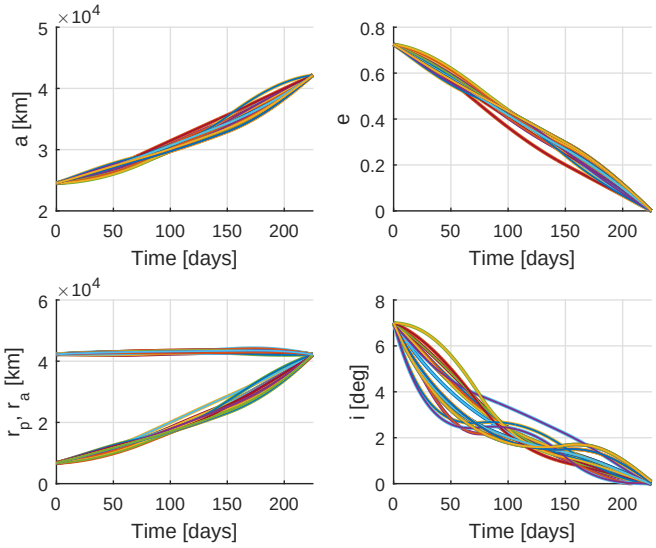

Figure 12.9: Orbital elements variation of the 21 solutions of MP-AIDEA characterised by $\Delta V < 1.6$ km/s - Strategy 4.

used in the previous section requires some changes when considering the perturbation due to J_2, if period of increase of inclination are to be avoided during the transfer. In particular, since ω changes during the transfer when perturbations are considered, the optimal point for the variation of i continuously changes during the transfer (Equation 12.2). In order to allow for a reduction of inclination at any value of ω, two additional thrust arcs are added to the control parametrisation. They are characterised by length ΔL_{pa} (thrust arc between perigee and apogee) and ΔL_{ap} (thrust arc between apogee and perigee). The angular distance δL between any two thrust arcs (from the final point of the previous arc to the initial point of the

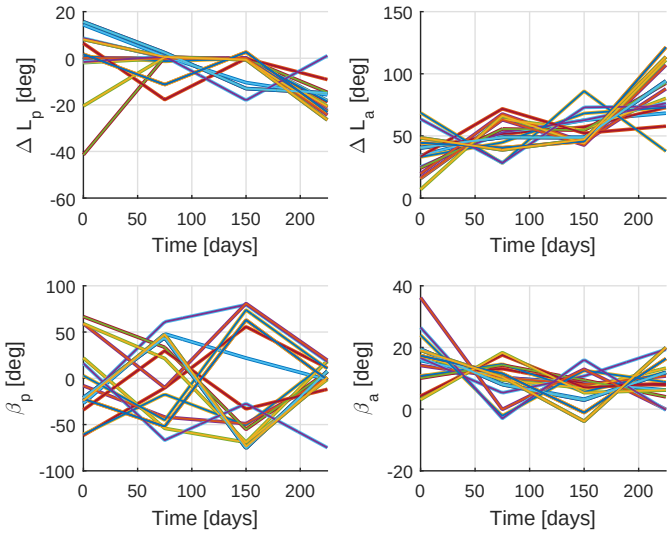

Figure 12.10: Control history.

Figure 12.11: Control history of the 21 solutions of MP-AIDEA characterised by $\Delta V < 1.6$ km/s - Strategy 4.

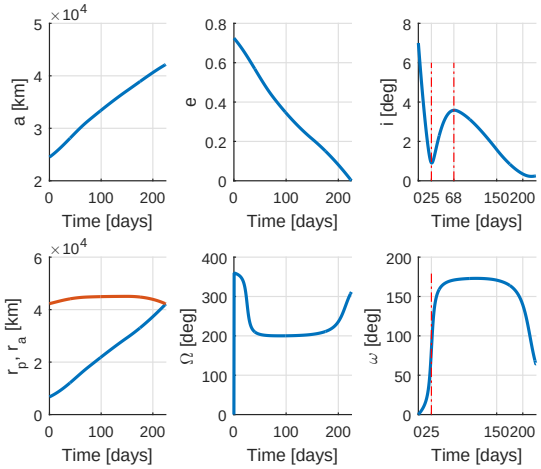

Figure 12.12: GTO-GEO transfer, J_2 and two thrust arcs: orbital elements variation.

next arc) is constrained to be

$$\delta L = \frac{2\pi - \Delta L_p - \Delta L_{pa} - \Delta L_a - \Delta L_{ap}}{4} \,. \tag{12.13}$$

The elevation angles on the two additional arcs is chosen such as to always cause a decrease

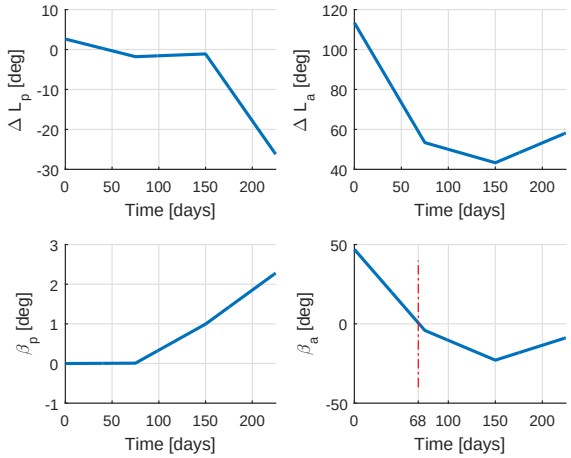

Figure 12.13: GTO-GEO transfer, J_2 and two thrust arcs: control history.

of inclination, according to:

$$\beta_{ap} = \beta_{pa} = -\frac{\pi}{2}\text{sgn}\left(\cos(\omega + \theta)\right) \ . \tag{12.14}$$

The control parameters are now 24, rather than 16:

$$\begin{aligned}\mathbf{x} = [&\Delta L_{p,1}\ \Delta L_{p,2}\ \Delta L_{p,3}\ \Delta L_{p,4}\ \Delta L_{a,1}\ \Delta L_{a,2}\ \Delta L_{a,3}\ \Delta L_{a,4}\ \beta_{p,1}\ \beta_{p,2}\ \beta_{p,3}\ \beta_{p,4}\ \beta_{a,1}\ \beta_{a,2}\ \beta_{a,3}\ \beta_{a,4}\\ &\Delta L_{pa,1}\ \Delta L_{pa,2}\Delta L_{pa,3}\ \Delta L_{pa,4}\ \Delta L_{ap,1}\ \Delta L_{ap,2}\ \Delta L_{ap,3}\ \Delta L_{ap,4}]^T \ .\end{aligned} \tag{12.15}$$

The inequality constraint $g_2(\mathbf{x})$ in Equation 12.5 is now formulated as

$$g_2\left(\mathbf{x}\right) = \max\left(|\Delta L_p(t)|+|\Delta L_a(t)|+|\Delta L_{pa}(t)|+|\Delta L_{ap}(t)|\right) - 2\pi \ . \tag{12.16}$$

This new parametrisation of the control is used to solve the GTO-GEO transfer with perturbations due to J_2. As in the previous section, at first a local optimisation process is considered. The initial guess for ΔL_p, ΔL_a, β_p and β_a are the results of the best solution of the previous section. $\Delta L^{IG}_{pa,s}$ and $\Delta L^{IG}_{ap,s}$ are expressed as:

$$\Delta L^{IG}_{ap,s} = \frac{\Delta L^{IG}_{ap,4}}{3}(s-1) \quad \Delta L^{IG}_{pa,s} = \frac{\Delta L^{IG}_{pa,4}}{3}(s-1) \tag{12.17}$$

and the values of ΔL^{IG}_{pa} and ΔL^{IG}_{ap} are taken in the range 0 to 180 deg. The results of the local optimisation of the problem, solved with SQP and IPM, starting from different initial guess for $\Delta L_{pa,4}$ and $\Delta L_{ap,4}$, are shown in Figure 12.14. The minimum ΔV solution (between SQP and IPM) is represented. Blank area in the plot represents conditions for which there was no convergence of the optimisation algorithm.

The minimum ΔV solution is represented in Figures 12.15 and 12.16. The cost of the trans-

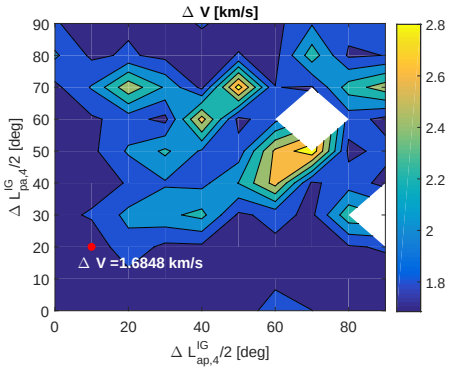

Figure 12.14: ΔV for transfer with J_2 perturbations for different values of the initial guess of ΔL_{ap} and ΔL_{pa}; $\omega_0 = 0$.

fer is $\Delta V = 1.6848$ km/s, lower than the cost of 1.7347 km/s found with two thrust arcs, and the inclination decreases during the entire transfer.

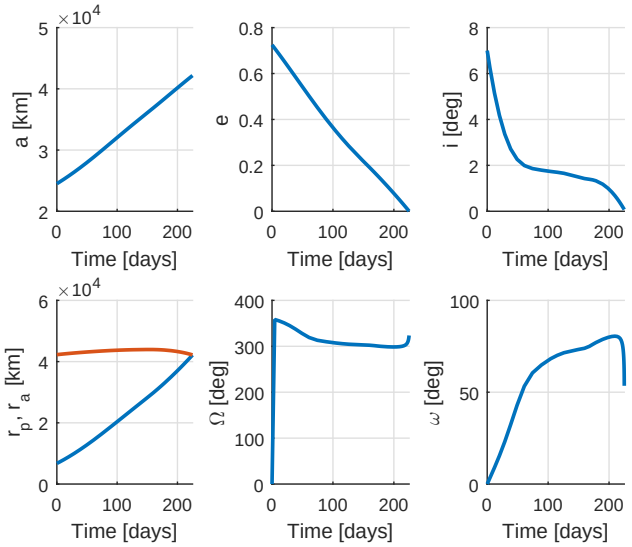

Figure 12.15: Variation of orbital elements: J_2, 4 thrust arcs, $\omega_0 = 0$.

Results show that the additional thrust arcs have non-negligible semi-amplitude only in the last phase of the transfer ($t > 150$ days), when indeed the value of ω approaches 90 deg and therefore it is not efficient to change the inclination in the vicinity of the perigee and apogee of the orbit (Figure 12.16). The solution has been validated by comparing it to the results of a numerical integration of the equations of motion using the control profile defined in Figure 12.16. The comparison between numerical and analytic integration is shown in Figure 12.17 and shows the good agreement between the two models.

The optimal solution to the GTO-GEO transfer with J_2 perturbation is then sought also using MP-AIDEA. In order to facilitate convergence to the feasible region, the search space is

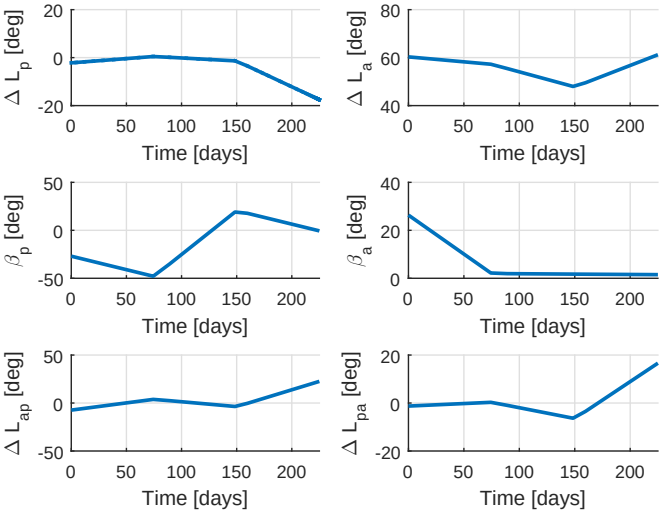

Figure 12.16: Control history: J_2, 4 thrust arcs, $\omega_0 = 0$.

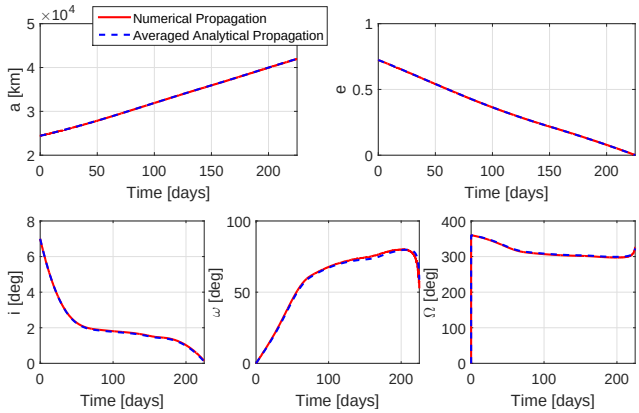

Figure 12.17: Numerical and averaged analytical propagation.

reduced with respect to the one presented in Equation 12.6. The new boundaries for the search space are $\Delta L_{p,s} \in [-\pi/4, \pi/4]$, $\Delta L_{a,s} \in [0, \pi/2]$, $\beta_{pi}, \beta_{a,s} \in [-\pi/2, \pi/2]$ and $\Delta L_{pa,s}, \Delta L_{ap,s} \in [-\pi/4, \pi/4]$. MP-AIDEA is now run with 1 population of 24 individuals. The costs of the feasible solutions found by one run of MP-AIDEA are shown in Figure 12.18. By comparing Figure 12.18 with Figure 12.8 it is possible to see that the number of solutions provided by a run of MP-AIDEA is now reduced with respect to the case without perturbations. The minimum cost solution found by MP-AIDEA is $\Delta V = 1.6588$ km/s, lower than the value of 1.6848 km/s found by the local optimisation (black line in Figure 12.18). With the additions of perturbations, the initial value of ω of the GTO plays an important role. Therefore the analysis presented above, valid for $\omega_0 = 0$, is realised also for $\omega_0 = 178$ deg, the initial value of ω for

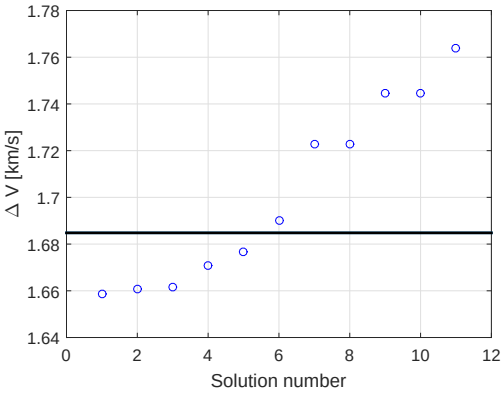

Figure 12.18: ΔV of feasible solution found by MP-AIDEA for GTO-GEO transfer with J_2 perturbations and $\omega_0 = 0$.

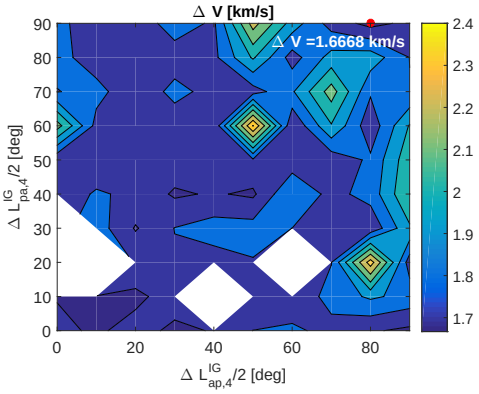

Figure 12.19: ΔV for transfer with J_2 perturbations for different values of the initial guess of ΔL_{ap} and ΔL_{pa}, $\omega_0 = 178$ deg.

the GTO of the Ariane launcher[1]. Figure 12.19 shows the results of the solution of several local optimisation problem with initial guess given by the solution without J_2 and $\omega_0 = 178$ and using values for the initial guess of $\Delta L^{IG}_{pa,4}$ and $\Delta L^{IG}_{ap,4}$ in the range from 0 to π.

The minimum ΔV solution found by local optimisation is represented in Figures 12.20 and 12.21 and is characterised by $\Delta V = 1.6668$ km/s.

The cost of the feasible solutions found by one run of MP-AIDEA are shown in Figure 12.22, together with a black line representing the minimum ΔV solution found by local optimisation. The orbital elements variation of the five solutions with lower ΔV are shown in Figures 12.23 and 12.24.

The minimum cost solution found by MP-AIDEA has $\Delta V = 1.6452$ km/s, lower than the solution of the local optimisation method. The minimum ΔV solution is analysed in more detail to study the effect of additional perturbations: J_3, J_4 and J_5. No significant difference in ΔV is evident when considering these additional perturbations and the profile of the variation

[1]http://www.arianespace.com/wp-content/uploads/2011/07/Ariane5_Users-Manual_October2016.pdf

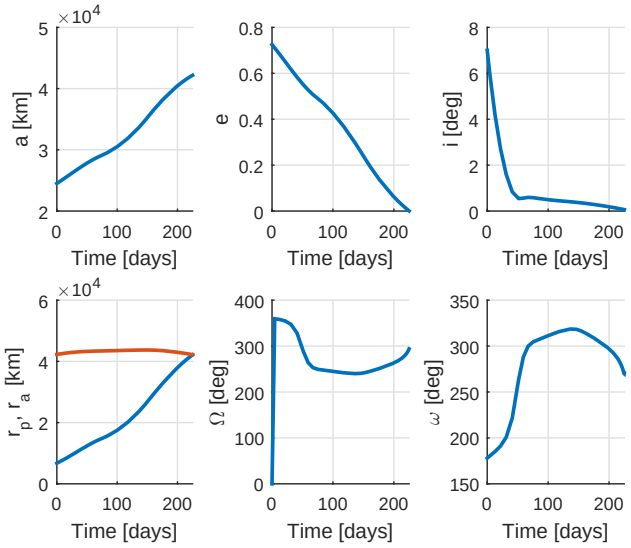

Figure 12.20: Orbital elements: J_2, 4 thrust arcs, $\omega_0 = 178$ deg.

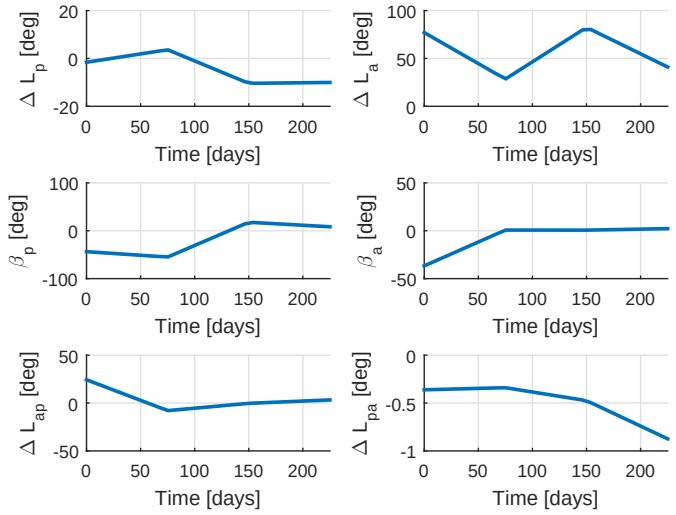

Figure 12.21: Control history from local optimisation: J_2, 4 thrust arcs, $\omega_0 = 178$ deg.

of the orbital elements remains approximately the same. In more detail, the ΔV and orbital elements at the end of the transfers are reported in Table 12.4.

12.3.2 Atmospheric drag

In this subsection the effect of the atmospheric drag is analysed. The considered atmospheric model is a static exponential model with zero density of the atmosphere at altitude higher than 4000 km [64, 204] (Section 4.3). No significant difference is measured when considering the

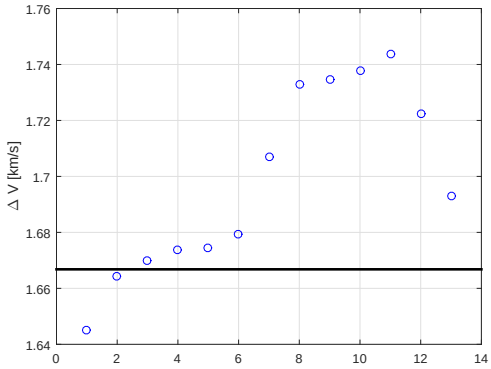

Figure 12.22: ΔV of feasible solutions found by MP-AIDEA for GTO-GEO transfer with J_2 perturbations and $\omega_0 = 178$ deg.

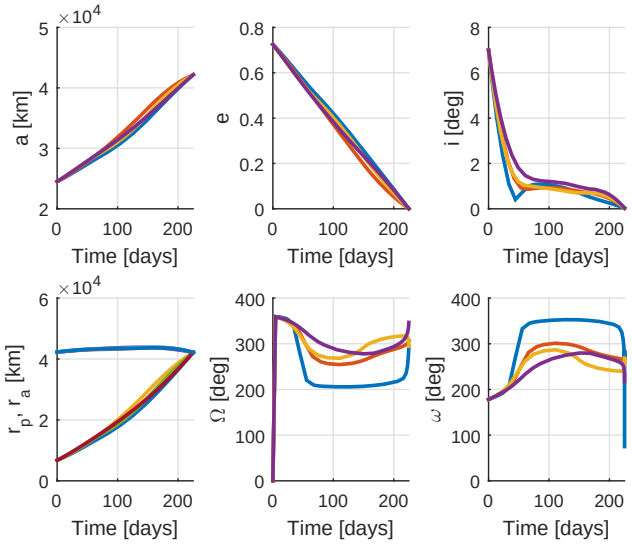

Figure 12.23: Orbital elements variation of the 5 best solutions found by MP-AIDEA for GTO-GEO transfer with J_2 perturbations and $\omega_0 = 178$ deg.

Table 12.4: Final orbital element and ΔV - Effect of the Earth's perturbation.

	J_2	J_2, J_3	J_2, J_3, J_4	J_2, J_3, J_4, J_5
a [km]	42166.42	42166.34	42166.32	42166.32
e	1.41e-5	1.62e-5	1.68e-5	1.67e-5
i [deg]	0.03	0.03	0.03	0.03
ΔV [km/s]	1.6452	1.6452	1.6452	1.6452

perturbation due to the atmospheric drag for area to mass ratio of the spacecraft with typical values of 10^{-2} m^2/kg, as shown in Table 12.5. Table 12.5 shows the final orbital elements considering the optimal control profile defined in Subsection 12.3.1 and J_2, J_3, J_4, J_5 and the

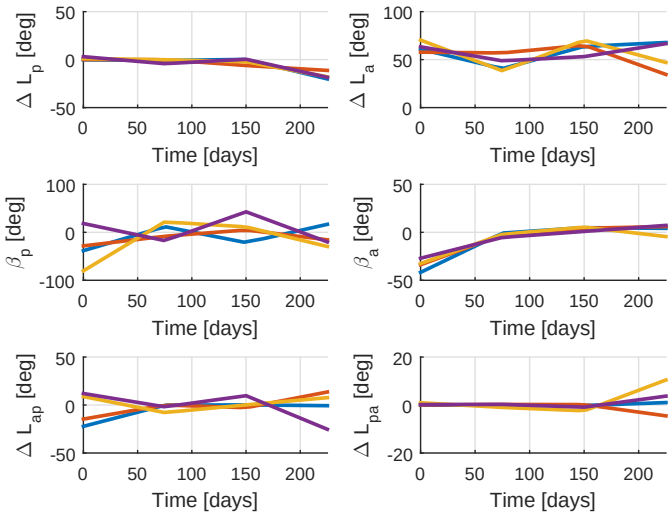

Figure 12.24: Control history of the 5 best solutions found by MP-AIDEA for GTO-GEO transfer with J_2 perturbations and $\omega_0 = 178$ deg.

drag perturbation.

Table 12.5: Final orbital elements and ΔV- Effect of the drag perturbation.

Parameter	J_2, J_3, J_4, J_5	J_2, J_3, J_4, J_5, drag
a [km]	42166.42	42164.77
e	1.41e-5	1.44e-5
i [deg]	0.03	0.03
ΔV [km/s]	1.6452	1.6452

Results show that, as expected, when using the control profile computed without the atmospheric drag, the addition of the atmospheric drag causes a reduction of the final semi-major axis. The reduction is however negligible and it is possible to state that the effect of the atmospheric drag is not significant for the considered GTO-GEO transfer.

12.3.3 Sun's gravitational perturbation

For the analysis of the perturbation due to the Sun, the position of the Sun with respect to the orientation of the GTO orbit, and therefore the initial date of the transfer, has to be taken into account. It is assumed that the spacecraft is injected into the GTO by an Ariane launch from Kourou. Figure 12.25 shows the right ascension of the GTO orbit at the opening and closing of the launch windows for each day of the year [204].

The GTO-GEO transfer with J_2 and Sun's perturbation is analysed at four different initial dates using different values of Ω for the GTO orbit, corresponding to the opening time of the launch windows (Table 12.6).

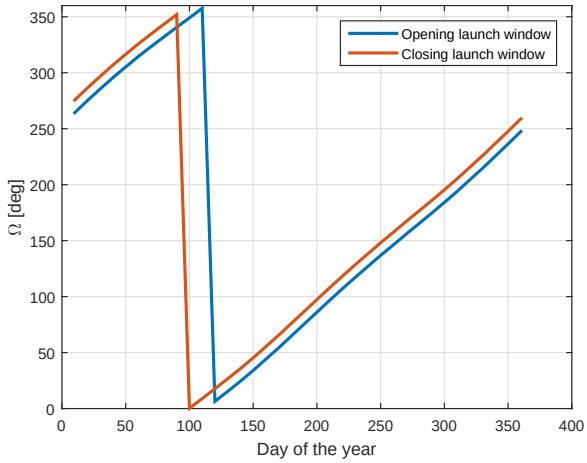

Figure 12.25: Variation of Ω of the GTO orbit during the year.

Table 12.6: Initial Ω at different initial dates for the transfer.

Date	21 March	21 June	21 Sept.	21 Dec.
Ω_0 [deg]	332.05	55.23	148.92	240.87

The feasible results of a single run of MP-AIDEA for different initial dates are shown in Figure 12.26 . The black line represent the result of MP-AIDEA without the perturbation from the Sun ($\Delta V = 1.6452$ km/s).

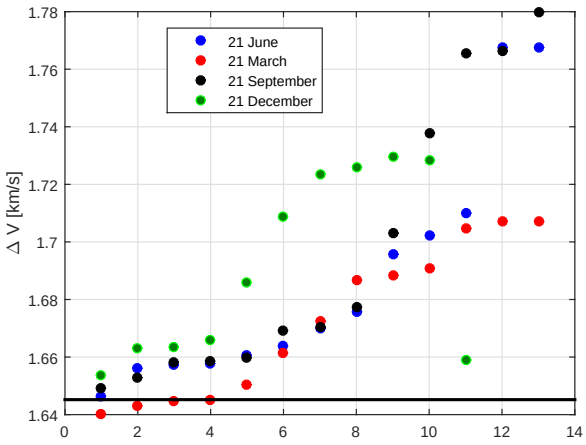

Figure 12.26: ΔV of the solution found by MP-AIDEA for transfer with J_2 and Sun perturbation.

The final orbital elements at the end of the transfer and the ΔV of the best solution found for each one of the four considered dates are reported in Table 12.7.

Table 12.7: Final orbital elements and ΔV - Sun's gravitational perturbation.

	21 March	21 June	21 Sept.	21 Dec.
a [km]	42166.26	42168.89	42165.05	42166.42
e	5.29e-5	4.12e-4	2.23e-5	1.11e-4
i [deg]	0.008	0.06	3.64e-4	0.02
ΔV [km/s]	1.6403	1.6463	1.6494	1.6536

12.4 Conclusions

This chapter has presented the results of the global optimisation of the low-thrust transfer from GTO to GEO, including different types of perturbation. Results have shown that MP-AIDEA can explore the solution space and locate better solutions than a local optimisation method, without the need to provide an initial guess to the solution. The addition of perturbations can cause differences in the results. In particular, the main difference with respect to the Keplerian case are caused by J_2; however, also the Sun's perturbation can cause small but non negligible difference ($\Delta\Delta V < 0.0133$ km/s) in the cost of the transfer.

Chapter 13

Conclusions

This chapter provides a short summary of the main findings of this thesis and a discussion on possible future works.

13.1 Summary of the thesis

This section provides a description of how the goals and objectives defined in the Introduction of this thesis have been met and addressed in the different chapters.

The first objective was the definition of multi-fidelity models and tools for the evaluation of low-thrust transfers. In Chapter 2, a detailed survey and analysis of low-fidelity analytical control laws for low-thrust transfers, available in the literature, has been presented. These laws consider the low-thrust perturbation to be the only perturbation to the Keplerian orbital motion. Chapter 3 has presented methods of higher fidelity, introducing the derivation of novel analytical equations for the cost of low-thrust transfers in Earth's orbit, under the effect of gravitational perturbations.

The second objective was the definition of a computationally efficient model for the motion of the spacecraft subject to low-thrust acceleration and orbital perturbations. This has been addressed in Chapter 4, where analytical equations based on a first-order expansion in the perturbing accelerations have been derived.

The definition of techniques and methods for the use of surrogate models in the optimisation of low-thrust trajectories has been addressed in Chapter 6. Surrogate models represent fast approximation of high fidelity models and in Chapter 6, "offline" and "online" surrogate models for low-thrust transfers have been presented.

Finally, the development of an optimisation algorithm for the global optimisation of low-thrust trajectories has been dealt with in Chapter 7, where a novel adaptive multi-population implementation of an hybrid algorithm, combining differential evolution and monotonic basin hopping, has been introduced.

These methods and techniques have been used for the design of space missions in Earth and interplanetary space, presented in Part II of this dissertation. The applications proposed are not just tools used to test the developed techniques, but are original contributions. The

techniques derived and the proposed applications constitute an efficient set of tools for the preliminary design of low-thrust missions. A summary of the main achievements of each chapter and of the major findings of this thesis are discussed in more details hereafter.

Analysis of analytical control laws for low-thrust orbit transfer. Low-fidelity laws present in the literature for the estimation of the cost of low-thrust transfers, where one or two orbital elements are to be changed, are collected and analysed in Chapter 2. Analytic equations are derived, where not already present in the literature, for the cost of the transfers or for the variation of the orbital elements during the transfer.

Analytical laws for the variation of a, i, Ω with J_2. The low-fidelity analytical laws available in the literature and presented in Chapter 2 do not take into account orbital perturbations to the motion of the spacecraft. This could lead to unacceptable approximations for particular cases, such as, for example, spacecraft in Earth's orbit subject to the drift of the right ascension of the ascending node due to the second order zonal harmonic of the Earth's gravitational perturbation, J_2. Novel laws for the estimation of the cost of low-thrust transfers in Earth's orbit, under the effect of J_2, are presented in Chapter 3. These laws have been compared to each other; the one providing the lowest ΔV has been used for additional applications (Chapter 11).

Analytical propagation via first-order expansions. In the process of global optimisation of low-thrust trajectory, it is convenient to have a quick and computationally efficient method to model the motion of the spacecraft subject to low-thrust acceleration. Moreover, in order for the model to be as accurate as possible, natural perturbing accelerations have to be taken into account. Chapter 4 presents analytical equations based on a first order expansion in the perturbing acceleration; the equations can be used to model the motion of the spacecraft subject to low-thrust acceleration and orbital perturbations. The considered orbital perturbations, that complements what already available in the literature, are J_3, J_4, J_5, atmospheric drag and third body perturbation. As regards the low-thrust acceleration, equations are derived for the motion of the spacecraft subject to an acceleration following an inverse square law, $1/r^2$, where r is the distance of the spacecraft from the Sun. The formulae and the results of the propagation are validated through a comparison with the NASA software GMAT, the AGI software STK, and with numerical propagation of the Gauss' equations.

Transcription methods using first-order expansions. Three transcription methods are presented in Chapter 5 for the optimisation of low-thrust transfers. Two of these methods are successfully validated through comparison with the results provided by an indirect optimisation tool developed at the Centre National d'Etudes Spatial. The third one is validated through comparison with a tool developed at the European Space Operation Centre of the European Space Agency. The transcription methods make use of the first-order expansion model presented in Chapter 4 and have been used for the applications presented in Part II of this thesis.

Surrogate model for low-thrust transfers. Chapter 6 presents preliminary methods and results for the use of surrogate models for low-thrust transfers. One of the proposed applications consists in the use of surrogate models to define a cartography of low-thrust transfers. The aim is for the surrogate model to provide a fast approximation of the ΔV and ToF of a transfer where more than one orbital element can change. The surrogate model is built using a Kriging model and preliminary results show that increasingly accurate results are obtained by increasing the number of training points used to generate the surrogate model. A preliminary analysis for the use of the expected improvement, to locate the region of space where the minimum cost of a transfer is located, is also presented.

Multi Population Adaptive Inflationary Differential Evolution Algorithm. The first part of the thesis ends with Chapter 7, where the novel adaptive multi-population global optimisation algorithm MP-AIDEA is presented. The algorithm is based on a hybridisation of Differential Evolution and Monotonic Basin Hopping and implements novel mechanism for the adaptation of its main parameters. MP-AIDEA is extensively tested over more than fifty academic test functions and real-world problems and compared to other algorithms of previous global optimisation competitions. The results of this comparison are presented in Chapter 7, where it is shown how MP-AIDEA compares well, and in many cases outperforms, other existing algorithms.

Low-thrust mission to the Atira asteroids. The first proposed application of the methods and techniques developed in Part I of this thesis is a mission to visit asteroids in the inner solar system. The design of the proposed mission is realised with a combination of combinatorial tools, the global optimisation algorithm MP-AIDEA, and the low-thrust transcription techniques presented in Chapter 5. The design of the mission is completed with a detailed study of the launch strategy and of a final phase of the mission dedicated to the observation of objects in the inner solar system. Results show that 6 asteroids of the Atira group can be visited through fly-bys over a period of approximately 8.4 years and that, using a swing-by of the Earth, the spacecraft can then be placed on a surveillance orbit with perihelion at Venus, in order to monitor asteroids in the inner solar system.

Low-thrust mission to the main belt asteroids. A second interplanetary application is proposed in Chapter 9, where a mission to visit the asteroids in the main belt is described. In this case too, a combinatorial problem has to be solved to define the sequence of objects to be visited. MP-AIDEA is used to optimise the parameters defining the trajectory so as to further reduce the cost of the mission. The trajectory is then optimised for low-thrust transfer using the transcription methods presented in Chapter 5. The transfer from Earth to main belt is also studied. Two database of asteroids are considered: one including few targets of scientific interest and a second one composed by more than 100,000 objects. Results show that when the two database are combined, 11 asteroids can be visited in about 5 years and that, among the 11 visited asteroids, 2 are of particular scientific interest.

Removal of non-cooperative objects from LEO using low-thrust spacecraft. The first proposed Earth's application of the methods and techniques developed in Part I of the thesis is a mission to actively de-orbit multiple objects from LEO using a servicing low-thrust spacecraft. Two possible de-orbiting strategies are considered, one analogous to the Travelling Salesman Problem and one analogous to the Vehicle Routing Problem. The transfer of the spacecraft between subsequent objects to be removed combines low-thrust propulsion with the natural dynamic due to J_2 in order to change the right ascension of the ascending node, a manoeuvre that would be very expensive using classic out-of-plane manoeuvres. Surrogate models for the cost of the transfers between any two objects are used in combination with a combinatorial algorithm to obtain sequences of objects to be removed with the minimum possible cost. Results show that by using an approach like the Travelling Salesman Problem, up to 10 objects can be removed from LEO in 1 year, while the Vehicle Routing Problem method allows one to de-orbit only 3 objects in the same period of time.

Constellation deployment. The analytic laws developed in Chapter 3 are applied to the deployment of the satellites of a constellation in MEO in Chapter 11, where a multi-objective optimisation problem is proposed. A constellation of 27 satellites in MEO is considered; the constellation can be deployed using two possible launchers, with different payload capabilities. Once left by the launchers into an injection orbit, the satellites use then their own electric propulsion system to reach the operational orbits. The objectives of the problem are the maximisation of the profit of the constellation and the minimisation of the ΔV required to deploy the satellites. The use of the analytical laws developed in Chapter 3 considerably speed-ups the run time of the multi-objective optimisation algorithm.

Low-thrust GTO-GEO transfer. The last case studied is the transfer from GTO to GEO using low-thrust propulsion. Both local and global optimisation algorithms are used to solve the problem, using a range of orbital perturbations (J_2, J_3, J_4, J_5, atmospheric drag and Sun third body perturbations). Different thrusting strategies are also considered. Results show that the problem is characterised by many local minima and that the use of a global optimisation algorithm is of paramount importance in order to be able to locate the minimum of the problem, if the initial guess to the local solver is not accurate enough.

Appendix A

Optimal control of time-continuous systems

Let us consider the optimal control problem defined in Equation 1.3 (reported hereafter) and the cost function J defined as in the problem of Bolza (Equation 1.6):

$$\begin{aligned} \min_{\mathbf{u}} \; & J\left(\mathbf{X}, \mathbf{u}, t\right) \\ \text{s.t.} \quad & \dot{\mathbf{X}} = \mathbf{h}(\mathbf{X}, \mathbf{u}, \mathbf{p}, t) \\ & \mathbf{c}(\mathbf{X}, \mathbf{u}, \mathbf{p}, t) = 0 \\ & \boldsymbol{\psi}\left(\mathbf{X}(t_0), \mathbf{X}(t_f), t_0, t_f\right) = 0 \\ & t \in [t_0, t_f] \end{aligned} \tag{A.1}$$

The cost function J can be augmented with the boundary constraints $\boldsymbol{\psi}$, the dynamic and equality constraints $\mathbf{h}$ and $\mathbf{c}$, and expressed in terms of the Hamiltonian $\mathcal{H}$ as in Equations 1.9 and 1.8:

$$J = \Phi\left(\mathbf{X}\left(t_f\right), t_f\right) + \boldsymbol{\nu}^T \boldsymbol{\psi}\left(\mathbf{X}\left(t_0\right), \mathbf{X}\left(t_f\right), t_0, t_f\right) + \int_{t_0}^{t_f} \left[\mathcal{H}\left(\mathbf{X}, \mathbf{u}, \boldsymbol{\lambda}, \boldsymbol{\mu}, t\right) - \boldsymbol{\lambda}\left(t\right)^T \dot{\mathbf{X}}\right] dt \,. \tag{A.2}$$

J can be further re-arranged integrating by parts the second term in Equation A.2:

$$\int_{t_0}^{t_f} \boldsymbol{\lambda}\left(t\right)^T \; \dot{\mathbf{X}} \, dt = \left[\boldsymbol{\lambda}\left(t\right)^T \mathbf{X}\left(t\right)\right]_{t_0}^{t_f} - \int_{t_0}^{t_f} \dot{\boldsymbol{\lambda}}\left(t\right)^T \mathbf{X}\left(t\right) dt, \tag{A.3}$$

so that:

$$\begin{aligned} J = {} & \Phi\left(\mathbf{X}\left(t_f\right), t_f\right) + \boldsymbol{\nu}^T \boldsymbol{\psi}\left(\mathbf{X}\left(t_0\right), \mathbf{X}\left(t_f\right), t_0, t_f\right) + \boldsymbol{\lambda}\left(t_0\right)^T \mathbf{X}\left(t_0\right) - \boldsymbol{\lambda}\left(t_f\right)^T \mathbf{X}\left(t_f\right) \\ & + \int_{t_0}^{t_f} \left[\mathcal{H}\left(\mathbf{X}, \mathbf{u}, \boldsymbol{\lambda}, \boldsymbol{\mu}, t\right) + \dot{\boldsymbol{\lambda}}\left(t\right)^T \mathbf{X}\right] dt \end{aligned} \,. \tag{A.4}$$

The first order variation of J is

$$\begin{aligned}\delta J = &\left[\left(\boldsymbol{\Phi}_{\mathbf{X}} + \boldsymbol{\nu}\left(t\right)^{T}\boldsymbol{\psi}_{\mathbf{X}} - \boldsymbol{\lambda}\left(t\right)^{T}\right)\delta\mathbf{X}\right]_{t=t_f} + \left[\boldsymbol{\lambda}\left(t\right)^{T}\delta\mathbf{X}\right]_{t=t_0} + \\ &\int_{t_0}^{t_f}\left[\boldsymbol{H}_{\mathbf{u}} + \left(\boldsymbol{H}_{\mathbf{X}} + \dot{\boldsymbol{\lambda}}\left(t\right)^{T}\right)\delta\mathbf{X}\right]d\tau\,,\end{aligned} \tag{A.5}$$

where $\bullet_{\mathbf{X}}$ represents the variation of a quantity with respect to $\mathbf{X}$ and $\bullet_{\mathbf{u}}$ the variation with respect to $\mathbf{u}$. The resulting first order variation of the cost function can be seen as composed of three terms:

$$\delta J = \delta J(t_f) + \delta J(t_0) + \delta J(t_0 \rightarrow t_f) = 0. \tag{A.6}$$

The necessary condition for the augmented cost function to be minimised is that its first order variation equals zero, that is $\delta J = 0$. This condition is satisfied when the three terms in δJ are zero, resulting in the necessary conditions, also referred to as Euler-Lagrange equations:

1. transversality conditions:

$$\boldsymbol{\lambda}\left(t_f\right)^{T} = \left[\boldsymbol{\Phi}_{\mathbf{x}} + \boldsymbol{\nu}\left(t\right)^{T}\boldsymbol{\psi}_{\mathbf{x}}\right]_{t=t_f} \tag{A.7}$$

2. control equation:

$$\boldsymbol{H}_{\mathbf{u}} = L_{\mathbf{u}} + \boldsymbol{\lambda}^{T}\mathbf{h}_{\mathbf{u}} + \boldsymbol{\mu}^{T}\mathbf{g}_{\mathbf{u}} = 0 \tag{A.8}$$

3. adjoint differential equations:

$$\dot{\boldsymbol{\lambda}}^{T}\left(t\right) = -\boldsymbol{H}_{\mathbf{X}} = -\mathcal{L}_{\mathbf{X}} - \boldsymbol{\lambda}^{T}\mathbf{h}_{\mathbf{x}} - \boldsymbol{\mu}^{T}\mathbf{g}_{\mathbf{X}}. \tag{A.9}$$

If the final time t_f is free, then the first order variation of J depends also on δt, and the following transversality condition is added to the Euler-Lagrange equations [19]:

$$\left[\phi_t + \boldsymbol{\nu}^{T}\boldsymbol{\psi}_t + \mathcal{H}\right]_{t=t_f} = 0\,. \tag{A.10}$$

The control equation is an application of the Pontryagin maximum principle. A more general expression is:

$$\mathbf{u} = \arg\min_{\mathbf{u}\in\mathcal{U}}\,\mathcal{H}\left(\mathbf{X},\mathbf{u},\boldsymbol{\lambda},\boldsymbol{\mu},t\right). \tag{A.11}$$

The maximum principle states that the control variables must be chosen to optimise the Hamiltonian at every instant of time [19].

The complete set of necessary conditions for optimality consists of a differential-algebraic system including the following equations:

$$\begin{aligned}&\dot{\mathbf{X}} = \mathbf{h}\left(\mathbf{X},\mathbf{u},t\right)\\ &\dot{\boldsymbol{\lambda}}\left(t\right) = -\boldsymbol{H}_{\mathbf{X}}^{T}\\ &\boldsymbol{H}_{\mathbf{u}} = 0\end{aligned} \tag{A.12}$$

and with boundary conditions at t_0 and t_f defined by:

$$\begin{aligned} &\boldsymbol{\psi}\left(\mathbf{X}\left(t_0\right), \mathbf{X}\left(t_f\right), t_0, t_f\right) = 0 \\ &\boldsymbol{\lambda}\left(t_f\right)^T = \left[\boldsymbol{\Phi}_{\mathbf{X}} + \boldsymbol{\nu}\left(t\right)^T \boldsymbol{\psi}_{\mathbf{X}}\right]_{t=tf} \\ &\left[\boldsymbol{\phi}_t + \boldsymbol{\nu}^T \boldsymbol{\psi}_t + \mathcal{H}\right]_{t=t_f} = 0\,. \end{aligned} \tag{A.13}$$

This is referred to as a two-point boundary value problem (TPBVP), as some boundary conditions on the states are specified at the initial time and some boundary conditions on the states and adjoints are specified at the terminal time [48].

Appendix B

Non-linear programming problem

The non-linear programming (NLP) problem, introduced in Equation 1.19, is reported hereafter for convenience:

$$\begin{aligned} \min_{\mathbf{x}\in\mathbb{X}} \ & \tilde{J}(\mathbf{x}) \\ \text{s.t.} \quad & \mathbf{c}(\mathbf{x}) = 0 \\ & \mathbf{g}(\mathbf{x}) \leq 0 \end{aligned} \tag{B.1}$$

Problem B.1 can be expressed in a compact form as

$$\min_{\mathbf{x}\in\mathcal{F}} \tilde{J}(\mathbf{x}) \tag{B.2}$$

where $\mathcal{F}$ is the feasible set (Definition 1.3.1). In the following, some important definitions are given (set of active indices, Lagrangian) and then the first-order necessary and sufficient conditions for optimality are presented [23].

Definition B.0.1 (Set of active indices)**.** *An inequality constraint $g_i(\mathbf{x})$ is said to be active if $g_i(\mathbf{x}) = 0$. The set of active indices $\mathcal{I}$ of the inequality constraints is:*

$$\mathcal{I}(\mathbf{x}) := \{i = 1, 2, \ldots, n_g | g_i(\mathbf{x}) = 0\} \tag{B.3}$$

Definition B.0.2 (Lagrangian function)**.** *The Lagrangian associated with Problem B.1 is given by the mapping $\mathcal{L} : \mathbb{R}^{n_x} \times \mathbb{R}^{n_c} \times \mathbb{R}^{n_g} \to \mathbb{R}$:*

$$\mathcal{L}(\mathbf{x}, \boldsymbol{\lambda}, \boldsymbol{\mu}) := \tilde{J}(\mathbf{x}) + \boldsymbol{\lambda}^T \mathbf{c}(\mathbf{x}) + \boldsymbol{\mu}^T \mathbf{g}(\mathbf{x}) \ , \tag{B.4}$$

where $\boldsymbol{\lambda} \in \mathbb{R}^{n_c}$ and $\boldsymbol{\mu} \in \mathbb{R}^{n_g}$ are Lagrange multipliers.

The first-order necessary conditions for optimality are defined by the Karush-Kuhn-Tucker theorem [20]

Theorem B.0.3 (Karush-Kuhn-Tucker (KKT) necessary conditions)**.** *Assume that the functions $\tilde{J}$, $\mathbf{c}$ and $\mathbf{g}$ are continuously differentiable with respect to $\mathbf{x}$. Then, at a local minimum $\mathbf{x}^*$, the follo-*

wing conditions, known as Karush-Kuhn-Tucker (KKT) conditions are satisfied (optimality conditions, constraints and complementarity conditions):

$$\begin{aligned}
&\nabla_x \mathcal{L}\left(\mathbf{x}^*, \boldsymbol{\lambda}, \boldsymbol{\mu}\right) = \mathbf{0} \\
&\nabla_\lambda \mathcal{L}\left(\mathbf{x}^*, \boldsymbol{\lambda}, \boldsymbol{\mu}\right) = \mathbf{c}\left(\mathbf{x}^*\right) = \mathbf{0} \\
&\nabla_\mu \mathcal{L}\left(\mathbf{x}^*, \boldsymbol{\lambda}, \boldsymbol{\mu}\right) = \mathbf{g}\left(\mathbf{x}^*\right) \leq \mathbf{0} \\
&\boldsymbol{\mu}^* \geq 0 \\
&\boldsymbol{\mu}^{*T} \mathbf{g}\left(\mathbf{x}^*\right) = 0 \,,
\end{aligned} \tag{B.5}$$

Proofs of theorem B.0.3 can be found in [119]. A stationary KKT point is an optimal solution of problem B.1 if second-order sufficient conditions are satisfied. In order to define the second-order sufficient conditions, the definition of the critical cone is required [23].

Definition B.0.4 (Critical cone)**.** *If* $\mathbf{x}$ *is a feasible point, then the critical cone is defined by:*

$$\begin{aligned}
\mathcal{T}_x := \{\mathbf{v} \in \mathbb{R}^{n_x} \mid \quad & \nabla g_i^T\left(\mathbf{x}\right) \mathbf{v} \leq 0 \quad i \in \mathcal{I}\left(\mathbf{x}\right) \,,\; \mu_i = 0 \\
& \nabla g_i^T\left(\mathbf{x}\right) \mathbf{v} = 0 \quad i \in \mathcal{I}\left(\mathbf{x}\right) \,,\; \mu_i > 0 \\
& \nabla h_i^T\left(\mathbf{x}\right) \mathbf{v} = 0 \quad i \in [1, 2, \ldots, n_h]\}
\end{aligned} \tag{B.6}$$

Theorem B.0.5 (Second-order sufficient conditions)**.** *Let* $\mathbf{x}^* \in \mathcal{F}$ *be a feasible point for Problem B.1 and let the functions* $\tilde{J}$, $\mathbf{c}$ *and* $\mathbf{g}$ *be twice continuously differentiable with respect to* $\mathbf{x}$*. Assume the Lagrange vectors* $\boldsymbol{\lambda}$ *and* $\boldsymbol{\mu}$ *exist, Theorem B.0.3 holds and that the Hessian of the Lagrangian is positive definite on the critical cone:*

$$\mathbf{v}^T \nabla_y^2 \mathcal{L}\left(\mathbf{x}^*, \boldsymbol{\lambda}, \boldsymbol{\mu}\right) \mathbf{v} > 0 \,,\; \forall \mathbf{v} \in \mathcal{T}_x^* \,,\; \mathbf{v} \neq \mathbf{0} \,. \tag{B.7}$$

Then, $\mathbf{x}^*$ *satisfies the second-order necessary conditions and is a strict local minimum of B.1.*

The non-linear programming problem can be solved by Active Set or Interior Point Method; these methods are briefly presented in the next sections. More information can be found in [20].

B.1 Active Set Method

The Active Set Method is an iterative method that finds a suitable search direction $\mathbf{d}$ at every iteration. The method approximates the objective with a quadratic function and the non-linear constraints with liner constraints. The approximation of the objective is

$$\tilde{J}(\mathbf{x}_{k+1}) \approx \tilde{J}(\mathbf{x}_k) + \nabla \tilde{J}(\mathbf{x}_k)^T \mathbf{d} + \frac{1}{2} \mathbf{d}^T \nabla_{xx}^2 \tilde{J}\left(\mathbf{x}_k\right) \mathbf{d} \,, \tag{B.8}$$

where $\mathbf{d} = \Delta\mathbf{x} = \mathbf{x} - \mathbf{x}_k$ is the search direction. The constraints are approximated as:

$$\begin{aligned} \mathbf{c}\left(\mathbf{x}_{k+1}\right) &\approx \mathbf{c}\left(\mathbf{x}\right) + \nabla_{\mathbf{x}}\mathbf{c}\left(\mathbf{x}\right)\mathbf{d} = 0 \\ \mathbf{g}\left(\mathbf{x}_{k+1}\right) &\approx \mathbf{g}\left(\mathbf{x}\right) + \nabla_{\mathbf{x}}\mathbf{g}\left(\mathbf{x}\right)\mathbf{d} \leq 0\,. \end{aligned} \tag{B.9}$$

Solving the problem defined by Equations B.8 and B.9 corresponds to solving a quadratic subproblem, defined as:

$$\begin{aligned} \min_{\mathbf{x}\in\mathbb{X}}\ & \tilde{J}\left(\mathbf{x}\right) + \nabla_{\mathbf{x}}\tilde{J}^{T}\left(\mathbf{x}\right)\mathbf{d} + \frac{1}{2}\mathbf{d}^{T}\nabla^{2}_{xx}\tilde{J}\,\mathbf{d} \\ \text{s.t.}\quad & \mathbf{c}\left(\mathbf{x}\right) + \nabla_{\mathbf{x}}\mathbf{c}\left(\mathbf{x}\right)\mathbf{d} = 0 \\ & \mathbf{g}\left(\mathbf{x}\right) + \nabla_{\mathbf{x}}\mathbf{g}\left(\mathbf{x}\right)\mathbf{d} \leq 0 \end{aligned} \tag{B.10}$$

The general problem with equality and inequality constraints can be transformed into an equality contraints only problem using slack variables $\mathbf{s}$, and substituting the inequality constraints with:

$$\begin{aligned} &\mathbf{g}(\mathbf{x}) - \mathbf{s} = 0 \\ &\mathbf{s} \geq 0\,. \end{aligned} \tag{B.11}$$

The set of equality constraints includes now both the original equality constraints $\mathbf{c}\left(\mathbf{x}\right) = 0$ and $\mathbf{g}(\mathbf{x}) - \mathbf{s} = 0$. With this new formulation, the solution of the problem defined in Equation B.10 can be obtained solving the Karush-Kuhn-Tucker system:

$$\begin{bmatrix} \nabla^{2}_{\mathbf{x}}\mathcal{L} & -\nabla_{\mathbf{x}}\mathbf{c}^{T} \\ \nabla_{\mathbf{x}}\mathbf{c} & 0 \end{bmatrix} \begin{bmatrix} \Delta\mathbf{x} \\ \Delta\boldsymbol{\lambda} \end{bmatrix} = \begin{bmatrix} -\nabla_{\mathbf{x}}f \\ -\mathbf{c} \end{bmatrix}\,, \tag{B.12}$$

where $\nabla^{2}_{\mathbf{x}}\mathcal{L}$ is the Hessian of the Lagrangian $\mathcal{L}$ in $\mathbf{x}$. The solution of the quadratic subproblem is therefore a search direction $\mathbf{d}_k$ so that the solution to the problem can be found using the following update rule:

$$\mathbf{x}_{k+1} = \mathbf{x}_k + \alpha_k\mathbf{d}_k \tag{B.13}$$

where α_k is a positive step length.

B.2 Interior Point Method

The Interior Point Method transforms the NLP problem B.1 into a barrier formulation:

$$\begin{aligned} \min_{\mathbf{x}\in\mathbb{X}}\ & B\left(\mathbf{x}, \mu_{IPM}\right) \\ \text{s.t.}\quad & \mathbf{c}\left(\mathbf{x}\right) = 0 \end{aligned} \tag{B.14}$$

where

$$B\left(\mathbf{x}, \mu_{IPM}\right) = \tilde{J}(\mathbf{x}) - \mu_{IPM}\sum_{i}\log\left(-g_i\left(\mathbf{x}\right)\right) \tag{B.15}$$

In Equation B.14 $B(\mathbf{x}, \mu_{IPM})$ is the barrier function while μ_{IPM} the barrier parameter, added to keep the search in the feasible space $\mathbf{g}(\mathbf{x}) < 0$. The minimum of $B(\mathbf{x}, \mu_{IPM})$ converges to a solution of B.1 as μ_{IPM} converges to zero. Problem B.14 is then solved defining the associated Lagrangian and making use of the KKT conditions (see Definition B.0.2 and Theorem B.0.3). At each iteration of the IPM, one iteration towards the solution of the relaxed KKT system is performed, and the current solution estimates and parameter μ_{IPM} are updated.

Appendix C

Analytical integrals

This appendix reports the analytical integrals for the propagation of the motion of the satellite subject to low-thrust and perturbing accelerations (Chapter 4).

C.1 J_3, J_4, J_5

This section gives the expressions for the integrals used to compute the analytical equations for the motion of the satellite subject to the Earth's gravitational potential perturbations. The integrals reported in the following subsections have been solved analytically using the software Mathematica; the results, too cumbersome to be reported here, have been exported directly from Mathematica to MATLAB. The complete results can be found at: `http://dx.doi.org/10.15129/354f9b2a-d1d5-4f51-9545-e963251f1e40`.

C.1.1 J_3

$$\begin{aligned} I_{J_3,a,1} = \int_{L_0}^{L} \{ & \Phi_0^3(\mathcal{L}) \left(P_{20}\sin\mathcal{L} - P_{10}\cos\mathcal{L}\right)\left(Q_{20}\sin\mathcal{L} - Q_{10}\cos\mathcal{L}\right) \\ & \left[20\left(Q_{20}\sin\mathcal{L} - Q_{10}\cos\mathcal{L}\right)^2 - 3S_0^2\right]\Big\}\, d\mathcal{L} \end{aligned} \tag{C.1}$$

$$I_{J_3,a,2} = \int_{L_0}^{L} \left\{ \Phi_0^4(\mathcal{L}) \left(Q_{20}\cos\mathcal{L} + Q_{10}\sin\mathcal{L}\right)\left[S_0^2 - 20\left(Q_{20}\sin\mathcal{L} - Q_{10}\cos\mathcal{L}\right)^2\right]\right\} d\mathcal{L} \tag{C.2}$$

$$\begin{aligned} I_{J_3,P_1} = \int_{L_0}^{L} \Big\{ & -4\cos(\mathcal{L})\Phi_0^3(\mathcal{L})\left(Q_{20}\sin\mathcal{L} - Q_{10}\cos\mathcal{L}\right)\left[20\left(Q_{20}\sin\mathcal{L} - Q_{10}\cos\mathcal{L}\right)^2 - 3S_0^2\right] + \\ & + 3\Phi_0^2(\mathcal{L})\left(Q_{20}\cos\mathcal{L} + Q_{10}\sin\mathcal{L}\right)\left(P_{10} + \sin\mathcal{L} + \Phi_0(\mathcal{L})\sin\mathcal{L}\right) \\ & \left[S_0^2 - 20\left(Q_{20}\sin\mathcal{L} - Q_{10}\cos\mathcal{L}\right)^2\right]\Big\}\, d\mathcal{L} \end{aligned} \tag{C.3}$$

$$I_{J_3,P_1,P_2} = \int_{L_0}^{L} \left\{ \left(Q_{10}\cos\mathcal{L} - Q_{20}\sin\mathcal{L}\right)\Phi_0^2(\mathcal{L}) \left[S_0^2 - 20\left(Q_{20}\sin\mathcal{L} - Q_{10}\cos\mathcal{L}\right)^2 \right] \right\} d\mathcal{L} \quad \text{(C.4)}$$

$$\begin{aligned} I_{J_3,P_2} = \int_{L_0}^{L} \Big\{ & 4\sin(\mathcal{L})\Phi_0^3(\mathcal{L}) \left(Q_{20}\sin\mathcal{L} - Q_{10}\cos\mathcal{L}\right) \left[20\left(Q_{20}\sin\mathcal{L} - Q_{10}\cos\mathcal{L}\right)^2 - 3S_0^2 \right] + \\ & 3\Phi_0^2(\mathcal{L}) \left(Q_{20}\cos\mathcal{L} + Q_{10}\sin\mathcal{L}\right) \left(P_{20} + \cos\mathcal{L} + \Phi_0(\mathcal{L})\cos\mathcal{L}\right) \\ & \left[S_0^2 - 20\left(Q_{20}\sin\mathcal{L} - Q_{10}\cos\mathcal{L}\right)^2 \right] \Big\} d\mathcal{L} \end{aligned} \quad \text{(C.5)}$$

$$I_{J_3,Q_1} = \int_{L_0}^{L} \sin(\mathcal{L})\Phi_0^2(\mathcal{L}) \left[S_0^2 - 20\left(Q_{20}\sin\mathcal{L} - Q_{10}\cos\mathcal{L}\right)^2 \right] d\mathcal{L} \quad \text{(C.6)}$$

$$I_{J_3,Q_2} = \int_{L_0}^{L} \cos(\mathcal{L})\Phi_0^2(\mathcal{L}) \left[S_0^2 - 20\left(Q_{20}\sin\mathcal{L} - Q_{10}\cos\mathcal{L}\right)^2 \right] d\mathcal{L} \quad \text{(C.7)}$$

C.1.2 J_4

$$\begin{aligned} I_{J_4,a,1} = \int_{L_0}^{L} \Big\{ & \Phi_0^4(\mathcal{L}) \left[2800\left(Q_{20}\sin\mathcal{L} - Q_{10}\cos\mathcal{L}\right)^4 - 600S_0^2\left(Q_{20}\sin\mathcal{L} - Q_{10}\cos\mathcal{L}\right)^2 + 15 \right] \\ & \left(P_{20}\sin\mathcal{L} - P_{10}\cos\mathcal{L}\right) \Big\} d\mathcal{L} \end{aligned} \quad \text{(C.8)}$$

$$\begin{aligned} I_{J_4,a,2} = \int_{L_0}^{L} \Big\{ & \Phi_0^5(\mathcal{L}) \left(Q_{20}\cos\mathcal{L} + Q_{10}\sin\mathcal{L}\right) \left(Q_{20}\sin\mathcal{L} - Q_{10}\cos\mathcal{L}\right) \\ & \left[280\left(Q_{20}\sin\mathcal{L} - Q_{10}\cos\mathcal{L}\right)^2 - 30S_0^2 \right] \Big\} d\mathcal{L} \end{aligned} \quad \text{(C.9)}$$

$$\begin{aligned} I_{J_4,P_1} = \int_{L_0}^{L} \Big\{ & \cos(\mathcal{L})\frac{\Phi_0^4(\mathcal{L})}{8} \Big[2800\left(Q_{20}\sin\mathcal{L} - Q_{10}\cos\mathcal{L}\right)^4 - 600S_0^2\left(Q_{20}\sin\mathcal{L} - Q_{10}\cos\mathcal{L}\right)^2 + \\ & 15G_0^4 \Big] + \Phi_0^3(\mathcal{L}) \left(P_{10} + \sin\mathcal{L} + \Phi_0(\mathcal{L})\sin\mathcal{L}\right) \left(Q_{20}\cos\mathcal{L} + Q_{10}\sin\mathcal{L}\right) \\ & \left(Q_{20}\sin\mathcal{L} - Q_{10}\cos\mathcal{L}\right) \left[280\left(Q_{20}\sin\mathcal{L} - Q_{10}\cos\mathcal{L}\right)^2 - 30S_0^2 \right] \Big\} d\mathcal{L} \end{aligned} \quad \text{(C.10)}$$

$$I_{J_4,P_1,P_2} = \int_{L0}^{L} \Phi_0^3(\mathcal{L}) \left(Q_{10}\cos\mathcal{L} - Q_{20}\sin\mathcal{L}\right)^2 \left[140\left(Q_{20}\sin\mathcal{L} - Q_{10}\cos\mathcal{L}\right)^2 - 15S_0^2 \right] d\mathcal{L} \quad \text{(C.11)}$$

$$I_{J_4,P_2} = \int_{L_0}^{L} \Big\{ \sin(\mathcal{L}) \frac{\Phi_0^4(\mathcal{L})}{8} \Big[2800 \left(Q_{20} \sin\mathcal{L} - Q_{10} \cos\mathcal{L}\right)^4 - 600 S_0^2 \left(Q_{20} \sin\mathcal{L} - Q_{10} \cos\mathcal{L}\right)^2 + 15 S_0^4 \Big] - \Phi_0^3(\mathcal{L}) \left(P_{20} + \cos\mathcal{L} + \Phi_0(\mathcal{L}) \cos\mathcal{L}\right) \left(Q_{20} \cos\mathcal{L} + Q_{10} \sin\mathcal{L}\right) \left(Q_{20} \sin\mathcal{L} - Q_{10} \cos\mathcal{L}\right) \Big[280 \left(Q_{20} \sin\mathcal{L} - Q_{10} \cos\mathcal{L}\right)^2 - 30 S_0^2 \Big] \Big\} d\mathcal{L} \tag{C.12}$$

$$I_{J_4,Q_1} = \int_{L_0}^{L} \Phi_0^3(\mathcal{L}) \sin\mathcal{L} \left(Q_{20} \sin\mathcal{L} - Q_{10} \cos\mathcal{L}\right) \Big[15 S_0^2 - 140 \left(Q_{20} \sin\mathcal{L} - Q_{10} \cos\mathcal{L}\right)^2 \Big] d\mathcal{L} \tag{C.13}$$

$$I_{J_4,Q2} = \int_{L_0}^{L} \Phi_0^3(\mathcal{L}) \cos\mathcal{L} \left(Q_{20} \sin\mathcal{L} - Q_{10} \cos\mathcal{L}\right) \Big[15 S_0^2 - 140 \left(Q_{20} \sin\mathcal{L} - Q_{10} \cos\mathcal{L}\right)^2 \Big] d\mathcal{L} \tag{C.14}$$

C.1.3 J_5

$$I_{J_5,a} = \int_{L_0}^{L} \Big\{ \Phi_0^5(\mathcal{L}) \Big[3024 \left(Q_{20} \sin\mathcal{L} - Q_{10} \cos\mathcal{L}\right)^4 - 840 S_0^2 \left(Q_{20} \sin\mathcal{L} - Q_{10} \cos\mathcal{L}\right)^2 + 45 S_0^4 \Big] \left(Q_{20} \sin\mathcal{L} - Q_{10} \cos\mathcal{L}\right) \left(P_{20} \sin\mathcal{L} - P_{10} \cos\mathcal{L}\right) - \frac{1}{2} \Phi_0^6(\mathcal{L}) \left(Q_{20} \cos\mathcal{L} + Q_{10} \sin\mathcal{L}\right)) \Big[5040 \left(Q_{20} \sin\mathcal{L} - Q_{10} \cos\mathcal{L}\right)^4 - 840 S_0^2 \left(Q_{20} \sin\mathcal{L} - Q_{10} \cos\mathcal{L}\right)^2 + 15 S_0^4 \Big] \Big\} d\mathcal{L} \tag{C.15}$$

$$I_{J_5,P_1} = \int_{L_0}^{L} \Big\{ \Phi_0^5(\mathcal{L}) \cos L \Big[3024 \left(Q_{20} \sin\mathcal{L} - Q_{10} \cos\mathcal{L}\right)^4 840 G_0^2 \left(Q_{20} \sin\mathcal{L} - Q_{10} \cos\mathcal{L}\right)^2 + 45 G_0^4 \Big] \left(Q_{20} \sin\mathcal{L} - Q_{10} \cos\mathcal{L}\right) + \frac{1}{2} \Phi_0^4(\mathcal{L}) \left(Q_{20} \cos\mathcal{L} + Q_{10} \sin\mathcal{L}\right) \left(P_{10} + \sin\mathcal{L} + \Phi_0(\mathcal{L}) \sin\mathcal{L}\right) \Big[5040 \left(Q_{20} \sin\mathcal{L} - Q_{10} \cos\mathcal{L}\right)^4 + -840 G_0^2 \left(Q_{20} \sin\mathcal{L} - Q_{10} \cos\mathcal{L}\right)^2 + 15 G_0^4 \Big] \Big\} d\mathcal{L} \tag{C.16}$$

$$I_{J_5,P_1,P_2} = \int_{L_0}^{L} \Big\{ \Phi_0^4(\mathcal{L}) \Big[5040 \left(Q_{20} \sin\mathcal{L} - Q_{10} \cos\mathcal{L}\right)^4 - 840 S_0^2 \left(Q_{20} \sin\mathcal{L} - Q_{10} \cos\mathcal{L}\right)^2 + 15 S_0^4 \Big] \left(Q_{10} \cos\mathcal{L} - Q_{20} \sin\mathcal{L}\right) \Big\} d\mathcal{L} \tag{C.17}$$

$$I_{J_5,P_2} = \int_{L_0}^{L} \Big\{ -\Phi_0^5(\mathcal{L}) \sin\mathcal{L} \Big[3024 \left(Q_{20}\sin\mathcal{L} - Q_{10}\cos\mathcal{L}\right)^4 + 840 S_0^2 \left(Q_{20}\sin\mathcal{L} - Q_{10}\cos\mathcal{L}\right)^2 + 45 S_0^4 \Big] \left(Q_{20}\sin\mathcal{L} - Q_{10}\cos\mathcal{L}\right) + \frac{1}{2}\Phi_0^4(\mathcal{L}) \left(Q_{20}\cos\mathcal{L} + Q_{10}\sin\mathcal{L}\right) \left(P_{20} + \cos\mathcal{L} + \Phi_0(\mathcal{L})\cos\mathcal{L}\right) \Big[5040 \left(Q_{20}\sin\mathcal{L} - Q_{10}\cos\mathcal{L}\right)^4 - 840 S_0^2 \left(Q_{20}\sin\mathcal{L} - Q_{10}\cos\mathcal{L}\right)^2 + 15 S_0^4 \Big] \Big\} d\mathcal{L} \tag{C.18}$$

$$I_{J_5,Q_1} = \int_{L_0}^{L} \Phi_0^4(\mathcal{L}) \sin\mathcal{L} \Big[5040 \left(Q_{20}\sin\mathcal{L} - Q_{10}\cos\mathcal{L}\right)^4 - 840 S_0^2 \left(Q_{20}\sin\mathcal{L} - Q_{10}\cos\mathcal{L}\right)^2 + 15 S_0^4 \Big] d\mathcal{L} \tag{C.19}$$

$$I_{J_5,Q_2} = \int_{L_0}^{L} \Phi_0^4(\mathcal{L}) \cos\mathcal{L} \Big[5040 \left(Q_{20}\sin\mathcal{L} - Q_{10}\cos\mathcal{L}\right)^4 - 840 S_0^2 \left(Q_{20}\sin\mathcal{L} - Q_{10}\cos\mathcal{L}\right)^2 + 15 S_0^4 \Big] d\mathcal{L} \tag{C.20}$$

C.2 Atmospheric drag

This section reports the expressions for the analytical integrals used to describe the effect of the atmospheric drag perturbation on the motion of the satellite. The integrals can be found also at http://dx.doi.org/10.15129/63879118-7549-47ec-ad6e-bc6f77e0a6e5. In the following equations, $F_I\left(\phi, m\right)$, $E_I\left(\phi, m\right)$ and $\Pi_I\left(n, \phi, m\right)$ are the elliptic integral of the first, second and third kind:

$$\begin{aligned} F_I\left(\phi, m\right) &= \int_0^{\phi} \left(1 - m\sin^2\vartheta\right)^{-1/2} d\theta \\ E_I\left(\phi, m\right) &= \int_0^{\phi} \left(1 - m\sin^2\vartheta\right)^{1/2} d\theta \\ \Pi_I\left(n, \phi, m\right) &= \int_0^{\phi} \left(1 - n\sin^2\vartheta\right)^{-1} \left[1 - m\sin^2\vartheta\right]^{-1/2} d\theta \end{aligned} \tag{C.21}$$

C.2.1 $I_{Drag,1}$

$$I_{Drag,1} = k_0 I_{Drag,10} + k_1 I_{Drag,11} + k_2 I_{Drag,12} + k_3 I_{Drag,13} + k_4 I_{Drag-14} \tag{C.22}$$

$$I_{Drag,10} = \int_{\theta_0}^{\theta} \frac{\sin\vartheta\sqrt{1+e_0^2+2e\cos\vartheta}}{(1+e_0\cos\theta)^2}d\vartheta = \left[\frac{3+e_0^2}{e_0^2(1+e_0)}F_I\left(\frac{\vartheta}{2},\frac{4e_0}{(1+e_0)^2}\right)+\right.$$
$$-\frac{3(1+e_0)}{e_0^2}E_I\left(\frac{\vartheta}{2},\frac{4e_0}{(1+e_0)^2}\right)+\frac{1}{e_0^2}\log\left(\frac{\sqrt{1+e_0^2+2e_0\cos\vartheta}+e_0\sin\vartheta}{\sqrt{1+e_0^2+2e_0\cos\vartheta}-e_0\sin\vartheta}\right)+ \quad \text{(C.23)}$$
$$\left.+\frac{\sin\vartheta\sqrt{1+e_0^2+2e_0\cos\vartheta}}{e_0(1+e_0\cos\vartheta)}\right]_{\theta_0}^{\theta}$$

$$I_{Drag,11} = \int_{\theta_0}^{\theta} \frac{\sin\vartheta\sqrt{1+e_0^2+2e\cos\vartheta}}{(1+e_0\cos\vartheta)^3}d\vartheta = \left\{-\frac{1}{e_0^2(1+e_0)}E_I\left[\arcsin\left(\cos\frac{\vartheta}{2}\right),-\frac{4e_0}{(1-e_0)^2}\right]+\right.$$
$$+\frac{2}{e_0^2(1-e_0)}F_I\left[\arcsin\left(\cos\frac{\vartheta}{2}\right),-\frac{4e_0}{(1-e_0)^2}\right]+$$
$$\left.-\frac{(1+e_0)^2}{e_0^2(1-e_0^2)}\Pi_I\left[-\frac{2e_0}{1-e_0},\arcsin\left(\cos\frac{\vartheta}{2}\right),-\frac{4e_0}{(1-e_0)^2}\right]-\frac{\sin\vartheta(1+e_0^2+2e_0\cos\vartheta)^{3/2}}{2e_0(1-e_0^2)(1+e_0\cos\vartheta)^2}\right\}_{\theta_0}^{\theta} \quad \text{(C.24)}$$

where

$$\Pi_I\left[-\frac{2e_0}{1-e_0},\arcsin\left(\cos\frac{\vartheta}{2}\right),-\frac{4e_0}{(1-e_0)^2}\right]=\frac{1}{1+e_0}F_I\left[\arcsin\left(\cos\frac{\vartheta}{2}\right),-\frac{4e_0}{(1-e_0)^2}\right]+$$
$$\frac{1}{4}\frac{(1-e_0)}{(1+e_0)}\log\left[\frac{\left(\tan(\vartheta/2)\sqrt{1+e_0^2+2e_0\cos\vartheta}+(1+e_0)\right)\left((1-e_0)\tan(\vartheta/2)-\sqrt{1+e_0^2+2e_0\cos\vartheta}\right)}{\left(\tan(\vartheta/2)\sqrt{1+e_0^2+2e_0\cos\vartheta}-(1+e_0)\right)\left((1-e_0)\tan(\vartheta/2)+\sqrt{1+e_0^2+2e_0\cos\vartheta}\right)}\right] \quad \text{(C.25)}$$

$$I_{Drag,12} = \int_{\theta_0}^{\theta} \frac{\sin\vartheta\sqrt{1+e_0^2+2e_0\cos\vartheta}}{(1+e\cos\vartheta)^4}d\vartheta =$$
$$\left\{-\frac{(e_0^4-2e_0^3+2e_0^2-2e_0+1)}{3e_0^2(1-e_0)^3(1+e_0)^2}E_I\left[\arcsin\left(\cos\frac{\vartheta}{2}\right),-\frac{4e_0}{(1-e_0)^2}\right]+\right.$$
$$+\frac{(e_0^4-2e_0^2+1)}{3e_0^2(1-e_0)^3(1+e_0)^2}F_I\left[\arcsin\left(\cos\frac{\vartheta}{2}\right),-\frac{4e_0}{(1-e_0)^2}\right]+ \quad \text{(C.26)}$$
$$\left.-\frac{e_0\sin\vartheta A_{12}(e_0,\vartheta)}{3e_0^2(1-e_0)^2(1+e_0)^2(1+e_0\cos\vartheta)^3\sqrt{1+e_0^2+2e_0\cos\vartheta}}\right\}_{\theta_0}^{\theta}$$

where

$$A_{12}(e_0,\vartheta) = (2e_0^5+2e_0^3)\cos^3\vartheta+(e_0^6+4e_0^4+7e_0^2)\cos^2\vartheta+(-e_0^5+8e_0^3+5e_0)\cos\vartheta+ \quad \text{(C.27)}$$
$$+(-e_0^6+e_0^4+3e_0^2+1)$$

$$
\begin{aligned}
I_{Drag,13} = & \int_{\theta}^{\theta_0} \frac{\sin\vartheta\sqrt{1+e_0^2+2e_0\cos\vartheta}}{(1+e_0\cos\vartheta)^5}d\vartheta = \\
& \left\{ -\frac{(e_0^4-2e_0^3+2e_0^2-2e_0+1)}{3e_0^2(1-e_0)^4(1+e_0)^3}E_I\left[\arcsin\left(\cos\frac{\vartheta}{2}\right), -\frac{4e_0}{(1-e_0)^2}\right] + \right. \\
& + \frac{(e_0^4-2e_0^2+1)}{12e_0^2(1-e_0)^4(1+e_0)^3}F_I\left[\arcsin\left(\cos\frac{\vartheta}{2}\right), -\frac{4e_0}{(1-e_0)^2}\right] + \\
& + \frac{(e_0^5+e_0^4-2e_0^3-2e_0^2+e_0+1)}{4e_0^2(1-e_0)^4(1+e_0)^3}\Pi_I\left[-\frac{2e_0}{1-e_0}, \arcsin\left(\cos\frac{\vartheta}{2}\right), -\frac{4e_0}{(1-e_0)^2}\right] \\
& \left. - \frac{e_0\sin\vartheta A_{13}\left(e_0,\vartheta\right)}{24e_0^2(1-e_0)^3(1+e_0)^3(1+e_0\cos\vartheta)^4\sqrt{1+e_0^2+2e_0\cos\vartheta}} \right\}_{\theta_0}^{\theta}
\end{aligned}
\tag{C.28}
$$

where

$$
\begin{aligned}
A_{13}\left(e_0,\vartheta\right) = & (16e_0^6+16e_0^4)\cos^4\vartheta + (2e_0^7+60e_0^5+66e_0^3)\cos^3\vartheta + (-3e_0^8+15e_0^6+75e_0^4+105\,e_0^2)\cos^2\vartheta + \\
& (10e_0^7-24e_0^5+82e_0^3+60e_0)\cos\vartheta + (6e_0^8-11e_0^6-e_0^4+27e_0^2+11)
\end{aligned}
\tag{C.29}
$$

$$
\begin{aligned}
I_{Drag,14} = & \int_{\theta_0}^{\theta} \frac{\sin\vartheta\sqrt{1+e_0^2+2e_0\cos\vartheta}}{(1+e_0\cos\vartheta)^6}d\vartheta = \\
& \left\{ -\frac{(2e_0^6-4e_0^5+5e_0^4-6e_0^3+10e_0^2-14e_0+7)}{15e_0^2(1-e_0)^5(1+e_0)^4}E_I\left[\arcsin\left(\cos\frac{\vartheta}{2}\right), -\frac{4e_0}{(1-e_0)^2}\right] + \right. \\
& + \frac{(4e_0^6-9e_0^4+6e_0^2-1)}{30e_0^2(1-e_0)^5(1+e_0)^4}F_I\left[\arcsin\left(\cos\frac{\vartheta}{2}\right), -\frac{4e_0}{(1-e_0)^2}\right] + \\
& + \frac{1}{2e_0^2(1-e_0)^3(1+e_0)}\Pi_I\left[-\frac{2e_0}{1-e_0}, \arcsin\left(\cos\frac{\vartheta}{2}\right), -\frac{4e_0}{(1-e_0)^2}\right] \\
& \left. - \frac{\sin\vartheta A_{14}\left(e_0,\vartheta\right)}{60\,e_0(1-e_0)^4(1+e_0)^4(1+e_0\cos\vartheta)^5\sqrt{1+e_0^2+2e_0\cos\vartheta}} \right\}_{\theta_0}^{\theta}
\end{aligned}
\tag{C.30}
$$

where

$$
\begin{aligned}
A_{14}\left(e_0,\vartheta\right) = & (192e_0^9+24e_0^7+56e_0^5)\cos^5\vartheta + (8e_0^{10}+62e_0^8+132e_0^6+278e_0^4)\cos^4\vartheta + \\
& + (29e_0^9+97e_0^7+279e_0^5+555e_0^3)\cos^3\vartheta + \\
& + (4e_0^{10}+23e_0^8+103e_0^6+269e_0^4+561e_0^2)\cos^2\vartheta + \\
& + (-22e_0^9+111e_0^7-97e_0^5+229e_0^3+259e_0)\cos\vartheta + \\
& + (-12e_0^{10}+34e_0^8-11e_0^6-29e_0^4+71e_0^2+143)
\end{aligned}
\tag{C.31}
$$

C.2.2 $I_{Drag,2}$

$$
I_{Drag,2} = k_0 I_{Drag,20} + k_1 I_{Drag,21} + k_2 I_{Drag,22} + k_3 I_{Drag,23} + k_4 I_{Drag,24} \tag{C.32}
$$

$$I_{Drag,20} = \int_{\theta_0}^{\theta} \sqrt{1+e_0^2+2e_0\cos\vartheta}d\vartheta = 2(1+e_0)\left[E_I\left(\frac{\vartheta}{2},\frac{4e_0}{(1+e_0)^2}\right)\right]_{\theta_0}^{\theta} \tag{C.33}$$

$$\begin{aligned} I_{Drag,21} = \int \frac{\sqrt{1+e_0^2+2e_0\cos\theta}}{(1+e_0\cos\theta)}d\theta = \frac{2}{(1+e_0)}\left[2F_I\left(\frac{\theta}{2},\frac{4e_0}{(1+e_0)^2}\right)+\right. \\ \left.+(-1+e_0)\Pi_I\left(\frac{2e_0}{1+e_0},\frac{\theta}{2},\frac{4e_0}{(1+e_0)^2}\right)\right]_{\theta_0}^{\theta} \end{aligned} \tag{C.34}$$

$$I_{Drag,22} = \int_{\theta_0}^{\theta} \frac{\sqrt{1+e_0^2+2e_0\cos\vartheta}}{(1+e_0\cos\vartheta)^2}d\vartheta = I_{Drag-40} \tag{C.35}$$

$$\begin{aligned} I_{Drag,23} = \int_{\theta_0}^{\theta} \frac{\sqrt{1+e_0^2+2e_0\cos\vartheta}}{(1+e_0\cos\vartheta)^3}d\vartheta = \\ \left\{-\frac{1}{(1-e_0)(1+e_0)^2}E_I\left[\arcsin\left(\cos\frac{\vartheta}{2}\right),-\frac{4e_0}{(1-e_0)^2}\right]+\right. \\ -\frac{1}{(1-e_0)^2}\Pi_I\left[-\frac{2e_0}{1-e_0},\arcsin\left(\cos\frac{\vartheta}{2}\right),-\frac{4e_0}{(1-e_0)^2}\right]+ \\ \left.-\frac{e_0\sin\vartheta(2e_0^2+8e_0\cos\theta+4e_0^2\cos^2\vartheta-e_0^4+3)}{2(1-e_0)^2(1+e_0)^2\sqrt{1+e_0^2+2e_0\cos\vartheta}(1+e_0\cos\vartheta)^2}\right\}_{\theta_0}^{\theta} \end{aligned} \tag{C.36}$$

$$\begin{aligned} I_{Drag,24} = \int_{\theta_0}^{\theta} \frac{\sqrt{1+e_0^2+2e_0\cos\vartheta}}{(1+e_0\cos\vartheta)^4}d\vartheta = \\ \left\{-\frac{2(1+e_0^2)}{3(1-e_0)^2(1+e_0)^3}E_I\left[\arcsin\left(\cos\frac{\vartheta}{2}\right),-\frac{4e_0}{(1-e_0)^2}\right]+\right. \\ +\frac{2}{3(1-e_0)^2(1+e_0)}F_I\left[\arcsin\left(\cos\frac{\vartheta}{2}\right),-\frac{4e_0}{(1-e_0)^2}\right]+ \\ -\frac{2}{(1-e_0)^3(1+e_0)}\Pi_I\left[-\frac{2e_0}{1-e_0},\arcsin\left(\cos\frac{\vartheta}{2}\right),-\frac{4e_0}{(1-e_0)^2}\right]+ \\ \left.+\frac{\sin\vartheta\ e_0\ A_{24}\left(e_0,\vartheta\right)\sqrt{1+e_0^2+2e_0\cos\vartheta}}{3(e_0^6-3e_0^4+3e_0^2-2)(1+e_0\cos\vartheta)^3}\right\}_{\theta_0}^{\theta} \end{aligned} \tag{C.37}$$

where

$$A_{24}\left(e_0,\vartheta\right) = (2e_0^4+2e_0^2)\cos^2\vartheta + (2e_0^3+6e_0)\cos\vartheta + (e_0^4-2e_0^2+5) \tag{C.38}$$

C.2.3 $I_{Drag,3}$

$$I_{Drag,3} = k_0 I_{Drag,30} + k_1 I_{Drag,31} + k_2 I_{Drag,32} + k_3 I_{Drag,33} + k_4 I_{Drag,34} \tag{C.39}$$

$$I_{Drag,30} = \int_{\theta_0}^{\theta} \frac{\sqrt{1+e_0^2+2e_0\cos\vartheta}}{(1+e_0\cos\vartheta)^2}d\vartheta = \left[\frac{1}{(1-e_0)}E_I\left(\frac{\vartheta}{2},\frac{4e_0}{(1+e_0)^2}\right)+\frac{1}{(1+e_0)}F_I\left(\frac{\vartheta}{2},\frac{4e_0}{(1+e_0)^2}\right)+ -\frac{e_0\sin\vartheta\sqrt{1+e_0^2+2e_0\cos\vartheta}}{(1-e_0^2)(1+e_0\cos\vartheta)}\right]_{\theta_0}^{\theta} \tag{C.40}$$

$$I_{Drag,31} = \int_{\theta_0}^{\theta} \frac{\sqrt{1+e_0^2+2e_0\cos\vartheta}}{(1+e_0\cos\vartheta)^3}d\vartheta = I_{Drag,23} \tag{C.41}$$

$$I_{Drag,32} = \int_{\theta_0}^{\theta} \frac{\sqrt{1+e_0^2+2e_0\cos\vartheta}}{(1+e_0\cos\vartheta)^4}d\vartheta = I_{Drag,24} \tag{C.42}$$

$$\begin{aligned} I_{Drag,33} = &\int_{\theta_0}^{\theta} \frac{\sqrt{1+e_0^2+2e_0\cos\vartheta}}{(1+e_0\cos\vartheta)^5}d\vartheta = \\ &\left\{-\frac{2e_0^2}{(1-e_0)^3(1+e_0)^4}E_I\left[\arcsin\left(\cos\frac{\vartheta}{2}\right),-\frac{4e_0}{(1-e_0)^2}\right]+\right. \\ &+\frac{5}{4(1-e_0)^3(1+e_0)^2}F_I\left[\arcsin\left(\cos\frac{\vartheta}{2}\right),-\frac{4e_0}{(1-e_0)^2}\right]+ \\ &-\frac{(3e_0^2+13)}{4(1-e_0)^4(1+e_0)^2}\Pi_I\left[-\frac{2e_0}{1-e_0},\arcsin\left(\cos\frac{\vartheta}{2}\right),-\frac{4e_0}{(1-e_0)^2}\right]+ \\ &\left.-\frac{e_0\sin\vartheta A_{33}\left(e_0,\vartheta\right)\sqrt{1+e_0^2+2e_0\cos\vartheta}}{8(e_0^8-4e_0^6+6e_0^4-4e_0^2+1)(1+e_0\cos\vartheta)^4}\right\}_{\theta_0}^{\theta} \end{aligned} \tag{C.43}$$

where

$$A_{33}\left(e_0,\vartheta\right) = 16\,e_0^5\cos^3\vartheta+(-3\,e_0^6+46\,e_0^4+5\,e_0^2)\cos^2\vartheta+(-2e_0^5+36e_0^3+14e_0)\cos\vartheta+ (-2e_0^6+7e_0^4+11) \tag{C.44}$$

$$\begin{aligned} I_{Drag,34} = &\int_{\theta_0}^{\theta} \frac{\sqrt{1+e_0^2+2e_0\cos\vartheta}}{(1+e_0\cos\theta)^6}d\vartheta \\ &\left\{-\frac{(8e_0^4+57e_0^2-17)}{15(1-e_0)^4(1+e_0)^5}E_I\left[\arcsin\left(\cos\frac{\vartheta}{2}\right),-\frac{4e_0}{(1-e_0)^2}\right]+\right. \\ &+\frac{4(2e_0^2+7)}{15(1-e_0)^4(1+e_0)^3}F_I\left[\arcsin\left(\cos\frac{\vartheta}{2}\right),-\frac{4e_0}{(1-e_0)^2}\right]+ \\ &\left.-\frac{(3e_0^2+5)}{(1-e_0)^5(1+e_0)^3}\Pi_I\left[-\frac{2e_0}{1-e_0},\arcsin\left(\cos\frac{\vartheta}{2}\right),-\frac{4e_0}{(1-e_0)^2}\right]\right\}_{\theta_0}^{\theta} \end{aligned} \tag{C.45}$$

C.2.4 $I_{Drag,4}$

$$I_{Drag,4} = k_0 I_{Drag,40} + k_1 I_{Drag,41} + k_2 I_{Drag,42} + k_3 I_{Drag,43} + k_4 I_{Drag,44} \tag{C.46}$$

$$I_{Drag,40} = \int_{\theta_0}^{\theta} \frac{\sin\vartheta\sqrt{1+e_0^2+2e_0\cos\vartheta}}{(1+e_0\cos\theta)^2}d\vartheta = \left[-\frac{2}{e_0\sqrt{1-e_0^2}}\arctan\left(\sqrt{\frac{1+e_0^2+2e_0\cos\vartheta}{1-e_0^2}}\right)+ \right.$$
$$\left. +\frac{\sqrt{1+e_0^2+2e_0\cos\theta}}{e_0(1+e_0\cos\vartheta)}\right]_{\theta_0}^{\theta} \tag{C.47}$$

$$I_{Drag,41} = \int_{\theta_0}^{\theta} \frac{\sin\vartheta\sqrt{1+e_0^2+2e_0\cos\vartheta}}{(1+e_0\cos\vartheta)^3}d\vartheta = \left[-\frac{1}{e_0\sqrt{(1-e_0^2)^3}}\arctan\left(\sqrt{\frac{1+e_0^2+2e_0\cos\vartheta}{1-e_0^2}}\right)+ \right.$$
$$\left. -\frac{(e_0+\cos\vartheta)\sqrt{1+e_0^2+2e_0\cos\vartheta}}{2(1-e_0^2)(1+e_0\cos\vartheta)^2}\right]_{\theta_0}^{\theta} \tag{C.48}$$

$$I_{Drag,42} = \int_{\theta_0}^{\theta} \frac{\sin\vartheta\sqrt{1+e_0^2+2e_0\cos\vartheta}}{(1+e_0\cos\vartheta)^4}d\vartheta = \left[-\frac{1}{e_0\sqrt{(1-e_0^2)^5}}\arctan\left(\sqrt{\frac{1+e_0^2+2e_0\cos\vartheta}{1-e_0^2}}\right)+ \right.$$
$$\left. -\frac{(1+2e_0^2+3e_0\cos\vartheta)(-2+e_0^2-e_0\cos\vartheta)\sqrt{1+e_0^2+2e_0\cos\vartheta}}{6e_0(1-e_0^2)^2(1+e_0\cos\vartheta)^3}\right]_{\theta_0}^{\theta} \tag{C.49}$$

$$I_{Drag,43} = \int_{\theta_0}^{\theta} \frac{\sin\vartheta\sqrt{1+e_0^2+2e_0\cos\vartheta}}{(1+e_0\cos\vartheta)^5}d\vartheta = \left\{-\frac{5}{4e_0\sqrt{(1-e_0^2)^7}}\arctan\left(\sqrt{\frac{1+e_0^2+2e_0\cos\theta}{1-e_0^2}}\right)+ \right.$$
$$\left. +\frac{\sqrt{1+e_0^2+2e_0\cos\theta}}{24e_0(1+e_0\cos\vartheta)^4}\left[6-\frac{2(1+e_0\cos\vartheta)}{(1-e_0^2)}-\frac{5(1+e_0\cos\vartheta)^2}{(1-e_0^2)^2}-\frac{15(1+e_0\cos\vartheta)^3}{(1-e_0^2)^3}\right]\right\}_{\theta_0}^{\theta} \tag{C.50}$$

$$I_{Drag,44} = \int \frac{\sin\theta\sqrt{1+e_0^2+2e_0\cos\theta}}{(1+e_0\cos\theta)^6}d\theta = \left\{ -\frac{7}{4e_0\sqrt{(1-e_0^2)^9}}\arctan\left(\sqrt{\frac{1+e_0^2+2e_0\cos\vartheta}{1-e_0^2}}\right) + \right.$$
$$-\frac{\sqrt{1+e_0^2+2e_0\cos\vartheta}}{120\,e_0(1+e_0\cos\vartheta)^5}\left[-24+\frac{6(1+e\cos\vartheta)}{1-e_0^2}+\frac{14(1+e_0\cos\vartheta)^2}{(1-e_0^2)^2}+\frac{35(1+e_0\cos\vartheta)^3}{(1-e_0^2)^3}+\right.$$
$$\left.\left.+\frac{105(1+e_0\cos\vartheta)^4}{(1-e_0^2)^4}\right]\right\}_{\theta_0}^{\theta} \tag{C.51}$$

C.2.5 $I_{Drag,5}$

$$I_{Drag,5} = k_0 I_{Drag,50} + k_1 I_{Drag,51} + k_2 I_{Drag,52} + k_3 I_{Drag,53} + k_4 I_{Drag,54} \tag{C.52}$$

$$I_{Drag,50} = \int_{\theta_0}^{\theta} \frac{\cos\vartheta\sqrt{1+e_0^2+2e_0\cos\vartheta}}{(1+e_0\cos\vartheta)^2}d\vartheta = \left\{ \frac{1}{e_0(1+e_0)}E_I\left[\arcsin\left(\cos\frac{\vartheta}{2}\right), -\frac{4e_0}{(1-e_0)^2}\right] + \right.$$
$$-\frac{3}{e_0(1-e_0)}F_I\left[\arcsin\left(\cos\frac{\vartheta}{2}\right), -\frac{4e_0}{(1-e_0)^2}\right] +$$
$$\left.+\frac{2(1+e_0)}{e_0(1-e_0)}\Pi_I\left[-\frac{2e_0}{1-e_0}, \arcsin\left(\cos\frac{\vartheta}{2}\right), -\frac{4e_0}{(1-e_0)^2}\right] + \frac{\sin\vartheta\sqrt{1+e_0^2+2e_0\cos\theta}}{(1-e_0)(1+e_0)(1+e_0\cos\vartheta)}\right\}_{\theta_0}^{\theta} \tag{C.53}$$

$$I_{Drag,51} = \int_{\theta_0}^{\theta} \frac{\cos\vartheta\sqrt{1+e_0^2+2e_0\cos\vartheta}}{(1+e_0\cos\vartheta)^3}d\vartheta = \left\{ \frac{e_0}{(1-e_0)(1+e_0)^2}E_I\left[\arcsin\left(\cos\frac{\vartheta}{2}\right), -\frac{4e_0}{(1-e_0)^2}\right] + \right.$$
$$-\frac{1}{e_0(1-e_0)}F_I\left[\arcsin\left(\cos\frac{\vartheta}{2}\right), -\frac{4e_0}{(1-e)^2}\right] +$$
$$+\frac{1}{e_0(1-e_0)^2}\Pi_I\left[-\frac{2e_0}{1-e_0}, \arcsin\left(\cos\frac{\vartheta}{2}\right), -\frac{4e_0}{(1-e_0)^2}\right] +$$
$$\left.+\frac{\sin\vartheta A_{51}\left(e_0,\vartheta\right)}{2(1-e_0)^2(1+e_0)^2(1+e_0\cos\vartheta)^2\sqrt{1+e_0^2+2e_0\cos\vartheta}}\right\}_{\theta_0}^{\theta} \tag{C.54}$$

where

$$A_{51}\left(e_0,\vartheta\right) = \left(4\,e_0^4\right)\cos^2\vartheta + \left(2\,e_0^5+4\,e_0^3+2\,e_0\right)\cos\vartheta + \left(e_0^4+2\,e_0^2+1\right) \tag{C.55}$$

$$
\begin{aligned}
I_{Drag,52} = \int_{\theta_0}^{\theta} \frac{\cos\vartheta\sqrt{1+e_0^2+2e_0\cos\vartheta}}{(1+e_0\cos\vartheta)^4}d\vartheta = \\
\left\{ \frac{(5e_0^4-10e_0^3+4e_0^2+2e_0-1)}{3e_0(1-e_0)^4(1+e_0)^3} E_I\left[\arcsin\left(\cos\frac{\theta}{2}\right), -\frac{4e_0}{(1-e_0)^2}\right] + \right. \\
-\frac{2}{3e_0(1-e_0)^2(1+e_0)} F_I\left[\arcsin\left(\cos\frac{\vartheta}{2}\right), -\frac{4e_0}{(1-e_0)^2}\right] + \\
+\frac{(1+e_0^2)}{e_0(1-e_0)^3(1+e_0)}\Pi_I\left[-\frac{2e_0}{1-e_0}, \arcsin\left(\cos\frac{\vartheta}{2}\right), -\frac{4e_0}{(1-e_0)^2}\right] + \\
\left. +\frac{\sin\vartheta A_{52}\left(e_0,\vartheta\right)}{6(1-e_0)^3(1+e_0)^3(1+e_0\cos\vartheta)^3\sqrt{1+e_0^2+2e_0\cos\vartheta}} \right\}_{\vartheta_0}^{\vartheta}
\end{aligned}
\tag{C.56}
$$

where

$$
\begin{aligned}
A_{52}\left(e_0,\vartheta\right) = (20e_0^5-4e_0^3)\cos^3\vartheta + (4e_0^6+52e_0^4-8e_0^2)\cos^2\vartheta + (-3e_0^7+17e_0^5+35e_0^3-e_0)\cos\vartheta + \\
+ (-e_0^6+7e_0^4+9e_0^2+1)
\end{aligned}
\tag{C.57}
$$

$$
\begin{aligned}
I_{Drag,53} = \int_{\theta_0}^{\theta} \frac{\cos\vartheta\sqrt{1+e_0^2+2e_0\cos\vartheta}}{(1+e_0\cos\vartheta)^5}d\vartheta = \\
\left\{ \frac{2(e_0^4+3e_0^2-1)}{3e_0(1-e_0)^3(1+e_0)^4} E_I\left[\arcsin\left(\cos\frac{\vartheta}{2}\right), -\frac{4e_0}{(1-e_0)^2}\right] + \right. \\
-\frac{(8e_0^2+7)}{12e_0(1-e_0)^3(1+e_0)^2} F_I\left[\arcsin\left(\cos\frac{\vartheta}{2}\right), -\frac{4e_0}{(1-e_0)^2}\right] + \\
+\frac{(11e_0^2+5)}{4e_0(1-e_0)^4(1+e_0)^3}\Pi_I\left[-\frac{2e_0}{1-e_0}, \arcsin\left(\cos\frac{\vartheta}{2}\right), -\frac{4e_0}{(1-e_0)^2}\right] + \\
\left. +\frac{\sin\theta A_{53}\left(e_0,\vartheta\right)\sqrt{1+e_0^2+2e_0\cos\theta}}{24(e_0^8-4e_0^6+6e_0^4-4e_0^2+1)(1+e_0\cos\theta)^4} \right\}_{\theta_0}^{\theta}
\end{aligned}
\tag{C.58}
$$

where

$$
\begin{aligned}
A_{53}\left(e_0,\vartheta\right) = (16e_0^7+48e_0^5-16e_0^3)\cos^3\vartheta + (23e_0^6+170e_0^4-49e_0^2)\cos^2\vartheta + \\
+ (8e_0^7-14e_0^5+196e_0^3-46e_0)\cos\vartheta + +(2e_0^6-3e_0^4+56e_0^2-7)
\end{aligned}
\tag{C.59}
$$

$$
\begin{aligned}
I_{Drag,54} = \int_{\theta_0}^{\theta} \frac{\cos\vartheta\sqrt{1+e_0^2+2e_0\cos\vartheta}}{(1+e_0\cos\vartheta)^6}d\vartheta = \\
\left\{ \frac{(38e_0^4+27e_0^2-17)}{15e_0(1-e_0)^4(1+e_0)^5} E_I\left[\arcsin\left(\cos\frac{\vartheta}{2}\right), -\frac{4e_0}{(1-e_0)^2}\right] + \right. \\
-\frac{(107e_0^2+37)}{60e_0(1-e_0)^4(1+e_0)^3} F_I\left[\arcsin\left(\cos\frac{\vartheta}{2}\right), -\frac{4e_0}{(1-e_0)^2}\right] + \\
+\frac{(3e_0^4+22e_0^2+7)}{4e_0(1-e_0)^5(1+e_0)^3} \Pi_I\left[-\frac{2e_0}{1-e_0}, \arcsin\left(\cos\frac{\vartheta}{2}\right), -\frac{4e_0}{(1-e_0)^2}\right] + \\
\left. -\frac{\sin\vartheta A_{54}\left(e_0,\vartheta\right)\sqrt{1+e_0^2+2e_0\cos\vartheta}}{120(e_0^{10}-5e_0^8+10e_0^6-10e_0^4+5e_0^2-1)(1+e_0\cos\vartheta)^5} \right\}_{\theta_0}^{\theta}
\end{aligned}
\tag{C.60}
$$

where

$$
\begin{aligned}
A_{54}\left(e_0,\vartheta\right) = (304\,e_0^8+216\,e_0^6-136\,e_0^4)\cos^4\vartheta + (-45\,e_0^9+1083\,e_0^7+1073\,e_0^5-575\,e_0^3)\cos^3\vartheta + \\
+(-43\,e_0^8+1245\,e_0^6+2007\,e_0^4-905\,e_0^2)\cos^2\vartheta + \\
+(-30\,e_0^9+121\,e_0^7+421\,e_0^5+1635\,e_0^3-611\,e_0)\cos\vartheta + \\
+(-6\,e_0^8+23\,e_0^6+99\,e_0^4+389\,e_0^2-121)
\end{aligned}
\tag{C.61}
$$

Appendix D

Chebyshev interpolation

Definition D.0.1 (Chebyshev polynomial $T_k(x)$)**.** *The Chebyshev polynomial of order k is defined as follows:*

$$T_k(x) = \cos\left(k \arccos(x)\right), \quad x \in [-1, 1], \quad k = 0, 1, \ldots \tag{D.1}$$

Some useful properties of the Chebyshev polynomials are presented hereafter:

- The Chebyshev polynomials satisfy the following recursive relation [84]:

$$T_{k+1}(x) = 2\, x\, T_k(x) - T_{k-1}(x) \tag{D.2}$$

  starting with $T_0(x) = 1$ and $T_1(x) = x$.

- The Chebyshev polynomials satisfy the following orthogonality relation:

$$\int_{-1}^{1} \frac{T_r(x) T_s(x)}{\sqrt{1 - x^2}} dx = N_r \delta_{rs} \tag{D.3}$$

  where $N_0 = \pi$, $N_r = \pi/2$ if $r \neq 0$, and δ_{rs} is the Kronecker index.

- The Chebyshev polynomials satisfy the following discrete orthogonality relation. Let $n > 0$, $r, s \leq n$ and $x_j = \cos\left((j + 1/2)\, \pi/(n + 1)\right)$. Then:

$$\sum_{j=0}^{n} T_r(x_j) T_s(x_j) = K_r \delta_{rs} \tag{D.4}$$

  where $K_0 = n + 1$ and $K_r = 1/2(n + 1)$ when $1 \leq r \leq n$.

Because of the orthogonality relation, the set $\{T_k\}_{k=0}^{n}$ is a set of linearly independent polynomials and represents therefore a base of the linear vector space $\mathbb{P}^n$ [84]. Given a function $f(x)$ on the interval $[-1, 1]$, the Chebyshev interpolating polynomial P_n of degree n is defined as a combination of this base:

$$P_n(x) = \sum_{k=0}^{n} c_k T_k(x)\,, \tag{D.5}$$

where c_k are the coefficients of the interpolation. They are computed, from the discrete orthogonality condition, as:

$$c_k = \frac{2}{n+1} \sum_{j=0}^{n} f(x_j) T_k(x_j) \ . \tag{D.6}$$

$P_n(x)$ interpolates the function f at the Chebyshev nodes (the zeros of $T_{n+1}(x)$):

$$x_j = \cos\left(\frac{(j+1/2)\pi}{n+1}\right) \ , \ j = 0, 1, \ldots, n. \tag{D.7}$$

If the function f is not defined in the interval $[-1, 1]$ but in a generic interval $[a, b]$, then the Chebyshev nodes are:

$$x_k = \frac{a+b}{2} + \frac{b-a}{2} \cos\left(\frac{(k+1/2)\pi}{n+1}\right) \ . \tag{D.8}$$

Using the Chebyshev nodes as interpolation points minimise the product term in the expression for the interpolation error $f(x) - P_n(x)$.

Theorem D.0.2 (Interpolation error)**.** . *Let $f(x) \in C^{n+1}[a, b]$ and $P_n(x)$ a polynomial that interpolated $f(x)$ at the $n + 1$ distinct points $x_0, x_1, \ldots, x_n \in [a, b]$. Then*

$$\forall x \in [a, b], \ \exists \xi_n \in (a, b) \ : \ f(x) - P_n(x) = \frac{1}{(n+1)!} f^{(n+1)}(\xi_n) \prod_{j=0}^{n} (x - x_j) \tag{D.9}$$

Appendix E

Online surrogate model

This appendix reports the technique used for the "online" low-thrust surrogate model (Section E.1) and examples of results related to the work presented in Chapters 6 and 12 (Section E.2).

E.1 Global optimisation method based on surrogate models

In [102] different two-stages global optimisation methods, based on the use of surrogate models, are presented. In the first stage of these methods, a response surface is estimated. The response surface can be estimated with the Kriging model presented in Chapter 6. In the second stage the estimated response surface is used to compute new search points for the optimisation. A potential drawback of this approach is that the initial sample of training points may give a misleading representation of the function to minimise. As a consequence, if the error in the response surface is underestimated, the search could be too local or stop prematurely [102].

In this thesis the two-stage method based on the maximisation of the expected improvement is considered. As described in Chapter 6, the uncertainty about the function's value at a point $\mathbf{x}$ is described by a random variable $Y(\mathbf{x})$ normally distributed with mean $\hat{y}(\mathbf{x})$ and variance $s^2(\mathbf{x})$. Let us consider an optimisation problem in which the aim is to find the global minimum of a function J and let us denote with J_{min} the current best function value. There is an improvement I at $\mathbf{x}$ if $Y(\mathbf{x}) = J_{min} - I$. The likelihood of achieving this improvement at $\mathbf{x}$ is given by the normal density function [102]:

$$\frac{1}{\sqrt{2\pi}s(\mathbf{x})} \exp\left[-\frac{(J_{min} - I - \hat{y}(\mathbf{x}))^2}{2\,s^2(\mathbf{x})}\right] . \tag{E.1}$$

The expected improvement is defined by integration of the normal density function over positive values of I going from 0 to ∞:

$$EI = \int_{I=0}^{I=\infty} I \frac{1}{\sqrt{2\pi}s(\mathbf{x})} \exp\left[-\frac{(J_{min} - I - \hat{y}(\mathbf{x}))^2}{2\,s^2(\mathbf{x})}\right] dI . \tag{E.2}$$

The previous integrals results in

$$EI = s\left(\mathbf{x}\right)\left[u_{EI}\,\Phi_{EI}\left(u_{EI}\right) + \phi_{EI}\left(u_{EI}\right)\right]\,, \tag{E.3}$$

where $u_{EI} = \left(J_{min} - \hat{y}\left(\mathbf{x}\right)\right)/s\left(\mathbf{x}\right)$ and Φ_{EI} and ϕ_{EI} are the normal cumulative distribution and density function. The two-stage approach for global optimisation using the expected improvement starts by fitting a Kriging model to the training points $\mathcal{TR}$. Then, the point that maximises the expected improvement is located, the real expensive function is evaluated at that point and a new surrogate model is generated, including the point of maximum EI. The process is iterated until the expected improvement is less than a small positive value. The maximum of the expected improvement is located using the algorithm MP-AIDEA (Chapter 7).

E.2 Online generation of surrogate models

This section presents preliminary results on the search for the global minimum of the ΔV of a low-thrust transfer, using the maximisation of the expected improvement presented in Section E.1.

The first example is relative to the transfers with variation of semi-major axis and eccentricity presented in Section 6.2.5. In particular, the change of semi-major axis is from 0.86 AU to 0.98 AU, $i_0 = i_f = \bar{\omega}_0 = \theta_0 = \theta_f = 0$, $\bar{\omega}_f = \pi$ and e_0 and e_f are in the range defined by $\mathbf{x}^L = [0\ 0]^T$ and $\mathbf{x}^U = [0.1\ 0.1]^T$. In Section 6.2.5 it was shown how to accurately model the cost of these transfers, using 36 or 100 training points and two surrogate models. The aim here is not to accurately model the ΔV for every point in the region defined by $\mathbf{x}^L$ and $\mathbf{x}^U$, but to locate the region where the minimum of the ΔV is located. To this aim, an initial response surface is generated considering only 9 training points and one surrogate model, as shown in Figure E.1a. The points where the expected improvement is maximised are then found, and evaluated using the real expensive model. This is shown in Figure E.1b, where it is possible to see the addition of red points, corresponding to the location where the expected improvement had a maximum during the iterative process, and where the real expensive function was re-evaluated.

The method correctly samples new points in the region where the ΔV is expected to be lower ($e_0 \approx 0$ and $e_f \approx 0$). The search for the maximum of the expected improvement is performed using the global optimisation algorithm MP-AIDEA (Chapter 7), with the following settings: $n_{pop} = 4$, $N_{pop} = 10$, $\rho = 0.2$, $nFeVal = 1000$. Figure E.2 shows the expected improvement during two steps of the iterative process.

The second example is based on the low-thrust transfer from GTO to GEO presented in Chapter 12. In this case the parameters of the problems are not the initial and final orbital elements, as described in Section 6.2, but the low-thrust control parameters described in Equation 5.21 in Section 5.3. The dimension of the problem is $d = 16$. The maximisation of the expected improvement is applied on a reduced space of $d = 4$. In particular, the reduced vector of para-

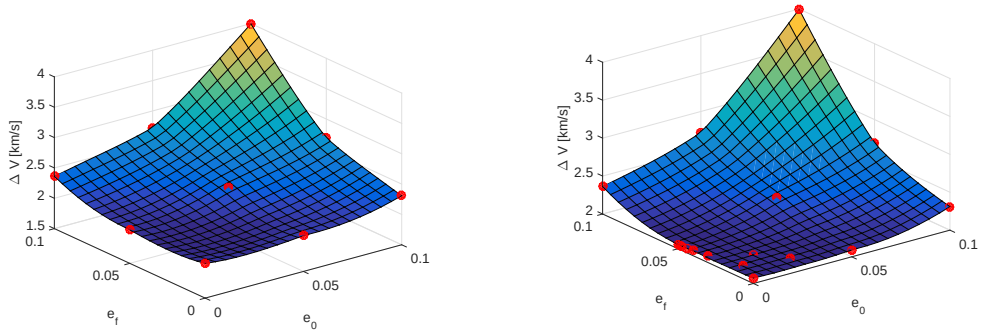

(a) Initial surrogate model (9 training points).

(b) Surrogate model after maximisation of expected improvement.

Figure E.1: ΔV surrogate model used for the global optimisation of transfers with variation of eccentricity.

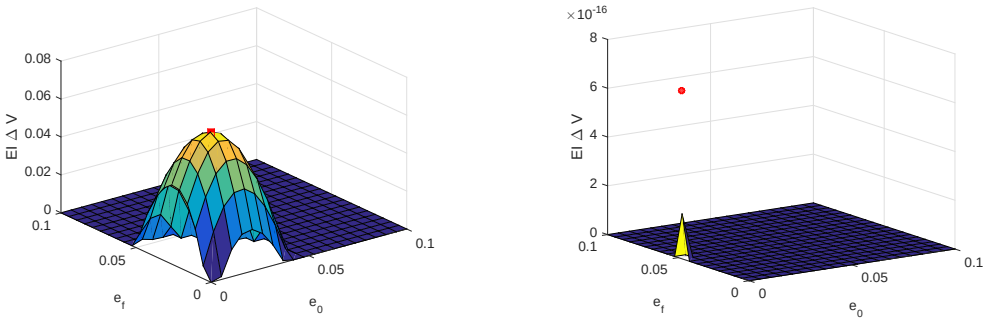

(a) Step 2.

(b) Step 5.

Figure E.2: Expected improvement during the iterative process to locate the global minimum of the ΔV for transfers with variation of eccentricity.

meters is $\tilde{\mathbf{x}} = [\Delta L_{a1},\ \Delta L_{a2},\ \Delta L_{a3},\ \Delta L_{a4}]^T$. The other parameters in $\mathbf{x}$ (defined in Equation 5.21) are equal to the corresponding values in the optimal solution $\mathbf{x}_{opt}$ presented in Section 12.2 (strategy 2). In particular, in Section 12.2, the optimal solution for the GTO-GEO transfer, corresponds to a cost of the transfer of $\Delta V = 1.5672$ km/s (Table 12.2) and has the following solution vector:

$$\begin{aligned}\mathbf{x}^{opt} = [&\Delta L_{p1},\ \Delta L_{p2},\ \Delta L_{p3},\ \Delta L_{p4},\ \Delta L_{a1},\ \Delta L_{a2},\ \Delta L_{a3},\ \Delta L_{a4},\\ &\beta_{p1},\ \beta_{p2},\ \beta_{p3},\ \beta_{p4},\ \beta_{a1},\ \beta_{a2},\ \beta_{a3}\ \beta_{a4}]^T =\\ &[27.94,\ 53.44,\ 59.70,\ 76.92,\ -0.1,\ -0.1,\ 0, -18.06,\\ &20.96,\ 24.76,\ 20.84,\ 14.20,\ 2.66,\ 2.66,\ 3.22,\ 4.10]^T \text{deg}\ .\end{aligned} \tag{E.4}$$

It is investigated how the search space can be explored, in an effort to locate the global minimum using the concept of maximisation of the expected improvement, when $\Delta L_{p1}, \Delta L_{p2}, \Delta L_{p3}$, $\Delta L_{p4}, \beta_{p1}$, β_{p2}, β_{p3} and β_{p4} are equal to the values given in Equation E.4 while ΔL_{a1}, ΔL_{a2}, ΔL_{a3}, ΔL_{a4} are allowed to change in the range $\tilde{\mathbf{x}}^L = [0,\ 0,\ 0, 0]^T$ and $\tilde{\mathbf{x}}^U = [2\pi,\ 2\pi,\ 2\pi, 2\pi]^T$.

To start the process, 5 points are defined by latin-hypercube in the space defined by $\tilde{\mathbf{x}}^L$ and $\tilde{\mathbf{x}}^U$. From these 5 points, 10 training points and 10 corresponding responses are then available to generate the initial surrogate model. In particular the 10 points are obtained as follows:

- the cost function is directly evaluated at the 5 points defined by latin-hypercube sampling; the points will likely be points where the constraints of the problem are not satisfied, therefore a penalty is added to the objective function (according to Equation 12.7 in Chapter 12).
- the 5 points defined by latin-hypercube sampling are used as initial guess for the solution of the NLP problem defined in Section 12.2. The training points set $\mathcal{TP}$ and the response vectors $\mathbf{y}$ are populated using the solution vectors of the 5 NLP problems and the resulting objective function, expressed as in Equation 12.7.

The iterative process described in Section E.1 is then applied. Results are shown in Figure E.3 and E.4. Figures E.3a and E.4a show the results relative to the first two parameters, ΔL_{a1} and ΔL_{a2} while Figures E.3b and E.4b show the results for ΔL_{a3} and ΔL_{a4}. The blue dots are the initial 10 sampling points while the black dots are the points of maximum expected improvement. The two red dots represent the optimal values of $\Delta L_{a1}, \Delta L_{a2}, \Delta L_{a3}, \Delta L_{a4}$ defined in Equation E.4. Note that Figure E.4 shows a zoom (in ΔV) of the region closer to the known optimal point.

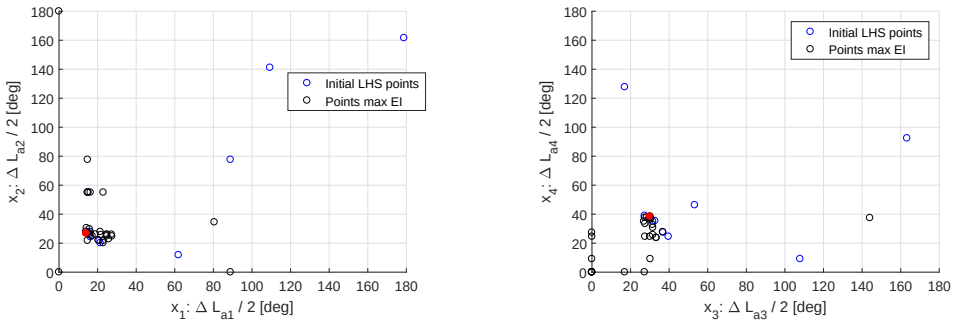

(a) ΔL_{a1} and ΔL_{a2} space. (b) ΔL_{a3} and ΔL_{a4} space.

Figure E.3: Representation of the space of parameters $\tilde{\mathbf{x}}$ with the LHS points (blue), the points of maximum EI (black) and the known optimal point (red).

It is possible to see that the point of maximum expected improvement (black dots) are indeed close to the optimal point defined in Equation E.4 (red dot). The proposed method samples, therefore, the most promising regions of the search space and ignores less interesting regions. It is therefore to be expected that the surrogate representation of the region where the minimum is located is more accurate than the representation of the rest of the search space.

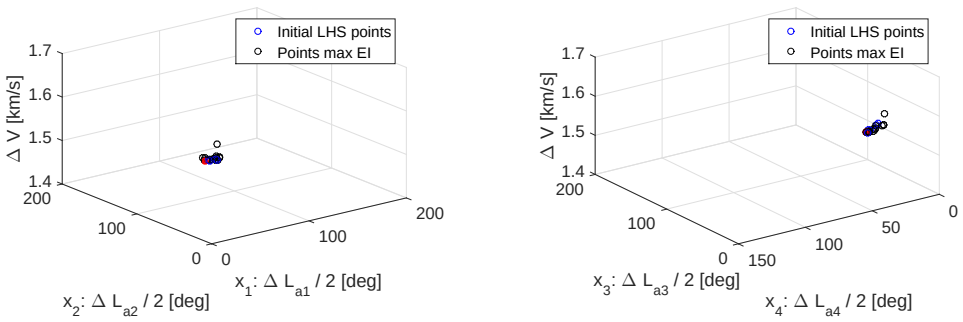

(a) ΔL_{a1} and ΔL_{a2} space.

(b) ΔL_{a3} and ΔL_{a4} space.

Figure E.4: Representation of the ΔV space with the LHS points (blue), the points of maximum EI (black) and the known optimal point (red).

Appendix F

Wilcoxon Test Results

The following tables report the results of the Wilcoxon test for the comparison of MP-AIDEA with UMOEAs (Tables F.1 and F.2), L-SHADE (Tables F.3 and F.4), MVMO (Tables F.5 and F.6) and CMLSP (Tables F.7 and F.8).

Table F.1: Wilcoxon Test Results, CEC 2014: MP-AIDEA vs. UMOEAs, 10D and 30D

	both		left		right		
	h	p	h	p	h	p	Result type
$n_D = 10$							
1	**0**	**1.00e+00**	-	-	-	-	**Case 1**
2	**0**	**1.00e+00**	-	-	-	-	**Case 1**
3	**0**	**1.00e+00**	-	-	-	-	**Case 1**
4	**1**	**2.18e-02**	**1**	**1.09e-02**	**0**	**9.89e-01**	**Case 3**
5	**1**	**3.74e-14**	**1**	**1.87e-14**	**0**	**1.00e+00**	**Case 3**
7	1	9.89e-16	0	1.00e+00	1	4.95e-16	Case 2
8	1	1.79e-02	0	9.91e-01	1	8.94e-03	Case 2
9	**1**	**7.80e-04**	**1**	**3.90e-04**	**0**	**1.00e+00**	**Case 3**
10	0	3.17e-01	0	8.43e-01	0	1.59e-01	Not sign.
11	**1**	**1.63e-05**	**1**	**8.16e-06**	**0**	**1.00e+00**	**Case 3**
13	1	8.19e-16	0	1.00e+00	1	4.10e-16	Case 2
14	**1**	**1.20e-17**	**1**	**5.98e-18**	**0**	**1.00e+00**	**Case 3**
15	**1**	**3.30e-18**	**1**	**1.65e-18**	**0**	**1.00e+00**	**Case 3**
16	**1**	**2.27e-03**	**1**	**1.14e-03**	**0**	**9.99e-01**	**Case 3**
17	0	5.60e-01	0	2.80e-01	0	7.22e-01	Not sign.
18	**1**	**5.36e-07**	**1**	**2.68e-07**	**0**	**1.00e+00**	**Case 3**
20	0	2.06e-01	0	8.98e-01	0	1.03e-01	Not sign.
21	0	2.11e-01	0	1.05e-01	0	8.96e-01	Not sign.
23	1	1.34e-20	0	1.00e+00	1	6.68e-21	Case 2
24	**1**	**1.54e-07**	**1**	**7.71e-08**	**0**	**1.00e+00**	**Case 3**
25	**1**	**2.39e-17**	**1**	**1.19e-17**	**0**	**1.00e+00**	**Case 3**
28	**1**	**2.22e-04**	**1**	**1.11e-04**	**0**	**1.00e+00**	**Case 3**
$n_D = 30$							
1	1	1.12e-05	0	1.00e+00	1	5.60e-06	Case 2
2	1	9.47e-16	0	1.00e+00	1	4.74e-16	Case 2
3	1	6.52e-03	0	9.97e-01	1	3.26e-03	Case 2
4	1	1.10e-10	0	1.00e+00	1	5.51e-11	Case 2
5	**1**	**8.62e-16**	**1**	**4.31e-16**	**0**	**1.00e+00**	**Case 3**
7	1	3.25e-18	0	1.00e+00	1	1.63e-18	Case 2
8	0	6.99e-01	0	3.49e-01	0	6.53e-01	Not sign.
9	1	2.38e-16	0	1.00e+00	1	1.19e-16	Case 2
10	0	2.55e-01	0	8.74e-01	0	1.28e-01	Not sign.
11	0	6.67e-02	1	3.33e-02	0	9.67e-01	Not sign.
13	1	3.50e-18	0	1.00e+00	1	1.75e-18	Case 2
14	**1**	**1.64e-13**	**1**	**8.19e-14**	**0**	**1.00e+00**	**Case 3**
15	**1**	**3.64e-13**	**1**	**1.82e-13**	**0**	**1.00e+00**	**Case 3**
16	**1**	**1.05e-08**	**1**	**5.26e-09**	**0**	**1.00e+00**	**Case 3**
17	**1**	**1.56e-16**	**1**	**7.78e-17**	**0**	**1.00e+00**	**Case 3**
18	0	1.48e-01	0	9.27e-01	0	7.41e-02	Not sign.
20	1	2.84e-03	0	9.99e-01	1	1.42e-03	Case 2
21	**1**	**5.93e-05**	**1**	**2.96e-05**	**0**	**1.00e+00**	**Case 3**
23	1	1.39e-20	0	1.00e+00	1	6.95e-21	Case 2
24	**1**	**5.44e-12**	**1**	**2.72e-12**	**0**	**1.00e+00**	**Case 3**
25	**1**	**9.60e-03**	**1**	**4.80e-03**	**0**	**9.95e-01**	**Case 3**
28	**1**	**3.87e-09**	**1**	**1.94e-09**	**0**	**1.00e+00**	**Case 3**

Table F.2: Wilcoxon Test Results, CEC 2014: MP-AIDEA vs. UMOEAs, 50D and 100D

	both		left		right		
	h	p	h	p	h	p	Result type
$n_D = 50$							
1	0	1.59e-01	0	9.24e-01	0	7.97e-02	Not sign.
2	1	1.95e-19	0	1.00e+00	1	9.77e-20	Case 2
3	1	8.85e-08	0	1.00e+00	1	4.43e-08	Case 2
4	**1**	**1.27e-08**	**1**	**6.37e-09**	**0**	**1.00e+00**	**Case 3**
5	**1**	**1.11e-12**	**1**	**5.57e-13**	**0**	**1.00e+00**	**Case 3**
7	1	1.33e-20	0	1.00e+00	1	6.66e-21	Case 2
8	0	7.14e-02	0	9.65e-01	1	3.57e-02	Not sign.
9	1	3.45e-18	0	1.00e+00	1	1.73e-18	Case 2
10	**1**	**5.37e-03**	**1**	**2.68e-03**	**0**	**9.97e-01**	**Case 3**
11	**1**	**1.43e-02**	**1**	**7.15e-03**	**0**	**9.93e-01**	**Case 3**
13	1	3.30e-18	0	1.00e+00	1	1.65e-18	Case 2
14	**1**	**3.72e-15**	**1**	**1.86e-15**	**0**	**1.00e+00**	**Case 3**
15	**1**	**2.06e-07**	**1**	**1.03e-07**	**0**	**1.00e+00**	**Case 3**
16	0	2.28e-01	0	1.14e-01	0	8.87e-01	Not sign.
17	**1**	**7.51e-18**	**1**	**3.76e-18**	**0**	**1.00e+00**	**Case 3**
18	**1**	**4.45e-05**	**1**	**2.23e-05**	**0**	**1.00e+00**	**Case 3**
20	1	2.77e-02	0	9.86e-01	1	1.38e-02	Case 2
21	**1**	**8.87e-17**	**1**	**4.43e-17**	**0**	**1.00e+00**	**Case 3**
23	1	1.39e-20	0	1.00e+00	1	6.95e-21	Case 2
24	**1**	**1.79e-17**	**1**	**8.95e-18**	**0**	**1.00e+00**	**Case 3**
25	0	5.03e-01	0	2.52e-01	0	7.50e-01	Not sign.
28	**1**	**3.16e-09**	**1**	**1.58e-09**	**0**	**1.00e+00**	**Case 3**
$n_D = 100$							
1	0	8.22e-02	0	9.61e-01	1	4.11e-02	Not sign.
2	1	5.25e-20	0	1.00e+00	1	2.63e-20	Case 2
3	0	1.24e-01	0	6.19e-02	0	9.39e-01	Not sign.
4	**1**	**2.91e-18**	**1**	**1.46e-18**	**0**	**1.00e+00**	**Case 3**
5	0	4.99e-01	0	2.50e-01	0	7.53e-01	Not sign.
7	1	1.36e-20	0	1.00e+00	1	6.81e-21	Case 2
8	1	3.57e-08	0	1.00e+00	1	1.78e-08	Case 2
9	1	3.30e-18	0	1.00e+00	1	1.65e-18	Case 2
10	**1**	**5.36e-07**	**1**	**2.68e-07**	**0**	**1.00e+00**	**Case 3**
11	0	9.79e-01	0	5.13e-01	0	4.89e-01	Not sign.
13	1	3.30e-18	0	1.00e+00	1	1.65e-18	Case 2
14	1	3.94e-18	0	1.00e+00	1	1.97e-18	Case 2
15	1	1.57e-15	0	1.00e+00	1	7.87e-16	Case 2
16	**1**	**3.34e-04**	**1**	**1.67e-04**	**0**	**1.00e+00**	**Case 3**
17	**1**	**4.70e-18**	**1**	**2.35e-18**	**0**	**1.00e+00**	**Case 3**
18	**1**	**7.96e-18**	**1**	**3.98e-18**	**0**	**1.00e+00**	**Case 3**
20	1	1.35e-03	0	9.99e-01	1	6.73e-04	Case 2
21	**1**	**5.29e-18**	**1**	**2.64e-18**	**0**	**1.00e+00**	**Case 3**
23	1	1.39e-20	0	1.00e+00	1	6.95e-21	Case 2
24	**1**	**1.90e-17**	**1**	**9.50e-18**	**0**	**1.00e+00**	**Case 3**
25	**1**	**2.65e-04**	**1**	**1.32e-04**	**0**	**1.00e+00**	**Case 3**
28	**1**	**5.01e-06**	**1**	**2.50e-06**	**0**	**1.00e+00**	**Case 3**

Table F.3: Wilcoxon Test Results, CEC 2014: MP-AIDEA vs. L-SHADE, 10D and 30D

	both		left		right		
	h	p	h	p	h	p	Result type
$n_D = 10$							
1	**0**	**1.00e+00**	-	-	-	-	**Case 1**
2	**0**	**1.00e+00**	-	-	-	-	**Case 1**
3	**0**	**1.00e+00**	-	-	-	-	**Case 1**
4	**1**	**5.69e-12**	**1**	**2.85e-12**	**0**	**1.00e+00**	**Case 3**
5	**1**	**5.12e-15**	**1**	**2.56e-15**	**0**	**1.00e+00**	**Case 3**
7	1	6.14e-06	0	1.00e+00	1	3.07e-06	Case 2
8	1	3.47e-03	0	9.98e-01	1	1.73e-03	Case 2
9	**1**	**8.86e-09**	**1**	**4.43e-09**	**0**	**1.00e+00**	**Case 3**
10	1	4.95e-17	0	1.00e+00	1	2.47e-17	Case 2
11	1	1.85e-02	0	9.91e-01	1	9.24e-03	Case 2
13	1	1.85e-07	0	1.00e+00	1	9.26e-08	Case 2
14	**1**	**6.31e-17**	**1**	**3.16e-17**	**0**	**1.00e+00**	**Case 3**
15	**1**	**3.43e-05**	**1**	**1.72e-05**	**0**	**1.00e+00**	**Case 3**
16	1	2.91e-02	0	9.86e-01	1	1.46e-02	Case 2
17	1	5.73e-05	0	1.00e+00	1	2.87e-05	Case 2
18	0	8.10e-01	0	5.98e-01	0	4.05e-01	Not sign.
20	1	4.20e-05	0	1.00e+00	1	2.10e-05	Case 2
21	0	1.01e-01	0	9.50e-01	0	5.05e-02	Not sign.
23	**1**	**1.34e-20**	**1**	**6.68e-21**	**0**	**1.00e+00**	**Case 3**
24	**1**	**1.40e-05**	**1**	**7.00e-06**	**0**	**1.00e+00**	**Case 3**
25	**1**	**7.22e-13**	**1**	**3.61e-13**	**0**	**1.00e+00**	**Case 3**
28	**1**	**8.47e-11**	**1**	**4.23e-11**	**0**	**1.00e+00**	**Case 3**
$n_D = 30$							
1	1	1.79e-07	0	1.00e+00	1	8.94e-08	Case 2
2	1	9.47e-16	0	1.00e+00	1	4.74e-16	Case 2
3	1	6.52e-03	0	9.97e-01	1	3.26e-03	Case 2
4	1	4.92e-20	0	1.00e+00	1	2.46e-20	Case 2
5	**1**	**3.30e-18**	**1**	**1.65e-18**	**0**	**1.00e+00**	**Case 3**
7	1	3.25e-18	0	1.00e+00	1	1.63e-18	Case 2
8	1	4.21e-20	0	1.00e+00	1	2.10e-20	Case 2
9	1	3.30e-18	0	1.00e+00	1	1.65e-18	Case 2
10	1	1.62e-18	0	1.00e+00	1	8.12e-19	Case 2
11	1	3.40e-07	0	1.00e+00	1	1.70e-07	Case 2
13	1	1.27e-17	0	1.00e+00	1	6.34e-18	Case 2
14	**1**	**5.03e-17**	**1**	**2.52e-17**	**0**	**1.00e+00**	**Case 3**
15	**1**	**4.26e-02**	**1**	**2.13e-02**	**0**	**9.79e-01**	**Case 3**
16	1	2.30e-16	0	1.00e+00	1	1.15e-16	Case 2
17	1	2.48e-14	0	1.00e+00	1	1.24e-14	Case 2
18	1	4.18e-18	0	1.00e+00	1	2.09e-18	Case 2
20	1	4.43e-18	0	1.00e+00	1	2.22e-18	Case 2
21	1	9.72e-13	0	1.00e+00	1	4.86e-13	Case 2
23	1	1.39e-20	0	1.00e+00	1	6.95e-21	Case 2
24	1	**1.64e-10**	**1**	**8.21e-11**	**0**	**1.00e+00**	**Case 3**
25	1	7.97e-13	0	1.00e+00	1	3.99e-13	Case 2
28	**1**	**2.19e-11**	**1**	**1.09e-11**	**0**	**1.00e+00**	**Case 3**

Table F.4: Wilcoxon Test Results, CEC 2014: MP-AIDEA vs. L-SHADE, 50D and 100D

	both		left		right		
	h	p	h	p	h	p	Result type
$n_D = 50$							
1	**1**	**2.79e-20**	**1**	**1.39e-20**	**0**	**1.00e+00**	**Case 3**
2	1	1.95e-19	0	1.00e+00	1	9.77e-20	Case 2
3	1	4.53e-20	0	1.00e+00	1	2.26e-20	Case 2
4	**1**	**1.99e-18**	**1**	**9.93e-19**	**0**	**1.00e+00**	**Case 3**
5	**1**	**3.30e-18**	**1**	**1.65e-18**	**0**	**1.00e+00**	**Case 3**
7	1	1.33e-20	0	1.00e+00	1	6.66e-21	Case 2
8	1	4.62e-19	0	1.00e+00	1	2.31e-19	Case 2
9	1	3.30e-18	0	1.00e+00	1	1.65e-18	Case 2
10	1	3.30e-18	0	1.00e+00	1	1.65e-18	Case 2
11	1	2.57e-08	0	1.00e+00	1	1.29e-08	Case 2
13	1	3.30e-18	0	1.00e+00	1	1.65e-18	Case 2
14	**1**	**4.01e-17**	**1**	**2.00e-17**	**0**	**1.00e+00**	**Case 3**
15	0	5.31e-02	1	2.65e-02	0	9.74e-01	Not sign.
16	1	3.30e-18	0	1.00e+00	1	1.65e-18	Case 2
17	**1**	**2.37e-09**	**1**	**1.19e-09**	**0**	**1.00e+00**	**Case 3**
18	**1**	**8.86e-11**	**1**	**4.43e-11**	**0**	**1.00e+00**	**Case 3**
20	1	3.30e-18	0	1.00e+00	1	1.65e-18	Case 2
21	1	6.57e-12	0	1.00e+00	1	3.28e-12	Case 2
23	**1**	**2.76e-05**	**1**	**1.38e-05**	**0**	**1.00e+00**	**Case 3**
24	**1**	**3.24e-18**	**1**	**1.62e-18**	**0**	**1.00e+00**	**Case 3**
25	1	3.75e-14	0	1.00e+00	1	1.87e-14	Case 2
28	1	1.62e-03	0	9.99e-01	1	8.10e-04	Case 2
$n_D = 100$							
1	0	8.22e-02	0	9.61e-01	1	4.11e-02	Not sign.
2	1	5.25e-20	0	1.00e+00	1	2.63e-20	Case 2
3	0	1.24e-01	0	6.19e-02	0	9.39e-01	Not sign.
4	**1**	**2.91e-18**	**1**	**1.46e-18**	**0**	**1.00e+00**	**Case 3**
5	0	4.99e-01	0	2.50e-01	0	7.53e-01	Case 2
7	1	1.36e-20	0	1.00e+00	1	6.81e-21	Case 2
8	1	3.57e-08	0	1.00e+00	1	1.78e-08	Case 2
9	1	3.30e-18	0	1.00e+00	1	1.65e-18	Case 2
10	**1**	**5.36e-07**	**1**	**2.68e-07**	**0**	**1.00e+00**	**Case 3**
11	0	9.79e-01	0	5.13e-01	0	4.89e-01	Not sign.
13	1	3.30e-18	0	1.00e+00	1	1.65e-18	Case 2
14	1	3.94e-18	0	1.00e+00	1	1.97e-18	Case 2
15	1	1.57e-15	0	1.00e+00	1	7.87e-16	Case 2
16	**1**	**3.34e-04**	**1**	**1.67e-04**	**0**	**1.00e+00**	**Case 3**
17	**1**	**4.70e-18**	**1**	**2.35e-18**	**0**	**1.00e+00**	**Case 3**
18	**1**	**7.96e-18**	**1**	**3.98e-18**	**0**	**1.00e+00**	**Case 3**
20	1	1.35e-03	0	9.99e-01	1	6.73e-04	Case 2
21	**1**	**5.29e-18**	**1**	**2.64e-18**	**0**	**1.00e+00**	**Case 3**
23	1	1.39e-20	0	1.00e+00	1	6.95e-21	Case 2
24	**1**	**1.90e-17**	**1**	**9.50e-18**	**0**	**1.00e+00**	**Case 3**
25	**1**	**2.65e-04**	**1**	**1.32e-04**	**0**	**1.00e+00**	**Case 3**
28	**1**	**5.01e-06**	**1**	**2.50e-06**	**0**	**1.00e+00**	**Case 3**

Table F.5: Wilcoxon Test Results, CEC 2014: MP-AIDEA vs. MVMO, 10D and 30D

	both		left		right		
	h	p	h	p	h	p	Result type
$n_D = 10$							
1	**1**	**1.39e-20**	**1**	**6.95e-21**	**0**	**1.00e+00**	**Case 3**
2	**1**	**1.39e-20**	**1**	**6.95e-21**	**0**	**1.00e+00**	**Case 3**
3	**1**	**1.35e-20**	**1**	**6.73e-21**	**0**	**1.00e+00**	**Case 3**
4	**1**	**6.66e-08**	**1**	**3.33e-08**	**0**	**1.00e+00**	**Case 3**
5	**1**	**3.64e-13**	**1**	**1.82e-13**	**0**	**1.00e+00**	**Case 3**
7	**1**	**2.31e-07**	**1**	**1.16e-07**	**0**	**1.00e+00**	**Case 3**
8	1	1.35e-02	0	9.93e-01	1	6.75e-03	Case 2
9	**1**	**5.49e-07**	**1**	**2.75e-07**	**0**	**1.00e+00**	**Case 3**
10	**1**	**2.32e-02**	**1**	**1.16e-02**	**0**	**9.89e-01**	**Case 3**
11	0	9.15e-01	0	4.57e-01	0	5.45e-01	Not sign.
13	1	1.75e-15	0	1.00e+00	1	8.77e-16	Case 2
14	**1**	**8.38e-17**	**1**	**4.19e-17**	**0**	**1.00e+00**	**Case 3**
15	**1**	**1.60e-04**	**1**	**8.01e-05**	**0**	**1.00e+00**	**Case 3**
16	0	4.14e-01	0	2.07e-01	0	7.95e-01	Not sign.
17	0	1.37e-01	0	9.32e-01	0	6.87e-02	Not sign.
18	**1**	**1.54e-05**	**1**	**7.68e-06**	**0**	**1.00e+00**	**Case 3**
20	0	7.72e-02	0	9.62e-01	1	3.86e-02	Not sign.
21	0	7.08e-02	0	9.65e-01	1	3.54e-02	Not sign.
23	1	1.34e-20	0	1.00e+00	1	6.68e-21	Case 2
24	**1**	**1.88e-06**	**1**	**9.41e-07**	**0**	**1.00e+00**	**Case 3**
25	**1**	**1.36e-12**	**1**	**6.81e-13**	**0**	**1.00e+00**	**Case 3**
28	0	1.95e-01	0	9.03e-01	0	9.77e-02	Not sign.
$n_D = 30$							
1	**1**	**1.28e-18**	**1**	**6.41e-19**	**0**	**1.00e+00**	**Case 3**
2	**1**	**3.08e-18**	**1**	**1.54e-18**	**0**	**1.00e+00**	**Case 3**
3	**1**	**1.15e-19**	**1**	**5.75e-20**	**0**	**1.00e+00**	**Case 3**
4	0	1.22e-01	0	6.09e-02	0	9.40e-01	Not sign.
5	0	7.72e-02	0	9.62e-01	1	3.86e-02	Not sign.
7	**1**	**1.43e-18**	**1**	**7.17e-19**	**0**	**1.00e+00**	**Case 3**
8	1	2.73e-16	0	1.00e+00	1	1.36e-16	Case 2
9	**1**	**2.42e-15**	**1**	**1.21e-15**	**0**	**1.00e+00**	**Case 3**
10	1	4.33e-02	0	9.79e-01	1	2.16e-02	Case 2
11	0	2.11e-01	0	1.05e-01	0	8.96e-01	Not sign.
13	0	3.81e-01	0	8.11e-01	0	1.90e-01	Not sign.
14	**1**	**4.33e-05**	**1**	**2.16e-05**	**0**	**1.00e+00**	**Case 3**
15	**1**	**3.91e-08**	**1**	**1.96e-08**	**0**	**1.00e+00**	**Case 3**
16	0	1.25e-01	0	9.38e-01	0	6.27e-02	Not sign.
17	1	6.57e-12	0	1.00e+00	1	3.28e-12	Case 2
18	1	1.62e-08	0	1.00e+00	1	8.09e-09	Case 2
20	1	8.56e-06	0	1.00e+00	1	4.28e-06	Case 2
21	1	4.53e-04	0	1.00e+00	1	2.27e-04	Case 2
23	1	1.39e-20	0	1.00e+00	1	6.95e-21	Case 2
24	**1**	**3.34e-15**	**1**	**1.67e-15**	**0**	**1.00e+00**	**Case 3**
25	**1**	**3.29e-10**	**1**	**1.65e-10**	**0**	**1.00e+00**	**Case 3**
28	**1**	**3.64e-13**	**1**	**1.82e-13**	**0**	**1.00e+00**	**Case 3**

Table F.6: Wilcoxon Test Results, CEC 2014: MP-AIDEA vs. MVMO, 50D and 100D

	both		left		right		
	h	p	h	p	h	p	Result type
$n_D = 50$							
1	**1**	**2.79e-20**	**1**	**1.39e-20**	**0**	**1.00e+00**	**Case 3**
2	**1**	**3.29e-18**	**1**	**1.65e-18**	**0**	**1.00e+00**	**Case 3**
3	**1**	**2.92e-18**	**1**	**1.46e-18**	**0**	**1.00e+00**	**Case 3**
4	**1**	**9.96e-03**	**1**	**4.98e-03**	**0**	**9.95e-01**	**Case 3**
5	1	1.24e-05	0	1.00e+00	1	6.20e-06	Case 2
7	**1**	**3.01e-18**	**1**	**1.51e-18**	**0**	**1.00e+00**	**Case 3**
8	1	1.15e-15	0	1.00e+00	1	5.75e-16	Case 2
9	**1**	**6.06e-06**	**1**	**3.03e-06**	**0**	**1.00e+00**	**Case 3**
10	0	6.06e-01	0	3.03e-01	0	6.99e-01	Not sign.
11	1	2.65e-04	0	1.00e+00	1	1.32e-04	Case 2
13	1	1.79e-07	0	1.00e+00	1	8.93e-08	Case 2
14	0	6.98e-01	0	3.49e-01	0	6.54e-01	Not sign.
15	0	9.79e-01	0	4.89e-01	0	5.13e-01	Not sign.
16	1	2.63e-02	0	9.87e-01	1	1.31e-02	Case 2
17	1	2.20e-08	0	1.00e+00	1	1.10e-08	Case 2
18	1	6.68e-15	0	1.00e+00	1	3.34e-15	Case 2
20	1	3.50e-18	0	1.00e+00	1	1.75e-18	Case 2
21	1	9.14e-10	0	1.00e+00	1	4.57e-10	Case 2
23	1	1.39e-20	0	1.00e+00	1	6.95e-21	Case 2
24	**1**	**8.28e-08**	**1**	**4.14e-08**	**0**	**1.00e+00**	**Case 3**
25	1	1.93e-09	0	1.00e+00	1	9.66e-10	Case 2
28	**1**	**6.34e-15**	**1**	**3.17e-15**	**0**	**1.00e+00**	**Case 3**
$n_D = 100$							
1	**1**	**3.83e-20**	**1**	**1.92e-20**	**0**	**1.00e+00**	**Case 3**
2	**1**	**3.28e-18**	**1**	**1.64e-18**	**0**	**1.00e+00**	**Case 3**
3	**1**	**3.30e-18**	**1**	**1.65e-18**	**0**	**1.00e+00**	**Case 3**
4	**1**	**2.03e-16**	**1**	**1.01e-16**	**0**	**1.00e+00**	**Case 3**
5	1	2.27e-12	0	1.00e+00	1	1.14e-12	Case 2
7	**1**	**6.75e-18**	**1**	**3.37e-18**	**0**	**1.00e+00**	**Case 3**
8	1	2.26e-17	0	1.00e+00	1	1.13e-17	Case 2
9	**1**	**5.01e-04**	**1**	**2.51e-04**	**0**	**1.00e+00**	**Case 3**
10	**1**	**7.25e-13**	**1**	**3.63e-13**	**0**	**1.00e+00**	**Case 3**
11	0	7.79e-01	0	3.89e-01	0	6.13e-01	Not sign.
13	1	1.65e-16	0	1.00e+00	1	8.23e-17	Case 2
14	1	3.30e-18	0	1.00e+00	1	1.65e-18	Case 2
15	0	6.06e-01	0	6.99e-01	0	3.03e-01	Not sign.
16	0	9.20e-01	0	5.43e-01	0	4.60e-01	Not sign.
17	**1**	**2.04e-04**	**1**	**1.02e-04**	**0**	**1.00e+00**	**Case 3**
18	1	3.30e-18	0	1.00e+00	1	1.65e-18	Case 2
20	1	3.30e-18	0	1.00e+00	1	1.65e-18	Case 2
21	1	8.37e-03	0	9.96e-01	1	4.18e-03	Case 2
23	1	1.39e-20	0	1.00e+00	1	6.95e-21	Case 2
24	1	5.32e-17	0	1.00e+00	1	2.66e-17	Case 2
25	**1**	**6.58e-16**	**1**	**3.29e-16**	**0**	**1.00e+00**	**Case 3**
28	**1**	**1.41e-15**	**1**	**7.06e-16**	**0**	**1.00e+00**	**Case 3**

Table F.7: Wilcoxon Test Results, CEC 2014: MP-AIDEA vs. CMLSP, 10D and 30D

	both		left		right		
	h	p	h	p	h	p	Result type
$n_D = 10$							
1	**1**	**1.39e-20**	**1**	**6.95e-21**	**0**	**1.00e+00**	**Case 3**
2	**1**	**1.39e-20**	**1**	**6.95e-21**	**0**	**1.00e+00**	**Case 3**
3	**1**	**1.39e-20**	**1**	**6.95e-21**	**0**	**1.00e+00**	**Case 3**
4	**1**	**4.38e-18**	**1**	**2.19e-18**	**0**	**1.00e+00**	**Case 3**
5	**1**	**3.30e-18**	**1**	**1.65e-18**	**0**	**1.00e+00**	**Case 3**
7	**1**	**1.71e-15**	**1**	**8.56e-16**	**0**	**1.00e+00**	**Case 3**
8	**1**	**1.47e-19**	**1**	**7.36e-20**	**0**	**1.00e+00**	**Case 3**
9	**1**	**2.05e-18**	**1**	**1.02e-18**	**0**	**1.00e+00**	**Case 3**
10	**1**	**3.28e-18**	**1**	**1.64e-18**	**0**	**1.00e+00**	**Case 3**
11	**1**	**3.30e-18**	**1**	**1.65e-18**	**0**	**1.00e+00**	**Case 3**
13	**1**	**6.01e-15**	**1**	**3.01e-15**	**0**	**1.00e+00**	**Case 3**
14	**1**	**3.30e-18**	**1**	**1.65e-18**	**0**	**1.00e+00**	**Case 3**
15	**1**	**3.30e-18**	**1**	**1.65e-18**	**0**	**1.00e+00**	**Case 3**
16	**1**	**1.01e-17**	**1**	**5.03e-18**	**0**	**1.00e+00**	**Case 3**
17	**1**	**5.09e-08**	**1**	**2.55e-08**	**0**	**1.00e+00**	**Case 3**
18	**1**	**2.57e-13**	**1**	**1.29e-13**	**0**	**1.00e+00**	**Case 3**
20	**1**	**9.67e-15**	**1**	**4.84e-15**	**0**	**1.00e+00**	**Case 3**
21	**1**	**1.14e-06**	**1**	**5.71e-07**	**0**	**1.00e+00**	**Case 3**
23	1	1.34e-20	0	1.00e+00	1	6.68e-21	Case 2
24	**1**	**3.29e-18**	**1**	**1.64e-18**	**0**	**1.00e+00**	**Case 3**
25	**1**	**8.30e-07**	**1**	**4.15e-07**	**0**	**1.00e+00**	**Case 3**
28	**1**	**1.13e-04**	**1**	**5.64e-05**	**0**	**1.00e+00**	**Case 3**
30D							
1	**1**	**1.28e-18**	**1**	**6.41e-19**	**0**	**1.00e+00**	**Case 3**
2	**1**	**3.08e-18**	**1**	**1.54e-18**	**0**	**1.00e+00**	**Case 3**
3	**1**	**1.15e-19**	**1**	**5.75e-20**	**0**	**1.00e+00**	**Case 3**
4	**1**	**3.12e-18**	**1**	**1.56e-18**	**0**	**1.00e+00**	**Case 3**
5	**1**	**3.30e-18**	**1**	**1.65e-18**	**0**	**1.00e+00**	**Case 3**
7	**1**	**1.42e-18**	**1**	**7.11e-19**	**0**	**1.00e+00**	**Case 3**
8	**1**	**2.76e-18**	**1**	**1.38e-18**	**0**	**1.00e+00**	**Case 3**
9	1	3.86e-02	0	9.81e-01	1	1.93e-02	Case 2
10	**1**	**3.30e-18**	**1**	**1.65e-18**	**0**	**1.00e+00**	**Case 3**
11	**1**	**3.30e-18**	**1**	**1.65e-18**	**0**	**1.00e+00**	**Case 3**
13	**1**	**6.32e-03**	**1**	**3.16e-03**	**0**	**9.97e-01**	**Case 3**
14	**1**	**3.30e-18**	**1**	**1.65e-18**	**0**	**1.00e+00**	**Case 3**
15	**1**	**3.30e-18**	**1**	**1.65e-18**	**0**	**1.00e+00**	**Case 3**
16	**1**	**3.30e-18**	**1**	**1.65e-18**	**0**	1.00e+00	**Case 3**
17	1	3.19e-17	0	1.00e+00	1	1.59e-17	Case 2
18	1	4.55e-09	0	1.00e+00	1	2.28e-09	Case 2
20	1	3.21e-14	0	1.00e+00	1	1.61e-14	Case 2
21	1	4.99e-02	0	9.75e-01	1	2.49e-02	Case 2
23	1	1.85e-17	0	1.00e+00	1	9.24e-18	Case 2
24	1	1.40e-02	0	9.93e-01	1	7.02e-03	Case 2
25	1	3.58e-10	0	1.00e+00	1	1.79e-10	Case 2
28	1	5.36e-07	0	1.00e+00	1	2.68e-07	Case 2

Table F.8: Wilcoxon Test Results, CEC 2014: MP-AIDEA vs. CMLSP, 50D and 100D

	both		left		right		
	h	p	h	p	h	p	Result type
$n_D = 50$							
1	**1**	**2.79e-20**	**1**	**1.39e-20**	**0**	**1.00e+00**	**Case 3**
2	**1**	**3.29e-18**	**1**	**1.65e-18**	**0**	**1.00e+00**	**Case 3**
3	**1**	**2.92e-18**	**1**	**1.46e-18**	**0**	**1.00e+00**	**Case 3**
4	**1**	**3.29e-18**	**1**	**1.65e-18**	**0**	**1.00e+00**	**Case 3**
5	**1**	**3.30e-18**	**1**	**1.65e-18**	**0**	**1.00e+00**	**Case 3**
7	**1**	**3.20e-18**	**1**	**1.60e-18**	**0**	**1.00e+00**	**Case 3**
8	**1**	**3.16e-18**	**1**	**1.58e-18**	**0**	**1.00e+00**	**Case 3**
9	**1**	**1.69e-17**	**1**	**8.46e-18**	**0**	**1.00e+00**	**Case 3**
10	**1**	**3.30e-18**	**1**	**1.65e-18**	**0**	**1.00e+00**	**Case 3**
11	**1**	**3.30e-18**	**1**	**1.65e-18**	**0**	**1.00e+00**	**Case 3**
13	**1**	**1.07e-04**	**1**	**5.33e-05**	**0**	**1.00e+00**	**Case 3**
14	**1**	**3.30e-18**	**1**	**1.65e-18**	**0**	**1.00e+00**	**Case 3**
15	**1**	**3.30e-18**	**1**	**1.65e-18**	**0**	**1.00e+00**	**Case 3**
16	**1**	**3.30e-18**	**1**	**1.65e-18**	**0**	**1.00e+00**	**Case 3**
17	**1**	**5.00e-16**	**1**	**2.50e-16**	**0**	**1.00e+00**	**Case 3**
18	**1**	**4.14e-15**	**1**	**2.07e-15**	**0**	**1.00e+00**	**Case 3**
20	1	1.27e-17	0	1.00e+00	1	6.34e-18	Case 2
21	**1**	**1.58e-12**	**1**	**7.89e-13**	**0**	**1.00e+00**	**Case 3**
23	**1**	**7.50e-19**	**1**	**3.75e-19**	**0**	**1.00e+00**	**Case 3**
24	**1**	**2.13e-17**	**1**	**1.07e-17**	**0**	**1.00e+00**	**Case 3**
25	1	5.67e-04	0	1.00e+00	1	2.84e-04	Case 2
28	**1**	**9.60e-03**	**1**	**4.80e-03**	**0**	**9.95e-01**	**Case 3**
$n_D = 100$							
1	**1**	**3.83e-20**	**1**	**1.92e-20**	**0**	**1.00e+00**	**Case 3**
2	**1**	**3.28e-18**	**1**	**1.64e-18**	**0**	**1.00e+00**	**Case 3**
3	**1**	**3.30e-18**	**1**	**1.65e-18**	**0**	**1.00e+00**	**Case 3**
4	**1**	**3.30e-18**	**1**	**1.65e-18**	**0**	**1.00e+00**	**Case 3**
5	**1**	**3.30e-18**	**1**	**1.65e-18**	**0**	**1.00e+00**	**Case 3**
7	**1**	**3.25e-18**	**1**	**1.63e-18**	**0**	**1.00e+00**	**Case 3**
8	**1**	**3.30e-18**	**1**	**1.65e-18**	**0**	**1.00e+00**	**Case 3**
9	**1**	**3.30e-18**	**1**	**1.65e-18**	**0**	**1.00e+00**	**Case 3**
10	**1**	**3.30e-18**	**1**	**1.65e-18**	**0**	**1.00e+00**	**Case 3**
11	**1**	**3.30e-18**	**1**	**1.65e-18**	**0**	**1.00e+00**	**Case 3**
13	**1**	**2.70e-13**	**1**	**1.35e-13**	**0**	**1.00e+00**	**Case 3**
14	1	7.72e-10	0	1.00e+00	1	3.86e-10	Case 2
15	**1**	**3.30e-18**	**1**	**1.65e-18**	**0**	**1.00e+00**	**Case 3**
16	**1**	**3.30e-18**	**1**	**1.65e-18**	**0**	**1.00e+00**	**Case 3**
17	**1**	**3.30e-18**	**1**	**1.65e-18**	**0**	**1.00e+00**	**Case 3**
18	**1**	**3.30e-18**	**1**	**1.65e-18**	**0**	**1.00e+00**	**Case 3**
20	1	4.70e-18	0	1.00e+00	1	2.35e-18	Case 2
21	**1**	**3.30e-18**	**1**	**1.65e-18**	**0**	**1.00e+00**	**Case 3**
23	**1**	**3.30e-18**	**1**	**1.65e-18**	**0**	**1.00e+00**	**Case 3**
24	**1**	**3.30e-18**	**1**	**1.65e-18**	**0**	**1.00e+00**	**Case 3**
25	**1**	**1.36e-04**	**1**	**6.81e-05**	**0**	**1.00e+00**	**Case 3**
28	**1**	**9.90e-14**	**1**	**4.95e-14**	**0**	**1.00e+00**	**Case 3**

Appendix G

Algorithm LambTAN: Lambert problem to Target Asteroids at Nodal points

This appendix describes the algorithm Lambert problem to Target Asteroids at Nodal points (LambTAN), used to solve the combinatorial problem for the mission design presented in Chapter 8. The algorithm starts, for a transfer j, from a given departure orbit $\mathcal{OE}_j$, identified by its orbital elements:

$$\mathcal{OE}_j = \{a, e, i, \Omega, \omega\}, \tag{G.1}$$

For a given set of target asteroids $\mathcal{A}_j = \{A_1, A_2, ..., A_d\}$, the ascending and descending nodal points are computed. For the *k*-th asteroid, A_k, the epochs of passage through the ascending and descending nodal points, $T^{asc}_{A_k}$ and $T^{desc}_{A_k}$, are computed within the interval of time going from the considered epoch, t, to the end of the mission, T_{end}. For each node passing epoch $T^{asc}_{A_k}$ and $T^{desc}_{A_k}$, a window for the departure times from the departure orbit $\mathcal{OE}_j$ can be computed. In particular, the start and end epochs for the departure window DW, T^{DW}_{start} and T^{DW}_{end}, are computed by subtracting the minimum and maximum time of flight ToF_{min} and ToF_{max} from each node passing epoch $T^{asc}_{A_k}$ and $T^{desc}_{A_k}$. For an encounter at the ascending node at time $T^{asc}_{A_k}$, T^{DW}_{start} and T^{DW}_{end} are

$$\begin{aligned} T^{DW}_{start} &= \max\left[\left(T^{asc}_{A_k} - ToF_{max}\right), T_{A_{k-1}}\right] , \\ T^{DW}_{end} &= T^{asc}_{A_k} - ToF_{min} , \end{aligned} \tag{G.2}$$

where $T_{A_{k-1}}$ is the passing time at the previous visited asteroid. In Equation G.2, $T^{asc}_{A_k}$ has to satisfy $T^{asc}_{A_k} \leq T_{end}$, where T_{end} is the mission end epoch. The Lambert arc associated with departure time T^{DW}_{start} is represented in red in Figure 8.2 in Chapter 8, while the Lambert arc associated with departure time T^{DW}_{end} is shown in blue. The next step is to compute, from the window of departure times going from T^{DW}_{start} to T^{DW}_{end}, n Lambert arcs that connect the departure orbit $\mathcal{OE}_j$ with the nodal point at the considered nodal passing epoch, as shown in

Figure 8.2. The value n is given by

$$n = \frac{T_{end}^{DW} - T_{start}^{DW}}{ToF_{step}}, \tag{G.3}$$

where ToF_{step} is the considered step size for the time of flights. As an example, in Figure 8.2, ToF_{step} is such as to give $n = 6$. For each Lambert arc, the algorithm proceeds to the next step only if three constraint criteria are met:

1. the ΔV at departure for the current Lambert arc, ΔV_{arc_k}, does not exceed a given maximum value, ΔV_{max}:
$$\Delta V_{arc_k} \leq \Delta V_{max}; \tag{G.4}$$

2. the Lambert transfer is characterised by a perihelion q greater than a given minimum perihelion, q_{min}:
$$q > q_{min}; \tag{G.5}$$

3. the impulsive Lambert transfer can be realised with the low-thrust propulsion system. This is deemed possible if the following condition is satisfied:
$$ToF_{arc_k}\epsilon \geq \max\left[C\Delta V_{arc_k}, \sqrt{V_0^2 - 2V_f V_0 + V_f^2}\right], \tag{G.6}$$
where ToF_{arc_k} is the time of flight for the current Lambert arc, ΔV_{arc_k} is the change in velocity required for the impulsive Lambert arc at departure, ϵ is the acceleration provided by the low-thrust engine, C is an appropriate empirical coefficient, V_0 is the spacecraft's velocity when it passes the previous asteroid and V_f is the velocity at the end of the Lambert arc. The second term in square brackets in the previous equation is the Edelbaum's ΔV for low-thrust transfer between circular orbits (Section 2.2.2).

If the considered Lambert arc meets all of the above constraints, then the Lambert arc is set as the new departure orbit for the next transfer, $\mathcal{OE}_{j+1}$. A new set of possible target asteroids, $\mathcal{A}_{j+1}$, is defined by removing the asteroid visited at step j, A_j, from the set of possible targets, $\mathcal{A}_{j+1} = \{x : x \in \mathcal{A}_j \wedge x \neq A_j\}$. The process is then repeated for all possible combinations of asteroids. A full solution is generated when the set of target asteroids $\mathcal{A}$ is empty, $\mathcal{A} = \emptyset$, or if the end time of the mission epoch has been reached.

The main setting parameters of the LambTAN solver are summarized in Table G.1.

Table G.1: LambTAN parameters settings.

$\mathcal{A}$	Target asteroids $[A_1, A_2, \dots A_d]$
T_0	Mission start epoch
T_{end}	Mission end epoch
ToF_{max}	Maximum time of flight for each Lambert arc
ToF_{min}	Minimum time of flight for each Lambert arc
ToF_{step}	Time step for the time of flight
ΔV_{max}	Maximum departure velocity vector $[\Delta V_{Earth}, \Delta V_{arc1}, \Delta V_{arc2}, ..., \Delta V_{arcn}]$
q_{min}	Minimum perihelion
ϵ	Low-thrust acceleration
C	Scaling factor

Bibliography

[1] Competition on testing evolutionary algorithms on real-world numerical optimization problems @ cec11, new orleans, usa, june 2011.
URL http://www3.ntu.edu.sg/home/epnsugan/index_files/CEC11-RWP/CEC11-RWP.htm

[2] Hybrid differential evolution algorithm with adaptive crossover mechanism.
URL http://uk.mathworks.com/matlabcentral/fileexchange/39217-hybrid-differential-evolution-algorithm-with-adaptive-crossover-mechanism/content/DE_TCRparam.m

[3] Ponnuthurai nagaratnam sugantha shared documents.
URL http://web.mysites.ntu.edu.sg/epnsugan/PublicSite/Shared%20Documents/Forms/AllItems.aspx

[4] Abramowitz, M., Stegun, I. A., Handbook of Mathematical Functions: with Formulas, Graphs, and Mathematical Tables, New York: Dover, 1972.

[5] Adamatzky, A., Martinez, G. J., Chapa-Vergara, S. V., Asomoza-Palacio, R., Stephens, C. R., Approximating Mexican highways with slime mould, Natural Computing 10 (3) (2011) 1195–1214. doi:10.1007/s11047-011-9255-z.

[6] Alemany, K., Braun, R. D., Survey of Global Optimization Methods for Low-Thrust, Multiple Asteroid Tour Missions, 17th AAS/AIAA Space Flight Mechanics MeetingJanuary 28 - February 1, 2007, Sedona, Arizona, USA.

[7] Alonso, S., Jimenez, J., Carmona, H., Galvan, B., Winter, G., Performance of a flexible evolutionary algorithm, 2005 IEEE Congress on Evolutionary Computation (CEC), September 2-5, 2005, Edinburgh, United Kingdom.

[8] Asafuddoula, M., Ray, T., Sarker, R., An adaptive differential evolution algorithm and its performance on real world optimization problems, 2011 IEEE Congress on Evolutionary Computation (CEC), June 5-8, 2011, New Orleans, LA, USA. doi:10.1109/CEC.2011.5949734.

[9] Auger, A., Hansen, N., A restart CMA evolution strategy with increasing population size, 2005 IEEE Congress on Evolutionary Computation (CEC), September 2-5, 2005, Edinburgh, United Kingdom. doi:10.1109/CEC.2005.1554902.

[10] Auger, A., Hansen, N., Performance evaluation of an advanced local search evolutionary algorithm, 2005 IEEE Congress on Evolutionary Computation (CEC), September 2-5, 2005, Edinburgh, United Kingdom. doi:10.1109/CEC.2005.1554903.

[11] Ballester, P. J., Stephenson, J., Carter, J. N., Gallagher, K., Real-parameter optimization performance study on the CEC-2005 benchmark with SPC-PNX, 2005 IEEE Congress on Evolutionary Computation (CEC), September 2-5, 2005, Edinburgh, United Kingdom. doi:10.1109/CEC.2005.1554724.

[12] Bandaru, S., Tulshyan, R., Deb, K., Modified sbx and adaptive mutation for real world single objective optimization, 2011 IEEE Congress on Evolutionary Computation (CEC), June 5-8, 2011, New Orleans, LA, USA. doi:10.1109/CEC.2011.5949771.

[13] Battin, R. H., An introduction to the mathematics and methods of astrodynamics, AIAA, 1987. doi:10.2514/4.861543.

[14] Becerra, V. M., Myatt, D. R., Nasuto, S. J., Bishop, J. M., Izzo, D., An efficient pruning technique for the global optimisation of multiple gravity assist trajectories, Proceedings of the Internaional Workshop on Global OptimizationHonolulu, HI.

[15] Becker, W., Yu, X., Tu, J., EvLib: A parameterless self-adaptive real-valued optimisation Library, 2005 IEEE Congress on Evolutionary Computation (CEC), September 2-5, 2005, Edinburgh, United Kingdom.

[16] Benney, D. J., Escape from a circular orbit using tangential thrust, Journal of Jet Propulsion 28 (3) (1958) 167–169. doi:10.2514/8.7261.

[17] Bernelli-Zazzera, F., Vasile, M., Fornasari, N., Masarati, P., Design of interplanetary and lunar missions combining low thrust and gravity assists, Tech. rep., Politecnico di Milano (2002).

[18] Bertrand, R., Epenoy, R., New smoothing techniques for solving bang-bang optimal control problems - numerical results and statistical interpretation, Optimal Control Applications and Methods 23 (2002) 171–197. doi:10.1002/oca.709.

[19] Betts, J. T., Survey of Numerical Methods for Trajectory Optimization, Journal of Guidance, Control and Dynamics 21 (2) (1998) 193–207. doi:10.2514/2.4231.

[20] Betts, J. T., Practical Methods for Optimal Control and Estimation Using Nonlinear Programming, Advances in Design and Control, Society for Industrial and Applied Mathematics (SIAM), 2010.

[21] Bezdek, A., Vokrouhlicky, B., Semianalytic theory of motion for close-Earth spherical satellites includingdragand gravitational perturbations, Planetary and Space Science 52 (2004) 1233–1249. doi:10.1016/j.pss.2004.08.004.

[22] Bezdek, J. C., Pattern Recognition with Fuzzy Objective Function Algorithms, Springer US, 1981. doi:10.1007/978-1-4757-0450-1.

[23] Bohme, T. J., Frank, B., Introduction to Nonlinear Programming, Springer International Publishing, Cham, 2017, pp. 27–77. doi:10.1007/978-3-319-51317-1_2. URL https://doi.org/10.1007/978-3-319-51317-1_2

[24] Boltz, F. W., Orbital motion under continuous radial thrust, Journal of Guidance, Control, and Dynamics 14 (3) (1991) 667–670. doi:10.2514/3.20690.

[25] Boltz, F. W., Orbital motion under continuous tangential thrust, Journal of Guidance, Control, and Dynamics 15 (6) (1992) 1503–1507. doi:10.2514/3.56583.

[26] Bombardelli, C., Baù, G., Pelaez, J., Asymptotic solution for the two-body problem with constant tangential thrust acceleration, Celestial Mechanics and Dynamical Astronomy 110 (3) (2011) 239–256. doi:10.1007/s10569-011-9353-3.

[27] Bombardelli, C., Palaez, J., Ion Beam Shepherd for Contactless Space Debris Removal, Journal of Guidance, Control, and Dynamics 34 (3) (2011) 916–920. doi:10.2514/1.51832.

[28] Bonanno, C., An analytical approximation for the MOID and its consequences, Astronomy and Astrophysics 360 (2000) 411–416.

[29] Bonnard, B., Faubourg, L., Trélat, E., Mécanique céleste et controle des véhicules spatiaux,, Springer Science and Business Media,, 2005.

[30] Braun, V., A., L., Flegel, S., Gelhaus, J., Mockel, M., Kebschull, C., Wiedemann, C., Vorsmann, P., Active debris removal of multiple priority targets, Advances in Space Research 51 (9) (2013) 1638–1648. doi:10.1016/j.asr.2012.12.003.

[31] Brest, J., Greiner, S., Bošković, B., Mernik, M., Zumer, V., Self-adapting control parameters in differential evolution: a comparative study on numerical benchmark problems, IEEE Transactions on Evolutionary Computation 10 (6) (2006) 646–657. doi:10.1109/TEVC.2006.872133.

[32] Brophy, J., Rayman, M., Pavri, B., Dawn: An ion-propelled journey to the beginning of the solar system, 2008 IEEE Aerospace ConferenceBig Sky, MT. doi:10.1109/AERO.2008.4526264.

[33] Broucke, R., Cefola, P. J., On the equinoctial orbit elements, Celestial Mechanics 5 (3) (1972) 303–310. doi:10.1007/BF01228432.

[34] Brouwer, D., Solution of the problem of artifical satellite theory without drag, Astronomical Journal 64 (1959) 378–396.

[35] Bruno, C., Spacecraft Propulsion, in: The International Handbook of Space Technology, Springer PRaxis, 2014, pp. 279–321. doi:10.1007/978-3-642-41101-4.

[36] Bryson, A. E., Ho, Y., Applied Optimal Control, Taylor and Francis Group, New York, 2000.

[37] Bui, L. T., Shan, Y., Qi, F., Abbass, H. A., Comparing two versions of differential evolution in real parameter optimization, 2005 IEEE Congress on Evolutionary Computation (CEC), September 2-5, 2005, Edinburgh, United Kingdom.

[38] Bujok, P., Tvrdik, J., Polakova, R., Differential evolution with rotation-invariant mutation and competing-strategies adaptation, 2014 IEEE Congress on Evolutionary Computation (CEC), July 6-11, 2014, Beijing, China. doi:10.1109/CEC.2014.6900626.

[39] Burt, E. G. C., On space manoeuvres with continuous thrust, Planetary and Space Science 15 (1) (1967) 103–122. doi:10.1016/0032-0633(67)90070-0.

[40] Castronuovo, M., Active space debris removal—A preliminary mission analysis and design, Acta Astronautica 69 (9-10) (2011) 848–859. doi:10.1016/j.actaastro.2011.04.017.

[41] Cefola, P. J., Long, A. C., Holloway, G. J., The long-term prediction of artificial satellite orbits, AIAA 12th Aerospace Sciences Meeting, January 30-February 1, 1974, Washington.

[42] Chamot, B., Richard, M., Mission and system architecture design for active removal or rocket bodies in Low Earth Orbit, Master's thesis, Massachusetts Institute of Technology, USA (2012).

[43] Chen, L., Liu, H.-l., Zheng, Z., Xie, S., An evolutionary algorithm based on Covariance Matrix Leaning and Searching Preference for solving CEC 2014 benchmark problems, 2014 IEEE Congress on Evolutionary Computation (CEC), July 6-11, 2014, Beijing, China. doi:10.1109/CEC.2014.6900594.

[44] Chen, Y., Baoyin, H., Junfeng, L., Accessibility of main-belt asteroids via gravity assists, Journal of Guidance, Control, and Dynamics 37 (2) (2014) 623–632. doi:10.2514/1.58935.

[45] Colombo, C., Vasile, M., Radice, G., Semi-Analytical Solution for the Optimal Low-Thrust Deflection of Near-Earth Objects, Journal of Guidance, Control, and Dynamics 32 (3) (2009) 796–809.

[46] Committee, I.-A. S. D. C., IADC Space Debris Mitigation Guidelines, Tech. rep., 45th Session of the Scientific and Technical Subcommittee, United Nations Committee on the Peaceful Uses of Outer Space, http://www.iadc-online.org/Documents/IADC-2002-01,%20IADC%20Space%20Debris%20Guidelines,%20Revision%201.pdf (2007).

[47] Conway, B. A., Spacecraft Trajectory Optimization Using Direct Transcription and Nonlinear Programming, in: Spacecraft trajectory optimization, Cambridge University Press, 2010, pp. 37–76. doi:10.1017/CBO9780511778025.

[48] Conway, B. A., The Problem of Spacecraft Trajectory Optimization, in: Spacecraft trajectory optimization, Cambridge University Press, 2010, pp. 1–13. doi:10.1017/CBO9780511778025.

[49] Cook, G. E., King-Hele, D. G., The contraction of satellite orbits under the influence of air drag. IV. With scale height dependent on altitude, Proceedings of the Royal Society A 275 (1362). doi:10.1098/rspa.1963.0175.

[50] Cook, G. E., King-Hele, D. G., The contraction of satellite orbits under the influence of air drag. V. With day-to-night variation in air density, Proceedings of the Royal Society A 259 (1096). doi:10.1098/rsta.1965.0053.

[51] Cook, G. E., King-Hele, D. G., The contraction of satellite orbits under the influence of air drag. VI. Near circular orbit with day-to-night variation in air density, Proceedings of the Royal Society A 303 (1472). doi:10.1098/rspa.1968.0037.

[52] Cook, G. E., King-Hele, D. G., Walker, D. M. C., ÑThe contraction of satellite orbits under the influence of air drag. I. With spherically symmetrical atmosphere, Proceedings of the Royal Society A 257 (1289). doi:10.1098/rspa.1960.0146.

[53] Cook, G. E., King-Hele, D. G., Walker, D. M. C., The contraction of satellite orbits under the influence of air drag. I. With oblate atmosphere, Proceedings of the Royal Society A 264 (1316). doi:10.1098/rspa.1961.0186.

[54] Costa, L., A parameter-less evolution strategy for global optimization, 2005 IEEE Congress on Evolutionary Computation (CEC), September 2-5, 2005, Edinburgh, United Kingdom.

[55] Curell, P., Grace orbit analysis tool and parametric analysis, Tech. rep., Center for Space Research - The University of Texas at Austin (1998).

[56] Dachwald, B., Optimization of very-low-thrust trajectories using evolutionary neurocontrol, Acta Astronautica 57 (2-8) (2005) 175–185. doi:10.1016/j.actaastro.2005.03.004.

[57] Danielson, D. A., Semianalytic satellite theory, Tech. rep., Naval Postgraduate School, Monterey, CA, USA (1995).

[58] Das, S., Suganthan, P. N., Problem definitions and evaluation criteria for cec 2011 competition on testing evolutionary algorithms on real world optimization problems, Technical Report, Jadavpur University, Nanyang Technological University, 2010.

[59] Das, S., Suganthan, P. N., Differential evolution: a survey of the state-of-the-art, IEEE Transactions on Evolutionary Computation 15 (1) (2011) 4–31. doi:10.1109/TEVC.2010.2059031.

[60] De Pascale, P., Vasile, M., Preliminary Design of Low-Thrust Multiple Gravity-Assist Trajectories, Journal of Spacecraft and Rockets 43 (5) (2006) 1065–1076. doi:10.2514/1.19646.

[61] De Pascale, P., Vasile, M., Casotto, S., Optimal Options for Rendezvous and Impact Missions to NEOs, IBIS, Journal of the British Interplanetary Society 59 (11).

[62] Di Carlo, M., Ricciardi, L. A., Vasile, M., Multi-Objective Optimisation of Constellation Deployment using Low-Thrust Propulsion, 2016 AIAA/AAS Astrodynamics Specialist Conference, September 13-16, 2016, Long Beach, CA.

[63] Di Carlo, M., Romero Martin, J. M., Ortiz Gomez, N., Vasile, M., Optimised Low-Thrust Mission to the Atira Asteroids, Advances in Space Research 59 (7) (2017) 1724–1739. doi:10.1016/j.asr.2017.01.009.

[64] Di Carlo, M., Romero Martin, J. M., Vasile, M., Automatic trajectory planning for low-thrust active removal mission in Low-Earth Orbit, Advances in Space Research 59 (1) (2017) 1234–1258. doi:10.1016/j.asr.2016.11.033.

[65] Di Carlo, M., Vasile, M., Dunlop, J., Low-thrust tour of the main belt asteroids, Advances in Space Researchdoi:10.1016/j.asr.2017.12.033.

[66] Di Carlo, M., Vasile, M., Kemble, S., Optimised GTO-GEO Transfer using Low-Thrust Propulsion, 26th International Symposium on Space Flight Dynamics (ISSFD), June 3-9, 2017, Matsuyama, Japan.

[67] Di Carlo, M., Vasile, M., Minisci, E., Multi-Population Adaptive Inflationary Differential Evolution Algorithm with Adaptive Local Restart, IEEE Congress on Evolutionary Computation, May 25-28, 2015, Sendai, Japan.

[68] Di Lizia, P., Radice, G., Advanced Global Optimisation for Mission Analysis and Design, Tech. rep., European Space Agency, the Advanced Concepts Team (2004).

[69] Di Lizia, P., Radice, G., Advanced global optimisation tools for mission analysis and design, Tech. rep., European Space Agency, the Advanced Concepts Team (2004).

[70] Dourado Maia, R., Nunes de Castro, L., Matos Caminhas, W., Real-parameter optimization with OptBees, 2014 IEEE Congress on Evolutionary Computation (CEC), July 6-11, 2014, Beijing, China. doi:10.1109/CEC.2014.6900549.

[71] Eberhart, R., Kennedy, J., A New Optimizer Using Particle Swarm Theory, 6th International Symposium on Micromachine and Human Science, October 4-6, 1995, Nagoya, Japan.

[72] Edelbaum, T. N., Propulsion requirements for controllable satellites, ARS Journal 31 (8) (1961) 1079–1089. doi:10.2514/8.5723.

[73] Elsayed, S. M., Sarker, R. A., Essam, D. L., Differential evolution with multiple strategies for solving CEC2011 real-world numerical optimization problems, 2011 IEEE Congress on Evolutionary Computation (CEC), June 5-8, 2011, New Orleans, LA, USA. doi:10.1109/CEC.2011.5949732.

[74] Elsayed, S. M., Sarker, R. A., Essam, D. L., GA with a new multi-parent crossover for solving IEEE-CEC2011 competition problems, 2011 IEEE Congress on Evolutionary Computation (CEC), June 5-8, 2011, New Orleans, LA, USA. doi:10.1109/CEC.2011.5949731.

[75] Elsayed, S. M., Sarker, R. A., Essam, D. L., Hamza, N. M., Testing united multi-operator evolutionary algorithms on the CEC2014 real-parameter numerical optimization, 2014 IEEE Congress on Evolutionary Computation (CEC), July 6-11, 2014, Beijing, China. doi:10.1109/CEC.2014.6900308.

[76] Epenoy, R., Bertrand, R., Decomposition-coordination techniques in optimal control for computing multi-phases interplanetary trajectories of low-thrust probes, FGP 2002, French-German-Polish conference on Optimization, September 9-13 2002, Technical University Cottbus, Germany.

[77] Erlich, I., Rueda, J. L., Wildenhues, S., Shewarega, F., Evaluating the mean-variance mapping optimization on the IEEE-CEC 2014 test suite, 2014 IEEE Congress on Evolutionary Computation (CEC), July 6-11, 2014, Beijing, China. doi:10.1109/CEC.2014.6900516.

[78] Falck, R. D., Sjauw, W. K., Smith, D. A., Comparison of Low-Thrust Control Laws for Applications in Planetocentric Space, 50th AIAA/ASME/SAE/ASEE Joint Propulsion Conference, AIAA Propulsion and Energy Forum, July 28-30, 2014, Cleveland, Ohio, USA.

[79] Forrester, A. I. J., Keane, A. J., Recent advances in surrogate-based optimization, Progress in Aerospace Sciences 45 (1-3) (2009) 50–79. doi:10.1016/j.paerosci.2008.11.001.

[80] Forrester, A. I. J., Sobester, A., Keane, A. J., Engineering Design via Surrogate Modelling - A Practical Guide, Wiley, 2008.

[81] Fortescue, P., Swinerd, G., Stark, J., Spacecraft Systems Engineering, Wiley, 2011.

[82] Fossati, M., Evaluation of Aerodynamic Loads via Reduced-Order Methodology, AIAA Journal 53 (8) (2015) 2389–2405. doi:10.2514/1.J053755.

[83] García-Martínez, C., Lozano, M., Hybrid real-coded genetic algorithms with female and male differentiation, 2005 IEEE Congress on Evolutionary Computation (CEC), September 2-5, 2005, Edinburgh, United Kingdom. doi:10.1109/CEC.2005.1554778.

[84] Gil, A., Segura, J., Temme, M., Numerical Methods for Special Functions, SIAM, Society for Industrial and Applied Mathematics, 2007.

[85] Giunta, A. A., Watson, L. T., A Comparison of Approximation Modeling Techniques: Polynomial Versus Interpolating Models, 7th AIAA/USAF/NASA/ISSMO Symposium on Multidisciplinary Analysis and Optimization, September 2-4, 1998, St Louis, Missouri, USA.

[86] Goldberg, D. E., Genetic Algorithms in Search, Optimization, and Machine Learning, Addison Wesley, Boston, MA, 1989.

[87] Greenstreet, S., Ngo, H., Gladman, B., The orbital distribution of Near- Earth Objects inside Earth's orbit, Icarus 217 (1) (2012) 355–366. doi:10.1016/j.icarus.2011.11.010.

[88] Grigoriev, I. S., Zapletin, M. P., Choosing promising sequences of asteroids, Automation and Remote Control 74 (8) (2013) 1284–1296. doi:10.1134/S0005117913080055.

[89] Gronchi, G. F., On the stationary points of the squared distance between two ellipses with a common focus, SIAM Journal on Scientific Computing 24 (2002) 61–80. doi:10.1137/S1064827500374170.

[90] Gronchi, G. F., An algebraic method to compute the critical points of the distance function between two Keplerian orbits, Celestial Mechanics and Dynamical Astronomydoi:10.1007/s10569-005-1623-5.

[91] Grover, P., Ross, S., Designing Trajectories in a Planet-Moon Environment Using the Controlled Keplerian Map, Journal of Guidance, Control, and Dynamic 32 (2) (2009) 436–443. doi:10.2514/1.38320.

[92] Guinn, J. and Chung, M. and Vincent, M., Conversion Between Osculating and Mean Orbital Elements, Tech. rep., Jet Propulsion Laboratory, Pasadena, CA, United States (2006).

[93] Guo, T., Jiang, F., Li, J., Homotopic approach and pseudospectral method applied jointly to low thrust trajectory optimization, Acta Astronautica 71 (2012) 38–50. doi:10.1016/j.actaastro.2011.08.008.

[94] Haider, U., Das, S., Maity, D., Abraham, A., Dasgupta, P., Self adaptive cluster based and weed inspired differential evolution algorithm for real world optimization, 2011 IEEE Congress on Evolutionary Computation (CEC), June 5-8, 2011, New Orleans, LA, USA. doi:10.1109/CEC.2011.5949694.

[95] Harris, A., NEA populations and impact frequency, Asteroid Grand Challenge Seminar Series, March 28, 2014, https://sservi.nasa.gov/wp-content/uploads/2014/03/Harris.pdf.

[96] Hennes, D., Izzo, D., Landau, D., Fast approximators for optimal low-thrust hops between main belt asteroids, 2016 IEEE Symposium Series on Computational Intelligence (SSCI), December 6-9, 2016, Athens, Greece.

[97] Herman, A. L., Conway, B. A., Direct Optimization Using Collocation Based on High-Order Gauss-Lobatto Quadrature Rules, Journal of Guidance, Control, and Dynamics 19 (3) (1996) 592–599. doi:10.2514/3.21662.

[98] Hildreth, S. A., Arnold, A., Threats to U.S. National Security Interests in Space: Orbital Debris Mitigation and Removal, Tech. rep., Congressional Research Service, https://www.files.ethz.ch/isn/176178/219951.pdf (2014).

[99] Hongmei, C., Mascagni, M., Warnock, T., On the optimal Halton sequence, Mathematics and computers in simulation 70 (1) (2005) 9–21.

[100] Hoots, F. R., Roehrich, R. L., Spacetrack Report No. 3 - Models for Propagation of NORAD Element Sets, Tech. rep., Office of Astrodynamics, Aerospace Defence Center, USA (1998).

[101] Hu, Z., Bao, Y., Xiong, T., Partial opposition-based adaptive differential evolution algorithms: evaluation on the CEC 2014 benchmark set for real-parameter optimization, 2014 IEEE Congress on Evolutionary Computation (CEC), July 6-11, 2014, Beijing, China. doi:10.1109/CEC.2014.6900489.

[102] Jones, D. R., A Taxonomy of Global Optimization Methods Based on Response Surfaces, Journal of Global Optimization 21 (4) (2001) 345–383.

[103] Kawaguchi, J., The Hayabusa mission - Its seven years flight, 2011 IEEE Symposium on VLSI CircuitsHonolulu, HI.

[104] Kechichian, J. A., Low-thrust eccentricity-constrained orbit raising, Journal of Spacecraft and Rockets 35 (3) (1998) 327–335. doi:10.2514/2.3330.

[105] Kechichian, J. A., Orbit raising with low-thrust tangential acceleration in presence of earth shadow, Journal of Spacecraft and Rockets 35 (4) (1998) 516–525. doi:10.2514/2.3361.

[106] Kéchichian, J. A., Reformulation of Edelbaum's Low-Thrust Transfer Problem Using Optimal Control Theory, Journal of Guidance, Cotnrol and Dynamics 20 (5) (1997) 988–994. doi:10.2514/2.4145.

[107] Kéchichian, J. A., Analytic representations of optimal low-thrust transfer in circular orbit, in: Spacecraft trajectory optimization, Cambridge University Press, 2010. doi:10.1017/CBO9780511778025.

[108] Kemble, S., Interplanetary Mission Analysis and Design, Springer Praxis Books, 2006.

[109] Kennedy, J., Eberhart, R., Swarm Intelligence, IEEE Internaional Conference on Neural Networks, November 27-December 1, 1995, Piscataway, NJ, USA.

[110] Kessler, D. J., Johnson, N. L., Liou, J. C., Matney, M., The Kessler Syndrome: Implications to Future Space Operations , Advances in the Astronomical Sciences 167 (2010) 47–62.

[111] King-Hele, D. G., The contraction of satellite orbits under the influence of air drag. III. High eccentricity orbits (0.2¡e¡1), Proceedings of the Royal Society A 267 (1331). doi:10.1098/rspa.1962.0117.

[112] King-Hele, D. G., Walker, D. M. C., The contraction of satellite orbits under the influence of air drag. VII. Orbits of high eccentricity, with day-to-night variation in air density, Proceedings of the Royal Society A 411 (1840). doi:10.1098/rspa.1987.0050.

[113] Kluever, C. A., Optimal Low-Thrust Interplanetary Trajectories by Direct Method Techniques, Journal of the astronautical sciences 45 (3).

[114] Kluever, C. A., Geostationary Orbit Transfers Using Solar Electric Propulsion with Specific Impulse Modulation, Journal of Spacecraft and Rockets 41 (3) (2004) 461–466. doi:10.2514/1.10939.

[115] Kluever, C. A., Oleson, S. R., Direct Approach for Computing Near-Optimal Low-Thrust Earth-Orbit Transfers, Journal of Spacecraft and Rockets 35 (4) (1998) 509–515. doi:10.2514/2.3360.

[116] Koppel, C. R., Advantages of a continuous thrust strategy from a geosynchronous transfer orbit, using high specific impulse thrusters, 14th International Symposium on Space Flight Dynamics (ISSFD), February 8-12, 1999, Foz do Iguacu, Brazil.

[117] Korošec, P., Šilc, J., The continuous differential ant-stigmergy algorithm applied to real-world optimization problems, 2011 IEEE Congress on Evolutionary Computation (CEC), June 5-8, 2011, New Orleans, LA, USA. doi:10.1109/CEC.2011.5949770.

[118] Kozai, Y., The motion of a close Earth satellite, Astronomical Journal 64 (1959) 367–377. doi:10.1086/107957.

[119] Kuhn, H. W., Tucker, A. W., Nonlinear Programming, in: Traces and Emergence of Nonlinear Programming, Birkhauser, Basel, 2014, pp. 16–36. doi:10.1007/978-3-0348-0439-4_11.

[120] Kumar, K., Ortiz Gomez, N., Jankovic, M., Romero Martin, J. M., Topputo, F., Walker, S., Kirchner, F., Vasile, M., Agora: Mission to demonstrate technologies to actively remove Ariane rocket bodies, 66th International Astronautical Congress (IAC), October 12-16, 2015, Jerusalem, Israel.

[121] Lantoine, G., Russell, R. P., A Hybrid Differential Dynamic Programming Algorithm for Constrained Optimal Control Problems. Part 2: Application, Journal of Optimization

Theory and Applications 154 (2) (2012) 418–442. doi:10.1007/s10957-012-0038-1.

[122] LaTorre, A., Muelas, S., Peña, J.-M., Benchmarking a hybrid de-rhc algorithm on real world problems, 2011 IEEE Congress on Evolutionary Computation (CEC), June 5-8, 2011, New Orleans, LA, USA. doi:10.1109/CEC.2011.5949730.

[123] LaValle, S. M., Planning Algorithms, Cambridge Univeristy Press, 2006.

[124] Lawden, D. F., Optimal trajectories for space navigation, Butterworths, 1963.

[125] Li, Z., Shang, Z., Qu, B. Y., Liang, J.-J., Differential evolution strategy based on the constraint of fitness values classification, 2014 IEEE Congress on Evolutionary Computation (CEC), July 6-11, 2014, Beijing, China. doi:10.1109/CEC.2014.6900507.

[126] Liang, J.-J., Suganthan, P. N., Dynamic multi-swarm particle swarm optimizer with local search, 2005 IEEE Congress on Evolutionary Computation (CEC), September 2-5, 2005, Edinburgh, United Kingdom. doi:10.1109/CEC.2005.1554727.

[127] Liang, J., Qu, B., Suganthan, P., Problem definitions and evaluation criteria for the cec 2014 special session and competition on single objective real-parameter numerical optimization, Technical Report, 2013.

[128] Lin, Q., Loxton, R., Teo, K. L., The Control Parametrisation Method for Nonlinear Optimal Control: A Survey, Journal of Industrial and Management Optimization 10 (1) (2014) 275–309. doi:10.3934/jimo.2014.10.275.

[129] Liou, J. C., Johnson, N. L., Instability of the present LEO satellite populations, Advances in Space Research 41 (7) (2008) 1046–1053. doi:10.1016/j.asr.2007.04.081.

[130] Liu, J., Lampinen, J., A fuzzy adaptive differential evolution algorithm, Soft Computing 9 (6) (2005) 448–462. doi:10.1007/s00500-004-0363-x.

[131] Locatelli, M., Vasile, M., (non) convergence results for the differential evolution method, Optimization Letters 9 (3) (2015) 413–425. doi:10.1007/s11590-014-0816-9.

[132] Lophaven, S. N., Nielsen, H. B., Sondergaard, J., DACE - A Matlab Kriging Toolbox, Tech. rep., Technical University of Denmark (2002).

[133] Mallipeddi, R., Suganthan, P. N., Ensemble differential evolution algorithm for cec2011 problems, 2011 IEEE Congress on Evolutionary Computation (CEC), June 5-8, 2011, New Orleans, LA, USA. doi:10.1109/CEC.2011.5949801.

[134] Mallipeddi, R., Wu, G., Lee, M., Suganthan, P., Gaussian adaptation based parameter adaptation for differential evolution, 2014 IEEE Congress on Evolutionary Computation (CEC), July 6-11, 2014, Beijing, China. doi:10.1109/CEC.2014.6900601.

[135] Mandal, A., Das, A. K., Mukherjee, P., Das, S., Suganthan, P. N., Modified differential evolution with local search algorithm for real world optimization, 2011 IEEE Congress on Evolutionary Computation (CEC), June 5-8, 2011, New Orleans, LA, USA. doi:10.1109/CEC.2011.5949802.

[136] Martinusi, V., Dell'Elce, L., Kerschen, G., Analytic propagation of near-circular satellite orbits in the atmosphere of an oblate plane, Celestial Mechanics and Dynamical Astronomy 123 (2015) 85–103. doi:10.1007/s10569-015-9630-7.

[137] Martinusi, V., Dell'Elce, L., Kerschen, G., First-order analytic propagation of satellites in the exponential atmosphere of an oblate planet, Celestial Mechanics and Dynamical Astronomy 127 (2017) 451–476. doi:10.1007/s10569-016-9734-8.

[138] McConaghy, T. T., Debban, T. J., Petropoulos, A. E., Longuski, J. M., Design and Optimization of Low-Thrust Trajectories with Gravity Assists, Journal of Spacecraft and Rockets 40 (3) (2003) 380–387. doi:10.2514/2.3973.

[139] Mereta, A., Izzo, D., Wittig, A., Machine Learning of Optimal Low-thrust Transfers between Near-Earth Objects, in: Hybrid Artificial Intelligent Systems, Springer International Publishing, 2017, pp. 543–553. doi:10.1007/978-3-319-59650-1_46.

[140] Millis, R. L., Wasserman, L. H., Franz, O. G., The size, shape, density, and albedo of Ceres from its occulation of BD+8 471, Icarus 72 (3). doi:10.1016/0019-1035(87)90048-0.

[141] Minisci, E., Vasile, M., Adaptive inflationary differential evolution, in: 2014 IEEE Congress on Evolutionary Computation (CEC), pp. 1792–1799. doi:10.1109/CEC.2014.6900587.

[142] Minton, D. A., Dynamical History of the Asteroid Belt and Implications for Terrestrial Planet Bombardment, Ph.D. thesis, University of Arizona (2009).

[143] Molina, D., Herrera, F., Lozano, M., Adaptive local search parameters for real-coded memetic algorithms, 2005 IEEE Congress on Evolutionary Computation (CEC), September 2-5, 2005, Edinburgh, United Kingdom. doi:10.1109/CEC.2005.1554777.

[144] Molina, D., Lacroix, B., Herrera, F., Influence of regions on the memetic algorithm for the CEC'2014 Special Session on Real-Parameter Single Objective Optimisation, 2014 IEEE Congress on Evolutionary Computation (CEC), July 6-11, 2014, Beijing, China. doi:10.1109/CEC.2014.6900536.

[145] Montenbruck, O., Gill, E., Satellite Orbits, Springer-Verlag Berlin Heidelberg, 2000.

[146] Nakagaki, T., Yamada, H., Toth, A., Intelligence: Maze-solving by an amoeboid organism, Nature 407. doi:10.1038/35035159.

[147] Novak, D. M., Vasile, M., Improved Shaping Approach to the Preliminary Design of Low-Thrust Trajectories, Journal of Guidance, Control, and Dynamicsdoi:10.2514/2.4231.

[148] Olympio, J. T., Optimal Control Problem for Low-Thrust Multiple Asteroid Tour Missions, Journal of Guidance, Control and Dynamics 34 (6) (2011) 1709–1719. doi:10.2514/1.53339.

[149] Olympio, J. T., Frouvelle, N., Space debris selection and optimal guidance for removal in the SSO with low-thrust propulsion, Acta Astronautica 99 (2014) 263–275. doi:10.1016/j.actaastro.2014.03.005.

[150] Omran, M. G., Salman, A., Engelbrecht, A. P., Self-adaptive differential evolution, in: Computational intelligence and security, Springer, 2005, pp. 192–199. doi:10.1007/11596448_28.

[151] Pesch, H. J., A Practiacal Guide to the Solution of Real-Life Optimal Control Problems, Control and Cybernetics 23 (1994) 7–60. doi:10.1.1.53.5766.

[152] Peterson, G. E., Target identification and Delta-V sizing for active debris removal and improved tracking campaigns, 23rd International Symposium on Space Flight Dynamics (ISSFD), October 29 - November 2, 2012, Pasadena, CA, USA.

[153] Petropolous, A., Some Analytic Integrals of the Averaged Variational Equations for a Thrusting Spacecraft, Tech. Rep. 42-150, Jet Propulsion Laboratory, California Institute of Technology (2002).

[154] Petropolous, A. E., Longuski, J. M., Shape-Based Algorithm for Automated Design of Low-Thrust, Gravity-Assist Trajectories, Journal of Spacecraft and Rockets 41 (5) (2004) 787–796.

[155] Petropoulos, A., Low-Thrust Orbit Transfers Using Candidate Lyapunov Functions with a Mechanism for Coasting, AIAA/AAS Astrodynamics Specialist Conference and Exhibit, August 16-19, 2004, Providence, Rhode Island, USA.

[156] Petropoulos, A. E., Longuski, J. M., Shape-Based Algorithm for Automated Design of Low-Thrust, Gravity-Assist Trajectories, Journal of Spacecraft and Rockets 41 (5) (2004) 787–796. doi:10.2514/1.13095.

[157] Petropoulos, A. E., Sims, J., A Review of Some Exact Solutions to the Planar Equations of Motion of a Thrusting Spacecraft, 2nd International Symposium Low Thrust Trajectories, June 18, 2002, Toulouse, France.

[158] Petropoulos, A. E., Simple control laws for low-thrust orbit transfers, AAS/AIAA Astrodynamics Specialist Conference, August 3-7, 2003, Big Sky, Montana.

[159] Polakova, R., Tvrdik, J., Bujok, P., Controlled restart in differential evolution applied to CEC2014 benchmark functions, 2014 IEEE Congress on Evolutionary Computation (CEC), July 6-11, 2014, Beijing, China. doi:10.1109/CEC.2014.6900632.

[160] Pollard, J. E., Simplified analysis of low-thrust orbital maneuvers, Tech. rep., Aerospace Corp El Segundo CA Technology Operations (2000).

[161] Pošik, P., Real-parameter optimization using the mutation step co-evolution, 2005 IEEE Congress on Evolutionary Computation (CEC), September 2-5, 2005, Edinburgh, United Kingdom. doi:10.1109/CEC.2005.1554775.

[162] Preux, P., Munos, R., Valko, M., Bandits attack function optimization, 2014 IEEE Congress on Evolutionary Computation (CEC), July 6-11, 2014, Beijing, China. doi:10.1109/CEC.2014.6900558.

[163] Price, K. V., Storn, R. M., Differential Evolution. A Simple and Efficient Heuristic for Global Optimization Over Continuous Spaces, Journal of Global Optimization 11 (4) (1997) 341–359. doi:10.1023/A:1008202821328.

[164] Price, K. V., Storn, R. M., Lampinen, J. A., Differential Evolution. A Practical Approach to Global Optimization, Natural Computing Series, Springer-Verlag, Berlin, 2005.

[165] Price, K., Storn, R. M., Lampinen, J. A., Differential evolution: a practical approach to global optimization, Springer Science & Business Media, 2006. doi:10.1007/3-540-31306-0.

[166] Prussing, J. E., Primer Vector Theory and Applications, in: Spacecraft Trajectory Optimization, Cambridge University Press, 2010, pp. 16–36. doi:10.1017/CBO9780511778025.

[167] Prussing, J. E., Coverstone-Carroll, V., Constant Radial Thrust Acceleration Redux, Journal of Guidance, Control, and Dynamics 21 (3) (1998) 516–518. doi:10.2514/2.7609.

[168] Qin, A. K., Suganthan, P. N., Self-adaptive differential evolution algorithm for numerical optimization, 2005 IEEE Congress on Evolutionary Computation (CEC), September 2-5, 2005, Edinburgh, United Kingdom. doi:10.1109/CEC.2005.1554904.

[169] Qing, A., Fundamentals of differential evolution, Differential Evolution: Fundamentals and Applications in Electrical Engineering (2010) 41–60doi:10.1002/9780470823941.ch2.

[170] Qu, B., Liang, J., Xiao, J., Shang, Z., Memetic differential evolution based on fitness Euclidean-distance ratio, 2014 IEEE Congress on Evolutionary Computation (CEC), July 6-11, 2014, Beijing, China. doi:10.1109/CEC.2014.6900476.

[171] Quarta, A., Mengali, G., New Look to the Constant Radial Acceleration Problem, Journal of Guidance, Control, and Dynamics 35 (3) (2012) 919–929. doi:10.2514/1.54837.

[172] Ranieri, C. L., Ocampo, C. A., Optimization of Roundtrip, Time-Constrained, Finite Burn Trajectories via an Indirect ethod, Journal of Guidance, Control, and Dynamics 28 (2) (2005) 306–314. doi:10.2514/1.5540.

[173] Ranieri, C. L., Ocampo, C. A., Indirect Optimization of Spiral Trajectories, Journal of Guidance, Control, and Dynamics 29 (6). doi:10.2514/1.19539.

[174] Rauwolf, G. A., Converstone-Carroll, V. L., Near-Optimal Low-Thrust Orbit Transfers Generated by a Genetic Algorithm, Journal of Spacecraft and Rockets 33 (6) (1996) 859–862. doi:10.2514/3.26850.

[175] Rayman, M., Williams, S., Design of the first interplanetary solar electric propulsion mission, Journal of Spacecraft and Rockets 39 (4) (2002) 589–595. doi:10.2514/2.3848.

[176] Reynoso-Meza, G., Sanchis, J., Ferragud, X. B., Durá, J. M. H., Hybrid de algorithm with adaptive crossover operator for solving real-world numerical optimization problems., 2011 IEEE Congress on Evolutionary Computation (CEC), June 5-8, 2011, New Orleans, LA, USA. doi:10.1109/CEC.2011.5949800.

[177] Ricciardi, L., Vasile, M., Improved archiving and search strategies for Multi Agent Collaborative Search, International Conference on Evolutionary and Deterministic Methods for Design, Optimization and Control with Applications to Industrial and Societal Problems (EUROGEN), September 14-16, 2015, Glasgow, United Kingdom.

[178] Ronkkonen, J., Kukkonen, S., Price, K. V., Real-parameter optimization with differential evolution, 2005 IEEE Congress on Evolutionary Computation (CEC), September 2-5, 2005, Edinburgh, United Kingdom. doi:10.1109/CEC.2005.1554725.

[179] Ross, S. D., Scheeres, D. J., Multiple Gravity Assists, Capture, and Escape in the Restricted Three-Body Problem, SIAM Journal of Applied Dynamical Systems 6 (3) (2007) 576–596. doi:10.1137/060663374.

[180] Rossi, A., Valsecchi, G. B., Collision risk against space debris in Earth orbits, Celestial Mechanics and Dynamical Astronomy 95 (1-4) (2016) 345–356. doi:10.1007/s10569-006-9028-7.

[181] Rossi, A., Valsecchi, G. B., Alessi, E. M., The Criticality of Spacecraft Index, Advances in Space Research 56 (3) (2015) 449–460. doi:10.1016/j.asr.2015.02.027.

[182] Ruggiero, A., Pergola, P., Marcuccio, S., Andrenucci, M., Low-Thrust Maneuvers for the Efficient Correction of Orbital Elements, 32nd International Electric Propulsion Conference, September 11-15, 2011, Wiesbaden, Germany.

[183] Russell, R., Primer Vector Theory Applied to Global Low-Thrust Trade Studies, Journal of Guidance, Control, and Dynamics 30 (2) (2007) 460–472. doi:10.2514/1.22984.

[184] Saha, A., Ray, T., How does the good old genetic algorithm fare at real world optimization?, 2011 IEEE Congress on Evolutionary Computation (CEC), June 5-8, 2011, New Orleans, LA, USA. doi:10.1109/CEC.2011.5949733.

[185] Sanchez Cuartielles, J. P., Gibbings, A., Snodgrass, C., Bowles, N., Asteroid belt multiple fly-by optiosn for M-class missions, 67th International Astronautical Congress (IAC)26-30 September 2016, Guadalajara, Mexico.

[186] Sehnal, L., Thermospheric Total Density Model TD, Astronomical Institutes of Czechoslovakia 39 (2) (1988) 120–127.

[187] Shang, H., Liu, Y., Assessing Accessibility of Main-Belt Asteroids Based on Gaussian Process Regression, Journal of Guidance, Control and Dynamics 40 (5) (2017) 1144–1154.

[188] Sims, J., Flanagan, S., Preliminary Design of Low-Thrust Interplanetary Missions, AAS/AIAA Astrodynamic Specialist Conference, August 16, 1999, Girdwood, Alsaka, USA.

[189] Sims, J. A., Finlayson, P. A., Rinderle, E. A., Vavrina, M. A., Kowalkowski, T. D., Implementation of a Low-Thrust Trajectory Optimization Algorithm for Preliminary Design, AIAA/AAS Astrodynamics Specalist Conference, August 21-24, 2006, Keystone, Colorado, USA.

[190] Singh, H. K., Ray, T., Performance of a hybrid ea-de-memetic algorithm on cec 2011 real world optimization problems, 2011 IEEE Congress on Evolutionary Computation (CEC), June 5-8, 2011, New Orleans, LA, USA. doi:10.1109/CEC.2011.5949769.

[191] Sinha, A., Tiwari, S., Deb, K., A population-based, steady-state procedure for real-parameter optimization, 2005 IEEE Congress on Evolutionary Computation (CEC), September 2-5, 2005, Edinburgh, United Kingdom. doi:10.1109/CEC.2005.1554726.

[192] Sorensen, K., Hyperbolic injection issues for MXER tethers, 39th AIAA/ASME/SA/ASEE Joint Propulsion Conference, July 21-23, 2003, Huntsville, Alabama, USA.

[193] Stock, A., Investigation on low cost transfer options to the earth-moon libration point region, Master's thesis, University of Stuttgart (2009).

[194] Stuart, J., Howell, K., R., W., Application of multi-agent coordination methods to the design of space debris mitigation tours, Advances in Space Research 57 (8) (2016) 1680–1697. doi:10.1016/j.asr.2015.05.002.

[195] Stuart, J. S., Observational constraints on the number, albedos, sizes, and impact hazards of the near-earth asteroids,, Ph.D. thesis, Massachusetts Institute of Technology,, https://www.ll.mit.edu/mission/space/linear/files/StuartThesis.pdf (2003).

[196] Suganthan, P., Testing evolutionary algorithms on real-world numerical optimization problems, Nanyang Technological University, School of Electrical and Electronics Engineering, Singapore.

[197] Suganthan, P. N., Hansen, N., Liang, J. J., Deb, K., Chen, Y.-P., Auger, A., Tiwari, S., Problem definitions and evaluation criteria for the CEC 2005 special session on real-parameter optimization, Technical report, Nanyang Technological University, 2005.

[198] Tanabe, R., Fukunaga, A. S., Improving the search performance of SHADE using linear population size reduction, 2014 IEEE Congress on Evolutionary Computation (CEC), July 6-11, 2014, Beijing, China. doi:10.1109/CEC.2014.6900380.

[199] Tedesco, E. F., IRAS Minor Planet Survey, Proceedings of the 160th Symposium of the International Astronomical Union, June 14-18, 1993, Belgirate, Italy. doi:10.1007/978-94-011-1148-5_32.

[200] Tero, A., Kobayashi, R., Nakagaki, T., Physarum solver: A biologically inspired method of road-network navigation, Physica A: Statistical Mechanics and its Applications 363 (1) (2006) 115–119. doi:10.1016/j.physa.2006.01.053.

[201] Tero, A., Yumiki, K., Kobayashi, R., Saigusa, T., Nakagaki, T., Flow-network adaptation in Physarum amoebae, Theory in Biosciences 127 (2) (2008) 89–94. doi:10.1007/s12064-008-0037-9.

[202] Topputo, F., Zhang, C., Survey of Direct Transcription for Low-Thrust Space Trajectory Optimization with Applications, Abstract and Applied Analysis 2014 (ID 851720). doi:10.1155/2014/851720.

[203] Tsien, H. S., Take-off from satellite orbit, Journal of the American Rocket Society 23 (4) (1953) 233–236. doi:10.2514/8.4599.

[204] Vallado, D. A., Fundamentals of Astrodynamics and Applications, Springer, 2007.

[205] Vasile, M., A Global Approach to Optimal Space Trajectory Design, 13th AAS/AIAA Space Flight Mechanics Meeting, February 9-13, 2003, Puerto Rico, NM, USA.

[206] Vasile, M., Bernelli-Zazzera, F., Optimizing low-thrust and gravity assist maeuvers to design interplanetary trajectories, Journal of the Astronautical Sciences 51 (1).

[207] Vasile, M., Campagnola, S., Design of Low-Thrust Gravity Assist Trajectories to Europa, Journal of the British Interplanetary Society 62 (1).

[208] Vasile, M., Ceriotti, M., Incremental Techniques for Global Space Trajectory Design, in: Spacecraft Trajectory Optimization, Cambridge University Press, 2010, pp. 202–235. doi:10.1017/CBO9780511778025.

[209] Vasile, M., De Pascale, P., Preliminary Design of Multiple Gravity-Assist Trajectories, Journal of Spacecraft and Rockets 43 (4) (2006) 794–805. doi:10.2514/1.17413.

[210] Vasile, M., De Pascale, P., Casotto, S., On the optimality of a shape-based approach based on pseudo-equinoctial elements, Acta Astronautica 61 (1-6) (2007) 286–297. doi:10.1016/j.actaastro.2007.01.017.

[211] Vasile, M., Ercoli Finzi, A., Direct Lunar Descent Optimisation by Finite Elements in Time Approach, International Journal of Mechanics and Control.

[212] Vasile, M., Maddock, C., Saunders, C., Orbital debris removal with solar concentrators, 61st International Astronautical Congress (IAC), September 27 - October 1, 2010, Pragues, Czech Republic.

[213] Vasile, M., Minisci, E., Locatelli, M., An Inflationary Differential Evolution Algorithm for Space Trajectory Optimization, IEEE Transaction on Evolutionary Computation 15 (2) (2011) 267–281. doi:10.1109/TEVC.2010.2087026.

[214] Vasile, M., Minisci, E., Locatelli, M., On the Global Optimization of Multigravity Assist Trajectories with Evolutionary Algorithms, in: Computational Intelligence in Aerospace Sciences, AIAA, 2014, pp. 707–743. doi:10.2514/5.9781624102714.0707.0744.

[215] Vasile, M., Novak, D., Incremental Solution of LTMGA Transfers Transcribed with an Advanced Shaping Approach, 61st International Astronautical Congress (IAC), September 27 - October 1, Prague, Czech Republic.

[216] Vasile, M., Schutze, O., Junge, O., Radice, G., Dellnitz, M., Spiral Trajectories in Global Optimisation of Interplanetary and Orbital Transfers, Tech. rep., University of Glasgow, UK (2006).

[217] Vasile, M., Minisci, E., Locatelli, M., An inflationary differential evolution algorithm for space trajectory optimization, IEEE Transactions on Evolutionary Computation 15 (2) (2011) 267–281. doi:10.1109/TEVC.2010.2087026.

[218] Vavrina, M. A., Howell, K. C., Global low-thrust trajectory optimization through hybridization of a genetic algorithm and a direct method, AAS/AIAA Astrodynamics Specialist Conference, August 18-21, 2008, Honolulu, Hawaii.

[219] Veres, P., Jedicke, R., Fitsimoons, A., Danneau, L., Granvik, M., Bolin, B., Chastel, S., Wainscoat, J., Burgett, W. S., Chambers, K. C., Flewelling, H., Absolute magnitudes and slope parameters for 250,000 asteroids observed by Pan-STARRS PS1 – Preliminary results, Icarus 261 (2015) 34–47. doi:10.1016/j.icarus.2015.08.007.

[220] Virgili, B. B., Krag, H., Strategies for Active Removal in LEO, Proceedings of the 5th European Conference on Space Debris, March 30 - April 2, 2009, Darmstadt, Germany.

[221] Vroom, A., Di Carlo, M., Romero Martin, J. M., Vasile, M., Optimal Trajectory Planning for Multiple Asteroid Tour Mission by Means of an Incremental Bio-Inspired Tree Search Algorithm, 2016 IEEE Symposium Series on Computational Intelligence, December 6-9, 2016, Athens, Greece.

[222] Wales, D. J., Doye, J. P. K., Global Optimization by Basin-Hopping and the Lowest Energy Structures of Lennard-Jones Clusters Containing up to 110 Atoms, Journal of Physical Chemistry A 101 (28) (1997) 5111–5116. doi:10.1021/jp970984n.

[223] Wales, D. J., Doye, J. P., Global optimization by basin-hopping and the lowest energy structures of lennard-jones clusters containing up to 110 atoms, The Journal of Physical Chemistry A 101 (28) (1997) 5111–5116. doi:10.1021/jp970984n.

[224] Wall, B., Conway, B. A., Near-Optimal Low-Thrust Earth-Mars Trajectories via a Genetic Algorithm, Journal of Guidance, Control, and Dynamics 28 (5). doi:10.2514/1.11891.

[225] Wall, B. J., Conway, B. A., Shape-Based Approach to Low-Thrust Rendezvous Trajectory Design, Journal of Guidance, Control and Dynamics 32 (1) (2009) 95–101. doi:10.2514/1.36848.

[226] Wallace, B., Scott, R., Sale, M., The Near Earth Object Surveillance Satellite: Mission status and CCD evolution after 18 months on-orbit, Advanced Maui Optical and Space Surveillance Technologies Conference, September 9-12, 2014, Maui, Hawaii, USA.

[227] Wang, Y., Li, B., Zhang, K., Estimation of distribution and differential evolution cooperation for real-world numerical optimization problems, 2011 IEEE Congress on Evolutionary Computation (CEC), June 5-8, 2011, New Orleans, LA, USA. doi:10.1109/CEC.2011.5949768.

[228] Wormnes, K., Le Letty, R., Summerer, L., Schonenborg, R., Dubois-Matra, O., Luraschi, E., Cropp, A., Krag, H., Delaval, J., ESA Technologies for Space Debris Remediation, Proceedings of the 6th European Conference on Space Debris, April 22-25, 2013, Darmstadt, Germany.

[229] Xu, C., Huang, H., Ye, S., A Differential Evolution with Replacement Strategy for Real-Parameter Numerical Optimization, 2014 IEEE Congress on Evolutionary Computation (CEC), July 6-11, 2014, Beijing, China. doi:10.1109/CEC.2014.6900468.

[230] Yam, C. H., Izzo, D., Biscani, F., Towards a High Fidelity Direct Transcription Method for Optimisation of Low-Thrust Trajectories, 4th International Conference on Astrodynamics Tools and Techniques, April 28, 2010, Madrid, Spain.

[231] Yam, C. H., Lorenzo, D. D., Izzo, D., Low-thrust trajectory design as a constrained global optimization problem, Proceedings of the Institution of Mechanical Engineers, Part G: Journal of Aerospace Engineeringdoi:10.1177/0954410011401686.

[232] Yang, H., Li, J., Baoyin, H., Low-cost transfer between asteroids with distant orbits using multiple gravity assists, • 56 (5) (Advances in Space Research) 837–848. doi:10.1016/j.asr.2015.05.013.

[233] Yashesh, D., Deb, K., Bandaru, S., Non-uniform mapping in real-coded genetic algorithms, 2014 IEEE Congress on Evolutionary Computation (CEC), July 6-11, 2014, Beijing, China. doi:10.1109/CEC.2014.6900621.

[234] Yu, C., Kelley, L., Zheng, S., Tan, Y., Fireworks algorithm with differential mutation for solving the cec 2014 competition problems, July 6-11, 2014, Beijing, China. doi:10.1109/CEC.2014.6900590.

[235] Yuan, B., Gallagher, M., Experimental results for the special session on real-parameter optimization at CEC 2005: a simple, continuous EDA, 2005 IEEE Congress on Evolutionary Computation (CEC), September 2-5, 2005, Edinburgh, United Kingdom. doi:10.1109/CEC.2005.1554905.

[236] Zandbergen, I., Some typical solid propellant rocket motors, Tech. rep., Delft University of Technology (2013).

[237] Zhan, Z., Habashi, W. G., Fossati, M., Real-Time Regional Jet Comprehensive Aeroicing Analysis via Reduced-Order Modeling, AIAA Journal 54 (12) (2016) 3787–3802. doi:10.2514/1.J055013.

[238] Zhang, J., Sanderson, A. C., Jade: adaptive differential evolution with optional external archive, IEEE Transactions on Evolutionary Computation 13 (5) (2009) 945–958. doi:10.1109/TEVC.2009.2014613.

[239] Zuiani, F., Vasile, M., Preliminary Design of Debris Removal Missions by Means of Simplified Models for Low-Thrust, Many-Revolution Transfers, International Journal of Aerospace Engineering 2012. doi:10.1155/2012/836250.

[240] Zuiani, F., Vasile, M., Extended analytical formulas for the perturbed keplerian motion under a constant control acceleration, Celestial Mechanics and Dynamical Astronomy 121 (3) (2015) 275–300. doi:10.1007/s10569-014-9600-5.

[241] Zuiani, F., Vasile, M., Palmas, A., Avanzini, G., Direct transcription of low-thrust trajectories with finite trajectory elements, Acta Astronautica 72 (2012) 108–120. doi:10.1016/j.actaastro.2011.09.011.